IntechOpen

Current Developments in Optical Fiber Technology

Edited by Sulaiman Wadi Harun and Hamzah Arof

CURRENT DEVELOPMENTS IN OPTICAL FIBER TECHNOLOGY

Edited by **Sulaiman Wadi Harun**
and **Hamzah Arof**

Current Developments in Optical Fiber Technology
http://dx.doi.org/10.5772/46191
Edited by Sulaiman Wadi Harun and Hamzah Arof

Contributors

Miguel Perez, OLaya González Pérez, José R. Arias, Mitsuru Kihara, Pablo Sartor, Franco Robledo - Pedeciba Informatica, Claudio Risso, Tarek Ennejah, Rabah Attia, Danish Rafique, Andrew D. Ellis, Rosa Ana Perez-Herrera, Manuel Lopez-Amo, Manuel Durán Sánchez, Ricardo Ivan Alvarez Tamayo, Evgeny Kuzin, Baldemar Ibarra Escamilla, Andres Gonzalez Garcia, Olivier Jean Michel Pottiez, Fouad El-Diasty, Joao M. P. Coelho, Marta Castiñeiras, Catarina Eira Silva, José Rebordão, Dionísio Pereira, Xianfeng Chen, Katerina Krebber, Aurenice Oliveira, Ivan Lima Jr., Hadi Guna, Dr. Mohammad Syuhaimi Ab-Rahman, Malik Sulaiman, L.S. Supian, Norhana Arsad, Kasmiran Jumari, David Sánchez Montero, Carmen Vázquez García, Aron Michael, Silvio Abrate, Guido Perrone, Roberto Gaudino, Masaharu Ohashi, Masataka Iinuma, Seung-Woo Lee, Carlos Gouveia, Pedro Jorge, José Baptista

First published in Croatia, 2013 by INTECH d.o.o.
eBook (PDF) Published by IN TECH d.o.o.
Place and year of publication of eBook (PDF): Rijeka, 2019.
IntechOpen is the global imprint of IN TECH d.o.o.
Printed in Croatia

Legal deposit, Croatia: National and University Library in Zagreb

Additional hard and PDF copies can be obtained from orders@intechopen.com

Current Developments in Optical Fiber Technology
Edited by Sulaiman Wadi Harun and Hamzah Arof

p. cm.

ISBN 978-953-51-1148-1

eBook (PDF) ISBN 978-953-51-6348-0

Meet the editors

Sulaiman Wadi Harun received his B.E degree in Electrical and Electronics System Engineering from Nagaoka University of Technology, Japan in 1996, and M.Sc. and Ph.D degrees in Photonic Technology from University of Malaya in 2001 and 2004, respectively. He is actively working on optical amplifiers, fiber lasers and fiber-optic sensors with more than 350 publications in ISI journals and citations of more than 2000. He is currently working as a full Professor in the Department of Electrical Engineering, University of Malaya, Malaysia.

Hamzah Arof received his B.Sc from Michigan State University, and Ph.D from the University of Wales, all in Electrical Engineering. His current research interests include signal processing and photonics. Currently he is affiliated with the Department of Electrical Engineering, University of Malaya, Malaysia.

Contents

Preface

This book provides an overview of recent researches and developments in optical fiber technology related to next generation optical communication, system and network, sensor, laser, measurement, characterization and device. It is divided into five sections where the first section consists of five chapters that focus on the optical fiber communication systems and networks. The second section contains two chapters related to plastic optical fibers technologies for communication and sensors. Section three comprises seven chapters that cover recent advances on fiber optic sensors for various applications. Fiber laser works are highlighted in section four which focuses on mode-locked, dual wavelength and multi-wavelength lasers. The last section deals with fiber measurements techniques and fiber optic devices on silicon chip.

The exponential growth of Internet traffic volume has increased the demand for higher capacity networks, which then leads to the deployment of dense wavelength division multiplexing (DWDM) technology. The increasing number of per-physical-link connections intrinsic to DWDM may cause multiple logical link failures from a single physical link failure. This issue inspires the development of new multi-layer models that consist of stacks of network layers. The first chapter of this book, addresses the problem of finding the optimal configuration of a logical topology over a fixed physical layer. Another challenge with the DWDM networks is associated with the nonlinear transmission impairments, which strongly link the achievable channel reach for a given set of modulation formats to symbol-rates across a number of channels. Various methods of compensating fiber transmission impairments have been proposed, both in optical and electronic domains. Chapter 2 demonstrates the application of electronic compensation schemes in a dynamic optical network, focusing on adjustable signal constellations with non identical launch powers, and describes the impact of periodic addition of 28-Gbaud polarization multiplexed m-ary quadrature amplitude modulation (PM-mQAM) channels on existing traffic. This chapter also discusses the impact of cascaded reconfigurable optical add-drop multiplexers on networks operating close to the maximum permissible capacity in the presence of electronic compensation techniques for a range of higher-order modulation formats and filter shapes.

Chapter 3 reviews a typical Fiber To The Home (FTTH) network and various fiber connection faults and countermeasures in Japan. Chapter 4 reports on the use of multimode optical fiber as a successor to traditional copper-based transmission media for access networks. A predictive model of a full-optical convergent deployment scenario is also proposed in this chapter. Polarization-mode dispersion (PMD) is a major source of impairments in optical fiber communication systems. PMD causes distortion and broadens the optical pulses carrying information and lead to inter-symbol interference. In chapter 5, statistical methods of multi-canonical Monte Carlo (MMC) and importance sampling (IS) are used to accurately and efficiently compute penalties caused by the PMD.

Chapter 6 discusses the Wavelength Division Multiplexing (WDM) application over the Polymer Optical Fiber (POF) networks and data communications of selected equipment onboard of a navy ship. In chapter 7 a general overview of interesting applications of Step-Indexed POFs made of PolyMethylMethAcrylate (PMMA) material is given. This fiber can address interesting niche markets such as automobile entertainment, local networking and sensing.

Optical fibers are widely extended for several applications, outside the typical applications in communications. In recent years, a large number of sensors that use optical fibers have been developed for measuring a lot of physical, chemical and biological quantities. Chapter 8 reviews fibre grating technologies, including fibre Bragg grating (FBG), tilted fibre grating (TFG) and long-period grating (LPG), for applications in chemical and bio- sensing. Three techniques including holographic, phase-mask and point-by-point methods are employed to fabricate these gratings structures in optical fibre. The most important contribution presented in this chapter is the implementation of optical fibre grating based refractive index sensors, which has been successfully used for chemical and bio- sensing. Chapter 9 describes recent approaches to the development of fibre-optic chemical sensors utilizing different measurement designs based on evanescent wave, tapered and long period gratings. Advantages and characteristic features of each measurement design are discussed and examples of the sensitive and selective detection of various chemical analyzes are demonstrated. Chapter 10 presents several operation principles (absorbance, reflectance and luminescence), data processing strategies, and the potential use for measurement purposes by means of some real implementation. A new method of highly sensitive detection of bioluminescence at an optical fiber end is introduced in Chapter 11 for ATP detection. The general concept of construction for an optical fiber-based system is discussed. The results of the sensitivity test using a compact and cooled photomultiplier tube (PMT) are also presented in this chapter. Chapter 12 discusses the development of novel smart technical textiles with embedded optical fibers. These textiles have a potential new market niche for fiber optic sensors such as in structural safety and healthcare monitoring. It is currently recognized that label free optical sensing based on the measurement of refractive index is an important technology for the measurement of chemical and biological parameters in diversified environments, ranging from industrial processes, medicine to environmental applications, where the need for complete and real time information about a variety of parameters is present. In chapter 13, the basic principles and most relevant advances of fiber refractometers based on evanescent wave interactions are presented. Chapter 14 describes recent advances in optical fiber laser micromachining for various sensors developments.

Chapter 15 focuses on mode-locked fiber lasers, which can be realized using various active and passive techniques. Chapter 16 describes an experimental work on dual wavelength fiber laser. In the proposed laser, a Sagnac fiber optical loop mirror with a high-birefringence fiber on the loop (Hi-Bi FOLM) is used as a spectral filter to finely control the laser cavity loss. This control allows characterizing the competitive behavior with temperature variations to achieve a better adjustment to obtain dual-wavelength laser emission. Chapter 17 presents various configurations of all-fiber multi-wavelength fiber lasers. These lasers have attracted much interest recently because of their potential applications in wavelength-division-multiplexing (WDM) communications, microwave generation, high-resolution spectroscopy, fiber optic sensing, etc.

Precise and accurate measurement of optical fiber parameters is highly needed for both communication and sensing applications. Chapter 18 discusses fiber measurement based on interferometry techniques. Chapter 19 describes fiber measurement technique based on optical time domain refractometer (OTDR). This technique is based on the measurement of the back-scattered light power to obtain information about various fiber parameters. In the last chapter, micro-machining and film deposition techniques that are useful for integrating and forming passive optical components on silicon chips are reviewed.

Sulaiman Wadi Harun and Hamzah Arof
Department of Electrical Engineering,
University of Malaya,
Kuala Lumpur, Malaysia

Section 1

Optical Fiber Systems and Networks

Chapter 1

Optimal Design of a Multi-Layer Network an IP/MPLS Over DWDM Application Case

Claudio Risso, Franco Robledo and Pablo Sartor

Additional information is available at the end of the chapter

http://dx.doi.org/10.5772/54340

1. Introduction

Some decades ago the increasing importance of the telephony service pushed most telecommunications companies (TELCOs) to deploy optical fibre networks. In order to guarantee appropriate service availability, these networks were designed in such a way that several independent paths were available between each pair of nodes, and in order to optimize these large capital investments several models and algorithms were developed.

Already the optimal design of a single layer network is a challenging task that has been considered by many research groups, see for instance the references: [1-3]. Throughout this work this optical network is referred to as the *physical layer*.

Some years afterwards, the exponential growth of Internet traffic volume demanded for higher capacity networks. This demand led to the deployment of dense wavelength division multiplexing (DWDM) technology. Today, DWDM has turned out to be the dominant network technology in high-capacity optical backbone networks. Repeaters and amplifiers must be placed at regular intervals for compensating the loss in optical power while the signal travels along the fibre; hence the cost of a lighpath is proportional to its length over the physical layer. DWDM supports a set of standard high-capacity interfaces (e.g. 1, 2.5, 10 or 40 Gbps). The cost of a connection also depends of the capacity but not proportionally. For economies of scale reasons, the higher the bit-rate the lower the per-bandwidth-cost. The client nodes together with these lightpath connections form a so-called *logical layer* on top of the physical one.

The increasing number of per-physical-link connections -intrinsic to DWDM- may cause multiple logical link failures from a single physical link failure (e.g., fibre cut). This issue led to the development of new multi-layer models aware of the stack of network layers. Most of these models share in common the 1+1 protection mechanism, that is: for every demand two independent lightpaths must be routed such that in case of any single physical link -or even node- failure, at least one of them survive. The following references: [4] and [5] are good examples of this kind of models. Those multi-layer models are suitable for certain families of logical layer technologies such as: synchronous optical networking (SONET) or synchronous digital hierarchy (SDH) since both standards have 1+1 protection as their native protection mechanism.

During many years the connections of IP networks were implemented over SONET/SDH -for simplicity we will only mention SDH from now on-. Most recently: multiprotocol label switching (MPLS), traffic engineering extensions for dynamic routing protocols (e.g. OSPF-TE, ISIS-TE), fast-reroute algorithms (FRR) and other new features were added to the traditional IP routers. This new *technology bundle* known as IP/MPLS, opens a competitive alternative against traditional protection mechanisms based on SDH.

Since IP/MPLS allows recovering from a failure in about 50ms, capital savings may come from the elimination of the intermediate SDH layer. Another improvement of this technology is that the number of paths to route demands between nodes is not pre-bounded; so it might exist in fact a feasible different configuration for most failure scenarios. Since IP/MPLS allows the elimination of an intermediate layer, manages Internet traffic natively, and makes possible a much easier and cheaper operation for virtual private network (VPN) services, it is gaining relative importance every day.

Setting aside technical details and for the purpose of the model presented in this work, we remark two important differences between SDH and IP/MPLS. The first one is the need of SDH to keep different demands between the same nodes. In IP/MPLS networks, all the traffic from one node to another follows the same path in the network referred to as *IP/MPLS tunnel*. The second remarkable difference is how these technologies handle the existence of parallel links in the logical layer. In SDH the existence of parallel links is typical but in IP/MPLS parallel links may conflict with some applications so we will avoid them.

In this paper we address the problem of finding the optimal -minimum cost- configuration of a logical topology over a fixed physical layer. The input data set is constituted by: the physical layer topology -DWDM network-, the client nodes of the logical layer -IP/MPLS nodes- and the potential links between them, as well as the traffic demand to satisfy between each pair of nodes and the per-distance-cost in the physical network associated with the bitrates of the lightpaths to deploy over it. The decision variables are: what logical links do we have to implement, which bitrate must be assigned to each of them and what path do these lightpaths have to follow in the physical layer. For being a feasible solution a configuration must be capable of routing every traffic demand over the remaining active links of the logical layer for every single physical link failure scenario.

The problem previously described is NP-hard and due to its complexity we developed a metaheuristic based on GRASP to find good quality solutions for real size scenarios. Actually, we analysed the performance of the proposed metaheuristic using real-world scenarios provided by the Uruguayan national telecommunications company (ANTEL).

The main contributions of this article are: i) a model to represent a common network overlay design problem; ii) the design of a GRASP metaheuristic to find good quality solutions for this model; iii) the experimental evaluation based on real-world network scenarios.

The remaining of this document is organized as follows. A mixed-integer programming model will be presented in Section-2. In Section-3 we will show some exact solutions found with CPLEX for small/simple but illustrative problems; in this section we also analyze the intrinsic complexity of the problem. In Section-4 a GRASP metaheuristic to solve this problem is presented. Finally, in Section-5 we will show the solutions found with the previous metaheuristic for real-world network scenarios.

2. Mathematical model

We will now introduce the basic mixed-integer programming model that arises from the detailed interaction of technologies.

2.1. Parameters

The physical network is represented by an undirected graph (V, P), and the logical network is represented by another undirected graph (V, L). Both layers share the same set of nodes. The links of the logical layer are potential -admissible logical links- while the links of the physical layer are definite. In both graphs the edges are simple since multigraphs are not allowed in this model.

For every different pair of nodes $p, q \in V$ is known the traffic volume d_{pq} to fulfil along the unique path (tunnel) this traffic follows throughout a logical layer configuration.

These paths are unique at every moment, but in case of link failures they may change to follow an alternate route. For simplicity we assume that the traffic volume is symmetric (i.e. $d_{pq} = d_{qp}$). Let $\hat{B} = \{b_1, \ldots, b_{\bar{B}}\}$ be the set of possible bitrate capacities for the lightpaths on the physical layer and therefore for the links of the logical one. Every capacity $b \in \hat{B}$ has a known per-distance cost c_b. For economies of scale reasons it holds that if $b' < b''$ then $(c_{b'} / b') > (c_{b''} / b'')$. Since both graphs of this model are simple and undirected, we will express links as pairs of nodes. For every physical link (ij) is known its length l_{ij}.

2.2. Variables

This model comprises three classes of variables. The first class is composed of the logical link capacity variables. We will use boolean variables τ_{pq}^{b} to indicate whether or not the logical link $(pq) \in L$ has been assigned with the capacity $b \in \hat{B}$. As a consequence the capacity of the link (pq) could be computed as: $\sum_{b \in \hat{B}} b \cdot \tau_{pq}^{b}$.

The second class of variables determines how are going to be routed the logical links over the physical network. If $\sum_{b \in \hat{B}} \tau_{pq}^{b} = 1$ then the logical link $(pq) \in L$ was assigned with a capacity, it is going to be used in the logical network and requires a lightpath in the physical one. y_{pq}^{ij} is a boolean variable that indicates whether or not the physical link $(ij) \in P$ is being used to implement the lightpath of $(pq) \in L$. Since lightpaths cannot automatically recover from a link failure, whenever a physical link (ij) fails all the logical links (pq) such that $y_{pq}^{ij}=1$ do fail as well. The only protection available in this model is that of the logical layer. For demands being protected against single physical link failures, it is necessary to have a feasible route through the remaining active logical links.

The third and final class of variables is that that determines how the IP/MPLS tunnels are going to be routed against any particular failure in the physical layer. ${}^{rs}x_{pq}^{ij}$ is a boolean variable that indicates whether the logical link $(pq) \in L$ is going to be used or not, to route traffic demand $d_{rs}>0$, under a fault condition in the physical link $(ij) \in P$.
NOTE: To keep the nomenclature of the variables as easy as possible we always placed: logical links subindexes at bottom right position, physical links subindexes at top right position and demands subindexes at top left position.

2.3. Constraints

This problem comprises three groups of constraints. The first group of constraints establishes the rules that the routes of the lightpaths must follow to be feasible.

$$\sum_{b \in \hat{B}} \tau_{pq}^{b} \leq 1 \qquad \forall (pq) \in L. \tag{1}$$

$$\sum_{j/(pj) \in P} y_{pq}^{pj} = \sum_{b \in \hat{B}} \tau_{pq}^{b} \qquad \forall (pq) \in L. \tag{2}$$

$$\sum_{i/(iq) \in P} y_{pq}^{iq} = \sum_{b \in \hat{B}} \tau_{pq}^{b} \qquad \forall (pq) \in L. \tag{3}$$

$$\sum_{j/(ij) \in P} y_{pq}^{ij} = 2\hat{\theta}_{pq}^{i} \qquad \forall (pq) \in L, \forall i \in V, \; i \neq p, i \neq q. \tag{4}$$

$$\tilde{\theta}_{pq}^{i} + \hat{\theta}_{pq}^{i} = 1 \qquad \forall (pq) \in L, \forall i \in V, \; i \neq p, i \neq q. \tag{5}$$

$$y_{pq}^{ij} - y_{pq}^{ji} = 0 \qquad \forall (pq) \in L, \forall (ij) \in P. \tag{6}$$

$$\forall(pq)\in L, \forall(ij)\in P. \qquad \begin{smallmatrix}\forall(pq)\in L,\forall(ij)\in P,\\ \forall b\in\hat{B},\forall i\in V.\end{smallmatrix} \tag{7}$$

The meaning of the previous constraints is the following: (1) establishes that the number of capacities assigned to every logical link is at most 1 -it could be 0 if the link is not going to be used-; (2) and (3) guarantee that if any particular link $(pq)\in L$ was assigned with a capacity $(\sum_{b\in\hat{B}}\tau^{b}_{pq}=1)$ then there must exist one and only one outgoing -or incoming- physical link used for its lightpath.

Before going any further we have to introduce a set of auxiliary variables: $\tilde{\theta}^{i}_{pq}$ and $\hat{\theta}^{i}_{pq}$. These variables are defined for every combination of logical links $(pq)\in L$ and physical nodes $i\in V$. (5) guarantees that exactly one of the following conditions must meet: $(\tilde{\theta}^{i}_{pq}, \hat{\theta}^{i}_{pq})=(1, 0)$ or $(\tilde{\theta}^{i}_{pq}, \hat{\theta}^{i}_{pq})=(0, 1)$. Hence, (4) guarantees flow balance for routing the lightpaths through the remaining -not terminal- nodes. Finally (6) guarantees that the lightpaths go back and forth through the same path, while (7) stands the integrity of the variables.

The second group of constraints establishes the rules that the routes of the IP/MPLS tunnels must follow in the logical layer and their meaning is similar to the previous ones except for (1) and (8). The inequalities in (8) were added to guarantee that whatever the failure scenario is $(\forall\,(ij)\in P)$, its associated routing configuration over the logical network keeps the aggregated traffic load below the link capacity for every data link $(\forall\,(pq)\in L\,)$. Constrains (2) and (3) are equivalent to (9) and (10), except for the fact that in the latter the existence of a tunnel relies on the existence of demand and this is known in advance. Another remarkable point is that the second group of constraints has as many possible routing scenarios as arcs in P, so the number of variables is much greater.

$$\sum_{rs:d_{rs}>0} d_{rs}\cdot {}^{rs}x^{ij}_{pq} \le \sum_{b\in\hat{B}} b\cdot\tau^{b}_{pq} \qquad \forall(pq)\in L,\forall(ij)\in P. \tag{8}$$

$$\sum_{q/(rq)\in L} {}^{rs}x^{ij}_{rq} = 1 \qquad \forall d_{rs}>0,\forall(ij)\in P. \tag{9}$$

$$\sum_{p/(ps)\in L} {}^{rs}x^{ij}_{ps} = 1 \qquad \forall d_{rs}>0,\forall(ij)\in P. \tag{10}$$

$$\sum_{q/(pq)\in L} {}^{rs}x^{ij}_{pq} = 2\cdot {}^{rs}\hat{\mu}^{ij}_{p} \qquad \begin{smallmatrix}\forall d_{rs}>0,\forall(ij)\in P,\\ \forall p\in V, p\neq r, p\neq s.\end{smallmatrix} \tag{11}$$

$${}^{rs}\tilde{\mu}^{ij}_{p} + {}^{rs}\hat{\mu}^{ij}_{p} = 1 \qquad \begin{smallmatrix}\forall d_{rs}>0,\forall(ij)\in P,\\ \forall p\in V, p\neq r, p\neq s.\end{smallmatrix} \tag{12}$$

$$ {}^{rs}x_{pq}^{ij} - {}^{rs}x_{qp}^{ij} = 0 \qquad \begin{matrix} \forall d_{rs}>0, \forall(pq)\in L, \\ \forall(ij)\in P. \end{matrix} \tag{13} $$

$$ {}^{rs}x_{pq}^{ij}, {}^{rs}\tilde{\mu}_{p}^{ij}, {}^{rs}\hat{\mu}_{p}^{ij} \in \{0,1\} \qquad \begin{matrix} \forall d_{rs}>0, \forall(pq)\in L, \\ \forall(ij)\in P, \forall p\in V. \end{matrix} \tag{14} $$

Variables sets ${}^{rs}\tilde{\mu}^{i}_{pq}$ and ${}^{rs}\hat{\mu}^{i}_{pq}$ are homologous to $\tilde{\theta}^{i}_{pq}$ and $\hat{\theta}^{i}_{pq}$; so are constraints from (4) to (7) with those from (11) to (14). Before proceeding any further we must notice that both groups are not independent. Many logical links may not be available for routing after a physical link failure. Which logical links are in this condition, relies on how the lightpaths were routed in the physical layer. Specifically, if some logical link (pq) uses a physical link (ij) for its lightpath implementation then this logical link cannot be used to route any tunnel under (ij) failure scenario.

$$ \left\{ {}^{rs}x_{pq}^{ij} \le 1 - y_{pq}^{ij} \qquad \forall rs : d_{rs} > 0, \forall(pq) \in L, \forall(ij) \in P, \right. \tag{15} $$

The group of constrains (15) prevents from using (pq) to route any traffic (${}^{rs}x^{ij}_{pq}=0$, $\forall\, rs: d_{rs}>0$) in any failure scenario which affects the link (when $y^{ij}_{pq}=1$).

2.4. Objective

The function to minimize is the sum of the cost of every logical link. According on what capacity was assigned to a logical link there is an associated per-distance-cost (c_b), and according on how the corresponding lightpath was routed over the physical layer there is an associated length ($\sum_{(ij)\in P} l_{ij} y^{ij}_{pq}$). The product of both terms is the cost of a particular logical link and the sum of these products for all of the logical links is the total cost of the solution. The direct arithmetic expression for the previous statement would be: $\sum_{(pq)\in L} (\sum_{b\in \hat{B}} c_b \tau^{b}_{pq})(\sum_{(ij)\in P} l_{ij} y^{ij}_{pq}) = \sum_{(pq)\in L\ ,(ij)\in P, b\in \hat{B}} c_b l_{ij} \cdot \tau^{b}_{pq} y^{ij}_{pq}$.

Although straightforward, this approximation is inappropriate because it is not linear. The following sub-problem expresses the objective value with an equivalent linear expression.

$$ \min \sum_{\substack{(pq)\in L \\ (ij)\in P \\ b\in \hat{B}}} c_b l_{ij} \cdot {}^{b}\eta_{pq}^{ij} \tag{16} $$

$$ {}^{b}\eta_{pq}^{ij} \ge \tau_{pq}^{b} + y_{pq}^{ij} - 1 \qquad \begin{matrix} \forall(pq)\in L, \forall(ij)\in P, \\ \forall b\in \hat{B}. \end{matrix} \tag{17} $$

$$ {}^{b}\eta_{pq}^{ij} \geq 0 \qquad \begin{array}{l} \forall (pq) \in L, \forall (ij) \in P, \\ \forall b \in \hat{B}. \end{array} \tag{18} $$

We used the real variable ${}^{b}\eta_{pq}^{ij}$ instead of $\tau_{pq}^{b} y_{pq}^{ij}$ and added some extra constraints to guarantee the consistency. This consistency comes from the following observations: the result of $\tau_{pq}^{b} y_{pq}^{ij}$ is also a boolean variable, and since ${}^{b}\eta_{pq}^{ij}$ is being multiplied by a positive constant in a minimization problem it will take its lowest value whenever this is possible. This value would be zero because of constrains (3) of (D).

The only exception is when the values of τ_{pq}^{b} and y_{pq}^{ij} are both 1, in which case the value of ${}^{b}\eta_{pq}^{ij}$ should be 1 as well to keep consistency. This is guaranteed by constrain (17). The complete MIP is the result of merging (1) to (18).

3. Finding exact solutions

We will start by showing particular solutions for some simple example cases. The first example has four nodes $V = \{v_1, v_2, v_3, v_4\}$, the physical layer is the cycle (C^4) while the logical layer is the clique (K^4). The remaining parameters are: $\hat{B} = \{3\}$, $d_{pq} = 1 \ \forall \ 1 \leq p < q \leq 4$ and $l_{ij} = 1, \ \forall \ (ij) \in P$. c_b is irrelevant in this case because there is only one bitrate available. The optimal solution found for this case uses all of the logical links. Figure 1 shows with dashed lines the route in that solution followed for each lightpath over the physical cycle. This is an example where lightpaths routes are not intuitive, even for a very simple input data set.

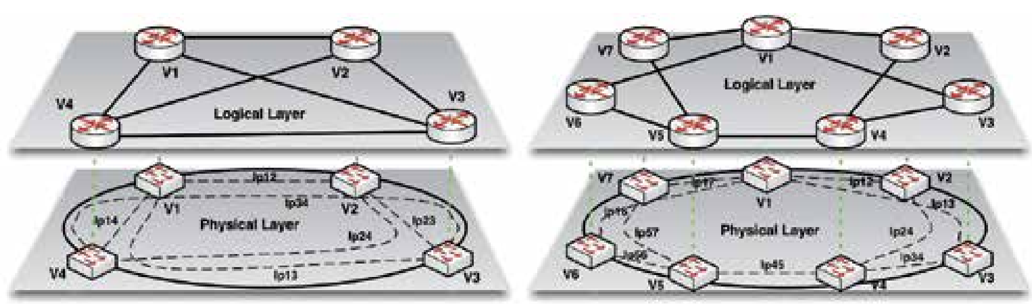

Figure 1. Optimal solutions found for: K^4 over C^4, with $d_{pq} = 1$ and $\hat{B} = \{3\}$, and for: K^7 over C^7, with $d_{1q} = 1$ and $\hat{B} = \{3\}$.

The following example comprises seven nodes and explores again the clique-over-cycle case. The remaining parameters are analogous: $\hat{B} = \{3\}$, $l_{ij} = 1 \ \forall \ (ij) \in P$, except for demands that in this case are to/from one single node ($d_{1q} = 1, \forall \ 1 < q \leq 7$). Unlike the previous example, the optimal solution in this case (also sketched in Figure 1) does not make use of all the logical links. Although the route followed by each lightpath looks more natural in this example, it is not immediate why this set of logical links ought to be the appropriate to construct the optimal solution.

Through these two examples we attempted to show that solutions are not intuitive even for very simple cases. To find optimal solutions we used ILOG CPLEX v12.1. All computations were performed on a Linux machine with an INTEL CORE i3 Processor and 4GB of DDR3 RAM. Table 1 shows information for several test instances analogous to those represented in Figure 1, that is: K^n over C^n with $d_{pq}=1,\ \forall\, 1 \le p < q \le n$ and $l_{ij}=1,\ \forall\, (ij) \in P$ over a range of integer b_1 values ($|\hat{B}|=1$).

$\|V\|$	b_1 range	#variables	#constrains	Elapsed time (hh:mm:ss)
5	2 – 6	1230	1640	00:00:00 – 000:00:11
6	3 – 9	3390	4035	00:00:02 – 000:19:31
7	2 – 12	7896	8652	(*) 00:00:05 – 087:19:05
8	3 – 16	16296	16772	(*) 00:00:02 – 100:10:17

(*)Note: The solver aborted for some intermediate cases

Table 1. Overall results for some particular cases

We proved that: it is always possible to find minimal feasible solutions for these particular topologies and demands when: $b_1=2$ and $|V|$ is odd, or when $b_1=3$ and $|V|$ is even. In the first situation the complete logical graph is needed, whereas in the second only diagonal links can be disposed of. The lowest computation times were found for these extreme cases.

We also proved that: the cycle configuration for the logical network -the simplest possible- is feasible for every b_1 greater or equal to: $|V|^2/4$ when $|V|$ is even, or $(|V|^2-1)/4$ when $|V|$ is odd. Very low computation times were found for these cases also. The time required for finding optimal solutions for non-extreme cases were much higher. CPLEX even aborted for many of them. Aside from a bunch of worthless exceptions, we couldn't find solutions for topologies other than K^n over C^n.

Keeping these physical and logical topologies while trying with simpler matrices of demand (e.g. $d_{1q}=1, \forall\, 1<q \le n$) it was possible to increase the size of the problems to 15 nodes and yet being able to find optimal solutions. Suffices to say this size bound as well as the simplicity in the topologies and traffic matrices of the previous examples, are incompatible with real life network problems.

Proposition 1: The problem presented in this section is NP-Hard.

Demonstration lies under reduction of NPP (Number Partitioning Problem) to our particular problem that will be referred to as MORNP (Multi-Overlay Robust Network Problem) within this proof. NPP problem consist in finding two subsets with the same sum for a known multiset

http://dx.doi.org/10.5772/54340

of numbers. Formally: given a list of positive integers: $a_1, a_2, \ldots, a_N$, a partition $A \subseteq \{1, 2, \ldots, N\}$ must be found so that discrepancy:

$$E(A) = \left| \sum_{i \in A} a_i - \sum_{i \notin A} a_i \right|, \tag{19}$$

finds its minimum value within the set $\{0, 1\}$. NPP is a very well known NP-Complete problem (see for instance [6]).

$(\Rightarrow)$ Given such a list of positive integers we create an instance of MORNP by taking: $B = \left\{ b_1 = \left\lceil \left(\sum_{1 \le i \le N} a_i \right) / 2 \right\rceil \right\}$, logical and physical graphs with the same topology schematized in Figure 2, $l_{ij} = 1 \ \forall \ (ij) \in P$ and $d_{iD} = a_i, \forall \ 1 \le i \le N$.

Since logical and physical topologies are the same and all distances are equal, the logical layer projected over the physical one for any optimal solution must copy the underlying shape. So, if there exists a solution for such an instance of MORNP, this solution should have a feasible routing scenario when transport -and logical- link $(v_{A1}v_{A2})$ fails and therefore a way to accommodate traffic requirements over $(v_{H1}v_D)$ and $(v_{H2}v_D)$, due to the fact that both links are still in operational state and they are the only way to reach v_D.

Because there is only one capacity both links must have been assigned with b_1, this can only be done when discrepancy is not grater than one, so we indirectly found a solution for the original NPP problem.

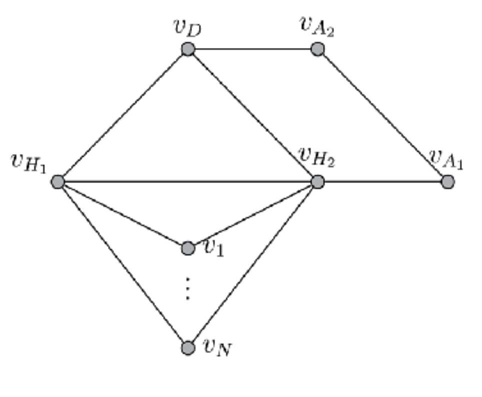

Figure 2. Graph used for NPP reduction to MORNP.

$(\Leftarrow)$ The complementary part of the proof is easier. Given a solution to an instance of NPP, this partition is used to distribute tunnels between $(v_{H1}v_D)$ and $(v_{H2}v_D)$. Once in v_{H1} or $v_{H2}$the tunnel is terminated directly in the corresponding node, except for some fault condition in one of these links, in which case a detour through the other v_{Hx} node is always possible. When the fault condition arises in $(v_{H1}v_D)$ or $(v_{H2}v_D)$, a detour may be taken through: (v_Dv_{A2}), $(v_{A2}v_{A1})$, $(v_{A1}v_{H2})$ or (v_Dv_{A2}), $(v_{A2}v_{A1})$, $(v_{A1}v_{H2})$, $(v_{H2}v_{H1})$.

Since all the transformation are of polynomial complexity it stands that $NPP \prec MORNP$ and MORNP is NP-Hard.

We proved the complexity of MORNP is intrinsic to the problem, since it is NP-Hard. Because of the previous result and like for most other network design problems, an exhaustive search for the optimal solution of the problem presented in this work is infeasible for real size problems.

4. Metaheuristics

We decided to use a metaheuristic algorithm based on GRASP to find good quality solutions for real instances of this problem. A very high level diagram of our algorithm is shown in Figure 3.

4.1. GRASP implementation

As for every GRASP implementation this algorithm has a loop with two phases. The *construction phase* builds a *randomized feasible solution*, from which a local minimum is found during the *local search phase*. This procedure is repeated *MaxIter* times, while the best overall solution is kept as the result. Further information and details in GRASP algorithms can be found in [7] or in [8].

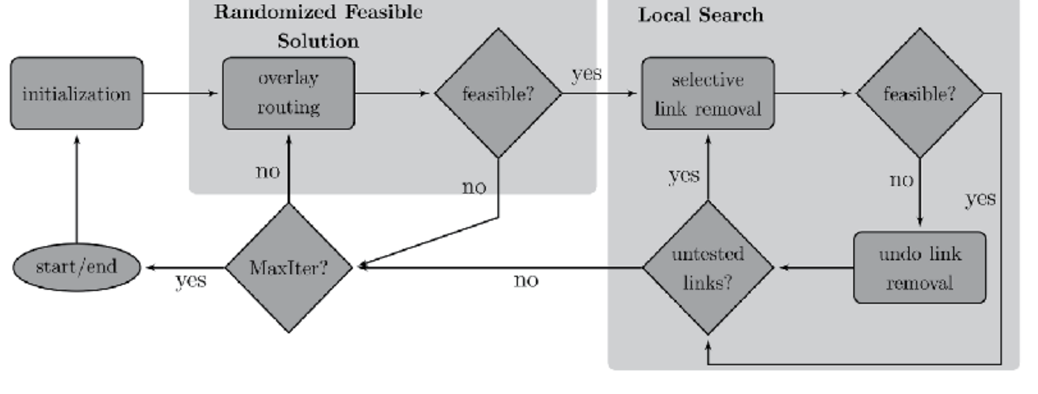

Figure 3. Block-diagram of the GRASP implementation used.

The *initialization phase* performs computations whose results are invariants among the iterations, like the shortest path and distance over the physical layer between each pair of nodes.

4.2. Construction phase

The *randomized feasible solution phase* performs a heuristic low cost balanced routing of the logical layer over the physical one. The exact solution for this sub-problem is also NP-Complete as it can be seen in [9]. The goal is to find a path for every lightpath, such that the number of physical link intersections is minimum. It is also desirable that the total cost be as low as possible but as a secondary priority. The strategy chosen in this heuristic is the following: nodes are taken randomly (.e.g.: uniformly), and for each node their logical links are also taken randomly but with probabilities in inverse ratio to the minimal possible distance of their lightpaths over the physical layer.

Instead of using the real distances of the physical links (l_{ij}), from this point on and until the next iteration pseudo-distances: l_{ij}, $\forall\,(ij) \in P$ will be used. Prior to start routing lightpaths, all these pseudo-distances are set to 1.

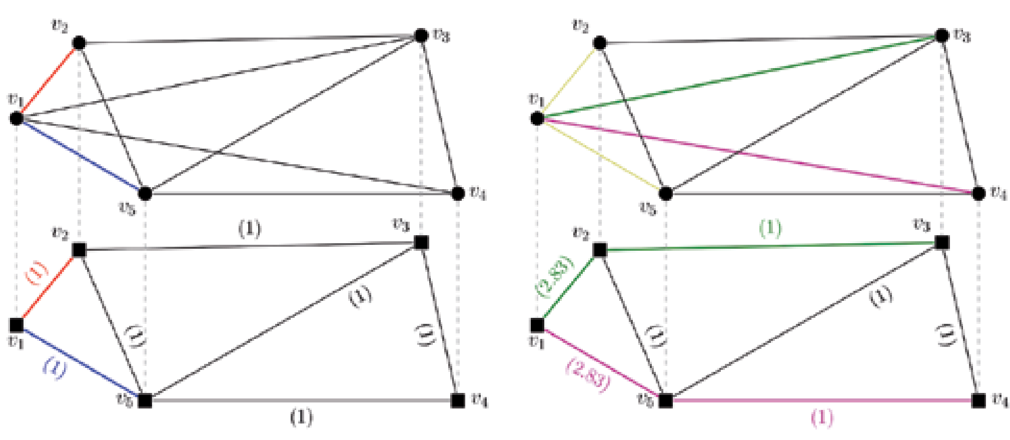

Figure 4. An example of the balanced routing heuristic.

According to these new weights, logical links are routed following the minimal distance without repeating physical links among them. Usually, after routing some lightpaths the set of not-yet-used physical links empties, and it is necessary to start over a new *control window* by filling again the not-yet-used set. Prior to do this, the pseudo-distances are updated using the following rule: $l_{ij} = (1 + n_{ij})^p$ for some fixed penalty p, where n_{ij} is the number of lightpaths that are making use of $(ij) \in P$ up to the moment.

For instance, let us guess our networks are like those sketched in Figure 4 and the links drawn are: (12), (15), (13), (14), (23), (35), and so on. The left half of Figure 4 shows with red and blue lines how are routed the lightpaths (12) and (15). At this point we need to update the pseudo-distances and restart the window. If $p = 1.5$ and since $n_{12} = n_{15} = 1$, then $l_{12} = l_{15} = 2^{1.5} \approx 2.83$ for the next window.

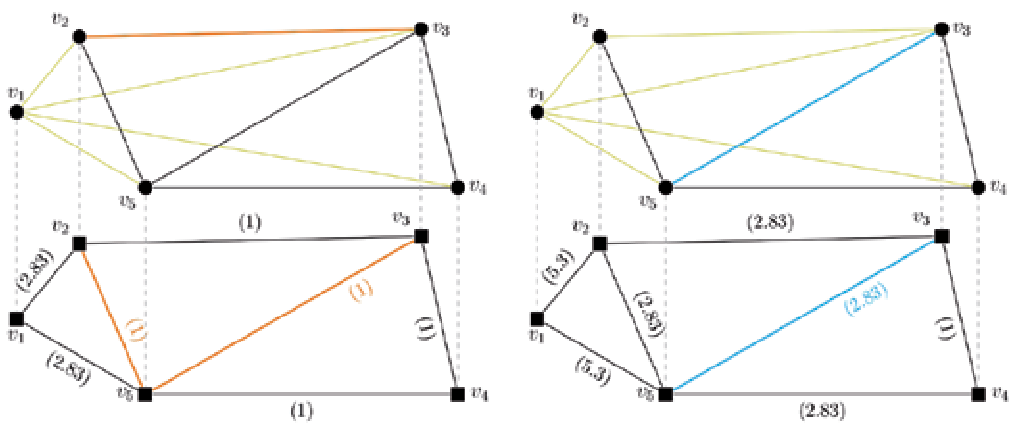

Figure 5. Lightpaths for logical links (23) and (35).

The next two logical links are (13) and (14). They are routed using the updated values. Their lightpaths are also represented with green and magenta lines in the right half of Figure 4. The link (23) is the following and it can be routed in two hops. A window restart is necessary to route the lightpath of (35), as it can be seen in Figure 5.

The elements of the input data in Algorithm-1 are: the logical graph (V, L), the physical graph (V, P), the minimum distance over the physical layer to connect each pair of nodes -computed in the *initialization phase*-. The output is an application between logical links and the subset of physical links used by their lightpaths.

The algorithm detailed in Algorithm-1 is the one depicted in Figure 4 and Figure 5. The outcome of the randomized feasible solution phase is a candidate configuration for the route of each lightpath over the physical network. We did not make use of capacity and traffic information yet; and before going any further we must state that -as in the exact examples- in our practical applications we limited the capacities set to only one capacity ($|\hat{B}|=1$).

The main reason was that the telecommunications company we developed this application for, wanted the maximum possible bitrate for all the interfaces of its core network. The next issue is determining whether the configuration found is feasible or not. The answer to this question is far from being easy, since this sub-problem is NP-Complete. We have based on a heuristic to answer this question. The heuristic is the following: demands are taken in decreasing order of volume (d_{pq}) and each tunnel is routed over the logical layer following the minimal number of hops, but using only links with remaining capacity to allocate the new tunnel demand.

For instance, Figure 6 shows an example logical topology whose link capacities are 3. Let the demands be: $d_{24}=2$, $d_{12}=1$, $d_{13}=1$ and $d_{23}=1$. The path followed by every tunnel is sketched in Figure 6 using: violet, orange, red, and green curves respectively; so it is the remaining capacity in every link after routing each tunnel -two tunnels in the central image-.

Overlay routing (logical over physical). Algorithm 1

Input: $(V, L), (V, P), d : V \times V \rightarrow \mathbb{R}_0^+$. **Output:** $\Psi : L \rightarrow 2^P$.

Set $\Psi(e) = \emptyset, \forall e \in L$ and $pd : P \rightarrow \mathbb{R}_0^+, pd(e) = 1 \; \forall e \in P$.
while $\exists v \in V$ / not-processed(v) **do**
  Select randomly $v \in V$ / not-processed(v));
  Set $prob(vw) = \frac{1}{d(v,w)}, \forall (vw) \in L \,/\, \Psi(vw) = \emptyset$;
  Normalize $prob$ such that: $\sum_{e \in L} prob(e) = 1$;
  Create new *control window*;
  while $\exists w \in V \,/\, ((vw) \in L$ AND $\Psi(vw) = \emptyset)$ **do**
    Draw such $w \in V$ randomly weighted by $prob(vw)$;
    Find *shortest-lp*, a *pd-distance* shortest lightpath for (vw) avoiding repeating physical links within this window;
    if (*shortest-lp*=$\emptyset$) AND (there are not unprocessed (vw)) **then**
      Update $\text{pd}(v, w) = \text{pd}(w, v) = (1 + \sum_{e \in L} |\Psi(e) \cap \{(vw)\}|)^p$;
      Create new *control window*;
    else
      $\Psi(v_e v_f) = \Psi(v_f v_e) = shortest\text{-}lp$;
    end if
  end while
end while
return $\Psi : L \rightarrow 2^P$.

Algorithm 1.

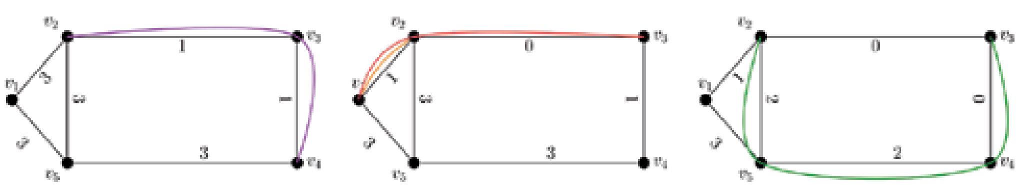

Figure 6. Routes for the tunnels (24), (12), (13), and (23)over a Logical Layer.

This constraint based routing algorithm is straightforward and it is based on Dijkstra's algorithm. Nevertheless an efficient implementation is quite complicated because of the following fact: to be sure a solution is feasible this algorithm must be repeated for each single failure scenario. In order to improve the efficiency: routes cache, optimized data structures and several others low-level programming techniques were used. This isFeasible function is used in both: construction and local search phases. The performance of this function is critic since it is used several times within the same iteration in the local search, as it is represented in Figure 3. Up to this point and before entering the local search phase, we have a feasible configuration for the routes of every lightpath; but we are still using all of the initial logical links and this input network is very likely to be over-sized. Moreover, in the construction phase we attempted to distribute the routes of the lightpaths uniformly over the physical layer, but it is still possible that many logical links fail simultaneously because of a single physical link failure. Therefore, it is very likely that many of these "redundant links" may be disposed of, if they are not really adding useful capacity. It is worth mentioning that from this point on and until the next iteration, lightpaths costs are revealed because we have their lengths -from the configuration for their routes- and there is only one possible capacity.

4.3. Local search

Through the local search phase we intend to remove the most expensive and unnecessary logical links for the current configuration. The process is the following: logical links are taken in decreasing order of cost for their lightpaths, each one is removed and the feasibility of the solution is tested again. If the solution remains feasible the current logical link is permanently removed, otherwise it is reinserted and the sequence follows for the remaining logical links. Once this processes is finished the result is a minimal solution. After *MaxIter* iterations the best solution found is chosen to be the output of the algorithm. Since the construction procedure we have used in this work privileges the nodes drawn earlier to shape the routes of the lightpaths, we presume that adding path-relinking to this algorithm could significantly improve the quality of the result, if the initial lightpaths routes of the elite solutions are prioritized to explore new solutions. We are planning to check this assumption in a future work. For further information in path-relinking enhancement to GRASP, please refer to: [7] and [10].

5. Application case context and results

We will focus now in the context of ANTEL -the telecommunication company we applied this metaheuristic to-. Prior to doing so we are giving some basic elements of the overall Internet architecture. Internet is actually a network that could be disaggregated into several separate smaller networks also known as *Autonomous Systems* (AS). Typically every AS is a portion of the global Internet owned/governed by a particular Internet Service Provider (ISP). Internet users access content residing in servers of: companies, universities, government sites or even from other residential customers (e.g. P2P applications). A portion of this content is located within the own network of the ISP this customer lease the service to -into some of the *Points Of Presence* (POP) of the ISP-, but most content is scattered over the Internet. Since traffic interchange is necessary among different ISPs, the Internet architecture needs special POPs known as *Network Access Points* (NAPs). Within these NAPs: Carriers, ISPs and important content providers (e.g.: Google, Akamai) connect to each other in order to interchange traffic.

This company had two different IP/MPLS networks referred to as: *aggregation network* and *public Internet network*. The *aggregation network* is geographically dispersed all over the country and it is responsible of gathering and delivering the traffic of the customers to the *public Internet network*. The *public Internet network* is where the AS of this ISP is implemented; centralizes the international connections with other ISPs as well as those to Datacenters of local content providers. The *public Internet network* is geographically concentrated and only has POPs in the Capital City and in an important NAP of the US territory (see grey clouds in Figure 7). In terms of the model covered in this article we may stand that the physical network has all of its nodes but one -the NAP- within the national boundaries.

There are four independent paths for international connections -leased to Carriers- between the NAP and the national boundaries. The *aggregation* and *public Internet* networks are both logical. The *public Internet network* only has presence in a few POPs of the Capital City and in the NAP; and although the *aggregation network* has full-national presence it does not span to the NAP. A Non-Disclosure Agreement (NDA) signed between the telecommunications company and our research institute protects more accurate information and details. The costs and traffic information shown in the rest of this article are only referential.

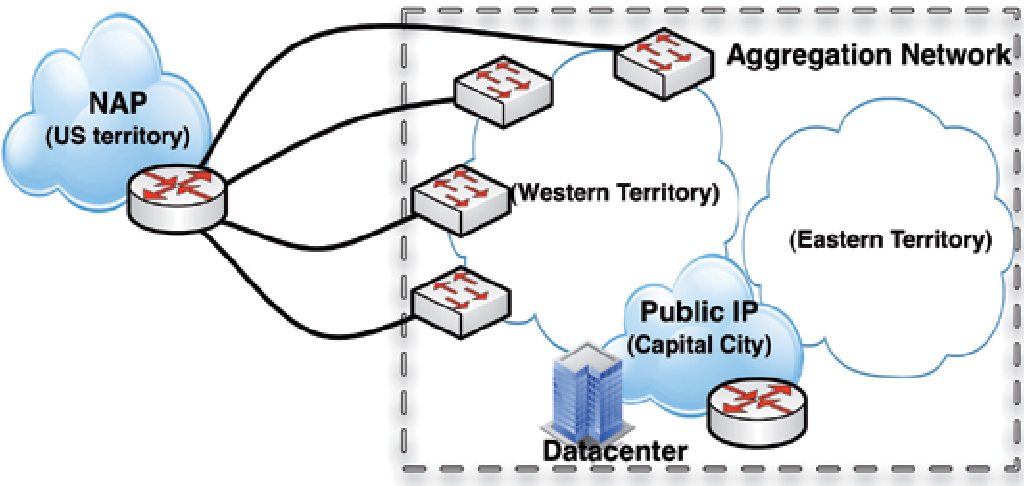

Figure 7. Remarkable aspects of the particular network architecture.

Several planning concerns arose from the situation exposed: Is it convenient the current architecture? Or it would be better to merge both IP/MPLS networks? Are profitable the IT infrastructure investments necessary to increase the percentage of local content? Which would be the optimal network to fulfil every demand requirements scenario? We helped to answer these questions by identifying representative scenarios and creating their associated data sets to feed the metaheuristic.

The overall performance of the algorithm described in Section-4 was very good -under the two hours of execution time in every scenario-.

We tried several scenarios based on the following considerations: traffic volume, network architecture and the percentage of locally terminated traffic. We selected eight remarkable scenarios to detail in Table 2.

According on traffic forecasts it is expected that some years from now the total volume of traffic to be placed somewhere between 57 and 100 (reference values). If some IT investments and agreements were made it is expected that the percentage of locally terminated traffic (national traffic) could be greater (High). These new potential sources of traffic would be placed in the Capital City, specifically in the same POPs where the public Internet network is present. Those scenarios where merged networks is set to False inherit the current network architecture.

scenario index	aggregated traffic demand	%local content	merged networks	number of nodes	required lightpaths	total cost
1	100	Low	False	56	81	10,000,000
2	100	Low	True	68	118	7,662,651
3	100	High	False	56	81	7,578,234
4	100	High	True	68	133	5,713,563
5	57	Low	False	56	75	6,319,470
6	57	Low	True	63	94	4,872,987
7	57	High	False	56	75	5,108,587
8	57	High	True	63	105	4,064,597

Table 2. Referential results for representative scenarios

Another remarkable aspect of this architecture is that whereas the aggregation network is deployed directly over the physical layer, there is an extra SDH layer between the public Internet network and the physical one. Since the public Internet network only has a few nodes and its protection relies on the 1+1 protection mechanism of SDH, its optimal value can be estimated easily. The only portion where we needed computer assistance is that of the aggregation network. The columns number of nodes and required lightpaths refers exclusively to the values for this last network.

On the other hand and in order to compare solutions fairly, the column *total cost* represents the combined cost of both networks -when they are not joined-. It is worth observing those scenarios: 1 and 3, as well as 5 and 7 require the same number of lightpaths. Moreover, their solutions use exactly the same lightpaths. This result should be expected because in both pairs of scenarios share the same traffic and non-merged network architecture; since Datacenters - the only difference- are connected to the *public Internet network*, the *aggregation network* is unaware of the percentage of local content. The only changes are in the *total cost* because of the saving of international capacity.

Less intuitive are those savings arising exclusively from the merging of both networks like: 1 and 2, 3 and 4, and so on. The reason is the following: "the routing search-space of the IP/MPLS technology is much greater than that of the SDH equivalent, so it is much more efficient". For simplicity let us guess for a while that traffic does not need to be fitted in tunnels and instead can behave as a fluid. Since the length of international connections is measured in thousands of kilometres, this links are the most expensive of the physical network. As it was showed in Figure 7 there are four independent connections to the NAP; hence if we needed to guarantee 60Gbps of international traffic we could reserve 20Gbps in every one of these links, because a single failure could only affect one of them. Therefore the efficiency in the usage of international connections could rise to 75% if the efficiency of IP/MPLS would be available. The protection mechanism of SDH (1+1) cannot exploit this degree of connectivity. To protect 60Gbps of traffic using SDH active/stand-by independent paths, we always need other 60Gbps of reserved capacity, so the efficiency of SDH it is limited to 50%. The improved efficiency of IP/MPLS to exploit the extra connectivity degree between local and international traffic explains by itself most of the savings.

6. Conclusion

Perhaps the most remarkable result of this work relies on exposing through a real-world application, how much more cost-efficient could be networks deployed using IP/MPLS, than those based on traditional protection schemes like SDH. This efficiency comes not only from the savings linked to the elimination of an intermediate layer, but also from the extra degrees of freedom available to route the traffic.

We presume that the application this work dealt with is not an exception, and the potential savings might replicate from one ISP to the other. The results for the examples of Section-5 and their later analysis justify the convenience to update network design models this work introduced, in order to follow the new technology trends and exploit their benefits.

Regarding on the metaheuristic, we presume that applying path-relinking could significantly increase the computational efficiency of the proposed GRASP, so this is the line of our immediate future work.

Author details

Claudio Risso*, Franco Robledo and Pablo Sartor*

*Address all correspondence to: crisso@fing.edu.uy

Engineering Faculty – University of the Republic, Montevideo, Uruguay

References

[1] Okamura H. and Seymour P., (1981), "Multicommodity flows in planar graphs", Journal of Combinatorial Theory 31(1), pp. 75–81.

[2] Stoer M., (1992), "Design of survivable networks", Lecture Notes in Mathematics.

[3] Kerivin H. et al., (2005), "Design of survivable networks: A survey", Networks 46(1), pp. 1–21.

[4] Orlowski S. et al., (2007), "Two-layer network design by branch-and-cut featuring MIP-based heuristics", Proceedings of the 3rd International Network Optimization Conference (INOC).

[5] Koster A. et al., (2008), "Single-layer Cuts for Multi-layer Network Design Problems", Proceedings of the 9th INFORMS Telecommunications Conference, Vol. 44, Chap. 1, pp.1-23.

[6] Mertens. S., (2006) "The Easiest Hard Problem: Number Partitioning", "Computational Complexity and Statistical Physics", pp.125-139, Oxford University Press, New York, http://arxiv.org/abs/cond- mat/0302536.

[7] Resende M., Riberio C., (2003), "Greedy randomized adaptive search procedures", ATT Research, http://www2.research.att.com/~mgcr/doc/sgrasp-hmetah.pdf.

[8] Resende M., Pardalos P., (2006), "Handbook of Optimization in Telecommunication", Springer Science + Business Media.

[9] Oellrich M., (2008), "Minimum Cost Disjoint Paths under Arc Dependence", University of Technology Berlin.

[10] Glover F., (1996), "Tabu search and adaptive memory programming - Advances, applications and challenges", Interfaces in Computer Science and Operations Research, pp.1-75.

Chapter 2

Scaling the Benefits of Digital Nonlinear Compensation in High Bit-Rate Optical Meshed Networks

Danish Rafique and Andrew D. Ellis

Additional information is available at the end of the chapter

http://dx.doi.org/10.5772/52743

1. Introduction

The communication traffic volume handled by trunk optical transport networks has been increasing year by year [1]. Meeting the increasing demand not only requires a quantitative increase in total traffic volume, but also ideally requires an increase in the speed of individual clients to maintain the balance between cost and reliability. This is particularly appropriate for shorter links across the network, where the relatively high optical signal-to-noise ratio (OSNR) would allow the use of a higher capacity, but is less appropriate for the longest links, where products are already close to the theoretical limits [2]. In such circumstances, it is necessary to maximize resource utilization and in a static network one approach to achieve this is the deployment of spectrally efficient higher-order modulation formats enabled by digital coherent detection. As attested by the rapid growth in reported constellation size [3,4], the optical hardware for a wide variety of coherently detected modulation formats is identical [5]. This has led to the suggestion that a common transponder may be deployed and the format adjusted on a link by link basis to either maximize the link capacity given the achieved OSNR, or if lower, match the required client interface rate [6] such that the number of wavelength channels allocated to a given route is minimized. It is believed that such dynamic, potentially self-adjusting, networks will enable graceful capacity growth, ready resource re-allocation and cost reductions associated with improved transponder volumes and sparing strategies. However additional trade-offs and challenges associated with such networks are presented to system designers and network planners. One such challenge is associated with the nonlinear transmission impairments which strongly link the achievable channel reach for a given set of modulation formats, symbol-rates [6,7] across a number of channels.

Various methods of compensating fiber transmission impairments have been proposed, both in optical and electronic domain. Traditionally, dispersion management was used to suppress the impact of fiber nonlinearities [8,9]. Although dispersion management is appreciably beneficial, the benefit is specific to a limited range of transmission formats and rates and it enforces severe limitations on link design. Similarly, compensation of fiber impairments based on spectral inversion (SI) [10], has been considered attractive because of the removal of in-line dispersion compensation modules (DCM), transparency to modulation formats and compensation of nonlinearity. However, although SI has large bandwidth capabilities, it often necessitates precise positioning and customized link design (e.g., distributed Raman amplification, etc.). Alternatively, with the availability of high speed digital signal processing (DSP), electronic mitigation of transmission impairments has emerged as a promising solution. As linear compensation methods have matured in past few years [11], the research has intensified on compensation of nonlinear impairments. In particular, electronic signal processing using digital back-propagation (DBP) with time inversion has been applied to the compensation of channel nonlinearities [12,13]. Back-propagation may be located at the transmitter [14] or receiver [15], places no constraints on the transmission line and is thus compatible with the demands of an optical network comprising multiple routes over a common fiber platform. In principle this approach allows for significant improvements in signal-to-noise ratios until the system performance becomes limited only by non-deterministic effects [16] or the power handling capabilities of individual components. Although the future potential of nonlinear impairment compensation using DBP in a dynamic optical network is unclear due to its significant computational burden, simplification of nonlinear DBP using single-channel processing at the receiver suggest that the additional processing required for intra-channel nonlinearity compensation may be significantly lower than is widely anticipated [17,18]. Studies of the benefits of DBP have largely been verified for systems employing homogenous network traffic, where all the channels have the same launch power [19]. However, as network upgrades are carried out, it is likely that channels employing different multi-level formats will become operational. In such circumstances, it has been demonstrated that the overall network capacity may be increased if the network traffic will become inhomogeneous, not only in terms of modulation format, but also in terms of signal launch power [6,7,20]. In particular, if each channel operates at the minimum power required for error free propagation (after error correction) rather than a global average power or the optimum power for the individual channel, the overall level of cross phase modulation in the network is reduced [20].

In this chapter we demonstrate the application of electronic compensation schemes in a dynamic optical network, focusing on adjustable signal constellations with non identical launch powers, and discuss the impact of periodic addition of 28-*Gbaud* polarization multiplexed m-ary quadrature amplitude modulation (PM-mQAM) channels on existing traffic. We also discuss the impact of cascaded reconfigurable optical add-drop multiplexerson networks operating close to the maximum permissible capacity in the presence of electronic compensation techniques for a range of higher-order modulation formats and filter shapes.

2. Simulation conditions

Figure 1 illustrates the simulation setup. The optical link comprised nine (unless mentioned otherwise) 28-*Gbaud* WDM channels, employing PM-mQAM with a channel spacing of 50 GHz. For all the carriers, both the polarization states were modulated independently using de-correlated 2^{15} and 2^{16} pseudo-random bit sequences (PRBS), for x- and y-polarization states, respectively. Each PRBS was de-multiplexed separately into two multi-level output symbol streams which were used to modulate an in-phase and a quadrature-phase carrier. The optical transmitters consisted of continuous wave laser sources, followed by two nested Mach-Zehnder Modulator structures for x- and y-polarization states, and the two polarization states were combined using an ideal polarization beam combiner. The simulation conditions ensured 16 samples per symbol with 2^{13} total simulated symbols per polarization. The signals were propagated over standard single mode fiber (SSMF) transmission link with 80 km spans, no inline dispersion compensation and single-stage erbium doped fiber amplifiers (EDFAs). The fiber had attenuation of 0.2 dB/km, dispersion of 20 ps/nm/km, and a nonlinearity coefficient (γ) of 1.5/W/km(unless mentioned otherwise). Each amplifier stage was modeled with a 4.5 dB noise figure and the total amplification gain was set to be equal to the total loss in each span.

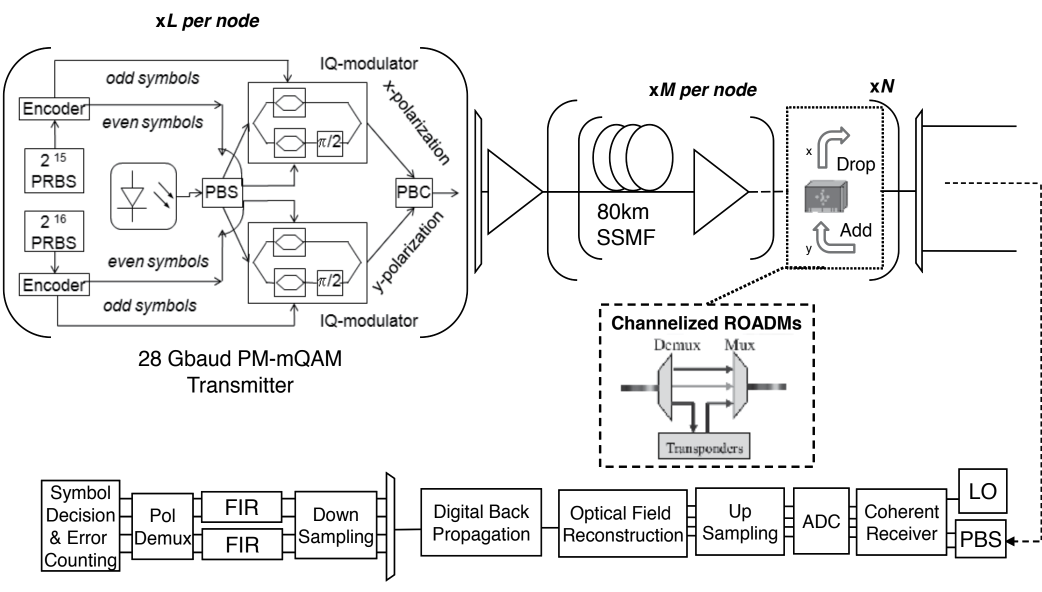

Figure 1. Simulation setup for 28-*Gbaud* PM-mQAM (m= 4, 16, 64, 256) transmission system with *L* wavelengths and *M* spans per node (total spans is given by *N*).

At the coherent receiver the signals were pre-amplified (to a fixed power of 0 dBm per channel), filtered with a 50 GHz 3rd order Gaussian de-multiplexing filter, coherently-detected and sampled at 2 samples per symbol. Transmission impairments were digitally compensated in two scenarios. Firstly by using electronic dispersion compensation (EDC) alone, employing finite impulse response (FIR) filters (T/2-spaced taps) adapted using a least mean square algorithm. In the second case, electronic compensation was applied via single-channel digital back-propagation (SC-DBP), which was numerically implemented by split-step Fourier method based solution of nonlinear Schrödinger equation. In order to establish the maximum potential benefit of DBP, the signals were up sampled to 16 samples per bit and an upper bound on the step-size was set to be 1 km with the step length chosen adaptively based on the condition that in each step the nonlinear effects must change the phase of the optical field by no more than 0.05 degrees. To determine the practically achievable benefit, in line with recent simplification of DBP algorithms, e.g. [17,18,21], we also employed a simplified DBP algorithm similar to [21], with number of steps varying from 0.5 step/span to 2 steps/span. Following one of these stages (EDC or SC-DBP) polarization de-multiplexing, frequency response compensation and residual dispersion compensation was then performed using FIR filters, followed by carrier phase recovery [22]. Finally, the symbol decisions were made, and the performance assessed by direct error counting (converted into an effective Q-factor (Q_{eff})). All the numerical simulations were carried out using VPItransmissionMaker®v8.5, and the digital signal processing was performed in MATLAB®v7.10.

3. Analysis of trade-offs in hybrid networks

3.1. Constraints on transmission reach

In a dynamic network, there are a large range of options to provide the desired flexibility including symbol rate [23], sub-carrier multiplexing [24], network configuration [25] signal constellation and various combinations of these techniques. In this section we focus on the signal constellation and discuss the impact of periodic addition of PM-mQAM (m= 4, 16, 64, 256) transmission schemes on existing PM-4QAM traffic in a 28-*Gbaud* WDM optical network with a total transparent optical path of 9,600 *km*. We demonstrate that the periodic addition of traffic at reconfigurable optical add-drop multiplexer (ROADM) sites degrades through traffic, and that this degradation increases with the constellation size of the added traffic. In particular, we demonstrate that undistorted PM-mQAM signals have the greatest impact on the through traffic, despite such signals having lower peak-to-average power ratio (PAPR) than dispersed signals, although the degradation strongly correlated to the total PAPR of the added traffic at the launch point itself. Using this observation, we propose the use of linear pre-distortion of the added channels to reduce the impact of the cross-channel impairments [26,27].

Note that the total optical path was fixed to be 9,600 *km* and after every *M* spans, a ROADM stage was employed and the channels to the left and right of the central channel were dropped and new channels with independent data patterns were added, as shown in Figure 2. in order to analyze the system performance, the dropped channels were coherently-detected after first ROADM and the central channel after the last ROADM link.

Figure 2. Network topology for flexible optical network, employing PM-4QAM traffic as a through channel, and PM-mQAM traffic as neighboring channels, getting added/dropped at each ROADM site. Note that in this schematic only right-hand wavelength is shown to be added/dropped, however in the simulations both right and left wavelengths were add/dropped. The total path length was fixed to 9,600 km, and the number of ROADMs was varied.

The optimum performance of the central PM-4QAM channel at 9,600 *km* occurred for a launch power of -1 *dB*m. In this study, the launch power of all the added channels was also fixed at -1 *dB*m, such that all channels had equal launch powers. Figure 3 illustrates the performance of the central test channel after the last node (solid), along with the performance of co-propagating channel employing various modulation formats after the first ROADM node (open) for a number of ROADM spacing's, using both single-channel DBP (Figure 3a) and EDC (Figure 3b). It can be seen that single-channel DBP offers a Q_{eff} improvement of ~1.5 *dB* compared to EDC based system. This performance improvement is strongly constrained by inter-channel nonlinearities, such that intra-channel effects are not dominant. Moreover, the figure shows that as the number of ROADM nodes are increased, or the distance between ROADMs decreases, the performance of higher-order neighboring channels improves significantly due to the improved OSNR.

It can also be seen from Figure 3 that added channels with higher-order formats induce greater degradation of the through channel. In particular if there are 30 ROADM sites (320 *km* ROADM spacing) allocated to transmit PM-64QAM, whilst this traffic operates with significant margin, the through traffic falls below the BER of $3.8x10^{-3}$. This increased penalty is due to the increased nonlinear degradation encountered in the first span after the ROADM node, where higher formats induce greater cross phase modulation(XPM) than PM-4QAM by virtue of their increased PAPR. However, even when the add drop traffic is PM-4QAM, the performance of the through channel degrades slightly as the number of ROADM nodes is increased, despite the reduction in PAPR due to the randomization of the nonlinear crosstalk.

The estimated PAPR evolutions for the various formats are shown in Figure 4. Asymptotic values are reached after the first span, and reach a slightly higher value for m ≥ 16. The PAPR is reduced at the ROADM site itself, particularly for PM-4QAM. Figure 4 implies that harmful increases in the instantaneous amplitude of the interfering channels are not the entire cause of the penalty experienced by the through channel; we can therefore only conclude that the additional distortion results from interplay between channel walk off and nonlinear effects. Given that walk-off is known to induce short and medium range correlation in crosstalk between subsequent bits, effectively low pass filtering the crosstalk [28]. We thus believe that the penalty experienced by the through channel is not only because of variation in PAPR, but also due to the randomization of the crosstalk by the periodic replacement of the interfering data pattern.

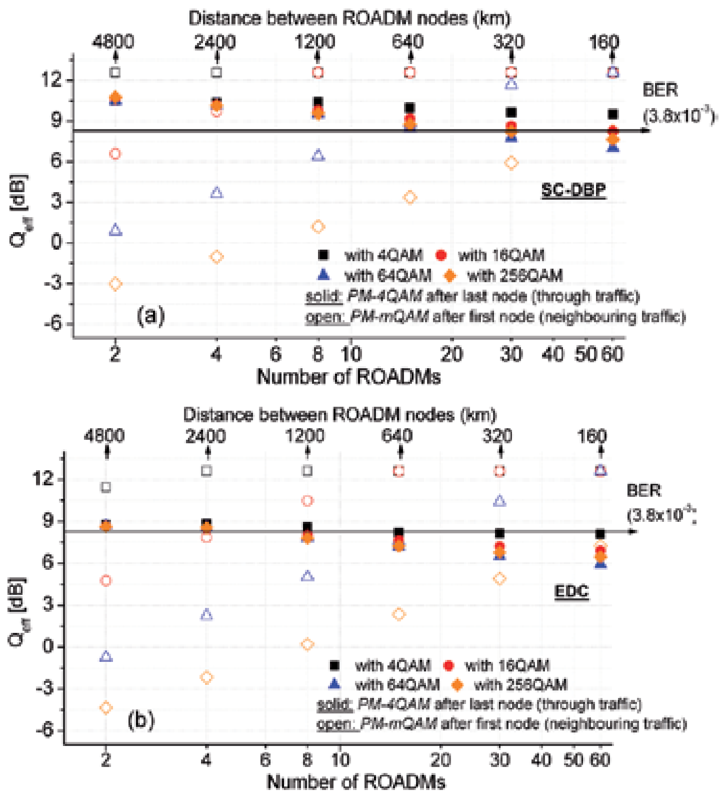

Figure 3. Q_{eff} as a function of number of ROADMs (and distance between ROADM nodes) for 28-*Gbaud* PM-mQAM showing performance of central PM-4QAM (solid, after total length), and neighboring PM-mQAM (open, after first node). a) with single-channel DBP, b) with electronic dispersion compensation. Square: 4QAM, circle: 16QAM, up triangle: 64QAM, diamond:256QAM. Up arrows indicate that no errors were detected, implying that the Q_{eff} was likely to be above 12.59 *dB*. Total link length is 9,600 km.

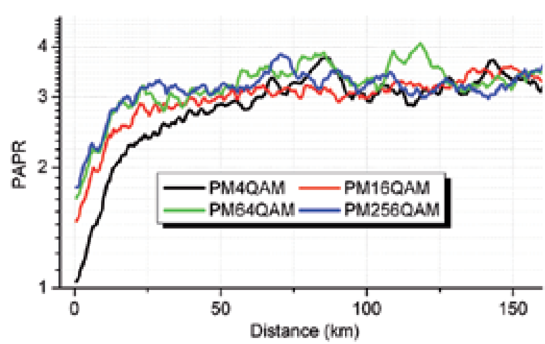

Figure 4. Variation in PAPR, for 4QAM (black), 16QAM (red), 64QAM (green) and 256QAM (blue) for a loss-less linear fiber with 20 ps/nm/*km* dispersion.

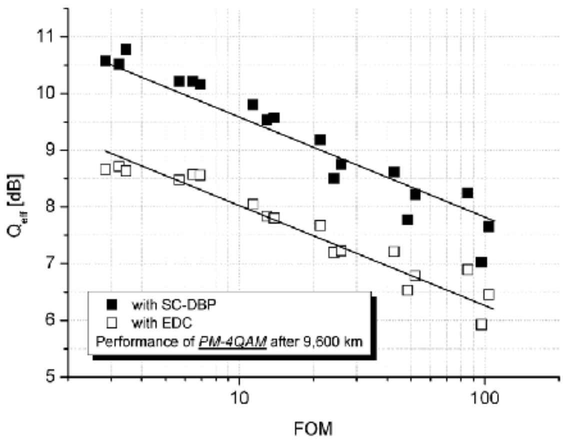

Figure 5. Q_{eff} of the PM-4QAM through channel for 28-*Gbaud* PM-mQAM add/drop traffic after 9,600 *km* as a function of a figure of merit (FOM) defined in the text for various add drop configurations. Solid: with single-channel DBP, open: with EDC.

This is confirmed by Figure 5, which plots the Q_{eff} of PM-4QAM after last node, for both EDC and single-channel DBP, in terms of a figure of merit (FOM) related to the increased amplitude modulation experienced by the test channel in the spans immediately following the ROADM node, defined as,

$$FOM_{PM-mQAM}(m) = (ROADM_N) \times \left[I_{\max}(m) / \overline{I_{all}(m)} \right] \tag{1}$$

where$m$ represents the modulation order, $ROADM_N$ represents number of add-drop nodes, I_{max} and $I_{all}$are the maximum and mean intensity of the given modulation format at the ROADM site. A strong correlation between the penalty and change in PAPR is observed. For instance, for a high number of ROADMs the system would be mostly influenced by relatively un-dispersed signals and the difference between peak-to-average fluctuations for multi-order QAM varies significantly. This leads to higher-order modulation formats impinging worse cross-channel effects on existing traffic for shorter routes.

Having observed that the nonlinear penalty is determined by the reduction in the correlation of nonlinear phase shift between bits arising from changing bit patterns, and to changes in PAPR arising from undistorted signals, it is possible to design a mitigation strategy to minimize these penalties. Figure 6 illustrates, for both EDC and single-channel DBP systems, that if the co-propagating higher-order QAM channels are linearly pre-dispersed, the performance of the PM-4QAM through traffic can be improved. The figure shows that when positive pre-dispersion is applied, such that the neighboring channel constellation is never, along its entire inter node transmission length, restored to a well-formed shape, the impact of cross-channel impairments on existing traffic is reduced significantly.

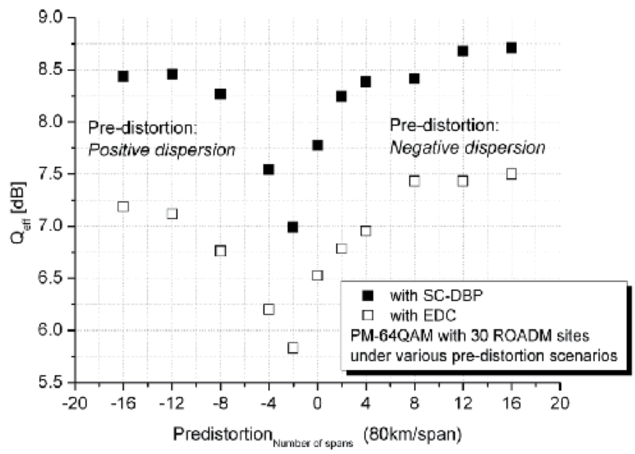

Figure 6. Q_{eff} of the PM-4QAM through channel with 30 ROADM sites, when the neighboring PM-64QAM channel is linearly pre-dispersed. Solid: with single-channel DBP, open: with EDC.

On the other hand, when negative pre-dispersion of less than the node-length (distance per node) is employed, the central test channel is initially degraded further. This behavior can be attributed to the increased impact of the PAPR of the un-dispersed constellation which is restored in the middle of the link. However, if negative pre-dispersion of more than the node-length is employed, the penalty is reduced due to lower PAPR induced XPM, and the performance saturates for higher values of pre-dispersion, similar to the case of positive pre-dispersion. Note that avoiding well formed signals along the entire link corresponds to maximizing the path averaged PAPR of the signals. The benefits of this strategy have subsequently been predicted from a theoretical standpoint [[27]].

3.2. Constraints on transmitted power

In this section, we demonstrate that independent optimization of the transmitted launch power enhances the performance of higher modulation order add-drop channels but severely degrades the performance of through traffic due to strong inter-channel nonlinearities. However, if an altruistic launch power policy is employed such that the higher-order add-drop traffic still meets the BER of 3.8×10^{-3}, a trade-off can be recognized between the performance of higher-order channels and existing network traffic enabling higher overall network capacity with minimal crosstalk [19].

As a baseline for this study, we initially consider transmission distances up to 9,600km with the same 80km spans, suitable to enable a suitable performance margin (at bit-error rate of 3.8×10^{-3}) for the network traffic given various modulation schemes at a fixed launch power of -1 *dB*m, (optimum power as determined in previous section. For a dynamic network with *N* ROADMs and m^{th} order PM-QAM, the overall results are summarized in Table 1. The table shows under which conditions the central PM-4QAM channel (right-hand symbol), and the periodically added traffic (left-hand symbol) are simultaneously able to achieve error-free operation after FEC. Two ticks indicate that both types of traffic is operational, whilst a

http://dx.doi.org/10.5772/52743

cross indicates that at least one channel produces severely errorred signals. As expected, with decreasing ROADM spacing, the operability of higher-order neighboring channels increases due to the improved OSNR. However, it can also be seen that as a consequence, added channels with higher-order formats induce greater degradation of the through channel through nonlinear crosstalk as shown in Section 3.1. In particular, if the ROADM spacing is 320 *km*, allocated to transmit PM-64QAM, whilst this traffic is operable, the through traffic falls below the BER threshold. Conversely for large ROADM spacing, there is little change in nonlinear crosstalk, since the m-QAM signals are highly dispersed, but the higher order format traffic has insufficient OSNR for error free operation. We refer to this approach as "fixed network power".

mQAM/ ROADM spacing	4800 km	2400 km	1200 km	640 km	320 km	160 km	80 km
4QAM	++	++	++	++	++	++	++
16QAM	x+	++	++	++	++	+x	+x
64QAM	x+	x+	x+	++	+x	+x	+x
256QAM	x+	x+	x+	x+	xx	xx	+x

Table 1. Operability of PM-mQAM/4QAM above BER threshold of $3.8x10^{-3}$for a total trnamsission distance of 9,600km. Tick/Cross (Left) represents performance of mQAM, Tick/Cross (Right) represents corresponding performance of central 4QAM. Tick: Operational, Cross: Non-operational

Since higher-order modulation formats have higher required OSNR, we expect the optimum launch power for those channels to be different than those used in the fixed network power scenario which was operated at a launch power of -1 *dBm*. Thus, for example, for large ROADM spacing, we improved performance might be expected if the add-drop traffic operates with increased launch power. Figure 7 illustrates the performance of through channel and the higher-order add-drop channels as a function of launch power of the add-drop traffic (through channel operates with a fixed, previously optimized, launch power of -1 *dBm*). For clarity we report two ROADM spacings, selected to give zero margin (Figure 7a) or ~2 *dB* margin (Figure 7b) for 256QAM add drop traffic. The ROADM spacing for 16 and 64QAM signals were scaled in proportion (approximately) to their required OSNR levels under linear transmission. The exact ROADM spacing is reported in the figure captions.

Figure 7 clearly illustrates that the higher-order formats operating over a longer (shorter) reach enable lower (higher) Q_{eff}, but also that the nonlinear effects increase in severity as the modulation order is increased. In particular, the long distance through traffic is strongly degraded before the nonlinear threshold is reached for such formats. Comparing Figure 7a and Figure 7b, we can see that the reduced ROADM spacing in Figure 7b enables improved performance of the add-drop channels; however the degradation of the through channel is increasingly severe. This change in behavior between formats can be attributed to the increased amplitude modulation imposed by un-dispersed signals added at each ROADM site, as discussed previously.

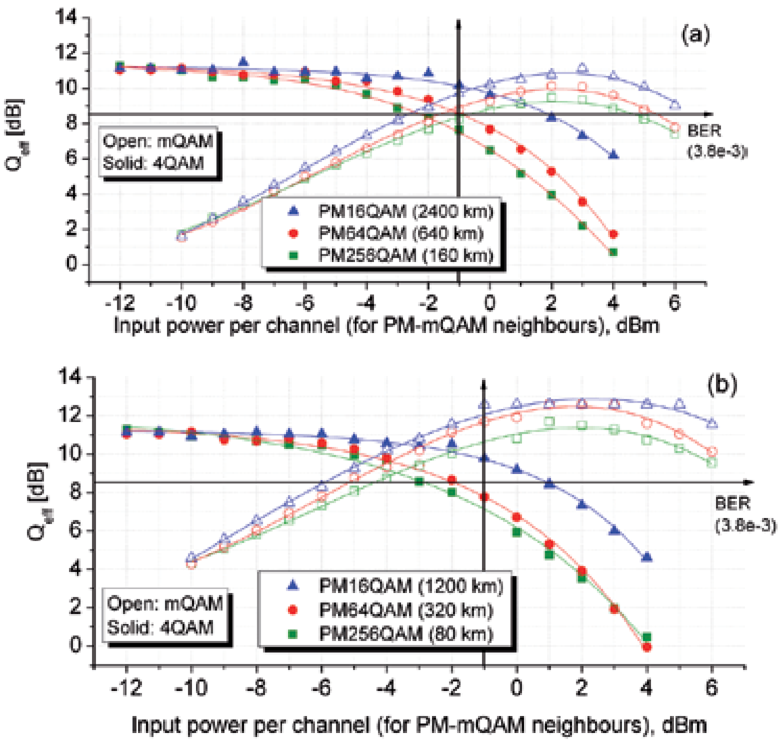

Figure 7. Q_{eff} as a function of launch power of two neighboring channels for 28-*Gbaud* PM-mQAM, showing performance of central PM-4QAM (Solid), and neighboring PM-mQAM (Half Solid). Triangle: 16QAM, Circle: 64QAM, Square: 256QAM. The launch power per channel for PM-4QAM is fixed to -1 *dBm*. ROADM spacing of, a) 2400, 640, 160 *km*, b) 1200, 320, 80 *km* for 16, 64, 256 QAM, respectively.

We can use the results of Figure 7 to analyze the impact of various power allocation strategies. Clearly if we allow each transponder to adjust its launch power to optimize its own performance autonomously, a high launch power will be selected and the degradation to the traffic from other transponders increases in severity, and in all six scenarios in Figure 7 the through channel fails if the performance of the add drop traffic is optimized independently. This suggests that launch power should be centrally controlled. Howevercentrally controlled optimization of individual launch powers for each transponder is complex; so a more promising approach would be a fixed launch power irrespective of add-drop format or reach to minimize the complexity of this control. We have already seen (Table 1) that if the launch power is set to favor the performance of PM-4QAM (-1 *dBm*) the flexibility in transmitted format for the add/drop transponders is low, and to confirm this in Figure 7 four of the scenarios fail. The best performance for these two scenarios is achieved at a fixed launch power of -3 *dBm*, but we still find that 3 scenarios fail to establish error free connections. However, if the transponders are altruistically operated at the minimum launch power required for the desired connection (not centrally controlled), the majority of the scenarios studied result in successful connections. The one exception is the add-drop of 256QAM channels with a ROADM spacing of 160 *km*, which is close to the maximum possible reach of the format. Note that shorter through paths would tend to use higher-order formats for all the routes, where nonlinear sensitivity is higher [29], and therefore we expect similar conclusions.

4. Application in meshed networks

In the previous section, we identified that optimum performance for a given predetermined modulation format was obtained by using the minimum launch power. However, this arbitrary selection of transmitted format fails to take into account the ability of a given link to operate with different formats, leading to a rich diversity of connections. In this section, we focus on the impact of flexibility in the signal constellation, allowing for evolution of the existing ROADM based static networks. We consider a configuration where network capacity is increased by allowing higher-order modulation traffic to be transmitted on according to predetermined rules based on homogenous network transmission performance. In particular we consider a 50 GHz channel grid with coherently-detected 28-*Gbaud* PM-mQAMand 20 wavelength channels. We demonstrate that even if modulation formats are chosen based on knowledge of the maximum transmission reach aftersingle-channel digital back-propagation, for the network studied, the majority of the network connections (75%) are operable with significant optical signal-to-noise ratio margin when operated with electronic dispersion compensation alone. However, 23% of the links require the use of single-channel DBP for error free operation. Furthermore, we demonstrate that in this network higher-order modulation formats are more prone to impairments due to channel nonlinearities and filter crosstalk; however they are less affected by the bandwidth constrictions associated with ROADM cascades due to shorter operating distances. Finally, we show that, for any given modulation order, a minimum filter Gaussian order of ~3 or bandwidth of ~35 *GHz* enables the performance with approximately less than 1 *dB* penalty with respect to ideal rectangular filters [30].

4.1. Network design

To establish a preliminary estimate of maximum potential transmission distance of each available format, we employed the transmission reaches identified in Section 3. These are suitable to enable a BER of $3.8x10^{-3}$ at a fixed launch power of -1 *dBm* assuming the availability of single-channel DBP. These conditions gave maximum reaches of 2,400 *km* for PM-16QAM, 640 *km* for PM-64QAM and 160 *km* for 256 QAM. Note that only single-channel DBP was considered in this study since in a realistic mesh network access to neighboring traffic might be impractical. WDM based DBP solution may be suitable for a point to point submarine link or for a network connection where wavelengths linking the same nodes co-propagate using adjacent wavelengths. Implementation of this condition would require DBP aware routing and wavelength assignment algorithms. This approach could enable significant Q_{eff} improvements or reach increases. For 64QAM, up to 7 *dB*Q_{eff}improvements were shown in [29], although the benefit depends on the number of processed channels [31].

We then applied this link capacity rule to an 8-node route from a Pan-European network topology (see highlighted link in Figure 8). To generate a representative traffic matrix, for each node, commencing with London, we allocated traffic demand from the node under consideration to all of the subsequent nodes, operating the link at the highest order constellation permissible for the associated transmission distance, and selecting the next wavelength. We note that none of the links in this chosen route were suitable for 256QAM, indeed only the Strasberg to Zurich and Vienna to Prague links are expected to be suitable for this format.

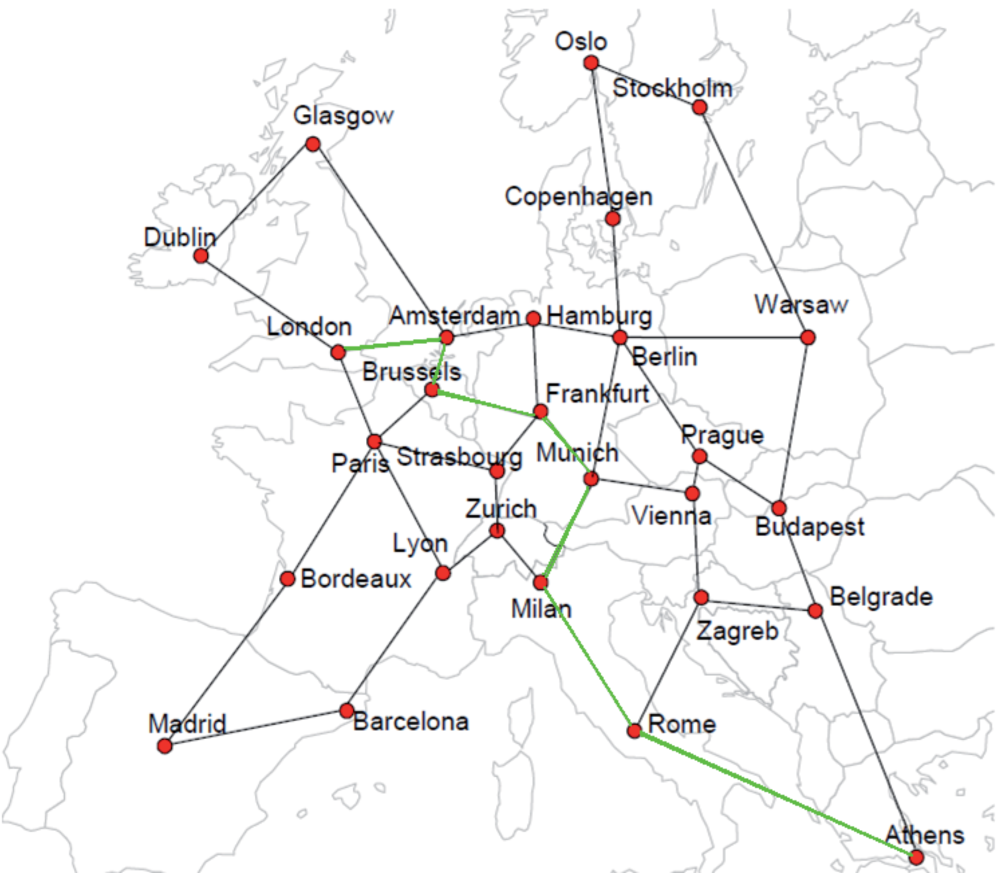

Figure 8. node Pan-European network topology. Link 1: London-to-Amsterdam: 7 spans, Link 2: Amsterdam-to-Brussels: 3 spans, Link 3: Brussels-to-Frankfurt: 6 spans. Link 4: Frankfurt-to-Munich: 6 spans, Link 5: Munich-to-Milan: 7 spans, Link 6: Milan-to-Rome: 9 spans, Link 7: Rome-to-Athens: 19 spans. (80 *km*/span).

Once all nodes were connected by a single link, this process was repeated (in the same order), adding additional capacity between nodes where an unblocked route was available until all 20 wavelengths were allocated, and no more traffic could be assigned without blockage.

http://dx.doi.org/10.5772/52743

Table 2 illustrates the resultant traffic matrix showing the location where traffic was added and dropped (gray highlighting) and the order of the modulation format (numbers) carried wavelength (horizontal index) on each link (vertical index). For example, emerging from node 6 are nine wavelengths carrying PM-4QAM and 5 wavelengths carrying PM-16QAM whilst on the center wavelength, PM-16QAM data is transmitted from node 1 (London) to node 5 (Munich) where this traffic is dropped and replaced with PM-64QAM traffic destined for node 6 (Milan). This ensured that various nodes were connected by multiple wavelengths. As it can be seen, the adopted procedure allowed for a reasonably meshed optical network (36 connections) with shortest route of 3 spans and longest path of 57 spans, emulating a quasi-real traffic scenario with highly heterogeneous traffic. At each node, add-drop functionality was enabled using a channelized ROADM architecture where all the wavelengths were de-multiplexed and channels were added/dropped, before re-multiplexing the data signals again. We considered Rectangular and Gaussian-shaped filters for ROADM stages, and the order of the Gaussian filters was varied from 1 through 6.

X (λ) / Y (Link)	*-10*	*-9*	*-8*	*-7*	*-6*	*-5*	*-4*	*-3*	*-2*	*-1*	*0*	*+1*	*+2*	*+3*	*+4*	*+5*	*+6*	*+7*	*+8*	*+9*
1	4	16	16					64	4	16	16	4	64		16	16	16		16	4
2	4	16	16	16	64	64	4	16	4	16	16	4	16	4	16	16	16		16	4
3	4	16	16	16	4	16	4	16	4	16	16	4	16	4	16	16	16	64	16	4
4	4	16	4	16	4	16	4	16	4	16	16	4	16	4	16	16	64	16	16	4
5	4	16	4	16	4	16	4	16	4	16	64	4	16	4	4	16		16		4
6	4		4		4		4		4	16	16	4	16	4	4	16		16		4
7	4		4		4		4		4	16	16				4					

Table 2. Traffic matrix (Each element represents the modulation order, Grayed: Traffic dropped and added at nodes highlighted in gray.

4.2. Results and discussions

4.2.1. Nonlinear transmission with ideal ROADMs

Figure 9 depicts the required OSNR of each connection as a function of transmission distance, after electronic dispersion compensation. Note that in this case we employed rectangular ROADM filters to isolate the impact of inter-channel nonlinear impairments from filtering crosstalk (no cascade penalties were observed with ideal filters).

Numerous conclusions can be ascertained from this figure. First, these results confirm that with mixed-format traffic and active ROADMs, as the transmission distance is increased the required OSNR increases irrespective of the modulation order due to channel nonlinearities.

Second, as observed by the greater rate of increase in required OSNR with distance, the higher-order channels are most degraded by channel nonlinearities, even at the shortest distance traversed. Furthermore, even for the shortest distances the offset between the theoretical OSNR for a linear system and the simulated values are greater for higher order formats. These two effectsare attributed to the significantly reduced minimum Euclidian distance which leads to increased sensitivity to nonlinear effects. However, for a system designed according to single-channel DBP propagation limits, as the one studied here, one can observe that majority of the links operate using EDC alone (except the ones highlighted by up-arrows). Note that managing the PAPR for such formats through linear pre-dispersion could further improve the transmission performance, as shown in Section 1.3. Additionally, in order to examine the available system margin, Figure 9 also shows the received OSNR for various configurations, where it can be seen that majority of the links (except 3) have more than 2 *dB* available margins, and that our numerical results show an excellent match to the theoretical predictions.

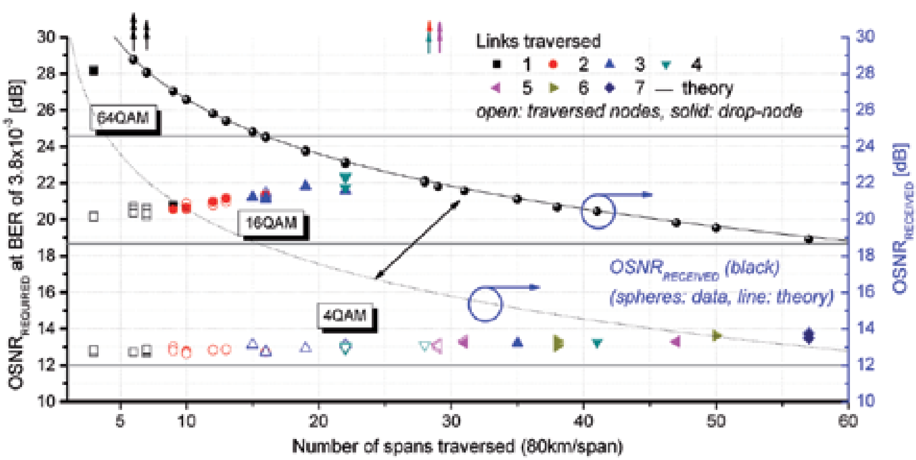

Figure 9. Nonlinear tolerance of PM-mQAM in a dynamic mesh network after EDC. a) Colored: OSNR at BER of $3.8x10^{-3}$ vs. Distance (Links traversed: 1(square), 2(circle), 3(up-tri), 4(down-tri), 5(left-tri), 6(right-tri), 7(diamond), horizontal lines (theoretical required OSNR)), open: intermediate nodes, solid: destination nodes. Black: Received OSNR (black spheres), Line (theoretical received OSNR), Dotted Line (theoretical received OSNR with 5 *dB* margin). Up arrows indicate failed connections (corresponding to drop nodes).

As discussed, the results presented in Figure 9 exclude 9 network connections classified as failed (25% of the total traffic), where the calculated BER was always found to be higher than the $3.8x10^{-3}$. In order to address the failed routes, we employed single-channel DBP, as shown in [21], on such channels, as shown in Figure 10 (red: simplified, blue: full-precision 40 steps per span).It can be seen that all but one of the links can be restored by using single-channel DBP, with the Q_{eff}increasing by an average of ~1 *dB*, consistent with the improvements observed for heterogeneous traffic in Section 1.3. The link which continues to give a BER even after after single-channel DBP is operated with the highest order modulation format studied, and its two nearest neighbors are both highly dispersed. Note that even though the maximum node lengths are chosen based on nonlinear transmission employing single-channel DBP, most of the network traffic also abide by the EDC constraints (64QAM: ≥ 1 span, 16QAM: ≥ 6 spans, 4QAM ≥ 24 spans). The failed links have one-to-one correlation with violation of these EDC constraints, allowing for prediction of DBP requirements with a quarter of the total network traffic requiring the implementation of single-channel DBP. Also, note that all but two of the links are operable with less than 15 DBP steps for the whole link.

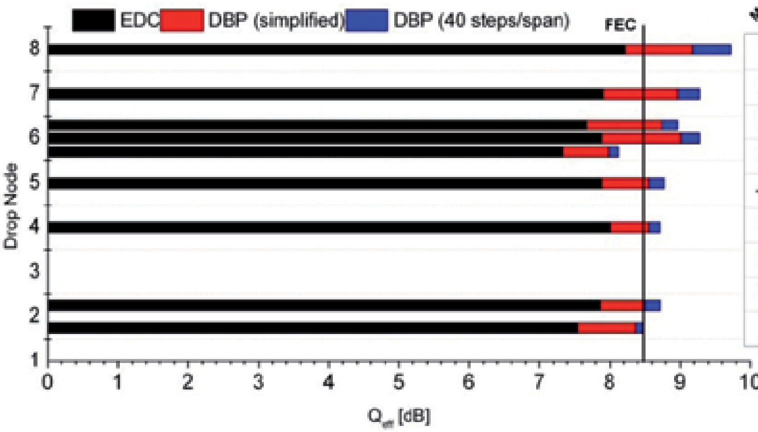

Margin	Links traversed	Spans	mQAM	DBP steps
1	2	28	16	14
0.8	4	28	16	14
0.4	5	29	16	14
0.8	5	29	16	14
-0.4	1	7	64	14
0.3	1	6	64	12
0.2	1	6	64	12
0.2	1	7	64	14
0	1	7	64	14

Figure 10. Q_{eff} as a function of network nodes for failed routes, shown by up-arrows in Fig. 5, for PM-mQAM in a dynamic mesh network. After EDC (black) and single-channel DBP (red: simplified, blue: full-precision 40 steps per span). Table shows the network parameters for each scenario and number of steps for single-channel simplified DBP.

These results give some indication of the benefit of flexible formats and DBP. For particular network studied (assuming one of the two failed links works with high precision DBP), if homogeneous traffic, employing 4QAM, is considered, a total network capacity of 4-*Tb/s*could be achieved. On the other hand, flexible m-ary QAM employing bandwidth allocation based on EDC performance limits only (not shown) enables ~60% increase in transmission capacity (6.8-*Tb/s*), while designs accounting for SC-DBP add a further 12% increase in capacity (7.7-*Tb/s*). Note that for traffic calculations based on EDC constraints, we assumed that the routes of Figure 10 would operate satisfactorily for the next format down and that there would be no increase in the nonlinear penalty experienced by any other channel. Further increase in capacity can be attained if pre-dispersion or limited WDM DBP are used, or if more format granularity is introduced (e.g. 8QAM and 32QAM) to exploit the remaining margin. In this example, 25% of transponders operating in single-channel DBP mode enable a 12% increase in capacity. One may therefore argue that in order to provide a the same increase in capacity without employing DBP, approximately 12% more channels would be required, consuming 12% more energy (assuming that the energy consumption is dominated by the transponders). In the case studied, since a ¼ of transponders require DBP, breakeven would occur if the energy consumption of a DBP transponder was 50% greater than a conventional transponder. Given that commercial systems allocate approximately 3-5% of their power to the EDC chipset [32], this suggests that the DBP unit used could be up to 16 times the complexity of the EDC chip. The results reported in Figure 10 with simplified DBP fall within this bound and highlight the practicality of simplified DBP algorithms.

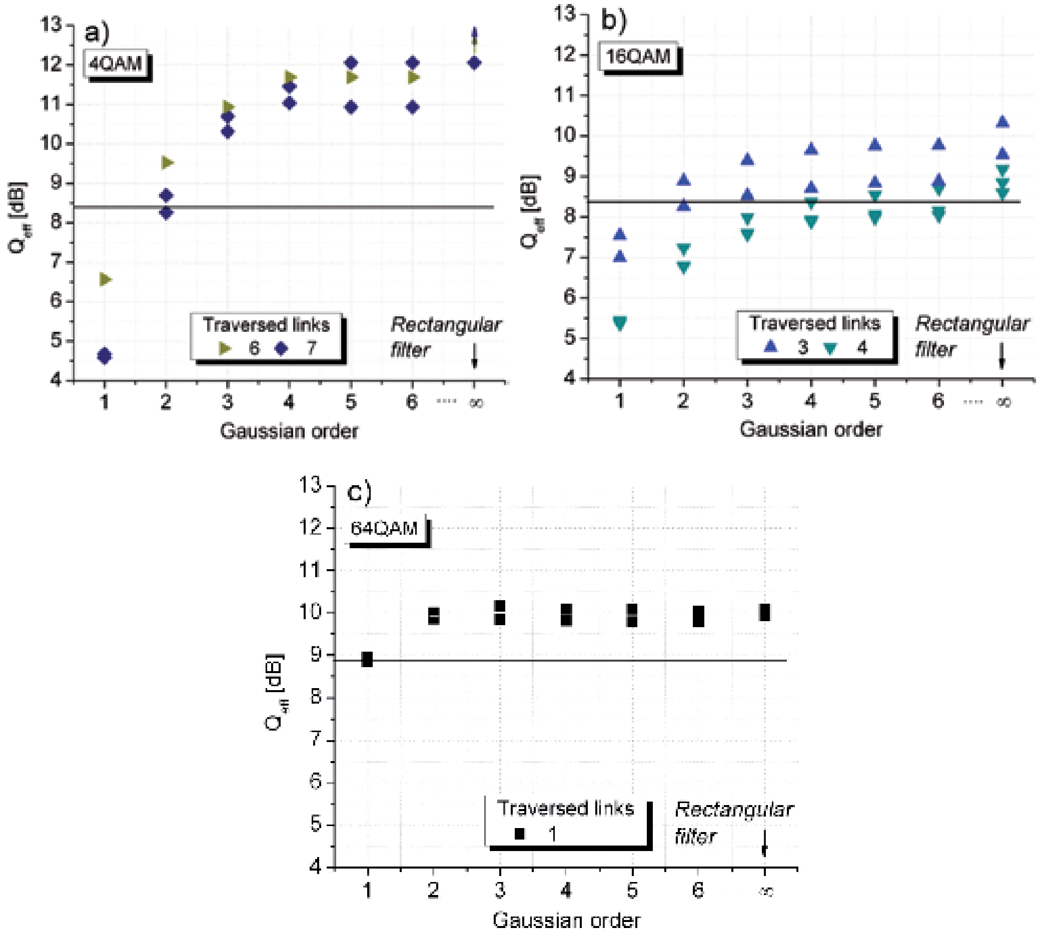

Figure 11. Q_{eff} as a function of Gaussian filter order (35 *GHz* bandwidth) for a 6 *dB* margin from theoretical achievable OSNR. a) 4QAM; b) 16QAM; c) 64QAM. (up-arrows indicate that no errors were detected).

4.2.2. Filter order and BW dependence

Figure 11 shows the performance of a selection of links with less than 6 *dB* margin from the theoretical achievable OSNR (see Figure 9 for links used, we show only the links with the worst required OSNR in the case of 16QAM for clarity), as a function of the Gaussian filter order within each ROADM. As it is well-known, the transmission penalty decreases as filter order increases [33]. However, it can be seen that for higher-order modulation formats, the transmission performance saturates at lower filter orders, compared to lower-order formats. This trend is related to the fact that modulation formats traversing through greater number of nodes are more strongly dependent on the Gaussian order (attributed to known penalties from filter cascades [34,35]). For instance, the performance of 4QAM traffic is severely degraded as a function of Gaussian order, due to the higher number of nodes traversed by such format. 16QAM channels show relatively good tolerance to filter order due to reduced number of hops, however when greater than 3 nodes are employed, the performance again becomes a strong function of filter order. 64QAM is least dependent on filter order since no intermediate ROADMs are traversed. For any given modulation order, a minimum Gaussian order of ~3 enables the optimum performance to be within 1 *dB* of the performance for an ideal rectangular filter.

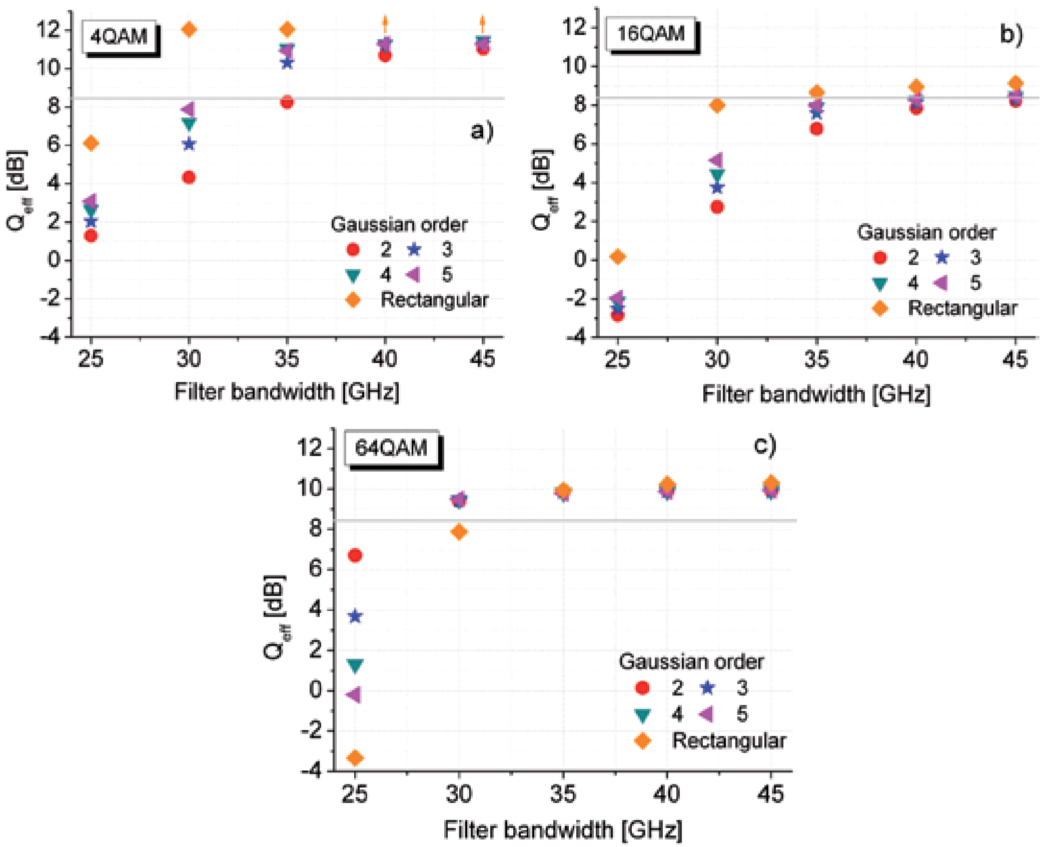

Figure 12. Q_{eff} as a function of Gaussian filter bandwidth (and filter order) for worst-case OSNR margin seen in Figure 6.8. a) 4QAM; b) 16QAM; c) 64QAM.

The simulated Q_{eff} versus 3 *dB* bandwidth of the ROADM stages and filter order is shown in Figure 12, again for the worst-case required OSNR observed in Figure 9 for each modulation format. For lower bandwidths, the Q_{eff} is degraded due to bandwidth constraints. With the exception of second order filters, bandwidths down to 35 *GHz* are sufficient for all the formats studied. However, consistent with previous analysis (in Figure 10), the impact of filter order on 64QAM is minimal and lower-order filters seem to have better performance than higher-order ones at 25*GHz* bandwidth. This is because when the signal bandwidth (28-*GHz*) exceeds the filter bandwidth, the lower order filters capture more of the signal spectra. However, this effect is visible in the case of 64QAM only since no nodes were traversed in this case, thereby avoiding the penalty from ROADM stages with lower filter orders.

5. Summary and future work

In this chapter we explored the network aspect of advanced physical layer technologies, including multi-level formats employing varying DSP, and solutions were proposed to enhance the capacity of static transport networks. It was demonstrated that that if the order of QAM is adjusted to maximize the capacity of a given route, there may be a significant degradation in the transmission performance of existing traffic for a given dynamic network architecture. Such degradations were shown to be correlated to the accumulated peak-to-average power ratio of the added traffic along a given path, and that management of this ratio through pre-distortion was proposed to reduce the impact of adjusting the constellation size on through traffic. Apart from distance constraints, we also explored limitations in the operational power range of network traffic. The transponders which autonomously select a modulation order and launch power to optimize their own performance were reported to have a severe impact on co-propagating network traffic. A solution was proposed to operate the transponders altruistically, offering lower penalties than network controlled fixed power approach. In the final part of our analysis, the interplay between different higher-ordermodulation channels and the effect of filter shapes and bandwidth of(de)multiplexers on the transmission performance, in a segment of pan-European optical network was explored. It was verified that if the link capacities are assigned assuming that digital back propagation is available, 25% of the network connections fail using electronic dispersion compensation alone. However, majority of such links can indeed be restored by employing single-channel digital back-propagation. Our results indicated some benefit of flexible formats and DBP in realistic mesh networks. We showed that for particular network studied, if homogeneous traffic, employing 4QAM is considered, a total network capacity of 4 *Tb/s* can be achieved. On the other hand, flexible m-ary QAM employing bandwidth allocation based on EDC performance limits enable ~60% increase in transmission capacity (6.8 *Tb/s*), while designs accounting for SC-DBP add a further 12% increase in capacity (7.7 *Tb/s*). Further enhancement in network capacity may be obtained through the use of intermediate modulation order, dispersion pre-compensation for nonlinearity control and the use of altruistic launch powers.

In terms of network evolution, the ultimate goal is to enable software-defined transceivers, where each node would switch itself to *just-right* modulation scheme and associated DSP, based on various physical layer, distance, power, and etc. constraints. Modeling of real-time traffic employing the content covered in this chapter, should motivate and pave the way for

http://dx.doi.org/10.5772/52743

high capacity upgrade of currently deployed networks. In addition, modulation/DSP aware routing and wavelength assignment algorithms (e.g. DBP bandwidth aware wavelength allocation) would further enhance the transmission capacity.

Acknowledgements

This work was supported by Science Foundation Ireland under Grant numbers 06/IN/I969 and 08/CE/11523.

Author details

Danish Rafique[1,2] and Andrew D. Ellis[1]

1 Photonic Systems Group, Tyndall National Institute and Department of EE/Physics, University College Cork, Dyke Parade, Ireland

2 now with Nokia Siemens Networks, S.A., Lisbon, Portugal

References

[1] R.W. Tkach, "Scaling optical communications for the next decade and beyond," Bell Labs Technical Journal 14, 3-9 (2010).

[2] P. Winzer, “Beyond 100G Ethernet,” IEEE Communications Magazine 48, 26 (2010).

[3] S. Makovejsm, D. S. Millar, V. Mikhailov, G. Gavioli, R. I. Killey, S. J. Savory, and P. Bayvel, “Experimental Investigation of PDMQAM16 Transmission at 112 Gbit/s over 2400 km,” OFC/NFOEC, OMJ6 (2010).

[4] J. Yu, X. Zhou, Y. Huang, S. Gupta, M. Huang, T. Wang, and P. Magill, “112.8-Gb/s PM-RZ 64QAM Optical Signal Generation and Transmission on a 12.5GHz WDM Grid,” OFC/NFOEC, OThM1 (2010).

[5] M. Seimetz, Higher-order modulation for optical fiber transmission. Springer (2009).

[6] A. Nag, M. Tornatore, and B. Mukherjee, “Optical network design with mixed line rates and multiple modulation formats,” Journal of Lightwave Technology 28, 466–475 (2010).

[7] C. Meusburger, D. A. Schupke, and A. Lord, “Optimizing the migration of channels with higher bitrates,” Journal of Lightwave Technology 28, 608–615 (2010).

[8] M. Suzuki, I. Morita, N. Edagawa, S. Yamamoto, H. Taga, and S. Akiba, "Reduction of Gordon-Haus timing jitter by periodic dispersion compensation in soliton transmission," Electronics Letters 31, 2027-2029 (1995).

[9] C. Fürst, C. Scheerer, G. Mohs, J-P. Elbers, and C. Glingener, "Influence of the dispersion map on limitations due to cross-phase modulation in WDM multispan transmission systems," Optical Fiber Communication Conference, OFC ’01, MF4 (2001).

[10] D.D. Marcenac, D. Nesset, A. E. Kelly, M. Brierley, A. D. Ellis, D. G. Moodie, and C. W. Ford, "40 Gbit/s transmission over 406 km of NDSF using mid-span spectral inversion by four-wave-mixing in a 2 mm long semiconductor optical amplifier," Electronics Letters 33, 879 (1997).

[11] M. Kuschnerov, F. N. Hauske, K. Piyawanno, B. Spinnler, M. S. Alfiad, A. Napoli, and B. Lankl, “DSP for coherent single-carrier receivers,” Journal of Lightwave Technology 27, 3614-3622 (2009).

[12] X. Li, X. Chen, G. Goldfarb, Eduardo Mateo, I. Kim, F. Yaman, and G. Li, ‘‘Electronic post-compensation of WDM transmission impairments using coherent detection and digital signal processing,” Opt. Express, 16, 880 (2008).

[13] D. Rafique, J. Zhao, and A. D. Ellis, "Digital back-propagation for spectrally efficient WDM 112 Gbit/s PM m-ary QAM transmission," Opt. Express 19, 5219-5224 (2011).

[14] C. Weber, C.-A. Bunge, and K. Petermann, ‘‘Fiber nonlinearities in systems using electronic predistortion of dispersion at 10 and 40 Gbit/s,” Journal of Lightwave Technology 27, 3654-3661 (2009).

[15] G. Goldfarb, M.G. Taylor, and G. Li, ‘‘Experimental demonstration of fiber impairment compensation using the split step infinite impulse response method,” IEEE LEOS, ME3.1 (2008).

[16] D. Rafique and A. D. Ellis, "Impact of signal-ASE four-wave mixing on the effectiveness of digital back-propagation in 112 Gb/s PM-QPSK systems," Opt. Express 19, 3449-3454 (2011).

[17] L.B. Du, and A. J. Lowery, "Improved single channel backpropagation for intra-channel fiber nonlinearity compensation in long-haul optical communication systems," Opt. Express 18, 17075-17088 (2010).

[18] L. Lei, Z. Tao, L. Dou, W. Yan, S. Oda, T. Tanimura, T. Hoshida, and J. C. Rasmussen, "Implementation Efficient Nonlinear Equalizer Based on Correlated Digital Backpropagation," OFC/NFOEC, OWW3 (2011).

[19] S. J. Savory, G. Gavioli, E. Torrengo, and P. Poggiolini, "Impact of Interchannel Nonlinearities on a Split-Step Intrachannel Nonlinear Equalizer," Photonics Technology Letters, IEEE 22, 673-675 (2010).

[20] D. Rafique and A. D. Ellis, "Nonlinear Penalties in Dynamic Optical Networks Employing Autonomous Transponders," Photonics Technology Letters, IEEE 23, 1213-1215 (2011).

[21] D. Rafique, M. Mussolin, M. Forzati, J. Martensson, M.N. Chugtai, A.D. Ellis, “Compensation of intra-channel nonlinear fibre impairments using simplified digital backpropagation algorithm”, Optics Express, Opt. Express 19, 9453-9460 (2011).

[22] C. S. Fludger, T. Duthel, D. vanden Borne, C. Schulien, E.-D. Schmidt, T. Wuth, J. Geyer, E. DeMan, G.-D. Khoe, and H. de Waardt,, "Coherent Equalization and POL-MUX-RZ-DQPSK for Robust 100-GE Transmission," J. Lightwave Technol. 26, 64-72 (2008).

[23] T. Wuth, M. W. Chbat, and V. F. Kamalov, “Multi-rate (100G/40G/10G) Transport over deployed optical networks,” OFC/NFOEC, NTuB3 (2008).

[24] W. Wei, Z. Lei, and Q. Dayou, “Wavelength-based sub-carrier multiplexing and grooming for optical networks bandwidth virtualization,” OFC/NFOEC, PDP35 (2008)

[25] R. Peter, and C. Brandon, “Evolution to colorless and directionless ROADM architectures,” OFC/NFOEC, NWE2 (2008).

[26] D. Rafique and A.D. Ellis “Nonlinear penalties in long-haul optical networks employing dynamic transponders,” Optics Express 19, 9044-9049, (2011).

[27] S. Turitsyn, M. Sorokina, and S. Derevyanko, "Dispersion-dominated nonlinear fiber-optic channel," OpticsLetters 37, 2931-2933 (2012) .

[28] L.E. Nelson, A. H. Gnauck, R. I. Jopson, and A. R. Chraplyvy, “Cross-phase modulation resonances in wavelength-division-multiplexed lightwave transmission,” ECOC, 309–310 (1998).

[29] D. Rafique, J. Zhao, and A. D. Ellis, "Digital back-propagation for spectrally efficient WDM 112 Gbit/s PM m-ary QAM transmission," Opt. Express 19, 5219-5224 (2011).

[30] D. Rafique and A.D. Ellis “Nonlinear and ROADM induced penalties in 28 Gbaud dynamic optical mesh networks employing electronic signal processing," Optics Express 19, 16739-16748, (2011).

[31] D. Rafique and A. D. Ellis, "Various Nonlinearity Mitigation Techniques Employing Optical and Electronic Approaches," Photonics Technology Letters, IEEE 23, 1838-1840 (2011).

[32] K. Roberts, “Digital signal processing for coherent optical communications: current state of the art and future challenges,” SPPCOM, SPWC1 (2011).

[33] F. Heismann, “System requirements for WSS filter shape in cascaded ROADM networks,” OFC/NFOEC, OThR1 (2010).

[34] T. Otani, N. Antoniades, I. Roudas, and T. E. Stern, "Cascadability of passband-flattened arrayed waveguidegrating filters in WDM optical networks," Photonics Technology Letters 11, 1414-1416 (1999).

[35] M. Filer, and S. Tibuleac, "DWDM transmission at 10Gb/s and 40Gb/s using 25GHz grid and flexible-bandwidth ROADM," OFC/NFOEC, NThB3 (2011).

Chapter 3

Faults and Novel Countermeasures for Optical Fiber Connections in Fiber-To-The-Home Networks

Mitsuru Kihara

Additional information is available at the end of the chapter

http://dx.doi.org/10.5772/54241

1. Introduction

The number of subscribers to broadband services in Japan now exceeds 34 million, and about 20 million were using fiber-to-the-home (FTTH) services in December 2011 [1]. The number of optical fiber cables continues to increase as the number of FTTH subscribers increases; however, unexpected faults have occurred along with this increase. One such fault is damage caused by wildlife including rodents, insects, and birds [2], and another is that caused by defective optical fiber connectors [3]. It is very important to detect and investigate the causes of these faults and to apply correct countermeasures.

The Technical Assistance and Support Center (TASC), Nippon Telegraph and Telephone (NTT) East Corporation is engaged in technical consultation and the analysis of optical fiber network faults for the NTT group in Japan and is contributing to eliminating the causes and reducing the number of faults in the optical fiber facilities of FTTH networks. The TASC has investigated and reported faults in various fiber connections using refractive index matching material with wide gaps between fiber ends and faults in fiber connectors with imperfect physical contact [4-6].

This chapter describes some of the faults with optical fiber connections in FTTH networks that the TASC has investigated. In addition, it introduces novel countermeasures for dealing with the faults. The various faults and countermeasures described in this chapter are shown in Fig. 1. First, section 2 briefly reviews a typical FTTH network and various fiber connections in Japan. Then section 3.1 reports faults with fiber connections that employ refractive index matching material. These faults have two major causes: One is a wide gap between fiber ends and the other is incorrectly cleaved fiber ends. Next, section 3.2 describes faults with fiber connections that employ physical contact (PC). This fault has the potential to occur when connector endfaces are contaminated. The characteristics of these faults are outlined. Novel countermeasures against the above-mentioned faults are introduced in section 4. In section 4.1, a new connection method using solid refractive index matching material is proposed as a countermeasure against faults caused by a wide gap between fiber ends. In section 4.2, a fiber optic Fabry-Perot interferometer based sensor is introduced as a way of detecting faults caused by incorrectly cleaved fiber ends. The sensor mainly uses laser diodes, an optical power meter, a 3-dB coupler, and an XY lateral adjustment fiber stage. In section 4.3, a novel tool for inspecting optical fiber ends is proposed as a countermeasure designed to detect faults caused both by incorrectly cleaved fiber ends and contaminated connector endfaces. The proposed tool has a simple structure and does not require focal adjustment. It can be used to inspect a fiber and clearly determine whether it has been cleaved correctly and whether the connector endfaces are contaminated or scratched. This chapter is summarized in section 5.

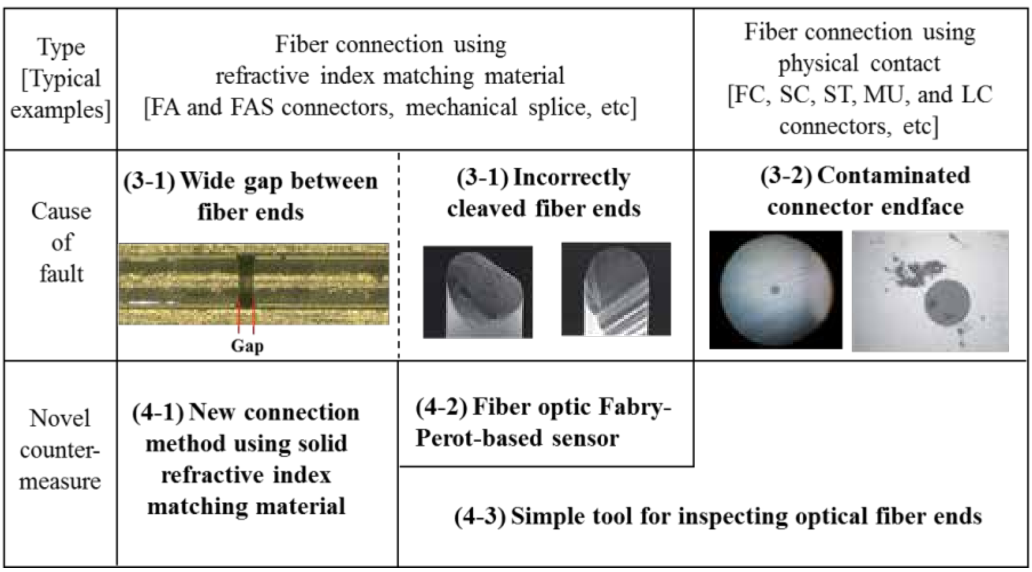

Figure 1. Various faults and their countermeasures dealt with in this chapter

2. Fiber-to-the-home network and various fiber connections

Figure 2 shows the configuration of a typical FTTH network in Japan, which is mainly composed of an optical line terminal (OLT) in a central office, underground and aerial optical fiber cables, and an optical network unit (ONU) inside a customer's home. The network requires various fiber connections at the central office, outdoors, and in homes. With the aerial and home-sited fiber connections in particular, field installable connectors or mechanical splices are used to make it possible to employ the most suitable wiring for the aerial condition and room arrangement. Field assembly (FA) termination connectors and field assembly small (FAS) connectors are types of field installable connectors [7-8].

http://dx.doi.org/10.5772/54241

In contrast, manufactured physical contact (PC)-type connectors, such as miniature-unit coupling optical fiber (MU) and single fiber coupling optical fiber (SC) connectors [9-10], are used in central offices and homes. These connectors require more frequent reconnection than field installable connectors.

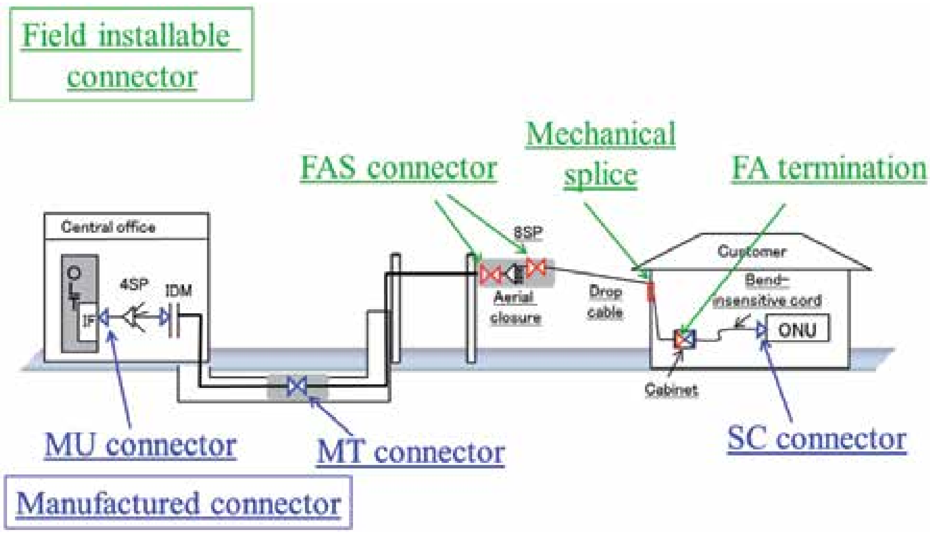

Figure 2. Typical FTTH network and various fiber connections

Figure 3(a) shows the basic structure of a PC-type connector, 3(b) shows that of a mechanical splice and 3(c) shows that of a field installable connector. With PC-type connectors, two ferrules are aligned in an alignment sleeve and connected using compressive force. Normally, two fiber ends in ferrules are connected without a gap and without offset or tilt misalignment. A mechanical splice is suitable for joining optical fibers simply in the field. It consists of a base with a V-groove guide, three coupling plates, and a clamp spring. When a wedge is inserted between the plates and the base, optical fibers can be inserted though the V-groove guide to connect and fix them in position by releasing the wedge between the plates and base [11]. Refractive index matching material is used to reduce Fresnel reflection. This connection procedure requires no electricity.

A field installable connector is composed of three main parts, a polished ferrule containing a short optical fiber (built-in optical fiber), a mechanical splicer, and a clamp. This connector holds the optical fiber drop cable or indoor cable sheath. To assemble the connection, the optical fiber end is cleaved and connected to the built-in optical fiber using a mechanical splice, and the cable sheath is fixed in the clamp. The structure allows connection to another optical fiber connector in the field. In addition, the field installable connector is fabricated based on the above-mentioned mechanical splice technique; therefore, the connection can be assembled without the use of special tools or electricity.

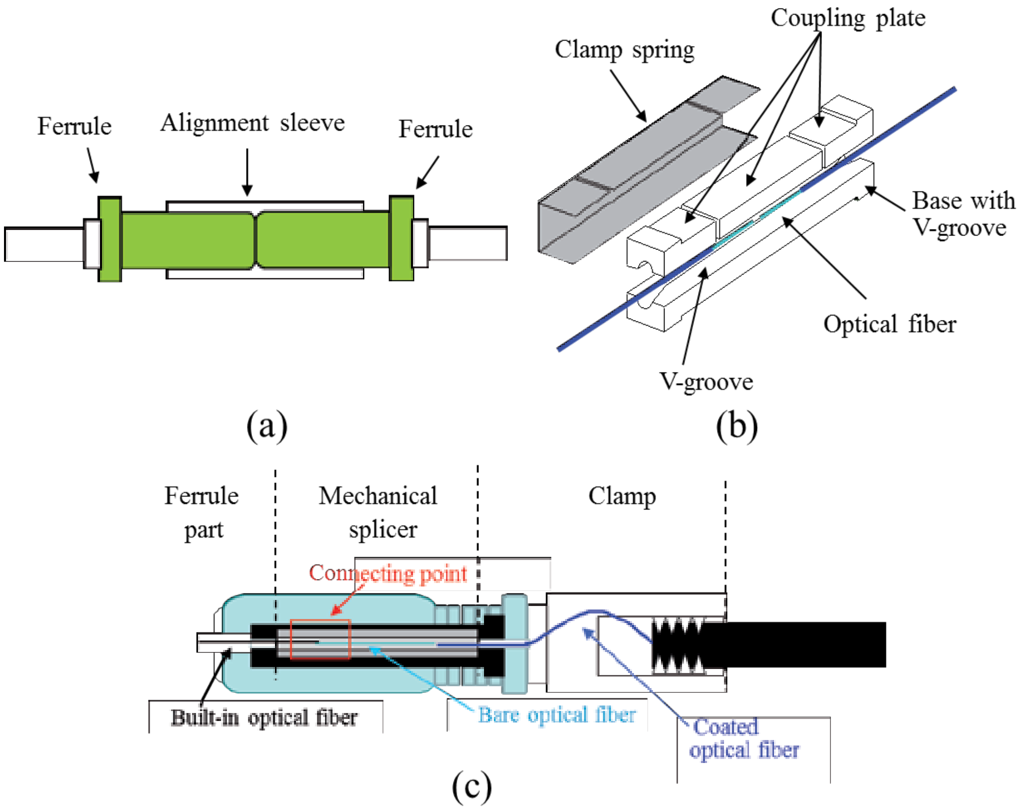

Figure 3. Basic structures of physical contact type connector, (b) mechanical splice, and (c) field installable connector

Both the mechanical splice and the field installable connector use the same fiber end preparation process before fiber installation. Figure 4 shows the fiber end preparation procedures. The coating of a fiber is stripped. Then the stripped fiber (bare fiber) is cleaned with alcohol, cut with a cleaver, inserted into the mechanical splice or the splicer inside a field installable connector, and joined to the opposite fiber or built-in fiber. Finally, the inserted fibers are fixed in position with a clamp. Stripping, cleaning, and cutting are important for successful fiber connection (to provide good performance) in the field. If any of these procedures are not conducted correctly, the performance of the fiber connection might deteriorate.

3. Faults with optical fiber connections

This section reports some of the faults with optical fiber connections in FTTH networks that the TASC has investigated. First, faults related to fiber connection using refractive index matching material are reported in section 3.1. Faults involving PC fiber connection are described in section 3.2.

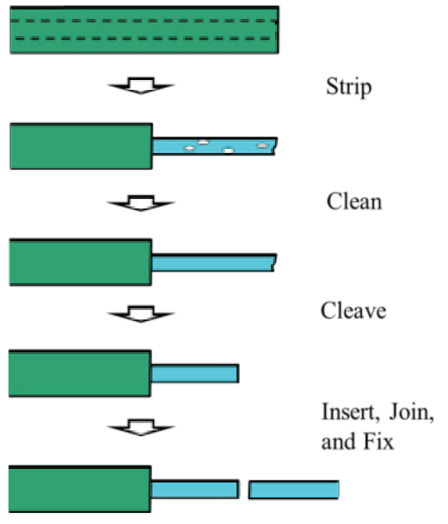

Figure 4. Optical fiber end preparation procedure

3.1. Fiber connection with refractive index matching material

There are two major causes of faults related to fiber connection using refractive index matching material: one is a wide gap between fiber ends and the other is an incorrectly cleaved fiber end. Figure 5 shows three connection models using refractive index matching material; (a) shows the normal connection state with a narrow gap between flat fiber ends, (b) shows an abnormal connection state with a wide gap between flat fiber ends, and (c) shows an abnormal state with an incorrectly cleaved (uneven) fiber end. With the normal connection (a), there is a very narrow (sub-micron) gap between the fiber ends because a normal fiber end is not completely flat. The very narrow gap is filled with silicone oil compound, which is used as the refractive index matching material in a normal connection. In the abnormal connection state (b) there is a very wide gap between the flat fiber ends, and the gap is not filled with refractive index matching material but is a mixed state consisting of refractive index matching material and air. In the abnormal connection state (c) there is a wide gap between flat and incorrectly cleaved (uneven) fiber ends. However, the gap between the fiber ends is filled with matching material.

The optical performance of various fiber connections using refractive index matching material was investigated experimentally. Wide gaps were formed between flat fiber ends by using MT connectors [12] and feeler gauges. A feeler gauge (thickness gauge tape) was installed and fixed in place between the two MT ferrules of a connector with a certain gap size by using a clamp spring. By changing the thickness of the feeler gauge, gaps of various sizes were obtained [13]. In contrast, incorrectly cleaved fiber ends were intentionally formed by adjusting the fiber cleaver so that the bend radius would be too small [14]. The cracks in these incorrectly cleaved fiber ends were from 30 to 200 μm in the axial direction. Using these incorrectly cleaved fiber ends, we fabricated field installable connectors as experimental samples. The fabricated

MT connector with a feeler gauge and field installable connector samples were subjected to a heat-cycle test in accordance with IEC 61300-2-22 (-40 to 70°C, 10 cycles, 6 h/cycle) to simulate conditions in the field. The insertion and return losses were measured.

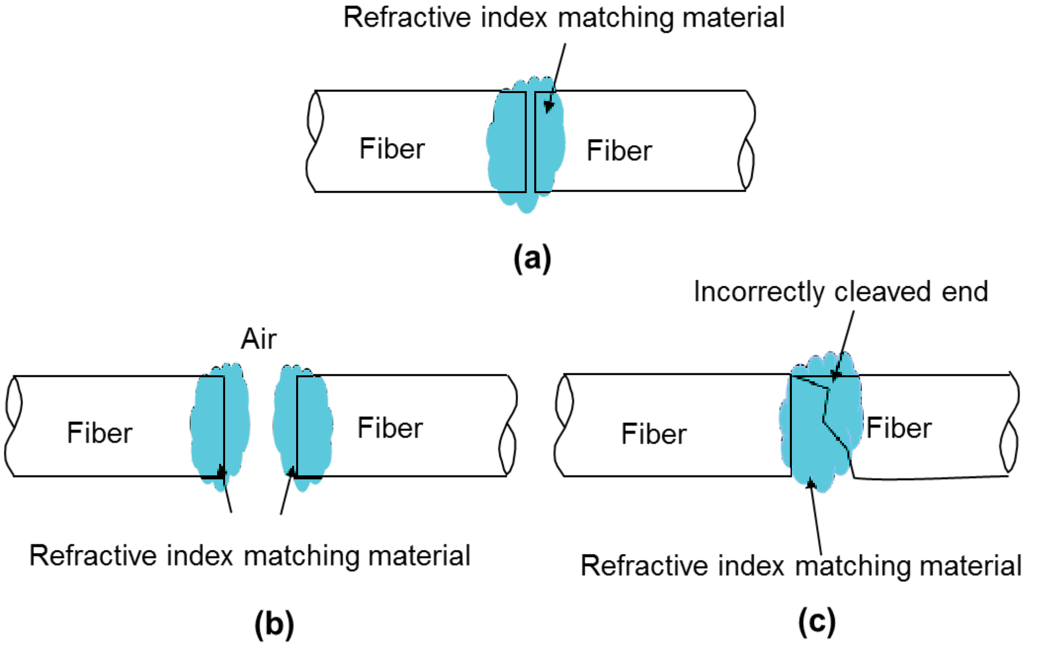

Figure 5. Fiber connection models using refractive index matching material: (a) normal connection with narrow gap between flat fiber ends, (b) abnormal connection with wide gap between flat fiber ends, and (c) abnormal connection with an incorrectly cleaved (uneven) fiber end

The insertion and return losses of an abnormal connection sample with a wide gap between flat fiber ends are shown in Fig. 6. The optical performance changed and was unstable. The insertion loss was initially 2.7 dB and then varied when the temperature changed. The maximum insertion loss exceeded 30 dB. The return losses also varied from 20 dB to more than 60 dB. This performance deterioration is thought to be caused by the mixture of refractive index matching material and air-filled gaps between the fiber ends in the MT connector sample.

http://dx.doi.org/10.5772/54241

Refractive index matching material moved in the gap when the temperature changed, and the mixed state change of the refractive index matching material and the air between the fiber ends induced the change in optical performance. When there is a mixed state consisting of refractive index matching material and air between the fiber ends, the boundary between the refractive index matching material and air could be uneven. In this state, the transmitted light spread randomly in every direction at the boundary. Therefore, the insertion loss increased to more than 30 dB. Consequently, the optical performance of fiber connections with a wide gap between flat fiber ends might be extremely unstable and vary widely. Therefore, it is important to prevent the gap from becoming wider and avoid mixing air with the refractive index matching material in the gap between fiber ends for these fiber connections.

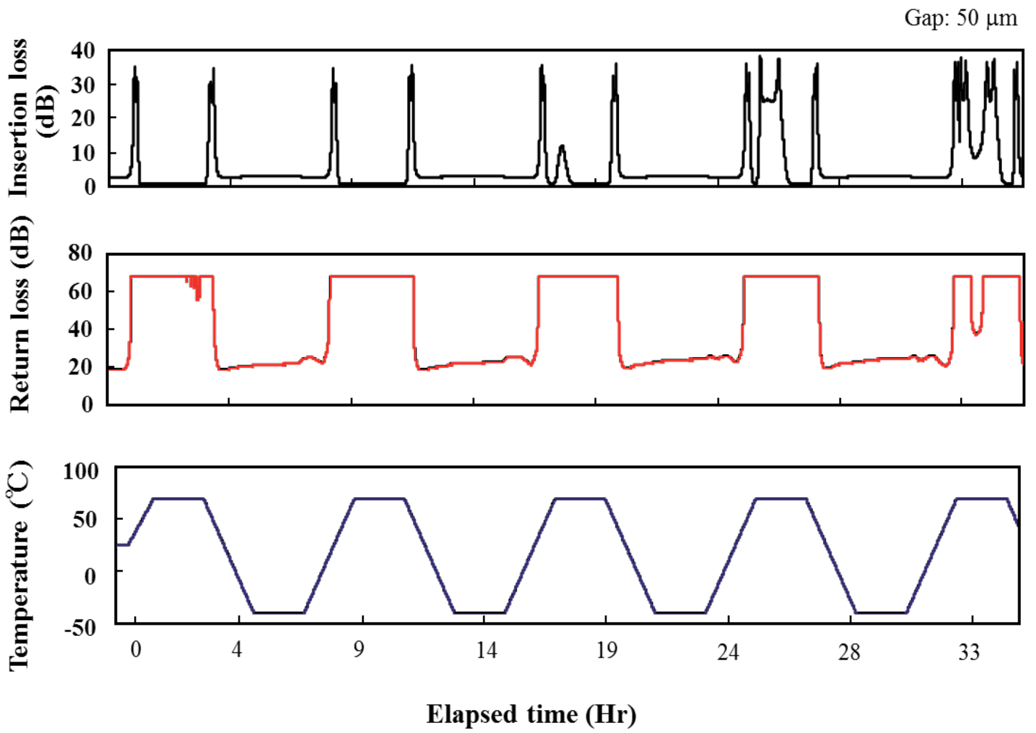

Figure 6. Heat-cycle test results for fiber connection with wide gap between flat fiber ends

The insertion and return losses of an abnormal connection sample with an incorrectly cleaved (uneven) fiber end also changed greatly and were unstable. Figure 7 shows a scatter diagram plotted from the measured insertion and return loss values to enable the values to be easily and simultaneously understood. The horizontal lines indicate insertion loss and the vertical lines indicate return loss. The scatter diagram plots minute insertion and return losses that occurred during the heat cycle test. There are both huge vertical and horizontal fluctuations in the plotted data in Fig. 7. The insertion and return loss values changed periodically during temperature cycles. The initial insertion loss was low at about 1 dB and the initial return loss was high at more than 40 dB. The insertion loss increased greatly and then the return loss decreased as the temperature changed. At worst, the insertion loss changed to 43 dB and the return loss changed to 28 dB.

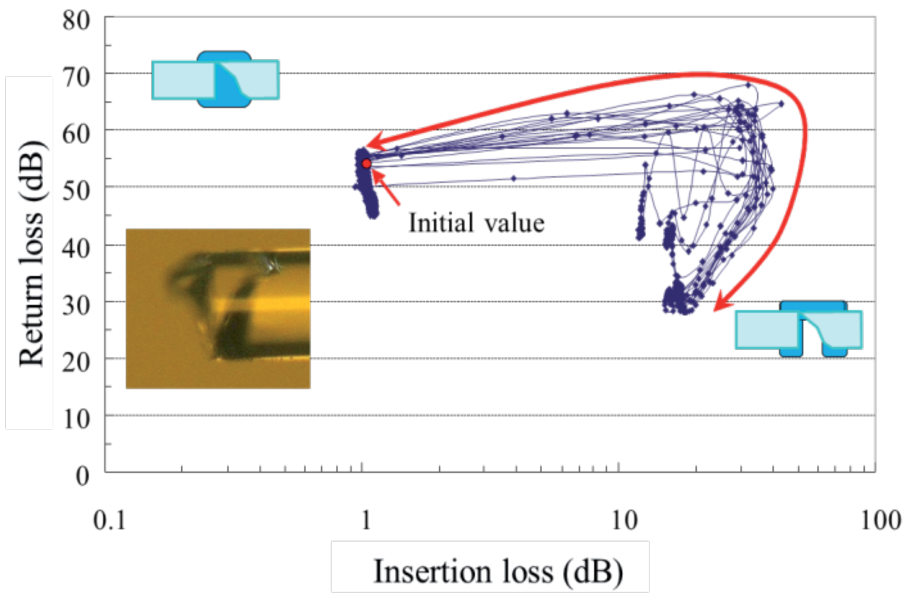

Figure 7. Scatter diagrams of results from heat cycle test for fiber connection with an incorrectly cleaved (uneven) fiber end

The great changes in the insertion and return losses are also attributed to a partially air-filled gap. The gap was not completely filled with refractive index matching material and thus consisted of a mixed state of refractive index matching material and air because of the incorrectly cleaved fiber ends. The boundary between the refractive index matching material and air could be uneven. The transmitted light in this state spread randomly in every direction at the boundary. Therefore, the insertion and return losses became much worse. When the gap was filled with refractive index matching material and there was no air, the optical performance was not so bad. When the gap was a mixed state of refractive index matching material and air, the optical performance deteriorated. The connection state is thought to vary with temperature. These results suggest that the insertion and return losses of fiber connections using incorrectly cleaved fiber ends might change to, at worst, more than 40 dB for the former and less than 30 dB for the latter. Consequently, it is important to prevent gaps between the correctly and incorrectly cleaved ends of fiber connections from becoming wider, and air from mixing with the refractive index matching material in the gaps. Therefore, incorrectly cleaved fiber ends must not be used. An effective countermeasure is to check the fiber ends cleaved with fiber cleavers. Reference [6] is recommended to those readers requiring a more detailed analysis of these abnormal connection states.

3.2. Physical Contact (PC) type connector

This section discusses the deterioration in optical performance caused by the contamination of manufactured physical contact (PC)-type connectors. It has been reported that contamination on a PC-type connector may significantly degrade the performance of mated connectors [15-17]. In this report, contamination was found on the connector endface and the sides of the connector ferrule. To study the effect of contamination on the optical performance of mated connectors, various connection conditions for PC-type connectors in abnormal states are discussed. The abnormal connection conditions are shown in Fig. 8. With PC-type connectors, two ferrules are aligned in an alignment sleeve and connected using compressive force. Normally, two fiber ends in ferrules are connected without a gap and without offset or tilt misalignment. However, if contamination is present, the connection state might become abnormal. An abnormal state can be induced by four conditions: (A) light-blocking caused by contamination on the fiber core, (B) an air-filled gap caused by contamination, (C) tilt misalignment caused by contamination, and (D) offset misalignment caused by contamination. Conditions (A) to (C) are caused by contamination on the ferrule endface. Conditions (C) and (D) are caused by contamination on the side of the ferrule. The performance deterioration caused by contamination (abnormal state) is calculated using the ratio of core contamination coverage and the Marcuse equations [18]. Figure 9 shows the individual calculated insertion losses for the four abnormal conditions. In condition (A), as the core contamination coverage ratio increases, the insertion loss increases. When the ratios are 0.5 and 0.8, the insertion losses are 3 and 7 dB, respectively. This connection condition could degrade the return loss due to the difference between the refractive indices of the fiber core and contamination. Condition (B) may be caused by contamination on the ferrule endface or fiber cladding. As the gap width becomes larger, the calculated insertion loss increases. The insertion loss caused by an air-filled gap is dependent on wavelength. When the wavelengths are 1.31 and 1.55 μm, the insertion losses of a 50-μm gap are 1.0 and 0.4 dB, respectively. This connection condition could also degrade the return loss caused by the difference in the refractive index between the fiber core and air [19]. Condition (C) may be caused by contamination on the edge of the ferrule endface and on the side of the ferrule. As the tilt angle increases, the calculated insertion loss increases. The insertion loss caused by tilt misalignment is dependent on wavelength. When the wavelengths are 1.31 and 1.55 μm, the insertion losses for a 3º misalignment angle are 1.4 and 1.3 dB, respectively. This connection condition might also have a detrimental effect on the return loss due to the difference between the refractive indices of the fiber core and air. Condition (D) may be caused by contamination on the side of the ferrule. When the offset is larger, the calculated insertion loss is higher. The insertion loss caused by offset misalignment is also dependent on wavelength. When the wavelengths are 1.31 and 1.55 μm, the insertion losses of a 3-μm offset are 1.9 and 1.5 dB, respectively. Current PC-type connectors usually have a small clearance between the outer diameter of the ferrule and inner diameter of the alignment sleeve. Therefore, the offset and tilt angle cannot be so large that the insertion losses become low. Conditions (A) and (B), which are caused by contamination on the fiber and ferrule endfaces, are thought to mainly affect the optical performance of connectors.

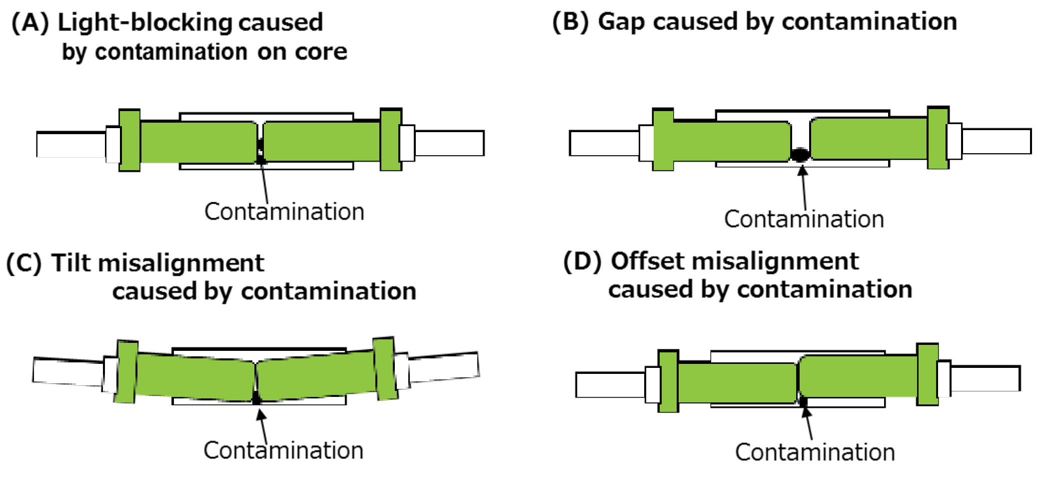

Figure 8. Abnormal connection states for PC type connector with contamination

Faults with PC-type connectors caused by contamination were investigated experimentally. Figure 10 shows examples of the investigated connectors. Figure 10 (a) is a normal sample (no contamination on the connector ferrule endface), and (b) to (e) are samples with contamination on the connector ferrule endface. The insertion losses at 1.31 and 1.55 μm were both 0.1 dB and the return loss at 1.55 μm was 58 dB for the uncontaminated sample. This optical performance is good and satisfies the required specifications for an SC connector. However, with the contaminated ferrule endfaces of samples (b) to (d), the insertion losses varied and exceeded 0.5 dB. The return losses were less than 40 dB. This optical performance does not satisfy the specifications for an SC connector. The losses with samples (b) and (c) are thought to be due to condition (A), and the loss with sample (d) is thought to be due to condition (B). With contamination sample (e), the optical performance was not bad and satisfied the SC connector specifications. Consequently, if there is contamination on a PC-type connector, the performance might deteriorate. An effective countermeasure against the loss increase caused by contamination is to inspect the PC-type connector endface prior to connection. When the connector endface is contaminated it must be cleaned with a special cleaner [20]. The countermeasures against connector endface contamination and incorrect cleaving are effective in reducing connector faults.

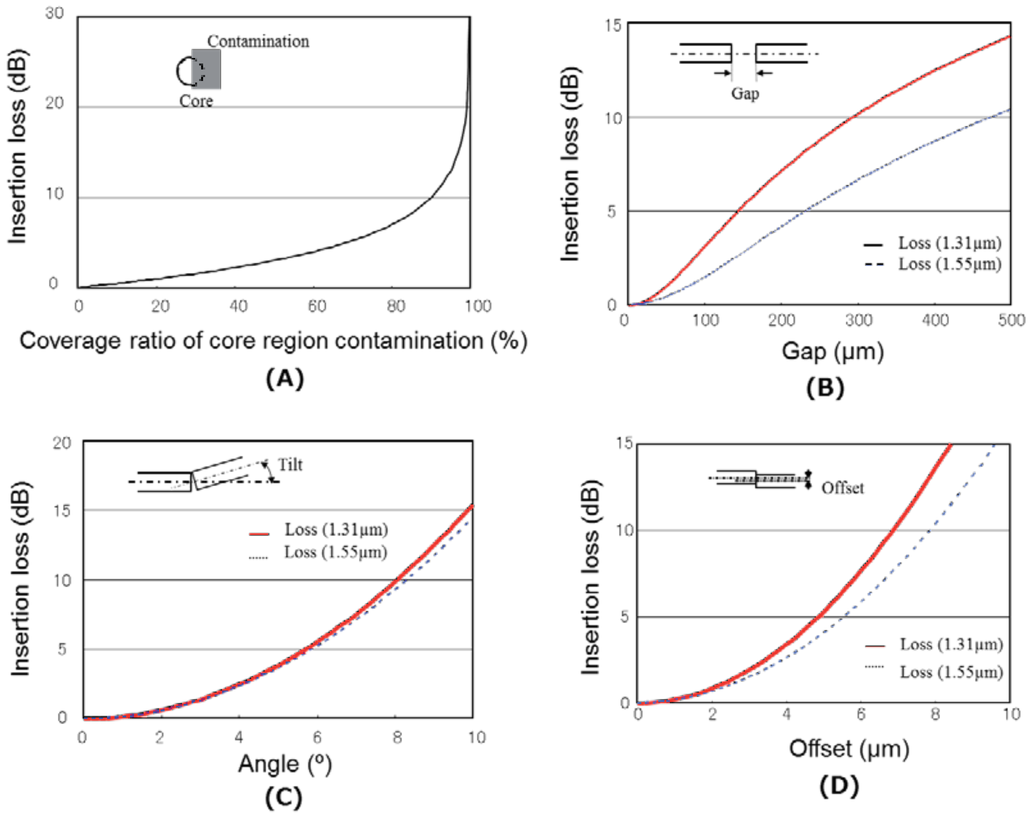

Figure 9. Calculated insertion loss, (A) cover ratio of contamination to fiber core, (B) caused by air-filled gap, (C) caused by tilt, and (D) caused by offset

4. Novel countermeasures

This section introduces novel countermeasures designed to deal with the faults described above. In section 4.1, a new connection method using solid refractive index matching material is proposed as a way of dealing faults caused by wide gaps between fiber ends. In section 4.2, a fiber optic Fabry-Perot interferometer based sensor is introduced as a countermeasure designed to prevent faults caused by incorrectly cleaved fiber ends. In section 4.3, a novel tool for inspecting optical fiber ends is proposed as a technique for detecting both faults caused by incorrectly cleaved fiber ends and those caused by contaminated connector endfaces.

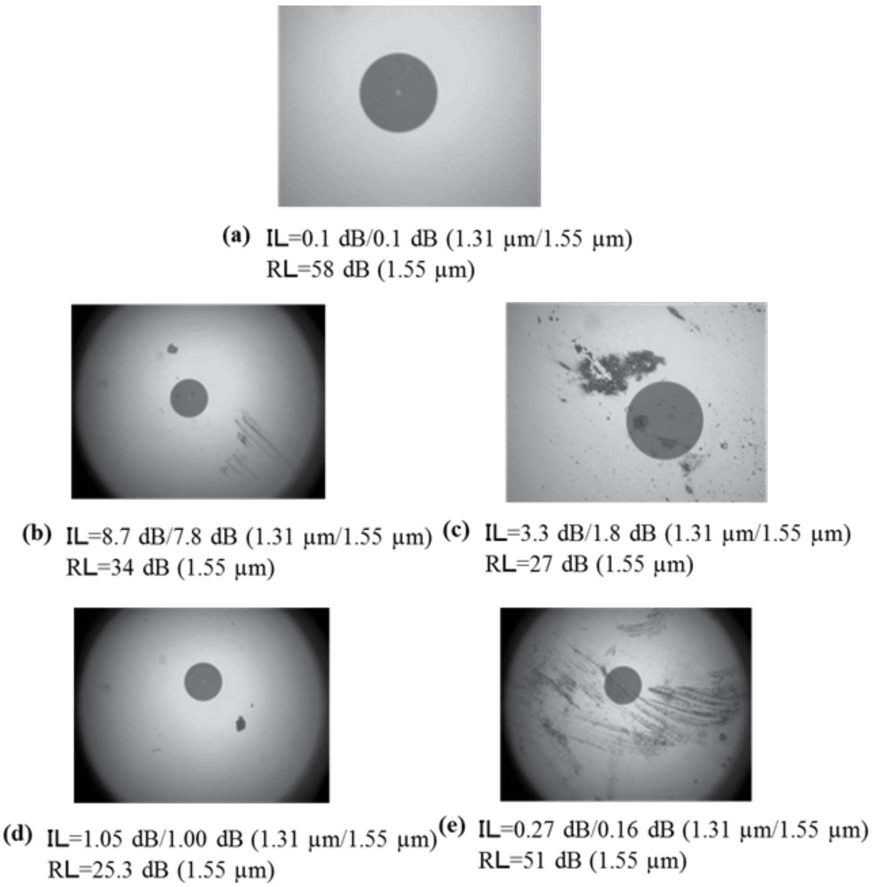

Figure 10. Examples of contamination on connector endface, (a) uncontaminated connector endface, and (b-e) different contaminations on connector endface

4.1. New connection method using solid refractive index matching material

The optical performance of fiber connections with a wide gap between flat fiber ends might be extremely unstable and vary widely. This performance deterioration may not occur immediately after installation but intermittently over time. In the event of an unusual fault, it is difficult to find the defective connection, and it takes long time to repair the fault. Therefore, it is important to prevent the gap between fiber ends from becoming wider in joints that employ refractive index matching material. A novel optical fiber connection method that uses a solid resin as refractive index matching material has been proposed [21]. The new connection method provides a high insertion loss that exceeds the loss budget between network devices when there is a wide gap between fiber ends (defective connection) and a suitable low insertion loss when the gap is less than a par-

http://dx.doi.org/10.5772/54241

ticular width (normal connection). The experimental optical performance of the proposed connection method is also discussed in this section.

The following two points are important as regards the new refractive index matching material.

i. An elastic solid resin must be used that has almost the same refractive index as the fiber core.

ii. Refractive index matching material with a particular width should be inserted between fiber ends (A and B) and tilted at a special tilt angle to the optical axis of the fiber.

The refractive index matching material must maintain its shape; therefore, a solid resin is used since the connection state cannot be easily changed. Figure 11(a) and (b) show the principles of this connection method. The incident light is refracted at the boundary surface of the refractive index matching material when the fiber ends do not touch it (there is a wide gap between the fiber ends, as shown in Fig. 11(a)). In this case, there is a high insertion loss because of the offset misalignment. In contrast, the incident light will travel straight into the refractive index matching material when it is touched by both fiber ends (the gap between the fiber ends is less than a particular width, as shown in Fig. 11(b)). The insertion loss in Fig. 11(b) is much lower than that in Fig. 11(a).

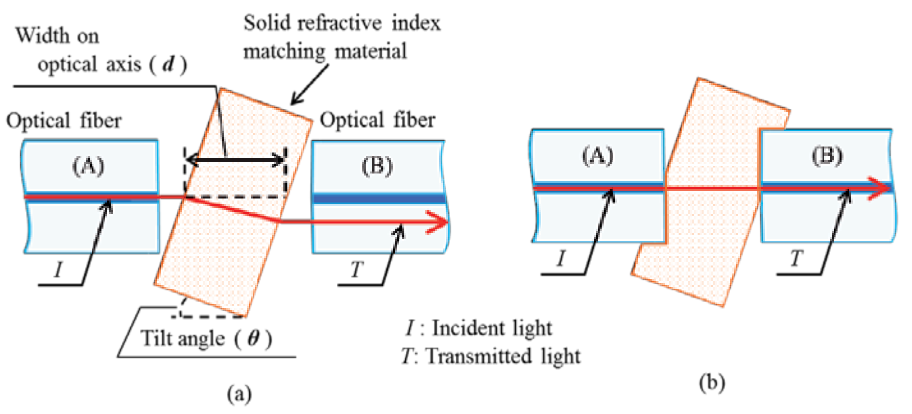

Figure 11. Proposed connection method: (a) fiber ends do not touch matching material, and (b) fiber ends touch matching material

A connection method using solid refractive index matching material based on the above-mentioned considerations was designed and used in the following procedure.

First, a target low insertion loss was set when the gap was narrower than a particular width d and then the particular width of the solid matching material on the optical axis of the fiber was determined.

Then the target high insertion loss was set when the gap was a wider than a particular width d and a special tilt angle θ was determined for the solid refractive index matching material.

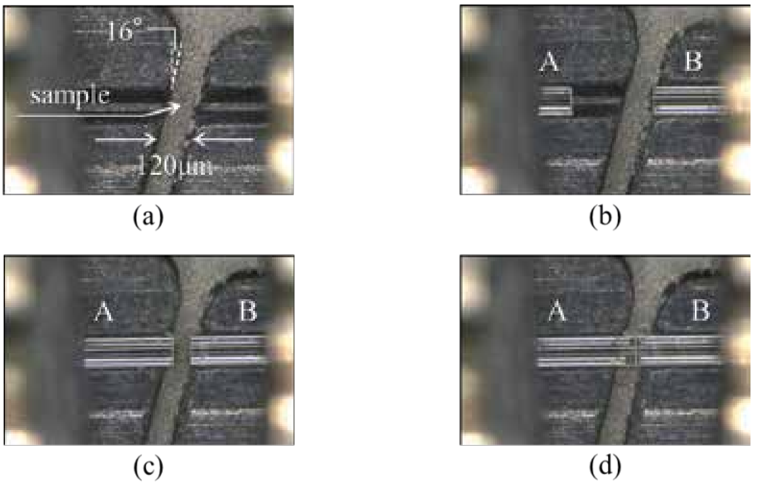

Figure 12. Composition of experimental conditions: (a) V-grooved substrate and sample, (b) fiber A does not touch sample, (c) fiber A just touches sample, and (d) fiber A is close to fiber B and very narrow gap is filled with sample

In step 1, the insertion loss caused by the gap between the fiber ends was calculated by using a Marcuse equation [18]. The insertion loss should be less than 0.5 dB to satisfy the mechanical splice specifications. However, when the insertion loss was 0.5 dB, d was 60 μm, which was too small to handle the refractive index matching material. Therefore, the target d was doubled to 120 μm. The insertion loss then became 2 dB.

In step 2, the insertion loss caused by the misalignment of the offset was calculated by using another Marcuse equation [3]. Another target insertion loss of 20 dB was determined in order to exceed the loss budget between network devices. The insertion loss became 20 dB when θ was 16°.

A sample made of the solid refractive index matching material (silicone resin) was fabricated based on the above parameters. Experiments were carried out with mechanical splices and samples of solid matching material. A groove was dug with the same shape as the sample, and the sample was tilted at 16° to the optical axis of the fiber, as shown in Fig. 12(a). A state was maintained whereby fiber end B always touched the sample, and fiber end A gradually moved toward the sample (Fig. 12(b)-(d)). The insertion and return losses were measured for different gap widths. Figure 12(b) shows the state in which fiber end A did not touch the sample. Figure 12(c) shows the state where fiber end A just touched the sample, and fiber end A was close to fiber end B, and Fig. 12(d) shows the state where the very narrow gap between the fiber ends was filled by the sample.

Figure 13(a) and (b) show the insertion and return loss results at wavelengths of 1.31 and 1.55 μm, respectively. When fiber end A did not touch the sample, the insertion loss always exceeded 20 dB. Moreover, the return losses were constant at 15 dB. When fiber end A just touched the sample, the insertion losses decreased to 2.5 and 2.3 dB, and the return losses increased to 51.7 and 48.6 dB at wavelengths of 1.31 and 1.55 μm, respectively. In addition, when fiber end A was close to fiber end B and the very narrow gap between fiber ends was filled by the sample, both insertion losses decreased to around 0.1 dB, and the return losses were 53.4 and 45.5 dB at wavelengths of 1.31 and 1.55 μm, respectively. These experimental results were consistent with the target values based on the design. If there is a defective connection that has a wide gap, the insertion loss can always be extremely high. In this case, communication services may be immobilized. With the connection method, engineers can detect the defective connection immediately after installation.

Consequently, a new connection method using solid refractive index matching material is proposed as a countermeasure against faults caused by a wide gap between fiber ends. This connection method can provide insertion losses of more than 20 dB or less than 2 dB, respectively, when the gap between the fiber ends is more or less than 120 μm.

4.2. Fiber optic fabry-perot interferometer based sensor

Field installable connections that have incorrectly cleaved fiber ends might lead to insertion losses of more than 40 dB induced by temperature changes, which may eventually result in faults in the optical networks. Therefore, it is important to use correctly cleaved fiber ends to prevent network failures caused by improper optical fiber connections. This means that we need a technique for inspecting cleaved optical fiber ends.

Cleaved optical fiber ends are usually inspected before fusion splicing with a CCD camera and a video monitor installed in fusion splice machines [22]. On the other hand, cleaved optical fiber ends are not usually inspected when mechanical splices and field installable connectors are assembled. These connections are easy to assemble and does not require electric power. Therefore, an inspection method is needed for these connections. A fiber optic Fabry-Perot interferometer based sensor for inspecting cleaved optical fiber ends has been proposed [23-24].

The basic concept of the proposed sensor for inspecting cleaved optical fiber ends is shown in Fig. 14. Figure 14(a) and (b), respectively, show fiber connections in which a fiber with a flattened end for detection is used in the inspection of incorrectly cleaved (uneven) and correctly cleaved (flat) fiber ends. The ratio of the reflected light power (P_r or P_r') to the incident light power (P_i or P_i') within each connection is measured. Two optical fibers are connected with an air gap S remaining between them. Misalignments of the offset and tilt between the fibers and the mode field mismatch are not taken into account. Under both conditions, Fresnel reflections occur at the fiber ends because of refractive discontinuity. In Fig. 14(a), the reflected light from the uneven end spreads in every direction, and the back-reflection efficiency ratio, P_r/P_i, is determined using the Fresnel reflection at the fiber end for detection in air. The Fresnel reflection R_0 is defined by the following equation.

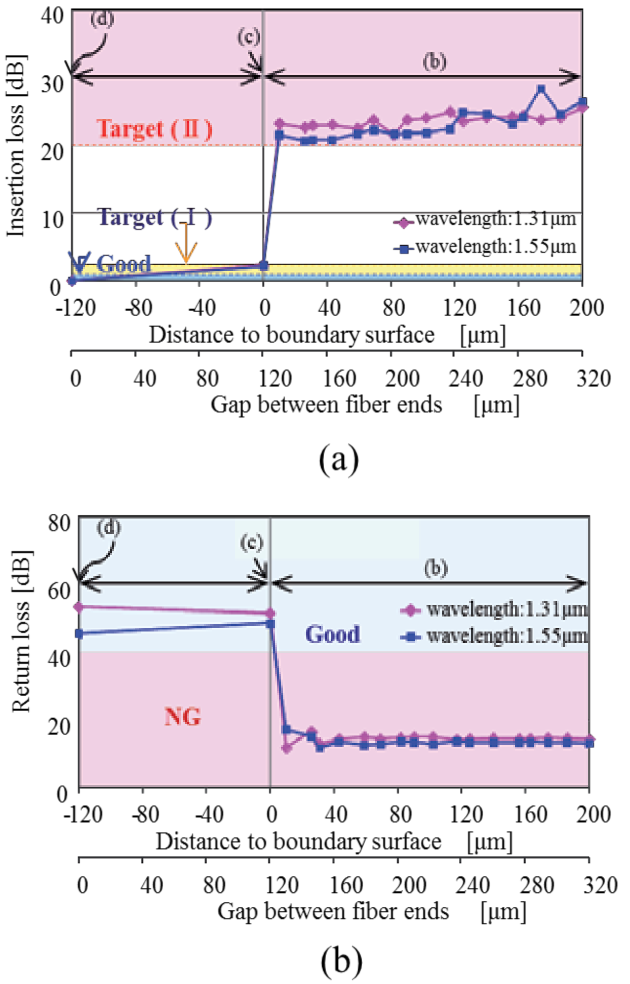

Figure 13. Results of (a) insertion loss and (b) return loss

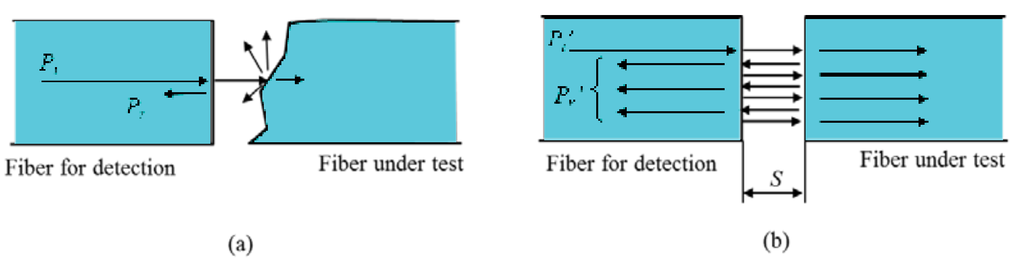

Figure 14. Basic concept of proposed sensor: (a) inspecting uneven fiber end, and (b) inspecting flat fiber end

$$R_0 = \left(\frac{n_1 - n}{n_1 + n} \right)^2 \tag{1}$$

Here n_1 and n denote the refractive indices of the fiber core and air, respectively.

In Fig. 14(b), some of the incident light is multiply reflected in the gap. The phase of the multiply reflected light changes whenever it is reflected, which interferes with the back-reflected light at the optical fiber connection. These multiple reflections between fiber ends are considered to behave like a Fabry-Perot interferometer [25-27]. Two flat fiber ends make up a Fabry-Perot interferometer. Based on the model, the returned efficiency R (= P_r'/P_i') is defined by the following equation.

$$R = \frac{4R_0 \sin^2(2\pi nS/\lambda)}{(1-R_0)^2 + 4R_0 \sin^2(2\pi nS/\lambda)} \tag{2}$$

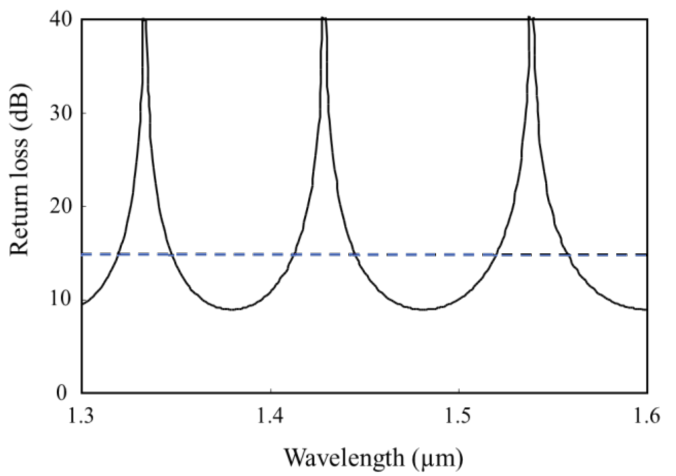

Figure 15. Return losses from uneven (dashed line) and flat (solid line) fiber ends

The return losses in dB are derived by multiplying the log of the reflection functions by -10. Here S and λ denote the gap size and wavelength, respectively. According to Equation (2), the return loss depends on S and λ. Figure 15 shows the calculated return losses from the uneven (incorrectly cleaved) and flat (correctly cleaved) fiber ends. The dashed and solid lines in the figure represent the calculations for the uneven and flat ends based on Equations (1) and (2), respectively. Here, the refractive indices n_1 and n were 1.454 and 1.0, and the gap size used for Equation (2) was 10 μm. The return losses of the uneven end were independent of wavelength and had a constant value of 14.7 dB. The return losses of the flat end varied greatly and periodically and resulted in a worst value of ~8.7 dB because of the Fabry-Perot interference.

The return loss values at wavelengths of 1.31 and 1.55 μm were 11.2 and 18.9 dB, respectively. Even if the gap size and wavelength period were changed, the return losses varied as greatly as the values at a 10-μm gap [28]. These results indicate that an inspected fiber end can be considered uneven or flat depending on whether or not the measured return losses from the fiber end at two wavelengths are both ~14.7 dB.

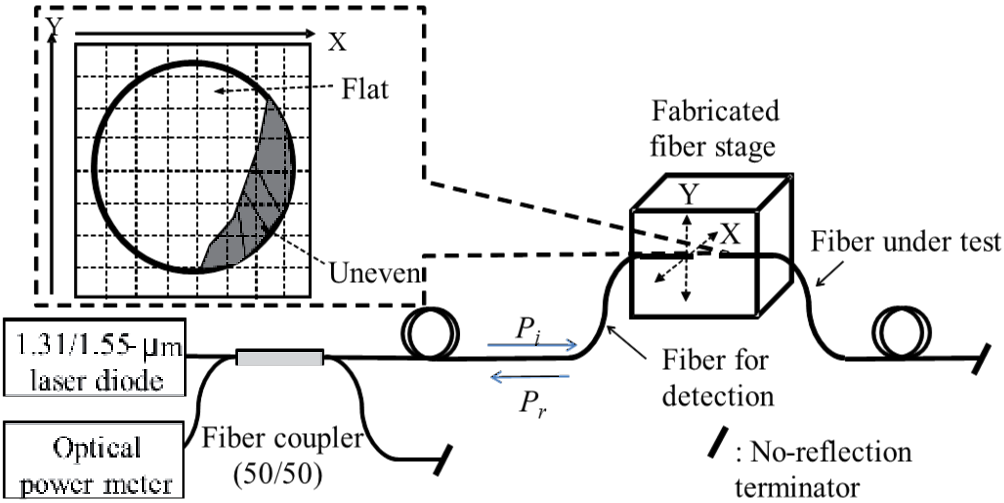

Figure 16. Experimental setup including fiber stage

Based on the above principle, we have designed the inspection sensor shown in Fig. 16. This sensor is composed of two light sources emitting at different wavelengths, an optical power meter, an optical coupler, and a fiber stage. In this proposed sensor, one light source is turned on and the other is turned off. The return loss values are measured separately at two wavelengths. The fiber stage is the most important component because a Fabry-Perot interferometer must be created in it by the fiber for detection and the fiber under test. The other equipment can be adapted from commercially available devices. Therefore, we fabricated a new fiber stage with the following characteristics to implement the proposed technique, as shown in Fig. 17. The dimensions of the fabricated fiber stage are 90 x 100 x 110 mm, which is small enough to be portable in the field. It is also suitable for operation in an outside environment because it does not require a power source. Manual driving was adopted for moving the fiber ends. Two V-grooves for the alignment of two fiber ends were used to create a Fabry–Perot interferometer. These two V-grooves were originally one V-groove that was divided into two. By using the same V-groove for alignment, any tilting of the two fibers along their Z-axes can be reduced. The X- and Y-axes for the scanning direction of the fiber ends were chosen from several alternatives, the direction of the radius, spirally, or with one stroke, due to the streamlining of the fiber stage mechanism. The minimum distance the V-groove can move was designed to be 10 μm along both the X- and Y-axes. The stage was designed to move along both the X- and Y-axes to a maximum distance of 250 μm to cover the entire end of 125-μm-diameter fibers.

Two levers are provided for manually operating only the left V-groove. The left lever moves the left V-groove along the Y-axis at 10 μm per pitch up to a maximum distance of 250 μm. Similarly, the right lever moves the left V-groove along the X-axis at 10 μm per pitch up to a maximum distance of 250 μm.

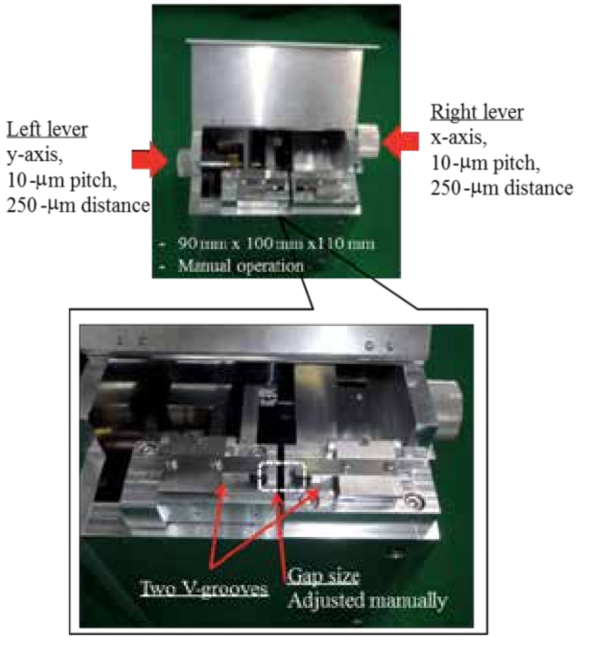

Figure 17. Fabricated fiber stage

In the experiments, the gap between the fiber for detection and the fiber under test was set at 40 μm, and each scanning distance was set at 10 μm. Typical experimental results are shown in Fig. 18. In the figure, (a) and (c) show the flat parts of the inspected fiber end found using the proposed inspection sensor and (b) and (d) show SEM images of the flat end. The fiber ends seen in Fig. 18(a) and (c) were found to be correctly and incorrectly cleaved, respectively. The experimental image with a correctly cleaved fiber end shows that the flat parts form a circle with a diameter of about 140 μm, which is slightly larger than the actual 125-μm-diameter fiber end. This is because the mode field area of light may radiate from the fiber end for detection. In contrast, the experimental results for the incorrectly cleaved fiber end show that half the fiber end parts are flat and half are uneven. The results obtained with the proposed inspection method and those obtained by SEM observation are in good agreement.

The above results show that the proposed sensor made it possible to determine accurately whether the fiber ends were correctly or incorrectly cleaved for all the samples examined. Since the proposed sensor for cleaved optical fiber ends is based on the Fabry-Perot interferometer and a new fiber stage, it allows us to determine whether 10 x 10 μm areas of a cleaved optical fiber end are flat or uneven. The measured results of the inspected flat and uneven fiber ends were in good agreement with those obtained using an SEM.

4.3. Simple tool for inspecting optical fiber ends

The conventional inspection method for a cleaved fiber end involves checking it regularly (about once a week) to ensure good cleaving quality by using a CCD camera and the video monitor of a fusion splicer. If the cleaved fiber end is imperfect, first the fiber cleaver blade is replaced. If no improvements result from this countermeasure, the fiber cleaver itself must be repaired by the manufacturer. In contrast, the conventional inspection method for optical fiber connector endfaces is to check the surface before connecting the mated connector. This method uses a CCD camera and the video monitor of a specialized piece of inspection equipment [29]. If the connector endface is contaminated, it must be cleaned with a special cleaner. These methods using a CCD camera and a video monitor are expensive and unsuitable for use with straightforward fiber connections in the field. Therefore, a simple and economical inspection tool for cleaved fiber ends and connector endfaces suitable for use in the field have been proposed [30-31].

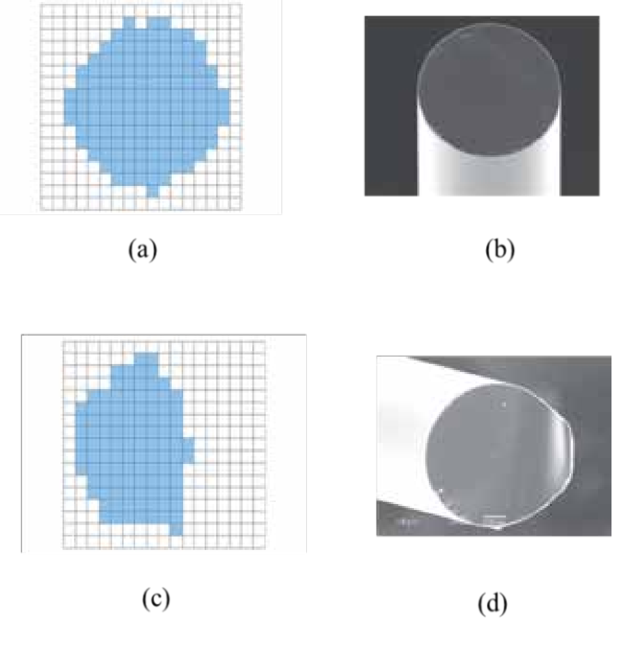

Figure 18. Experimental results of correctly cleaved fiber end: (a) result with proposed sensor and (b) result of SEM observation, and experimental results for incorrectly cleaved fiber end: (c) result with proposed sensor and (d) result of SEM observation

There are three important requirements for an inspection tool, namely it must provide a clear view, be portable, and easy to operate. We took these requirements into consideration when developing the tool. For the clear view requirement, the fiber ends or connector endfaces under test should be viewable with both the naked eye and a camera. Naked-eye inspection is easily applicable and effective during fiber end preparation and assembly procedures. Camera inspection is effective because it allows us to photograph an inspected cleaved fiber end or connector endface. To meet the portability requirement, the tool must be compact and easy to carry to any location including aerial sites. For the ease of operation requirement, the tool should not require any focal adjustment of a microscope, and the tool must be as easy as possible to handle to prevent the need for complex operations in the field.

Several concrete specifications were determined on the basis of these requirements, as listed in Table 1. The tool must be small enough to carry with one hand. Its total weight should be less than 500 g. It should include a microscope that has a lens with a magnification power of a few hundred times. The target fiber is a 125-μm bare/250-μm coated fiber, which is placed in the FA holder used in field installable connectors or a holder for mechanical splicing. The target connectors are SC, MU, FA, and FAS connectors. The tool uses a cell phone equipped with a CCD camera and small video monitor. This enables the inspected fiber end to be photographed and sent over a cell phone network. LED light sources are used to allow visibility in dark places. A rechargeable battery is used for the LED light sources.

Description	Value/Comment
Size	Small enough to be carried with one hand
Weight	Less than 500 g
Microscope	Few hundred power magnification lens
Target fiber	125/250 (bare/coated) fiber in FA holder or holder for mechanical splicing
Target connector	SC, MU, FA, FAS connectors
Camera	Cell phone capable of taking photos
Light	LED
Battery	Rechargeable battery

Table 1. Specifications of new inspection tool

The tool is designed to inspect both cleaved fiber ends and connector endfaces. Schematic views of the inspection method for a cleaved fiber end and an optical connector endace are shown in Fig. 19(a) to (c). The fundamental optical microscope system for the tool is shown in Fig. 19(a). The microscope system is composed of an objective lens, an eyepiece lens for a cell phone camera or a naked eye, a sample that can be inspected, and an LED light source. Their components must be arranged in a line at designated lengths. In this figure, S_{ob}, L_a, S_{ey}, f_{ob}, and f_{ey} indicate the distance from the objective lens to the object point, the distance between the objective and eyepiece lenses, the distance from the eyepiece lens to the viewpoint for a cell phone camera or the naked eye, the focal distance of the objective lens, and the focal distance of the eyepiece lens, respectively. Here, S_{ob} is designed to be slightly larger than f_{ob}, and S_{ey} is designed to be slightly larger than f_{ey}. The figure also shows the light path. An LED light source emitting an almost parallel light beam, is used in this microscope system. After passing through the inspected sample, the light is focused at the back focal plane of the objective lens. It then proceeds to and is magnified by the eyepiece lens before passing into a cell phone camera or a naked eye. The magnified image of the inspected sample can be observed with the cell phone monitor or with the naked eye by using appropriate lenses and by designating appropriate distances; S_{ob}, L_a, and S_{ey}. With normal optical microscopes, the inspected sample is placed on the stage and must be adjusted to S_{ob} and aligned at the object point while L_a and S_{ey} are designated as constants. By contrast, with this microscope system, the inspected sample, which in placed in a special holder, can always be positioned at the object point without active alignment, i.e., without focal length adjustment. This special holder is described in detail in the following section. For the cleaved fiber inspection shown in Fig. 19(b), the side of the cleaved fiber end is designed to be viewed through the objective lens of the microscope system with the use of the LED light source. The distance between the fiber end and the objective lens a is designed to be equal to S_{ob}. The fiber end, LED, and lens are designed to align passively and to set at each designated distance and not require focal adjustment. However, for the optical-fiber connector inspection in Fig. 19(c), the endface of the connector is designed to be viewed through the objective lens by using a half-mirror and another LED light source. The summation of the distance between the connector endface and the half-mirror b and that between the half-mirror and the object lens c is designed to be equal to S_{ob}. The connector end, LED, half-mirror, and lens are also designed to align passively and to set at each designated distance and not require focal adjustment.

On the basis of the described specifications and design, we developed a simple, mobile and cost-effective tool. The outer components of the proposed inspection tool and the internal makeup of the optical microscope system are shown in Fig. 20. It is composed of three main parts: a body that includes a microscope that has objective and eyepiece lenses and LED light sources, a cell phone and its attachment, and special holders for cleaved fiber ends or connector endfaces. The cell phone is equipped with a CCD camera and a small video monitor. This inspection tool is simple and light, and weighs about 500 g including the cell phone. The optical microscope system is also shown in this figure. The eyepiece lens, objective lens, and object point of the cleaved fiber end are aligned in the body of the tool. The two LEDs for the cleaved fiber end and connector endface are also installed in the body. The half-mirror is aligned in the special holder for the connector endface. The inspection procedure is as follows.

i. The cleaved optical fiber or the optical connector to be inspected is placed in the appropriate special holder.

ii. The special holder is installed at the center of the body.

iii. The attachment with the cell phone is installed on top of the body.

The special holders and body are designed to automatically align the inspected cleaved fiber end or connector end at each of the object points after step (ii). The attachment for a cell phone is also designed to automatically align the camera in the cell phone at the viewpoint after step (iii). This structure and procedure result in the inspection tool not requiring focal adjustment.

The fiber ends or connector endfaces under test can be viewed through the top of the body (step ii) using the cell phone monitor (step iii).

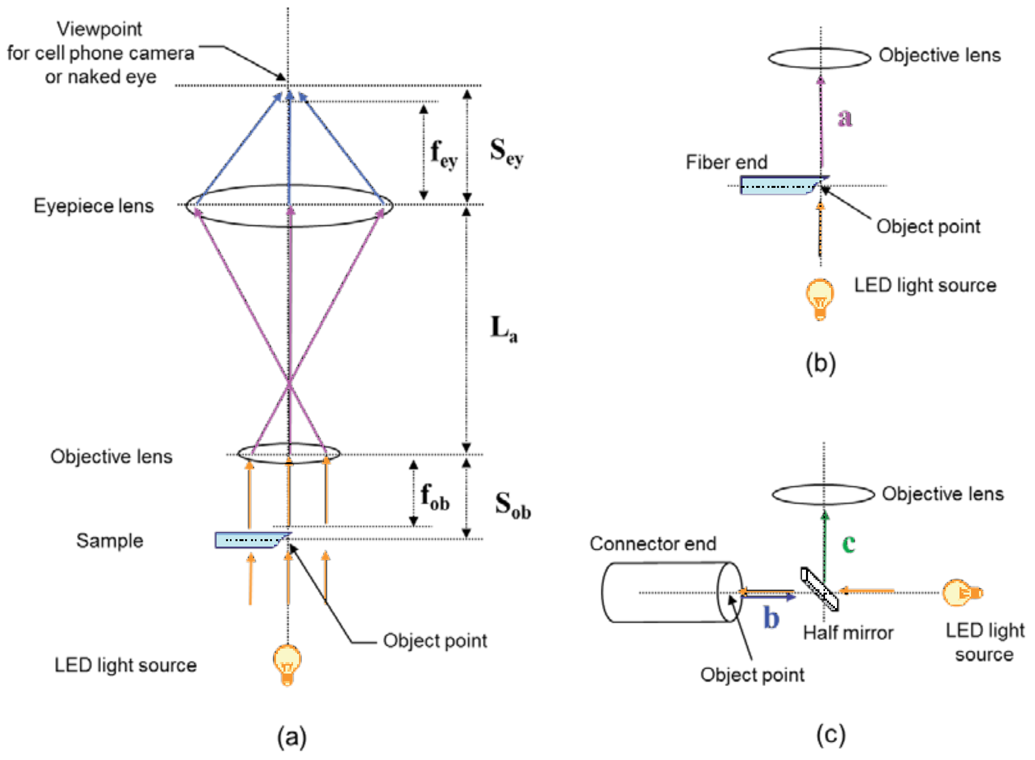

Figure 19. Basic concept of inspection method with developed tool: (a) fundamental optical microscope system and inspecting (b) cleaved fiber end (side) and (c) connector endface (front)

The conventional fiber end preparation procedure for an FAS connector has six steps: (1) cut the support wire of the dropped cable, (2) strip the cable coating, (3) place the fiber in the FA holder, (4) strip the fiber coating, (5) clean the stripped fiber (bare fiber) with alcohol, and (6) cut the bare optical fiber with a fiber cleaver. The assembly procedure comprises the next three steps: (7) insert the properly prepared bare optical fiber into the mechanical splice part in the FAS connector, (8) join it to the built-in optical fiber, and (9) fix the position of the bare optical fiber. The inspection procedure for the proposed inspection tool (i)-(iii) for a cleaved fiber end can be conducted between the fiber end preparation and assembly procedures, i.e., between steps (6) and (7). This indicates that the proposed inspection tool can work well with the conventional fiber end preparation and assembly procedures.

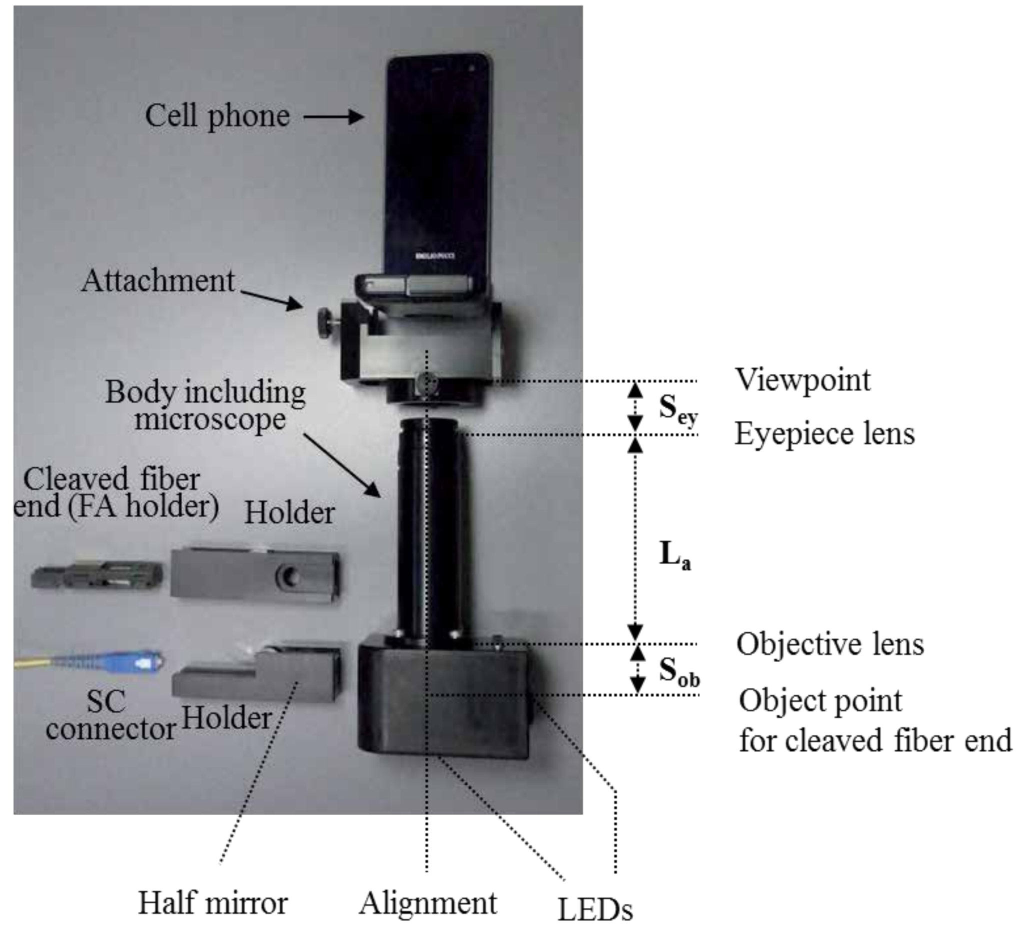

Figure 20. Outer components of fabricated inspection tool and internal makeup of optical microscope system

The inspection results and operation time of the fabricated inspection tool were evaluated. Experimental observation results from the cell phone screen are shown in Fig. 21. The tool with a cell phone attached is shown in Fig. 21(a), and its observation results are shown in Fig. 21(b) to (e). The fiber end or connector endface in each photo is magnified about 100 times. These results indicate that the tool can be used to inspect and determine whether fiber ends have been cleaved incorrectly (Fig. 21(b)) or correctly (Fig. 21(c)), and whether there is contamination (Fig. 21(d)) or no contamination (Fig. 21(e)) on the connector endfaces.

http://dx.doi.org/10.5772/54241

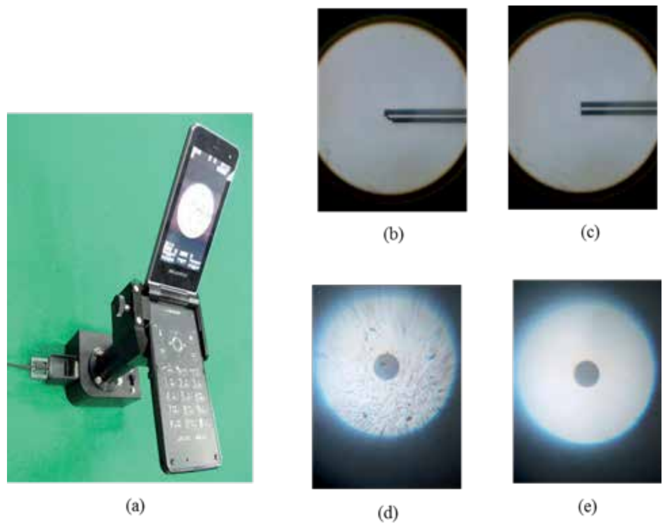

Figure 21. Experimental observation results on cell phone screen: (a) developed inspection tool with cell phone attached, (b) incorrectly cleaved fiber end, (c) correctly cleaved fiber end, (d) contamination on connector endface, and (e) uncontaminated connector endface

For conventional FAS connector procedures, the fiber end preparation and assembly procedures take 72 and 28% of the total installation time, respectively. With the proposed tool, inspection took 11% longer than with the conventional procedure. These results indicate that using the inspection tool may result in a slight increase of 11% in operation time compared with that required with conventional fiber end preparation and assembly procedures.

The fabricated inspection tool is compact, highly portable, and can inspect a fiber and clearly determine whether it has been cleaved correctly and whether contamination or scratches can be found on the connector endfaces. Thus, this tool will be highly practical for field use.

5. Conclusion

This chapter reported example faults and novel countermeasures with optical fiber connectors and mechanical splices in FTTH networks.

After a brief introduction (section 1), section 2 described the FTTH network and optical fiber connectors and mechanical splices used in Japan, and section 3 reported example faults with these optical connections in FTTH networks. First, the faults with fiber connection using refractive-index matching material were reported in section 3.1. There are two major causes of these faults: one is a wide gap between fiber ends and the other is incorrectly cleaved fiber ends. Next, faults with fiber connection using physical contact were explained in section 3.2. This fault might occur when the connector endfaces are contaminated. The characteristics of these faults were outlined.

Novel countermeasures against these above-mentioned faults were introduced in section 4. In section 4.1, a new connection method using solid refractive index matching material was proposed as a countermeasure against faults caused by the wide gap between fiber ends. This connection method can provide an insertion loss of more than 20 dB or less than 2 dB when the gap between the fiber ends is wider or narrower than 120 μm, respectively. If there is a defective connection that has a wide gap, the insertion loss will always be extremely high. In such cases, communication services may be immobilized. With the connection method, engineers undertaking detection work can notice the defective connection immediately after installation.

In section 4.2, a fiber optic Fabry-Perot interferometer-based sensor was introduced as a countermeasure for detecting faults caused by incorrectly cleaved fiber ends. The sensor mainly uses laser diodes, an optical power meter, a 3-dB coupler, and an XY lateral adjustment fiber stage. Experimentally obtained fiber end images were in good agreement with scanning electron microscope observation images of incorrectly cleaved fiber ends.

In section 4.3, a novel tool for inspecting optical fiber ends was proposed as a countermeasure for detecting faults caused both by incorrectly cleaved fiber ends and by contaminated connector endfaces. The proposed tool has a simple structure and does not require focal adjustment. It can be used to inspect a fiber and clearly determine whether it has been cleaved correctly and whether contamination or scratches are present on the connector endfaces. The tool requires a slight increase of 11% in operation time compared with conventional fiber end preparation and assembly procedures. The proposed tool provides a simple and cost-effective way of inspecting cleaved fiber ends and connector endfaces and is suitable for field use.

These results support the practical use of optical fiber connections in the construction and operation of optical network systems such as FTTH.

Acknowledgements

This work was supported by the TASC, NTT East Corporation, Japan. The author is deeply grateful to the following members of the TASC for their support; to Y. Yajima for discussing the experiments related to fiber connection with refractive index matching material, to H. Onose for discussing the experiments related to contaminated connector endfaces, to H. Watanabe and M. Tanaka for helpful discussions regarding the new connection method using solid refractive index matching material and a fiber optic Fabry-Perot interferometer based sensor, and to M. Okada and M. Hosoda for discussions regarding the simple inspection tool.

Author details

Mitsuru Kihara

NTT Access Network Service Systems Laboratories, Nippon Telegraph and Telephone Corporation, Japan

http://dx.doi.org/10.5772/54241

References

[1] Ministry of Internal Affairs and Communications, 2011 WHITE PAPER Information and Communications in Japan [online], Available at: http://www.soumu.go.jp/johotsusintokei/whitepaper/ja/h23/pdf/index.html (accessed 10 Aug. 2012).

[2] Matsuhashi K., Uchiyama Y., Kaiden T., Kihara M., Tanaka H., & Toyonaga M. "Fault cases and countermeasures against damage caused by wildlife to optical fiber cables in FTTH networks in Japan," in Proceeding of the 59th IWCS/Focus, Nov. 7-10, 2010, Providence, Rhode Island, USA, pp. 274-278.

[3] NTT East Corporation, "Fault cases and countermeasures for field assembly connectors in optical access facilities," NTT Technical Review, vol. 9, No. 7, 2011.

[4] Kihara M., Nagano R., Uchino M., Yuki Y., Sonoda H., Onose H., Izumita H., & Kuwaki N., "Analysis on performance deterioration of optical fiber joints with mixture of refractive index matching material and air-filled gaps," in Proceedings of the OFC/NFOEC, March 22-26, 2009, San Diego, CA, USA, JWA4.

[5] Kihara M., Uchino M., Watanabe H., & Toyonaga M., "Fault analysis: optical performance investigation of optical fiber connections with imperfect physical contact," Opt. Lett., vol. 36, no. 24, 2011, pp. 4791-4793.

[6] Kihara M., "Optical performance analysis of single-mode fiber connections," in the book "Optical fiber communications and devices" edited by Moh. Yasin, Sulaiman W. Harun and Hamzah Arof, ISBN 978-953-307-954-7, InTech, February 2, 2012.

[7] Nakajima T., Terakawa K., Toyonaga M., & Kama M., "Development of optical connector to achieve large-scale optical network construction," in Proceedings of the 55th IWCS/Focus, Nov. 12-15, 2006, Providence, Rhode Island, USA, pp. 439–443.

[8] Hogari K., Nagase R., & Takamizawa K., "Optical connector technologies for optical access networks," IEICE Trans. Electron., Vol. E93-C, No. 7, 2010, pp. 1172–1179.

[9] Sugita E., Nagase R., Kanayama K., & Shintaku T., "SC-type single-mode optical fiber connectors," IEEE/OSA J. Lightw. Technol., vol. 7, 1989, pp. 1689–1696.

[10] Nagase R., Sugita E., Iwano S., Kanayama K., & Ando Y., "Miniature optical connector with small zirconia ferrule," IEEE Photon. Technol. Lett., vol. 3, No. 11, 1991, pp. 1045–1047.

[11] "Optical fiber mechanical splice", US patent No.5963699.

[12] Satake T., Nagasawa S., & Arioka R., "A new type of a demountable plastic molded single mode multifiber connector," IEEE/OSA J. Lightw. Technol., vol. LT-4, 1986, pp. 1232-1236.

[13] Kihara M., Nagano R., Izumita H., & Toyonaga M., "Unusual fault detection and loss analysis in optical fiber connections with refractive index matching material," Optical Fiber Technol., vol. 18, 2012, pp. 167–175.

[14] Yajima Y., Watanabe H., Kihara M., & Toyonaga M., "Optical performance of field assembly connectors using incorrectly cleaved fiber ends," in Proceedings of the OECC2011, July 4-8, 2011, Kaohsiung, Taiwan, 7P3_053.

[15] Berdinskikh T., Bragg J., Tse E., Daniel J., Arrowsmith P., Fisenko A., & Mahmoud S., "The contamination of fiber optics connectors and their effect on optical performance," in Technical digest series of OFC 2002, March 17- 22, 2002, Anaheim, California, pp. 617-618.

[16] Albeanu N., Aseere L., Berdinskikh T., Nguyen J., Pradieu Y., Silmser D., Tkalec H., & Tse E., "Optical connector contamination and its influence on optical signal performance," J SMTA, vol. 16, issue 3, 2003, pp. 40-49.

[17] Berdinskikh T., Chen J., Culbert J., Fisher D., Huang S. Y., Roche B. J., Tkalec H., Wilson D., & Ainley S. B., "Accumulation of particles near the core during repetitive fiber connector matings and de-matings" in Technical Digest of OFC/NFOEC2007, March 25-29, 2007, Anaheim, CA, USA, NThA6, pp. 1-11.

[18] Marcuse D., "Loss analysis of optical fiber splice," Bell Sys. Tech. J, vol. 56, 1976, pp. 703-718.

[19] Kihara M., Nagasawa S., & Tanifuji T., "Return loss characteristics of optical fiber connectors," IEEE/OSA J. Lightw. Technol., vol. 14, Sep. 1996, pp. 1986-1991.

[20] For example, CLETOP (Optical connector cleaner), see URL: http://www.ntt-at.com/product/cletop/

[21] Tanaka M., Watanabe H., Kihara M., & Takaya M., "New connection method using solid refractive index matching material," in Proceedings of the OECC2012, July 2-6, 2012, Busan, Korea, 4C2-5.

[22] Tanifuji T., Kato Y., & Seikai S., "Realization of a low-loss splice for single-mode fibers in the field using an automatic arc-fusion splicing machine," in Proceedings of the OFC, Feb. 28-March 2, 1983, New Orleans, Louisiana, USA, MG3.

[23] Kihara M., Watanabe H., Tanaka M., & Toyonaga M., "Fiber optic Fabry-Perot interferometer based sensor for inspecting cleaved fiber ends," Microwave and Optical Technol. Lett., vol. 54, No. 6, 2012, 1541-1543.

[24] Watanabe H., Kihara M., Tanaka M., & Toyonaga M., "Inspection technique for cleaved optical fiber ends based on Fabry-Perot interferometer," IEEE/OSA J. Lightw. Technol., vol. 30, No. 8, 2012, 1244-1249.

[25] Yariv A., "Introduction to optical electronics," New York: Holt, Rinehart, and Winstone, 1985.

[26] Kashima N., "Passive optical components for optical fiber transmission," Norwood, MA: Artech House, 1995.

[27] Kihara M., Tomita S., & Haibara T., "Influence of wavelength and temperature changes on optical performance of fiber connections with small gap," IEEE Photon. Tech. Lett. 18, 2006, 2120-2122.

[28] Kihara M., Uchino M., Omachi M., & Izumita H., "Analyzing return loss deterioration of optical fiber joints with various air-filled gaps over a wide wavelength range," in Proceedings of the OFC/NFOEC, March 21-25, 2010, San Diego, CA, USA, NWE4.

[29] For example, JDSU Fiberscope (Fiber Optic Connector End Face Cleaning System), see URL: http://www.jdsu.com/en-us/Test-and-Measurement/Products/families/westover/Pages/default.aspx/

[30] Okada M., Kihara M., Hosoda M., &Toyonaga M., "Simple inspection tool for cleaved optical fiber ends and optical fiber connector end surface," in Proceedings of the 60th IWCS, Nov. 7-9, Charlotte, North Carolina, USA, 2011, 270-274.

[31] Kihara M., Okada M., Hosoda M., Iwata T., Yajima Y., & Toyonaga M., "Tool for inspecting faults from incorrectly cleaved fiber ends and contaminated optical fiber connector end surfaces," Optical Fiber Technol., vol. 18, 2012, 470-479.

Multimode Graded-Index Optical Fibers for Next-Generation Broadband Access

David R. Sánchez Montero and
Carmen Vázquez García

Additional information is available at the end of the chapter

http://dx.doi.org/10.5772/54245

1. Introduction

Growing research interests are focused on the high-speed telecommunications and data communications networks with increasing demand for accessing to the Internet even from home. For instance, in Nov 2011 Strategy Analytics forecasted that there would be more than 807 million broadband fixed line subscriptions worldwide in 2017, based on a figure of 578 million at the end of 2011 showing a cumulative annual growth rate of around 8 percent [1]. This increasing demand for high-speed information transmission over the last two decades has been driven by the huge successes during the last decade of new multimedia services, commonly referred as Next-Generation Access (NGA) services, such as Internet Protocol Television (IPTV) or Video on Demand (VoD), as well as an increased data traffic driven by High-Definition TV (HDTV) and Peer-to-Peer (P2P) applications which have changed people's habits and their demands for service delivery. Consequently, consumer adoption of broadband access to facilitate use of the Internet for knowledge, commerce and, obviously, entertainment is contingent with the increment of the optical broadband access network capacity, which should extent into the customer's premises up to the terminals. Thus, steady increases in bandwidth requirements of access networks and local area networks (LANs) have created a need for short-reach and medium-reach links supporting data rates of Gbps (such as Gigabit Ethernet, GbE), 10Gbps (such as 10-Gigabit Ethernet, 10GbE) and even higher (such as 40- and 100- Gigabit Ethernet standards, namely 40GbE and 100GbE respectively, which started in November 2007 and have been very ratified in June 2010). Detailed studies [2, 3] have defined the required bit-rates to be transmitted to the customer’s premises for different profiles for the traffic flows, reaching a total future-proof very-high-bit-rate link in the order of 2Gbps per user. It is estimated that end-user access bandwidths could reach 1 Gbps by 2015, and 10 Gbps by 2020.

Related to this latter premise, a growing number of service providers are turning to solutions capable of exploiting the full potential of optical fiber for service delivery, being the copper based x-Digital Subscriber Line (xDSL) infrastructure progressively replaced by a fiber-based outside plant with thousands of optical ports and optical fiber branches towards residential and business users, constituting the core of the FTTx (Fiber to the Home/Node/Curb/Business) deployments, see Fig. 1(a). These include passive optical networks (PONs), whose standardization has accelerated product availability and deployment. The ongoing evolution to deliver Gigabit per second Ethernet and the growing trend to migrate to Wavelength Division Multiplexing (WDM) schemes have benefited significantly from the Coarse WDM (CWDM) and Dense WDM (DWDM) optoelectronics technologies, as they provide a more efficient way to deliver traffic to Customer Premises Equipment (CPE) devices. These systems, commonly referred to as WDM-PON, are still under standardization process and field trials and are the basis of the so-called next-generation broadband optical access networks to prepare for the future upgrade of the FTTx systems currently being deployed. A basic scheme of the WDM-PON architecture is depecited in Fig. 1(b). However, networking architectures such as PON, BPON, WDM-PON, etc. are outside the scope of this chapter. There is a widely-spread consensus concerning service providers that FTTx is the most powerful and future-proof access network architecture for providing broadband services to residential users.

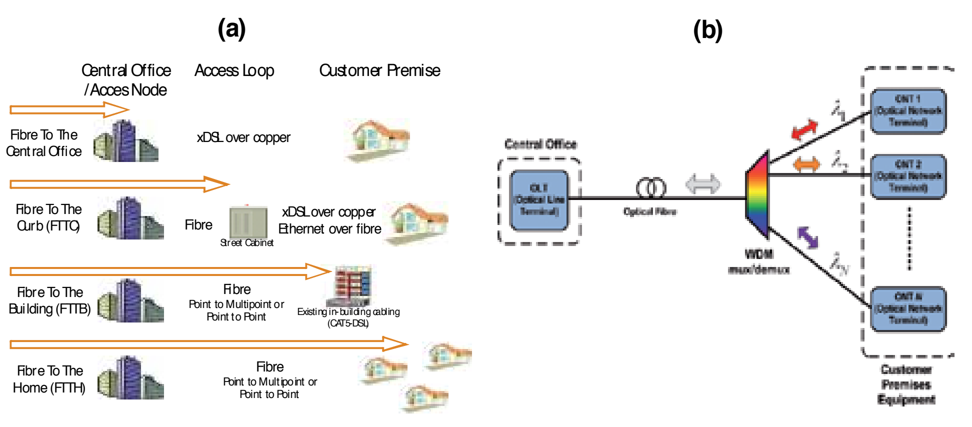

Figure 1. (a) Different FTTx network deployments. (b) Architecture of WDM-PON.

In the FTTx system concepts deployed up to now, singlemode optical fiber (SMF) is used, which has a tremendous bandwidth and thus a huge transport capacity for many services such as the ITU G.983.x ATM[1]-PON system. Research is ongoing to further extend the capabilities of shared SMF access networks. The installation of SMF has now conquered the core and

1 ATM: Asynchronous Transfer Mode.

http://dx.doi.org/10.5772/54245

metropolitan area networks and is subsequently penetrating into the access networks. However, it requires great care, delicate high-precision equipment, and highly-skilled personnel, being mainly deployed for long-haul fiber optic communications, constituting the so-called Optical Distribution Network (ODN) and the core telecommunication network of the next generation of optical broadband access networks. Nevertheless, as it comes closer to the end user and his residential area, the costs of installing and maintaining the fiber network become a driving factor, which seriously hampers the large-scale introduction of FTTx.

Also inside the customer's premises, there is a growing need for convergence of the multitude of communication networks. Presently, Unshielded Twisted copper Pair (UTP) cables are used for voice telephony, cat-5 UTP cables for high-speed data, coaxial cables for CATV[2] and FM[3] radio signals distribution, wireless Local Area Network (LAN) for high-speed data, FireWire for high-speed short-range signals, and also Power Line Communications (PLC) technology for control signals and lower-speed data. These different networks are each dedicated and optimised for a particular set of services, which also put different Quality-of-Service (QoS) demands, and suffer from serious shortcomings when they are considered to serve the increasing demand for broadband services. Also no cooperation between the networks exists. A common infrastructure that is able to carry all the service types would alleviate these problems. It is therefore not easy to upgrade services, to introduce new ones, nor to create links between services (e.g., between video and data). By establishing a common broadband in-house network infrastructure, in which a variety of services can be integrated, however, these difficulties can be surmounted. The transmission media used at present are not suited for provisioning high-bandwidth services at low cost. For instance, today's wiring in LANs is based mainly on copper cables (twisted pair or coaxial) and silica (glass) fiber of two kinds: singlemode optical fiber (SMF) and multimode optical fiber (MMF). Copper based technologies suffer strong susceptibility to electromagnetic interferences and have limited capacity for digital transmission as well as the presence of crosstalk. Compared to these copper based technologies, optical fiber has smaller volume, it is less bulky and has a smaller weight. In comparison with data transmission capability, optical fiber offers higher bandwidth at longer transmission distances.

On the other hand, optical fiber is extensively used for long-distance data transmission and it represents an alternative for transmission at the customer's premises as well. Optical fiber connections offer complete immunity to EMI and present increase security, since it is very difficult to intercept signals transmitted through the fiber. Moreover, optical communication systems based on silica optical fibers allow communication signals to be transmitted not only over long distances with low attenuation but also at extremely high data rates, or bandwidth capacity. In SMF systems, this capability arises from the propagation of a single optical mode in the low-loss windows of silica located at the near-infrared wavelengths of 1.3μm, and 1.55μm. Furthermore, since the introduction of Erbium-Doped Fiber Amplifiers (EDFAs), the last decade has witnessed the emergence of SMF as the standard data trans-

2 CATV: Community Antena TeleVision.

3 FM: Frequency Modulation.

mission medium for wide area networks (WANs), especially in terrestrial and transoceanic communication backbones. The success of the SMF in long-haul communication backbones has given rise to the concept of optical networking, which is a central theme with currently driving research and development activities in the field of photonics. The main objective is to integrate voice, video, and data streams over all-optical systems as communication signals make their way from WANs down to the end user by Fiber-To-The-x (FTTx), offices, and in-homes.

Although conventional SMF solutions have the potential of achieving very large bandwidths, they suffer from high connections costs compared to copper or wireless solutions. For this reason, SMF has not been widely adopted by the end user (premises) where most of the interconnections are needed and less cost-sharing between users is obtainable. The underlying factor is the fact that the SMF core is typically only a few micrometers in diameter with the requirement of precise connecting, delicate installation and handling. Yet as the optical network gets closer to the end user, the system is characterized by numerous connections, splices, and couplings that make the use of thin SMF impractical. An alternative technology is then the use of conventional silica-based multimode optical fiber (MMF) with larger core diameters. This fact allows for easier light coupling from an optical source, large tolerance on axial misalignments, which results in cheaper connectors and associated equipment, as well as less requirements on the skills of the installation personnel. However, the use of MMFs is at a cost of a bandwidth penalty with regards to their SMF counterparts, mainly due to the introduction of modal dispersion. This is the reason why MMF is commonly applied to short-reach and medium-reach applications due to its low intrinsic attenuation despite its limited bandwidth. In particular, in the access network, the use of MMF may yield a considerable reduction of installation costs although the bandwidth-times length product of SMF is significantly higher than that of MMF. As in the access network, the fiber link lengths are less than 10km, however, the bandwidth of presently commercially available silica MMFs is quite sufficient.

On the other hand, compared to multimode silica optical fiber, polymer optical fiber (POF) offers several advantages over conventional multimode optical fiber over short distances (ranging from 100m to 1000m) such as the even potential lower cost associated with its easiness of installation, splicing and connecting. This is due to the fact that POF is more flexible and ductile [4], making it easier to handle. Consequently, POF termination can be realized faster and cheaper than in the case of silica MMF. This POF technology could be used for data transmission in many applications areas ranging like in-home, fiber to the building, wireless LAN backbone or office LAN among others. In addition, improvement in the bandwidth of POF fiber can be obtained by grading the refractive index, thus introducing the so-called Graded-Index POFs (GIPOFs). Although by grading the index profile significantly enhanced characteristics have been obtained, the bandwidth and attenuation still limit the transmission distances and capacity. Reduction of loss has been achieved by using amorphous perfluorinated polymers for the core material. This new type of POF has been named perfluorinated GIPOF (PF GIPOF). This new fiber with low attenuation and large bandwidth has opened the way for high capacity transmission over POF based systems. In addition to, as PF GIPOF has a relative low loss wavelength region ranging from 650nm to 1300nm (even theoretically in the third transmission window), it allows for WDM transmission of several data channels. However, attenuation and bandwidth characteristics of the current state-of-the-art PF GIPOF are not at par with those of standard silica SMFs, but they still are superior to those of copper based technologies. Nevertheless, although these losses are coming down steadily due to ongoing improvements in the production processes of this still young technology, the higher than silica attenuation inhibits their use in relative long link applications, being mainly driven for covering in-building optical networks link lengths for in-building/home optical networks (with link lengths less than 1 km), and thus the loss per unit length is of less importance. It should be noted that available light sources for silica fiber based systems can be used with PF GIPOF systems. The same is true of connectors as in the case of Gigabit Ethernet equipment.

Therefore, it can be stated that polymer optical fiber technology has reached a level of development where it can successfully replace copper based technology and silica MMF for data transmission in short distance link applications such as in the office, in-home and LAN scenarios. Moreover, PF GIPOF is forecasted to be able to support bit-rate distance products in the order of 10Gbps km [5]. Short distance communications system like in-home network and office LANs represent a unique opportunity for deployment of PF GIPOF based systems for broadband applications. We can conclude that PF GIPOF technology is experiencing rapid development towards a mature solution for data transmission at short haul communications. The challenge remains in bringing this POF technology (transceiver, connectors,…) to a competitive price and performance level at the customer's premises.

Nevertheless, the potentials of these multimode fibers, both silica- and polymer-based, to support broadband radio-frequency, microwave and even millimetre wave transmission over short- and medium-reach distances are yet to be fully known. The belief is that a better understanding of the factors that affect the fiber bandwidth will prove very useful in increasing the bandwidth of silica MMF and PF GIPOF links in real situations. In the whole fiber network society to be realized in the near future, it is said that silica-based SMF fibers for long-haul backbone will be only several percents of the total use, and the remaining more than 90% would correspond to all-optical networks covering the last mile [6]. Link lengths may range from well below 1 km in LANs and residential houses, to only a few kilometres in larger building such as offices, hospitals, airport halls, etc. And it is now clear that the expected market is huge and researches and companies all over the world are competing to find a solution to this issue.

In this framework, the first part of this chapter, comprising sections 2 and 3 will briefly address the fundamentals of mutimode optical fibers as well as present transmission capacities. Like any communication channel, the multimode optical fiber also suffers from various signal distortions limiting its usefulness. The primary mechanisms contributing to the channel impairment in multimode fibers are discussed. Both silica-based MMFs and PF GIPOFs are essentially large-core optical waveguide supporting multiple transverse electromagnetic modes and they suffer from similar channel impairments. On the other hand, present capabilities of actual multimode optical fiber-based deployments are shown. In addition, different techniques reported in literature to carry microwave and millimetre-wave over optical networks, surmounting the multimode fiber bandwidth bottleneck, are also briefly described.

The second part of this chapter, which comprises sections 4, 5 and 6, respectively, focuses on the frequency response mathematical framework and the experimental results, respectively, of both types of multimode optical fibers. Some of the key factors affecting the frequency characteristics of both fiber types are addressed and studied. Theoretical simulations and measurements are shown for standard silica-based MMF as well as for PF GIPOF. Although some of these issues are interrelated, they are separately identified for clarity.

Finally, the main conclusions of this chapter are reported in Section 7.

2. Fundamentals of multimode optical fibers

Despite the above advantages, the use of multimode optical fiber has been resisted for some years by fiber-optic link designers in favour of their SMF counterparts since Epworth discovered the potentially catastrophic problem of modal noise [7]. Modal noise in laser-based MMF links has been recently more completely addressed and theoretical as well as experimental proofs have shown that long-wavelength operation of MMFs is robust to modal noise [8-10]. This explains the spectacular regain of interest for MMFs as the best solution for the cabling of the access, in-home networks and LANs. The question that needs answer now in view of increasing the usefulness of MMF concerns the improvement of their dispersion characteristics, which is related to their reduced bandwidth.

For the transmission of communication signals, attenuation and bandwidth are important parameters. Both parameters will be briefly described in the following subsections, focusing on their impact over multimode fibers. In any case, the optical signal is distorted and attenuated when it propagates over the fiber. These effects have to be modeled when describing the signal transmission. They behave quite differently in different types of fibers. Whereas signal distortions in singlemode fibers (SMFs) are primarily caused by chromatic dispersion, i.e. the different speeds of individual spectral parts, the description of dispersion in multimode fibers (MMFs) is considerably more complex. Not only does chromatic dispersion occur in them, but also has the generally much greater modal (or intermodal) dispersion.

It should be noted that, apart from attenuation, an important characteristic of an optical fiber as a transmission medium is its bandwidth. Bandwidth is a measure of the transmission capacity of a fiber data link. As multimode fibers can guide many modes having different velocities, they produce a signal response inferior to that of SMFs, being this modal dispersion effect the limiting bandwidth factor. So bandwidth and dispersion are two parameters closely related.

2.1. Attenuation

Attenuation in fiber optics, also known as transmission loss, is the reduction in the intensity of the light beam with respect to distance traveled through a transmission medium, being an important factor limiting the transmission of a digital signal across large distances. The attenuation coefficient usually use units of dB/km through the medium due to the relatively high quality of transparency of modern optical transmission media. Empirical research over the years has shown that attenuation in optical fiber is caused primarily by both scattering and absorption. However, the fundamentals of both attenuation mechanisms are outside the scope of this chapter.

On the one hand, silica exhibits fairly good optical transmission over a wide range of wavelengths. In the near-infrared (near IR) portion of the spectrum, particularly around 1.5 μm, silica can have extremely low absorption and scattering losses of the order of 0.2 dB/km. Such remarkably-low losses are possible only because ultra-pure silicon is available, being essential for manufacturing integrated circuits and discrete transistors. Nevertheless, fiber cores are usually doped with various materials with the aim of raising the core refractive index thus achieving propagation of light inside the fiber (by means of total internal reflection mechanisms). A high transparency in the 1.4-μm region is achieved by maintaining a low concentration of hydroxyl groups (OH). Alternatively, a high OH concentration is better for transmission in the ultraviolet (UV) region.

On the other hand, until recently, the only commercially available types of POF were based on non-fluorinated polymers such as PolyMethylMethAcrylate (PMMA) (better known as Plexiglass®), widely used as core material for graded-index fiber [11] in addition with the utilization of several kinds of dopants. Although firstly developed PMMA-GIPOFs were demonstrated to obtain very high transmission bandwidth compared to that of Step-Index (SI) counterparts, the use of PMMA is not attractive due to its strong absorption driving a serious problem in the PMMA-based POFs at the near-IR (near-infrared) to IR regions. This is because of the large attenuation due to the high harmonic absorption loss by carbon-hydrogen (C-H) vibration (C-H overtone). As a result, PMMA-based POFs could only be used at a few wavelengths in the visible portion of the spectrum, typically 530nm and 650nm, with typical attenuations around 150dB/km at 650nm. Today, unfortunately, almost all gigabit optical sources operate in the near-infrared (typically 850nm or 1300nm), where PMMA and similar polymers are essentially opaque. Nevertheless, in this scenario, undistorted bit streams of 2.5Gbps over 200m of transmission length were successfully demonstrated over PMMA-GIPOF [12].

On the other hand, it has been reported that one can eliminate this absorption loss by substituting the hydrogen atoms in the polymer molecule for heavier atoms [13]. In this case, if the absorption loss decreases with the substitution of hydrogen for deuterium or halogen atoms (such as fluorine), the possible distance for signal transmission would be limited by dispersion, and not by attenuation. Many polymers have been researched and reported in literature in order to improve the bandwidth performance given by the first PMMA-based graded-index polymer optical fibers [14]. Nevertheless, today, amorphous perfluorinated (PF) GIPOF is widely used because of its high bandwidth and low attenuation from the visible to the near IR wavelengths compared to PMMA GIPOF [15]. As a result, it is immediately compatible with gigabit transmission sources, and can be used over distances of hundreds of meters. This fact is achieved mainly by reducing the number of carbon-hydrogen bonds that exist in the monomer unit by using partially fluorinated polymers. In 1998, the PF-based GIPOF had an attenuation of around 30dB/km at 1310nm. Attenuation of 15dB/km was achieved only three years after and lower and lower values of attenuation are being achieved. The theoretical limit of PF-based GIPOFs is ~0.5 dB/km at 1250-1390nm [16]. In the estimation, the attenuation factors are divided in two: material-inherent scattering loss and material-inherent absorption loss. The first factor is mainly given by the Rayleigh scattering, following the relation $\alpha_R \sim (\lambda)^{-4}$. The second factor is given by the absorption caused by molecular vibrations. A detailed explanation on the estimation processes is described [17].

2.2. Dispersion

As aforementioned, pulse broadening in MMFs is generally caused by modal dispersion and chromatic dispersion. For MMFs it is necessary to consider the factors of material, modal and profile dispersion. The latter considers the wavelength dependence on the relative refractive index difference in graded index fibers. Waveguide dispersion additionally occurs in singlemode fibers, whereas profile dispersion and modal dispersion do not.

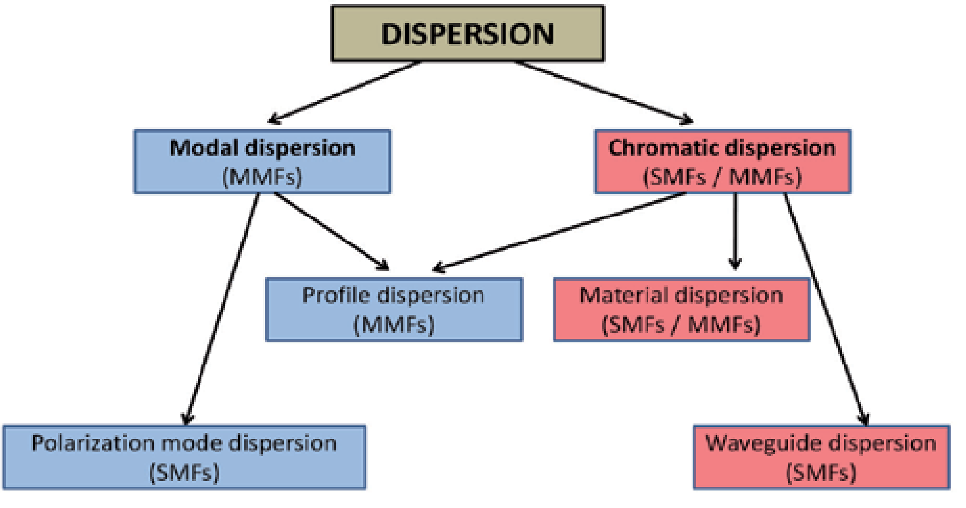

Figure 2. Dispersion mechanisms in optical fibers.

All the kinds of dispersion appearing in optical fibers are summarized in Fig. 2. The mechanisms dependent on the propagation paths are marked in blue, whereas the wavelength-dependent processes are marked in red. Those mechanisms only affecting SMFs are outside from the scope of this work so they will be avoided. For multimode fibers modal dispersion and chromatic dispersion are the relevant processes to be considered.

In a generic description, chromatic dispersion is introduced by the effect that the speed of propagation of light of different wavelengths differs resulting in a wavelength dependence of the modal group velocity. The end result is that different spectral components arrive at

http://dx.doi.org/10.5772/54245

slightly different times, leading to a wavelength-dependent pulse spreading, i.e. dispersion. As a matter of fact, the broader the spectral width (linewidth) of the optical source the greater is the chromatic dispersion. In PF-based POFs the chromatic dispersion is much smaller than in silica MMF for wavelengths up to 1100nm. For wavelengths above 1100nm, the dispersion of the PF-based GIPOF retains and the dispersion of silica MMF increases. The expression of such dispersion is given by:

$$\Delta t_{\text{chrom}} = D(\lambda)\cdot\Delta\lambda\cdot L\ ;\ D(\lambda) = -\frac{\lambda}{c}\cdot\frac{d^2 n(\lambda)}{d\lambda^2} \qquad (1)$$

where $D(\lambda)$ is the material dispersion parameter (usually given in ps/nm·km), $\Delta\lambda$ is the spectral width of the light source, and L is the length of the fiber. Fig. 3(a) depicts a typical material dispersion curve as a function of the operating wavelength. for a PF GIPOF as well as a silica-based MMF with a SiO_2 core doped with 6.3mol-% GeO_2 and a SiO_2 cladding. It is clearly seen the better performance in terms of material dispersion of the PF GIPOF compared to the silica-based counterpart, especially in the range up to 1100nm.

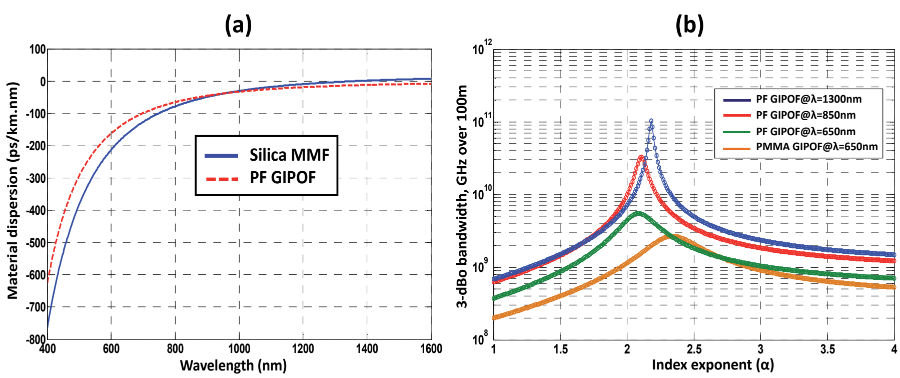

Figure 3. (a) Typical material dispersion of the central core region for a silica-based MMF (blue solid line) and PF GIPOF (red dashed line). (b) Relation between the refractive index profile and bandwidth of 100m-long PF GIPOF. PMMA-GIPOF at 650nm is plotted for comparison.

On the other hand, modal dispersion is caused by the fact that the different modes (light paths) within the fiber carry components of the signals at different velocities, which ultimate results in pulse overlap and a garbled communications signal. Lower order modes propagate mainly along the waveguide axis, while the higher-order modes follow a more zigzag path, which is longer. If a short light pulse is excited at the input of the fiber, the lowest order modes arrive first at the end of the fiber and the higher order modes arrive later. The output pulse will thus be built up of all modes, with different arrival times, so the pulse is broadened.

To overcome and compensate for modal dispersion, the refractive index of the fiber core (or, alternatively, graded index exponent of the fiber core) is graded parabola-like from a high index at the fiber core center to a low index in the outer core region, i.e. by forming a graded-index (GI) fiber core profile. In such fibers, light travelling in a low refractive-index structure has a higher speed than light travelling in a high index structure and the higher order modes bend gradually towards the fiber axis in a shorter period of time because the refractive index is lower at regions away from the fiber core. The objective of the GI profile is to equalise the propagation times of the various propagating modes. Therefore, the time difference between the lower order modes and the higher order modes is smaller, and so the broadening of the pulse leaving the fiber is reduced and, consequently, the transmission bandwidth can be increased over the same transmission length. For negligible modal dispersion the ideal refractive index profile is around 2. This refractive index profile formed in the core region of multimode optical fibers plays a great role determining its bandwidth, because modal dispersion is generally dominant in the multimode fiber although an optimum refractive index profile can produce the minimum modal dispersion, i.e. larger bandwidth being almost independent of the launching conditions [18]. Fig. 3(b) shows the calculated bandwidth of a PF-based GIPOF operating at different wavelengths, in which it is assumed that the source spectral width is 1nm, with regards to the refractive index profile, α. The data of the bandwidth of a PMMA-based GIPOF at 650nm is also shown for comparison showing a maximum limited to approximately 1.8GHz for 100m by the large material dispersion. On the other hand, the smaller material dispersion of the PF polymer-based GIPOF permits a maximum bandwidth of 4GHz even at 650nm. Furthermore, when the signal wavelength is 1300nm, theoretical maximum bandwidth achieves 92GHz for 100m. The difference of the optimum index exponent value between 650nm and 1300nm wavelengths is caused by the inherent polarization properties of material itself. It should be mentioned that a uniform excitation has been assumed and no differential mode attenuation (DMA) and mode coupling (MC) effects have been considered. These effects will be briefly described later on.

To summarize, the different types of dispersion that appear in a MMF and their relation to the fiber bandwidth are analyzed in Fig. 4. This figure reports the PF GIPOF chromatic and modal dispersion and the total bandwidth of a 100m-long link as a function of the refractive index profile, at a wavelength of 1300nm. Fig. 4(b) depicts the corresponding 3-dBo (3-dB optical bandwidth) baseband bandwidth, related to Fig. 4(a). These plots are based on the same analysis of Fig. 3, which assumed a uniform excitation and neglected both the DMA and mode coupling effects. From these figures, the chromatic bandwidth is seen to show little dependence on α, which means that the material dispersion is the dominant contribution (with regards to the profile dispersion) in the transmission window considered. On the other hand, the modal bandwidth shows a highly peaked resonance with α. This is the well known characteristic feature of the grading. With the present choice of parameters values, that maximum bandwidth (i.e. minimum dispersion) approximately occurs at 2.18 at 1300nm, as shown in Fig. 4(a). Furthermore, the presence of crossover points (namely α_1 and α_2) shows that the total bandwidth may be limited either by the modal dispersion or the chromatic dispersion depending on the value of the refractive index profile. Focusing on

Fig. 4(a), the chromatic dispersion will essentially limit the total bandwidth for $\alpha_1 < \alpha < \alpha_2$, whilst for $\alpha < \alpha_1$ or $\alpha > \alpha_2$ the modal dispersion will cause the main limitation. In other words, when the index exponent is around the optimum value (α-resonance), the modal dispersion effect on the possible 3-dB bandwidth (and so on the bit rate) is minimized and the chromatic dispersion dominates this performance. On the other hand, when the index exponent is deviated from the optimum, the modal dispersion increases becoming the main source of bandwidth limitation.

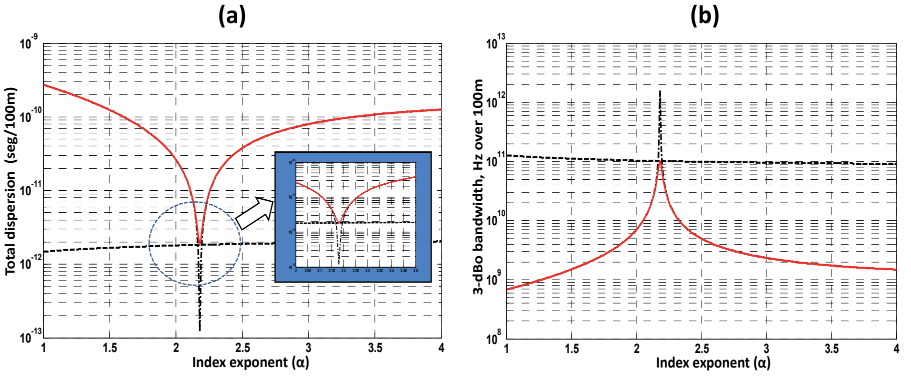

Figure 4. (a) Dispersion effects versus refractive index profile for a 100m-long PF GIPOF, assuming equal power in all modes and a 1300nm light source with 1nm of spectral linewidth. Inset: zoom near the optimum profile region. (b) Corresponding 3-dBo bandwidth. (—) Total dispersion ; **(- -)** Modal dispersion ; (---) Chromatic dispersion.

It is also noteworthy that, since the PF polymer has low material and profile dispersions and the wavelength dependence of the optimum profile is decreased, a high bandwidth performance can be maintained over a wide wavelength range, compared to multimode silica or PMMA-based GIPOF fibers.

2.2.1. Dispersion modelling approach

The propagation characteristics of optical fibers are generally described by the wave equation which results directly from Maxwell's equations and characterizes the wave propagation in a fiber as a dielectric wave guide in the form of a differential equation. In order to solve the equation, the field distributions of all modes and the attendant propagation constants, which results from the use of the boundary conditions, have to be determined.

The wave equation is basically a vector differential equation which can, however, under the condition of weak wave guidance be transformed into a scalar wave equation in which the polarization of the wave plays no role whatsoever [19]. The prerequisite for the weak wave guiding is that the refractive indices between the core and cladding hardly differ, being fulfilled quite well in silica fibers when the difference in refractive index between the core and cladding region is below 1%. Calculations based on the scalar wave equation only show very small inaccuracies with regards to the group delay. Then, the equations which describe the electric and magnetic fields are decoupled so that you can write a scalar wave equation.

The models based on the solution of the wave equation in the form of a mode solver differ fundamentally only in regard to the solution method and whether or not you are proceeding from a more computer-intensive vector wave equation or the more usual scalar wave equation. In the technical literature solutions for the vector wave equation with the aid of finite element method (FEM) [20], with finite differences (Finite Difference Time Domain Method - FDTD) [21] and the beam propagation method (BPM) [22] are well known. These are generally used for very small, mostly singlemode waveguides in which polarization characteristics play a role. Multimode fibers (including polymer fibers) are quite large and the polarization of light counts for only a few centimeters. That is why analytical estimations of the scalar wave equation, the so-called WKB (Wentzel-Kramers-Brillouin, from whom the name derives) Method and Ray Tracing [23], are primarily used for the modeling of multimode fibers. In the latter, the propagating light through an optical system can be seen as the propagation of individual light rays following a slightly different path; these paths can be calculated using standard geometrical optics.

Focusing on the WKB method, the latter primarily makes available expressions, that can be calculated efficiently, for describing the propagations constants and group delays of the propagating modes within the fiber. In this method, whereas the field distributions in step index profile fibers can be determined analytically, the refractive index distribution over the radius of a graded index fiber can generally be described with a power-law, as Eq. 2 states. Fibers with power-law profiles possess the characteristic that the modes can be put in mode groups which have the same propagation constant and also similar mode delay (at least for exponents close to α=2). The propagation times of the modes are only then dependent on the propagation constant and then the group delay can be determined with the aid of the WKB Method by differentiating the propagation constant from the angular frequency [24].

$$n(r,\lambda)=\begin{cases} n_1(\lambda)\left[1-2\Delta(\lambda)\left(\frac{r}{a}\right)^{\alpha}\right]^{1/2} & \text{for } 0\le r\le a \\ n_1(\lambda)\left[1-2\Delta(\lambda)\right]^{1/2} & \text{for } r\ge a \end{cases} \quad \text{with} \quad \Delta(\lambda)=\frac{n_1^{\,2}(\lambda)-n_2^{\,2}(\lambda)}{2n_1^{\,2}(\lambda)} \tag{2}$$

where r is the offset distance from the core center, a is the fiber core radius (i.e. the radius at which the index $n(r, \lambda)$ reaches the cladding value $n_2(\lambda)=n_1(\lambda)[1-2\Delta(\lambda)]^{1/2}$), $n_1(\lambda)$ is the refractive index in the fiber core center, λ is the free space wavelength of the fiber excitation light, α is the refractive index exponent and $\Delta(\lambda)$ is the relative refractive index difference between the core and the cladding. It is usually assumed that the core and cladding refractive index materials follow a three-term Sellmeier function of wavelength [25] given by:

$$n_i(\lambda)=\left(1+\sum_{k=1}^{3}\frac{A_{i,k}\lambda^2}{\lambda^2-\lambda_{i,k}^2}\right)^{1/2} \quad \text{with i=1 (core), 2 (cladding)} \tag{3}$$

where $A_{i,k}$ and $\lambda_{i,k}$ are the oscillator strength and the oscillator wavelength, respectively (both parameters are often gathered under the term of Sellmeier constants).

On the other hand, from the WKB analysis, the modal propagation constants can be approximately derived as following [26], in which each guided mode has its own propagation constant and therefore propagates at its own particular velocity:

$$\beta_m = \beta(m,\lambda) = n_1(\lambda)k\left[1 - 2\Delta(\lambda)\left(\frac{m}{M(\alpha,\lambda)}\right)^{\frac{2\alpha}{\alpha+2}}\right]^{1/2} \tag{4}$$

where m stands for the principal mode number [27] and $k=2\pi/\lambda$ is the free space wavenumber. This so-called principal mode number (mode group number or mode number) can be defined as $m=2\mu+\nu+1$ in which the parameters μ and ν are referred to as radial and azimuthal mode number, respectively. Physically, μ and ν represent the maximum intensities that may appear in the radial and azimuthal direction in the field intensities of a given mode. For a deeper analysis works reported in [28, 29] are recommended. On the other hand, $M(\alpha,\ \lambda)$ is the total number of mode groups that can be potentially guided in the fiber, given by [26]:

$$M(\alpha,\lambda) = 2\pi a\frac{n_1(\lambda)}{\lambda}\left[\frac{\alpha\cdot\Delta(\lambda)}{\alpha+2}\right]^{1/2} \tag{5}$$

As a consequence of Eq. 4, the delay time $\tau(m,\ \lambda)$ of a mode depends only on its principal mode number. It should be mentioned that the differences in modal delay are those that determine the modal dispersion. The delay time of the guided modes (or modal delay per unit length) can be derived from Eq. 4 using the definition:

$$\tau(m,\lambda) = -\frac{\lambda^2}{2\pi c}\frac{d\beta(m,\lambda)}{d\lambda} \tag{6}$$

where c is the speed of light in vacuum, deriving in:

$$\tau_m = \tau(m,\lambda) = \frac{N_1(\lambda)}{c}\left[1 - \frac{\Delta(\lambda)(4+\varepsilon(\lambda))}{\alpha+2}\left(\frac{m}{M}\right)^{\frac{2\alpha}{\alpha+2}}\right]\left[1 - 2\Delta(\lambda)\left(\frac{m}{M}\right)^{\frac{2\alpha}{\alpha+2}}\right]^{-1/2} \tag{7}$$

where $\varepsilon(\lambda)$ is the profile dispersion parameter given by [30]:

$$\varepsilon(\lambda) = -\frac{2n_1(\lambda)}{N_1(\lambda)} \frac{\lambda \dfrac{d\Delta(\lambda)}{d\lambda}}{\Delta(\lambda)} \tag{8}$$

and $N_1(\lambda)$ is the material group index defined by:

$$N_1(\lambda) = n_1(\lambda) - \lambda \frac{dn_1(\lambda)}{d\lambda} \tag{9}$$

2.3. Differential mode attenuation

The distribution of the power among the different modes propagating through the fiber will also be affected by the Differential Mode Attenuation (DMA), also called mode-dependent attenuation, which causes the attenuation coefficient to vary from mode to mode in a different manner. It originates from conventional loss mechanisms that are present in usual optical fibers such as absorption, Rayleigh scattering [31] or losses on reflection at the core-cladding interface [32]. The following functional expression or empirical formula for the DMA is proposed, in which the DMA increases when incresing the mode order [33]:

$$\alpha_m = \alpha_m(m,\lambda) = \alpha_o(\lambda) + \alpha_o(\lambda) I_\rho \left[\eta \left(\frac{m-1}{M} \right)^{\frac{2\alpha}{\alpha+2}} \right] \tag{10}$$

where $\alpha_o(\lambda)$ is the attenuation of low-order modes (i.e intrinsic fiber attenuation), I_ρ is the ϱ-th order modified Bessel function of the first kind and η is a weighting constant. This empirical formula is set up by noticing that most measured DMA data displayed in the literature for long wavelengths conform to the shape of modified Bessel functions [31, 34, 35]. It is also worth mentioning that, during propagation, modes with fastest power loss may be stripped off or attenuated so strongly that they no longer significantly contribute to the dispersion. In other words, the DMA is a filtering effect, which may yield a certain bandwidth enhancement depending on the launching conditions and the transmission length. From Fig. 5 it can be seen that low-order mode groups show similar attenuation (intrinsic fiber attenuation) whereas for high-order mode groups attenuation increases rapidly.

2.4. Mode coupling

Mode coupling is rather a statistical process in which modes exchange power with each other. Due to the mode coupling, the optical energy of the low-order modes would be coupled to higher-order modes, even if only the low-order modes would have launched selectively. This effect generally occurs through irregularities in the fiber, whether they are roughness of the core-cladding interface or impurities in the core material leading, for instance, to refrac-

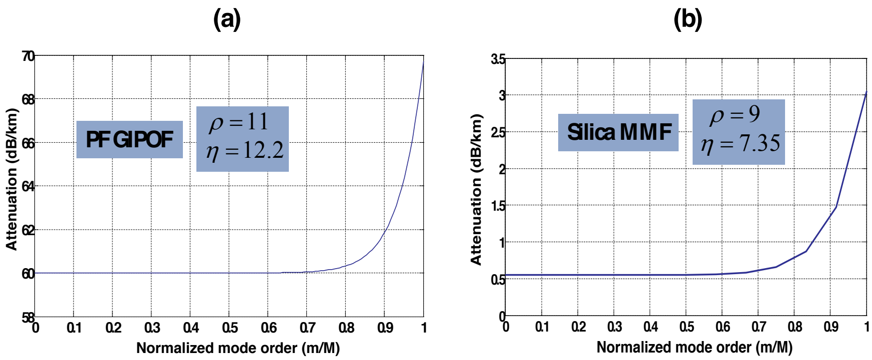

Figure 5. (a) Differential mode attenuation (DMA) as a function of the normalized mode order m/M for a PF GIPOF with a=250μm, α=2, and λ=1300nm. An intrinsic attenuation of 60dB/km@1300nm has been considered. (b) Differential mode attenuation (DMA) as a function of the normalized mode order m/M for a silica MMF with a=31.25μm, α=2, and λ=1300nm. An intrinsic attenuation of 0.55dB/km@1300nm has been considered.

tive index fluctuations. This effect can therefore only be described with statistical means. In addition, it is agreed that silica-based MMFs exhibit far less mode coupling compared to POF fibers [36]. This is attributed to the difference in the material properties.

The main effects for generating mode coupling are Rayleigh and Mie scattering which differ in the size of the scattering centers. Rayleigh scattering arises through the molecular structure of matter which is why no material can have perfectly homogenous properties. Its optical density fluctuates around a mean value which represents the refractive index of the material. These fluctuations are very small and have typical sizes in the range of molecules (<μm). Rayleigh scattering depends on the wavelength and decreases with greater wavelengths as of the fourth power ($\sim \lambda^{-4}$). In constrast, Mie scattering comes from the fluctuations of the refractive index which has greater typical lengths that mostly come about because of impurities in the material such as air bubbles or specks of dust which are large compared with the wavelength of light. The ensuing scattering has more of an effect on the direction of propagation of the light and is independent of the wavelength. Thinking of these aspects mode coupling reveals itself as a complex process which plays a great role in polymer fibers.

There are some approaches for the modeling of mode coupling which cannot be applied equally well in all propagation models [37, 38] while some descriptions present themselves rather in mode models [39]. Moreover, the coupling coefficients which describe the coupling between modes can either be described by analytical attempts which are based on observations of mode overlapping [40, 41]. However, it is demonstrated that in real fibers only very few modes effectively interact with each other and, moreover, neighboring or adjacent modes (those with similar propagation constants, modes m and $m\pm1$, respectively) primarily show strong mode coupling [42, 43]. As a matter of fact, larger core refractive index and higher fiber numerical aperture (NA) values are expected to decrease the mode coupling in GIPOFs. In addition, larger mode coupling effects are observed in SIPOFs compared to that GIPOFs counterparts.

Mode coupling alters the achievable bandwidth of a multimode fiber. According to the laws of statistics, the differential delay (or more precisely, the standard deviation) between the different propagating modes does not increase in a linear relationship to the length but approximately only proportional to the square root of the length. The best known approach for approximately determining the coupling length of the fiber is the description with the aid of a length-dependent bandwidth, in the way $BW \propto L^{\gamma}$. Here the coupling length is the point in which the linear decrease ($\gamma \approx -1$) in the bandwidth turns to a root dependency ($\gamma \approx -0.5$) under mode coupling. From this point, a state of equilibrium arises through mode coupling effects. Typical values of coupling length in silica-based GI-MMFs are in the order of units of kilometers [44] whereas in the case of PF GIPOFs usually range from 50m up to 150m.

3. Multimode optical fiber capabilities

Emerging themes in next-generation access (NGA) research include convergence technologies, in which wireline-wireless convergence is addressed by Radio-over-Fiber (RoF) technologies. Photonics will transport gigabit data across the access network, but the final link to the end-user (measured in distances of metres, rather than km's) could well be wireless, with portable/mobile devices converging with photonics. RoF technologies can address the predicted multi-Gbps data wave, whilst conforming to reduced carbon footprints (i.e. green telecoms). NGA networks will provide a common resource, with passive optical networks (PONs) supplying bandwidth to buildings, and offering optical backhaul for such systems.

Parameter	Remarks
Transmission distances	Typ. <10km, max. 20km, e.g. for alternative topologies
Peak data rate	100Mbps (private customers) Nx1 Gbps up to 10Gbps (business)
Temperature range	Controlled: +10ºC to +50ºC Uncontrolled operation in buildings: -5ºC to +85ºC Uncontrolled operation in the field: -33ºC to +85ºC
Long lifetime	
Humidity and vibrations (shock) have to be considered at non-weather protected locations	
No optical amplifiers in the field	
No optical dispersion compensation	

Table 1. Access network requirements.

It has been indicated by several roadmaps that the peak link data rate should be at least 100Mbps (symmetrical) for private customers and 1 to 10Gbps for business applications. Inherent access network requirements are highlighted in Table 1. These hundreds of megabits per second per user are reasonably reachable in the coming future and the Fiber To The

Home (FTTH, or some intermediate version such as FTT-curb) network constitutes a fiber access network, connecting a large number of end users to a central point, commonly known as an access node. Each access node will contain the required active transmission equipment used to provide the applications and services over optical fiber to the subscriber.

On the one hand, Ethernet is the most widespread wired LAN technology, including in-home networks, and the development of Ethernet standards goes hand in hand with the adoption and development of improved MMF channels [45]. And Ethernet standards for 1Gbps and 10Gbps designed for multimode and singlemode fibers are now in use. Table 2 shows the minimum performance specified by IEEE 802.3 standard for the various interfaces. For example, 10-Gigabit Ethernet (GbE) standard operating at 10.3125Gbps@1300nm supports a range of transmission lengths of 300m over multimode silica fiber and 10km over singlemode silica fiber. Actually OM4 fiber type is under consideration although is not yet within a published standard. OM4 fiber type defines a 50μm core diameter MMF with a minimum modal bandwidth (under OverFilled Launching condition, OFL) of 3500MHz·km@850nm and 500MHz·km@1300nm, respectively. Nevertheless, data rate transmission research achievements are not at par as those covered by the standard and report even greater values. Some significant works are reported in [46-48]. Different techniques or even a combination of some of them were applied to achieved these transmission records. Some of them will be briefly discussed in next section.

Fiber type	10GBaseSR 850nm Modal Bandwidth / Operating Range (MHz·km)/(Meters)	10GBaseLR(/ER) 850nm Modal Bandwidth / Operating Range (MHz·km)/(Km)	10GBaseLRM 1300nm Modal Bandwidth /Operating Range (MHz·km)/ (Meters)
62.5μm*	160/26	n.a.	n.a.
62.5μm (OM-1)**	200/33	n.a.	500/300
50μm	400/66	n.a.	400/240
50μm (OM-2)	500/82	n.a.	500/300
50μm (OM-3)	2000/300.	n.a.	500/300
SMF	n.a.***	10 (/40)	n.a/10000.

*TIA (Telecommunications Industry Association), Document 492AAAA compliance. Commonly referred to as 'FDDI-grade' fiber.

** ISO (International Standards Organization), Document 11801 compliance.

*** n.a.: not available.

Table 2. 10-Gigabit Ethernet transmission over fiber standards (IEEE 802.3aq). Approved in 2006.

Figure 6 provides a brief description of the current 10GbE and the possible future Ethernet standards over copper and fiber links [6]. The trend of extending the reach and data rate of the links is obvious in the previous standards and the 10GbE standards shown in the figure. Although the twisted pair of copper wires is a relatively low-cost and low-power solution compared to the MMF solutions, the motivation for the transition from the copper-based links to the MMF links is their much higher available bandwidth. However, the need for even higher performance MMF solutions is apparent, and much more is to be expected, for example, with new ultra-HDTV format such as 4K (4000 horizontal pixels, with an expected increase in the required bandwidth of a factor of approximately 16).

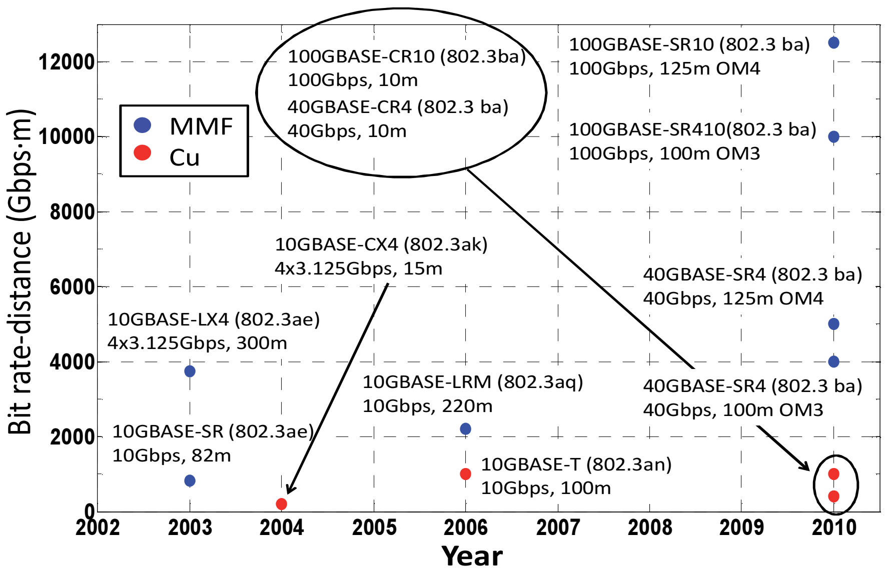

Figure 6. Gigabit Ethernet (10GbE) standards over MMF and copper links [44].

On the other hand, another important point in access networks communications is within the field of the wireless signal transmission (for both mobile and data communication), namely Wireless Local Area Networks (WLANs). Wireless technologies are developing fast but there is a need to link base stations/servers to the antenna by using fixed links together with the future exploitation of capacities well beyond present day standards (IEEE802.11a/b/g), which offer up to 54Mbps and operate at 2.4GHz and 5GHz, as well as 3G mobile networks such as IMT2000/UMTS[4], which offer up to 2Mbps and operate around 2GHz. Moreover, IEEE802.16, otherwise known as WiMAX, is another recent standard aiming to bridge the last mile through mobile and fixed wireless access to the end user at frequencies between 2-11GHz. In addition, WiMAX also aims to provide Fixed Wireless Access at bit-rate in the excess of 100Mbps and at higher frequencies between 10-66GHz. All these services use signals at the radio-frequency (RF) level that are analogue in nature, at least in the sense that they cannot be carried directly by digital baseband modulation. Optical cabling solutions can also offer the possibility for semi-transparent transport of these signals

4 IMT2000: International Mobile Telecommunications-2000 ; UMTS:Universal Mobile Telecommunications System.

by using Radio-over-Fiber (RoF) technology. This RoF technology has been proposed as a solution for reducing overall system complexity by transferring complicated RF modem and signal processing functions from radio access points (RAPs) to a centralised control station (CS), thereby reducing system-wide installation and maintenance costs. Furthermore, although RoF in combination with multimode fibers can be deployed within homes and office buildings for baseband digital data transmission within the Ultra Wide Band (UWB), in general low carrier frequencies offer low bandwidth and the 6GHz UWB unlicensed low band is not available worldwide due to coexistence concerns [49]. These include radio and TV broadcasts, and systems for (vital) communication services such as airports, police and fire, amateur radio users and many others. In contrast, the 60 GHz-band, within millimetre wave, offers much greater opportunities as the resulting high radio propagation losses lead to numerous pico-cell sites and thus to numerous radio access points due to the limited cell coverage. These pico-cells are a natural way to increase capacity (i.e. to accommodate more users) and to enable better frequency spectrum utilisation. Therefore, for broadband wireless communication systems to offer the needed high capacity, it appears inevitable to increase the carrier frequencies even to the range of millimetre-wave and to reduce cell sizes [50]. Considering in-house wireless access networks, coaxial cable is very lossy at such frequencies and the bulk of the installed base of in-building fiber is silica-based MMF. Meanwhile PF GIPOF is also emerging as an attractive alternative, due to the aforementioned low cost potential and easier handling required in in-building networks. It is also mandatory to overcome the modal bandwidth limitation in multimode fibers to deliver modulated high frequency carriers to remote access points.

Following on this, it should be mentioned that PF GIPOFs have been demonstrated capable for transmission of tens of Gbps over distances of hundreds of meters. Some examples are reported in [51-53] in which more than 40Gbps over 100m of PF GIPOF are reported. An overview of some significant works over the years regarding GIPOF transmission can be seen in [54]. This is in contrast with all commercially available step-index POFs (SIPOFs) in which the bandwidth of transmission is limited to about 5MHz·km [6] due to modal dispersion. Therefore, even in the short-range communication scenario, the SIPOF is not able to cover the data rate of more than 100Mbps that would be necessary in many standards of the telecommunication area. Therefore, the SIPOF is mainly aimed at very short-range data-range transmission (less than 50m), image guiding and illumination.

3.1. Multimode optical fiber expanded capabilities

Although multimode fibers, both silica-based and polymer-based counterparts, are the best candidate for the convergence and achievement of a full service access network context, it has been previously addressed their main disadvantage concerning the limited bandwidth performance, limited by modal dispersion. For instance, for standard 62.5/125μm silica-based MMFs, the minimum bandwidths are only specified to be 200MHz·km and 500MHz·km (up to 800MHz·km) in the 850nm and 1300nm transmission windows, respectively, under OverFilled Launch (OFL) condition[5]. Even though these specifications do satisfy the information rate of many classical short-range links, it is clear that a 2km-long campus backbone cannot be realized for operation at the speed of Gigabit Ethernet. This limited bandwidth hampers the desired integration of multiple broadband services into a common multimode fiber access or in-building/home network. Overcoming the bandwidth limitation of such fibers requires the development of techniques oriented to extend the capabilities of multimode fiber networks to attend the consumer's demand for multimedia services.

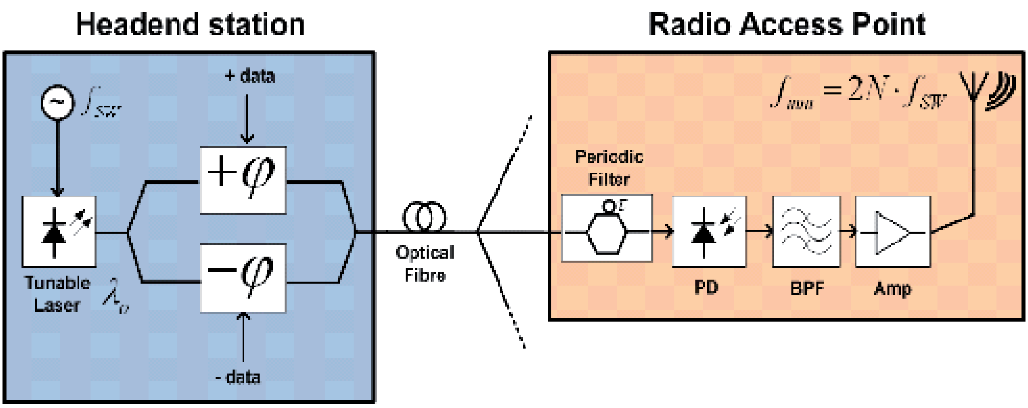

Figure 7. Feeding microwave data signals over a multimode network by OFM technique.

Novel techniques to expand the MMF capabilities and surmount this bandwidth bottleneck are continuously reported demonstrating that the frequency response of MMF does not diminish monotonically to zero after the baseband bandwidth, but tends to have repeated passbands beyond that [55]. In recent times, these high-order passbands and flat regions have been used in research to transmit independent streams of data (digital or analogue) complementary to the baseband bandwidth in order to exceed the aggregated transmission capacity of MMF [56] as well as to transport microwave and mm-wave radio carriers, commonly employed for creating high-capacity picocell wireless networks in RoF systems, as in [57]. Related to this latter technique, the Optical Frequency Multiplying (OFM) is a method by which a low-frequency RF signal is up-converted to a much higher microwave frequency through optical signal processing [58]. At the headend station, a wavelength-tunable optical source is used, of which the wavelength is periodically swept over a wavelength range with a sweep f_{SW} while keeeping its output power constant. The data is then impressed on this wavelength-swept optical signal, see Fig. 7. After having passed through the optical fiber link, the signal impinges on a periodic optical multi-passband filter (e.g. optical comb or Fabry-Perot filter). In sweeping across N transmission peaks of this filter (back and forth during one wavelength sweep cycle), light intensity burts arrive on the photodiode with a frequency $2{\cdot}N{\cdot}f_{SW}$. Thus, the output signal of the photodiode contains a microwave frequency component at the above frequency and higher harmonics of which the strength depends on the bandpass characteristics of the periodic filter. Then, in order to select the desired har-

5 ISO/IEC (International Standards Organization/International Electrotechnical Commission) 11801-"Generic cabling for customer premises".

monic, a bandapss filtering plus some amplification could be implemented. Note that only the optical sweep frequency is limited by the bandwidth of the optical fiber link, and that microwave carrier frequency can exceed this bandwidth by far due to the optical frequency multiplication mechanism. Extremely pure generated microwave signals have been demonstrated, notwithstanding a moderate laser spectral linewidth, due to the inherent phase noise cancellation in the OFM technique [59, 60].

On the other hand, subcarrier multiplexing (SCM) is a mature, simple, and cost effective approach for exploiting optical fiber bandwidth in analogue optical communication systems in general and RoF systems in particular. This technique was firstly addressed at the end of the 1990's in [61], which also takes advantage of the relative flat passband channels existing in the multimode fiber frequency response. Basically, in SCM, the RF signal (the subcarrier) is used to modulate an optical carrier at the transmitter's side. As a result, there is an optical spctrum consisting of the original optical carrier f_0 plus two side-tones located at $f_0 \pm f_{SC}$, where f_{SC} is the subcarrier frequency. If the subcarrier itlsef is modulated with data (either analogue or digital), then sidebands centered on $f_0 \pm f_{SC}$ are produced. Finally, to multiplex multiple channels on to one optical carrier, multiple subcarriers are first combined and then used to modulate the optical carrier [62]. At the receiver's side the sucarriers are recovered through direct detection. One of the main advantages of SCM is that it supports broadband mixed mode data traffic with independent modulation format. Moreover, one subcarrier may carry digital data, while another may be modulated with an analogue signal, such as telephone traffic. However, the frequency ranges suitable for passband transmission vary from fiber to fiber as well as with the fiber length, the launching conditions or if the fiber is subjected to mechanical stress. Nevertheless, to overcome this limitation, an adaptative channel/allocation system would be necessary. Another drawback is that being SCM an analogue communication technique, it becomes more sensitive to noise effects and distortions due to non-linearities in the communications system.

It is worth noting that some other methods try to electrically improve this bandwidth performance using, for example, equalization techniques [63, 64]. In addition to, it is well known than an m-ary digital modulation scheme with m>2 (multi-level coding) can enhance transmission capacity by overcoming the bandwidth limitations of a transmitter or a transmission medium and, therefore, multilevel modulation schemes that are used in radio-frequency communications have also been demonstrated in fiber-optic links [65]. Other attempts to overcome the bandwidth limit includes selective excitation of a limited number of modes, so-called Restricted Mode Launching (RML), in different ways: offset launch [66], conventional center launch [67] or even by means of a twin-spot technique [68]. Since the propagating modes are fewer under RML launch conditions, the difference in propagating times between the fastest and slowest modes is smaller, thus decreasing modal dispersion and increasing the corresponding bandwidth. In a similar way, Mode Group Diversity Multiplexing (MGDM) [69, 70] can be applied, in which the bandwidth increase is achieved by injecting a small light spot radially offset from the fiber core center thus limiting the number of modes excited within the fiber and, therefore, performing different simultaneous data transmission channels depending on the group of modes propagating. On the other hand, from the multimode fiber frequency response, the effect of having a wideband frequency-selective channel for data transmission can be overcome by using orthogonal frequency-division multiplexing (OFDM). In OFDM, the high-data-rate signal is error-correction encoded and then divided into many low-data-rate signals. By doing this, the wideband frequency-selective channel is separated into a series of many narrowband frequency-nonselective channels. OFDM technique has been applied to fiber-optic transmission [71] and shown to offer some protection against the frequency selectivity of a dispersive multimode fiber. Mode filtering techniques, either at the fiber input [72] or its output [73] have also been applied.

As cost is a key issue in local and residential networks, the use of Wavelength Division Multiplexing Passive Optical Network (WDM-PON) architectures for distribution of RoF signals has gained importance recently as WDM enables the efficient exploitation of the fiber network's bandwidth. This architecture acts as the starting point from the access node to the subscribing homes and buildings, constituting the all-optical fiber path. WDM-PON promises to combine both sharing feeder fibers while still providing dedicated point-to-point connectivity [74]. A basic scheme of the WDM-PON architecture can be seen in Fig. 1(b). In this case, optical microwave/mm-wave signals from multiple sources, which can be located in a Central Office (CO) or Optical Line Terminal (OLT) can be multiplexed and the composite signal is transported through an optical fiber and, finally, demultiplexed to address each Optical Network Terminal (ONT) or Remote Access Point (RAP), the latter for wireless applications. However, a challenging issue concerns the applications of these signals as the optical spectral width of a single mm-wave source may approach or exceed the WDM channel spacing.

Finally, it is worth mentioning that there is not the desire of making a competition between optical and wireless solutions, since wireless is and will always be present inside the building or home. In contrast, research and development are focusing on the coexistence of both technologies.

4. Theoretical approach of multimode optical fibers

4.1. Introduction

The restricted bandwidth of the multimode fiber has been one of the main causes that makes the specification and designing of the physical media dependent layer very difficult. Moreover, the potentials of MMFs to support broadband RF, microwave and millimetre wave transmission over short, intermediate and long distances to meet user requirements for higher data rates and to support emerging multimedia applications are yet to be fully known. To enable the design and utilization of MMFs with such enhanced speeds, the development of an accurate frequency response model to describe the signal propagation through multimode fibers is of prime importance. Through this multimode fiber modelling more likely performance limits can be established, thereby preventing eventual overdesign of systems and the resulting additional cost.

Since the mid-1970's, much work has been directed to the investigation of MMFs and their ability for high speed transmission. Different factors have clearly been identified to influence the information-carrying capacity, namely the material dispersion (in combination with the spectrum of the exciting source) [26], the launching conditions [66] as well as the mode-dependent characteristics, i.e. delay [26], attenuation [75] and coupling coefficient [27]. Unfortunately, the achievements, so far accomplished, are not quite complete to enable precise frequency response and bandwidth prediction if an arbitrary operating condition is to be considered.

The most popular technique reported so far for the analysis of signal propagation through MMF fibers is that based on the coupled power-flow equations developed by Gloge [76] in the early 70's and later improved by Olshansky [27] and Marcuse [28], to account for the propagation and time spreading of digital pulses through MMFs. Most of the published models and subsequent work on the modelling of MMFs [29, 77-79] are based on this method in which the MMF power transfer function is solved by means of a numerical procedure like the Crank-Nicholson method, for instance [29]. However, other methods rely on solving the system of coupled equations adopting the matrix formalism [80].

The power-flow equations are adequate for the description of digital pulse propagation through MMFs but present several limitations either when considering the propagation of analogue signals or when a detailed knowledge of the baseband and RF transfer function is required since in these situations the effect of the signal phase is important. To overcome these limitations it is necessary to employ a method relying on the propagation of electric field signals rather than optical power signals. Unfortunately, there are very few of such descriptions available in the literature with the exception of the works reported in [54, 81, 82].

From literature, it is demonstrated that the frequency characteristics of multimode fibers should show significant high-frequency components, i.e. higher-frequency transmission lobes, resonances or passbands are expected in the fiber frequency response. And these higher-frequency transmission lobes would allow to transport information signals by modulating them on specific carrier frequencies, as an independent transmission channel each. These modulated carriers can be positioned in such a way that they will optimally fit into the higher-frequency transmission lobes of the multimode fiber link thus increasing the aggregated transmission capacity over MMFs. Furthermore, it has been stated that the contrast ratio between resonances reveals a dramatically reduction as the frequency increases thus providing potential for broadband transmission at even higher frequencies than those determined by the transmission lobes.

The position of these higher-frequency lobes depends on the fiber link length, and on the exact fiber characteristics, which may vary due to external circumstances such as induced stress by bending or environmental temperature variations. Any system that would take advantage of such high-frequency transmission lobes would have to adapt to those variations, e.g. monitoring the fiber link frequency response by injecting some weak pilot tones, and allocating the subcarriers accordingly would be a feasible solution. Anyway, this in turn is contingent on the availability of accurate models to describe the microwave radio signals propagation over multimode fibers. With such a predictive tool, notwithstanding its restricted bandwidth, a single multimode fiber network that may carry a multitude of broadband services using the higher-order transmission lobes would become more feasible. Thus, easy-to-install multimode fiber networks for access and in-building/home can be realised in which wirebound and wireless services were efficiently integrated.

4.2. Mathematical framework

In this section a closed-form analytic expression to compute the baseband and RF transfer function of a MMF link based on the electric field propagation method is briefly presented. By obtaining an accurate model it is possible to evaluate the conditions upon which broadband transmission is possible in RF regions far from baseband. For a deeper comprehension works reported in [81, 82] are recommended.

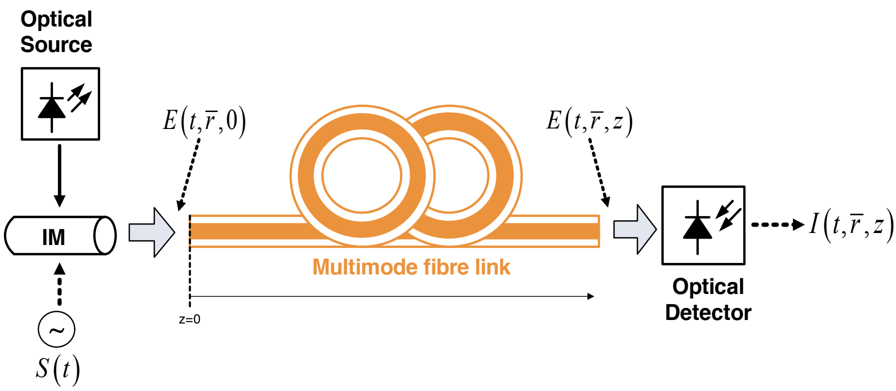

Figure 8. Scheme of a generic Multimode Optical Fiber link. IM: Intensity optical Modulator.

Fig. 8 shows a generic optical transmission system scheme which employs a multimode optical fiber as a transmission medium. $E(t, \bar{r}, z)$ represents the electric field at a point located at a distance z from the fiber origin and at a point $\bar{r}$ of its cross section. $E(t, \bar{r}, 0)$ represents the electric field at the fiber origin and at a point $\bar{r}$ of its cross section and $S(t)$ is the modulation signal composed of a RF tone with modulation index m_o.

Thus the optical intensity at a point z, $I(t, \bar{r}, z)$, depends directly on the electric field $E(t, \bar{r}, z)$ at a point located at a distance z from the fiber origin and at a point $\bar{r}$ of its cross section. Both the electric field and the optical intensity can be expressed, using the electric field propagation model and referred to the system described in Fig. 8, as [82]:

$$E(t,\bar{r},z) = \sum_{\nu=1}^{N}\sum_{\mu=1}^{N}[h_{\mu\nu}(t) * E_{\nu}(t,0)]e_{\nu}(\bar{r}) \tag{11}$$

$$\begin{aligned} I(t,\bar{r},z) \propto \left\langle \left|E(t,\bar{r},z\right|^2 \right\rangle = \sum_{\mu=1}^{N}\sum_{\nu=1}^{N}\sum_{\mu'=1}^{N}\sum_{\nu'=1}^{N} e_{\nu}^{*}(\bar{r})e_{\nu'}(\bar{r}) \cdot \\ \cdot \int_{-\infty}^{\infty}\int_{-\infty}^{\infty} \left\langle h_{\mu\nu}^{*}(t-t')h_{\mu'\nu'}(t-t'')\right\rangle \left\langle E_{\mu}^{*}(t',0)E_{\mu'}(t'',0)\right\rangle dt'dt'' \end{aligned} \tag{12}$$

http://dx.doi.org/10.5772/54245

where N is the number of guided modes, $h_{\mu\nu}(t)$ is the impulse response at z caused by mode ν at the fiber origin over mode μ at z and $e_\nu(r)$ is the modal spatial profile of mode ν. It has been assumed that non linear effects are negligible.

Let $S(t)$ be the modulation signal composed of a RF tone with modulation index m_o assuming a linear modulation scheme (valid for direct and external modulation), which incorporates the source chirp α_C, and approximated by three terms of its Fourier series, following:

$$\sqrt{S(t)} = \sqrt{S_o}\left\{1 + \frac{m_o}{8}(1 + j\alpha_C)e^{j\Omega t} + \frac{m_o}{8}(1 + j\alpha_C)e^{-j\Omega t}\right\} \tag{13}$$

where S_o is proportional to the average optical power and Ω represents the frequency of the RF modulating signal. It has also been assumed an optical source which has a finite linewidth spectrum (temporal coherence) defined by a Gaussian time domain autocorrelation function.

Assuming a stationary temporal coherence of the source and assuming that the detector collects the light impinging on the detector area A_r, and produces an electrical current proportional to the optical power given by:

$$P(t) = \int_{A_r} I\left(t, \bar{r}, z\right) d\bar{r} = \int_{-\infty}^{\infty}\int_{-\infty}^{\infty} \sqrt{S^*(t')S(t'')} \cdot Q(t - t', t - t'')dt'dt'' \tag{14}$$

being

$$Q(t', t'') = R(t', t'')Q_O(t', t'') \text{ and } Q_O(t', t'') = \sum_{\mu=1}^{N}\sum_{\nu=1}^{N}\sum_{\mu'=1}^{N}\sum_{\nu'=1}^{N} C_{\mu\mu'}\chi_{\nu\nu'}\left\langle h^*_{\mu\nu}(t')h_{\mu'\nu'}(t'')\right\rangle \tag{15}$$

From the above equations:

- The term $Q(t', t'')$ is referred to the influence of the source/fiber/detector system.
- The term $Q_O(t', t'')$ depends on the fiber and the power coupling from to the source to the fiber and from the fiber to the detector.
- The spatial coherence of the source related to the fiber modes is provided by $C_{\mu\mu'}$.
- $\chi_{\nu\nu'}$ is defined as $\chi_{\nu\nu'} = \int_{A_r} e^*_\nu(\bar{r})e_{\nu'}(\bar{r})d\bar{r}$. In the special case where the detector collects all the incident light $\chi_{\nu\nu'} = \delta_{\nu\nu'}$.

- The term $\left\langle h^*_{\mu\nu}(t-t^{'})h_{\mu^{'}\nu^{'}}(t-t^{''})\right\rangle$ is referred to the fiber dispersion and to the mode coupling.

This last term, relative to the propagation along the fiber, is composed of two parts, one describing the independent propagation of modes $h^*_{\mu\nu}(t-t^{'})$ and a second one describing the power coupling between modes $h_{\mu^{'}\nu^{'}}(t-t^{''})$. For analysing this term, it is required to consider the N coupled mode propagation equations (field amplitudes) in the frequency domain which refer to an N-mode multimode fiber. A detailed study of this analysis can be found in [54, 82].

Although Eq. (14) reveals a nonlinear relationship between the output and the input electrical signals being not possible to define a transfer function, under several conditions linearization is possible yielding to a linear system with impulse response $Q(t)$. This linear response is given by [81]:

$$P(t) = \int_{-\infty}^{\infty} S(t')Q(t-t', t-t')dt' \tag{16}$$

The impulse response terms of the fiber can then be found by inverse Fourier transforming the above matrix elements. Upon substitution in Eq. (16) it is found that $P(t)$ is composed of two terms $P(t) = P^U(t) + P^C(t)$ being $P^U(t)$ the optical power in absence of mode coupling and $P^C(t)$ the contribution of modal coupling. Moreover, both the coupled and uncoupled parts can be divided into a linear and a non-linear term, respectively. These non-linear terms will contribute to the harmonic distortion and intermodulation effects. Grouping the linear contributions of the uncoupled and the coupled parts, and comparing the power of the lineal part of the total power received (sum of contributions from the coupled and uncoupled parts) with the power of one of the sidebands of the electric modulating signal, it is possible to obtain the final overall RF transfer function, yielding Eq. (17). For a detailed description of the evaluation of both terms, see the works reported in [54, 82].

$$H(\Omega) = \sqrt{1+\alpha_C^2} \cdot e^{-\frac{1}{2}\left(\frac{\beta_o^2 \Omega z}{\sigma_c}\right)^2} \cdot \cos\left(\frac{\beta_o^2 \Omega^2 z}{2} + \arctan(\alpha_C)\right) \cdot \sum_{m=1}^{M} 2m(C_{mm}\chi_{mm} + G_{mm})e^{-2\alpha_m z}e^{-j\Omega\tau_m z} \tag{17}$$

The expression of Eq. (17) provides a description of the main factors affecting the RF frequency response of a multimode fiber link and can be divided as the product of three terms of factors. From the left to the right, the first term is a low-pass frequency response which depends on the first order chromatic dispersion parameter β_o^2 which is assumed to be equal for all the modes guided by the fiber, and the parameter σ_C which is the source coherence time directly related to the source linewidth. The second term is related to the Carrier Sup-

http://dx.doi.org/10.5772/54245

pression Effect (CSE) due to the phase offset between the upper and lower modulation sidebands, as the optical signal travels along a dispersive waveguide, i.e. optical fiber. When the value of this relative phase offset is 180 degrees, a fading of the tone takes place. Finally, the third term represents a microwave photonic transversal filtering effect [83], in which each sample corresponds to a different mode group m carried by the fiber. Coefficients C_{mm}, χ_{mm} and G_{mm} stand for the light injection efficiency, the mode spatial profile impinging the detector area and the mode coupling coefficient, respectively. This last term involves that the periodic frequency response of transversal filters could permit broadband RF, microwave and mm-wave transmissions far from baseband thus achieving a transmission capacity increase in such fiber links. Parameters α_{mm} and τ_{mm} represent the differential mode attenuation (DMA) effect and the delay time of the guided modes per unit length, respectively.

5. Analysis and results on silica-based multimode optical fibers

The MMF transfer function presented in Eq. (17) provides a description of the main factors affecting the RF frequency response of a multimode fiber link, including the temporal and spatial source coherence, the source chirp, chromatic and modal dispersion, mode coupling (MC), signal coupling to modes at the input of the fiber, coupling between the output signal from the fiber and the detector area, and the differential mode attenuation (DMA). Theoretical simulations and experimental results are studied with regards to several parameters in order to determine the optimal conditions for a higher transmission bandwidth in baseband and to investigate the potencials for broadband Radio-over-Fiber (RoF) systems in regions far from baseband using multimode fiber.

For the simulation results in this section it has been considered a 62.5/125μm core/cladding diameter graded-index multimode fiber (GI-MMF) with a typically SiO_2 core doped with 6.3 mol-% GeO_2 and a SiO_2 cladding, and intrinsic attenuation of 0.55dB/km. This typical doping value has been provided by the manufacturer. The refractive indices were approximated using a three-term Sellmeier function for 1300nm and 1550nm wavelengths. Sellmeier coefficients were provided by the manfacturer. Core and cladding refractive indices as a function of wavelength, from the Sellemier equation, Eq. (3), are illustrated in Fig. 9. A comparison of the core refractive index for a different core doped multimode fiber consisting of 7.5mol-% GeO_2 is given. The parameters relative to the differential mode attenuation were fitted to $\rho=9$ and $\eta=7.35$. Coefficient G_{mm} was obtained assuming a random coupling process defined by a Gaussian autocorrelation function [28] with a rms deviation of $\sigma=0.0009$ and a correlation length of $\varsigma=115\cdot a$, being a the fiber core radius. The rms linewidth of the source was set to 10MHz and its chirp parameter to zero. A refractive index profile of $\alpha=2$ was considered. Overfilled launching condition (OFL) was also assumed so that the light injection coefficient was set to $C_{mm}=1/M$, being M the total number of mode groups.

Fig. 10 illustrates the frequency response of a 3km-long GI-MMF link in absence and presence of DMA and mode coupling effects. An optical source operating at 1300nm and with

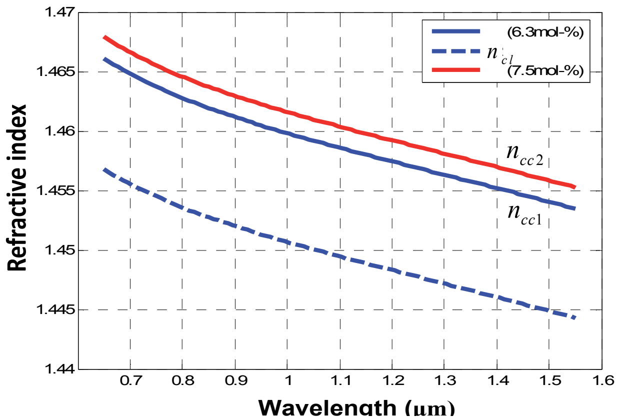

Figure 9. MMF core (n_{ccl}) and cladding (n_{cl}) refractive index for different dopant concentration.

10MHz of linewidth has been considered. The filtering effect caused by the DMA is decreased when considering the presence of the mode coupling phenomenon. Moreover, the RF baseband bandwidth is increased by mode coupling while DMA has little effect on the bandwidth itself. Anyway, not considering mode coupling effects, Fig. 10 illustrates the classical conflict relationship between dispersion and loss in MMFs in general. As a matter of fact, the large DMA of high-order modes necessarily causes a large power penalty during light propagation, but at the same time it yields a bandwidth enhancement as a result of the mode stripping effect. Finally if mode coupling effects are considered, there is no deviation on the resonance central frequencies no matter the fiber DMA whilst DMA has a significant effect when mode coupling is considered to be negligible. $f_o|_n$ refers to the possible transmission channels far from baseband that could be employed.

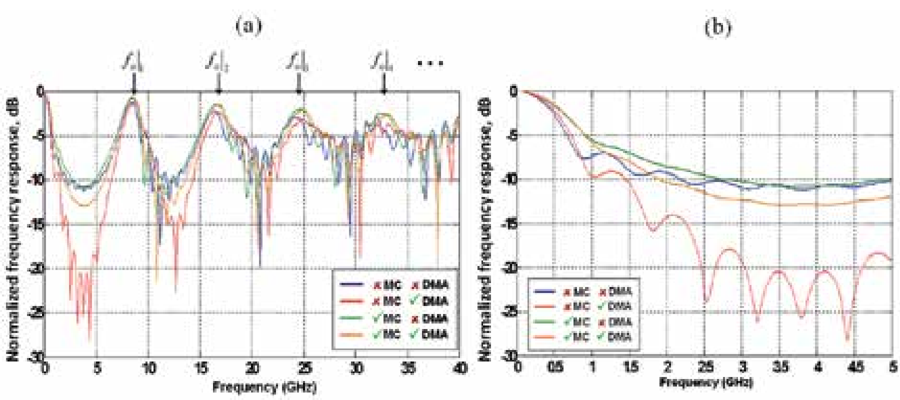

Figure 10. (a) Frequency responses up to 40GHz for a 62.5/125µm GIMMF showing the effect of mode coupling and DMA. L=3km. (b) Zoom up to 5GHz.

The influence of the optical fiber properties over its frequency response is of great importance. Parameters such as the core radius, the graded-index exponent, length and the core refractive index count for this matter. Nevertheless, the most critical parameter that define the behaviour and performance of a graded-index optical fiber type is its refractive index profile α. It should be outlined that this index profile may slightly vary with wavelength, always due to the eventually nonlinear Sellmeier coefficients. As a consequence of this, a profile conceived to be optimal (in terms of bandwidth, for example) at a given wavelength may will be far from optimal at another wavelength. This fact was also addressed in Section 2.2. The α-dispersion is imposed by the dopant and its concentration, so this impairment is not easy to overcome. Furthermore, these latter parameters can also be affected by temperature impairments, as recently reported in [84]. Frequency responses are displayed in Fig. 11(a) for a 2km-long GI-MMF link showing the influence of 1% fiber refractive index profile deviations on the RF transfer function. The rest of parameters for the simulations take the same value as aforementioned. Significant displacements of the high-order resonances over the frequency spectrum are noticed. From simulation conditions, attending to Fig. 11(a), an increase of $\alpha^{'} = \alpha + 0.04$ produces a change of the first-order resonance central frequency of 3.2GHz. It is also noticeable that the 3-dB passband bandwidth of the high-order resonances is also highly influenced. Both facts could cause a serious MMF link fault if multiple-GHz carriers are intended to be transmitted through this physical medium when performing a RoMMF system.

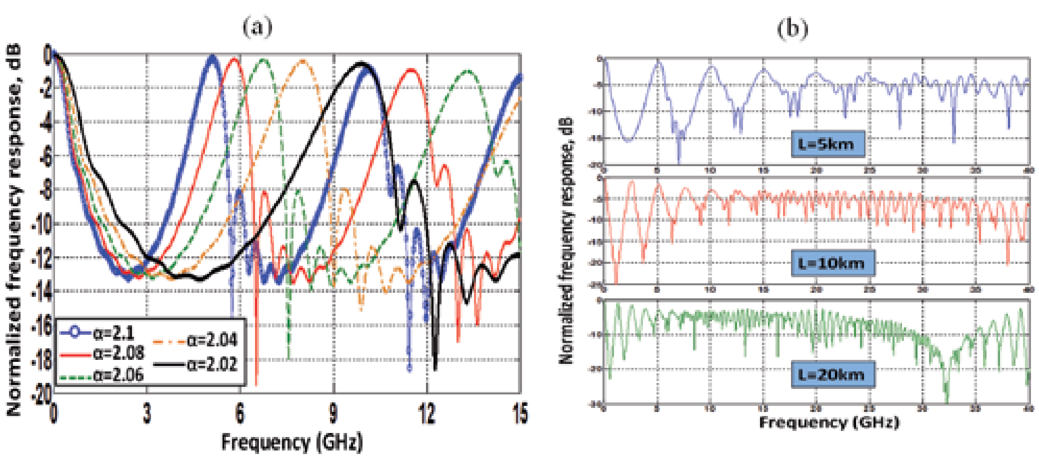

Figure 11. (a) Influence of the refractive index profile on the GI-MMF frequency response for a 2km-long link. (b) GI-MMF frequency response for different link lengths, covering access reach.

The MMF frequency response dependence on the link length is shown in Fig. 11(b), covering typical access network distances. High-order resonances far from baseband are slightly displaced over the frequency spectrum with changes in attenuation depending on the case. In addition, transmission regions can be easily identified as well as the effect of the carrier suppression (CSE) due to the presence of intermediate notches, as seen in the case of L=20km. This effect can not be overlooked but could be avoided using single sideband modulation

Finally, the following figures illustrate both the influence of the optical source linewidth characteristic as well as the launching condition with regards to the GI-MMF frequency response. The influence of other optical source characterisitics such as the source chirp and the operating wavelength can be seen in [54]. It should be noted that wavelength emission provided by the optical source links with different optical fiber properties to be considered. Parameters such as the core and cladding refractive indices, the material dispersion, the propagation constant, the intrinsic attenuation and the number of propagated modes strongly depend on the optical wavelength launched into the fiber, being not an easy task to determine a real comparison about the influence of this parameter on the frequency response.

Fig. 12(a) illustrates the GI-MMF frequency response of a 3km-long link for three different optical sources operating at 1300nm. The rest of parameters take the same value as those previously indicated. The response for the DFB laser (with a Full Width Half Maximum - FWHM- of 10MHz) behaves relatively flat at high frequencies. The frequency response employing a FP laser with 5.5nm linewidth however suffers from a low-pass effect, determined by a 40dB fall at 40GHz. In the case of using a broadband light source, such a Light Emitting Diode (LED) with 30nm of source linewidth, the response falls dramatically after a few GHz and no high-order resonances are observed. On the other hand, the influence of the launching condition on the frequency response can be seen in Fig. 12(b). A GI-MMF link of 1km and an input power spectral density conforming a Gaussian lineshape from a DFB optical source with 10MHz FWHM have been considered. From the frequency response it is noticeable the dramatic enhancement of the baseband bandwidth as well as the achievement of a flat response in all the 20GHz-spectrum considered.

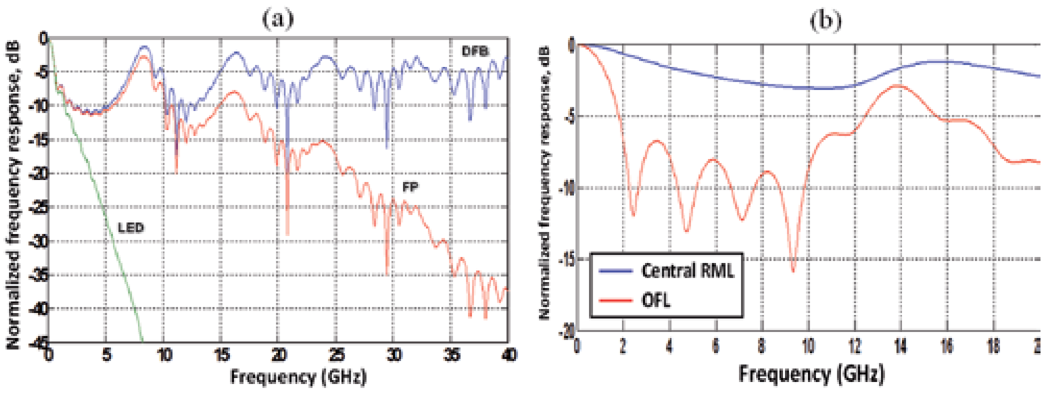

Figure 12. (a) Influence of the optical source temporal coherence on the frequency response of a 3km-long GI-MMF link. (b) Influence of the light injection on the frequency response of a 1km-long GI-MMF link.

By evaluating the latter results, it is observed that exploiting the possibility of transmitting broadband signals at high frequencies is contingent on the use of both narrow-linewidth optical sources and selective mode-launching schemes. These requirements were also confirmed in the work reported in [82].

Some measurement examples of the silica-based MMF transfer function are presented highlighting the conditions upon broadband MMF transmission in regions far from baseband can be featured thus validating the theoretical model described and proposed in [81]. The setup schematic for the experimental measurements is shown in Fig. 13.

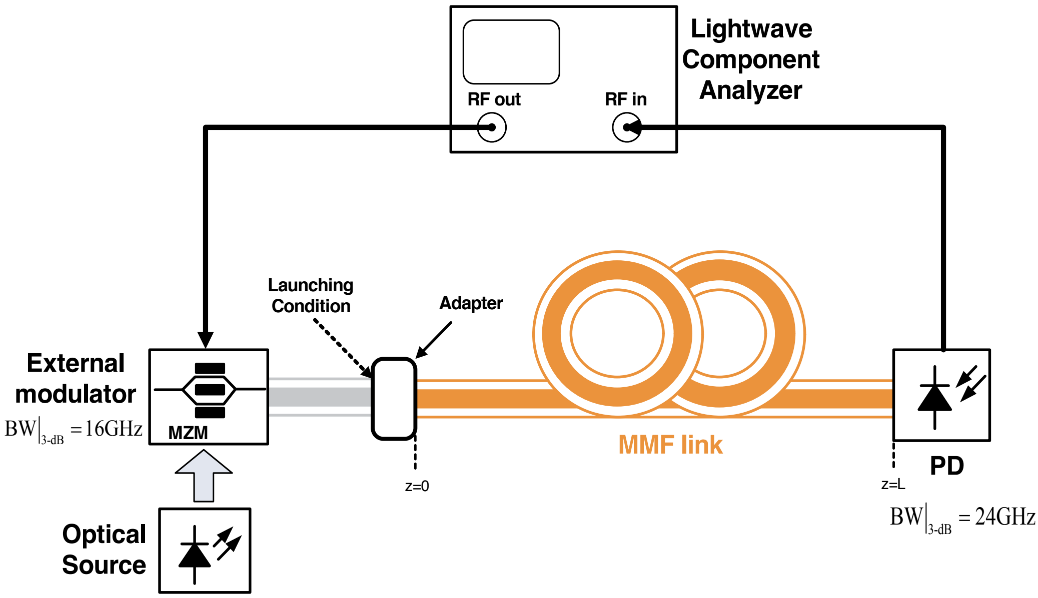

Figure 13. Block diagram of the experimental setup for the silica-based GI-MMF frequency response measurement up to 20GHz.

A Lightwave Component Analyzer (LCA, Agilent 8703B, 50MHz–20GHz) has been used to measure the frequency response, using a 100Hz internal filter. In all cases the laser was externally intensity modulated with an RF sinusoidal signal up to 20GHz of modulation bandwidth, by means of an electro-optic (E/O) Mach-Zehnder modulator (model JDSU AM-130@1300nm and JDSU AM-155@1550nm). At the receiver, the frequency response is detected by using a high-speed PIN photodiode, model DSC30S, from Discovery Semiconductors. It should be mentioned that the experimental results of the silica-based GI-MMF link shown in this section have been calibrated with regards to both the E/O intensity modulator and the photodetector electrical responses, being therefore solely attributed to the MMF fiber. It should be also noted that the ripples observed are caused by reflections in the optical system and are not features of the fiber response, although FC/APC connectors are used to minimize this effect. To perform different launching conditions, the optical output of the E/O modulator was passed through a 62.5/125µm silica-based MMF fiber patch cord plus a mode scrambler before being launched to the MMF link. This optical launching scheme provides an OFL condition for light injection. On the other hand, selective central mode launching was achieved by injecting light to the system via a SMF patchcord.

Fig. 14(a) shows the measured frequency response for a 3km silica-based GI-MMF link. As it was expected from the theory, while the response for the DFB laser (@1550nm) behaves relatively flat at high frequencies, with maximum variations of approximately ± 0.8 dB with regards to a mean level of approximately 2.5dB below the low frequency regime, the response relative to the FP laser (@1310nm) suffers from a low pass effect characterized by a 15dB fall at 20GHz. In the case of the Broadband Light Source (BLS), the response falls dramatically after a few GHz. Therefore, as previously stated, exploiting the possibility of transmitting broadband RF signals at high frequencies is contingent on the use of narrow-linewidth sources. This latter performance stands regardless the operating wavelength from the optical source.

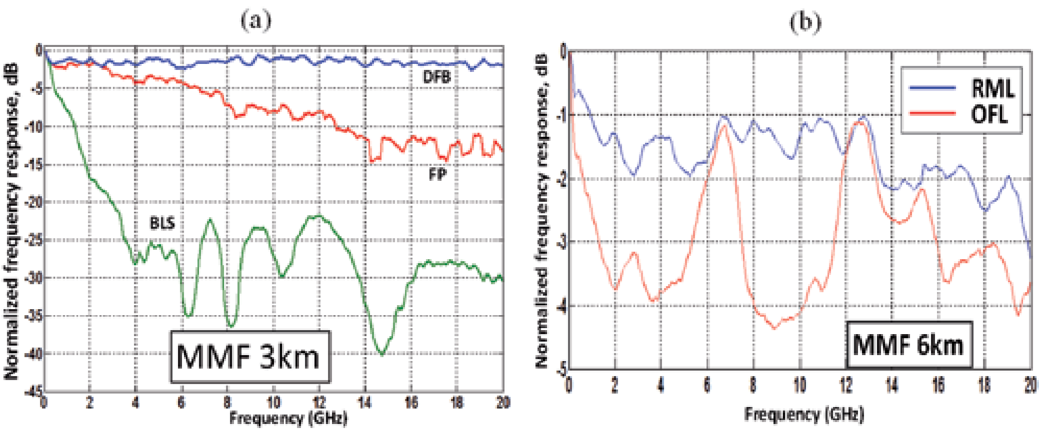

Figure 14. (a) Measured influence of the optical source linewidth on the silica-based GI-MMF frequency response. (b) Measured influence of the launching condition on the silica-based GI-MMF frequency response.

Additionally, two launching conditions, RML and OFL, were also applied to the fiber link. Results are shown in Fig. 14(b), and were performed by using a DFB laser operating at with FWHM of 100kHz. As expected, for the RML condition, in which a limited number of modes is excited, the typical transversal filtering effect of the MMF is significantly reduced, thus achieving an increased flat response over a broader frequency range spectrum. It should be noted that the distance values comprising Fig. 14 are representative of currently deployed moderate-length fiber links.

Finally, the above figures show a comparison between the curves predicted by the theoretical model and the experimental results showing good agreement between them. A FP source operating at 1300nm with $\Delta\lambda$=1.8nm of source linewidth has been employed in measurements reported in Fig. 15(a). An OFL excitation at the fiber input end has been applied. Theoretical curves have been obtained considering a silica-based MMF with a SiO_2 core doped with 6.3mol-% GeO_2 and a SiO_2 cladding, with a refractive index profile of

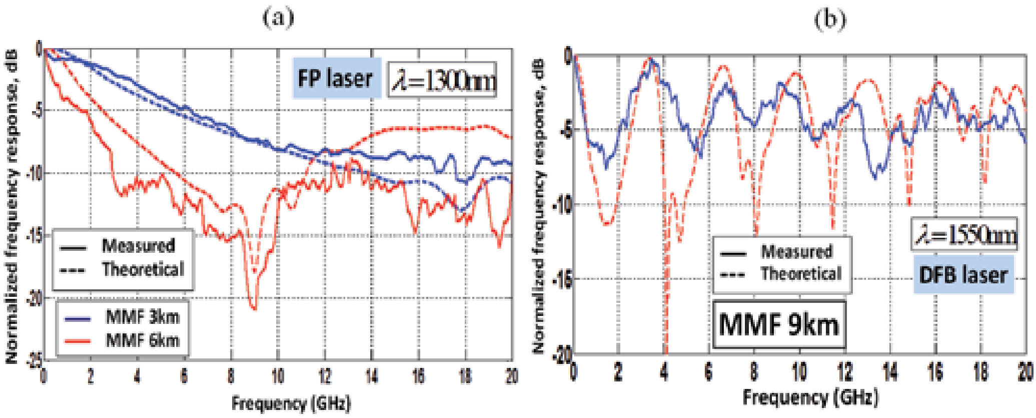

Figure 15. (a) Theoretical and measured frequency response of a 3km- and 6km-long silica based GI-MMF link with a FP laser source operating at 1300nm. (b) Theoretical and measured frequency response of a 9km-long silica-based GI-MMF link with a DFB laser source operating at 1550nm [84].

α=1.921 and an intrinsic attenuation coefficient of α_o=0.59dB/kmat 1300nm. The latter was measured employing Optical Time-Domain Reflectometer (OTDR) techniques. Core and cladding refractive indices have been calculated using a three-term Sellmeier function. It has also been assumed a free chirp source. Differential Mode Attenuation (DMA) effects have been considered by setting ρ=8.7; η=7.35. Additionally, a random coupling process defined by a Gaussian autocorrelation function has beeen defined for the mode coupling with a correlation length of ς=0.0036m and rms deviations of σ=0.0012@3km and σ=0.0017@6km. Fig. 15(a) also addresses the high-order resonances (passband) suppression effect as the source linewidth increases.. This is due to the fact that in this latter case the low pass term in Eq. (17) begins to dominate over the other two. In constrast, in Fig. 15(b), a DFB laser source with 100kHz of linewidth and operating at 1550nm has been employed. An intrinsic fiber attenuation coefficient of α_o=0.31dB/km at 1550nm was measured and a rms deviation of σ=0.0022@9km was considered for a link length of 9km. The rest of parameters take the same values as aforementioned. Several passband channels suitable for multiple-GHz carrier transmission over the frequency spectrum are observed as well as a relatively flat region over 17GHz. However, a significant discrepancy can be observed in the resonances excursions, being the measured ones not so pronounced compare to what the model predicts, i.e. the measured filtering effect is decreased compare to what it is expected. Many reasons can be attributed for this behaviour but mainly due to both the DMA and mode coupling modelling approaches considered.

Finally, although the 3-dB bandwidth of the baseband frequency response has not been paid much attention in this analysis, it is commonly agreed that the measurement uncertainty in characterizing this parameter is quite large and a standard deviation on the order of 10%-20% or more is not uncommon. This performance depends on the care of a particular lab in setting up the launch conditions and acquiring the data. This was verified in 1997 with an informal industry wide round robin [85]. Furthermore, it was, in fact, because of this that the industry standardized the overfilled launch (OFL) condition during the late 1990s [86].

6. Analysis and results on graded-index polymer optical fibers

This section, comprising Graded-Index Polymer Optical Fibers (GIPOFs) will follow the same scheme as previous section. Furthermore, this section proves that the same principles are essentially valid for silica-based MMFs and GIPOFs in order to extend their capabilities beyond the RF baseband bandwidth.

For the simulation results in this section it has been considered a 120/490μm core/cladding diameter graded-index polymer optical fiber (PF GIPOF) with intrinsic attenuation of 60dB/km at 1300nm and 150dB/km at 1550nm. The refractive indices for the fiber core and fiber cladding were calculated using a three-term Sellmeier. These coefficients were provided by the manfacturer. Core and cladding refractive indices as a function of wavelength, from the Sellemier equation, Eq. (3), are illustrated in Fig. 16. The parameters relative to the differential mode attenuation were fitted to $\rho=11$ and $\eta=12.2$. Coefficient G_{mm} was obtained assuming a random coupling process defined by a Gaussian autocorrelation function with a rms deviation of $\sigma=0.0005$ and a correlation length of $\varsigma=1.6\times10^4\cdot a$, being a the fiber core radius. This latter value of the correlation length provides similar mode coupling strengths than that of reported in other works for PF GIPOF fibers such as in [35, 44]. The rms linewidth of the optical source was set to 5nm and its chirp parameter to zero. A refractive index profile of $\alpha=2$ was considered, unless specified. Overfilled launching condition (OFL) was also assumed so that the light injection coefficient was set to $C_{mm}=1/M$, being M the total number of mode groups.

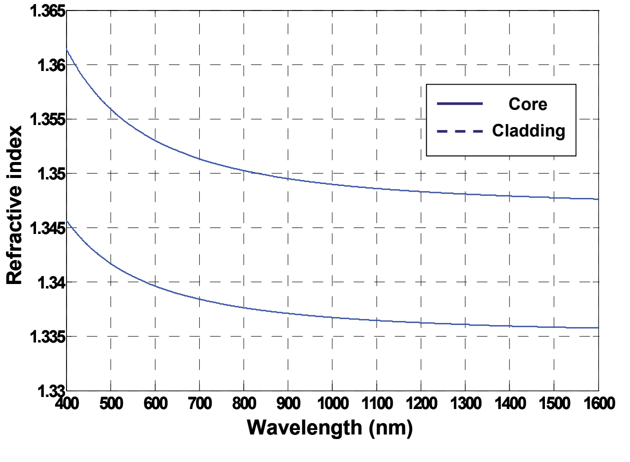

Figure 16. PF GIPOF core and cladding refractive index as a function of wavelength.

It is worth mentioning that with PF GIPOFs, a thermally determined alteration in the dopant material can come about, leading to changes in the refractive index, although new materials have just recently become available and behave with admirable stability in this issue [87]. This dopant concentration during the manufacturing process is also directly related to the fiber refractive index profile.

Fig. 17(a) depicts the frequency response of a 200m-long PF GIPOF link operating at 1300nm in absence and presence of DMA and mode coupling effects. The theoretical curve for a 200m-long PMMA GIPOF in presence of both DMA and mode coupling is also given for comparison. As expected, much greater baseband bandwidths are obtained by using fluorine dopants in the core instead of classical PMMA-based composites. The results indicate that the presence of both effects is favorable for improving the frequency response of the GIPOF. It can be observed a more than a three-fold RF baseband bandwidth enhancement caused if only DMA effect is considered. This result shows that the DMA is a determining factor for accurate assessment of the baseband in GIPOFs. No high-order resonances are shown due to both the high fiber attenuation and the OFL launching condition considered. As in the case of silica-based MMFs, the influence of the optical fiber properties over its frequency response is of great importance. Parameters such as the core radius, the graded-index exponent, length and the core refractive index count for this matter. Similar mechanisms as those stated for silica-based GI-MMFs rule for PF GIPOFs concerning these parameters. This fact is illustrated in Fig. 17(b), in which PF GIPOF frequency responses are displayed for a 200m-long link showing the influence of 5% fiber refractive index profile deviations on the RF transfer function. The rest of parameters for the simulations take the same value as aforementioned. Similarly to silica-based counterparts, significant displacements of the high-order resonances over the frequency spectrum are noticed. However, it is worth pointing out that PF GIPOFs are less sensitive to α-tolarences compared to that of silica counterparts.

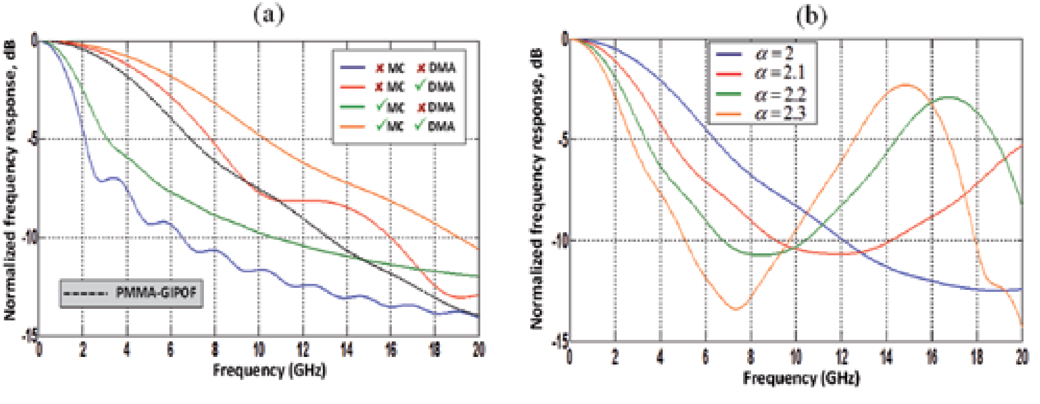

Figure 17. (a) Frequency responses up to 20GHz for a 200m-long PF GIPOF link showing the effect of mode coupling and DMA. Similar PMMA-based link is also illustrated for comparison. (b) Influence of the refractive index profile on the PF GIPOF frequency response for a 200m-long link.

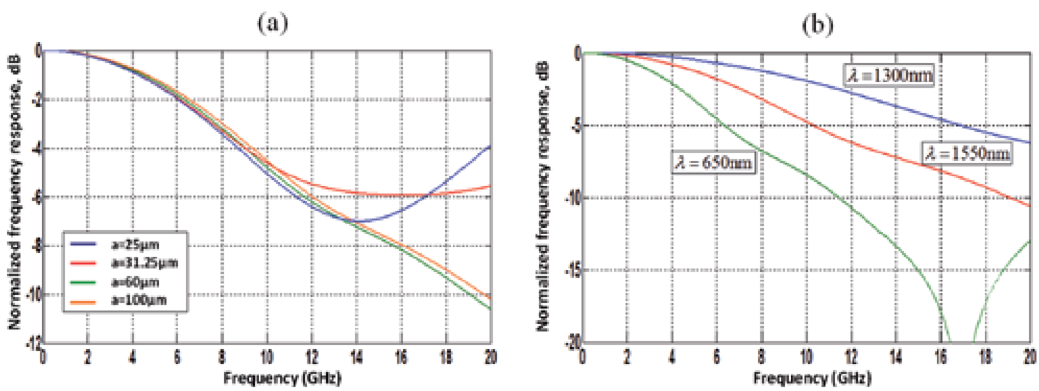

Figure 18. (a) Influence of the core radius on the PF GIPOF frequency response at OFL condition. (b) Influence of the operating wavelength on the PF GIPOF frequency response.

On the other hand, Fig. 18(a) illustrates the frequency response of present commercially available PF GIPOFs with different core radius. Identical simulation parameters have been considered. From the theoretical curves, similar RF baseband bandwidths at OFL condition are obtained, independent from the core radius considered, although high-order resonances start to notice as core radius decreases. However, this fact turns to be different if RML launching is applied. Simulations under this light injection condition predict that lower fiber core radius results in a RF baseband bandwidth enhancement. This result is quite in agreement with the fact that the bandwidth reduction is to be connected with the larger number of excited modes, directly related to the fiber core radius. Nevertheless, this dependence is strongly reduced as nearer OFL is reached. Moreover, the frequency response dependence on the operating wavelength is shown in Fig. 18(b). As expected, due to the high chromatic dispersion of PF GIPOFs at 650nm, see Fig. 3(a), RF baseband bandwidth at this wavelength falls dramatically after few GHz. On the other hand, baseband bandwidths achievable at 1300nm are greater than those obtained at 1550nm despite the similar PF GIPOF material dispersion (even slight smaller at 1550nm) and despite the use of a relatively narrow-linewidth optical source. Thus, bandwidth must mostly be limited by modal dispersion. The reason for this bandwidth difference is supported by the fact that DMA effects are supposed to be stronger at 1300nm than that of 1550nm, leading to a RF baseband bandwidth enhancement.

Finally, the following figures illustrate both the influence of the optical source linewidth characteristic as well as the launching condition with regards to the PF GIPOF frequency response. The influence of other optical source characterisitics such as the source chirp and the operating wavelength can be seen in [54]. Fig. 19(a) illustrates the PF GIPOF frequency response at 1300nm of a 200m-long link for: a DFB optical source with 10MHz of FWHM; a FP laser of 2nm of linewidth; and a LED with 20nm of source linewidth. The rest of parameters take the same value as those previously indicated. As expected, the frequency response is progressively penalised as source linewidth increases, hampering the possible observance of high-order resonances. On the other hand, the influence of the launching condition on the frequency response can be seen in Fig. 19(b). A PF GIPOF link of 200m and an input power spectral density conforming a Gaussian lineshape from a DFB optical source with 0.2nm have been considered. From the frequency response, a dramatic enhancement of the RF baseband bandwidth is observed when applying a RML condition as well as a reduction of the filtering effect, similarly of what it was expected from the silica-based MMF analysis.

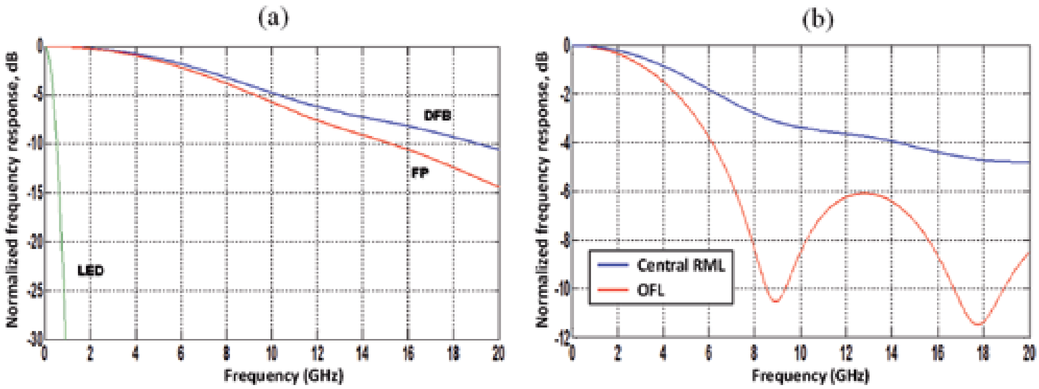

Figure 19. (a) Influence of the optical source temporal coherence on the frequency response of a 200m-long PF GIPOF link. (b) Influence of the light injection on the frequency response of a 200m-long PF GIPOF link.

Some measurement examples of the PF GIPOF transfer function are presented highlighting the conditions upon broadband transmission in regions far from baseband can be featured thus validating the theoretical model proposed [88]. A comparison between the curves predicted by the theoretical model and the experimental results is also provided. Good agreement between theory and experimental results is observed. The results have been tested over an amorphous perfluorinated (PF) graded-index polymer optical fiber. In all cases, such fiber type fulfils the requirements of the IEC[6] 60793-2-40 standard for the PF polymer-based POFs (types A4f, A4g and A4h) which fits a minimum bandwidth of 1500MHz@100m for A4f type and 1880Mhz@100m for A4g and A4h types, respectively. The setup schematic for the experimental measurements follows the same concept as that reported in Fig. 13. The experimental results have been calibrated with regards to both the E/O intensity modulator and the photodetector electrical responses. Similar optical sources as those used in silica-based MMFs experiments were employed. An OFL excitation at the fiber input end has been applied. Theoretical curves have been obtained considering a PF GIPOF with a refractive index profile of α=2.18 and an intrinsic attenuation coefficient of α_o=42dB/km at 1300nm. The latter was measured employing Optical Time-Domain Reflectometer (OTDR) techniques. Core and cladding refractive indices have been calculated using a three-term Sellmeier function. It has also been assumed a free chirp source. Differential Mode Attenuation (DMA) effects have been considered by setting ρ=11; η=12.2. Additionally, a random coupling process defined by a Gaussian autocorrelation function has beeen defined for the mode cou-

6 International Electrotechnical Commission

pling with a correlation length of $\varsigma = 0.005$m and rms deviation of $\varsigma = 1.6 \cdot 10^4 \times a$, being 'a' the core radius of the fiber considered.

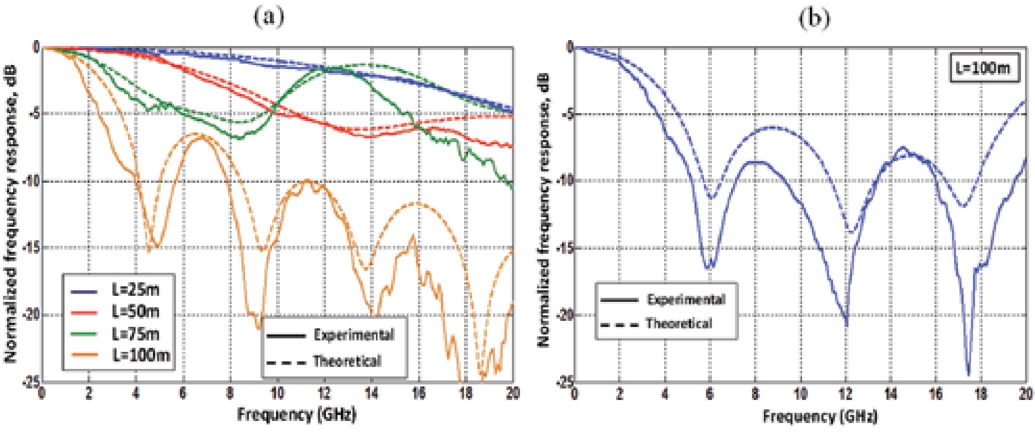

Figure 20. (a) Theoretical and measured frequency response of a 50μm core diameter PF GIPOF link for different lengths with a FP laser source operating at 1300nm. (b) Theoretical and measured frequency response of a 100m-long 62.5μm core diameter PF GIPOF link under identical operating conditions.

Fig. 20(a) depicts the theoretical (dashed line) and measured (solid line) frequency responses of a 50μm core diameter PF GIPOF link for different lengths. On the other hand, the theoretical and measured frequency response of a 100m-long 62.5μm core diameter PF GIPOF link is shown in Fig. 20(b). In both cases, a FP optical source operating at 1300nm and 1.8nm of linewidth was employed. Results reveal the presence of some latent high-order resonances in the PF GIPOF frequency response. Although these passbands suffer from a power penalty in the range of 5dB per passband order, attending to Fig. 20(a), this high attenuation could significantly be improved with lower fiber attenuation values. Nevertheless, the presence of these periodicities in the PF GIPOF frequency response opens up the extension of the transmission capabilities beyond baseband thus increasing the aggregated capacity over this optical fiber type.

Another example can be seen in Fig. 21(a), where the theoretical and measured frequency response of a 150m-long 120μm core diameter PF GIPOF link is depicted. Similar operating conditions as above were applied. In constrast, Fig. 21(b) reports the RF bandwidth enhancement when employing a narrow-linewidth DFB optical source. A 62.5μm core diameter PF GIPOF was used. As expected, the available bandwidth is increased if we compare the curves within this figure with those obtained in Fig. 20(a). However, it is important to observe that the frequency response at 1550nm falls at 17dB at 20GHz. This is due to the fact that the PF GIPOF intrinsic attenuation at this wavelength was measured to be 140dB/km. In both figures an OFL condition was also applied.

Finally, the following figure evaluates the conditions upon which broadband transmission over PF GIPOF beyond the RF baseband bandwidth is possible. Fig. 22(a) shows the meas-

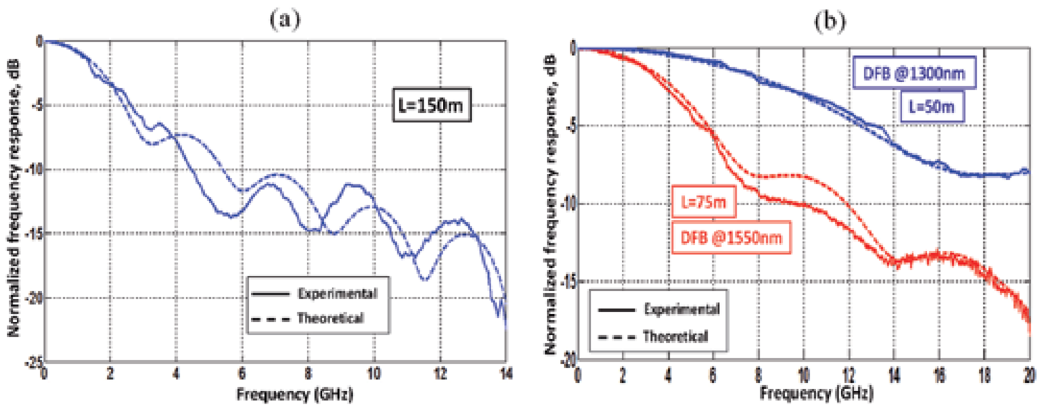

Figure 21. (a) Theoretical and measured frequency response of a 150m-long 120μm core diameter PF GIPOF link, under similar operation conditions as in Fig. 20. (b) Theoretical and measured frequency response of a 62.5μm core diameter PF GIPOF link employing DFB optical sources.

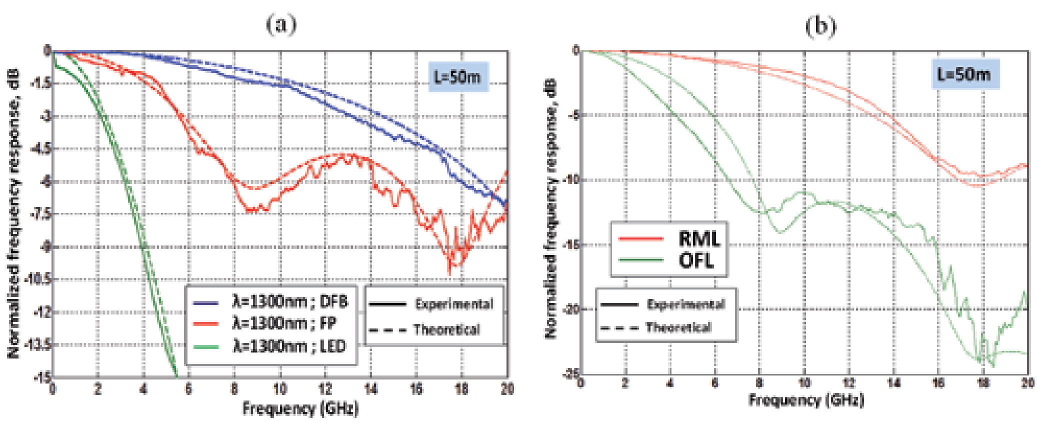

Figure 22. (a) Influence of the optical source temporal coherence on the frequency response of a 50m-long 62.5μm core diameter PF GIPOF link. (b) Measured influence of the launching condition on the 50m-long 120μm core diameter PF GIPOF frequency response.

ured frequency response for a 50m-long 62.5μm core diameter PF GIPOF link at an operating wavelength of 1300nm. As it was expected from the theory, the frequency response dramatically decreases when increasing the rms source linewidth. When a LED with W =98nm of spectral width is employed as the optical source, the frequency response falls after a few GHz. In contrast greater baseband bandwidths when employing a FP laser with W =1.8nm and a DFB source with 100kHz of FWHM are achievable. In addition, the presence of high-order resonances in the frequency response is also identified. On the other hand, Fig. 22(b) illustrates the frequency response of a 50m-long 120μm core diameter PF GIPOF link at launching conditions OFL and RML, respectively. In both cases a FP laser operating at 1300nm and 1.8nm of source linewidth was employed. As expected from theory, RML increases the RF baseband bandwidth as well as flattens the frequency response. However, possible transmission regions beyond baseband are penalised in power due to the high PF GIPOF attenuation compared to that of silica-based counterparts. From both figures, we can therefore conclude, and similarly to silica-based MMFs, that exploiting the possibility of transmitting broadband RF signals in PF GIPOFs at high frequencies is also contingent on the use of narrow-linewidth sources and selective mode-launching schemes.

7. Conclusions

Future Internet Access technologies are supposed to bring us a very performing connection to the main door of our homes. At the same tine, new services and devices and their increase use, commonly grouped as next-generation access (NGA) services, will require data transfers at speeds exceeding 1Gbps inside the building or home at the horizon 2015. Both drivers lead to the deployment of a high-quality, future-proof network from the access domain even to inside buildings and homes. There is a widely-spread consensus that FTTx is the most powerful and future-proof access network architecture for providing broadband services to residential users. Furthermore, FTTx deployments with WDM-PON topologies are considered in the long-term the target architecture for the next-generation access networks. This environment may end up taking advantage of optical cabling solutions as an alternative to more traditional copper or pure wireless approaches.

Multimode optical fibers (MMF), both silica- and polymer-based, can offer the physical infrastructure to create a fusion and convergence of the access network via FFTx for these next-generation access (NGA) services. Both fiber types may be used not only to transport fixed data services but also to transparently distribute in-building (and also for short- and medium-reach links) widely ranging signal characteristics of present and future broadband services leading to a significant system-wide cost reduction. The underlying reason is that multimode fibers have a much larger core diameter and thus alignment in fiber splicing and connectorising is more relaxed. Also the injection of light from optical sources is easier, without requiring sophisticated lens coupling systems. And these facts seem to be critical as all optical networks are being deployed even closer to the end users, where most of interconnections are needed. Moreover, polymer optical fiber (POF) may be even easier to install than silica-based multimode fiber, as it is more ductile, easier to splice and to connect even maintaining high bandwidth performances as in the case of PF GIPOFs. However, their main drawback is related to the fact that their bandwidth per unit length is considerably less with respect to singlemode fiber counterparts. However, this may not be decisive as link lengths are relatively short in the user environment.

On the other hand, it is obvious that the deployment of such emerging NGA network technology and its convergence would be not possible without the research and evaluation of predictive and accurate models to describe the signal propagation through both MMF fiber types to overcome the inherent limitations of such a transport information media. However,

http://dx.doi.org/10.5772/54245

the potentials of MMF to support broadband RF, microwave and millimetre-wave transmission beyond baseband over short and intermediate distances are yet to be fully known, as its frequency response seems to be unpredictable under arbitrary operating conditions as well as fiber characteristics. The different experimental characterizations and the theoretical model presented in this chapter allow understanding and an estimation of the frequency response and the total baseband bandwidth. In addition, can give an estimation of the aggregated transmission capacity over MMFs through analyzing the high-order resonances as well as the presence of relatively flat regions that are present beyond baseband, under certain conditions, in the MMF frequency response.

From the theoretical and experimental results, it is demonstrated that, next to its baseband transmission characteristics, an intrinsically multimode fiber link will show passband characteristics in higher frequency bands. However, the location and the shape of these passbands depend on the actual fiber characteristics, and may change due to environmental conditions and/or the light launching conditions as well as the number of guided modes excited and the power distribution among them. Also the length of the fiber, the mode coupling processes, the source wavelength, the launching scheme, and the fiber core diameter influence the fibre frequency response. This fact imposes a great challenge for the extension of the bandwidth-dependent multimode fiber performance. And, the influence of most of all these parameters that can have a large impact on the date rate transmission performance in MMF links has been addressed. Although no accurate agreement can be expected due to the many approximations made in the theoretical analysis as well as the amount of parameters involved in the frequency response, the results reveal a quite good assessment in the behavior of the multimode optical fiber frequency response compared to the curves predicted by the model

The use of selective mode-launching schemes combined with the use of narrow-linewidth optical sources is demonstrated to enable broadband RF, microwave and millimetre-wave transmission overcoming the typical MMF bandwidth per length product. Under these conditions it is possible to achieve flat regions in the frequency response as well as passband characteristics far from baseband. Transmission of multiple-GHz carrier in these MMF links can be featured at certain frequencies albeit a small power penalty, enabling the extension of broadband transmission, with direct application in Radio-over-Fiber (RoF) systems, in which broadband wireless services could be integrated on the same fiber infrastructure, thereby reducing system costs. The results also reveal that PF GIPOF has some latent high-order passbands and flat regions in its frequency response, which however suffer a high attenuation due to the higher intrinsic attenuation of polymer optical fibers compared to that of silica-based counterparts. Anyway, this power penalty could significantly be improved with lower fiber attenuation values.

To resume, MMFs (both silica- and polymer-based) are still far from SMF bandwidth and attenuation, but they are called to the next step on access network links due to its low cost systems requirements (light sources, optical detectors, larger fiber core,…) against the high cost of the singlemode components. It is worth mentioning that in-building networks may comprise quite a diversity of networks: not only networks within residential homes, but also networks inside office buildings, hospitals, and even more extensive ones such as networks in airport departure buildings and shopping malls. Thus the reach of in-building networks may range from less than 100 metres up to a few kilometers. A better understanding of the possibilities of signal transmission outside the baseband of such fibers are investigated, in order to extend their capabilities, together with the evaluation of current fiber frequency response theoretical models becomes of great importance.

Acknowledgements

The work comprised in this document has been developed in the framework of the activities carried out in the Displays and Photonics Applications group (GDAF) at Carlos III University of Madrid.

This research work has been supported by the following Spanish projects: TEC2006-13273-C03-03-MIC, TEC2009-14718-C03-03 and TEC2012-37983-C03-02 of the Spanish Interministerial Comission of Science and Technology (CICyT) and FACTOTEM-CM:S-0505/ESP/000417 and FACTOTEM-2/2010/00068/001 of Comunidad Autónoma de Madrid.

Additional financial support was obtained from the European Networks of Excellence: ePhoton/One+ (FP6-IST-027497)[7] and and BONE: Building the Future Optical Network in Europe (FP7-ICT-216863)[8]

Author details

David R. Sánchez Montero and Carmen Vázquez García

Displays and Photonics Applications Group (GDAF), Electronics Technology Dpt., Carlos III University of Madrid, Leganés (Madrid), Spain

References

[1] Broadband Network Strategies; Strategy Analytics. Global Broadband Forecast: 2H2011 18 Nov 2011.

[2] Charbonnier, B. End-user Future Services in Access, Mobile and In-Building Networks. FP7 ICT-ALPHA project, public deliv. 1.1p, http://www.ict-alpha.eu, July 2008.

7 ePhoton/One+ is supported by the Sixth Framework Programme (FP6) of the European Union.

8 BONE is supported by the Seventh Framework Programme (FP7) of the European Union.

[3] Meyer, S. Final usage Scenarios Report. FP7 ICT-OMEGA Project, public deliv. 1.1 Aug. 2008.

[4] Ishigure, T., Aruga, Y. and Koike Y. High-bandwidth PVDF-clad GI POF with ultra-low bending loss. Journal of Lightwave Technology 2007; 25(1) 335-345.

[5] Ishigure, T., Makino, K., Tanaka, S. and Koike, Y. High-Bandwidth Graded-Index Polymer Optical Fiber Enabling Power Penalty-Free Gigabit Data Transmission. Journal of Lightwave Technology 2003; 21(11) 2923-2930.

[6] Ziemann, O., Krauser J., Zamzow, P.E. and Daum, W. POF Handbook: Optical Short Range Transmission Systems. Berlin: Springer 2nd Edition; 2008.

[7] Epworth, R.E. The phenomenon of modal noise in analog and digital optical fiber systems. Proceedings of the 4th European Conference on Optical Communications (ECOC), Genova, Italy; 1978.

[8] Bates, R.J.S., Kutcha, D.M. Improved multimode fibre link BER calculations due to modal noise and non-self-pulsating laser diodes. Optical and Quantum Electronics 1995; 27 203-224.

[9] Pepeljugoski, P., Kuchta, D.M. and Risteski, A. Modal noise BER calculations in 10-Gb/s multimode fiber LAN links. IEEE Photonics Technology Letters 2005; 17(12) 2586-2588.

[10] Gasulla I. and Capmany, J. Modal noise impact in Radio over Fiber multimode fiber links. Optics Express 2008; 16(1) 121-126.

[11] Daum, W. Krauser, J., Zamzow P. and Ziemann, O. POF - Polymer Optical Fibers for Data Communication. Germany: Springer; 2002.

[12] Li, W., Khoe, G.D., van den Boom, H.P.A., Yabre, G., de Waardt, H., Koike, Y., Yamazaki, S., Nakamura, K. and Kawaharada, Y. 2.5 Gbit/s transmission over 200 m PPMA graded index polymer optical fiber using a 645 nm narrow spectrum laser and a silicon APD. Microwave and Optical Technology Letters 1999; 20(3) 163-166.

[13] Groh, W. Overtone absorption in macromolecules for polymer optical fibers. Makromoleculare Chemie 1988; 189 2861-2874.

[14] Ishigure, T., Nihei, E. and Koike, Y. Graded-index polymer optical fiber for high-speed data communication. Applied Optics 1994; 33(19) 4261-4266.

[15] Van den Boom, H.P.A., Li, W., van Bennekom, P.K., Tafur Monroy,I. and Khoe, G.D. High-capacity transmission over polymer optical fiber. IEEE Journal on Selected Topics in Quantum Electronics 2001; 7(3) 461-470.

[16] Nihei, E., Ishigure, T., Taniott, N. and Koike, Y. Present prospect of graded-lndex plastic optical fiber in telecommunication. IEICE Transactions on Electronics 1997; E80-C 117-121.

[17] Tanio, N. and Koike, Y. What is the most transparent polymer?. Polymer Journal 2000; 32(1) 119-125.

[18] Ishigure, T., Tanaka, S., Kobayashi, E. and Koike, Y. Accurate refractive index profiling in a graded-index plastic optical fiber exceeding gigabit transmission rates. Journal of Lightwave Technology 2002; 20(8) 1449-1456.

[19] Gloge, D. Dispersion in Weakly Guiding Fibers. Applied Optics 1971; 10(11) 2442-2445.

[20] Liu, Y.E., Rahmna, B.M.A., Ning, Y.N. and Grattan, K.T.V. Accurate Mode Characterization of Graded-Index Multimode Fibers for the Application of Mode-Noise Analysis. Applied Optics 1995; 34 1540-1543.

[21] Xiao, J.B. and Sun, X.H. A Modified full-vectorial finite-difference beam propagation method based on H-fields for optical waveguides with step-index profiles. Optics Communications 2006; 266(2) 505-511.

[22] Huang, W.P. and Xu, C.L. Simulation of 3-Dimensional Optical Wave-Guides by a Full-Vector Beam-Propagation Method. IEEE Journal of Quantum Electronics 1993; 29(10) 2639-2649.

[23] Zubia, J., Poisel, H., Bunge, C.A., Aldabaldetreku, G. and Arrue, J. POF Modelling. Proceedings of the 11th International Conference on Plastic Optical Fiber (ICPOF) Tokyo, Japan, 221-224; 2002.

[24] Marcatili, E.A.J. Modal Dispersion in Optical Fibers with Arbitrary Numerical Aperture and Profile Dispersion. Bell Labs Technical Journal 1977; 6(1) 49-63.

[25] Ishigure, T., Nihei, E. and Koike, Y. Optimum refractive-index profile of the graded-index polymer optical fiber, toward gigabit data links. Applied Optics 1996; 35(12) 2048-2053.

[26] Olshansky, R. and Keck, D.B. Pulse broadening in graded-index optical fibers. Applied Optics 1976; 15 483-491, and errata; Soudagar M.K. and Wali, A.A. Applied Optics 1993; 32 6678.

[27] Olshansky, R. Mode-Coupling Effects in Graded-Index Optical Fibers. Applied Optics 1975; 14 935-945.

[28] Marcuse, D. Theory of Dielectric Optical Waveguides. New York: Academic Press 2nd Edition; 1991.

[29] Yabre, G. Comprehensive Theory of Dispersion in Graded-Index Optical Fibers. Journal of Lightwave Technology 2000; 18(2) 166-177.

[30] Presby, H.M. and Kaminow, I.P. Binary silica optical fibers: refractive index and profile dispersion measurements. Applied Optics 1976; 15(12) 469-470.

[31] Olshansky, R. and Nolan, D.A. Mode-dependent attenuation of optical fibers: Excess Loss. Applied Optics 1976; 15 1045-1047.

[32] Gloge, D. Weakly Guiding Fibers. Applied Optics 1971; 10(10) 2252-2258.

[33] Yabre, G. Theoretical investigation on the dispersion of graded-index polymer optical fibers. Journal of Lightwave Technology 2000; 18(6) 869-877.

[34] Mickelson, A.R. and Eriksrud, M. Mode-dependent attenuation in optical fibers. Journal of the Optical Society of America 1983; 73(10) 1282-1290.

[35] Golowich, S.E., White, W., Reed, W.A. and Knudsen, E. Quantitative estimates of mode coupling and differential modal attenuation in perfluorinated graded-index plastic optical fiber. Journal of Lightwave Technology 2003; 21(1) 111-121.

[36] White, W.R., Dueser, M., Reed, W.A. and Onishi, T. Intermodal dispersion and mode coupling in perfluorinated graded-index plastic optical fiber. IEEE Photonics Technology Letters 1999; 11(8) 997-999.

[37] Cancellieri, G. Mode-Coupling in Graded-Index Optical Fibers Due to Perturbation of the Index Profile. Applied Physics 1980; 23 99-105.

[38] Cancellieri, G. Mode-Coupling in Graded-Index Optical Fibers Due to Micro-Bending. Applied Physics and Materials Science & Processing 1981; 26 51-57.

[39] Su, L., Chiang, K.S. and Lu, C. Microbend-induced mode coupling in a graded-index multimode fiber. Applied Optics 2005; 44(34) 7394-7402.

[40] Ohashi, M., Kitayama, K. and Seikai, S. Mode-Coupling Effects in a Graded-Index Fiber Cable. Applied Optics 1981; 20 2433-2438.

[41] Djordjevich A. and Savovic, S. Investigation of mode coupling in step index plastic optical fibers using the power flow equation. IEEE Photonics Technology Letters 2000; 12(11) 1489-1491.

[42] Donlagic, D. Opportunities to enhance multimode fiber links by application of overfilled launch. Journal of Lightwave Technology 2005; 23(11) 3526-3540.

[43] Ishigure, T., Ohdoko, K., Ishiyama, Y. and Koike, Y. Mode-coupling control and new index profile of GI POF for restricted-launch condition in very-short-reach networks. Journal of Lightwave Technology 2005; 23(12) 4155-4168.

[44] Polley, A. High Performance Multimode Fiber Systems: A Comprehensive Approach. PhD Thesis. Georgia Institute of Technology; December 2008.

[45] Cunningham, D.G., Lane, W.G. and LAne, B. Gigabit Ethernet Networking. Indianapolis: Macmillan; 1999.

[46] Gasulla I. and Capmany, J. 1 Tb/s km Multimode fiber link combining WDM transmission and low-linewidth lasers. Optics Express 2008; 16(11) 8033-8038.

[47] Sim, D.H., Takushima, Y. and Chung Y.C. High-Speed Multimode Fiber Transmission by Using Mode-Field Matched Center-Launching Technique. Journal of Lightwave Technology 2009; 27(8) 1018-1026.

[48] Zeng, J., Lee, S.C.J., Breyer, F., Randel, S., Yang, Y., van den Boom, H.P.A. and Koonen, A.M.J. Transmission of 1.25 Gb/s per Channel over 4.4. km Silica Multimode Fibre Using QAM Subcarrier Multiplexing. Proceedings of the 33th European Conference on Optical Communications (ECOC), paper 7.4.3, Berlin, Germany; 2007.

[49] WiMedia Alliance. Worlwide regulatory status. http://www.wimedia.org.

[50] Koonen, A.M.J. and Garcia Larrode, M. Radio-Over-MMF Techniques, Part II: Microwave to Millimeter-Wave Systems. Journal of Lightwave Technology 2008; 26(15) 2396-2408.

[51] Lee, S.C.J., Breyer, F., Randel, S., Spinnler, B., Polo, I.L.L., van Den Borne, D., Zeng, J., de Man, E., van Den Boom, H.P.A. and Koonen, A.M.J. 10.7 Gbit/s transmission over 220 m polymer optical fiber using maximum likelihood sequence estimation. Proceedings of Optical Fiber Communication and the National Fiber Optic Engineers Conference (OFC/NFOEC), Anaheim, USA; 2007.

[52] Polley, A. and Ralph, S.E. 100 m, 40 Gb/s Plastic Optical Fiber Link. Proceedings of Optical Fiber Communication and the National Fiber Optic Engineers Conference (OFC/NFOEC), San Diego, USA; 2008.

[53] Yang, H., Lee, S.C.J., Tangdiongga, E., Okonkwo, C., van den Boom, H.P.A., Breyer, F., Randel, S. and Koonen, A.M.J. 47.4 Gb/s Transmission Over 100 m Graded-Index Plastic Optical Fiber Based on Rate-Adaptive Discrete Multitone Modulation. Journal of Lightwave Technology 2010; vol. 28(4) 352-359.

[54] Montero, D.S. Multimode Fiber Broadband Access and Self-Referencing Sensor Networks. PhD Thesis. Electronics Technlogy Dpt., Universidad Carlos III de Madrid, Leganés (Madrid), Spain; 2011.

[55] Ingham, J.D., Webster, M., Wake, D., Seeds, A.J., Penty, R.V. and White, I.H. Bidirectional Transmission of 32-QAM Radio Over a Single Multimode Fibre Using 850-nm Vertical-Cavity Half-Duplex Transceivers. Proceedings of the 28th European Conference on Optical Communications (ECOC), Copenhagen, Denmark; 2002.

[56] Gasulla I. and Capmany, J. Simultaneous baseband and radio over fiber signal transmission over a 5 km MMF link. Proceedings of International Topics Meeting on Microwave Photonics Conference (MWP), pp. 209-212, Gold Coast, USA; 2008.

[57] Garcia Larrode, M., Koonen, A.M.J. and Vegas Olmos J.J. Overcoming Modal Bandwidth Limitation in Radio-over-Multimode Fiber Links. IEEE Photonics Technology Letters 2006; 18(22) 2428-2430.

[58] Garcia Larrode, M. and Koonen, A.M.J. Theoretical and Experimental Demonstration of OFM Robustness Against Modal Dispersion Impairments in Radio Over Multimode Fiber Links. Journal of Lightwave Technology 2008; 26(12) 1722-1728.

[59] Garcia Larrode, M., Koonen, A.M.J. and Vegas Olmos, J.J. Fiber-based broadband wireless access employing optical frequency multiplication. IEEE Journal of Selected Topics in Quantum Electronics 2006; 12(4) 875-881.

[60] Garcia Larrode, M., Koonen, A.M.J., Vegas Olmos, J.J. and Ng'Oma, A. Bidirectional radio-over-fiber link employing optical frequency multiplication. IEEE Photonics Technology Letters 2006; 18(1) 241-243.

[61] Raddatz L. and White, I.H. Overcoming the modal bandwidth limitation of multimode fiber by using passband modulation. IEEE Photonics Technology Letters 1999; 11(2) 266-268.

[62] Tyler, E.J., Webster, M., Penty, R.V. and White, I.H. Penalty free subcarrier modulated multimode fiber links for datacomm applications beyond the bandwidth limit. IEEE Photonics Technology Letters 2002; 14(1) 110-112.

[63] Zhao, X. and Choa, F.S. Demonstration of 10-Gb/s transmissions over a 1.5-km-long multimode fiber using equalization techniques. IEEE Photonics Technology Letters 2002; 14(8) 1187-1189.

[64] Pepeljugoski, P., Schaub, J., Tierno, J., Wilson, B., Kash, J., Gowda, S., Wu, H. and Hajimiri, A. Improved Performance of 10 Gb/s Multimode Fiber Optic Links Using Equalization. Proceedings of Optical Fiber Communication and the National Fiber Optic Engineers Conference (OFC/NFOEC), pp. 472-474, Atlanta, USA; 2003.

[65] Raddatz, L., White, I.H., Cunningham, D.G., Nowell, M.C, Tan, M.R.T. and Wang, S.Y. Fiber-optic m-ary modulation scheme using multiple light sources. Proceedings of Optical Fiber Communication and the National Fiber Optic Engineers Conference (OFC/NFOEC), pp. 198-199, Dallas, USA; 1997.

[66] Raddatz, L., White, I.H., Cunningham, D.G. and Nowell, M.C. An experimental and theoretical study of the offset launch technique for the enhancement of the bandwidth of multimode fiber links. Journal of Lightwave Technology 1998; 16(3) 324-331.

[67] Webster, M., Raddatz, L., White, I.H. and Cunningham, D.G. A statistical analysis of conditioned launch for gigabit ethernet links using multimode fiber. Journal of Lightwave Technology 1999; 17(9) 1532-1541.

[68] Sun, Q., Ingham, J.D., Penty, R.V., White, I.H. and Cunningham, D.G. Twin-Spot Launch for Enhancement of Multimode-Fiber Communication Links. Proceedings of Conference on Lasers and Electro-Optics CLEO; Baltimore, USA; 2007.

[69] Stuart, H.R. Dispersive multiplexing in multimode fiber. Science 2000; 289 305-307.

[70] De Boer, M., Tsekrekos, C.P., Martinez, A., Kurniawan, H., Bergmans, J.W.H, Koonen, A.M.J., van den Boom, H.P.A. and Willems, F.M.J. A first demonstrator for a

mode group diversity multiplexing communication system. Proceeding of IEE Seminar on Optical Fibre Communications and Electronic Signal Processing, pp. 0_46-16/5, London, UK; 2005.

[71] Dixon, B.J., Pollard, R.D. and Iezekiel, S. Orthogonal frequency-division multiplexing in wireless communication systems with multimode fiber feeds. IEEE Transactions on Microwave Theory and Techniques 2001; 49(8) 1404-1409.

[72] Shen, X., Kahn, J.M. and Horowitz, M.A. Compensation for multimode fiber dispersion by adaptive optics. Optics Letters 2005; 30(22) 2985-2987.

[73] Patel, K.M., Polley, A., Balemarthy, K. and Ralph, S.E. Spatially resolved detection and equalization of modal dispersion limited multimode fiber links. Journal of Lightwave Technology 2006; 24(7) 2629-2636.

[74] Gu, X.J., Mohammed, W. and Smith, P.W. Demonstration of all-fiber WDM for multimode fiber local area networks. IEEE Photonics Technology Letters 2006; 18(1) 244-246.

[75] Yadlowsky M.J. and Mickelson, A.R. Distributed loss and mode coupling and their effect on time-dependent propagation in multimode fibers. Applied Optics 1993; 32(33) 6664-6677.

[76] Gloge, D. Optical power flow in multimode optical fibers. Bell Labs Technical Journal 1972; 51 1767-1783.

[77] Tatekura, K, Itoh, K. and Matsumoto, T. Techniques and Formulations for Mode Coupling of Multimode Optical Fibers. IEEE Transactions on Microwave Theory and Techniques 1978; 26(7) 487-493.

[78] Djordjevich, A. and Savovic. S. Numerical solution of the power flow equation in step-index plastic optical fibers. Journal of the Optical Society of America: B-Optical Physics 2004; 21 1437-1442.

[79] Zubia, J., Durana, G., Aldabaldetreku, G., Arrue, J., Losada, M.A. and Lopez-Higuera, M. New method to calculate mode conversion coefficients in SI multimode optical fibers. Journal of Lightwave Technology 2003; 21(3) 776-781.

[80] Stepniak, G. and Siuzdak, J. An efficient method for calculation of the MM fiber frequency response in the presence of mode coupling. Optical and Quantum Electronics 2006; 38(15) 1195-1201.

[81] Saleh, B.E.A. and Abdula, R.M. Optical Interference and Pulse-Propagation in Multimode Fibers. Fiber and Integrated Optics 1985; 5 161-201.

[82] Gasulla, I. and Capmany, J. Transfer function of multimode fiber links using an electric field propagation model: Application to Radio over Fibre Systems. Optics Express 2006; 14(20) 9051-9070.

[83] Capmany, J., Ortega, B., Pastor, D. and Sales, S. Discrete-Time Optical Signal Processing of Microwave Signals. Journal of Lightwave Technology 2005; 23(2) 703-723.

[84] Montero, D.S. and Vázquez, C. Temperature impairment characterization in radio-over-multimode fiber systems. Optical Engineering 2012; 51(8) 085001-7.

[85] Hackert, M.J. Characterizing multimode fiber bandwidth for Gigabit Ethernet applications. Proceedings of Symposium on Optical Fiber Measurements 1998; 113-118.

[86] TIA/EIA Fiber Optic Test Procedure (FOTP) 54. Mode Scrambler Requirements for overfilled Launching Conditions to Multi-Mode Fibers; Dec 2001.

[87] Ishigure, T., Sato, M., Kondo, A. and Koike, Y. High-bandwidth graded-index polymer optical fiber with high-temperature stability. Journal of Lightwave Technology 2002; 20(8) 1443-1448.

[88] Montero, D.S. and Vázquez, C. Analysis of the electric field propagation method: theoretical model applied to perfluorinated graded-index polymer optical fiber links. Optics Letters 2011; 36(20) 4116-4118.

Chapter 5

Multicanonical Monte Carlo Method Applied to the Investigation of Polarization Effects in Optical Fiber Communication Systems

Aurenice M. Oliveira and Ivan T. Lima Jr.

Additional information is available at the end of the chapter

http://dx.doi.org/10.5772/53306

1. Introduction

Polarization-mode dispersion (PMD) is a major source of impairments in optical fiber communication systems. PMD causes distortion and broadens the optical pulses carrying information and lead to inter-symbol interference. In long-haul transmission systems it is necessary to limit the penalty caused by polarization effects [1], so that the probability of exceeding a maximum specified penalty, such as 1 dB, will be small, typically 10^{-5} or less. This probability is referred as the outage probability. Since PMD is a random process, Monte Carlo simulations are often used to compute PMD-induced penalties. However, the rare events of interest to system designers, which consists of large penalties, cannot be efficiently computed using standard (unbiased) Monte Carlo simulations or laboratory experiments. A very large number of samples must be explored using standard unbiased Monte Carlo simulations in order to obtain an accurate estimate of the probability of large penalties, which is computationally costly. To overcome this hurdle, advanced Monte Carlo methods, such as importance sampling (IS) [2], [3] and multicanonical Monte Carlo (MMC) [4] methods, have been applied to compute PMD-induced penalties [5], [6] using a much smaller number of samples. The analytical connections between MMC and IS are presented in [7], [8], [9], [10]. The MMC method has also been used to estimate the bit-error rate (BER) in optical fiber communication systems due to amplified spontaneous emission noise (ASE) [11], for which no practical IS implementation has been developed, and to estimate BER in spectrum-sliced wavelength-division-multiplexed (SS-WDM) systems with semiconductor optical amplifier (SOA) induced noise [12]. More recently, MMC has been used in WDM systems, where the performance is affected by the bit patterns on the various channels and, in order to account for this pattern dependence, a large number of simulations must be performed [13].

In optical fiber communication systems without PMD compensators, the penalty is correlated with the differential group delay (DGD) due to PMD. As a consequence, one can apply IS to bias the DGD [2] for the computation of PMD-induced penalties. However, biasing the DGD alone is inadequate to compute penalties in compensated systems. On the other hand, the use of multiple IS in which both first-and second-order PMD are biased [3] allows one to efficiently study important rare events with large first-and second-order PMD. In [5] and [14], we used multiple IS to bias first-and second-order PMD to compute the outage probability due to PMD in uncompensated systems and in compensated systems with a single-section PMD compensator. The development of IS requires some *a priori* knowledge of how to bias a given parameter in the simulations. In this particular problem, the parameter of interest is the penalty. However, to date there is no IS method that directly biases the penalty. Instead of directly biasing the penalty, one has to rely on the correlation of the first-and second-order PMD with the penalty, which may not hold in all compensated systems. In contrast to IS, MMC does not require *a priori* knowledge of which rare events contribute significantly to the penalty distribution function in the tails, since the bias is done automatically in MMC.

In this chapter, we investigated and applied MMC and IS to accurately and efficiently compute penalties caused by PMD. Using these techniques, we studied the performance of PMD compensators and compared the efficiency of these two advanced Monte Carlo methods to compute the penalty of several types of compensated systems. Since Monte Carlo methods are not deterministic, error estimates are essential to verify the accuracy of the results. MMC is a highly nonlinear iterative method that generates correlated samples, so that standard error estimation techniques cannot be applied. To enable an estimate of the statistical error in the calculations using MMC, we developed a method that we refer to as the MMC transition matrix method [15]. Because the samples are independent in IS simulations, one can successfully apply standard error estimation techniques and first-order error propagation to estimate errors in IS simulations. In this chapter, we also estimate the statistical errors when using MMC and IS. Practical aspects of MMC and IS implementation for optical fiber communication systems are also discussed; in addition, we provide practical guidelines on how MMC can be optimized to accurately and rapidly generate probability distribution functions.

2. MMC Implementation and Estimation of Errors in MMC simulations

In this section, we show how the MMC method can be implemented to PMD emulators and to compute PMD-induced penalty in systems with and without PMD compensators, and also show how one can efficiently estimate errors in MMC simulations using the MMC Transition Matrix method that we developed [15]. For example, when using a standard, unbiased Monte Carlo simulation to calculate the probability density function (pdf) of a statistical

http://dx.doi.org/10.5772/53306

quantity, such as the DGD, each sample drawn is independent from the other sample. Hence, when the histogram is smooth, one can infer that the error is acceptably low. The same is not true in MMC simulations because the MMC algorithm requires a substantial degree of correlation among the samples to effectively estimate the histogram, which induces a correlation between the calculated values of the probabilities of neighboring bins. Therefore, it is essential to be able to estimate errors particularly in MMC simulation to assess the accuracy of the calculation.

2.1. Multicanonical Monte Carlo method for PMD-Induced penalty

In this sub-section, we briefly review the multicanonical Monte Carlo (MMC) method proposed by Berg and Neuhaus [16], and we describe how we implemented MMC to compute the probability density function (pdf) of the differential group delay (DGD) for PMD emulators. Then, we present results showing the correlation among the histogram bins of the pdf of the DGD that is generated using the MMC method. Finally, we present results with the application of MMC to compute the PMD-induced penalty in uncompensated and single-section compensated system. In particular, we use contours plots to show the regions in the $|\boldsymbol{\tau}|-|\boldsymbol{\tau}_\omega|$ plane that are the dominant source of penalties in uncompensated and single-section PMD compensated systems.

2.1.1. *The multicanonical Monte Carlo method*

In statistical physics applications, a conventional canonical simulation calculates expectation values at a fixed temperature *T* and can, by re-weighting techniques, only be extrapolated to a vicinity of this temperature [17]. In contrast, a single multicanonical simulation allows one to obtain expectation values over a range of temperatures, which would require many canonical simulations. Hence, the name multicanonical [16], [17]. The multicanonical Monte Carlo method is an iterative method, which in each iteration produces a biased random walk that automatically searches the state space for the important rare events. Within each iteration, the Metropolis algorithm [18] is used to select samples for the random walk based on an estimated pdf of the quantity of interest or control parameter, which is updated from iteration to iteration. Each new sample in the random walk is obtained after a small random perturbation is applied to the previous sample. In each MMC iteration, a histogram of the control parameter is calculated that records how many samples are in each bin. In each iteration, one generates a pre-determined number of samples that can vary from iteration to iteration. Typically, each iteration has several thousand samples. Once the pre-determined number of samples in any iteration has been generated, the histogram of the control parameter is used to update the estimate of the probability of all the bins as in [16], which will be used to bias the following iteration. After some number of iterations, typically 15 - 50, the number of samples in each bin of the histogram of the control quantity becomes approximately constant over the range of interest, indicating that the estimated pdf of the control quantity is converging to the true pdf.

2.1.2. MMC implementation to PMD emulators

In the computation of the pdf of the DGD, the state space of the system is determined by the random mode coupling between the birefringent sections in an optical fiber with PMD, and the control parameter E is the DGD, as in [19]. When applying MMC, the goal is to obtain an approximately equal number of samples in each bin of the histogram of the control quantity. We compute probabilities by dividing the range of DGD values into discrete bins and constructing a histogram of the values generated by the different random configurations of the fiber sections. The calculations are based on coarse-step PMD emulators consisting of birefringent fiber sections separated by polarization scramblers [20]. We model the fiber using emulators with N_s=15 and N_s=80 birefringent sections. Prior to each section, we use a polarization scrambler to uniformly scatter the polarization dispersion vector on the Poincaré sphere. When polarization scramblers are present, the evolution of the polarization dispersion vector is equivalent to a three-dimensional random walk, and an exact solution [21] is available for the pdf of the DGD that can be compared with the simulations. In unbiased Monte Carlo simulations, the unit matrix $R = R_x(\phi)R_y(\gamma)R_x(\psi)$ rotates the polarization dispersion vector before each section, such that the rotation angles around the x-axis in the i-th section, ϕ_i and ψ_i, have their pdfs uniformly distributed between $-\pi$ and π, while the cosine of the rotation angle γ_i around y-axis has its pdf uniformly distributed between -1 and 1.

Within each MMC iteration, we use the Metropolis algorithm to make a transition from a state k to a state l by making random perturbations $\Delta\phi_i$, $\Delta\gamma_i$, and $\Delta\psi_i$ of the angles ϕ_i, γ_i, and ψ_i in each section, where $\Delta\phi_i$, $\Delta\gamma_i$, and $\Delta\psi_i$ are uniformly distributed in the range $[-\varepsilon\pi, \varepsilon\pi]$. To keep the average acceptance ratio close to 0.5 [22], we choose the coefficient of perturbation ε=0.09. This perturbation is small, since it does not exceed 10% of the range of the angles. In order to further optimize the MMC simulations and avoid sub-optimal solutions, the random perturbation should also be optimized. We are currently investigating the dependence of the relative error obtained in MMC simulations on the random perturbation and coefficient of perturnation used. The results of this investigation will be published in another publication.

To obtain the correct statistics in γ_i, since in the coarse step method the cosine of γ_i is uniformly distributed, we accept the perturbation $\Delta\gamma_i$ with probability equal to $\min[1, F(\gamma_i + \Delta\gamma_i)/F(\gamma_i)]$, where $F(\gamma) = 0.5(1-\cos^2\gamma)^{1/2}$. When the perturbation is not accepted, we set $\Delta\gamma_i$=0. The random variable with acceptance probability given by $\min[1, F(\gamma_i + \Delta\gamma_i)/F(\gamma_i)]$ can be implemented by obtaining a random number from a pdf uniformly distributed between 0 and 1, and then accepting the perturbation $\Delta\gamma_i$ if the random number obtained is smaller than $F(\gamma_i + \Delta\gamma_i)/F(\gamma_i)$. To introduce a bias towards large values of the control parameter E, each transition from state k to the state l in the iteration $j+1$ is accepted with probability $P_{accept}(k \to l) = \min[1,\ P^{\,j}(E_k) / P^{\,j}(E_l)]$, and rejected otherwise, where $P^{\,j}(E)$ is the estimate of the pdf of DGD obtained after the first j iterations. At the end of each iteration we update $P^{\,j}(E)$ using the same recursion algorithm as in [16], so that the number of hits in each bin of the control parameter histogram becomes approximately equal as the iteration number increases.

2.1.3. Summary of the MMC algorithm

In the first iteration we use M_1 samples and set the pdf of the DGD $P^1(E)$ of a PMD emulator with N_s sections as uniform, $P^1(E)=1/N_b$ (N_b= number of bins). Because every step in the Metropolis algorithm will be accepted with this initial distribution, we more effectively exploit the first iteration by choosing the coefficient of perturbation $\varepsilon=1$ To update the pdf of the DGD at the end of this iteration we use the recursive equation as in (1), which is the same equation used in any other iteration. We then carry out an additional $N-1$ iterations with M_l $(1<l\leq N)$ samples in each iteration. We note that in general the number of samples in each iteration does not have to be the same. We now present a pseudo-code summary of the algorithm:

Loop over iterations j = 1 to N -1:

Loop over fiber realizations (samples) m=1 to M_l:

(1) start random walk on ϕ, γ, and ψ with small steps $\Delta\phi$, $\Delta\gamma$, and $\Delta\psi$

$\Delta\phi=\{\Delta\phi_1,\cdots,\Delta\phi_{N_s}\}$; $\Delta\gamma=\{\Delta\gamma_1,\cdots,\Delta\gamma_{N_s}\}$; $\Delta\psi=\{\Delta\psi_1,\cdots,\Delta\psi_{N_s}\}$

(2) compute the provisional value of the DGD $((E_{\text{prov}}))$

with the angles $\phi+\Delta\phi$, $\gamma+\Delta\gamma$ and $\psi+\Delta\psi$.

(3) accept provisional step with probability equal to $\min[1, P^j(E_m)/P^j(E_{\text{prov}})]$

if step accepted: $E_{m+1}=E_{\text{prov}}$

$$\phi_{m+1}=\phi_m+\Delta\phi;\quad \gamma_{m+1}=\gamma_m+\Delta\gamma;\quad \psi_{m+1}=\psi_m+\Delta\psi$$

if step rejected: $E_{m+1}=E_m$

$$\phi_{m+1}=\phi_m;\quad \gamma_{m+1}=\gamma_m;\quad \psi_{m+1}=\psi_m$$

(4) increment the histogram of E with the sample E_{m+1}

End of loop over fiber realizations

update the pdf of the DGD $P^{j+1}(E)$

restart histogram

go to next iteration j

End

To update $P^j(E)$ at the end of each iteration j we use the recursive equation [16],

$$P_{k+1}^{j+1}=P_k^{j+1}\frac{P_{k+1}^j}{P_k^j}\left(\frac{H_{k+1}^j}{H_k^j}\right)^{\hat{g}_k^j}, \tag{1}$$

Where $\hat{g}_k^j$, the relative statistical significance of the k-th bin in the j-th iteration, is defined as

$$\hat{g}_k^j = \frac{g_k^j}{\sum_{l=1}^{j} g_k^l}, \quad \text{with} \quad g_k^j = \frac{H_{k+1}^j H_k^j}{H_{k+1}^j + H_k^j}. \tag{2}$$

If $H_{k+1}^j + H_k^j=0$ in a given iteration, then the k-th bin has no statistical significance in this iteration. Therefore, we set $g_k^j=0$ in that iteration. The statistical significance, $0\leq \hat{g}_k^j \leq 1$, depends on both previous bins and previous iterations, inducing a significant correlation among P_k^j. Finally, the P_k^j are normalized so that $\sum_{k=1}^{N_b} P_k^j=1$, where N_b is the number of bins. MMC is an extension of the Metropolis algorithm [18], where the acceptance rule accepts all the transitions to states with lower probabilities, but rejects part of the more likely transitions to states with higher probabilities. As the number of iterations increases, the histogram of the number of hits in each bin will asymptotically converge to a uniform distribution $\left(H_{k+1}^j / H_k^j \to 1\right)$, and the relative statistical significance will asymptotically converge to zero $\left(\hat{g}_k^j \to 0\right)$. Consequently, $P^{\,j+1}$will asymptotically converge to the true probability of the control parameter.

Equations (1) and (2) were derived by Berg and Neuhaus [16] assuming that the probability distribution is exponentially distributed with a slowly varying exponent that is a function of the control quantity (the temperature in their case and DGD or the penalty due to PMD in ours). This assumption is valid in a large number of problems in optical fiber communications, including the pdf of the DGD in fibers with an arbitrary number of sections [19], [23]. The recursions in (1) and (2) were derived by applying a quasi-linear approximation to the logarithm of the pdf in addition to a method for combining the information in the current histogram with that of previous iterations according to their relative statistical significance [16], [19].

2.1.4. Correlations

The goal of any scheme for biasing Monte Carlo simulations, including MMC, is to reduce the variance of the quantities of interest. MMC uses a set of systematic procedures to reduce the variance, which are highly nonlinear as well as iterative and have the effect of inducing a complex web of correlations from sample to sample in each iteration and between iterations. These, in turn, induce bin-to-bin correlations in the histograms of the pdfs. It is easy to see that the use of (1) and (2) generates correlated estimates for the P_k^j, although this procedure significantly reduces the variance [16]. In this section, we illustrate this correlation by showing results obtained when we applied MMC to compute the pdf of the DGD for a PMD emulator with 80 sections.

We computed the correlation coefficient between bin i and each bin j $(1\leq j\leq 80)$ in the histogram of the normalized DGD by doing a statistical analysis on an ensemble of many independent standard MMC simulations. The normalized DGD, $|\boldsymbol{\tau}|/\langle|\boldsymbol{\tau}|\rangle$, is defined as the

DGD divided by its expected value, which is 30 ps in this case. Suppose that on the l-th MMC simulation, we have P_i^l as the probability of the i-th bin and suppose that the average over all L MMC simulations is $\overline{P}_i$. Then, we define a normalized correlation between bin i and bin j as

$$C(i,j) = \frac{1}{L-1}\sum_{l=1}^{L}\frac{(P_i^l - \overline{P}_i)(P_j^l - \overline{P}_j)}{\sigma_{P_i}\sigma_{P_j}} \tag{3}$$

where σ_{P_i} and σ_{P_j} are the standard deviation of P_i and P_j, respectively. The normalized correlation defined in (3) is known as Pearson's correlation coefficient [24].

The values for $C(i,j)$ generated by (3) will range from -1 to 1. A value of +1 indicates a perfect correlation between the random variables. While a value of -1 indicates a perfect anti-correlation between the random variables. A value of zero indicates no correlation between the random variables.

In Figs. 1–3, we show the correlation coefficients between bin i and bin j, $1 \le j \le 80$, for the DGD in the bin i, DGD$_i$, equal to 30 ps, 45 ps, and 75 ps, respectively. In this case, we used a PMD emulator with 80 sections and the mean DGD is equal to 30 ps. To compute each value of $C(i,j)$ we used L =32 MMC simulations. We computed sample mean $\overline{C(i,j)}$ and standard deviation $\sigma_{C(i,j)}$ using 32 samples of $C(i,j)$. The values of the standard deviation for the results shown in Figs. 1–3 are in the range from 1.84×10^{-2} to 3.91×10^{-2}. Note that DGD$_i$ equal to 75 ps represents a case in the tail of the pdf of the DGD, where the unbiased Monte Carlo method has very low probability of generating samples, by contrast to a biased Monte Carlo method such as MMC. The results show that the correlations are not significant until we use a large value for DGD$_i$ compared to the mean DGD. However, these values of DGD$_i$ are precisely the values of greatest interest.

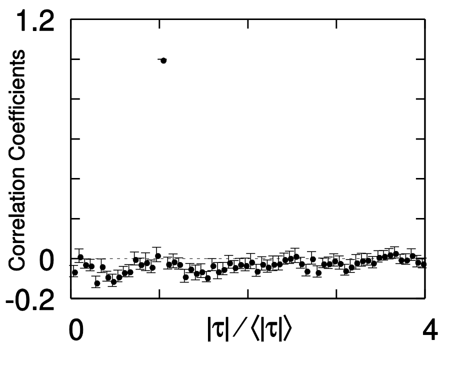

Figure 1. Correlation coefficients between bin i and bin j $(1 \le j \le 80)$ for the 80-section emulator, where the bin i corresponds to DGD$_i$=30 ps (1 × mean DGD). The correlation coefficients are computed using 32 standard MMC simulations. Each standard MMC simulation consists of 30 MMC iterations with 8,000 samples.

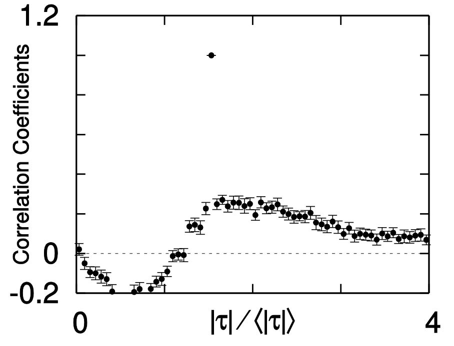

Figure 2. Correlation coefficients between bin i and bin j $(1 \leq j \leq 80)$ for the 80-section emulator, where the bin i corresponds to DGD_i=45 ps (1.5 × mean DGD). The correlation coefficients are computed using 32 standard MMC simulations. Each standard MMC simulation consists of 30 MMC iterations with 8,000 samples.

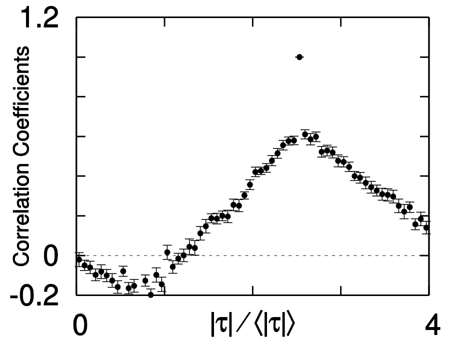

Figure 3. Correlation coefficients between bin i and bin j $(1 \leq j \leq 80)$ for the 80-section emulator, where the bin i corresponds to DGD_i=75 ps (2.5 × mean DGD). The correlation coefficients are computed using 32 standard MMC simulations. Each standard MMC simulation consists of 30 MMC iterations with 8,000 samples.

2.2. Estimation of errors in MMC simulations

In this sub-section, we explain why a new error estimation procedure is needed for multicanonical Monte Carlo simulations, and we then present the transition matrix method that we developed to efficiently estimate the error in MMC. Finally, we present the validation and application of this method.

2.2.1. Why a new error estimation procedure ?

Since MMC is a Monte Carlo technique, it is subject to statistical errors, and it is essential to determine their magnitude. In [25], we showed how to compute errors when using importance sampling. In this sub-section, we show how one can efficiently estimate errors in

MMC simulations using a transition matrix method that we developed. In practice, users of Monte Carlo methods often avoid making detailed error estimates. For example, when using an standard, unbiased Monte Carlo simulation to calculate the pdf of a quantity such as the DGD, the number of samples in each bin of the pdf's histogram is independent. Hence, when the histogram is smooth, one can infer that the error is acceptably low. This procedure is not reliable with MMC simulations because, as we showed in Section 2.1.4, the MMC algorithm induces a high degree of correlation from bin to bin. While it is always best to estimate error with any Monte Carlo method, it is particularly important in MMC simulations, due to the presence of large sample-to-sample correlations on the tails of the distributions.

The existence of correlations in the samples generated with the MMC method makes calculating the errors in MMC simulations significantly more difficult than in standard Monte Carlo simulations. Also, due to the correlations, one cannot apply to MMC standard error analysis that are traditionally used for simulations with uncorrelated samples. For the same reason, one cannot determine the contribution of the variance from each iteration using standard error propagation methods as in the case with importance sampling simulations [5]. Thus, the MMC variance cannot be estimated by applying a standard error analysis to a single MMC simulation. One can in principle run many independent MMC simulations in order to estimate the error by using the standard sample variance formula [26] on the ensemble of MMC simulations. However, estimating the error of the pdf of the quantity of interest by running many independent MMC simulations is computationally costly and in many cases not feasible. One can overcome this problem with the transition matrix method that we developed.

The transition matrix method is an efficient numerical method to estimate statistical errors in the pdfs computed using MMC. In this method, we use the estimated transition probability matrix to rapidly generate an ensemble of hundreds of pseudo-MMC simulations, which allows one to estimate errors from only one standard MMC simulation. The transition probability matrix, which is computed from a single, standard MMC simulation, contains all the probabilities that a transition occurs from any bin of the histogram of the quantity of interest to any other bin after a step (or perturbation) in the MMC random walk. The pseudo-MMC simulations are then made using the computed transition matrix instead of running full simulations. Each pseudo-MMC simulation must be made with the same number of samples per iteration and the same number of iterations as in the original standard MMC simulation. Once an ensemble of pseudo-MMC simulations has been calculated, one can use standard procedures to estimate the error. Since the transition matrix that is used in the pseudo-MMC simulations has its own statistical error, it might seem strange at first that it can be used as the basis from which to estimate the error in the MMC simulations. However, bootstrap theory assures us that such is the case [27]. Intuitively, the variation of any statistical quantity among the members of an ensemble of pseudo-MMC simulations is expected to be the same as the variation among members of an ensemble of standard MMC simulations because the simulations are carried out with the same number of samples and the same number of iterations.

To illustrate the transition matrix method, we calculated the pdf of DGD due to PMD and the associated confidence interval for two types of PMD emulators [28]. We validated our method by comparison to the results obtained by using a large ensemble of standard MMC simulations. We tested our method by applying it to PMD emulators because it was the first random phenomenon in optical fiber communication to which MMC was applied [19] and has become essential for testing biasing Monte Carlo methods. Moreover, it is computationally feasible to validate the proposed method with a large ensemble of standard MMC simulations. That is not the case for most other problems, *e.g.*, the error rate due to optical noise [29] and the residual penalty in certain PMD-compensated systems [6].

2.2.2. New error estimation procedure

Here we introduce an efficient numerical procedure that we refer to as the transition matrix method, to compute statistical errors in MMC simulations that properly accounts for the contributions of all MMC iterations. The transition matrix method is a bootstrap resampling method [27], [30] that uses a computed estimate of the probability of a transition from bin i to bin j of the histogram of the DGD. In a bootstrap method, one estimates a complex statistical quantity by extracting samples from an unknown distribution and computing the statistical quantity. In the case of computing the pdf of the DGD in PMD emulators, the complex statistical quantity is the probability of each bin in the histogram of the DGD, the pseudo-samples are the DGD values obtained in the pseudo-MMC simulations, and the unknown distribution is the true transition matrix. One then repeatedly and independently draws an ensemble of pseudo-samples with replacement from each original sample and computes the statistical quantity of interest using the same procedure by which the statistical quantity was first estimated. One can then estimate the variance of the quantity of interest from these pseudo-samples using standard techniques. The bootstrap method is useful when it is computationally far more rapid to resample the original set of samples than to generate new samples, allowing for an efficient estimate of the variance.

2.3. Bootstrap method

Efron's bootstrap [27] is a well-known general purpose technique for obtaining statistical estimates without making *a priori* assumptions about the distribution of the data. A schematic illustration of this method is shown in Fig.4. Suppose one draws a random vector $\mathbf{x}=(x_1,x_2,\ldots,x_n)$ with n samples from an unknown probability distribution F and one wishes to estimate the error in a parameter of interest $\hat{\theta}=f(\mathbf{x})$. Since there is only one sample of $\hat{\theta}$, one cannot use the sample standard deviation formula to compute the error. However, one can use the random vector $\mathbf{x}$ to determine an empirical distribution $\hat{F}$ from F (unknown distribution). Then, one can generate bootstrap samples from $\hat{F}$, $\mathbf{x}^*=(x_1^*,x_2^*,\ldots,x_n^*)$, to obtain $\hat{\theta}^*=f(\mathbf{x}^*)$ by drawing n samples with replacement from $\mathbf{x}$. The quantity $f(\mathbf{x}^*)$ is the result of applying the same function $f(.)$ to $\mathbf{x}^*$ as was applied to $\mathbf{x}$. For example, if $f(\mathbf{x})$ is the median of $\mathbf{x}$, then $f(\mathbf{x}^*)$ is the median of the bootstrap resampled data set. The star notation indicates that $\mathbf{x}^*$ is not the actual data set $\mathbf{x}$, but rather a resampled version of $\mathbf{x}$ obtained from the estimated distribution $\hat{F}$. Note that one can rapidly generate as many bootstrap samples $\mathbf{x}^*$ as one needs, since those simulations do not make use the system model, and then generate independent bootstrap sample estimates of $\hat{\boldsymbol{\theta}}$, $\hat{\boldsymbol{\theta}}_1^* = f(\mathbf{x}_1^*)$, ... , $\hat{\boldsymbol{\theta}}_B^* = f(\mathbf{x}_B^*)$, where B is the total number of bootstrap samples. Then, one can estimate the error in $\hat{\boldsymbol{\theta}}$ using the standard deviation formula on the bootstrap samples $\hat{\boldsymbol{\theta}}^*$.

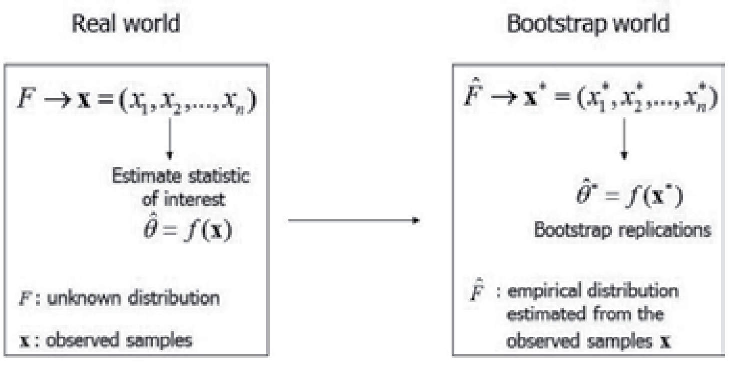

Figure 4. On the left, we show the drawing of a true realization form the actual, unknown distribution *F*. On the right, we show the same procedure applied to drawing bootstrap realizations.

The transition matrix method that we describe in this chapter is related to the bootstrap resampling method as follows:

1. $\hat{F}$ is an estimate of the transition matrix obtained from a single standard MMC simulation;
2. $\mathbf{x}_1^*$,..., $\mathbf{x}_B^*$, are the collection of samples that is obtained from the ensemble of pseudo-MMC simulations. We note that $\mathbf{x}_b^*$ should be computed using the exact same number of iterations and the exact same number of samples per iteration as in the original standard MMC simulation;
3. Each $\hat{\theta}_b^*$, where b=1,2,...,B, is a value for the probability p_k^* of the k-th bin of the histogram of the DGD obtained from each of the pseudo-MMC simulations;
4. Given that one has B independent p_k^*, one can obtain an error estimate for each bin in the estimated pdf of the DGD using the traditional sample standard deviation formula [26, 27].

$$\sigma_{\hat{\theta}^*} = \left[\frac{1}{B-1} \sum_{b=1}^{B} \left(\hat{\theta}_b^* - \overline{\hat{\theta}^*} \right)^2 \right]^{1/2}, \tag{4}$$

where,

$$\overline{\hat{\theta}^{\star}} = \frac{1}{B}\sum_{b=1}^{B}\hat{\theta}_b^{\star}. \tag{5}$$

2.4. The transition matrix method

In this sub-section, we explain the transition matrix method in the context of computing errors in the pdf of the DGD for PMD emulators. The transition matrix method has two parts. In the first part, one obtains an estimate of the pdf of the DGD and an estimate of the one-step transition probability matrix $\mathbf{\Pi}$. To do so, one runs a standard MMC simulation, as described in Section 2.1.2. At the same time, one computes an estimate of the transition probability $\pi_{i,j}$, which is the probability that a sample in the bin i will move to the bin j after a single step in the MMC algorithm. We stress that a transition attempt must be recorded whether or not it is accepted by the Metropolis algorithm after the fiber undergoes a random perturbation. The transition matrix is a matrix that contains the probability that a transition will take place from one bin to any other bin when applying a random perturbation. It is independent of the procedure for rejecting or accepting samples, which is how the biasing is implemented in the MMC method. An estimate of the transition matrix that is statistically as accurate as the estimate of the pdf using MMC can be obtained by considering all the transitions that were attempted in the MMC ensemble. One uses this information to build a $N_b \times N_b$ one-step transition probability matrix, where N_b is the number of bins in the histogram of the pdf. The transition matrix $\mathbf{\Pi}$ consists of elements $\pi_{i,j}$, where the sum of the row elements of $\mathbf{\Pi}$ equals 1. The elements $\pi_{i,j}$ are computed as

$$\pi_{i,j} = \frac{\sum_{m=1}^{M_t-1} I_i(E_m) I_j(E_{m+1})}{\sum_{m=1}^{M_t-1} I_i(E_m)}, \text{ if } \sum_{m=1}^{M_t-1} I_i(E_m) \neq 0, \tag{6}$$

And $\pi_{i,j}$=0, otherwise. In (6), M_t is the total number of samples in the MMC simulation and E_m is the m-th DGD sample. The indicator function $I_i(E)$ is chosen to compute the probability of having a DGD sample inside the bin i of the histogram. Thus, $I_i(E)$ is defined as 1 inside the DGD range of the bin i, otherwise $I_i(E)$ is defined as 0. In the second part of the procedure, one carries out a new series of MMC simulations (using the transition probability matrix), that we refer to as pseudo-MMC simulations. In each step, if one starts for example in bin i of the histogram, one picks a new provisional bin j using a procedure to sample from the pdf π_i, where $\pi_i(j)$=$\pi_{i,j}$. One then accepts or rejects this provisional transition using the same criteria as in full, standard MMC simulations, and the number of samples in the bins of histogram is updated accordingly. Thus, one is using the transition matrix $\mathbf{\Pi}$ to emulate the random changes in the DGD that result from the perturbations $\Delta\phi_i$, $\Delta\gamma_i$, and $\Delta\psi_i$ that were used in the original standard MMC simulation. In all other respects, each pseudo-MMC simulation is like the standard MMC simulation. In particular, the metric for accepting or rejecting a step, the number of samples per iteration, and the number of iterations must be kept the same. It is possible to carry out hundreds of these pseudo-MMC simulations in a small fraction of the computer time that it takes to carry out a single standard MMC simulation. This procedure requires us to hold the entire transition matrix in memory, which could in principle be memory-intensive, although this issue did not arise in any of the problems that we considered. This procedure will be useful when evaluating a transition using the transition matrix requires far less computational time than calculating a transition using the underlying physics. This is an assumption that was valid for the cases in which we considered, and we expect that it is applicable to most practical problems. An estimate of the pdf of the DGD is obtained in the final iteration of each pseudo-MMC simulation. Since the estimates of the probability in a given bin in the different pseudo-MMC simulations are independent, one may apply the standard formula for computation of the variance $\sigma^2_{p_i^*}$ of the i-th bin

$$\sigma^2_{p_i^*} = \frac{1}{(B-1)}\sum_{b=1}^{B}\left(p_{i,b}^* - \overline{p_i^*}\right)^2, \quad \text{with} \quad \overline{p_i^*} = \frac{1}{B}\sum_{b=1}^{B} p_{i,b}^*, \tag{7}$$

where $p_{i,b}^*$ is the probability of the i-th bin in the histogram of the DGD obtained in the b-th pseudo-MMC simulation and B is the total number of pseudo-MMC simulations. Thus, $\sigma_{p_i^*}$ is an estimate of the error in the i-th bin in the histogram of the DGD obtained in a single MMC simulation. We now illustrate the details of how we choose the provisional transition from bin i to bin j with the following pseudo-code:

bin DGD of current sample = i

use random number to generate x from a uniform pdf between 0 and 1: $x \leftarrow U[0,1]$

for j=1 to N_b

    if $(x < \boldsymbol{\pi}_{i,j}^{cdf})$

        new bin = j

        break

    end if

end for

current bin = new bin

where $\boldsymbol{\pi}_{i,j}^{\text{cdf}} = \sum_{m=1}^{j} \boldsymbol{\pi}_{i,m}$ is the cumulative transition probability. This procedure is used to sample from the pdf $\boldsymbol{\pi}_i$, where $\boldsymbol{\pi}_i(j) = \boldsymbol{\pi}_{i,j}$, and with $\boldsymbol{\pi}_{i,j}$ defined as the probability that a sample in the bin i will move to the bin j.

2.5. Assessing the error in the MMC error estimation

The estimate of the MMC variance also has an error, which depends on the number of samples in a single standard MMC simulation and on the number of pseudo-MMC simulations (bootstrap samples) [31]. Here, the error due to the bootstrap resampling is minimized by using 1,000 bootstrap pseudo-MMC simulations. Therefore, the residual error is due to the finite number of samples used to estimate both the pdf of the DGD and the transition matrix in the single standard MMC simulation, *i.e.*, in the first part of the transition matrix method. Thus, there is a variability in the estimate of the MMC variance due to the variability of the transition matrix $\hat{\mathbf{\Pi}}$ as an estimate of the true transition matrix $\mathbf{\Pi}$. To estimate the error in the estimate of the MMC variance, we apply a procedure known in the literature as *bootstrapping the bootstrap* or *iterated bootstrap* [32]. The procedure is based on the principle that if the bootstrap can estimate errors in one statistical parameter using $\hat{\mathbf{\Pi}}$, one can also use bootstrap to check the uncertainty in the error estimate using bootstrap resampled transition matrices $\hat{\mathbf{\Pi}}^*$. The procedure consists of:

1. Running one standard MMC simulation;
2. Generating N_B=100 pseudo-MMC simulations and computing transition matrices for each of the pseudo-MMC simulation. Therefore, we obtain N_B transition matrices that we call pseudo-transition matrices $\hat{\mathbf{\Pi}}^*_B$;
3. For each pseudo-transition matrix $\hat{\mathbf{\Pi}}^*_B$ we calculate N_B=100 pseudo-MMC simulations (N_B values for the probability of any given bin of the estimated pdf of the DGD, p^{**}). The double star notation indicates quantities computed with bootstrap resampling from a pseudo-transition matrix. We then estimate the error for the probability of any given bin in the estimated pdf of the DGD, $\sigma_{p^{**}}$, for each pseudo-transition matrix;
4. Since we have N_B=100 pseudo-transition matrices, we repeat step 3 N_B times and obtain N_B values for $\sigma_{p^{**}}$. Then, we compute the double bootstrap confidence interval Δp^{**} of the relative variation of the error of p (statistical error in p, where p is the probability of any given bin in the estimated pdf of the DGD computed using a single standard MMC simulation):

$$\Delta p^{**} = \left[\frac{\overline{\sigma_{p^{**}}} - \sigma_{\left(\sigma_{p^{**}}\right)}}{p}, \frac{\overline{\sigma_{p^{**}}} + \sigma_{\left(\sigma_{p^{**}}\right)}}{p} \right], \tag{8}$$

where,

http://dx.doi.org/10.5772/53306

$$\sigma_{\left(\sigma_{p^{**}}\right)} = \left[\frac{1}{N_B - 1} \sum_{n=1}^{N_B} \left(\sigma_{p^{**}}^{(n)} - \overline{\sigma_{p^{**}}} \right)^2 \right]^{1/2}, \tag{9}$$

and

$$\overline{\sigma_{p^{**}}} = \frac{1}{N_B} \sum_{n=1}^{N_B} \sigma_{p^{**}}^{(n)}. \tag{10}$$

In (9) and (10), $\sigma_{p^{**}}^{(n)}$ is the standard deviation of p^{**} computed using the n-th pseudo-transition matrix.

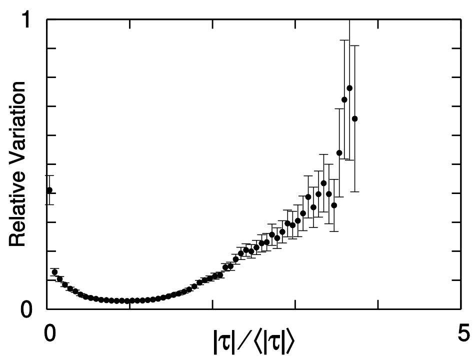

Figure 5. Relative variation $\left(\hat{\sigma}_{\hat{P}_{\mathrm{DGD}}} / \hat{P}_{\mathrm{DGD}}\right)$ of the pdf of the normalized DGD, $|\boldsymbol{\tau}| / \langle |\boldsymbol{\tau}| \rangle$, for the 15-section PMD emulator using 14 MMC iterations with 4,000 samples. The confidence interval is given by (8) when we compute an ensemble of standard deviations using bootstrap resampling for each of the 100 pseudo-transition matrices.

In Fig. 5, we show the relative variation of p^{**} and its confidence interval Δp^{**} for a PMD emulator with 15 sections. We used 14 MMC iterations with 4,000 samples each (total of 56,000 samples). The confidence interval of the relative variation is defined in (8). We used a total of 80 evenly-spaced bins where we set the maximum value for the normalized DGD as five times the mean DGD. We also use the same number for bins for all the figures shown in this chapter. As expected, we observed that the error in the estimate of the MMC variance is large when the MMC variance is also large. The confidence interval Δp^{**} is between $(2.73 \times 10^{-2},\ 3.19 \times 10^{-2})$ and $(3.61 \times 10^{-1},\ 4.62 \times 10^{-1})$ for $|\boldsymbol{\tau}| / \langle |\boldsymbol{\tau}| \rangle < 2$. It increases to $(2.68 \times 10^{-1}, 4.48 \times 10^{-1})$ when $|\boldsymbol{\tau}| / \langle |\boldsymbol{\tau}| \rangle = 3$ and to $(4.05 \times 10^{-1},\ 9.09 \times 10^{-1})$ at the largest value of $|\boldsymbol{\tau}| / \langle |\boldsymbol{\tau}| \rangle$. We concluded that the estimate of the relative variation of the probability of a bin is a good estimate of its own accuracy. This result is similar to what is observed with the standard analysis of standard Monte Carlo simulations [26]. Intuitively, one expects the relative error and the error in the estimated error to be closely related because both are drawn from the same sample space. In Fig. 5, we also observe that the relative variation increases with the DGD for values larger than the mean DGD, especially in the tail of the pdf. This phenomenon occurs because the regions in the configuration space that contribute to the tail of the pdf of the DGD are only explored by the MMC algorithm after several iterations. As the number of iterations increases, the MMC algorithm allows the exploration of less probable regions of the configuration space. Because less probable regions are explored in the last iterations, there will be a significantly smaller number of hits in the regions that contribute to the tail of the pdf of the DGD. As a consequence, the relative variation will increase as the DGD increases.

2.6. Application and validation

We estimated the pdf of the normalized DGD ($\hat{P}_{\mathrm{DGD}}$) and its associated confidence interval $\Delta\hat{P}_{\mathrm{DGD}}$ for PMD emulators comprised of 15 and 80 birefringent fiber sections with polarization scramblers at the beginning of each section. The normalized DGD, $|\boldsymbol{\tau}|/\langle|\boldsymbol{\tau}|\rangle$, is defined as the DGD divided by its expected value, which is equal 30 ps. We used 14 MMC iterations with 4,000 samples each to compute the pdf of the normalized DGD when we used a 15-section emulator and 30 MMC iterations with 8,000 samples each when we used an 80-section PMD emulator.

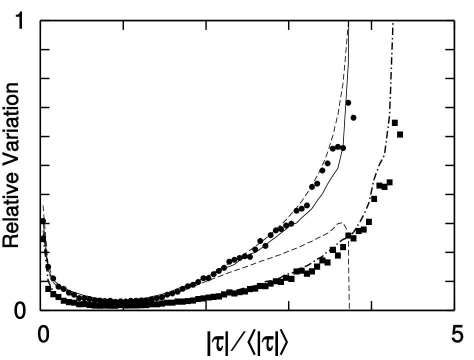

Figure 6. Relative variation ($\hat{\sigma}_{\hat{P}_{\mathrm{DGD}}}/\hat{P}_{\mathrm{DGD}}$) of the pdf of the normalized DGD, $|\boldsymbol{\tau}|/\langle|\boldsymbol{\tau}|\rangle$. (i) Circles: Transition matrix method based on a single standard MMC simulation for the 15-section PMD emulator; (ii) Solid: 10^3 standard MMC simulations for the 15-section emulator; (iii) Dashed: Confidence interval of the relative variation of the error estimated using the transition matrix method for the 15-section PMD emulator; (iv) Squares: Transition matrix method based on a single standard MMC simulation for the 80-section PMD emulator; (v) Dot-dashed: 10^3 standard MMC simulations for the 80-section PMD emulator.

We monitored the accuracy of our computation by calculating the relative variation of the pdf of the normalized DGD. The relative variation is defined as the ratio between the standard deviation of the pdf of the normalized DGD and the pdf of the normalized DGD ($\hat{\sigma}_{\hat{P}_{\mathrm{DGD}}}/\hat{P}_{\mathrm{DGD}}$). In Fig. 6, we show the relative variation when we used PMD emulators with

15 and with 80 birefringent sections. The symbols show the relative variation when we applied the procedure that we described in Section 2 with 1,000 pseudo-MMC simulations based on a single standard MMC simulation and the transition matrix method, while the solid and the dot-dashed lines show the relative variation when we used 1,000 standard MMC simulations. The circles and the solid line show the results for a 15-section PMD emulator, while the squares and dot-dashed line show the results when we used an 80-section PMD emulator. As expected, the result from an ensemble of pseudo-MMC simulations shows a systematic deviation from the result from an ensemble of standard MMC simulations for both emulators. The systematic deviation changes depending on which standard MMC simulation is used to generate the pseudo ensemble. In Fig. 6, the two dashed lines show the confidence interval of the relative variation with the 15-section PMD emulator computed using the transition matrix method, *i.e.*, the confidence interval for the results that are shown with the circles. The confidence interval Δp^{**} is between (3.04×10^{-2}, 3.28×10^{-2}) and (2.76×10^{-1}, 3.62×10^{-1}) for $|\boldsymbol{\tau}|/\langle|\boldsymbol{\tau}|\rangle<2$. It increases to ($2.39\times10^{-1}$, 4.31×10^{-1}) when $|\boldsymbol{\tau}|/\langle|\boldsymbol{\tau}|\rangle=3$ and to (2.69×10^{-1}, 9.88×10^{-1}) at the largest value of $|\boldsymbol{\tau}|/\langle|\boldsymbol{\tau}|\rangle$.

While the relative variation that is computed using the transition matrix method from a single MMC simulation will vary from one standard MMC simulation to another, the results obtained from different standard MMC simulations are likely to be inside this confidence interval with a well-defined probability. The confidence interval of the relative variation was obtained using a procedure similar to the one discussed in the Section 2.2, except that we computed the relative variation of the probability of a bin using the transition matrix method for every one of the 1,000 standard MMC simulations. Therefore, we effectively computed the true confidence interval of the error estimated using the transition matrix method. We have verified that the confidence interval calculated using the double bootstrap procedure on a single standard MMC simulation agrees well with the true confidence interval in all the cases that we investigated. We observed an excellent agreement between the results obtained with the transition matrix method based on a single standard MMC simulation and the results obtained with 1,000 standard MMC simulations for both 15 and 80 fiber sections when the relative variation $\left(\hat{\sigma}_{\hat{P}_{\mathrm{DGD}}}/\hat{P}_{\mathrm{DGD}}\right)$ is smaller than 15%. For larger relative variation, the true error is within the confidence interval of the error, which can be estimated using the double bootstrap method described in Section 2.2. The curves for the 80-section PMD emulator have a larger DGD range because a fiber with 80 birefringent sections is able to produce larger DGD values than is possible with a fiber with 15 birefringent fiber sections [28].

In Figs. 7 and 8, we show with symbols the results for the pdf of the normalized DGD and its confidence interval using the numerical procedure that we presented in Section 2.2. The solid line shows the pdf of the normalized DGD obtained analytically using a solution (see [21]) for 15 and 80 concatenated birefringent fiber sections with equal length. For comparison, we also show the Maxwellian pdf for the same mean DGD. In table 1, we present selected data points from the curves shown in Fig. 7. For both 15- and 80-section emulators, we find that the MMC yields estimates of the pdf of the normalized DGD with a small confidence interval. In Figs. 7 and 8, we see that the standard deviation $(\hat{\sigma}_{\hat{P}_{\mathrm{DGD}}})$ for the DGD pdf is always small compared to the DGD pdf. The values of the relative variation $(\hat{\sigma}_{\hat{P}_{\mathrm{DGD}}} / \hat{P}_{\mathrm{DGD}})$ ranges from 0.016 to 0.541. We used only 56,000 MMC samples to compute the pdf of the DGD in a 15-section emulator, but we were able nonetheless to accurately estimate probabilities as small as 10^{-8}. Since the relative error in unbiased Monte Carlo simulations is approximately given by $N_I^{-1/2}$, where N_I is the number of hits in a given bin, it would be necessary to use on the order of 10^9 unbiased Monte Carlo samples to obtain a statistical accuracy comparable to the results that I show in the bin with lowest probability in Figs. 7 and 8.

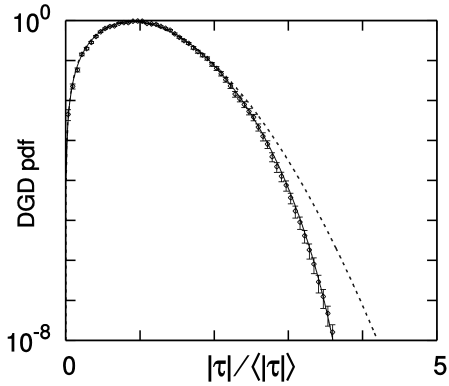

Figure 7. The pdf of the normalized DGD, $|\boldsymbol{\tau}| / \langle|\boldsymbol{\tau}|\rangle$, for the 15-section PMD emulator using 14 MMC iterations with 4,000 samples. (i) Diamonds: DGD pdf with error estimation using the transition matrix method, (ii) Dashed line: Maxwellian pdf, (iii) Solid line: Analytical pdf of the DGD for the 15-section PMD emulator.

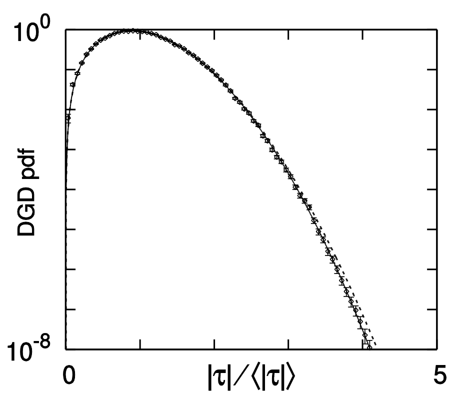

Figure 8. The pdf of the normalized DGD, $|\boldsymbol{\tau}| / \langle|\boldsymbol{\tau}|\rangle$, for the 80-section PMD emulator using 30 MMC iterations with 8,000 samples. (i) Diamonds: DGD pdf with error estimation using the transition matrix method, (ii) Dashed line: Maxwellian pdf, (iii) Solid line: Analytical pdf of the DGD for the 80-section PMD emulator.

$\lvert\tau\rvert / \langle\lvert\tau\rvert\rangle$	p_{DGD}	$\hat{p}_{DGD}$	$\hat{\sigma}_{\hat{p}_{DGD}}$	$\hat{\sigma}_{\hat{p}_{DGD}} / \hat{p}_{DGD}$
0.031	3.00×10^{-3}	4.50×10^{-3}	1.35×10^{-3}	0.301
0.344	3.16×10^{-1}	2.84×10^{-1}	1.75×10^{-2}	0.062
0.719	8.56×10^{-1}	8.57×10^{-1}	2.83×10^{-2}	0.033
1.094	8.63×10^{-1}	8.50×10^{-1}	2.76×10^{-2}	0.033
1.469	4.64×10^{-1}	4.66×10^{-1}	2.16×10^{-2}	0.046
1.844	1.43×10^{-1}	1.36×10^{-1}	1.21×10^{-2}	0.089
2.219	2.50×10^{-2}	2.32×10^{-2}	3.37×10^{-3}	0.145
2.594	2.26×10^{-3}	2.15×10^{-3}	4.43×10^{-4}	0.206
2.969	8.70×10^{-5}	7.57×10^{-5}	2.16×10^{-5}	0.286
3.344	8.92×10^{-7}	8.13×10^{-7}	3.49×10^{-7}	0.430
3.594	1.10×10^{-8}	1.59×10^{-8}	8.63×10^{-9}	0.541

Table 1. Selected data points from the curves shown in Fig. 6. The columns from left to right show: the normalized DGD value, the analytical probability density function, the estimated probability density function, the standard deviation computed using the transition matrix method, and the relative variation.

We would like to stress that the computational time that is required to estimate the errors using the transition matrix method does not scale with the time needed to carry out a single standard MMC simulation. For instance, it takes approximately 17.5 seconds of computation using a Pentium 4.0 computer with 3 GHz of clock speed to estimate the errors in the pdf of the DGD for the 80-section emulator using 1,000 pseudo-MMC simulations with the transition matrix method, once the transition matrix is available. The computational time that is required to compute the pdf of the DGD using only one standard MMC simulation is 60 seconds. To obtain 1,000 standard MMC simulations would require about 16.6 hours of CPU time in this case.

We also stress that it is difficult to estimate the statistical errors in MMC simulations because the algorithm is iterative and highly nonlinear. We introduced the transition matrix method that allows us to efficiently estimate the statistical errors from a single standard MMC simulation, and we showed that this method is a variant of the bootstrap procedure. We applied this method to calculate the pdf of the DGD and its expected error for 15-section and 80-section PMD emulators. Finally, we validated this method in both cases by comparing the results to estimates of the error from ensembles of 1,000 independent standard MMC simulations. The agreement was excellent. In Section 4, we apply the transition matrix method to estimate errors in the outage probability of PMD uncompensated and compensated systems. We anticipate that the transition matrix method will allow one to estimate errors with any application of MMC including the computation of the pdf of the received voltage in optical communication systems [29] and the computation of rare events in coded communication systems [33].

3. PMD Compensators

In this chapter, we investigated a single-section and three-section PMD compensators. A single-section PMD compensator [34], which is a variable-DGD compensator that was programmed to eliminate the residual DGD at the central frequency of the channel after compensation, and a three-section PMD compensator proposed in [35], which compensates for first- and second-order PMD. The three-section compensator consists of two fixed-DGD elements that compensate for the second-order PMD and one variable-DGD element that eliminates the residual DGD at the central frequency of the channel after compensation. The three-section compensator that we used has the first- and second-order PMD as feedback parameters. This compensator can also in principle operate in a feedforward configuration.

3.1. Single-section compensator

The increased understanding of PMD and its system impairments, together with a quest for higher transmission bandwidths, has motivated considerable effort to mitigate the effects of PMD, based on different compensation schemes [36], [37], [38]. One of the primary objectives has been to enable system upgrades from 2.5 Gbit/s to 10 Gbit/s or from 10 Gbit/s to 40 Gbit/s on old, embedded, high-PMD fibers. PMD compensation techniques must reduce the impact of first-order PMD and should reduce higher-order PMD effects or at least not increase the higher orders of PMD. The techniques should also be able to rapidly track changes in PMD, including changes both in the DGD and the PSPs. Other desired characteristics of PMD mitigation techniques are low cost and small size to minimize the impact on existing system architectures. In addition, mitigation techniques should have a small number of feedback parameters to control [39].

In this section, we describe a PMD compensator with an arbitrarily rotatable polarization controller and a single DGD element, which can be fixed [40] or variable [41]. Figure 9 shows a schematic illustration of a single-section DGD compensator. The adjustable DGD element or birefringent element is used to minimize the impact of the fiber PMD and the polarization controller is used to adjust the direction of the polarization dispersion vector of the compensator. The expression for the polarization dispersion vector after compensation, which is equivalent to the one in [42], is given by

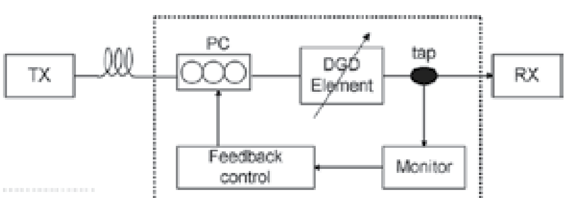

Figure 9. Schematic illustration of a single-section compensator with a monitor and a feedback element. In practical systems, the compensator will usually be part of the receiver, so that the monitor and the feedback control are integrated with the detection circuit.

http://dx.doi.org/10.5772/53306

$$\boldsymbol{\tau}_{tot}(\omega)=\boldsymbol{\tau}_{c}+T_c(\omega)R_{pc}\boldsymbol{\tau}_{f}(\omega), \tag{11}$$

where $\boldsymbol{\tau}_c$ is the polarization dispersion vector of the compensator, $\boldsymbol{\tau}_f(\omega)$ is the polarization dispersion vector of the transmission fiber, R_{pc} is the polarization transformation in Stokes space that is produced by the polarization controller of the compensator, and $T_c(\omega)$ is the polarization transformation in Stokes space that is produced by the DGD element of the compensator. We model the polarization transformation R_{pc} as

$$R_{pc}=R_x(\phi_{pc})R_y(\psi_{pc})R_x(-\phi_{pc}). \tag{12}$$

We note that the two parameters of the polarization controller's angles in (12) are the only free parameters that a compensator with a fixed DGD element possesses, while the value of the DGD element of a variable DGD compensator is an extra free parameter that must be adjusted during the operation. In (12), the parameter ϕ_{pc} is the angle that determines the axis of polarization rotation in the y-z plane of the Poincaré sphere, while the parameter ψ_{pc} is the angle of rotation around that axis of polarization rotation. An appropriate selection of these two angles will transform an arbitrary input Stokes vector into a given output Stokes vector. While most electronic polarization controllers have two or more parameters to adjust that are different from ϕ_{pc} and ψ_{pc}, it is possible to configure them to operate in accordance to the transformation matrix R_{pc} in (12) [43].

In all the work reported in this chapter, we used the eye opening as the feedback parameter for the optimization algorithm unless otherwise stated. We defined the eye opening as the difference between the lowest mark and the highest space at the decision time in the received electrical noise-free signal. The eye-opening penalty is defined as the ratio between the back-to-back and the PMD-distorted eye opening. The back-to-back eye opening is computed when PMD is not included in the system. Since PMD causes pulse spreading in amplitude-shift keyed modulation formats, the isolated marks and spaces are the ones that suffer the highest penalty [44]. To define the decision time, we recovered the clock using an algorithm based on one described by Trischitta and Varma [45].

We simulated the 16-bit string "0100100101101101." This bit string has isolated marks and spaces, in addition to other combinations of marks and spaces. In most of other simulations in this dissertation we use pseudorandom binary sequence pattern. The receiver model consists of an Gaussian optical filter with full width at half maximum (FWHM) of 60 GHz, a square-law photodetector, and a fifth-order electrical Bessel filter with a 3 dB bandwidth of 8.6 GHz. To determine the decision time after the electronic receiver, we delayed the bit stream by half a bit slot and subtracted it from the original stream, which is then squared. As a result a strong tone is produced at 10 GHz. The decision time is set equal to the time at which the phase of this tone is equal to $\pi/2$. The goal of our study is to determine the performance limit of the compensators. In order to do that, we search for the angles ϕ_{pc} and ψ_{pc}.

of the polarization controller for which the eye opening is largest. In this case, the eye opening is our compensated feedback parameter. We therefore show the global optimum of the compensated feedback parameter for each fiber realization.

To obtain the optimum, we start with 5 evenly spaced initial values for each of the angles ϕ_{pc} and ψ_{pc} in the polarization transformation matrix R_{pc}, which results in 25 different initial values. If the DGD of the compensator is adjustable, we start the optimization with the DGD of the compensator equal to the DGD of the fiber. We then apply the conjugate gradient algorithm [46] to each of these 25 initial polarization transformations. To ensure that this procedure yields the global optimum, we studied the convergence as the number of initial polarization transformations is increased. We examined 10^4 fiber realizations spread throughout our phase space, and we never found more than 12 local optima in the cases that we examined. We missed the global optimum in three of these cases because several optima were closely clustered, but the penalty difference was small. We therefore concluded that 25 initial polarization transformations were sufficient to obtain the global optimum with sufficient accuracy for our purposes. We observed that the use of the eye opening as the objective function for the conjugate gradient algorithm produces multiple optimum values when both the DGD and the length of the frequency derivative of the polarization dispersion vector are very large.

The performance of the compensator depends on how the DGD and the effects of the first- and higher-order frequency derivatives of the polarization dispersion vector of the transmission fiber interact with the DGD element of the compensator to produce a residual polarization dispersion vector and on how the signal couples with the residual principal states of polarization over the spectrum of the channel. Therefore, the operation of single-section PMD compensators is a compromise between reducing the DGD and setting one principal state of polarization after compensation that is approximately co-polarized with the signal. An expression for the pulse spreading due to PMD as a function of the polarization dispersion vector of the transmission fiber and the polarization state over the spectrum of the signal was given in [47].

3.2. Three-section compensator

Second-order PMD has two components: Polarization chromatic dispersion (PCD) and the principal states of polarization rotation rate (PSPRR) [35]. Let $\boldsymbol{\tau}_1$ be the polarization dispersion vector of the transmission line, and let $\boldsymbol{\tau}_2$ and $\boldsymbol{\tau}_3$ be the polarization dispersion vectors of the two fixed-DGD elements of the three-section compensator. Using the concatenation rule [42], the first- and second-order PMD vector of these three concatenated fibers are given by

$$\boldsymbol{\tau}_{tot} = R_3 R_2 \boldsymbol{\tau}_1 + R_3 \boldsymbol{\tau}_2 + \boldsymbol{\tau}_3, \tag{13}$$

$$\boldsymbol{\tau}_{tot,w} = \left(\boldsymbol{\tau}_3 + R_3 \boldsymbol{\tau}_2\right) \times R_3 R_2 \boldsymbol{\tau}_1 q_1 + \boldsymbol{\tau}_3 \times R_3 \boldsymbol{\tau}_2 + R_3 R_2 \boldsymbol{\tau}_{1w} q_1 + R_3 R_2 \boldsymbol{\tau}_1 q_{1w}, \tag{14}$$

where R_2 and R_3 are the rotation matrices of the polarization controllers before the first and the second fixed-DGD elements of the compensator, respectively. In (14), $\boldsymbol{\tau}_{1w}q_1$ and $\boldsymbol{\tau}_1 q_{1w}$ are the transmission line PCD and the PSPRR components, respectively, where we express the polarization dispersion vector of the transmission fiber as $\boldsymbol{\tau}_1=\boldsymbol{\tau}_1 q_1$. Here, the variable $\boldsymbol{\tau}$ is the DGD and $q=\boldsymbol{\tau}/|\boldsymbol{\tau}|$ is the Stokes vector of one of the two orthogonal principal states of polarization. The three-section PMD compensator has two operating points [35]. For the first operating point, the term $\boldsymbol{\tau}_3\times R_3\boldsymbol{\tau}_2$ in (14) is used to cancel the PSPRR component $R_3R_2\boldsymbol{\tau}_1 q_{1w}$, provided that we choose R_3 and R_2 so that $R_3^{\dagger}\boldsymbol{\tau}_3\times\boldsymbol{\tau}_2$ and $R_2\boldsymbol{\tau}_1 q_{1w}$ are antiparallel, where $R_3^{\dagger}$ is the Hermitian conjugate of R_3. Note that with this configuration one cannot compensate for PCD.

For the second operating point, $\boldsymbol{\tau}_3\times R_3\boldsymbol{\tau}_2$ in (14) is used to compensate for PCD by choosing $R_3^{\dagger}\boldsymbol{\tau}_3\times\boldsymbol{\tau}_2$ and $R_2\boldsymbol{\tau}_{1w}q_1$ to be antiparallel. Moreover, we can add an extra rotation to R_2 so that $\left[\left(R_3^{\dagger}\boldsymbol{\tau}_3+\boldsymbol{\tau}_2\right)\times R_2\boldsymbol{\tau}_1 q_1\right]$ and $R_2\boldsymbol{\tau}_1 q_{1w}$ are also antiparallel. In this way, the compensator can also reduce the PSPRR term. In our simulations, we computed the reduction of the PCD and PSPRR components for the two operating points and we selected the one that presented the largest reduction of the second-order PMD. Finally, the third, variable-DGD, section of the compensator cancels the residual DGD $\boldsymbol{\tau}_{\text{tot}}$ after the first two sections.

4. Simulation results and discussions

We evaluate the performance of optical fiber communication systems with and without PMD compensators using the statistical methods of importance sampling (IS) and multicanonical Monte Carlo (MMC). Both MMC and IS can be used to bias Monte Carlo simulations to the outage probability due to PMD in optical fiber communication systems with one-section and with three-section PMD compensators. When there exist a IS bias technique available, IS is more effective than MMC because each sample in IS is independent, while the samples in MMC slowly become uncorrelated. However, the effectiveness of MMC can be comparable or even exceed that of IS in the cases in which there isn't a high correlation between the parameters that are biased in IS and the parameter of interest. This is the case of optical communication systems with PMD compensation, in which IS has to exploit a vast region of the probability space that does not contribute to the events of interest.

In Fig.10, we show the pdf of the eye-opening penalty for a system with 30 ps mean DGD and a single-section compensator. We compute the pdf using IS in which only the DGD is biased, and we also compute the pdf using IS in which both the first- and the second-order PMD are biased. We observed that it is not sufficient to only bias the DGD in order to accurately calculate the compensated penalty and its pdf. This approach can only be used in systems where the DGD is the dominant source of penalties, which is the case in uncompensated systems and in systems with limited PMD compensation.

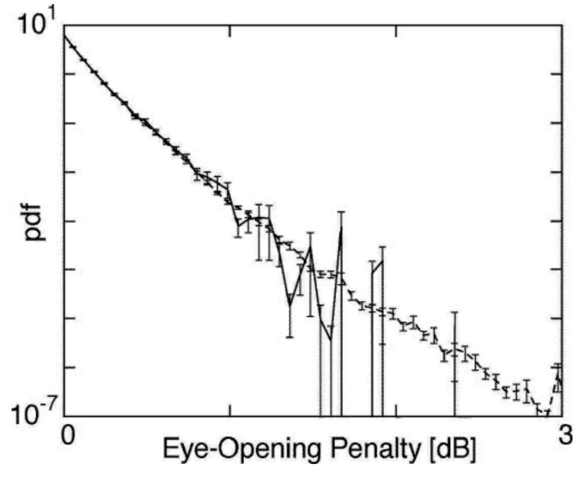

Figure 10. PDF of the eye-opening penalty for a system with a mean DGD of 30 ps and a single-section compensator. (i) Solid line: results using IS in which only the DGD is biased. (ii) Dashed line: results using IS in which both first-and second-order PMD are biased. The confidence interval is shown with error bars.

In Fig. 11, we show the outage probability as a function of the eye-opening penalty. We apply the MMC algorithm to compute PMD-induced penalties in a 10 Gbit/s NRZ system using 50 MMC iterations with 2,000 samples each. The results obtained using the samples in the final iteration of the MMC simulation (dashed and solid lines) are in excellent agreement with the ones obtained using importance sampling (open circles and squares). Here we used the results computed with importance sampling to validate the results obtained with MMC. The use of importance sampling to compute penalties in PMD single-section compensated systems was already validated with a large number of standard Monte Carlo simulations by Lima Jr. *et al.* [36], [14]. Therefore, the results computed with importance sampling can be used to validate the results computed with MMC. Our goal here is to show the applicability of MMC to accurately compute PMD-induced penalties in uncompensated and single-section PMD compensated systems.

In Fig. 12, we show contours (dotted lines) of the joint pdf of the magnitude of the uncompensated normalized first- and second-order PMD, $|\boldsymbol{\tau}|$ and $|\boldsymbol{\tau}_\omega|$, computed using importance sampling, as in [48]. We also show contours for the eye-opening penalty (solid lines) of an uncompensated system with a mean DGD, $\langle|\boldsymbol{\tau}|\rangle$, of 15 ps. The penalty contours were produced using the same samples we generated using the MMC method in the computation of the outage probability shown in Fig. 11. The MMC method automatically placed its samples in the regions of the $|\boldsymbol{\tau}|-|\boldsymbol{\tau}_\omega|$ plane that corresponds to the large DGD values that have the highest probability of occurrence, which is the region that is the dominant source of penalties in uncompensated systems.

http://dx.doi.org/10.5772/53306

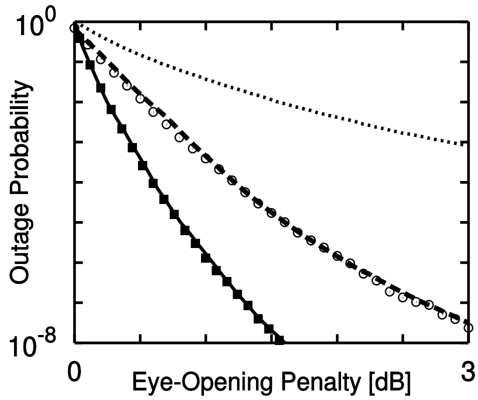

Figure 11. Outage probability as a function of the eye-opening penalty. (i) Dotted line: Uncompensated system with a mean DGD of 30 ps. (ii) Dashed line and (iii) Open circles: Results for a variable-DGD compensator, obtained using MMC and IS, respectively, for a system with mean DGD of 30 ps. (iv) Solid line and (v) Squares: Results for an uncompensated system with mean DGD of 15 ps, obtained using MMC and IS, respectively.

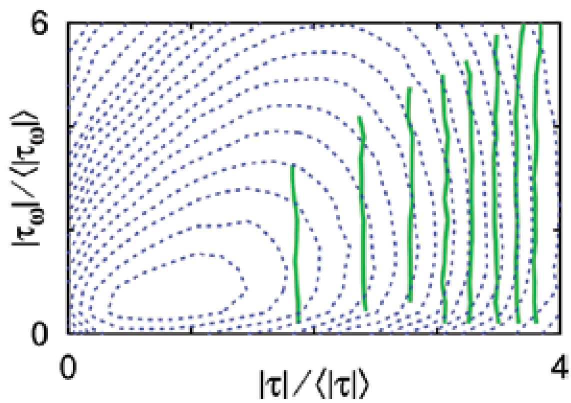

Figure 12. Penalty curves computed with MMC for an uncompensated system. Uncompensated system with a mean DGD of 15 ps. The dotted lines show the contour plots of the joint pdf of the normalized $|\boldsymbol{\tau}|$ and $|\boldsymbol{\tau}_\omega|$, obtained using IS. The solid lines show the average eye-opening penalty given a value of $|\boldsymbol{\tau}|$ and $|\boldsymbol{\tau}_\omega|$, obtained using MMC. The contours of joint pdf from the bottom to the top of the plot, are at 3×10^{-n}, and, n=1, …, 7 and 10^{-m}, m=1, …,11. The penalty contours in dB from the left to the right of the plot, are at 0.2, 0.4, 0.6, 0.8, 1.0, 1.2, 1.4, 1.6.

In Fig. 13, we show similar results for a system with $\langle|\boldsymbol{\tau}|\rangle$=30 ps and a variable-DGD compensator that was programmed to minimize the residual DGD at the central frequency of the channel after compensation. In contrast to Fig.12, the MMC method automatically placed its samples in the regions of the $|\boldsymbol{\tau}|-|\boldsymbol{\tau}_\omega|$ plane where $|\boldsymbol{\tau}_\omega|$ is large and the DGD is close to its average, corresponding to the region in the plane that is the dominant source of penalties in this compensated system. These results agree with the fact that the contour plots in the region dominating the penalty are approximately parallel to the DGD axis, indicating that the penalty is nearly independent of DGD. In Figs. 12 and 13, the samples obtained using the MMC method are automatically biased towards the specific region of the $|\boldsymbol{\tau}|-|\boldsymbol{\tau}_\omega|$ plane that dominates the penalty, *i.e.*, the region where the corresponding penalty level curve intersects the contour of the joint pdf of $|\boldsymbol{\tau}|$ and $|\boldsymbol{\tau}_\omega|$ with the highest probability. We did not compute the confidence interval for the results showed in this section.

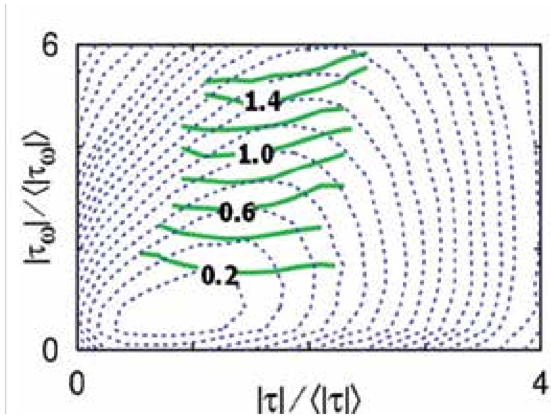

Figure 13. Same set of curves of Fig. 12 for a compensated system with a variable-DGD compensator. The penalty contours in dB from the bottom to the top of the plot, are at 0.2, 0.4, 0.6, 0.8, 1.0, 1.2, 1.4, 1.6.

In the following results, we evaluated the performance of a single-section and a three-section PMD compensator in a 10 Gbit/s nonreturn-to-zero system with a mean DGD of 30 ps. We used perfectly rectangular pulses filtered by a Gaussian shape filter that produces a rise time of 30 ps. We simulated a string with 8 bits generated using a pseudorandom binary sequence pattern. We modeled the fiber using the coarse step method with 80 birefringent fiber sections, which reproduces first- and higher-order PMD distortions within the probability range of interest [14]. The results of our simulations can also be applied to 40 Gbit/s systems by scaling down all time quantities by a factor of four. As in previous results, we used the eye opening for performance evaluation. The three-section compensator has two fixed-DGD elements of 45 ps and one variable-DGD element. The results that we present in this section were obtained using 30 MMC iterations with 8,000 samples each and using importance sampling with a total of 2.4×10^5 samples. We estimated the errors in MMC using the transition matrix method that we described in Section 2.2, while we estimated the errors in importance sampling as in [25].

In Fig. 14, we show the outage probability for a 1-dB penalty as function of the DGD element $(\boldsymbol{\tau}_c)$ for a system with the three-section compensator that we used. We observed that there is an optimum value for $\boldsymbol{\tau}_c$ that minimizes the outage probability, which is close to 45 ps. We set the values for the two fixed-DGD elements of the three-section PMD compensator that we used to this optimum value. The reason why the outage probability rises when $\boldsymbol{\tau}_c$

becomes larger than this optimum is because large values of $\boldsymbol{\tau}_c$ add unacceptable penalties to fiber realizations with relatively small second-order PMD values that could be adequately compensated at lower values of $\boldsymbol{\tau}_c$. We also observed that there is a relatively small dependence of the outage probability on $\boldsymbol{\tau}_c$. That is because the third, variable-DGD section of the compensator cancels the residual DGD after the first two sections, which significantly mitigates the penalty regardless of the value of $\boldsymbol{\tau}_c$.

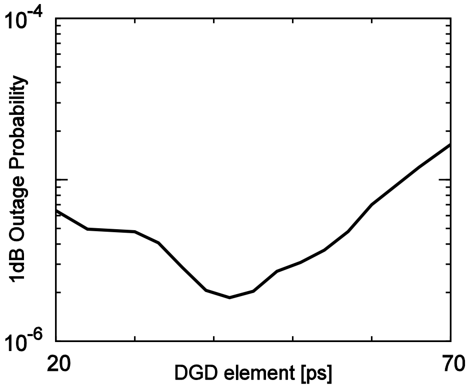

Figure 14. Outage probability for a 1-dB penalty as function of the DGD element ($\boldsymbol{\tau}_c$) of the three-section compensator for a system with mean DGD of 30 ps.

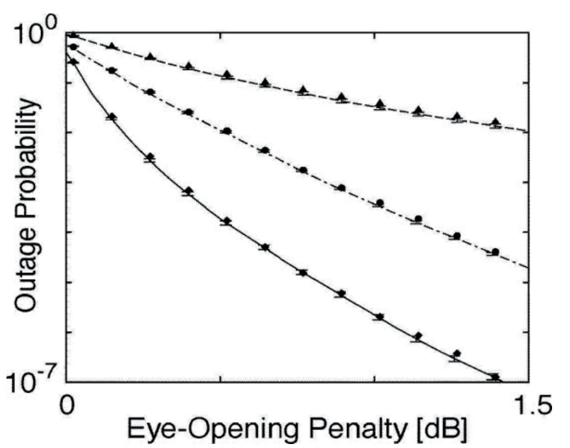

Figure 15. Outage probability as a function of the eye-opening penalty for a system with mean DGD of 30 ps. (i) Dashed line (MMC) and triangles (IS): Uncompensated system. (ii) Dot-dashed line (MMC) and circles (IS): System with a single-section compensator. (iii) Solid line (MMC) and diamonds (IS): System with a three-section compensator. The error bars show the confidence interval for the MMC results.

In Fig. 15, we plot the outage probability $(\hat{P}_{\text{out}})$ as a function of the eye-opening penalty for the compensators that we studied. The histogram of the penalty was divided into 34 evenly spaced bins in the range −0.1 and 2 dB, even though we show results from 0 to 1.5 dB of penalty. The maximum relative error $(\hat{\sigma}_{\hat{P}_{\text{out}}} / \hat{P}_{\text{out}})$ for the curves computed with MMC shown in this plot equals 0.13. The relative error for the curves computed with importance sampling is smaller than with MMC, and is not shown in the plot. The maximum relative error for the curves computed with importance sampling equals 0.1. The results obtained using MMC (solid lines) are in agreement with the ones obtained using importance sampling (symbols). The agreement between the MMC and importance sampling results was expected for the case that we used a single-section compensator, since this type of compensator can only compensate for first-order PMD [6], so that the dominant source of penalty after compensation is the second-order PMD of the transmission line. Hence, it is expected that MMC and importance sampling give similar results. We also observed good agreement between the MMC and importance sampling results for the three-section compensator. This level of agreement indicates that three-section compensators that compensate for the first two orders of the Taylor expansion of the transmission line PMD produce residual third and higher orders of PMD that are significantly correlated with the first- and second-order PMD of the transmission line. That is why the use of importance sampling to bias first- and second-order PMD is sufficient to accurately compute the outage probability in systems where the first two orders of PMD of the transmission line are compensated.

Significantly, we observed that the performance improvement with the addition of two sections, from the single-section compensator to the three-section compensator, is not as large as the improvement in the performance when one section is added, from the uncompensated to the single-section compensator. The diminishing returns that we observed for increased compensator complexity is consistent with the existence of correlations between the residual higher orders of PMD after compensation and the first two orders of PMD of the transmission line that are compensated by the three-section compensator.

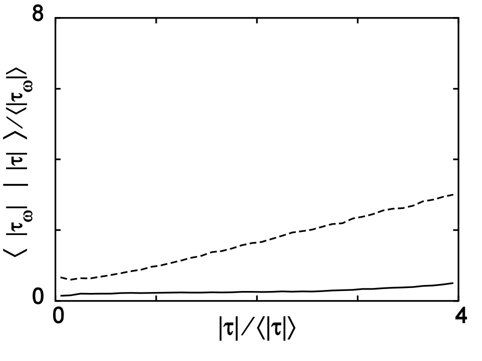

Figure 16. Conditional expectation of the magnitude of the normalized second-order PMD, $|\boldsymbol{\tau}_\omega|$, given a value of the DGD of the transmission line, $|\boldsymbol{\tau}|$. Conditional expectation before (dashed) and after (solid) the three-section compensator.

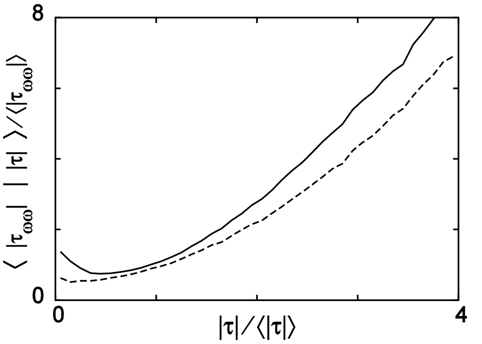

Figure 17. Conditional expectation of the magnitude of the normalized third-order PMD, $|\boldsymbol{\tau}_{\omega\omega}|$, given a value of the DGD of the transmission line, $|\boldsymbol{\tau}|$. Conditional expectation before (dashed) and after (solid) the three-section compensator.

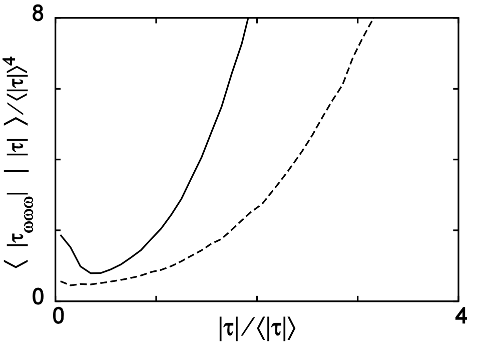

Figure 18. Conditional expectation of the magnitude of the normalized fourth-order PMD, $|\boldsymbol{\tau}_{\omega\omega\omega}|$, given a value of the DGD of the transmission line, $|\boldsymbol{\tau}|$. Conditional expectation before (dashed) and after (solid) the three-section compensator.

Figures 16–18 quantify the correlation between the lower and higher orders of PMD. In Fig. 16, we show the conditional expectation of the magnitude of second-order of PMD both before and after the three-section compensator given a value of the DGD of the transmission line. In these figures, the DGD $|\boldsymbol{\tau}|$ is normalized by the mean DGD $\langle|\boldsymbol{\tau}|\rangle$ and $|\boldsymbol{\tau}_{\omega}|$ is normalized by $\langle|\boldsymbol{\tau}_{\omega}|\rangle$ to obtain results that are independent of the mean DGD and of the mean of the magnitude of second-order PMD. We observed a large correlation between $|\boldsymbol{\tau}|$ and $|\boldsymbol{\tau}_{\omega}|$ before compensation, while after compensation $|\boldsymbol{\tau}_{\omega}|$ is significantly reduced and is less correlated with the DGD, demonstrating the effectiveness of the three-section compensator in compensating for second-order PMD. In Figs. 17and 18, we show the conditional expectation of the magnitude of the third-order PMD and of the fourth-order PMD, respectively, before and after the three-section compensator, given a value of the DGD of the transmission line. In both cases, we observed a high correlation of the third- and the fourth-order PMD with the DGD before and after compensation. In addition, we observed a significant increase of these higher-order PMD components after compensation, which leads to a residual penalty after compensation that is correlated to the original first- and second-order PMD.

In Fig. 19, we show contour plots of the conditional expectation of the penalty with respect to the first- and second-order PMD for a system with a three-section PMD compensator [35]. These results show that the residual penalty after compensation is significantly correlated with the first- and second-order PMD. The correlation between the higher orders of PMD with the DGD that we show in Figs. 16–18 can be estimated from the concatenation rule [42], which explicitly indicates a dependence of the higher-order PMD components on the lower order components. The increase in these higher-order components after compensation is also due to our choice of the operating point of this compensator, which is set to compensate only for first- and second-order PMD, regardless of the higher-order PMD components. It is possible that this three-section PMD compensator would perform better if all 7 parameters of the compensator are adjusted to achieve the global penalty minimum. However, finding this global optimum is unpractical due to the large number of local optima in such a multi-dimensional optimization space, as we found in our investigation of single-section PMD compensators [14]. On the other hand, the compensation of first- and second-order PMD using the three-section compensator that we studied here, which was proposed by Zheng, *et al.* [35], can be implemented in practice.

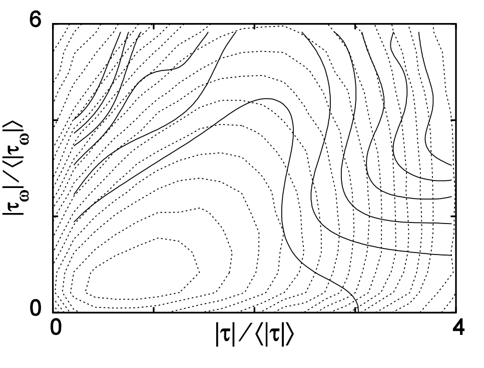

Figure 19. Three-section compensated system. The dotted lines are contour plots of the joint pdf of the normalized $|\boldsymbol{\tau}|$ and $|\boldsymbol{\tau}_\omega|$ from the bottom to the top of the plot, are at 3×10^{-n}, with n=1,⋯,7 and 10^{-m}, with m=1,⋯,11. The solid lines are contour plots of the conditional expectation of the eye-opening penalty in dB from the bottom to the top of the plot, are at 0.1, 0.2, 0.3, 0.4, 0.5, 0.6.

In this Section, we showed that both multiple importance sampling and MMC can be used with all the compensators that we investigated to reduce the computation time for the outage probability due to PMD in optical fiber communication systems. Importance sampling in which both the first- and second-order PMD are biased can be used to efficiently compute the outage probability even with a three-section PMD compensator in which both first- and second-order PMD are compensated, which is consistent with the existence of a large corre-

http://dx.doi.org/10.5772/53306

lation between first- and second-order PMD of the transmission line and higher orders of PMD after compensation. We directly verified the existence of these correlations. In contrast to what we presented in Fig.11, where importance sampling was used to validate the results with MMC, in the resulted subsequently presented, we used MMC to validate the results obtained with importance sampling. We used MMC to validate the results obtained with importance sampling because MMC can be used to compute penalties induced by all orders of PMD and not just penalties correlated to first- and second-order PMD as is the case with the importance sampling method. We showed that MMC yields the same results as importance sampling, within the statistical errors of both methods. Finally, we showed that the three-section compensator offers less than twice the advantage (in dB) of single-section compensators. We attribute the diminishing returns with increased complexity to the existence of correlations between the first two orders of PMD prior to compensation and higher orders of PMD after compensation.

5. Conclusions

In this chapter, we used MMC and IS in which both the first- and second-order PMD are biased to investigate the performance of single-section and three-section PMD compensators. We showed that both methods are effective to compute outage probabilities for the optical fiber communication systems that we studied with and without PMD compensators. The comparison of importance sampling to the MMC method not only allowed us to mutually validate both calculations, but yielded insights that were not obtained from either method alone. The development of IS requires some *a priori* knowledge of how to bias a given parameter in the simulations. In this particular problem, the parameter of interest is the penalty. However, to date there is no IS method that directly biases the penalty. Instead of directly biasing the penalty, one has to rely on the correlation of the first-and second-order PMD with the penalty, which may not hold in all compensated systems. In contrast to IS, MMC does not require *a priori* knowledge of which rare events contribute significantly to the penalty distribution function in the tails, since the bias is done automatically in MMC. Because the samples in IS are independent, IS converges more rapidly than MMC when the biased quantity is highly correlated to the parameter of interest. However this is not always the case. The applicability of IS to model a system with a three-section PMD compensator, in which both first- and second-order components of the Taylor's expansion of PMD in the frequency domain are compensated, is consistent with the existence of a large correlation between first- and second-order PMD components of the transmission line and the higher orders of PMD after compensation. Thus, even when the first two orders of PMD are compensated, these quantities prior to compensation still remain highly correlated with the residual penalty.

It is essential to carefully monitor statistical errors when carrying out Monte Carlo simulations in order to verify the accuracy of the results. Effective procedures for calculating the statistical errors in standard Monte Carlo simulations are well known and are easily implemented. Moreover, in this case, each sample is independently drawn, and the errors in each bin of the histogram will also be independent. Hence, the smoothness of the histogram is often a good indication that the errors are acceptably low. While calculating the statistical errors with importance sampling is more complicated, analytical formulae have been successfully implemented. By contrast, calculating statistical errors using MMC is not trivial. MMC generates correlated samples, so that standard error estimation techniques cannot be applied. To enable the estimate of the statistical errors in the calculations using MMC we developed a method that we refer to as the MMC transition matrix method. The method is based on the calculation of a transition matrix with a standard MMC simulations and the use of this transition matrix to draw a large number of independent samples.

Author details

Aurenice M. Oliveira[1] and Ivan T. Lima Jr.[2]

1 Michigan Technological University, U.S.A

2 North Dakota State University, U.S.A

References

[1] B. Huttner, C. Geiser, and N. Gisin, "Polarization-induced distortions in optical fiber networks with polarization-mode dispersion and polarization-dependent losses," *IEEE J. Selec. Topics Quantum Electron,* vol. 6, pp. 317-329, 2000.

[2] G. Biondini, W. L. Kath, and C. R. Menyuk, "Importance sampling for polarization-mode dispersion," *IEEE Photon. Technol. Lett,* vol. 14, pp. 310-312, 2002.

[3] S. L. Fogal, G. Biondini, and W. Kath, "Multiple importance sampling for first- and second-order polarization-mode dispresion," *IEEE Photon. Technol Lett,* vol. 14, pp. 1273-1275, 2002.

[4] B. A. Berg and T. Neuhaus, "The multicanonical ensemble: a new approach to simulate first-order phase transitions, "*Phys. Rev. Lett,* vol. 68, pp. 9-12, 1992.

[5] A. M. Oliveira, I. T. LimaJr, C. R. Menyuk, G. Biondini, B. Marks, and W. Kath, "Statistical analysis of the performance of PMD compensators using multiple importance sampling," *IEEE Photon. Technol. Lett.,* vol. 15, pp. 1716-1718, 2003.

[6] A. M. Oliveira, I. T. LimaJr, J. Zweck, and C. R. Menyuk, "Efficient computation of PMD-induced penalties using multicanonical Monte Carlo simulations," in *Proceedings ECOC 2003*, pp. 538-539.

[7] A. M. Oliveira, C. Menyuk, and I. LimaJr, "Comparison of Two Biasing Monte Carlo Methods for Calculating Outage Probabilities in Systems with Multisection PMD Compensators," *IEEE Photon. Technol. Lett.*, vol. 17, pp. 2580-2582, 2005.

[8] A. M. Oliveira, I. T. LimaJr, C. R. Menyuk, and J. Zweck, "Performance evaluation of single-section and three-section PMD compensators using extended Monte Carlo methods," in *Proceedings OFC 2005*.

[9] A. Bononi, L. Rusch, A. Ghazisaeidi, F. Vacondio, and N. Rossi, "A Fresh Look at Multicanonical Monte Carlo from a Telecom Perspective," in *IEEE Globecom 2009*, 2009.

[10] A. Bononi and L. Rusch, "Multicanonical Monte Carlo for Simulation of Optical Links," in *Impact of Nonlinearities on Fiber Optic Communications*, S. Kumar, Ed., ed: Springer Science Business Media, LLC, 2011, pp. 373-413.

[11] R. Holzlohner and C. R. Menyuk, "Use of multicanonical Monte Carlo simulations to obtain accurate bit error rates in optical communication systems," *Optics Letters,* vol. 28, pp. 1894-1896, 2003.

[12] A. Ghazisaeidi, F. Vacondio, A. Bononi, and L. Rusch, "SOA Intensity Noise Suppression in Spectrum Sliced Systems: A Multicanonical Monte Carlo Simulator of Extremely Low BER," *Journal of Lighwave Technologies,* vol. 27, pp. 2667-2677, 2009.

[13] L. Gerardi, M. Secondini, and E. Forestieri, "Performance Evaluation of WDM Systems Through Multicanonical Monte Carlo Simulations," *Journal of Lighwave Technologies,* vol. 29, pp. 871-879, 2011.

[14] I. T. LimaJr, A. M. Oliveira, G. Biondini, C. R. Menyuk, and W. L. Kath, "A comparative study of single-section polarization-mode dispersion compensators," *J. Lightwave Technol.*, vol. 22, pp. 1023-1032, 2004.

[15] A. M. Oliveira, I. T. LimaJr, C. R. Menyuk, and J. Zweck, "Error estimation in multicanonical Monte Carlo simulations with applications to polarization-mode-dispersion emulators," *Journal of Lighwave Technologies,* vol. 23, pp. 3781-3789, 2005.

[16] B. A. Berg and T. Neuhaus, "The multicanonical ensemble: a new approach to simulate first-order phase transitions," *Phys. Rev. Lett.*, vol. 68, pp. 9-12, 1992.

[17] B. A. Berg, "Multicanonical simulations step by step," *Comp. Phys. Commum.*, vol. 153, pp. 397-407, 2003.

[18] N. Metropolis, A. W. Rosenbluth, M. N. Rosenbluth, A. H. Teller, and E. Teller, "Equation of state calculations by fast computing machines," *J. Chem. Phys.,* vol. 21, pp. 1087-1092, 1953.

[19] D. Yevick, "The accuracy of multicanonical system models," *IEEE Photon. Technol. Lett.*, vol. 15, pp. 224-226, 2003.

[20] D. Marcuse, C. R. Menyuk, and P. K. A. Wai, "Application of the Manakov-PMD equation to studies of signal propagation in optical fibers with randomly varying birefringence," *J. Lightwave Technol.,* vol. 15, pp. 1735-1746, 1997.

[21] M. Karlsson, "Probability density functions of the differential group delay in optical fiber communication systems," *J. Lightwave Technol.,* vol. 19, pp. 324-331, 2001.

[22] M. H. Kalos and P. A. Whitlock, *Monte Carlo Methods*: John Wiley and Sons, 1986.

[23] D. Yevick, "Multicanonical communication system modeling---application to PMD statistics," *IEEE Photon. Technol. Lett.,* vol. 14, pp. 1512-1514, 2002.

[24] S. Kachigan, *Multivariate Statistical Analysis: A Conceptual Introduction*: Radius Press, 1991.

[25] A. M. Oliveira, I. T. LimaJr, C. R. Menyuk, G. Biondini, B. S. Marks, and W. L. Kath, "Statistical analysis of the performance of PMD compensators using multiple importance sampling," *IEEE Photon. Technol. Lett.,* vol. 15, pp. 1716-1718, 2003.

[26] R. Walpole and R. Myers, *Probability and Statistics for Engineers and Scientists*: Macmillian, 1993.

[27] B. Efron, "Bootstrap methods: another look at the Jackknife," *The Annals of Statistics,* vol. 7, pp. 1-26, 1979.

[28] I. T. LimaJr, R. Khosravani, P. Ebrahimi, E. Ibragimov, A. E. Willner, and C. R. Menyuk, "Comparison of polarization mode dispersion emulators," *J. Lightwave Technol.,* vol. 19, pp. 1872-1881, 2001.

[29] R. Holzlöhner and C. R. Menyuk, "The use of multicanonical Monte Carlo simulations to obtain accurate bit error rates in optical communications systems," *Opt. Lett.,* vol. 28, pp. 1894-1897, 2003.

[30] K. Singh, "On the asymptotic accuracy of Efron's Bootstrap," *The Annals of Statistics,* vol. 9, pp. 1187-1195, 1981.

[31] B. Efron and R. Tibshirani, *An Introduction to the Bootstrap*: Chapman and Hall, 1993.

[32] J. Booth and P. Hall, "Monte Carlo approximation and the Iterated Bootstrap," *Biometrika,* vol. 81, pp. 331-340, 1994.

[33] R. Holzlöhner, A. Mahadevan, C. R. Menyuk, J. M. Morris, and J. Zweck, "Evaluation of the very low BER of FEC codes using dual adaptive importance sampling," *Comm. Lett.,* vol. 9, pp. 163-165, 2005.

[34] R. Noé, D. Sandel, M. Yoshida-Dierolf, S. Hinz, V. Mirvoda, A. Schöpflin, C. Glingener, E. Gottwald, C. Scheerer, G. Fisher, T. Weyrauch, and W. Haase, "Polarization mode dispersion compensation at 10, 20, and 40 Gb/s with various optical equalizers," *J. Lightwave Technol.,* vol. 17, pp. 1602-1616, 1999.

http://dx.doi.org/10.5772/53306

[35] Y. Zheng, B. Yang, and X. Zhang, "Three-stage polarization mode dispersion compensator capable of compensating second-order polarization model dispersion," *IEEE Photon. Technol. Lett.*, vol. 14, pp. 1412-1414, 2002.

[36] I. T. LimaJr, G. Biondini, B. S. Marks, W. L. Kath, and C. R. Menyuk, "Analysis of PMD compensators with fixed DGD using importance sampling," *IEEE Photon. Technol. Lett.*, vol. 14, pp. 627-629, 2002.

[37] H. Sunnerud, C. Xie, M. Karlsson, R. Samuelssonm, and P. A. Andrekson, "A comparison between different PMD compensation techniques," *J. Lightwave Technol.*, vol. 20, pp. 368-378, 2002.

[38] A. M. Oliveira, I. T. LimaJr, T. Adalı, and C. R. Menyuk, "A Novel polarization diversity receiver for PMD mitigation," *IEEE Photon. Technol. Lett.*, vol. 14, pp. 465-467, 2002.

[39] I. P. Kaminow and T. Li, *Optical Fiber Telecommunications* vol. IV-B: Academic, 2002.

[40] T. Takahashi, T. Imai, and M. Aiki, "Automatic compensation technique for timewise fluctuation polarization mode dispersion in in-line amplifier systems," *Electron. Lett.*, vol. 30, pp. 348-349, 1994.

[41] F. Heismann, "Automatic compensation of first-order polarization mode dispersion in a 10 Gbit/s Transmission System," in *Proceedings ECOC 1998*, pp. 329-330.

[42] J. P. Gordon and H. Kogelnik, "PMD fundamentals: Polarization mode dispersion in optical fibers," *Proc. Nat. Acad. Sci.*, vol. 97, pp. 4541-4550, 2000.

[43] I. T. LimaJr, A. M. Oliveira, and C. R. Menyuk, "A comparative study of single-section polarization-mode dispersion compensators," *Journal of Lighwave Technologies*, vol. 22, pp. 1023-1032, 2004.

[44] H. Bülow, "System outage probability due to first- and second-order PMD," *IEEE Photon. Technol. Lett.*, vol. 10, pp. 696-698, 1998.

[45] P. R. Trischitta and E. L. Varma, *Jitter in Digital Transmission Systems*: Artech House, 1989.

[46] E. Polak, *Computational Methods in Optimization*: Academic Press, 1971.

[47] M. Karlsson, "Polarization mode dispersion-induced pulse broadening in optical fibers," *Optics Lett.*, vol. 23, pp. 688-690, 1998.

[48] A. M. Oliveira, I. T. LimaJr, B. S. Marks, C. R. Menyuk, and W. L. Kath, "Performance analysis of single-section PMD compensators using multiple importance sampling," in *Proceedings OFC 2003*, pp. 419-421.

Section 2

Plastic Optical Fiber Technologies

Chapter 6

Efficiency Optimization of WDM-POF Network in Shipboard Systems

Hadi Guna, Mohammad Syuhaimi Ab-Rahman,
Malik Sulaiman, Latifah Supian, Norhana Arsad and
Kasmiran Jumari

Additional information is available at the end of the chapter

http://dx.doi.org/10.5772/53545

1. Introduction

Polymer optical fibers (POFs) are in a great demand for the transmission and processing of optical-based data communications compatible with the Internet, which is one of the fastest growing industries in automobile and domestic industry. Other industry such as aviation and maritime have also taking the advantages of POF. POFs become an alternative transmission media replacing copper cable for future shipboard networks. A proposed POF based technology over submarine network for multimedia data transmission, measurement system, navigation, sensors and several applications. As shown in Figure 1, the system is able to transmit a number of signals represent a different data transmission (such as video, audio, etc) using a WDM based network (refer to Figure 1).

In this chapter, we proposed a wavelength division multiplexing (WDM) system over POF due to the rapid increase of traffic demands [2]. WDM is the solution that allows the transmission of data in onboard the ship over more than just a single wavelength (color) and thus greatly increases the POF's bandwidth.

2. Fiber optic onboard ship

The utilization of optical fiber as major data communication media onboard ship especially on naval combatant ships is not a new discovery [1,2]. Equipments such as communications system, radars, navigation system, combat management system, platform monitoring systems and LAN network have used fiber optic to transfer high rate data within equipment or as main data communication backbone. For instant, the platform control and monitoring system onboard ship is using dual redundancy Fiber Data Distribution Integration (FDDI) system to command, control and monitor the platforms onboard the ship. An example of FDDI architecture is shown in Figure 2. This FDDI architecture topology is glass fiber based that capable to transport high density data over long distance because the backbone is covering the entire ship. Numbers of commercial ships are also using FDDI topology as it is a proven system available commercially in the market [1-4].

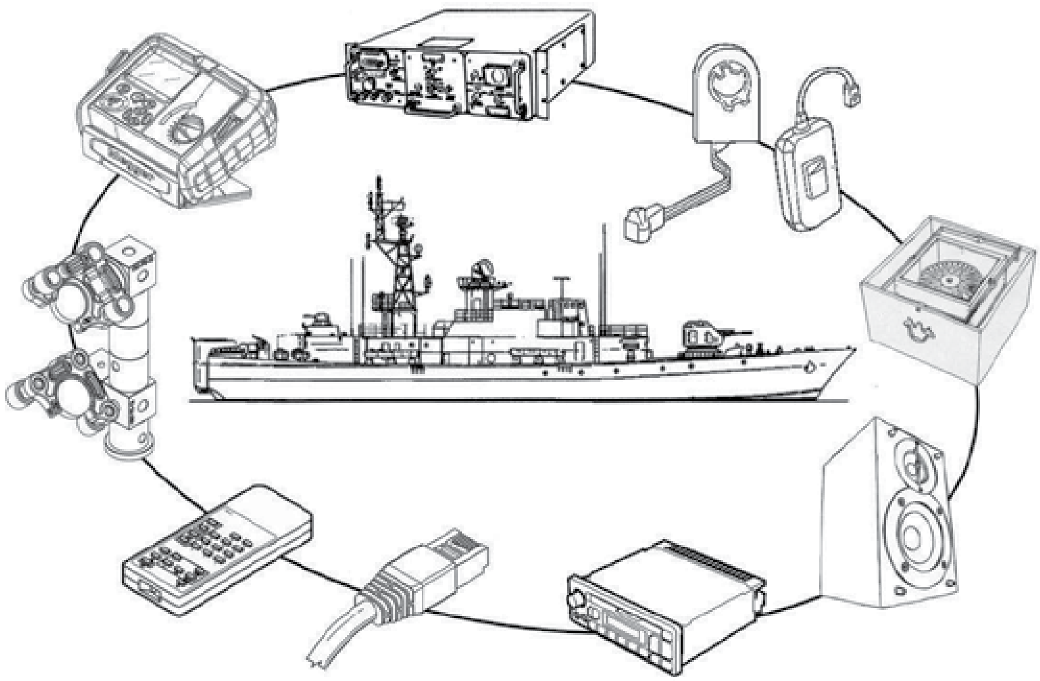

Figure 1. WDM-POF based network over novel system has been propose to ensure the high quality data transmission and communication system

In this chapter, the novel optical splitter/coupler based polymer optical fiber (POF) was successfully designed for the infotainment and data communication system over POF on-ship. The optical splitter consists of a single input port and *N* of output port (*N*=2,3,4,....). In principle, the bidirectional splitter performs two operational functions; either signal coupling (in multiple P2P direction) or signal splitting (in P2M direction). Thus, the usage of WDM onboard ship will become a new frontier in optical network.

This fiber optic onboard ship system is the most updated and promising innovation that will revolutionize in-vehicle data communication system which all data can be simply sent in visible light format rather than in electrical format at high speed data transmission. Data communication system is such all-in-one communication media system and the latest trend onboard ship network in which many appliances such as navigation system, platform surveillance & monitoring system, damage control & fire fighting system, onboard infotainment & training, sensors and many other appliances can be integrated *via* a WDM-POF. With this WDM-POF-based technology, all data such can be processed with environment-friendly LED conversion and low-cost multiplexing and filtering method besides the fact that it can extend the number of appliances in car interior. This invention enables simple POF cabling system for delivering each optical data as POF is the most updated cabling technology replacing conventional copper wire for short-haul communication. The advantages offered by POF over copper wire; economical installing cost, enabling eco-friendly LED conversion, Electromagnetic Interference (EMI) immunity, no grounding necessary, avoiding sparks, resistance to heat and vibration, lighter material, and narrow bending radius.

During the implementation of this project, several research activities to improve the efficiency of the system has been conduct. Temperature plays a significant role which can influence the performance of the data communication system in POF-based onboard ship. The characterization test was carried out is to determine the performance of the device in the test bench network. In the meantime, the fabricated splitter has been compared to other commercial one, in term of their performance; splitting ratio and power loss. An experiment has been set up in SPECTECH lab, Universiti Kebangsaan Malaysia, to evaluate the survivability of the device in environmental condition with varied temperature. Besides, the aim of experiment is to observe the temperature stability of the device while performing splitting/coupling function. The variation of temperature from 30 °C to 125 °C was exposed directly to the device.

In response to feedback from industries, the thermal aging experiment was undertaken to evaluate the durability of the device in very high temperature environment. The experiment was carried out within 9 hours while the device was exposed to high temperature at 105 °C. An analysis was made to observe the device performance with the variation of temperature. Several graph was plotted to analyze power loss and coupling ratio in varied temperature.

3. Results and discussion

In this study, single line POF is used to carry multiple wavelengths using WDM technology taking the advantage of its cheaper materials and fragility. Four different wavelengths are used to connect LAN connections, telephone line, surveillance cameras and central video/audio entertainments network throughout the ship for access by the user. The controller and server for ship LAN and surveillance cameras is at Machinery Control Room (MCR) that located at deck 1 aft of the ship. This is also the location of damage control and fire fighting headquarters onboard. The telephone PABX and central video/audio entertainment network controller is at Main Communication Center located at the centre of the ship on deck 1. The systems are also able to be monitored and controlled from the bridge located at 01 deck where the ship is navigated or from the combat Information Centre (CIC) where the ship warfare tactical information and status is collected, displayed, evaluated, disseminated and controlled for decision by the Commanding Officer.

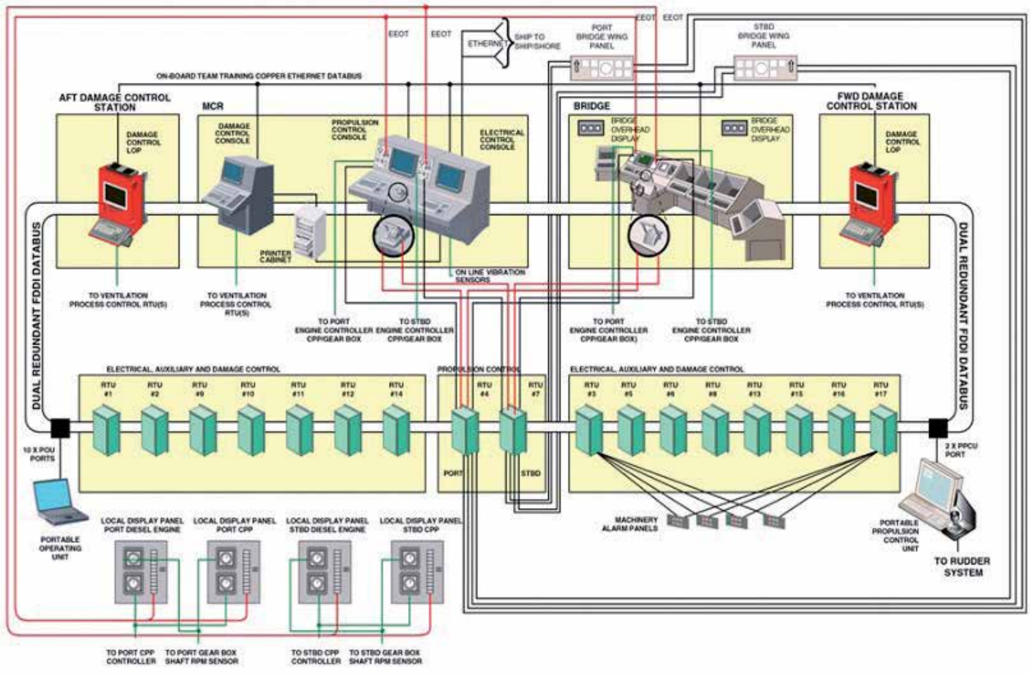

Figure 2. L3 Dual Redundant FDDI for Ship Control and Monitoring architectural network

The CCTV will provide surveillance and monitoring from flood, fire or unauthorized entrance of the high value compartments onboard. The LAN will enable ship staff to access all administration and orders, manuals, publications, maintenance requirements and training document from offices, common area and cabins. The central video/audio entertainments network is providing the ships' crews with central entertainment such as ship's live radio, movies and news broadcasted throughout the ship. The controller is placed at ship's main broadcast & recreation centre. The suggested backbone topology throughout the ship is as shown in Figure 3.

Each deck are interconnected to form a Dual Redundant POF-WDM (DRePOF-WDM) backbone arranged as one ring that interconnected to the equipments and end user devices. The backbone is arranged in mesh topology via an Optical Add Drop Multiplexer (OADM) which acts as optical switches. These switches will be able to be controlled and monitored at MCR, CIC or bridge for redundant connection through the backbone to ensure survivability and interconnectivity of the network. The connection [5] is shown in Figure 4. The devices need for this system is: fiber couplers, Multiplexer, Demultiplexer, Optical Add Drop Multiplexer (OADM) and POF's switches.

Figure 4 as shown above indicates overall arrangement of the system from the backbone to the equipments and the end users located on the various decks onboard the ship. On each deck, equipments and users in the rooms or compartments is linked to the DRePOF-WDM backbone topology using WDM sequenced by time division multiplexing TDM *via* a transceiver. The multiple different signals enter and exit from the devices onto the single wavelength data streams are done by passive devices multiplexer and demultiplexer. Many transmitters with different lights colour are used to carry single information. For example, red light with 650nm wavelength modulated with LAN signal while blue, green, and yellow lights carry image information, radio frequency (RF), and video signal, respectively. As shown is Figure 4, WDM is the first passive device required in WDM-POF system and it functions to combines optical signals from multiple different single-wavelength end devices onto a single fiber [6-7]. Conceptually, the same device can also perform the reverse process with the same WDM techniques, in which the data stream with multiple wavelengths decomposed into multiple single wavelength data streams, called demultiplexing.

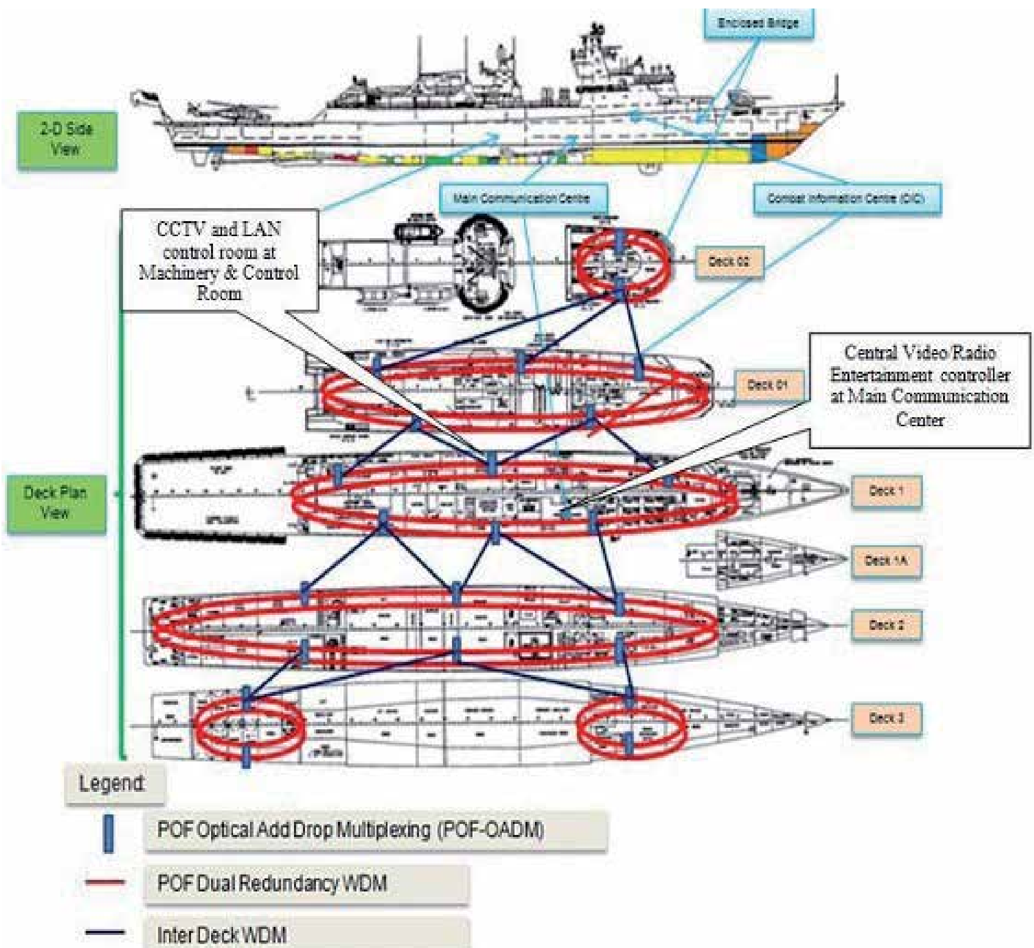

Figure 3. Deck-by-deck dual redundant POF-WDM backbone architectural network

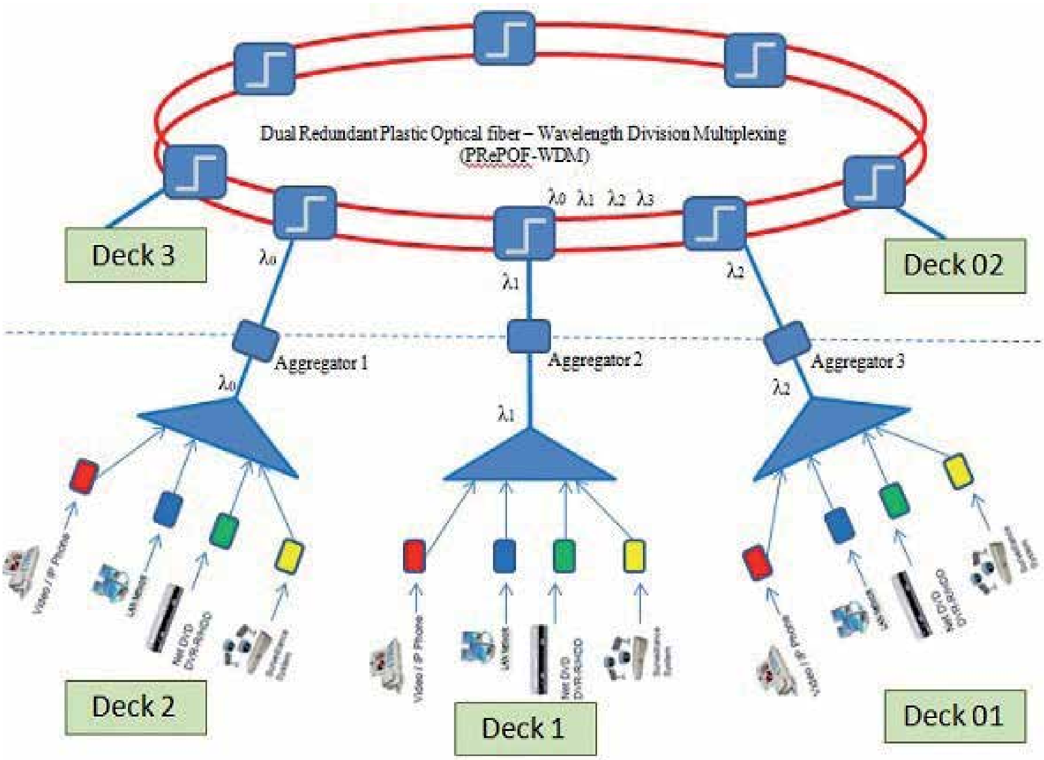

Figure 4. Connection from DRePOF-WDM backbone to each deck and equipments

During the development of the onboard project, several research activities to improve the efficiency of the system has been conduct. The characterization test was carried out is to determine the performance of the device in the test bench network.

3.1. Design and characterization of POF splitter

3.1.1. First generation

The first generation of low-cost fused taper (LFT™) splitters is initially demonstrated as novel innovation in optical splitter technology particularly for POF since it is fabricated via handmade fusion technique that is performed by handwork skill associated with simple tools; candle and metal rather than biconical fused taper. The fabrication method is cost-effective and less time-consuming (11 minutes per unit).

In comparison, the first generation of LFT™ splitter is more cost-effective than other POF-based commercial splitter e.g. Diemount™ grinded splitter, Harz-optic™ splitter, Industrial Fiber Optic™ (IFO) Fused Splitter and many others. The high costs of these commercial splitters are mainly due to the fabrication method that is complicated and implemented with fabrication machine that expensive. For LFT™ splitters, new handwork fusion method lead to low fabrication cost of splitter. The price for IFO™ fused splitter which uses same type as LFT™ splitter cost around USD110 while LFT™ splitter is only cost at ~ USD20. Figure 5 shows the price comparison between the commercial splitter and LFT™ splitters.

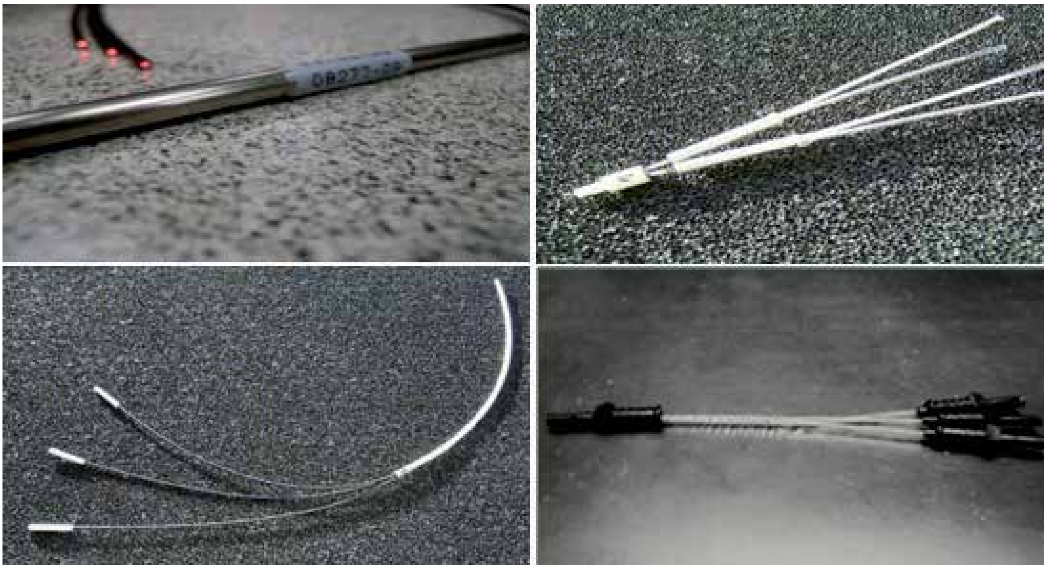

Figure 5. The price comparison between the commercial splitters (a) Industrial Fiber Optic™ (IFO) Fused Splitter (b) Diemount™ grinded splitter, (c) Harz-optic™ splitter, and (d) LFT™ splitters which cost at USD110, USD90, USD50 and USD20, respectively

3.1.2. Second generation

The second generation of LFT™ splitter is the successor of poor-performance fused splitter (first generation). The splitter is remain fabricated through handwork fusion technique. However, the procedures of fabrication method is changed with minor modification whereby the method include a new step particularly for the purpose of fusing the polymer fibers. As shown in Figure 6(a), second generation of LFT™ splitter is designed to have small area of POF imperfection, in which the length of fused and tapered fibers is reduced below 4 cm. The multimode step-indexed *polymethylmethacrylate* (PMMA) POF having a core diameter of 1 mm is used for splitter fabrication. Besides, polyvinyl chloride (PVC) is another material that used as jacket for insulating input and output fiber ports of fused splitter.

In the splitter, the tapered structure is the most critical region in producing low-loss and excellent power-splitting device. The structure has to be designed and fabricated having high fusion degree, in which all POFs are completely fused and coupled so that the wavelength of interest can pass through the coupling region with low power deviation and excellent power-splitting ratio. Therefore, no twisting effetcs are present in tapered region since the twisted spiral fiber is refined via fusion process. Figure 6(b) shows the cross-section of highly fused region in 3 × 3 or/and 1 × 3 tree coupler (splitter). Through fused and pulled region having a cross-section as depicted in Figure 6(b), the optical power input is coupled to each fiber output port with excellent power-splitting ratio. In the other word, one third of power capacity is distributed to every single of output fiber port.

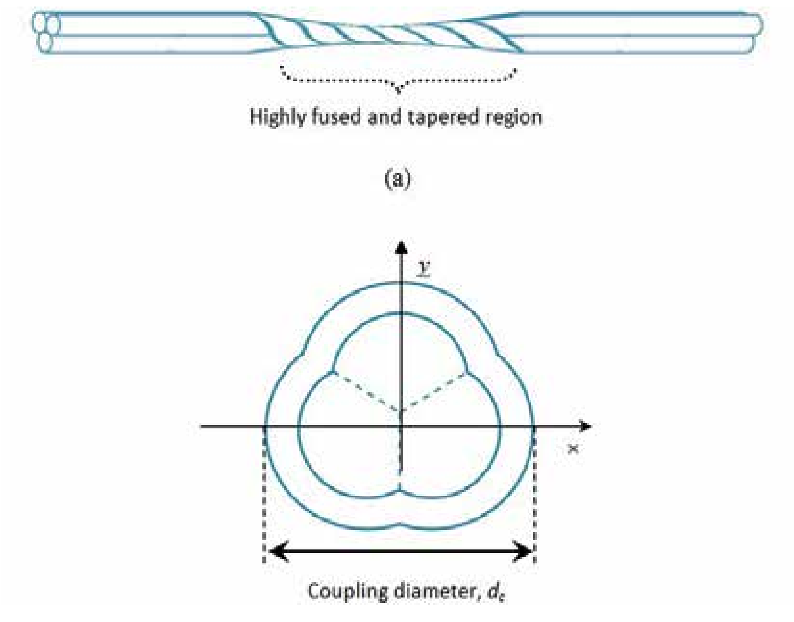

Figure 6. New schematic design of (a) highly-fused taper structure in the center of fiber bundle and (b) cross-section of fused region in fused 3 × 3 biconical coupler

Basically, the term of '*fusion*' defines the act or procedure of liquefying or melting by the application of heat. The maximum temperature required to ensure POFs reach melting point is 85°C [6]. In general, the technique includes four processes; fiber bundle configuration, fabrication of spiral fiber, fusion and fiber tapering. Among these process, fusion is new step that firstly demonstrated in fabrication method for the second generation splitters.

a. Fiber bundle configuration

b. Fabrication of spiral fiber

c. Fusion

d. Fiber tapering

Since the length of tapered fiber is reduced below 6 cm to minimize area of POF imperfection. An experimental characterization was undertaken on the relationship between the length of tapered and optical loss to observe a possible range of tapered length enabling low-loss power splitting. Figure 7 shows the relationship between the length of tapered and optical loss. Figure 8 shows the relationship between coupling ratio and the length of tapered. These results are essential in determine excellent dimension for the fabrication of second generation of LFT™ splitter. Coupling ratio is a parameter that indicates fusion characteristic in fused fibers. The ideal coupling ratio is 0.33 for each output port of splitter. The coupling ratio of 0.33 for each port shows that each fiber has been fused completely to be as a new single core.

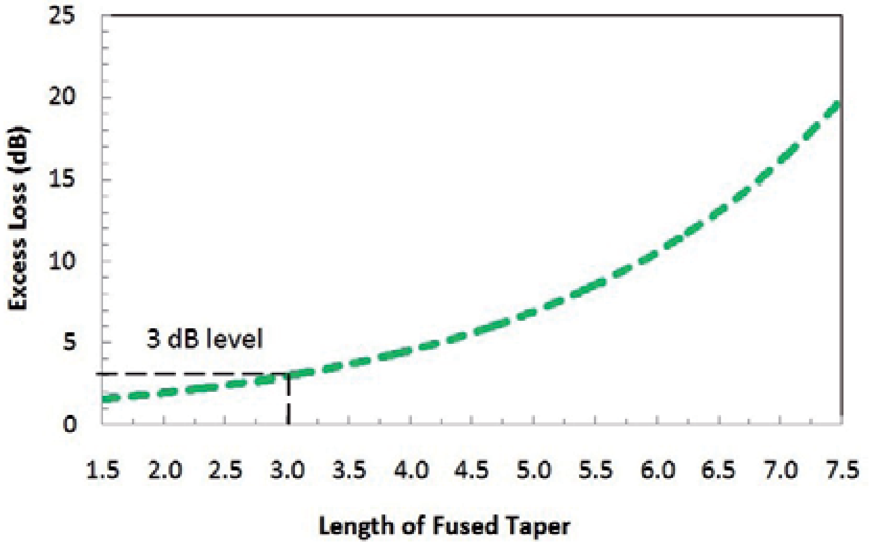

Figure 7. The excess loss of 3 × 3 coupler with range of tapered length vary from 1.5 cm to 7.5 cm; low excess loss < 3 dB occur in coupler in the range of tapered fiber length of 1.5 – 3.0 cm.

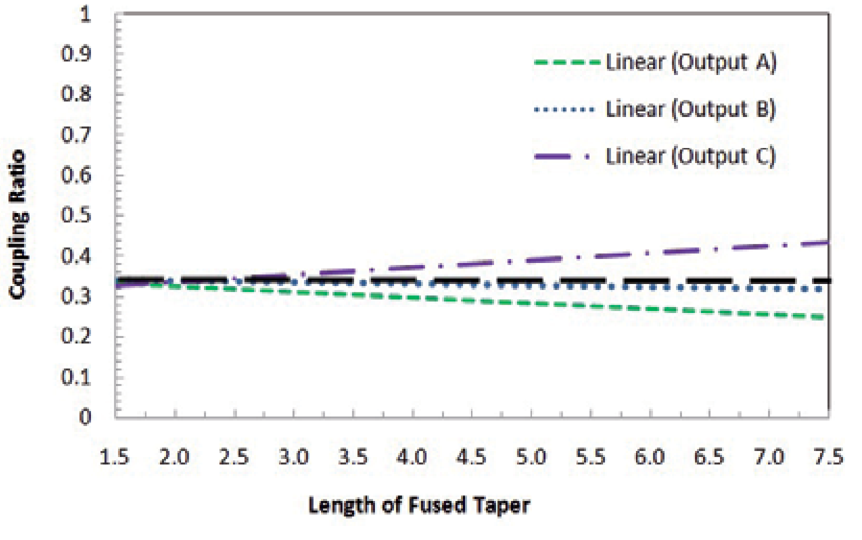

Figure 8. The coupling ratio of 3 × 3 coupler with range of tapered length vary from 1.5 cm to 7.5 cm; the coupler has good coupling ratio (~ 0.33) for each port within the range of 3 cm to 1.5 cm

From the graph, it is indicated that low optical loss < 3dB presents in tapered fiber length range of 1.5 – 3.0 cm. Furthermore, the fused and tapered fiber has good fusion characteristic in the range of 1.5 – 2.0 cm since the coupling ratio of each output fiber reach ~ 0.33 within this range. It is found that 1.5 cm is the minimum length required for fused input fiber to be suited into a small channel having ~1 mm diameter in DNP connector. Therefore, the range of 1.5 – 2.0 is selected for excellent dimension of fused and tapered length in order to permit low-loss power splitting and homogenous splitting ratio. Figure 9 (a) shows the structure of fused and tapered output fiber featured in the second generation of LFT™ splitter, in which the diameter of POF cross-section decrease to ~1 mm that fabricated through modified handwork fusion technique.

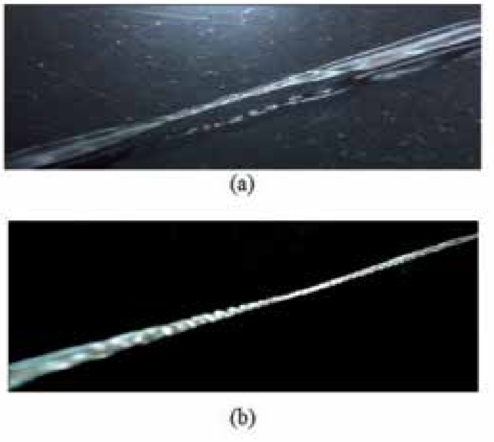

Figure 9. The features of (a) novel highly fused tapered having short taper length and plane surface (without twisting effect) and (b) conventional fused taper having long taper length and ripple surface (with twisting effects)

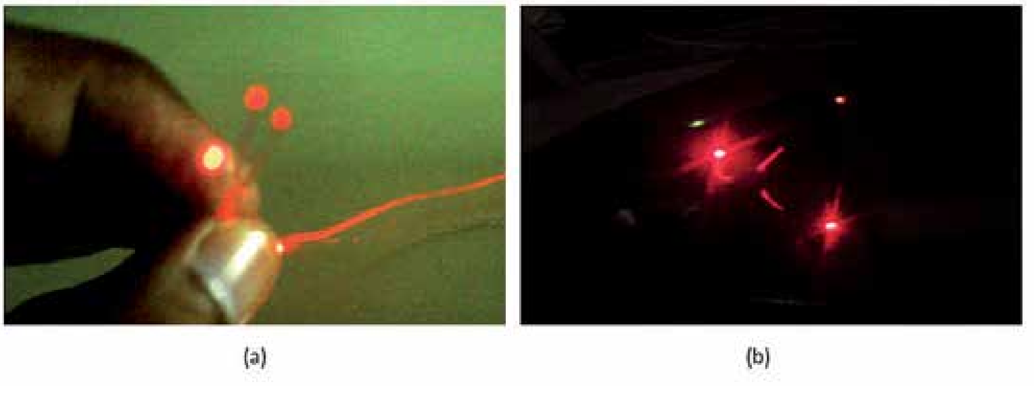

Figure 10. The results of experimental optical injection with 650 nm light source; (a) for the first generation of splitter and (b) for the second generation of LFT™ splitter.

As shown in Figure 10 (a), when the only one fused input port is injected with red LED transmitter having 650 nm, it is observed that each output port emits high-intensity red light. In comparison, as shown in Figure 10 (b), in the past experimental injection test, each output port of the first generation splitter emits red light with low power intensity except one output fiber among them. The power splitting with high intensity shows that the second generation of fused splitter is able to perform low-loss optical data splitting.

For the first generation splitters, as shown in Figure 11, the insertion loss of each output port is high which the range is 10 - 20 dB. In contrast to the first generation splitter, the second generation splitters perform with low insertion loss since each output fiber has insertion loss varying from 4 dB to 17 dB.

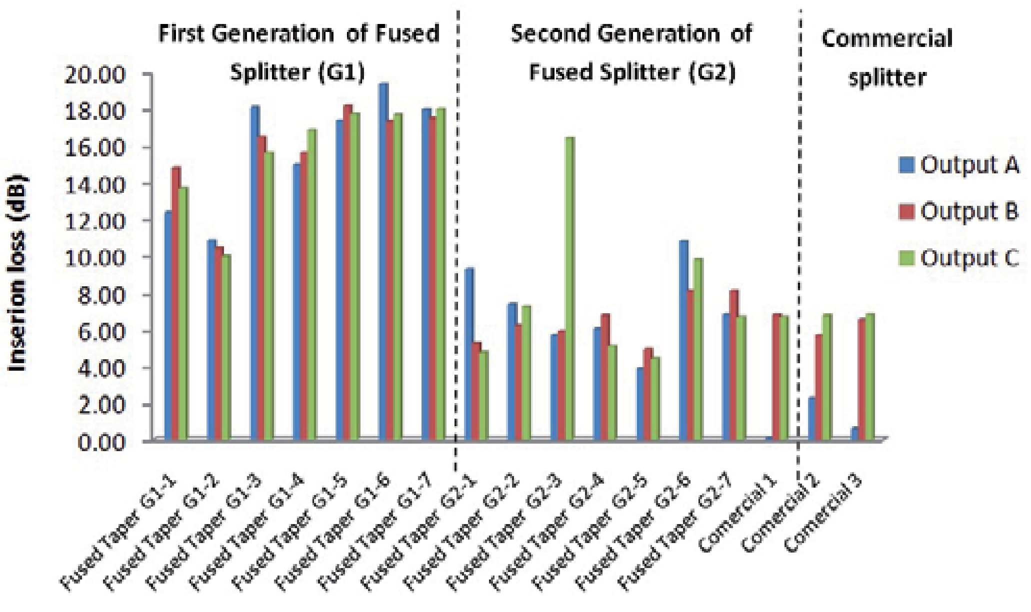

Figure 11. The comparison for insertion loss of each output fiber

Figure 12 shows the result for excess loss of the first and the second generations of LFT^{TM} splitter and commercial splitter. The result shows that the excess loss of the second generation splitter is lower than the first generation; this means that the performance of low-cost fused splitter has been improved effectively.

3.2. Temperature effect experiment

In the experiment, temperature of hot plate was increased by 5 °C to reach stable condition. Figure 13. shows the influence of temperature variation T from 30 °C to 125 °C on output power P_o for the splitter.

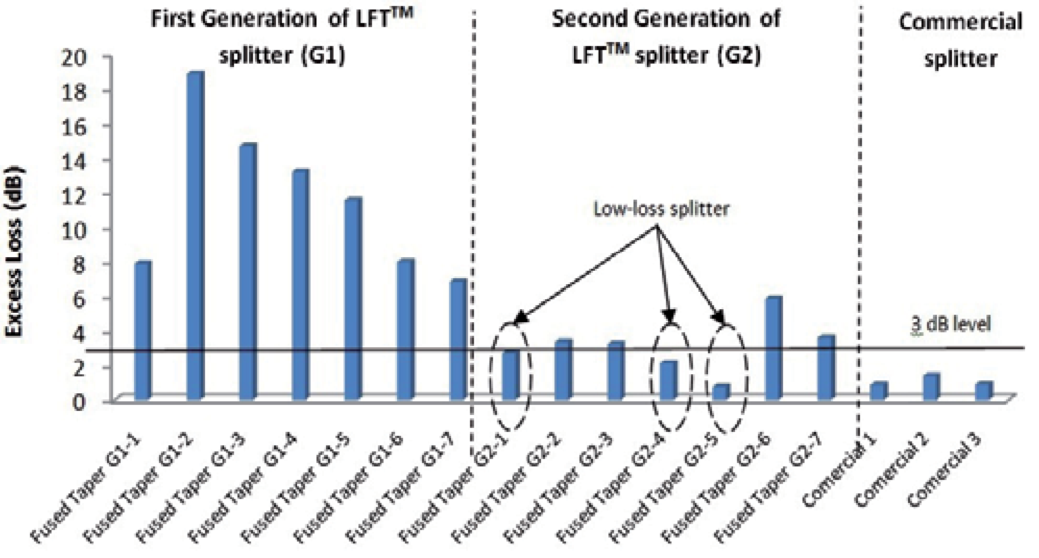

Figure 12. The comparison for excess loss

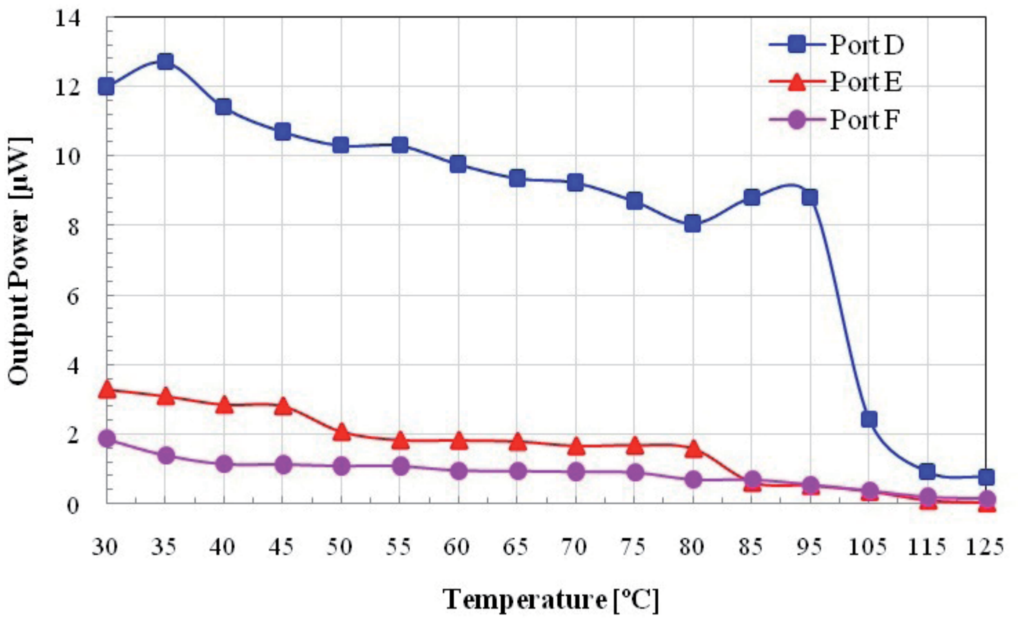

Figure 13. The relationship between temperature variation (30 °C to 125 °C) and output power for Low cost POF splitter

As shown in Figure 14, in each fiber port, output power decreases with respect to temperature rise. The type of fused polymer splitters were completely damaged when heating temperature increased T = 125 °C. The temperature point at 95 °C can thus be defined as damage threshold because the splitter loss temperature stability at this point. Figure 14. shows Excess loss variations as function of temperature for the splitter in bidirectional power injection.

As shown in Figure 15, the excess loss increase gradually with temperature increase. In this case, the splitter has temperature stability while maintaining their performance until T = 100 °C. Figure 15. shows temperature dependence of coupling ratio for the splitter in their throughput and cross-coupled fiber ports in bidirectional light guide propagation.

3.3. Thermal aging experiment

Figure 16. shows the durability of the Low cost POF splitter within 9 hours at fixed temperature T = 105 °. The graph shows that the splitter has high temperature stability within 9 hours when the splitter was exposed to very high temperature. The result shows that the splitter has high durability.

Figure 17. shows the durability of the Low cost POF splitter in term of output power in μW within 9 hours at fixed temperature T = 105 °.

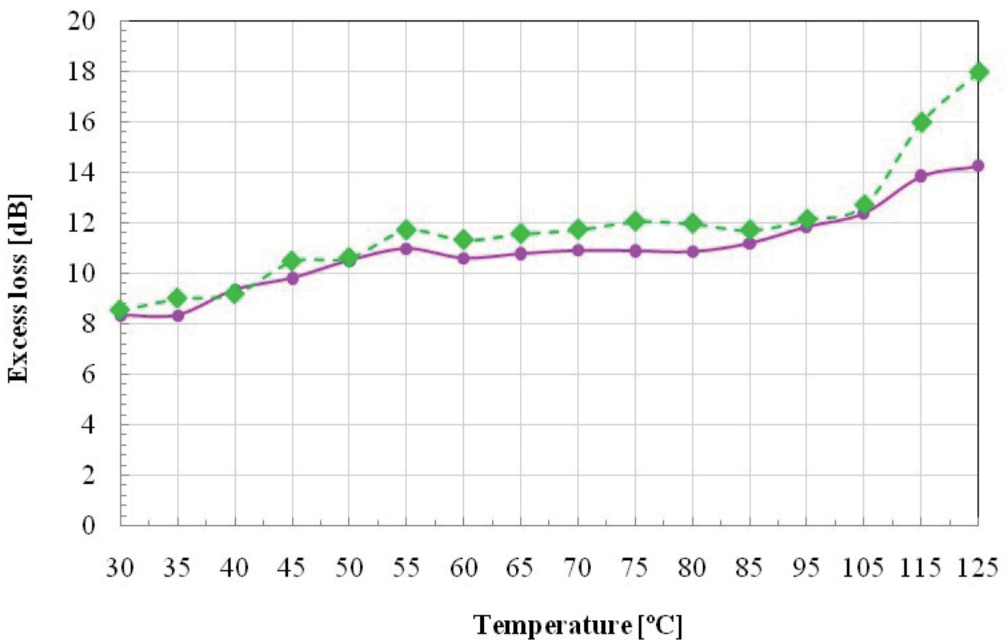

Figure 14. Excess loss variations as function of temperature for the splitter in bidirectional power injection

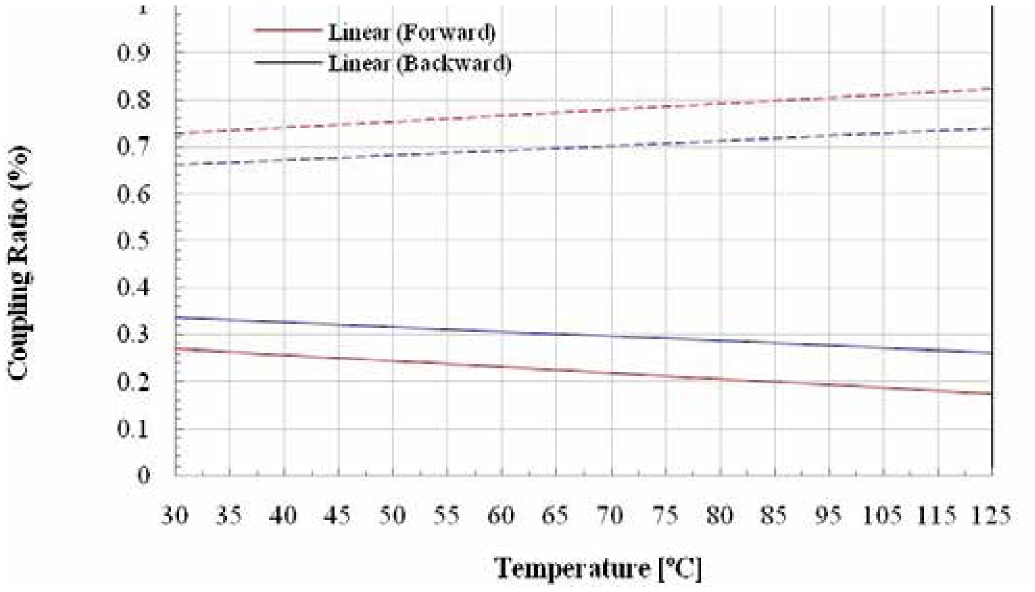

Figure 15. Excess loss variations with temperature increase for the splitter

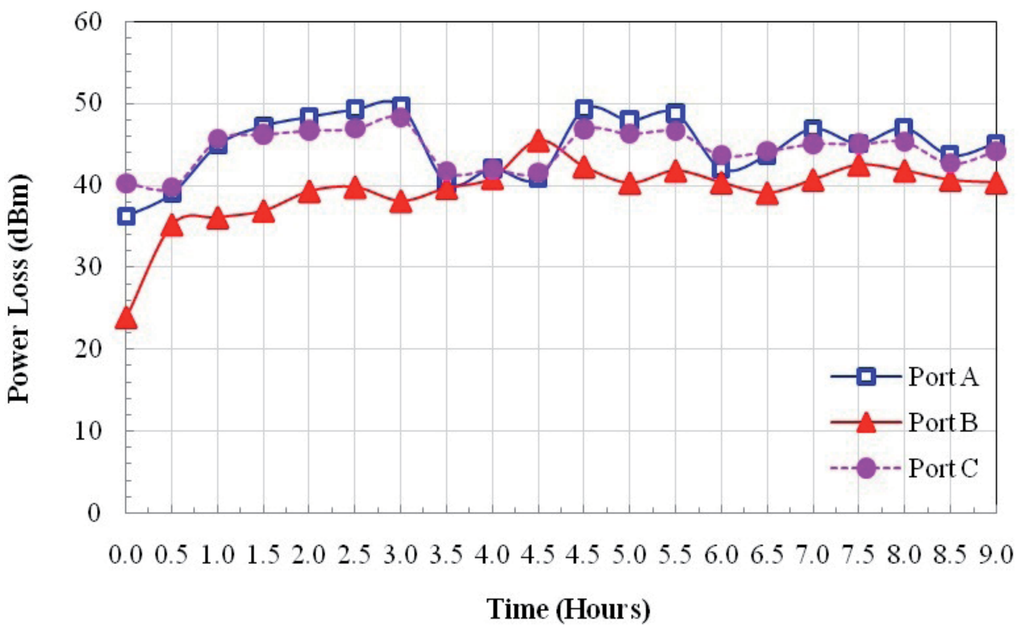

Figure 16. The relationship between heating time and power loss of the splitter

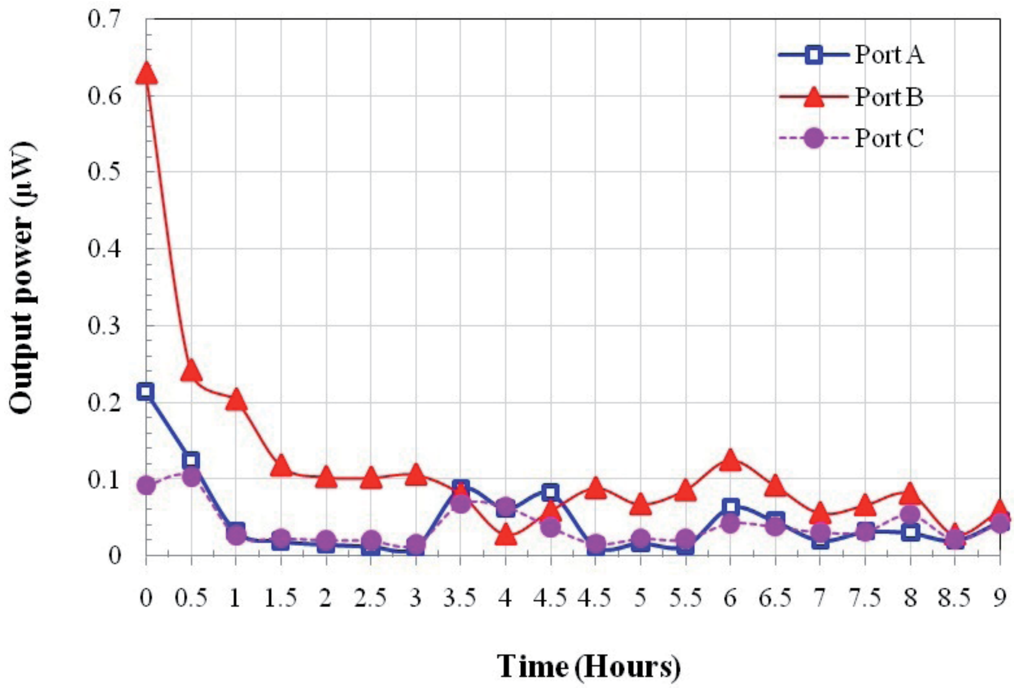

Figure 17. The relationship between heating time and power loss of the splitter

4. Conclusion

In conclusion, the Wavelength Division Multiplexing application over the Polimer Optical Fiber was used for data transmission onboard ship system. The network has been designed via dual redundancy POF-WDM interconnected deck-by-deck using mesh topology, introducing the design philosophy of Dual Redundant POF-WDM (DRePOF-WDM) backbone network. OADM acts as switches is used to make redundancy circuits [5, 8]. Four different wavelengths has been used to connect the overall equipments throughout the ship. This system is very promising hence the payback of less overall ship's weight and therefore will improve the speed and less fuel consumptions of the ship for future new build or ship embarking life extension program. The efficiency related to the temperature effect and thermal aging has been observed in order to optimized the onboard ship communication network. Any system or equipment to be fitted onboard can use this existing DRePOF-WDM backbone.

Acknowledgements

This research has been conducted in Computer& Network Security Laboratory, Universiti Kebangsaan Malaysia (UKM). This project is supported by Ministry of Science, technology and Environment, Government of Malaysia, PRGS/1/11/TK/UKM/03/1. All of the handmade fabrication method of POF splitter, LFT^{TM} splitter and also the low cost WDM-POF network solution were protected by patent numbered PI2010700001.

Author details

Hadi Guna, Mohammad Syuhaimi Ab-Rahman, Malik Sulaiman, Latifah Supian,
Norhana Arsad and Kasmiran Jumari

Universiti Kebangsaan Malaysia, Selangor Darul Ehsan, Malaysia

References

[1] Gopalkrishna, D.H., S.R. Muthangi, Vinayak, A. Paulraj. FDDI-A high speed data highway for warship system integration 1991, MILCOM '91.

[2] Gotthardt, M.R., K. Kathiresan, G.H. Campbell, J. Fluevog. Shipboard Fiber Optic Transmission Media (Cables). AT&T Bell Labs, AT&T Federal Systems and AT&T Networks Systems. CH2681-5/89/0000-0235 IEEE (1989): 0235.

[3] Baldwin, C., J. Kiddy, T. Salter, P. Chen, J. Niemczuk. Fiber Optic Structural Health Monitoring System: Raugh Sea Trials of the RV Triton 2002. Ocean MTS/IEEE.

[4] Jessop, Clifford N. All-Optical Wavelength Conversion in a Local Area Network, Report to United States Naval Academy Trident Scholar Committee, May 2006.

[5] Mohamad Syuhaimi Ab-Rahman, Mohamad Najib Mohamad Saupe, Kasmiran Jumari. Optical Switch Controller Using Embedded Internet Based System 2009. International Conference on Computer Technology and Development.

[6] Imran Ahmed, Hong Wong and Vikram Kapila. Internet-Based Remote Control using a Microcontroller and an Embedded Ethernet, Proceeding of the American Control Conference: 2004.

[7] Hong Wong and Vikram Kapila. Internet-Based Remote Control of a DC Motor using an Embedded Microcontroller 2004, Proceeding of the American Society for Engineering Education annual Conference and Exposition.

[8] Alam, M.F., M. Atiquzzaman, B. Duncan, H. Nguyen, R. Kunath. Fibre-optic network architectures for on-board radar and avionics signal distribution. IEEE Radar Conference, Washington, DC, 7-12 May, 2000.

Chapter 7

Step-Index PMMA Fibers and Their Applications

Silvio Abrate, Roberto Gaudino and Guido Perrone

Additional information is available at the end of the chapter

http://dx.doi.org/10.5772/52746

1. Introduction

With the general term "Optical Fibers" it is quite common to refer to a specific type of fibers, in particular Glass Optical Fibers (GOF), that can then be divided into several categories depending on the type of applications they are needed for (communications, sensing, lasing, etc.); but optical fibers are not only glass-based: a wide variety of Polymer-based Optical Fibers (POF), that can be mainly classified based on the specific material and the index profile, exists, for several applications.

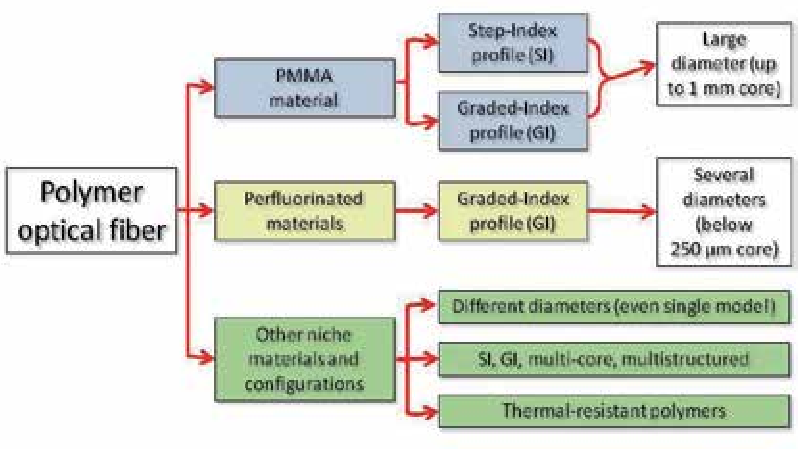

Figure 1. Overview of the different types of POF available.

Two major classes of POF can be identified: Step-Index POF with large core and Graded-Index POF. It is quite common to identify the first type of fiber as POF and the second one as PF-POF (made of perfluorinated material) or GI-POF, however in the following, for sake of clarity, PMMA-SI-POF will be used to address large core step index fibers made of PMMA material. Some other variants exist but are not commonly used, so we will not address them in this chapter.

The use of polymers instead of glass gives certain advantages in terms of mechanical robustness and installation in hostile environments (such as in presence of water or high humidity), so many studies are still in progress to reduce the transmission performance penalty that POF pay with respect to GOF. Since the behavior of the best performing GI-POF are getting very similar to multi-mode GOF, purpose of this chapter is to focus only on PMMA-SI-POF.

This chapter is organized as follows: first, we will give an overview on the fiber itself, describing the material, the production process, the main characteristic; secondly, we will describe components and tools for PMMA-SI-POF handling and using; then, we will analyze their adoption for communication systems and sensing applications.

2. Basics of PMMA-SI-POF

The most widely available PMMA-SI-POF has a core diameter of 980 μm and a global (core plus cladding) diameter of 1mm, while a variant with a diameter of 500μm is gaining interest; however, only the first type of fiber is standardized [1].

The success of 1mm fiber is due to the wide range of applications (Hi-Fi, car infotainment systems, video-surveillance, home networking) and to the interesting mechanical characteristics with respect to GOF. In particular, we can highlight the following main advantages that this type of POF has with respect to other fibers (we will not discuss about all the intrinsic advantages of optical propagation compared with electrical communications, that are maintained moving from GOF to POF):

- High mechanical resilience: the flexibility of the plastic material allows rough handling of the fiber, such as severe bending and stressing, without causing permanent damages. This enables brownfield installation (for example in existing power ducts, being an electrical insulator), also thanks to the 2,2 mm diameter of conventional PMMA-SI-POF simplex cable;

- High mechanical tolerances: the 980 μm core and the 0,5 numerical aperture allow a certain aligning mismatch in connection processes with transmitter and receivers of among fiber spools. This tolerance avoids the use of expensive precision tools for connectorization. Moreover, dust on the fiber ends is less compromising than with small-core fibers;

- Low bending losses: the core diameter also allows a certain bending tolerance. It has been demonstrated [2] that more than 20 bends at 90° with a radius of 14 mm are requested to cause a loss over 5dB for a 1 Gbps transmission system, even if standards foresee 0,5dB for every bend with a bending radius of 25 mm;

- Easy tooling: fiber cut can be made via conventional scissors, and polishing via sand paper, however very simple tools that avoid polishing after cutting exist. Connectorization is fast and easy via crimping or spin connectors, while also connector-less connection via clamping is foreseen in recent transceivers;
- Use of visible sources: the PMMA material works efficiently in the visible wavelength, namely red, green and blue (650 nm, 520 nm and 480 nm respectively). This actually helps unskilled personnel to have a preliminary evaluation of the good functioning of the components (you can actually see the light);
- Ease of installation: the previous characteristics result in a certain ease of installation for unskilled personnel and users, then yielding a consistent reduction in installation time and cost;
- Water resistance: PMMA is also very resistant towards water and salted water. This makes POF suitable for marine applications.

These advantages are reflected in 500 μm PMMA-SI-POF, with the obvious note that alignment tolerances are lower.

In turn, PMMA-SI-POF suffer of high attenuation and low bandwidth; while the attenuation is due to the material, the bandwidth limitations are due to the size of the core and the index profile: in 1 mm PMMA-SI-POF around 1 million modes are propagating in the operational wavelengths.

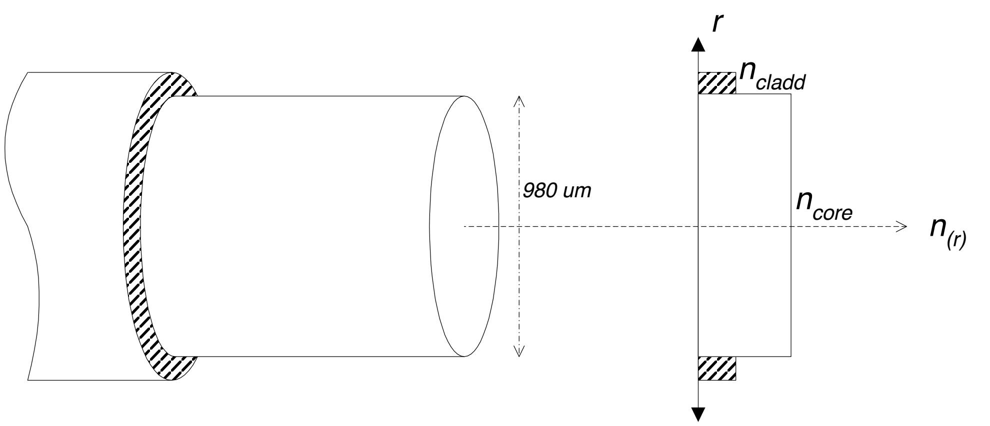

Figure 2. PMMA-SI-POF dimensions and index profile

We can then summarize that PMMA-SI-POF are not to be considered as competitors to GOF, but are rather competitors to copper, with the advantage of being a suitable medium for hostile environments. In Figure 3 it is possible to see a comparison among standard UTP Cat. 5e cable and a PMMA-SI-POF duplex cable.

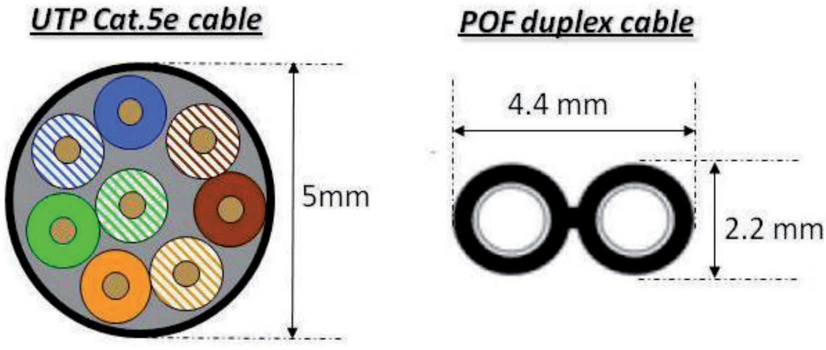

Figure 3. Comparison among a standard UTP Cat.5e copper cable and a PMMA-SI-POF duplex cable. POF cable is smaller and can easily replace copper cable.

2.1. Materials and production processes

2.1.1. Core materials

The most common material for POF is PolyMethylMethAcrylate (PMMA), also known as Plexyglas; it's refractive index is 1,492 and its glass transition temperature is around 105°C. PMMA based POF usually work with visible light (red, green and blue), however the attenuation can be very high (up to 200dB/Km for commercial fibers). Other materials have been investigates: Polystyrene (PS) has an higher refractive index than PMMA (1,59) but its attenuation performances are not expected to be better, so currently no mass production employing this polymer exists; Polycarbonate (PC) has a refractive index of 1,58, is interesting for special applications thanks to its high glass transition temperature (150°C) but its very high attenuation makes it not suitable for telecom/datacom applications.

MMA structure can be seen in Figure 4.

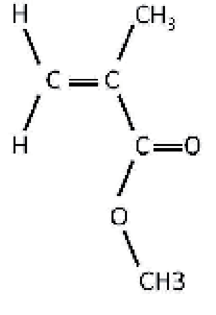

Figure 4. MMA momomer

http://dx.doi.org/10.5772/52746

2.1.2. Cladding materials

The other main materials for POF are Fluorinated Polymers; they can also be used for the core, since their performances are very interesting in terms of attenuation: in theory it could be comparable with the one achieved for glass fibers, and the refractive index is in the order of 1,42;to date, the best results have been achieved with CYTOP polymer, working at 850 nm and 1300 nm and used for GI-POF. However, from the point of view of PMMA-SI-POF, PF polymers are adopted as cladding materials.

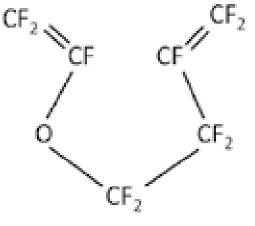

Figure 5. CYTOP momomer

PMMA can be used as cladding material when the core is made with PC.

2.1.3. Manufacturing by fiber drawing

The most well-known method for fiber productions is drawing from a preform, with a proper drawing tower; this method is used for mass production of glass fibers and can be easily adapted to polymer fibers.

A cylinder of polymer (the preform), having the very same structure and refractive indices difference of the fiber we want to draw has to be prepared, usually with an extrusion process; this cylinder has dimensions orders of magnitude bigger compared to the fiber it is meant to generate. The preform is then mounted on top of the drawing tower and heated through a specific furnace to a temperature that makes the polymer starts to soften, so that it becomes possible to reduce its diameter via controlled traction by a take-up winding drum. During the process, the diameter is controlled and it is eventually possible to deposit the coating (however this operation can also be performed in a subsequent phase).

Some variants of the process foresee the preform to be suitable for core drawing only, with the cladding applied subsequently via extrusion.

This way, the length of the fiber that can be obtained is limited by the dimension of the original preform.

With respect to GOF drawing towers, due to the lower melting temperature of polymer with respect to glass, POF towers are lower and also the ovens have a lower working temperature. Also the drawing speed is significantly lower, being in the order of 0,5 m/s while for GOF the conventional production speed overcomes 10 m/s.

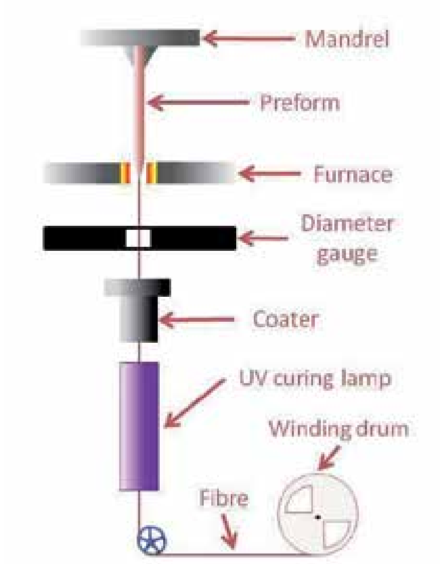

Figure 6. Fiber drawing.

2.1.4. Manufacturing by extrusion

Producing the fiber by extrusion requires the whole process to start from the monomer, that by means of a distillation process is inserted into a proper reactor together with the initiator and the polymerization controller. Once the process is concluded (at a temperature of about 150°C), the polymer is pushed through a nozzle by pressurized nitrogen injections, in order to control the diameter, and the cladding is applied (the cladding is extruded at around 200°C).

The extrusion is quite simple for PMMA-SI-POF, and is the most promising manufacturing process since it is quite cheap and allows continuous production starting from the monomer, thus enabling mass-production.

2.2. PMMASI-POF characteristics

2.2.1. Attenuation

Attenuation is a very important factor in determining the maximum length of a fiber link, and depends on the material properties and the transmission wavelength. The PMMA attenuation spectrum is depicted in Figure 7. It can be seen that, as happens with glass, three transmission windows can be clearly identified, even if with very different attenuation values: around 500 nm, 570 nm and 650 nm, starting from at least 80dB/Km; being in the visible wavelength interval, these windows can be associated to colors, respectively blue-green, yellow and red.

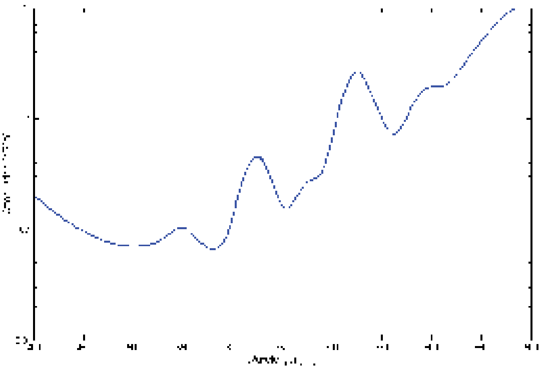

Figure 7. PMMA attenuation spectrum. Different windows can be identified.

The availability of components and the shape of the windows actually suggests to identify the transmission windows as follows: blue (480 nm), green (520 nm) and red (650 nm). Green and blue windows are characterized by the lowest attenuation, in the order of 80dB/Km (together with yellow, in which the attenuation is even lower but there is lack of components, and thus this window will be neglected in the following of this chapter), while in red the attenuation is nearly doubled but where there is a significantly higher availability of components at higher speeds. It has to be mentioned that standards [1] use to define the attenuations as reported in Table 1 for PMMA-SI-POF dubbed of category A4a.2.

Wavelength (nm)	Attenuation (dB/Km)
500	<110
650	<180

Table 1. Attenuation of PMMA-SI-POF according to IEC 60793-2-40 A4a.2

It is then evident that, when dealing with PMMA-POF, transmission length is limited to a few tens or a few hundred meters, depending on the baud-rate.

Given the attenuation of the fiber and the fact that home/office networking is one of the most interesting market for data-communications over PMMA-POF, bending loss becomes a parameter of paramount importance when dimensioning and then installing the system. As previously mentioned, standards foresee 0,5dB for a bend with a radius of 25 mm, but better results have been achieved; Figure 8 shows measured value of extra-losses for 360° bends, when the modal equilibrium is reached.

It can then be said that 0,5dB of extra-loss has to be considered for each 10 mm bend, while there is virtually no extra-loss to be considered when the bending radius exceeds 25 mm.

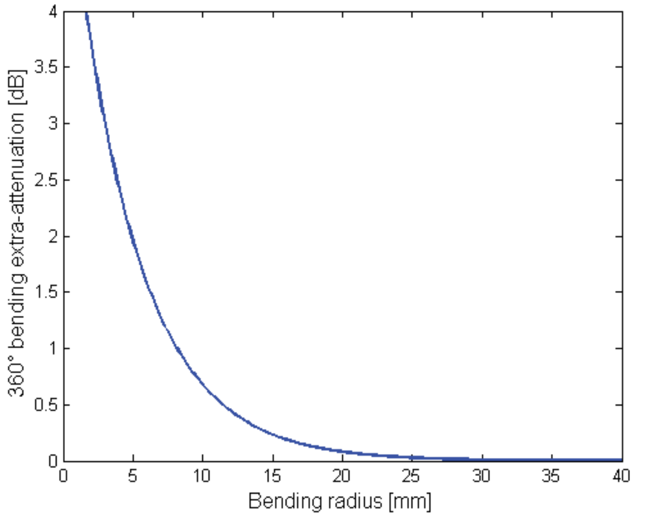

Figure 8. Extra attenuation vs. bending radius

As briefly mentioned, the modal equilibrium condition is important while measuring attenuation: due the multimodality of the fiber, the launching conditions are important especially for short lengths. In order to avoid having length-dependent attenuation measurements (after a certain length the Equilibrium Mode Distribution EMD is naturally obtained), usually two methods are adopted: differential measurement with consistent fiber lengths or the insertion of a mode scrambler at the transmitter side. An example of mode scrambler is reported in Figure 9.

Figure 9. Mode scrambler. Two cylinders with a radius of 21 mm are separated by 3 mm. The fiber is wounded in a 8-shape 10 times around those cylinders. The total attenuation of such an arrangement is about 10dB.

2.2.2. Bandwidth

PMMA-SI-POF are highly multi-modal (in the order of 1 million modes), and in the wavelength regime we consider, for what concerns bandwidth performances, multi-modality is by far the most limiting factor, while chromatic dispersion becomes negligible. It is not target of this chapter to perform a deep theoretical analyses of bandwidth in POF, then we will now focus only on experimental measurements, pointing out the fact that, as GOF, POF have a low-pass characteristic that can be approximated with a Gaussian curve.

A bandwidth measurement technique has not yet been defined in any standard; in literature, we can find results exploiting the following methods:

1. Frequency-domain direct spectral measurement with network analyzers;
2. Time-domain measurement with narrow pulse generation;
3. Optical Time Domain Reflectometry (OTDR).

The most comprehensive results available in literature [3] have been obtained with method 1, while results obtained with the other methods are usually a lot more limited in the length of the link [4], [5].

Frequency-domain measurement setup is quite simple: an electrical network analyzer drives an high-speed laser source connected to the fiber under test, then an high-bandwidth optical receiver closes the loop into the network analyzer, so that a direct bandwidth measurement can be performed. The results shown in Figure 10 are referred to a fiber with a declared NA=0,46. It is evident how POF systems can also be bandwidth limited, since we range from 30 MHz for 100 m of fiber to 9 MHz for 400 m of fiber. Also in this case it is useful to reach the EMD condition to avoid measurement being affected by launching conditions, such as transmitter numerical aperture.

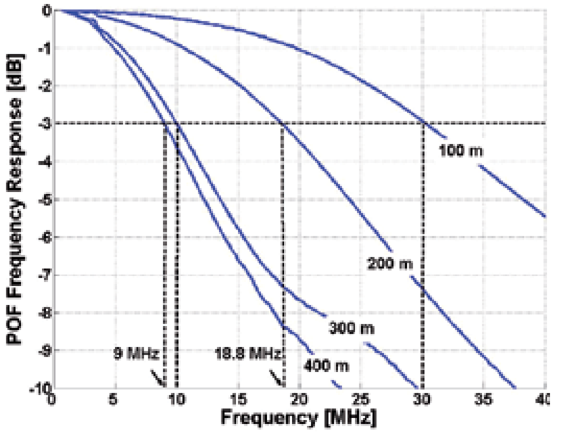

Figure 10. Electrical-to-electrical PMMA-SI-POF response for different link lengths with indication of 3dB bandwidth. Courtesy of the authors of [3].

It is not purpose of this chapter do go into deep analysis of the theoretical aspects of fibers bandwidth, and we suggest to refer to [6] if interested.

2.2.3. Handling, tooling and connectorization

The big advantage of 1 mm POF are due to their easy handling: this does not require expensive equipment and allows do-it-yourself installation; in particular:

- PMMA-SI-POF is robust and flexible, with good bending properties, and thus suitable for careless handling;
- its core dimension and numerical aperture allow certain mechanical tolerances and low sensitivity to contaminations;
- connectorization is easy, requiring simple tools (such as even conventional scissors) and, taken to the extreme, also allows connector-less contact.

Workmanlike connectorization of PMMA-SI-POF foresees the following steps:

- cutting and stripping the fiber with a proper tool, such as in Figure 11;
- inserting the fiber into the chosen connector (different types of connectors can be seen in Figure 12) and locking it (the connectors are usually self-crimping or screw-type);
- putting the connector into a polishing disk (Figure 13) and cleaving by moving the disk on delicate sand paper forming several times a 8-shape.

Figure 11. Cutting and stripping tools. On the left, a conventional copper cable stripper; on the right, a proper tool courtesy of Firecomms.

For such a connection, a 1 dB penalty is usually taken into account. Fusion splicing is not available with POF, so splicing is obtained facing to end-connectors into a proper in-line connector, and thus a 2 dB attenuation has to be taken into account.

Figure 12. Different type of 1 mm POF connectors. ST, SMA (2 versions), V-pin. Other type of connectors exist.

It is worth nothing that connectorless installation is gaining real interest since the induced penalties with respect to the previously mentioned procedure can be really negligible if the cutting is made with a certain care. If cutting and stripping is done with tools such as the ones shown in Figure 11, allowing a certain plain cut of the end face, then special transceiver housings such as the Optolock™ (by Firecomms, Figure 14) can be used, simply inserting the fiber into it and then locking.

Figure 13. Polishing disk for 1 mm POF. This disk will be moved forming several times a 8-shape on sand paper for final cleaving.

Figure 14. Optoloc™ transceiver housing, courtesy of Firecomms.

2.3. Overview on components

It is not in the scope of this chapter to present a full treatise on optical components, that would deserve a full book itself, so we suggest to consult [7] for this purpose and we will give a very general overview on what type of optical components are available for PMMA-SI-POF applications, given that the most interesting novelties of PMMA-SI-POF components are related to the optical sources only.

2.3.1. Sources

LEDs are the most common optical source to be employed with PMMA-SI-POF. LEDs are available for all the main wavelengths (red, green and blue), and can guarantee high output power and long lifetime. Components with an output power of up to +6 dBm can be found on market, and modulation bandwidths usually are in the order of the tenth of megahertz; thus, they usually are suitable for low-speed transmissions, such as 10 Mb/s, or require complex modulation formats of equalization techniques for higher speeds. Typical linewidth of LED sources is in the order of 40 nm.

A wide variety of red lasers exist, mostly developed of CD and DVD drives and laser pointers; usually, sources developed for such applications hardly meet the speed requirements for data communications but might be suitable for sensing applications. High power edge emitting lasers suitable for high-speeds exist, but not yet available in mass production or for low-cost applications. Vertical Cavity red lasers (VCSELs) are gaining interest since they can achieve interesting performances in terms of bit-rate [14], however low-cost commercial units usually have their peak wavelength at 665 nm, that remains in the red region but experiences a little attenuation penalty with respect to sources working at the optimal wave-

http://dx.doi.org/10.5772/52746

length of 650 nm. The spectral width of VCSELs is of course very narrow, and the typical output power is in the range of -5 dBm to -2 dBm.

Resonant Cavity LEDs (RC-LEDs) are gaining increasing interest for communications, since they join the robustness of LEDs with the high bandwidth provided by the resonant cavity. Commercial components work at 650 nm, with a spectral width in the order of 20 nm. Commercial RC-LED have 2 or 4 Quantum Wells (2QW or 4QW); in general 2QW sources are faster while 4QW sources are more powerful. On average, the typical bandwidth of a RC-LED source is in the order of 250 MHz, while the output power goes up to 0 dBm.

For comparison purposes, in Figure 15 and 16 are reported the eye diagrams at the output of commercial low-cost VCSEL and a RC-LED when transmitting 1,1 Gb/s.

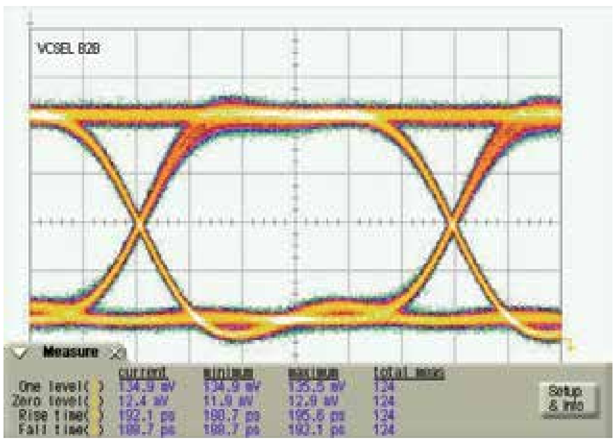

Figure 15. Gb/s transmission, eye-diagram at VCSEL output

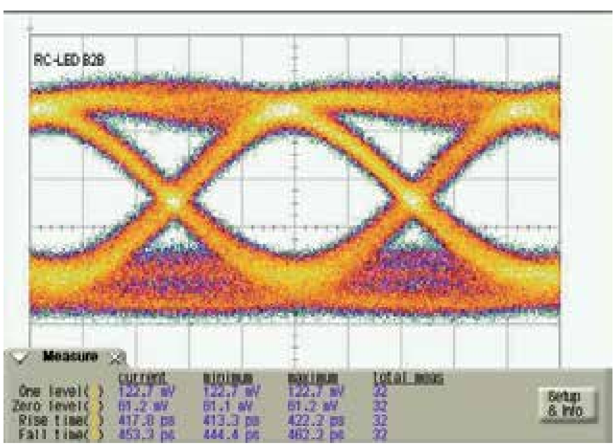

Figure 16. Gb/s transmission, eye-diagram at RC-LED output

As a summary, it is worth reminding that when needing high-speed components, such as VCSELs and RC-LEDs, then working in red wavelength is the only option.

2.3.2. Photodiodes

Typically, silicon photodiodes are used with PMMA-SI-POF. Their highest responsivity is usually around 950 nm, but their efficiency usually remains quite high also at 650 nm; some variants having their best performance at 800 nm exist. The performances decay when working at shorter wavelengths, but the lower attenuation of the fiber in green and blue.

Typical photodiodes have an area of 500 μm, up to 800 μm; considering the fiber diameter of 980 μm, it is quite common to use spherical coupling lenses in the photodiode package for improving coupling efficiency.

Pin structures are the most common to be found on market, but some Avalanche Photo Detectors (APD) can also be found.

2.3.3. Passive components

In the POF world there is not the same variety of passive components as in the GOF world. In particular, it can be said that only POF couplers exist off-the-shelf. The reasons for this lack of components is mainly due to the relatively low market needs. In particular, it can be said that only couplers/splitters exist off-the-shelf, mainly used for measurements setups or sensing applications. Couplers for PMMA-SI-POF are in general quite simple to be produced, mainly starting from the fiber itself: the most common structure foresees to polish two fibers, match and then glue them. It has to be mentioned that such couplers usually exhibit an excess loss in the order of 3 dB (to be added to the 3 dB due to the power splitting).

It is then worth mentioning that, however filtering in the visible regime should be quite common, no filters for PMMA-SI-POF exist. At the same time, no attenuator are available, and the common way to obtain (uncontrolled) attenuation is to insert in-line connectors into a fiber link and then creating an air-gap among the two facing fibers.

3. Data communications with PMMA-SI-POF

Considering attenuation and bandwidth characteristics illustrated in paragraph 2.2 and the performances of the components described in paragraph 2.3, it becomes quite evident that, if we consider the speeds defined by the Ethernet standard, 10 Mb/s systems are mainly attenuation limited, while transmitting at 100 Mb/s and over suffers of severe bandwidth limitations. Communications with PMMA-SI-POF then require the adoptions of mechanisms that are not usual to the optical community but that are widely adopted for example in copper or radio communications, such as multi-level modulation schemes or equalizations. In the following we will rapidly describe the most interesting multilevel modulation formats currently adopted for PMMA-SI-POF transmission, then we will report on the architectures that in literature have demonstrated the best bit rate vs. length results, considering the data-rates defined by the Ethernet standard.

3.1. Amplitude modulations: binary and multilevel

Amplitude modulations are the only formats reasonably applicable to PMMA-SI-POF systems, due to the unavailability of external modulators.

Conventional optical communications adopt On-Off Keying (OOK), that is a binary amplitude modulation, thus transmitting one bit per symbol and that in optics can be simplified switching the source ON when transmitting symbol 1 and OFF when transmitting symbol 0. In recent years more complex modulation formats, able to transmit more bits per symbol, have gained interest also when dealing with single-mode GOF for ultra-high capacity backbone systems. When dealing with PMMA-SI-POF, also due to the absence of proper optical modulators, only direct modulation of the source power can be adopted, thus introducing *Pulse Amplitude Modulation* (PAM).

PAM) consists in transmitting one of M possible amplitude levels (the "symbols") in each time slot. It is a well-known technique outside the fiber optic community, while it has found so far little (if any) application in fiber transmissions. For this reason, we briefly review its basic principle and terminology.

The number of levels M is set to $M=2^{N\_bit}$, where N_bit is the number of transmitted bits per symbol. Being T_s the duration of a symbol, the quantity D=1/T_s is the number of transmitted symbols per second, also called baud-rate, and the resulting bit rate is B_r = N_bit*D. The only reason for choosing multilevel is that, for a given available bandwidth B_av (related to the cascade of the transmitter, channel and receiver transfer functions), the maximum data rate that can be transmitted without excessive Inter-Symbol Interference (ISI) increases with the number of levels M. As a rule of thumb, the relation:

$$B\_av > 0.7\,D$$

should be satisfied to have acceptable ISI level (the constant 0.7 comes from the SDH standard; it can vary a little depending on filter types, without qualitatively affecting the following considerations nevertheless). Thus, for the same available bandwidth B_av, the resulting maximum bit rate increases with N_bit following the relation:

$$B\_r\_max < N\_bit * B\_av / 0.7$$

When adopting OOK, this means that for example 70 MHz are required for a line-rate of 100 Mb/s, while for multilevel modulations with the same bandwidth 100 Mbaud can be transmitted.

The use of multilevel transmission is very interesting for any bandwidth-limited system. On the other side, the drawbacks are:

- for a given Bit Error Rate and a given receiver noise floor, the required received power (or "receiver sensitivity") increases with N_bit

- the entire transmission channel, from the transmitter to the receiver, should be as linear as possible
- the complexity of the TX-RX pair is clearly increased with respect to binary transmission.

Multilevel transmission is then an appealing approach to improve the maximum bit rate without changing the optical part of the system. This key advantage has to be weighted up together with the previously mentioned drawbacks. In particular:

- regarding receiver sensitivity, for the same total bit rate, the penalty of multilevel compared to binary is equal to 1.76 dB for M=4, 3.93 dB for M=8 and 5.74 dB for M=16, if the receiver bandwidth is properly optimized. Without receiver bandwidth optimization, the penalty is respectively 4.77 dB, 9.03 dB and 12.04 dB. These penalties should clearly be taken into account.
- Regarding POF channel linearity, the only significantly nonlinear optoelectronic device is the LED, while the POF itself and the photodiode are linear to a fairly good approximation. Multilevel POF transmitter should therefore properly compensate for potential LED nonlinearity
- Regarding TX-RX electronic complexity, the cost of high-speed electronics is decreasing so much that there is a rationale to move "logical complexity" from the optical level to the electronic level, by using suitable digital signal processing (using programmable devices such as DSP and FPGA).

PAM has been described in deep since it is one of the options that is being considered for the standardization of 1 Gb/s PMMA-SI-POF systems, however other multilevel formats, such adduobinary [8], [9], [10] can be of interest and easy to be introduced.

Increase of performances could also be obtained using adaptive equalization; this topic is too complex to be fruitfully addressed in this chapter, so we will only mention when in literature equalization has been adopted and we suggest the reader to consult [11] for the theory of equalization.

3.2. Best results available in literature

3.2.1. 10 Mb/s transmission

According to the frequency response depicted in Figure 10 and the rule-of-the-thumb reported in the previous paragraph about the relationship among bandwidth and baud-rate, a conventional OOK modulation at 10 Mb/s could easily overcome, in terms of bandwidth, a distance of 400 m. In terms of attenuation, it makes sense then to use green wavelength due to the lowest attenuation it presence: the lack of fast components is not a limiting factor at this bit-rate. However, overcoming 400 m implies a power budget of over 40 dB, impossible with the best receivers available on market. Thus, we can affirm that at 10 Mb/s the system is attenuation limited.

UTP to POF Ethernet media converters currently available on market usually have a maximum reach in the order 200/250 m. They are mostly obtained by using standard Ethernet chipsets and directly driving the optical source. With the same technique, analog video-surveillance systems are being produced.

The best result available in literature [3] shows the possibility of transmitting 10 Mb/s over a distance of 425 Mb/s, by properly choosing the optical components (for mass production) and introducing Reed Solomon Forward Error Correction (FEC). Ethernet transport over such distances has required to correct the standard at level 1 and level 2, removing the Manchester line-coding (that doubles the line rate with respect to the bit-rate) to adopt a 8B / 10B line coding, and transforming the data stream from bursty to continuous in order to apply the FEC.

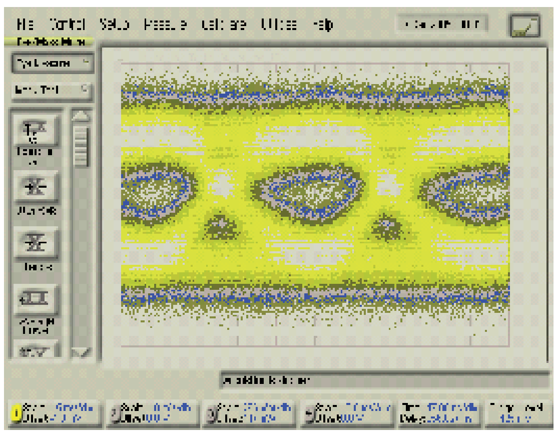

Figure 17. Eye-diagram of 10 Mb/s transmission over 400 m of PMMA-SI-POF, with one intermediate connector. Courtesy of the authors of [3].

3.2.2. 100 Mb/s transmission

Severe bandwidth limitations occur when transmitting at 100 Mb/s: from a power-budget point of view, transmitting in green could target 250 to 300 m, while over these distances the available bandwidth is well below the 20 MHz. This is then the typical case in which multi-level transmission techniques become of paramount importance. Adopting bandwidth-efficient modulation formats can allow, also in this case, the adoption of green components even giver their lack of speed with respect to red components. In fact, the best result available in literature [11] adopts a green LED with a bandwidth of 35 MHz and an average output power of +2 dBm at the transmitter side and a large area photodiode with integrated transimpedence amplifier, with a bandwidth of 26 MHz, at the receiver side, and reaches a distance of 275 m. The authors of the paper have opted for 8 levels PAM (8-PAM), and due to the linearity requirements mentioned in 2.4.1, LED non-linearity compensation has been implemented; even with these techniques, the received eye-diagram after a link in the order of 200 m resulted completely closed, showing that also equalization techniques [12] should be studied in order to recover the signal. In fact, the authors of [11] have adopted adaptive equalization (adaptive to cope with the intrinsic stochastic properties of multimodal dispersion), and the power budget has been increased with the adoption of FEC. In Figure 18 it is shown the eye-diagram of the 8-PAM signal after 200 m of PMMA-SI-POF when LED non-linearity compensation and adaptive equalization are adopted. Moving modulation formats with even more levels would be practically unfeasible for stricter linearity requirements.

It is worth mentioning that, when it is not requested to reach long distances, so that the available fiber bandwidth is bigger, it might be useful to employ red components, faster (such as VCSELs or RC-LEDs) than the ones working in green, and multilevel modulations might be avoided.

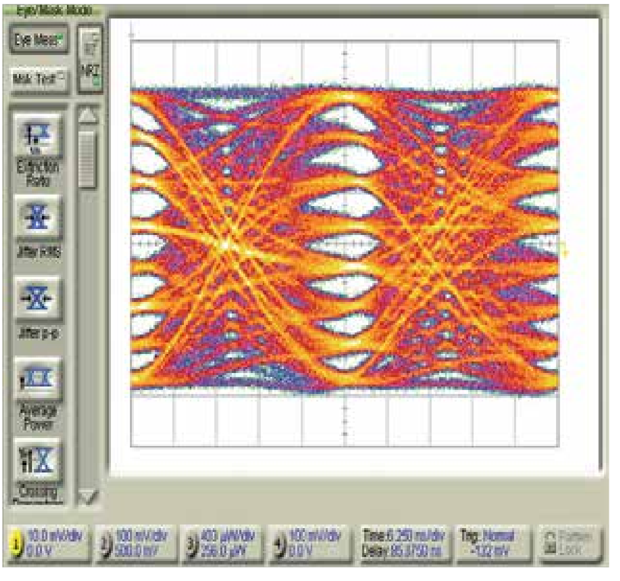

Figure 18. Received 8-PAM signal after 200 m of PMMA-SI-POF, with LED non-linearity compensation and adaptive equalization. Net data rate of 100 Mb/s. Courtesy of the authors of [11].

3.2.3. 1 Gb/s transmission

1 Gb/s transmission over PMMA-SI-POF experiences huge bandwidth limitations, and there is no other chance than using red components and strong equalization. The best results available in literature are due to the POF-PLUS European Project [13], in which it has been shown that in this case complex modulation formats do not give significant advantage with respect to OOK when already equalization is adopted. In [14] it has been shown that with a RC-LED OOK modulated and proper equalization and error correction it is possible to obtain a system overcoming 50 m (75 m with no margin have been obtained). Some little additional margin has been shown in [15] adopting duobinary modulation, a multilevel modulation that has a more complex theoretical background but an easier implementation,

with the current electronic capabilities, than PAM, and is feasible with low cost components. Transmissions over 100 m have been achieved using an edge-emitting laser with an output power of +6 dBm, but such a system cannot be acceptable for practical systems since not eye-safe.

A standardization process is currently going on inside the VDE/DKE initiative, for standardizing 1 Gb/s systems. Since adopting lasers at the transmitter side becomes of interest at this bit rate, then exploiting at most their linearity makes sense, and in fact a solution that adopts Discrete Multi-Tone (DMT) with PAM that adjusts the speed according to the channel performances is currently under investigation [16]: as previously mentioned, PAM vs OOK does not give significant advantages in terms of maximum distance, but in conjunction with DMT inserts in the system rate-adaption capabilities.

3.3. What about WDM over PMMA-SI-POF?

Wavelength Division Multiplexing (WDM) is a very common multiplexing technique adopted for high capacity optical communications with glass fibers; it might appear as an interesting chance with POF as well, but actually it is not a practical solution [17] for high-speed or long-distance applications for the following reasons:

- Array Waveguides (AVG), Mach-Zehender Interferometers (MZI) or Fiber Bragg Gratings (FBG) cannot be used with multimode fibers, so dense wavelength filtering is not possible;
- Red, Green and Blue (RGB) multiplexing is possible but no integrated wavelength splitter exists; experimental units with high insertion losses (5 dB), but in absence of in-line amplifiers this consistently reduces the distance.
- The different performances in terms of attenuation and speed of the components in the three transmission windows would make RGB WDM systems very unbalanced.

In turn, it is possible to say that RGB WDM on PMMA-SI-POF is of interest when low aggregate speeds and short distances are requested; in particular, video systems or medical applications could take advantage of such a technology.

When requiring high speeds and longer distances, the parallel optics approach can be a viable solution, for example for optical interconnects applications [18].

4. Sensing with PMMA-SI-POF

The peculiar characteristics of plastic optical fibers have attracted also the interest in sensing applications, and especially for measuring physical quantities in structural health monitoring [19]. Indeed, using multimode PMMA-SIPOF it is possible to realize fiber based sensing systems that balance costs and performances, since this type of fibers does not require complex machines for splicing and polishing, and makes use of simpler connectors and of visible LED sources. Although several sensing techniques have been described in the literature (and some are described in other chapters of this book), PMMA-SI-POF are best suited for the development of sensors that exploit the variation of the received light intensity with the quantity under measurement, which are the so-called intensiometric sensors, and in this paragraph we will address this technique only.

Typical PMMA-SI-POF intensiometric sensors are based on the variation of: (i) the propagation loss along the fiber (either for local microbending, as for example in [20] and [21], or in distributed form, as in [22]); (ii) the light collected after a free space propagation (as in [23], [24], and [25]); (iii) the interaction through evanescent field tails (as in [26], [27] and [28]). The first two approaches are most often used to measure physical quantities like displacements, vibrations and acceleration, whereas the latter for detecting chemicals.

Intensiometric sensors are conceptually very simple – hence the low cost – because their implementation in principle requires just an LED source and a receiver that acts as a power meter. They are, however, very sensitive to disturbances since any fluctuation in the received power (e.g. due to fluctuations in the source or to fiber degradations) is indistinguishable from actual changes in the quantity under measurement. This sensitivity to parasitic quantities is particularly relevant for long-term monitoring of slowly changing quantities, so in these cases proper compensation techniques using reference sensors [29], or more complex interrogation schemes with signals at different wavelengths [30], must be considered.

Limiting our analysis to the sensors used to measure static or dynamic displacements (vibrations), one of the simplest intensiometric sensors can be realized by facing two fibers along a common axis as in Figure 19. The displacement is measured by exploiting the change of the received power with the separation between the two fiber tips due to the beam divergence form the transmitting fiber (Figure 19 - right). This principle of operation has also been applied in early realizations with glass fibers, but with limitations in the measurement range, unless fiber bundles are used. Despite the simplicity, such a transducer, made using standard step-index 1 mm plastic fibers, has been successfully used to develop a sensing system with working range and accuracy within the typical specifications required for long term crack monitoring in cultural heritage preservation applications [23], [29]. In this case the use of PMMA-SI-POF allowed having most of the advantages of fiber sensors, and above all the impossibility to start fires, without the usual costs and complexities, both in terms of manufacturing and deployment.

Given the propagation loss in plastic optical fibers and the free space attenuation, the distance between the sensor and the interrogators is limited to some tens of meters, but this is typically enough to allow placing the electronics in a remote and safe place. Moreover, if unjacketed fibers are used, the visual impact is dramatically reduced, making the sensing system almost invisible.

An example of the results obtained with sensors arranged as in Figure 19 is shown in Figure 20, where a picture of a sensor mounted across a crack and the readings for a period of 18 months are reported. The data in Figure 20-right are corrected to compensate for the environmental parasitic effects using a "null" (reference) sensor, as reported in [29]. The null sensor is a sensor identical to the others but not fixed to edges of the crack under measure. This is an approach common to most types of the sensors and is effective provided that the reference sensor is exposed to the same kind of disturbances as the measuring sensor; so for meaningful readings, particular care must be devoted to ensure that the two sensors are exposed to the same parasitic phenomena (e.g. temperature, stray light, bending, etc.). The strict correlation between seasonal temperature fluctuations and the crack opening/closing are quite evident from the reported plots.

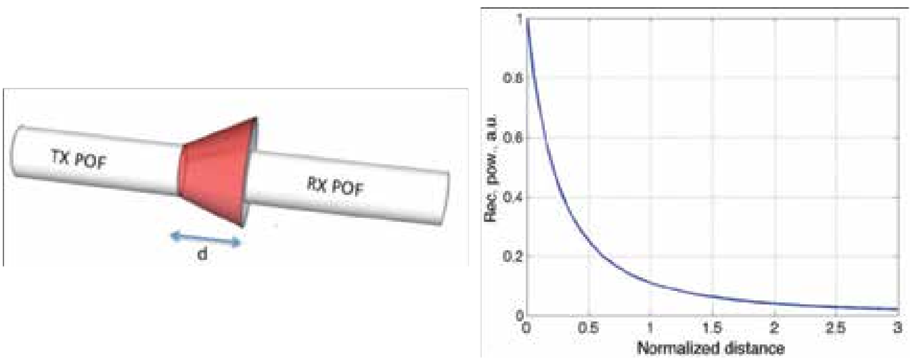

Figure 19. Schematic representation of a POF displacement sensor working in transmission mode (left) and the received power against distance curve (right).

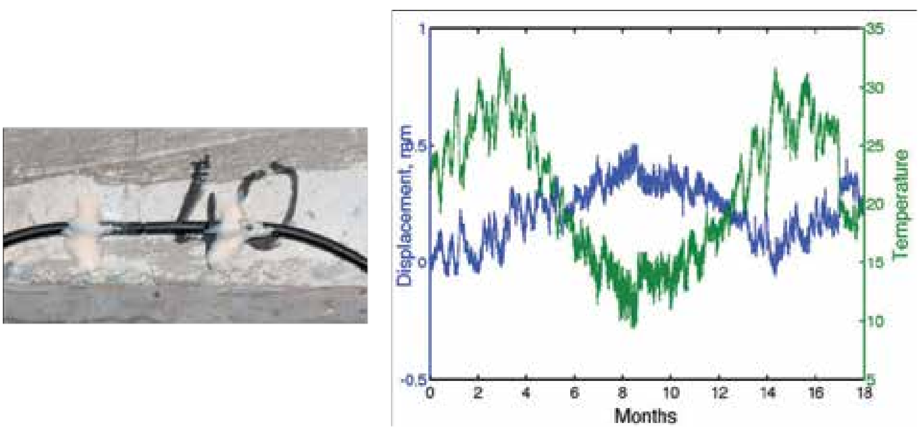

Figure 20. Example of practical POF displacement sensor arranged as in Figure 1 (left), and of the readings of a crack evolution for 18 months, after proper compensation with the null sensor technique as in [11] (right).

A variation of the same working principle is reported in Figure 21, where the light is collected by the receiving fiber after reflection from a target. This configuration can be reduced to the previous one working in transmission mode by considering an image receiving fiber positioned at a double distance and with a lateral offset. The transducer response curve can be modified by changing the sensor geometry (e.g. fiber diameters and separation), but, in any case, it exhibits a maximum that identifies two working regions. The leftmost part of the curve, which is characterized by higher sensitivity, though in a reduced working range, can be used to measure extremely small displacements, such as in high frequency vibrations; however, it requires positioning the sensing head very close to the target. For this reason, in most cases the sensor is arranged to operate exploiting the rightmost part of the curve. This type of sensor can be used both to measure displacements and for non-contact distance measurements.

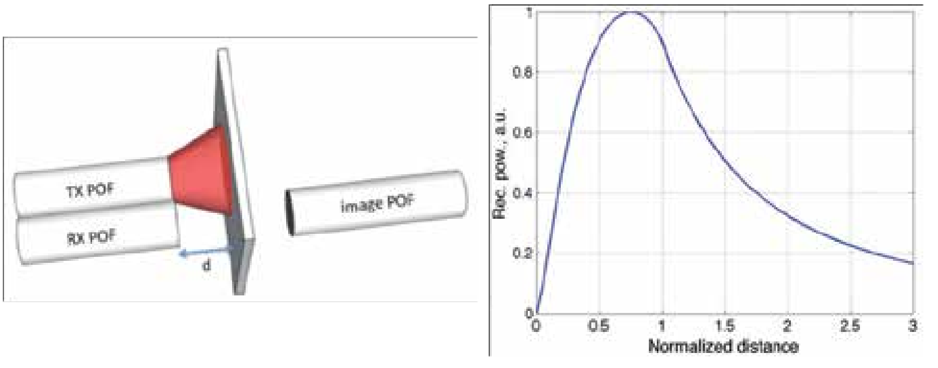

Figure 21. Schematic representation of a POF displacement sensor working in reflection mode (left) and the received power against distance curve (right).

An example of the use to measure displacements is an evolution of the crack monitoring system already shown in Figure 20. Indeed, using the reflection based sensor configuration it has been possible to develop compact transducers having the fiber connections on one side only, as depicted in Figure 4. These new sensors are currently used in a monitoing network deployed inside the chapel hosting the Holy Shroud of Turin in the framework of the Guarini's Project [31], a pilot project devoted to develop new technologies to support the restoration works after the fire that destroyed the Chapel in 1997. In this particular application the POF sensors are integrated within a wireless network to take advantages of both technologies.

Figure 22. Picture of a crack evolution POF sensor using the principle sketched in Figure 3 (left) and example of application in the Guarini Chapel to monitor a crack on a marble statue in a quite dusty environment (right) [13].

The reflection-based sensor configuration is also particularly well suited for the application of a dual-wavelength compensation technique, which turned out to be much more effective than the null sensor one, though slightly more complex to implement because it requires a dichroic mirror to be inserted in the setup sketched in Figure 22[30]. In this case two signals, at two different wavelengths, are coupled inside the transmitting fiber, then the reference signal is reflected at the fiber tip by a dichroic mirror, while the other wavelength is reflected by the target. This way, the two signals share the same path, hence the same perturbations, except for the sensing region. As for the use in non-contact distance measurements, it is important to highlight that the sensor response depends also on terms that cannot be calculated through theoretical models or may change in time, such as the target reflectivity, so they require continuous characterizations and subsequent calibrations. A sensor for static non-contact distance measurements with response independent from reflectivity changes has been studied in [32], while a calibration technique particularly effective in vibration tests, including cases when the surface has non-uniform reflectivity or non-flat profile, is presented in [33]. An example of a possible application is the mapping of the vibration amplitudes of a printed circuit board under vibration tests. An example of the system setup is pictured in Figure 23.

Recent developments of PMMA-SI-POF displacement sensors include the realization of a possible replacement of conventional crack gage based on sliding plates to measure crack evolutions in two dimensions [34].

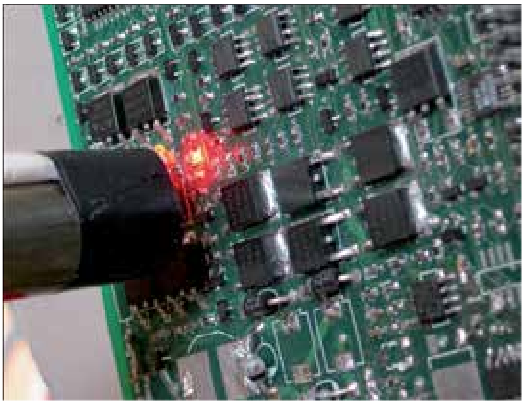

Figure 23. Picture of non-contact system for the mapping of the vibration amplitudes of printed circuit boards under vibration tests using the procedure described in [15].

5. Conclusions

In this chapter we have given a general overview of the most interesting applications of optical fibers made of PolyMethylMethAcrylate material, with a core diameter of 980 μm and with Step-Index profile. We have shown that, given the fact that the communication performances are orders of magnitude lower than the ones of the more common single-mode glass fibers, PMMA-SI-POF can address interesting niche markets such as automobile entertainment, local networking, sensing, provided that some complexity is added to the electrical part of the system, while the rules of optical propagation remain unchanged with respect to more common, yet more powerful, optical fibers.

Acknowledgements

The authors of this chapter would like to thanks Stefano Straullu and Valerio Miot for their help in the editing phase, and the partners of the POF-ALL and POF-PLUS European Projects for years of fruitful joint research activities, that have provided for the state-of-the art results in communications over PMMA-SI-POF.

Author details

Silvio Abrate[1], Roberto Gaudino[2] and Guido Perrone[2]

1 Istituto Superiore Mario Boella – Torino, Italy

2 Dipartimento di Elettronica e Telecomunicazioni, Politecnico di Torino - Torino, Italy

References

[1] IEC Recommendation “Optical fibres – Part 2-40: Product specifications – Sectional specification for category A4 multimode fibres”, IEC 60793-2-40

[2] A. Nespola, S. Straullu, P. Savio, D. Zeolla, S. Abrate, D. Cardenas, J. C. Ramirez Molina, N. Campione, R. Gaudino, First demonstration of real-time LED-based Gigabit Ethernet transmission of 50 m of A4a.2 SI-POF with significant system margin. 36th European Conference and Exhibition on Optical Communication (ECOC), Turin (Italy), 19-23 September 2010, E-ISBN 978-1-4244-8534-5, DOI 10.1109/ECOC.2010.5621396

[3] D. Cardenas, A. Nespola, P. Spalla, S. Abrate, R. Gaudino, A media converter prototype for 10Mb/s Ethernet transmission over 425m of Large-Core Step-Index Polymer Optical Fiber. IEEE Journal of Lightwave Technology, vol. 24, n. 12, December 2006

[4] J. Mateo, M. A. Losada, I. Garces, J. Arrue, J. Zubia, D. Kalymnios, High NA POF dependence of bandwidth on fiber length. POF Conference 2003, Seattle (USA), Sept. 2003

[5] E. Capello, G. Perrone, R. Gaudino, POF bandwidth measurement using OTDR. POF Conference 2004, Nurnberg (Germany), Sept. 2004

[6] A. Weinart. Plastic Optical Fibers. Editions Siemens Aktiengesellschaft, ISBN 3-89578-135-5; 1999

[7] O. Ziemann, J. Krauser, P. Zamzow, W. Daum. POF Handbook 2nd Edition. Springer; 2008

[8] A. Lender, Correlative digital communication techniques. IEEE Tran. Commun. Vol. COM-12 pp 128-135, 1964

[9] J. Proakis, M. Salhei. Digital Communication. McGraw Hill; 2007

[10] S. Abrate, S. Straullu, A. Nespola, P. Savio, D. Zeolla, R. Gaudino, J. Ramirez Molina, Duobinary modulation formats for gigabit Ethernet SI-POF transmission systems, International POF Conference, Bilbao (SPA), Sept. 2011

[11] D. Cardenas, A. Nespola, S. Camatel, S. Abrate, R. Gaudino, 100 Mb/s Ethernet transmission over 275 m of large core Step Index Polymer Optical Fiber: results from the POF-ALL European Project. IEEE Journal of Lightwave Technology, vol. 27, n. 14, July 2009

[12] H. Meyer, M. Moeneclaey, S. Fechtel, Digital communication receivers: synchronization, channel estimation and signal processing. Wiley-Interscience; 1997

[13] POF-PLUS European Project, www.ict-pof-plus.eu

[14] A. Nespola, S. Straullu, P. Savio, D. Zeolla, J. C. Ramirez Molina, S. Abrate, R. Gaudino, A new physical layer capable of record gigabit transmission over 1 mm Step Index Polymer Optical Fiber. IEEE Journal of Lightwave Technology, vol. 28, n. 20, 15 October 2010

[15] S. Straullu, A. Nespola, P. Savio, S. Abrate, R. Gaudino, Different modulation formats for Gigabit over POF. ANIC 2012, Colorado Springs (USA), June 2012

[16] KD-POF, http://www.kdpof.com/Papers_files/kdpof_demo_1Gbps.pdf

[17] O. Ziemann, L. Bartkiv, POF-WDM, the truth. POF Conference 2011, Bilbao (SPA), Sept. 2011

[18] S. Abrate, R. Gaudino, C. Zerna, B. Offenbeck, J. Vinogradov, J. Lambkin, A. Nocivelli, 10Gbps POF ribbon transmission for optical interconnects. IEEE Photonic Conference IPC 2011, Arlington (USA) Oct. 2011

[19] K. Peters, Polymer optical fiber sensors—a review, Smart Mater. Struct., vol. 20, 17 pages, 2011

[20] A. Vallan, M.L. Casalicchio, A. Penna, G. Perrone, An intensity based fiber accelerometer, IEEE International Instrumentation and Measurement Technology Conference (I2MTC), pp. 1078-1082, 2012

[21] A. Kulkarni, J. Na, Y. J. Kim, S. Baik, T. Kim, An evaluation of the optical power beam as a force sensor, Opt. Fiber Technol., vol. 15, pp. 131-135, 2009

[22] S. Liehr, P. Lenke, M. Wendt, K. Krebber, M. Seeger, E. Thiele, H. Metschies, B. Gebreselassie, J.C. Munich, Polymer optical fiber sensors for distributed strain measure-

ment and application in structural health monitoring, IEEE Sensors Journal, vol. 9, pp. 1330-1338, 2009

[23] S. Abrate, G. Perrone, R. Gaudino, D. Perla, European Patent n. EP 1630527

[24] M. Olivero, G. Perrone, A. Vallan, S. Abrate, Plastic optical fiber displacement sensor for cracks monitoring, Key Engineering Materials, vol. 347, pp. 487-492, 2007

[25] G. Perrone, A. Vallan, A low-cost optical sensor for noncontact vibration measurements, IEEE Trans. Instr. Meas., vol. 58, pp. 1650-1656, 2009

[26] J. Vaughan, C. Woodyatt, P.J. Scully, Polymer optical coatings for moisture monitoring, European Conference on Lasers and Electro-Optics, 2007

[27] E. Angelini, S. Grassini, A. Neri, M. Parvis, G. Perrone, Plastic optic fiber sensor for cumulative measurements, IEEE International Instrumentation and Measurement Technology Conference (I2MTC), pp. 1666-1670, 2009

[28] S. Corbellini, M. Parvis, S. Grassini, L. Benussi, S. Bianco, S. Colafranceschi, D. Piccolo, Modified POF Sensor for Gaseous Hydrogen Fluoride Monitoring in the Presence of Ionizing Radiations, IEEE Trans. Instr. Meas., vol. 61, pp. 1201-1208, 2012

[29] M.L. Casalicchio, A. Penna, G. Perrone, A. Vallan, Optical fiber sensors for long- and short-term crack monitoring, IEEE Workshop on Environmental, Energy, and Structural Monitoring Systems, EESMS 2009, pp. 87-92, 2009

[30] A. Vallan, M.L. Casalicchio, M. Olivero, G. Perrone, Assessment of a dual-wavelength compensation technique for displacement sensors using plastic optical fibers, IEEE Trans. Instr. Meas., vol. 61, pp. 1377-1383, 2012

[31] M.L. Casalicchio, D. Lopreiato, A. Penna, G. Perrone, A. Vallan, D. Lopreiato, POF sensor network for monitoring the Guarini Chapel, Proc. of the POF Conference, 2011

[32] M.L. Casalicchio, A. Neri, G. Perrone, D. Tosi, A. Vallan, Non-contact low-cost fiber distance sensor with compensation of target reflectivity, IEEE International Instrumentation and Measurement Technology Conference (I2MTC), pp. 1671-1675, 2009

[33] A. Vallan, M.L. Casalicchio, G. Perrone, Displacement and acceleration measurements in vibration tests using a fiber optic sensor, IEEE Trans. Instr. Meas., vol. 59, pp. 1389-1396, 2010

[34] M.L. Casalicchio, M. Olivero, A. Penna, G. Perrone, A. Vallan, Low-cost 2D fiber-based displacement sensor, IEEE International Instrumentation and Measurement Technology Conference (I2MTC), pp. 2078-2082, 2012

Section 3

Optical Fiber Sensors

Chapter 8

Optical Fibre Gratings for Chemical and Bio - Sensing

Xianfeng Chen

Additional information is available at the end of the chapter

http://dx.doi.org/10.5772/54242

1. Introduction

We live in an era of technological revolutions that continue to impact our lives and constantly redefine the breath of our social interactions. The past century has witnessed many technological breakthroughs, one of which is fibre optics. Due to the advantages of non-electromagnetic, light weight, flexibility, low-loss and high temperature tolerance, optical fibre gratings have been become one of the most important components in optical communications and optical sensing [1-7].

Fibre gratings are broadly classified into fibre Bragg gratings (FBGs) and long-period gratings (LPGs). The period of an FBG is approximately half a micrometer whereas the period of an LPG is typically several hundred micrometers. From the conventional coupled-mode theory, in an FBG the guided mode will be coupled to the corresponding backward mode [2, 3]. Contrary to the contradirectional coupling in FBGs, LPGs induce codirectional coupling in an optical fibre where the guided mode will be coupled to the cladding modes when the difference of their propagation constants is equal to the corresponding spatial frequency. FBGs have been demonstrated to measure a wide range of physical parameters including temperature, strain, pressure, loading, bending and vibration [6, 7]. LPGs, as core to cladding modes forward-coupling devices, have been used as band-rejection filters, Erbium-doped fibre amplifier (EDFA) gain flatteners and as optical sensors to monitor strain, temperature, bending and surrounding-medium refractive index (SRI). Radiation-mode out coupling from tilted fibre gratings (TFGs) has also been demonstrated for applications in wavelength-division-multiplexing (WDM) channel monitoring, gain flattening of EDFAs, polarisation discrimination, and optical sensor interrogation [8].

In recent years, with the advancement in UV-inscription technology and the drive from the various new fibres, a variety of in-fibre gratings have been investigated and developed, generating many smart device functionalities for applications in chemical detection, biosensing, bioengineering, environmental monitoring, medical science and health care.

This chapter is constructed as follows. In section 2, we give an overview of the optical fibre grating theories, including the mode coupling mechanism and phase matching condition. In Section 3, we present the fibre grating fabrication techniques. In section 4, we demonstrate several grating based optical fibre sensors for chemical and biosensing. Finally, a conclusion ends this chapter.

2. Theory of the optical fibre gratings

2.1. Coupled-mode theory

The coupled-mode theory is a basic theory for obtaining quantitative information about the diffraction efficiency and spectral dependence of optical fibre gratings. The derivation of the coupled-mode theory will not be provided, as it was detailed by Yariv and Kogelnik [1, 9]. Here the coupled-mode theory is briefly discussed following the work by Erdogan [3, 10].

The transverse component of the electric field in the ideal-mode approximation to coupled-mode theory can be written as a superposition of the ideal modes where the modes are in an ideal waveguide with no grating perturbation

$$\vec{E}_t(x,y,z) = \sum_j \left[A_j(z)\exp(i\beta_j z) + B_j(z)\exp(-i\beta_j z) \right] \cdot \vec{e}_{jt}(x,y) \tag{1}$$

where the coefficients $A_j(z)$ and $B_j(z)$ are the slowly varying amplitudes of the jth mode traveling in the +z and -z directions, respectively. $\vec{e}_{jt}(x, y)$ is the transverse mode field, which might describe a bound-core, cladding or radiation mode. The propagation constant β is simply

$$\beta = \frac{2\pi}{\lambda} n_{eff} \tag{2}$$

Where n_{eff} is effective index of jth mode. The presence of a dielectric perturbation will cause the coupling between the modes. The amplitudes $A_j(z)$ and $B_j(z)$ of the jth mode then evolve along the z direction according to

$$\frac{dA_j(z)}{dz} = i\sum_k A_k(K_{kj}^t + K_{kj}^z)\exp[i(\beta_k - \beta_j)z] + i\sum_k B_k(K_{kj}^t - K_{kj}^z)\exp[-i(\beta_k + \beta_j)z] \tag{3}$$

$$\frac{dB_j(z)}{dz} = -i\sum_k A_k(K_{kj}^t - K_{kj}^z)\exp[i(\beta_k + \beta_j)z] - i\sum_k B_k(K_{kj}^t + K_{kj}^z)\exp[-i(\beta_k - \beta_j)z] \tag{4}$$

The transverse coupling coefficient between *j* and *k* modes in the above equations is

$$K_{kj}^{t}(z) = \frac{\omega}{4}\iint_{\infty}\left[\Delta\varepsilon(x,y,z)\vec{e}_{k}^{\,t}(x,y)\cdot\vec{e}_{j}^{\,t*}(x,y)\right]dxdy \tag{5}$$

The longitudinal coefficient $K_{kj}^{z}(z)$ is analogous to $K_{kj}^{t}(z)$, but for fibre modes $K_{kj}^{z}(z)$ is usually neglected since $K_{kj}^{z}(z) << K_{kj}^{t}(z)$. In (5), $\Delta\varepsilon(x, y, z)$ is the permittivity perturbation, for $\delta n_{eff} << n_{eff}$, which is approximately

$$\Delta\varepsilon(x,y,z) = 2n_{eff}\delta n_{eff}(x,y,z) \tag{6}$$

In an ideal waveguide situation where no perturbation exists ($\Delta\varepsilon=0$), the coupling coefficient $K_{kj}^{t}(z)=0$, then the transverse modes are orthogonal and do not exchange energy.

Exposing photosensitive fibre to a spatially varying pattern of UV-light produces the refractive index change $\delta n_{eff}(z)$

$$\delta n_{eff}(z) = \overline{\delta n_{eff}}(z)\left[1+\upsilon\cos\left(\frac{2\pi}{\Lambda}z+\varphi(z)\right)\right] \tag{7}$$

where υ is the fringe visibility of the index change, Λ is the grating period, $\Phi(z)$ describes the grating chirp, and $\overline{\delta n}_{eff}(z)$ is the "dc" index change spatially averaged over a grating period, or the slowly varying envelope of the grating.

In most fibre gratings the UV-induced index change $\delta n_{eff}(x, y, z)$ is approximately uniform across the core and nonexistent outside the core. Thus the core index change can be described by an expression similar to (7) with $\overline{\delta n}_{eff}(z)$ replaced by $\overline{\delta n}_{co}(z)$.

Thus, with (6) and (7), the general coupling coefficient (5) may now be written

$$K_{kj}^{t}(z) = \sigma_{kj}(z) + 2\kappa_{kj}(z)\cos\left[\frac{2\pi}{\Lambda}z+\varphi(z)\right] \tag{8}$$

where δ is defined as a "dc" coupling coefficient and κ is an "ac" coupling coefficient

$$\sigma_{kj}(z) = \frac{\omega n_{eff}\overline{\delta n_{eff}}(z)}{2}\iint_{core}\vec{e}_{k}^{\,t}(x,y)\cdot\vec{e}_{j}^{\,t*}(x,y)dxdy \tag{9}$$

$$\kappa_{kj}(z) = \frac{\upsilon}{2}\sigma_{kj}(z) \tag{10}$$

2.1.1. Backward mode coupling

For the backward mode coupling, the dominant interaction is near the wavelength for which reflection occurs from a mode of amplitude $A(z)$ to an identical counter-propagating mode of amplitude $B(z)$. Under such conditions (3) and (4) can be simplified to the following equations [3]

$$\frac{dR}{dz} = i\hat{\sigma}R(z) + i\kappa S(z) \tag{11}$$

$$\frac{dS}{dz} = -i\hat{\sigma}S(z) - i\kappa^{*}R(z) \tag{12}$$

where the amplitudes R and S are

$$R(z) = A(z)\exp\left(i\delta z - \frac{\varphi(z)}{2}\right) \tag{13}$$

$$S(z) = B(z)\exp\left(-i\delta z + \frac{\varphi(z)}{2}\right) \tag{14}$$

In equations (11) and (12), κ is the "ac" coupling coefficient and $\hat{\sigma}$ is the general "dc" self-coupling coefficient defined as

$$\hat{\sigma} = \delta + \sigma - \frac{1}{2}\frac{d\varphi(z)}{dz} \tag{15}$$

with δ being the detuning, which is independent of z and is defined to be

$$\delta = \beta - \frac{\pi}{\Lambda} = \beta - \beta_d = 2\pi n_{eff}\left[\frac{1}{\lambda} - \frac{1}{\lambda_d}\right] \tag{16}$$

here $\lambda_d = 2n_{eff}\Lambda$ is the "design wavelength" for Bragg scattering by an infinitesimally weak grating ($\delta n_{eff} \rightarrow 0$).

http://dx.doi.org/10.5772/54242

For a single-mode Bragg grating, there are the following simplified relations

$$\sigma = \frac{2\pi}{\lambda}\overline{\delta n_{eff}} \tag{17}$$

$$\kappa = \kappa^* = \frac{\pi}{\lambda}\upsilon\overline{\delta n_{eff}} \tag{18}$$

If the grating is uniform along z direction, then $\overline{\delta n}_{eff}$ is constant and $d\varphi(z)/dz = 0$ which means no grating chirp. Thus κ, σ, and $\hat{\sigma}$ are constants. This simplifies (11) and (12) into coupled first-order ordinary differential equations with constant coefficients. The closed-form solutions may be found when appropriate boundary conditions are specified.

2.1.2. Forward mode coupling

For the forward mode coupling, close to the wavelength for which a forward- propagating mode of amplitude $A_1(z)$ is strongly coupled into a co-propagating mode with amplitude $A_2(z)$, (3) and (4) may be modified by retaining the terms that involve the amplitudes of these two modes and making the usual synchronous approximation

$$\frac{dR}{dz} = i\hat{\sigma}R(z) + i\kappa S(z) \tag{19}$$

$$\frac{dS}{dz} = -i\hat{\sigma}S(z) + i\kappa^* R(z) \tag{20}$$

where the new amplitudes R and S are

$$R(z) = A_1 \exp\left[-i(\sigma_{11} + \sigma_{22})\frac{z}{2}\right]\exp(i\delta z - \frac{\varphi}{2}) \tag{21}$$

$$S(z) = A_2 \exp\left[-i(\sigma_{11} + \sigma_{22})\frac{z}{2}\right]\exp(-i\delta z + \frac{\varphi}{2}) \tag{22}$$

In above equations, σ_{11} and σ_{22} are "dc" coupling coefficients defined in (9), $\kappa = \kappa_{21} = \kappa_{12}^*$ is the "ac" cross-coupling coefficient from (10) and $\hat{\sigma}$ is a general "dc" self-coupling coefficient now defined as

$$\hat{\sigma} = \delta + \frac{\sigma_{11} - \sigma_{22}}{2} - \frac{1}{2}\frac{d\varphi}{dz} \tag{23}$$

When the detuning δ is assumed to be constant along the z axis, it becomes

$$\delta = \frac{1}{2}(\beta_1 - \beta_2) - \frac{\pi}{\Lambda} = \pi\Delta n_{eff}\left[\frac{1}{\lambda} - \frac{1}{\lambda_d}\right] \tag{24}$$

where again $\lambda_d = \Delta n_{eff}\Lambda$ is the "design wavelength" for a grating approaching zero index modulation. In the case of Bragg gratings, $\delta = 0$, or $\lambda = \lambda_d = \Delta n_{eff}\Lambda$, corresponds to the grating condition.

For a uniform forward-coupled grating, $\hat{\sigma}$ and κ are constants. In contrast to the single-mode Bragg grating, here the coupling coefficient κ generally may not be written simply as in (18) and must be evaluated numerically. As the case of the FBG, the forward-coupled grating equations (19) and (20) are coupled first-order ordinary differential equations with constant coefficients. Thus when the appropriate boundary conditions are given, the closed form solutions can be found.

2.2. Phase-matching condition

If the perturbation exists in the fibre, the bound-wave can be coupled to the counter-propagating or co-propagating modes. Based on the direction of the mode coupling, fibre gratings may be classified in two types. One type is a backward-coupled grating which couples light to opposite directions. FBGs of normal and small-tilt uniform and chirped structures belong to this type. The other category is a forward-coupled grating, represented by LPGs and FBGs with largely tilted structures, where coupling occurs between the same directional modes.

For the coupled modes, the phase mismatch factor $\Delta\beta$ is referred as a detuning

$$\Delta\beta = \beta_i \pm \beta_d - \frac{2\pi}{\Lambda_g} N\cos\theta \tag{25}$$

where β_I and β_d are the propagation constants for the incident and diffracted modes, respectively, Λ_g is the period of the grating, θ is the grating tilt angle and N represents an integer number. It is noteworthy that the " $\pm$ " sign describes the case wherein the mode propagates in the $\mp$ z direction.

When the phase-matching condition satisfied $\Delta\beta$=0, (25) becomes

$$\beta_i \pm \beta_d = \frac{2\pi}{\Lambda_g}\cos\theta \tag{26}$$

If both β_I and β_d have identical signs, then the phase will be matched for counter- propagating modes; if they have opposite signs, then the interaction is between co-propagating modes. In most cases, first-order diffraction is dominant, hence N is assumed to be unity [1].

The resonant wavelength should be satisfied

$$\lambda = (n_i^{eff} \pm n_d^{eff})\frac{\Lambda_g}{\cos\theta} \tag{27}$$

2.2.1. Fibre Bragg gratings

In the case of backward-coupling (Fig. 1), represented by normal FBG (θ=0^o), the Bragg wavelength of the core mode is given by

$$\lambda_B = 2n_{eff}\Lambda \tag{28}$$

where n_{eff} is the effective index of the core.

Figure 1. Schematic of a contradirectional mode coupling for FBG.

2.2.2. Long-period gratings

In the case of forward-coupling, represented by LPG (Fig. 2), the resonant wavelength for coupling between the core and cladding modes satisfy

$$\lambda_{res} = (n_{co}^{eff} - n_{cl,m}^{eff}) \cdot \Lambda \tag{29}$$

where n_{co}^{eff} and $n_{cl,m}^{eff}$ are the effective indices of the core and the mth cladding mode, respectively.

The differences between core and cladding mode effective indices are much smaller than unity, hence the grating period for a forward-coupled grating at a given wavelength is much larger than that of a backward-coupled grating. Typically, LPG periods are hundreds of microns, whereas the period of FBG is less than a micron [11, 12].

Figure 2. Schematic of a codirectional mode coupling for an LPG.

2.2.3. *Tilted fibre gratings*

In the case of tilted gratings, as shown in Fig. 3, the mode coupling becomes more complex. The resonant wavelengths are [8, 13]

$$\lambda_{co-cl} = (n_{co}^{eff} \pm n_{cl,m}^{eff}) \cdot \frac{\Lambda_g}{\cos\theta} \tag{30}$$

where n_{co}^{eff} and $n_{cl,m}^{eff}$, respectively, are the effective indices of core and the mth cladding mode. The grating period along the fibre axis is simply

$$\Lambda = \frac{\Lambda_g}{\cos\theta} \tag{31}$$

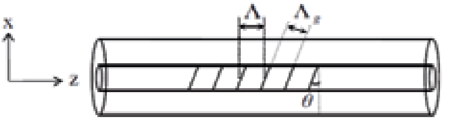

Figure 3. Schematic diagram of tilted grating in fibre core.

In equation (30), the sign of "+" and "-" describe the case wherein the mode propagates in -z or +z direction, relating to the grating tilt angle θ and then the backward- and forward- coupled TFG, respectively.

Mode coupling in a TFG can be understood by analysis of the phase-matching conditions as shown in Fig. 4(a). The strongest coupling takes place at the phase-matching condition

$$\vec{K}_R = \vec{K}_{co} + \vec{K}_G \tag{32}$$

where $\vec{K}_R$, $\vec{K}_{co}$ and $\vec{K}_G$ are wave vectors of the radiated light, core mode and grating itself, respectively. Because the refractive indices of the core and the cladding are very close, in general we may neglect the amplitude difference between $\vec{K}_R$ and $\vec{K}_{co}$.

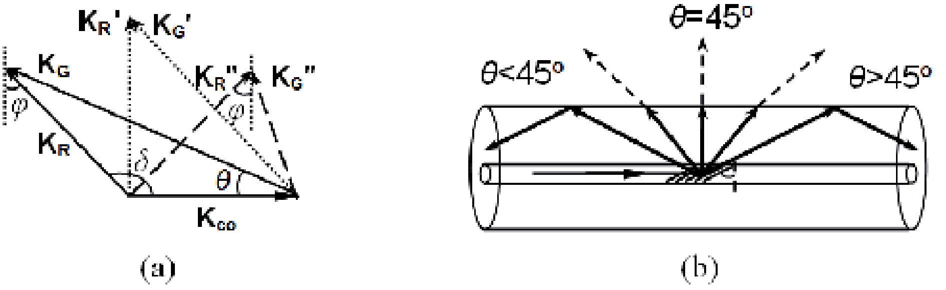

Figure 4. (a) Phase-matching conditions. (b) Mode coupling regimes for TFGs with tilt angles θ <, =, and >45°.

The direction of the coupled light depends on the tilt angle of the grating structure. As shown in Fig. 4(b), if the grating's tilt angle θ <45° (i.e. the radiation angle δ is an obtuse angle), the core mode will be coupled to the backward-propagating direction; if the grating angle θ>45° (δ is an acute angle), the core light can be coupled to the forward-propagating direction; if the θ=45° (δ=90°), all the phase matched light will be completely radiated out of the fibre. However, due to the total internal reflection effect at the cladding boundary, the coupled light by the TFG will exist in two different ranges: in one case the light radiated out of the core will be confined and propagates in the cladding; in the other case the light will not be bound by the cladding and will be tapped out from the side of the fibre. The range for radiation mode coupling depends on the critical angle, which is defined as

$$\alpha_c = \arcsin \frac{n_1}{n_2} \tag{33}$$

where n_1 and n_2 are refractive indices of the surrounding-medium and cladding, respectively. If the fibre is surrounded by air (n_1~1.0), the critical angle α_c=43.8°. If the surrounding-medium changes to the water (n_1~1.33), the critical angle α_c=67.0°.

If we define the incident angle as φ, shown in Fig. 4(a), for the light phase matched and radiated out of the core to the cladding /surrounding-medium boundary, φ is related to the grating tilt angle θ by $\varphi=|2\theta-\pi/2|$. If $\varphi < \alpha_c$, the radiation mode coupling range will be given by $\theta_{1c} < \theta < \theta_{2c}$ can be calculated as

$$\theta_{1c} = \frac{1}{2}\left(\frac{\pi}{2} - \alpha_c\right) \qquad \theta_{2c} = \frac{1}{2}\left(\frac{\pi}{2} + \alpha_c\right) \tag{34}$$

We have calculated this range to be 23.1°~66.9° in air and 11.5°~78.5° in water surrounding-medium. Within this range, the light will not be confined by the cladding and will radiate from the fibre. Below or beyond this range, the light will be coupled to the backward- or forward-propagating cladding modes, respectively, and be bound within the fibre.

3. Grating fabrication techniques

The fibre grating fabrication techniques may be classified to three main categories: two-beam holographic, phase mask and point-by-point techniques. Each technique has its merits and limitations and will be employed according to the specification requirement of the gratings to be fabricated.

3.1. Two-beam holographic technique

Fig. 5 shows the two-beam holographic UV-inscription system. The UV-beam is split into two with equivalent power when it passes through a 50:50 beam splitter. The two beams are then reflected by highly reflective mirrors M_1 and M_2 to meet on to the same section of the photo-sensitive fibre to produce the interfering fringes. A beam expanding telescope system consisting of two cylindrical lenses (C and D), where $df=CD-(f_c+f_d)=0$, is inserted into the optical path to expand the width of UV Gaussian beam, and thus the length of the two-beam interference pattern on the forthcoming meet at point O. Two cylindrical lenses (F_1 and F_2) are employed to focus the beams to the fibre core with enhanced power intensity.

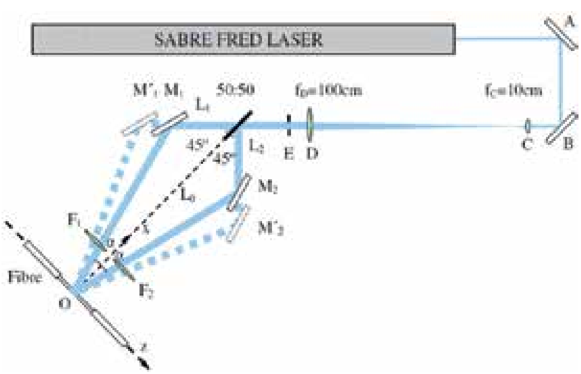

Figure 5. Two-beam holographic FBG inscription system.

The major advantage of the two-beam holographic method is the ability to write gratings with arbitrarily selected wavelengths simply by adjusting the angle (2α) between the two beams [14]. Limited by the range of the optical spectrum analyser (OSA) and the light source, the gratings fabricated are normally in the range of 750nm to 2000nm.

3.2. Phase-mask technique

The phase-mask technique, based on near-contact UV-beam scanning a phase mask, is one of the most effective techniques for reproducible FBG inscription.

The grating written by phase mask technique has a period of

$$\Lambda = \frac{\lambda_{UV}}{2\sin\theta_m} = \frac{\Lambda_{PM}}{2} \tag{35}$$

where Λ_{PM} is the period of the phase mask. The Bragg wavelength is then given by [3]

$$\lambda_B = 2n_{eff}\Lambda = n_{eff}\Lambda_{PM} \tag{36}$$

The phase mask is a corrugated grating etched in a silica substrate produced by high resolution lithography. Important features in a phase mask are the period of the etched grooves and the etch depth. With normal incidence, the UV-radiation is diffracted into several orders, m=0, ±1, ±2… The commercial phase masks have been optimized to achieve 0-order suppression of <5% and ~40% transmission in each of the ±1 diffracted orders. The superposition of ±1 diffraction orders, in the proximity of the surface of the phase mask, produces an interference pattern that can be used for writing FBGs.

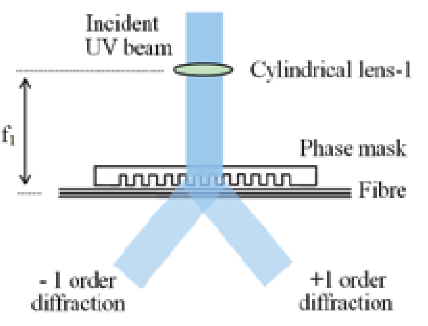

Figure 6. Fibre grating inscription by UV-beam scanning across a phase mask.

As shown in Fig. 6, a cylindrical lens with a focal length f_1 is added before phase mask and focuses the UV-irradiation to the fibre core with increased intensity in one dimension in the beam-fibre plane. Very uniform index modulation can be achieved by the phase mask method. Fig. 7(a) shows the image of the fringe structure inscribed in the fibre core using the phase mask method. The image was examined and measured by use of the Axioskop2 mot plus microscope (Carl Zeiss) in conjunction with Axio vision Cameras &Framegrabbers system with high magnification. Fig. 7(b) shows the typical transmission spectra for a uniform FBG fabricated by the phase mask technique. The grating is 5mm long and is designed to reflect with a Bragg wavelength of 1550nm. The multiple resonances with smaller amplitude on the short wavelength side of the main Bragg resonance are due to the radiated mode being reflected at the cladding-air interface and re-entering the core, creating a cylindrical Fabry-Perot effect.

Besides the distinctive advantage of reproducible grating inscription, a further advantage of the phase-mask technique is the ability to make high quality, complex grating structures, including grating arrays, chirped [15-17], apodised [18, 19], phase-shifted [20, 21], Moire [22, 23], sampled [24], and long-length gratings [25]. Of particular relevance to the work presented in this chapter, the phase-mask method has also been employed to fabricate TFGs with tilted structures ranging from 0° to 84°. In the phase mask fabrication system, TFGs can be realised simply by rotating the phase mask with respect to the fibre. Chirped gratings can also been readily fabricated using a chirped phase mask in this system.

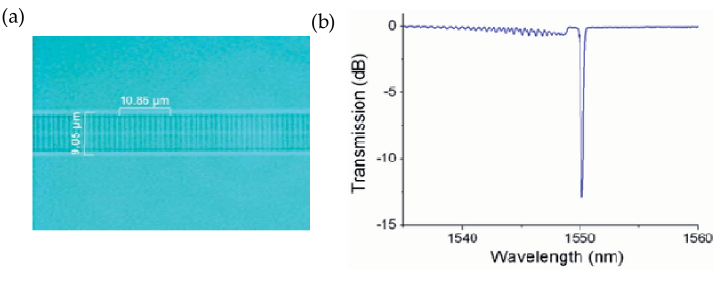

Figure 7. (a) Image of an FBG written by phase mask method (b) The typical transmission profiles of an FBG.

A disadvantage of the phase mask method is the limit to variation of Bragg wavelength, as it needs a separate phase mask for different wavelength required. The strain-fibre method has been incorporated into the system to give a 2nm-tuning range to the Bragg wavelength for each mask.

3.3. Point-by-point technique

The third main grating fabrication technique is the point-by-point technique. Because the grating is written a point at a time, it is a flexible method to alter the grating parameters, such as length, periodicity and strength. Limited by the focused spot size of UV-beam, it is difficult to control translation stage movement accurately enough to write FBG structures which in general have typical periods of ~0.5μm at 1550nm. Thus, the point-by-point technique is mainly used to fabricate long-period gratings with periods ranging from 10μm to 600μm.

As shown in Fig. 8(a), the point-by-point inscription system, two cylindrical lenses are added to focus the writing beam on the fibre to an approximate spot size of 20μm×20μm in z- and y-dimension and a shutter is computer- programmed to switch on/off with a 50:50 duty cycle to realise period-by-period print. The system has a great flexibility in fabricating LPGs with different periods, lengths and strengths. Fig. 8(b) shows the typical transmission spectrum of an LPG in SMF-28 with a length of 40mm and a periodicity of 380μm made by the point-by-

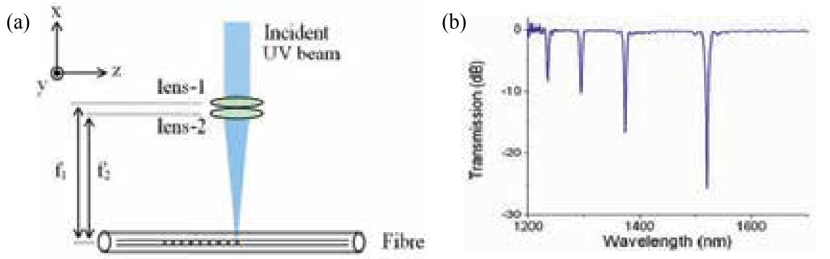

Figure 8. (a) Schematic of LPG fabrication using point-by-point technique. (b) The typical transmission spectrum of an LPG in SMF-28 fibre.

point method. The four broad attenuation resonances within 1200~1700nm wavelength range correspond to coupling to the different cladding modes. The bandwidth of resonances of an LPG is typically >10nm, much broader than that of an FBG. LPGs are transmission loss type devices and have been employed for a range of applications in optical communications and sensing.

3.4. Inscription of tilted fibre gratings

FBGs with tilted structures have their unique device functionalities. This section will present the fabrication and spectral characterisation of TFGs.

3.4.1. Design principle of TFGs

As illustrated in Fig. 9 the tilted structures can be achieved either (a) by tilting the phase mask with respect to the fibre in the phase mask inscription system, or (b) by rotation of the fibre about the axis normal to the plane defined by the two interfering UV beams in the holographic system.

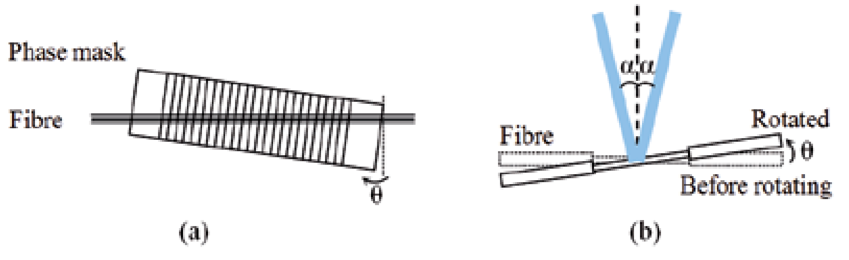

Figure 9. (a) Phase mask and (b) two-beam holographic techniques for TFG fabrication.

Owing to the cylindrical geometry of the optical fibre, the internal grating angle θ_{int} is not the same as the external phase-mask angle or fibre rotated angle θ_{ext}. For the phase-mask fabrication, the internalgrating angle θ_{int} is related to the external phase mask tilt angle θ_{ext}(the angle between the mask and the fibre) by the following relationship [26]

$$\theta_{\text{int}} = \frac{\pi}{2} - \tan^{-1}\left[\frac{1}{n\tan\theta_{ext}}\right] \tag{37}$$

In the case of holographic fabrication, θ_{int} can be expressed as [8]

$$\theta_{\text{int}} = \frac{1}{2}\left[\arcsin\left(\frac{1}{n}\sin(\alpha+\theta_{ext})\right) - \arcsin\left(\frac{1}{n}\sin(\alpha-\theta_{ext})\right)\right] \tag{38}$$

where α is the half angle between the two interfering beams, θ_{ext} is the fibre tilt angle.

The comparative study on TFG inscribed by phase mask and holographic method has been reported in [27], here we main focus on the phase mask fabrication of TFGs. The relationship of external and internal tilt angles for TFGs written by phase mask method has been depicted in Fig. 10.

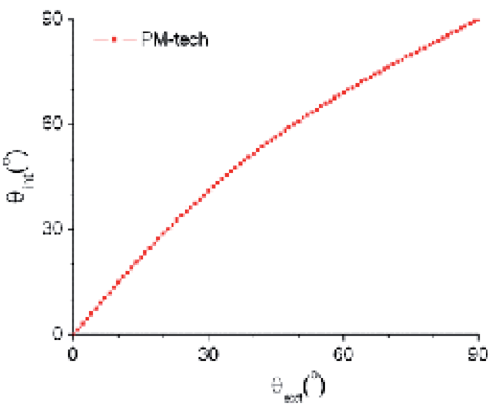

Figure 10. The relationship of the internal angle θ_{int} against the external angle θ_{ext} for TFG.

3.4.2. Unique spectral characteristics of TFGs

One of the unique characteristics of TFGs is the strong polarisation dependent loss (PDL) effect when the tilt angle becomes large. This property has been implemented as an in-line polarimeter [28] and a PDL equaliser [29, 30]. In addition, a near-ideal in-fibre polariser based on 45°-TFG has been reported by [31, 32], exhibiting a polarisation-extinction ratio higher than 33dB over 100nm range and an achievement of 99.5% degree of polarisation for the unpolarised light.

It is well known that there are two components of the electric field vector in the plane of polarisation. The components of the electric field parallel and perpendicular to the incidence plane are termed p-like and s-like. Light with a p-like electric field is defined to be p-polarised

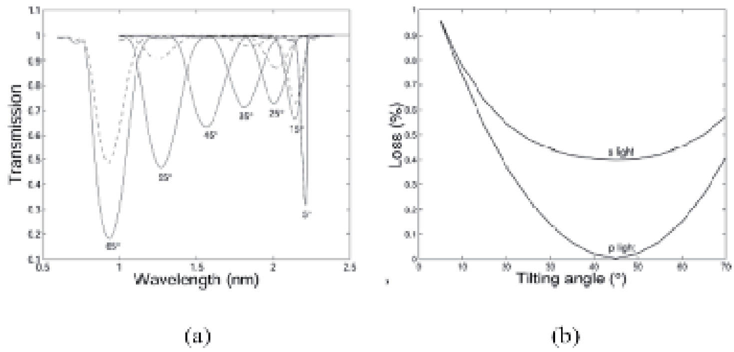

Figure 11. (a) The simulated transmission spectra of p- (dashed line) and s-polarised mode (solid line) travelling in the TFGs with various tilting angles; (b) Transmission losses of s- and p-polarised mode versus tilting angles. (After: [32])

whereas light with an s-like electric field is s-polarised. Fig. 11(a) shows the simulated transmission profiles of both the s- and p- polarised modes after they pass through a TFG. It is clear that both of two polarised modes show similarly evolving trends although the change in amplitude for p-polarised mode is more noticeable. The maximum transmission losses for different tilt angles for s- and p- modes have been simulated and plotted in Fig. 11(b). The transmission loss reaches minimum when the tilt angle is at 45°. At this critical angle, the loss of p-mode is eliminated completely and s-mode loss is still noticeably high [32], ie. p-mode is transmitted and s-mode is completely attenuated.

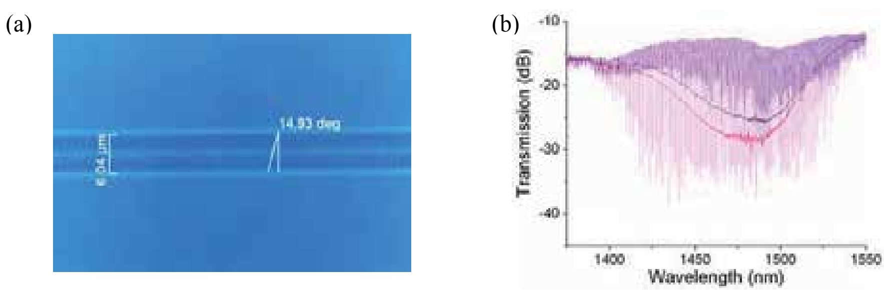

Figure 12. Image of $10°_{ext}$-TFG in B/Ge fibre (a) and transmission spectra (b).

As an example, a photo-induced tilted index modulation is shown in Fig. 12(a). This is θ_{ext}=10° tilted grating, the measured internal angle θ_{int} is 14.93° which is in a good agreement with the theoretical result (θ_{int}=14.9°) from Equation (37). Fig. 12(b) plots its transmission spectra where the dense resonances covering 1375-1550nm are caused by the core-cladding coupling and by the reflection at the cladding-air boundary. The multiple resonances can be removed by immersing the grating in index-matching gel to simulate an infinite cladding, where the light is coupled from the core to radiation modes, thus the dense resonances evolve to a smooth transmission loss profile.

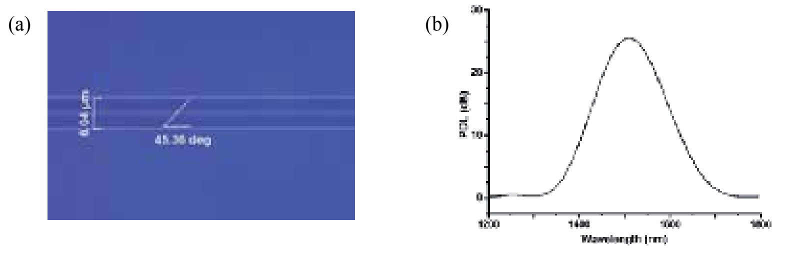

Figure 13. Image of 45°-TFG (a) and its PDL profile (b).

An 45°-TFG was fabricated in Ge-doped photosensitive fibre using the scanning phase mask technique and 244-nm cw UV laser source. A phase mask with 1.8μm period was used to ensure the 45°-TFG spectral response fell into near 1550nm region, the phase mask was rotated by 33.3° to induce slanted fringes at 45° within the fibre core. The 45° tilted fringes, shown in Fig. 13(a), were verified by examination with an oil-immersion high-magnification microscope. Fig. 13(b) shows the PDL of a 25mm-length 45°-TFG, the entire PDL profile is near-Gaussian-like distribution over ~300nm with the maximum PDL of 26dB at 1520nm [33].

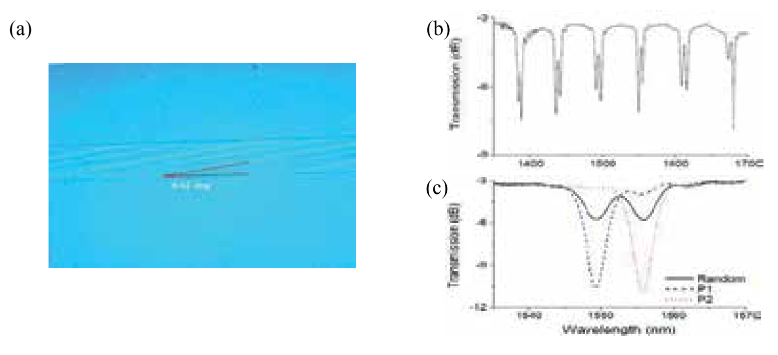

Figure 14. Image of the 81°-TFG (a) and it transmission spectra (b-c).

We fabricated a 10mm long 81°-TFBG in SMF-28 with UV laser scanning the phase mask (with period of 6.6μm) method. Fig. 14. (a) shows the image of the tilted fringes with a measured internal angle of 81.98°.

Since the angle 81° >θ_{2c} (=66.9° in the air), the light was coupled to forward-propagating cladding modes corresponding a series of the resonances with a noticeable paired-peak feature on the spectra, Fig. 14(b), it may be expected that the highly tilted structures will increase the birefringence of the fibre, thus resulting in the light coupled to two sets of modes of different polarisation states. It can be noticed that the strengths of the paired-peaks in Fig. 14(b) are around 3dB, which suggests that the light may be coupled equally into two sets of birefringence modes corresponding to the two orthogonal polarisation states. To confirm this, a polariser and a polarisation controller were inserted in the measurement system to measure the transmission spectrum. By varying the polarisation state of the probe light, the strengths of the paired-peaks varied accordingly with the polarisation of the light. Fig. 14(c) shows the transmission spectra of one of the paired-peak around 1550nm for random and two orthogonally polarised states. With random polarisation, both peaks exhibit a ~3dB loss as the light is coupled equally to the birefringence modes. When the light is switched to either polarisation state, one resonance grows into its full strength ~7.3dB whereas the other almost disappears. The polarisation effect induced spectral separation between the paired-peaks is about 6.3nm, giving an estimated birefringence of ~10^{-4}.

4. Optical fibre grating based chemical and bio- sensors

A key characteristic of optical chemical and bio- sensor design is the sensitivity to, or the change rate of optical signal as a function of, surrounding chemical and bio- analyte. There has also been an increasing activity aimed at implementing optical biosensors by exploring the fibre grating's response to the change of surrounding-medium refractive index (SRI) [34, 35, 36-38].SRI-sensitive devices have been recently developed by UV-inscribing normal Bragg, tilted, and long-period structures in standard single, multimode, and D-fibres[39-43]. Appropriate choice of fibre type can provide intrinsic or enhanced SRI sensitivity to grating structures and allow, in some instances, the realisation of multifunctionality. The fibre grating based RI sensors can be coated with bioactive materials to interact with certain type of biological agents, thus become true biosensors with high sensitivity and selectivity [44, 45].

4.1. Refractive index sensing principle of in-fibre gratings

As a core-to-core mode coupling, the light in an FBG is well screened by the cladding, effectively precluding strong interaction with the surrounding medium. Thus it is intrinsically insensitive to SRI. Several techniques have been demonstrated to sensitise FBGs, including polishing and chemical etching the fibres to expose the core to surrounding medium.

In contrast to FBGs, LPGs, as core-cladding mode coupling devices, are intrinsically sensitive to SRI. Any variation in the core-cladding guiding properties will affect the transmission characteristics of LPGs, providing an optical signal encoded with the information of external parameters. LPGs have been used to monitor the physical parameters such as strain, temperature, load, curvature and with a variety structures for SRI sensing [35, 38].

4.2. Chemical etching technique for sensitisation

The chemical etching technique has been extensively employed to remove the claddings of the FBG structures, enabling the interaction of the core mode with the surrounding medium [46-48]. Although LPGs are intrinsically sensitive to SRI, modifying the cladding properties can further enhance their SRI sensitivity greatly. Chiang *et al*. reported the enhancement of the external refractive index sensitivity of an LPG resulting from a small reduction in the cladding radius via an HF-etching process [49, 50]. We also employed the HF etching technique to reduce the thickness of the cladding of LPG devices and have demonstrated effective enhancement of the SRI sensitivity to these LPG structures.

In order to effectively control the thickness of the fibre gratings, an etching procedure was first established and the etching rates were investigated for different type fibres using HF acids of different concentrations. The HF etching technique inevitably suffers from mechanical reliability since any micro-crack of fibre will be very vulnerable to the HF acid, thus it will degrade the fibre tensile strength by orders of magnitude [51]. To effectively control the cladding size of fibre, the etching rate was first evaluated for virgin fibre samples including standard SMF and D-fibre using HF at 10% concentration. Twenty samples of each type fibre were immersed in the HF bath and were withdrawn in turn every 10min. The samples with differently etched claddings were then examined and measured by microscope with high magnification.

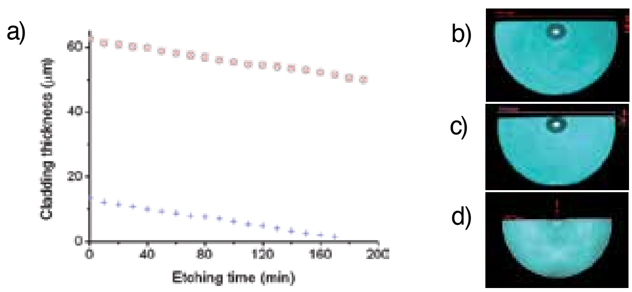

Figure 15. (a) Etching rates of SMF and D-fibre. (symbol × and o: round-side radii of SMF and D-fibre; symbol +: D-shaped cladding thickness of flat-side); The cross-section images of etched D-fibre: (b) etched-40min, (c) etched-90min, (c) etched-170min.

Fig. 15 plots the etched cladding thickness against etching time for the two types of fibre. The natural silica claddings of SMF and D-fibre show nearly isotropic etching processes with a similar etching rate of ~0.068μm/min. The cross-sectional images of the D-fibre samples that had been etched for 40min, 90min and 170min are shown in Fig. 15(b-d), respectively. It was estimated that at ~85min, the side of the inner elliptical fluorine-doped cladding on the flat side of the D-fibre was completely etched off, and the total inner cladding was almost removed after ~167min. After~170min, the core was almost etched off, as can be seen in Fig. 15(d), and the residual D-fibre cladding layer on the round-side was about 50.7μm.

Calibration of RI and sugar concentration

Since the chemical sensing mechanism of the in-fibre gratings is based on the resonances response to the change of SRI and the most devices discussed in this chapter have been evaluated for their SRI sensitivity by measuring the concentrations of sugar solution, the calibrated correlation between the concentration of sugar solution and the refractive index (RI) is necessary to be discussed first. Table 1 lists the conversion relationship between the percentage sugar concentration and the refractive index, which is from the data reported in reference [52].

Mass% of sugar solution	0	10	20	30	40	50	60	70	80
Refraction Index	1.333	1.348	1.364	1.381	1.400	1.420	1.442	1.465	1.491

Table 1. Calibration of refractive index against concentration of sugar solution ($C_{12}H_{22}O_{11}$).

4.3. Chemical sensor based on FBGs in D-fibre

In-fibre optical chemical sensor based on FBG in D-fibre and sensitised by HF etching treatment has been implemented and characterised.

The FBG structures were UV-inscribed in D-fibres using the standard phase mask fabrication method. The D-fibre FBG samples were then sensitised by removing the cladding layer on the flat side by employing etching process using HF acid of 10% concentration. In order to control the etching depth, the transmission spectra were monitored *in-situ* using an EDFA source and an optical spectrum analyser. Fig. 16 shows the spectral evolution of etched FBG samples the wavelength shift and strength of the transmission loss peak against etching time. There are three stages can be seen from the etching process: (i) 0~140min, (ii) 140~168min, and (iii) 168~173min. For the first stage, the spectrum of FBG remained intact, signifying the core mode was still well bounded by the cladding layer. With further etching (140~168min), the thickness of the flat-side claddingwas reduced to just a few microns, thereby allowing the evanescent field to penetrate to surrounding-medium (HF acid). In this stage, the Bragg resonance shifted noticeably towards the shorter wavelength side, indicating that the device has entered the SRI sensitive regime. For the final etching period from 168 to 173min, a fractional layer of the core was been etched off. As it can be seen from Fig. 16(b), the transmission loss drops dramatically due to the combined effects of the reduction of the effective core mode index and the degradation of the light confinement.

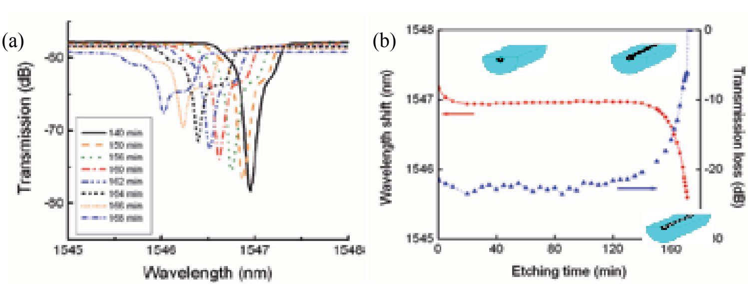

Figure 16. (a) Spectral evolution of the D-fibre FBG under etching period from 140~168min. (b) Bragg wavelength shift and transmission loss over the entire etching process. Inset, schematic images of D-fibre corresponding the different etching stage.

The SRI sensing characteristics of one un-etched and two etched D-fibre FBG devices (labeled as G1 and G2) were comparatively investigated. G1 and G2 were etched for 159min and 169min respectively. Sugar solutions with concentration ranging from 0% to 60% were prepared for refractive index measurement. The three grating devices were immersed in turn into each sugar solution and their Bragg wavelengths were measured and are shown in Fig. 17 It is clearfrom this figure that the un-etched grating is totally insensitive to SRI whereas the Bragg wavelengths of G1 and G2 red-shift at different rates with increasing SRI. The deeper etched grating G2 exhibits a much higher SRI sensitivity than the less etched G1.

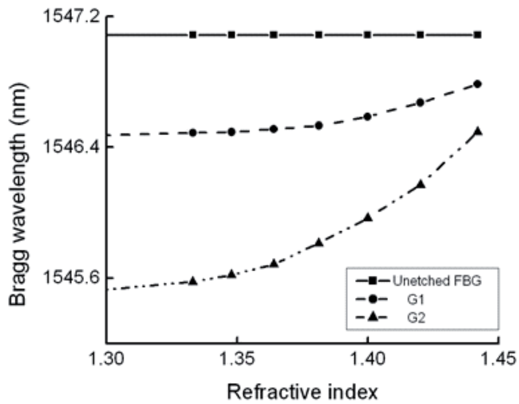

Figure 17. SRI sensitivity for un-etched, shallowly (G1) and deeply (G2) etched FBG in D-fibre.

If the SRI sensitivity is defined as the wavelength shift induced by 1% RI change, the maximum sensitivities exhibited by G1 and G2 are 0.03nm/% and 0.11nm/%, respectively. The latter is almost four times that of the former. Using the calibration of RI against sugar concentration, the SRI sensitivity can be converted to the sugar concentration sensitivity. For practical applications, up to 5% concentration change in sugar concentration can be easily detected by G2 using a standard optical interrogation system with an optical resolution of ~0.1nm and 0.5% change with a resolution of 0.01nm.

4.4. Dual-peak LPG for Haemoglobin sensing

In this section, an implementation of optical biosensor based on etched dual-peak LPG will be discussed. This device has been used to detect concentration of Haemoglobin (Hgb) protein in sugar solution, showing an ultrahigh sensitivity.

Due to the parabolic characteristic of the group index of the high-order cladding modes [34, 35], there exists a set of dispersion-turning-points on the LPG phase curves, where $d\lambda / d\Lambda \to \infty$. The nature of the coupled cladding modes close to the dispersion-turning-point makes the dual-peak LPGs ultrasensitive to cladding property, allowing fine tailoring the mode dispersion and index sensitivity by light-cladding-etching method using HF acid. It has been reported that the responses of such LPGs can be modified by reducing the cladding size via chemical etching [39, 41, 49, 50].

Based on the mode coupling theory, the phase curves have been simulated for an LPG of 160μm period in SMF-28 fibre with cladding radius reducing from 62.5μm to 51.5μm, as shown in Fig. 18(a). The dispersion-turning-point feature is apparentthat the slope direction of the phase curve changes from negative ($d\lambda / d\Lambda < 0$) to positive ($d\lambda / d\Lambda > 0$). For a given radius as dotted line in Fig. 18(a), two cladding modes, one in the positive and the other in negative dispersion region, could satisfy simultaneously the same phase match condition, resulting in dual-peak resonances.

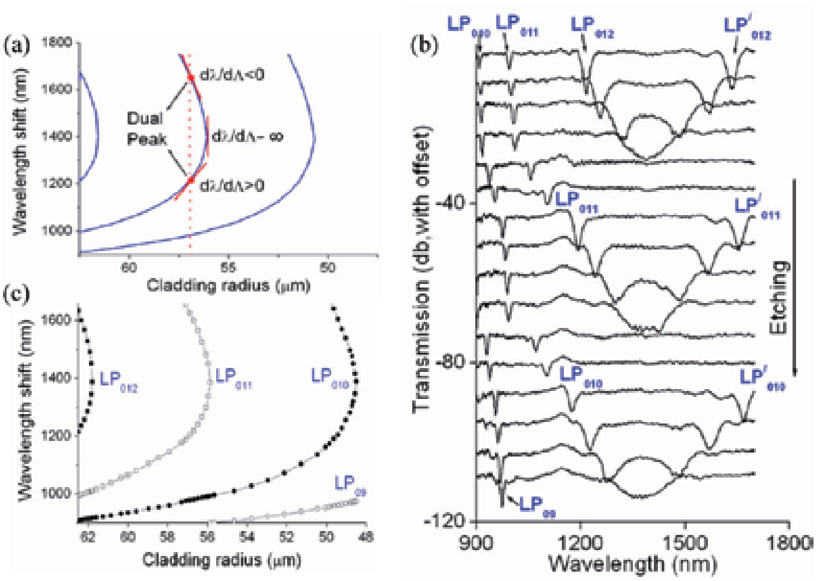

Figure 18. (a) Simulated phase curves of a dual-peak LPG of 160μm period for reduced cladding radius from 62.5μm to 51.5μm. (b) Spectral evolution of dual-peak LPG (c) Wavelength shift of LPG resonances against fibre cladding radius.

A dual-peak LPG with a period of 159μm was subjected to the etching experiment using an HF solution with 12% concentration. As the first trace shown in Fig. 18(b), this grating has four coupled cladding modes identified as LP_{010}, LP_{011}, LP_{012} and LP'_{012}in the wavelength range from 900nm to 1700nm, two of which are the dual-peak modes located at 1214.9nm and 1634.4nm. Under etching, it can be seen clearly that a transition of generation, coalescing and annihilation of the dual-peak resonances from higher order modes to lower ones. Firstly, LP_{012} and LP'_{012} are moving towards each other and eventually coalesced and annihilate, and a new pair of dual-peak modes (LP_{011} and LP'_{011}) are generated in conjunction with the red-shifting of LP_{010}; then this transition is repeated leading to the appearance of paired LP_{010} and LP'_{010}, and LP_{09} modes.

Fig. 18(c) plots the resonance shifts of dual-peak LPG against cladding radius, the shift speed increases when they are close to the dispersion-turning-point. It was also noticed that the movements of the same order dual peaks are not linear and symmetric: the loss peak with longer wavelength in $d\lambda / d\Lambda < 0$ region moves faster than its counterpart at shorter wavelength in $d\lambda / d\Lambda > 0$ region.

When the dual-peak cladding modes are close to the dispersion-turning-point, it is possible to fine tuning the sensitivity by light etching the cladding. A light-etching experiment was performed using HF acid of only 1% concentration. A 20mm-long LPG with a 147μm period was subjected to etching for 96.5min, removing cladding thickness by only 1.1μm (from 62.5μm to 61.4μm). The spectral evolution was monitored for the etching process and plotted in Fig. 19(a). The dual peaks were originally at M and M′ spaced by 493.6nm and finally moved to N and N′ separated by only 98.1nm, indicating they are now much closer to the dispersion-turning-point and should be significantly more sensitive to SRI change.

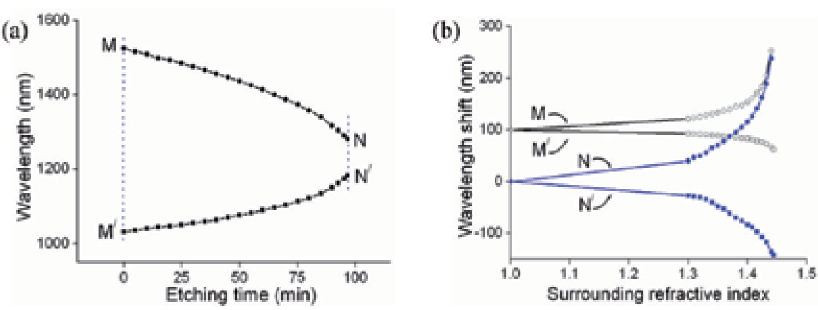

Figure 19. (a) Dual peak wavelengths against etching time (towards dispersion-tuning-point); (b) SRI induced spectral separation of the dual peaks for etched (N, N′) and unetched (M, M′) gratings (note: the curves have been offset).

The SRI sensitivity of the lightly etched dual-peak LPG was compared with that of an unetched device of the same grating parameters. The two gratings were immersed in the air and a set of index gels with refractive indices ranging from 1 to 1.44 and the separation of the dual peaks was measured for each SRI value, as plotted in Fig. 19(b). The separation increases nonlinearly with increasing SRI, however, that is far larger for the lightly-etched device than for the non-etched one. For SRI varying from 1 to 1.44, the total separation between N and N′ is 373.9nm, whereas that between M and M′ is 185.4nm, only half of the former. This indicates that the SRI sensitivity of the finely-etched LPG has more or less doubled that of the unetched one.

The lightly-etched dual-peak LPG was then used to measure the concentration of Hgb in sugar solution. Firstly, a set of Hgb solutions with concentrations from 0.0% to 1.0% (step 0.2%) was prepared by adding Hgbto water. Then 5ml each of these solutions was added into six beakers, each beaker had 30g of 60% aqueous sugar solution. LPG sensor was submerged in these solutions in turn and the shifts of ‘N’ peak were measured. Fig. 20(a) shows the spectral evolution the N-peak under different solutions and Fig. 20(b) plots its central wavelength shift against Hgb concentration. When the Hgb concentration changing from 0.0% to 1.0%, the peak red-shifts by 19.8nm. Defining the concentration sensitivity as the shift induced by 1% Hgb, we have a device sensitivity of ~20nm/1%. Thus, using a standard interrogation system with a resolution of 0.1nm, this finely tailored device could detect the Hgb concentration change as small as 0.005%.

http://dx.doi.org/10.5772/54242

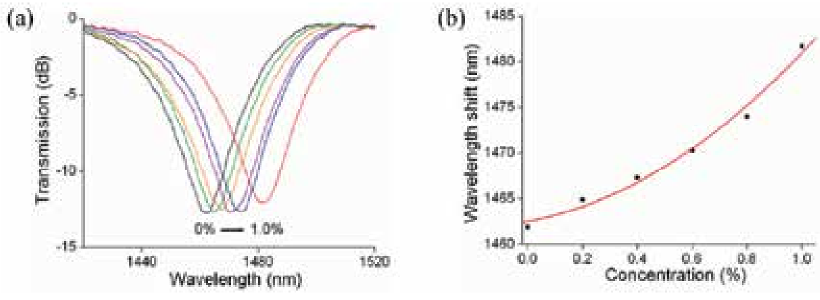

Figure 20. (a) Spectral evolution of N-peak of the lightly-etched dual-peak LPG with different Hgb concentrations; (b) N-peak wavelength shifts against Hgb concentration.

4.5. LPG based biosensor for DNA hybridisation detection

The development of biosensors is motivated by their potential applications in biochemical, biomedical, and environmental areas. In the past decade, the immobilisation techniques have been developed to enable the functionalisation of silica support and several DNA biosensors have been presented based on the hybridisation of target sequence to the bound DNA at the surface of modified electrode, surface plasmon resonance, microchips, ring-resonator, planar waveguide and optical fibre [53-55]. Chryssis*et al.* recently reported a detection of hybridisation of DNA by highly sensitive etched core FBG sensors [44, 45, 56-58]. Fibre grating based biochemical and biomedical sensors could be the alternative to and even the replacement for conventional biosensors with advantages, such as highly-sensitive, label-free, fast and real-time detection, dynamic analysis, etc. With the robustness and low-cost fabrication, the sensitised dual-peak LPGs could be another desirable candidate for advanced optical biosensors.

Here, we implement an optical biosensor based on LPG for detecting DNA interactions at a silica-liquid interface. The probe DNA is covalently immobilised onto the functionalised surface of the fibre grating region. Since LPG couples the light from core to cladding, it is intrinsically sensitive to changes in the refractive index at the sensor surface, thereby allowing the interaction between bound probe DNA and target DNA in ambient solution to be monitored *in situ*. This novel biosensor presents many advantages, such as detection of DNA hybridisation in low concentrations, real-time monitoring, high sensitivity and reusability.

Generation scheme of biosensor based on LPG: Fig. 21 displays the procedure of the in-fibre grating biosensor for silanisation, covalent activation, immobilisation and DNA hybridisation. All the biochemical experiments were performed in a fume cupboard. To minimise the bend cross-sensitivity, the LPG sensors were placed straight in a V-groove container on a Teflon plate and all the chemicals and solvents were added and withdrawn from the container by carefully pipetting.

Silanisation of LPG Surface: Prior to silanisation, LPGs were cleaned by immersion in 5M hydrochloric acid (HCl) for 30min at room temperature followed by rinsing in deionized (DI) water three times and drying in the air. Silanisation of glass surface was implemented by immersion in fresh 10% 3-Aminopropyl-triethoxysilane (APTS) (Sigma-Aldrich Company

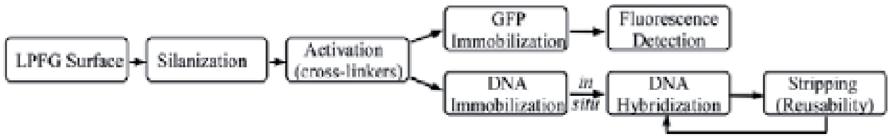

Figure 21. Basic scheme of the functionalisation of LPG for the generation of biosensor.

Ltd.) for 30min at room temperature [57]. In this work, a 30mm-long LPG with a period of 161μm has been used and the peak at 1590.5nm has been selected for biosensing experiment.

LPG Surface Activation: To immobilise biomolecules covalently to the glass surface, a chemical bond has to be formed between a functional group of biomolecule and the amino-group of the linker [54]. As it well known in bioconjugate chemistry, Dimethyl suberimidate (DMS, the molecular structure shown in Fig. 22(a)) is water soluble, membrane permeable and is one of the best crosslinking agents to convert the amino-groups into reactive imidoester cross-linkers. The imidoester functional group is one of the most specific acylating groups available for the modification of primary amines and has minimal cross reactivity toward other nucleophilic groups in proteins [59, 60]. In addition, DMS does not alter the overall charge of the protein, potentially retaining the native conformation and activity of the protein. For activation of glass surface, the silanised LPGs were immersed in 25mM DMS in phosphate buffered saline solution (PBS) for 35min at room temperature. Then the activated LPGs were rinsed by DI water three times and dried in the air.

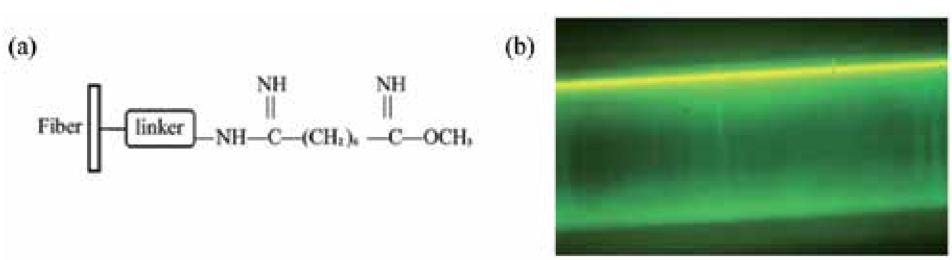

Figure 22. (a) Activation of the silanised glass surface using DMS. (b) The image of GFP fluorescence on the fibre surface;

GFP Immobilisation and Fluorescent Test: In order to provide a simple method to determine whether biomolecules are able to be successfully immobilised on the fibre glass surface, Green Fluorescent Protein (GFP), which is an intrinsically fluorescent protein that has been used extensively as a tool in biology to enable imaging, was employed to detect the attachment of protein onto the fibre surface. A DMS activated fibre, as described above, was incubated in 1mg/ml GFP in PBS for 16hrs at room temperature. The GFP-deposited fibre surface was observed under optical microscope with UV light source using appropriate filters for GFP fluorescence detection and the image was captured and shown in Fig. 22(b), exhibiting successful protein immobilisation.

Immobilisation of Probe DNA: The immobilisation process was carried out by incubation of an activated LPG in 1μM probe DNA (as shown in Table 2) in PBS for 16hrs at room temperature. The spectra of LPG as shown in Fig. 23(a) were measured at the beginning and end of the immobilisation process, respectively, by OSA with a resolution of 0.1nm. The grating wavelength was defined by the centroid calculation method. After 16hrs deposition, a blue-shift in wavelength of 254pm was observed, showing the fibre surface has been modified successfully.

Oligonucleotide	5´ end modification	Sequence	3´ end modification
Probe	none	GCA CAG TCA GTC GCC	NH_2
Target	none	GGC GAC TGA CTG TGC	none

Table 2. Sequences and modifications of the Probe and Target Oligonucleotides.

Hybridisation of Target DNA: Hybridisation was executed with target DNA. After cleaning with DI water, the grating sensor was rinsed in 6xSSPE (0.9M NaCl, 0.06M NaH_2PO_4, and 0.006M EDTA) then immersed in fresh 1μM target DNA in 6xSSPE buffer for 60min at room temperature. The grating wavelength shift, as shown in Fig. 23(b), was monitored *in situ* through whole hybridisation process. An increase of 715pm was observed in wavelength from the start of hybridisation process until the end and most of the change takes place in the first 20min showing that hybridisation takes place very quickly. Hybridisation of target DNA has been monitored successfully in real-time by this grating sensor.

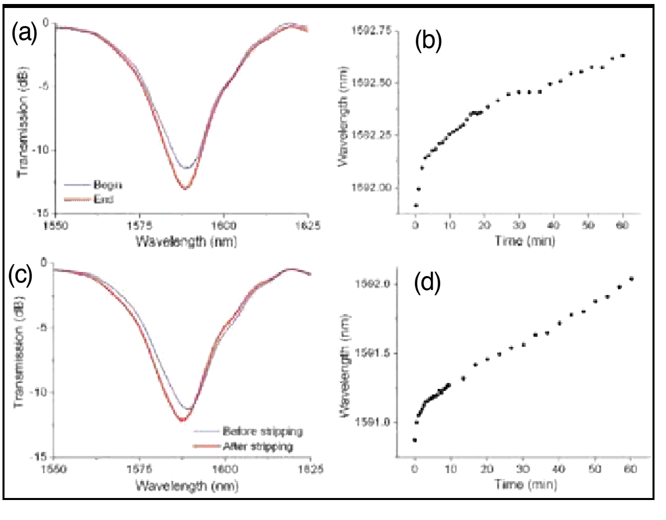

Figure 23. (a) Spectra of biosensor before and after probe DNA immobilisation; (b) Wavelength evolution of biosensor against time during the hybridisation of target DNA; (c) Spectra of biosensor before and after the stripping procedure; (d) Wavelength shift against time during the re-hybridisation process.

Stripping Procedure and Reusability: For re-use, grating sensor was incubated in a freshly prepared stripping buffer of 5mM Na_2HPO_4 and 0.1%(w/v) Sodium dodecyl sulfate (SDS) at 95°C for 30s, three times, then was washed with DI water and dried for the re-hybridisation. The grating spectra, as shown in Fig. 23(c), were measured in DI water before and after the stripping procedure. A blue-shift of 1257pm has been observed, which is caused by the stripping procedure. After stripping, the sensor was re-hybridised by immersion in 2μM target DNA in 6xSSPE buffer for 60min at room temperature. A 1165pm wavelength increase has been measured, as shown in Fig. 23(d), demonstrating the re-usability of the LPG biosensor.

A novel optical biosensor based on LPG has been demonstrated and used for detection of DNA hybridisation. A change of wavelength of 1165pm was observed in the 60min hybridisation of target DNA, showing a significantly higher sensitivity than the reported biosensor based on core-etched FBG [57].

5. Conclusions

In-fibre grating technology has developed very rapidly in recent years and the range of its applications will continue to grow, such as biomedical, biosensing, environmental monitoring and health care. This chapter, we have reviewed the theory, the fabrication techniques and the types of fibre gratings. In addition we have demonstrated the success of grating based devices for chemical and bio- sensing. It may be possible to further enhance the sensitivity by selecting the special fibre such as D-fibre, by refining the etching process, or by designing integrated microfluidic channels [61] or by developing the novel grating structures [62]. We are also interested in developing the new biosensor for selective bio-sensing, such as protein-protein, protein-DNA and protein-substrate interaction.

Acknowledgements

I gratefully acknowledge Professor Ian Bennion, Professor Lin Zhang, and Dr. Anna V. Hine et al. at Aston University, United Kingdom, for their contributions in many relevant works presented in this chapter.

Author details

Xianfeng Chen*

Address all correspondence to: x.chen@bangor.ac.uk

School of Electronic Engineering, Bangor University, Bangor, United Kingdom

References

[1] A. Yariv, "Coupled-mode theory for guided-wave optics," *IEEE J. Quantum Electron.*, 9, 919-933, 1973.

[2] K. O. Hill, Y. Fujii, D. C. Johnson, and B. S. Kawasaki, "Photosensitivity in optical fiber waveguides: Application to reflection filter fabrication," *Appl. Phys. Lett.*, 32, 647-649, 1978.

[3] T. Erdogan, "Fiber grating spectra," *J. Lightwave Technol.* 15, 1277-1294, 1997.

[4] I. Bennion, J. A. R. Williams, L. Zhang, K. Sugden, and N. J. Doran, "UV-written in-fibre Bragg gratings," *Optical and Quantum Electronics*, 28, 93-135, 1996.

[5] L. Zhang, W. Zhang, and I. Bennion, "In-fiber grating optic sensors," in *Fiber Optic Sensors*, F. T. S. Yu and S. Yin eds., 123-181, Marcel Dekker, New York, 2002.

[6] A. Othonos and K. Kalli, Fiber Bragg gratings, Artech House, Inc. 1999.

[7] R. Kashyap, Fiber Bragg gratings, Academic Press, 1999.

[8] T. Erdogan, and J. E. Sipe, "Tilted fiber phase gratings," *J. Opt. Soc. Am.A*, 13,296-313, 1996.

[9] H. Kogelnik, and C. W. Shank, "Coupled wave theory of distributed feedback lasers," *J.Appl.Phys.*, 43, 2327-2335, 1972.

[10] T. Erdogan, "Cladding-mode resonances in short- and long- period fiber grating filters," *J. Opt. Soc. Am. A*, 14, 1760-1773, 1997.

[11] A. M. Vengsarkar, P. Lemaire, J. Judkins, V. Bhatia, T. Erdogan, and J. Sipe, "Long-period fiber gratings as band-rejection filters," *J. Lightwave Technol.*, 14, 58-65, 1996.

[12] V. Bhatai and A. M. Vengsarkar, "Optical fiber long-period grating sensors," *Opt. Lett.*, 21, 692-694, 1996.

[13] K. Lee, and T. Erdogan, "Fiber mode coupling in transmissive and reflective tilted fibre gratings," *Appl. Opt.*, 39, 1394-1404, 2000.

[14] G. Meltz, W. W. Morey, and W. H. Glenn, "Formation of Bragg gratings in optical fibers by transverse holographic method," *Opt. Lett.*, 14, 823-825, 1989.

[15] L. Zhang, K. Sugden, J. A. R. Williams, and I. Bennion, "Postfabrication exposure of a gap-type bandpass filters in broadly chirped fiber gratings," *Opt. Lett.*, 20(18), 1927-1929, 1995.

[16] K. Sugden, I. Bennion, A. Molony, and N. J. Copner, "Chirped gratings produced in photosensitive optical fibers by fiber deformation during exposure," *Electron.Lett.*, 30(5), 440-442, 1994.

[17] K. C. Byron, K. Sugden, T. Bricheno, and I. Bennion, “Fabrication of chirped Bragg gratings in photosensitive fiber,” *Electron. Lett.*,29(18), 1659-1660, 1993.

[18] J. Albert, K. O. Hill, B. Malo, S. Theriault, F. Bilodeau, D. C. Johnson, L. E. Erickson, “Apodization of the spectral response of fiberbragg gratings using a phase mask with variable diffraction efficiency,” *Electron. Lett.*,31(3), 222-223, 1995.

[19] J. Albert, K. O. Hill, D. C. Johnson, F. Bilodeau, and M. J. Rooks, “Moire phase masks for automatic pure apodisation of fiber Bragg gratings,” *Electron. Lett.*,32(24), 2260-2261, 1996.

[20] R. Kashyap, P. F. Mckee, and D. Armes, “UV written reflection grating structures in photosensitive optical fibers using phase-shifted phase mask,” *Electron. Lett.*,30(23), 1977-1978, 1994.

[21] J. Canning and M. G. Sceats, “_ phase shifted periodic distributed structures in optical fibers by UV post-processing,” *Electron.Lett*.,30(16), 1344-1345, 1994.

[22] L. Zhang, K. Sugden, I. Bennion, and A. Molony, “Wide-stopband chirped fibermoire grating transmission filters,” *Electron. Lett*.,31(6), 477-479, 1995. 184

[23] S. Legoubin, E. Fertein, M. Douay, P. Bernage, P. Niay, F. Bayon, T. Georges, “Formation of moire grating in core of germanosilicatefiber by transverse holographic double exposure method,” *Electron. Lett*.,27(21), 1945-1946, 1991.

[24] B. J. Eggleton, P. A. Krug, L. Poladian, and F. Ouellette, “Long periodic superstructure Bragg gratings in optical fibers,” *Electron. Lett.*,30(19), 1620-1622, 1994.

[25] M. Durkin, M. Ibsen, M. J. Cole, R. I. Laming, “1m long continuously-written fibre Bragg gratings for combined second- and third-order dispersion compensation,” *Electron.Lett.*,33(22), 1891- 1893, 1997.

[26] S. J. Mihailov, T. J. Stocki, and D. C. Johnson, “Fabrication of tilted fibre-grating polarisation-dependant loss equaliser,” *Electron. Lett*.,37, 284 -286, 2001.

[27] K. Zhou, A. Simpson, X. Chen, L. Zhang, and I. Bennion, “Radiation mode out-coupling from blazed FBGs and its spatial-to-spectral encoding function investigated by side-tap detection,” *Bragg Gratings, Poling and Photosensitivity (BGPP-2003),* 2003.

[28] J. Peupelmann, E. Krause, A. Bandemer, and C. Schäffer, “Fibre-polarimeter based on grating taps,” *Electron.Lett*.,38, 1248-1250, 2002.

[29] S. L. Mihailov, R. B. Walker, T. J. Stocki, and D. C. Johnson, “Fabrication of tilted fibre-grating polarisation-dependent loss equaliser,” *Electron. Lett.*,37, 284-286, 2001.

[30] P. I. Reyes and P. S. Westbrook, “Tunable PDL of Twisted-Tilted Fiber Gratings,” *IEEE Photon. Technol. Lett*., 15, 828-830, 2003.

[31] K. Zhou, X. Chen, A. G. Simpson, L. Zhang, and I. Bennion, "High extinction ratio in-fiber polarizer based on a 45°-tilted fiber Bragg grating," in *Optical Fibre Communication Conference*, (Anaheim, California), paper OME22, 2005.

[32] K. Zhou, G. Simpson, X. Chen, L. Zhang, and I. Bennion, "High extinction ratio in-fiber polarizers based on 45°-tilted fiber Bragg gratings," *Opt. Lett.* 30, 1285-1287, 2005.

[33] Z. Yan, C. Mou, K. Zhou, X. Chen, and L. Zhang, "UV-inscription, polarization- dependant loss characteristics and applications of 45° tilted fiber gratings", *J. Lightwave Technol.*, Vol. 29(18), 2715-2724, 2011.

[34] X. Shu, L. Zhang, and I. Bennion, "Sensitivity characteristics near the dispersion turning points of long-period fiber gratings in B/Gecodopedfiber", *Opt. Lett.,* 26, 1755-1757, 2001.

[35] X. Shu, L. Zhang, and I. Bennion, "Sensitivity characteristics of Long-period fibre gratings", *J. Lightwave Technol*., 20, 255-266, 2002.

[36] D. J. Webb, M. W. Hathaway, D. A. Jackson, S. Jones, L. Zhang, and I. Bennion, "First in-vivo trials of a fiber Bragg grating based temperature profiling system," *J. Biomed. Opt*., 5, 45-50, 2000.

[37] Z. Zhang and J. S. Sirkis, "Temperature-compensated long period grating chemical sensor, " *Proc. Int. Conf. Optical Fiber Sensors (OFS'12)*, Williamsburg, VA, 294-297, 1997.

[38] H. J. Patrick, A. D. Kersey, and F. Bucholtz, "Analysis of the response of long period fiber gratings to external index of refraction," *J. Lightwave Tech*., 16, 1606-1611, 1998.

[39] X. Chen, K. Zhou, L. Zhang, and I. Bennion, "Simultaneous measurement of temperature and external refractive index by use of a hybrid grating in D-fibre with enhanced sensitivity by HF etching," *Appl. Opt*., 44, 178-182. 2005.

[40] X. Chen, K. Zhou, L. Zhang, and I. Bennion, "Optical chemsensor based on etched tiled Bragg grating structures in multimode fiber", *IEEE Photon. Technol. Lett*., 17, 864-866. 2005.

[41] X. Chen, K. Zhou, L. Zhang, and I. Bennion, "Optical chemsensors utilizing long-period fiber gratings UV-inscribed in D-fiber with enhanced sensitivity through cladding etching," *IEEE Photon. Technol. Lett*., 16, 1352-1354. 2004.

[42] X. Chen, K. Zhou, L. Zhang, and I. Bennion, "High sensitivity biosensors based on dual-peak LPGs sensitised by light cladding etching," *17th International Conference on Optical Fibre Sensors (OFS-2005)*, Proc. SPIE 5855, 383-386, Belgium, 2005.

[43] X. Chen, K. Zhou, M. Hughes, E. Davies, L. Zhang, A. Hine, K. Sugden, and I. Bennion, "DNA hybridisation biosensor based on dual-peak long-period grating", *AOE2007*, pp. 87-89, China, Oct.17-19, 2007.

[44] X. Chen, L. Zhang, K. Zhou, E. Davies, K. Sugden, I. Bennion, M. Hughes, and A. Hine, "Real-time detection of DNA interactions with long-period fiber-grating-based biosensor", *Opt. Lett.*, Vol. 32 (17), 2541-2543, 2007.

[45] A. Hine, X. Chen, M. D. Hughes, K. Zhou, E. Davies, K. Sugden, I. Bennion, and L. Zhang, "Optical fibre-based detection of DNA hybridization", *Biochem. Soc. Trans.*Vol.37, 445-449, 2009

[46] Meltz, W. W. Morey, and J. R. Dunphy, "Fiber Bragg grating chemical sensor," in *Chemical, biochemical, and Environmental Fiber Sensor III*, Proc. SPIE (Int. Soc. Opt. Eng.) 1587, 350-361, 1991.

[47] K. Schroeder, W. Ecke, R. Mueller, R. Willsch, and A. Andreev, "A fiber Bragg grating refractometer," *Meas. Sci, Technol.*, 12, 757-764, 2001.

[48] W. Liang, Y. Y. Huang, Y. Xu, R. K. Lee, and A. Yariv, "Highly sensitive fiber Bragg grating refractive index sensors," *Appl. Phys. Lett.*, 86, 151122, 2005.

[49] K. S. Chiang, Y. Liu, M. N. Ng, and X. Dong, "Analysis of etched long-period fibre grating and its response to external refractive index," *Electron.Lett.*,36, 966-967, 2000.

[50] S. Kim, Y. Jeong, S. Kim, J. Kwon, N. Park, and B. Lee, "Control of the characteristics of a long-period grating by cladding etching," *Appl. Opt.*, 39, 2038-2042, 2000.

[51] T. Volotinen, W. Griffoen, M. Ganonna, and H. G. Limberger, Eds., Reliability of optical fiber and components-final report of COST 246, London, U. K: Springer-Verlag, 1999.

[52] D. R. Lide, Ed., CRC Handbook of Chemistry and Physics, CRC Press, Boca Raton, 1999.

[53] H. R. Luckarift, J. C. Spain, R. R. Naik, and M. O. Stone, "Enzyme immobilization in a biomimetic silica support," *NatureBiotechnol.*, 22, 211-213, 2004.

[54] M. Beier and J. D. Hoheisel, "Versatile derivatisation of solid support media for covalent bonding on DNA-microchips," *Nucleic Acids Res.*, 27, 1970-1977, 1999.

[55] A. Ksendzov and Y. Lin, "Integrated optics ring-resonator sensors for protein detection," *Opt. Lett.*, 30, 3344-3346, 2005.

[56] A. N. Chryssis, S. M. Lee, S. B. Lee, S. S. Saini, and M. Dagenais, "High sensitivity evanescent field fiber Bragg grating sensor," *IEEE Photon. Technol. Lett.*, 17 (6), 1253-1255, 2005.

[57] A. N. Chryssis, S. S. Saini, S. M. Lee, H. Yi, W. E. Bentley, and M. Dagenais, "Detecting hybridization of DNA by highly sensitive evanescent field etched core fibre Bragg grating sensors," *IEEE Journal of Selected Topics in Quantum Electronics*, 11 (4), 864-872, 2005.

[58] M. P. DeLisa, Z. Zhang, M. Shiloach, S. Pilevar, C. C. Davis, J. S. Sirkis, and W. E. Bentley, "Evanescent wave long-period fiber Bragg grating as an immobilized antibody biosensor," *Anal. Chem.*, 72, 2895-2900 (2000).

[59] Hand, E. S. and Jencks, W. P. Mechanism of the reaction of imidoesters with amines. *J. Am. Chem. Soc.*, 84, 3505-3514 (1962).

[60] Mattson, G., Conklin, E., Desai, S., Nielander, G., Savage, D., and Morgensen, S. A practical approach to crosslinking.*Mol. Biol. Rep.*, 17, 167-183 (1993).

[61] K. Zhou, Y. Lai, X. Chen, K. Sugden, L. Zhang, and I. Bennion, "A refractometer based on a micro-slot in a fiber Bragg grating formed by chemically assisted femtosecond laser processing", *Opt. Express*, Vol. 15 (24), 15848-15853, 2007

[62] X. Chen, K. Zhou, A. Adebayo, and L. Zhang, "Chemical sensor using Mach-Zehnder interferometer based on a pair of largely tilted fibre gratings", *2012 Bragg Gratings, Photosensitivity and Poling in Glass Waveguides (BGPP-2012) Topical Meeting*, JTu5A.51, Colorado, USA, 17-21 June 2012

Chapter 9

Fibre-Optic Chemical Sensor Approaches Based on Nanoassembled Thin Films: A Challenge to Future Sensor Technology

Sergiy Korposh, Stephen James, Ralph Tatam and Seung-Woo Lee

Additional information is available at the end of the chapter

http://dx.doi.org/10.5772/53399

1. Introduction

Optical phenomena have been employed extensively by human civilization throughout the centuries for lighting, communication, calculations, observations, etc. and have played a crucial role in industrial development. The applications of the optics increased significantly after the first demonstration of the light guiding phenomenon based on total internal reflection in the 1840s, which was the precursor for the development of modern optical fibres. In modern life, optical fibres found their niche in telecommunications and, more recently, as sensors.

The sensing of chemical compounds is very important for monitoring outdoor and indoor environments (air and soil pollutions and sick building syndrome) [1], diseases (allergy and cancer) [2], and dangerous substances (drugs, hidden bombs, and landmines) [3]. Sensitive, reliable and cheap sensors for application in different areas of human activities are still sought.

Optical fibre-based measurement techniques have attracted a great deal of attention in a variety of analytical areas such as chemical and biological sensing, environmental monitoring and medical diagnosis. The variety of different designs and measurement schemes that may be employed using optical fibres provides the potential to create very sensitive and selective measurement techniques in real environments.

Different approaches exist for creation of fibre-optic sensors (FOS), which generally can be classified into two groups depending on the sensing mechanism: intrinsic and extrinsic fibre-optic sensors [4]. Interferometric sensors can be made that respond to an external stimulus by a change in the optical path length and thus a phase difference in the interferometer. Traditional interferometers such as Michelson, Mach Zehnder [5, 6, 7], Fizeau, Sagnac [8] and Fabry Perot [9, 10, 11] used for measuring of both chemical and physical parameters can be constructed utilizing optical fibres.

Fibre-optic sensors based on the evanescent wave absorption effect are an example of simple, cost effective yet very efficient type of intrinsic fibre-optic sensor [12]. As light travels along the core of the optical fibre, a small portion of energy penetrates the cladding in the form of an *evanescent wave*, the intensity of which decays exponentially with the distance from the interface between the cladding and the surrounding environment. Typically the penetration depth of evanescent wave into surrounding medium is in order of hundreds of nanometers.

This allows the direct analysis of the spectroscopy of an analyte in contact with the surface of the optical fibre. Alternatively an indirect measurement approach can be employed, whereby a chemically sensitive functional coating, which changes its optical properties when it comes into contact with the analyte, can be deposited onto the surface of the optical fibre. Analysis of the transmission spectrum can provide quantitative and qualitative information on the chemical species under examination. The use of chemically sensitive coatings means that the operating wavelength of the sensor is defined by the coating properties, rather than the absorption spectrum of the analyte, which can be advantageous. Fibre optic sensors based on the intrinsic evanescent wave offer the prospect for the development of cheap and compact devices, due to combination of low cost light emitting diodes (LED) and photodetectors. The sensitivity of the device is dependent on the length of the sensing area and for efficient operation coating materials with the strong absorption features should be selected. Generally, the simplest implementation of the fibre optic evanescent wave spectroscopy is application of the multimode optical fibre with the silica core and plastic cladding. The plastic cladding can easily be removed to allow the access to the evanescent wave and replaced with the functional coating providing sensor with its sensitivity and selectivity. In the case of the singlemode fibres with silica core and silica cladding polishing, etching or tapering is employed in order to get an access to the evanescent wave.

Intrinsic FOS allows to implement different measurements designs within an optical fibre based on the gratings (Bragg Gratings, FBG and long period gratings, LPG) written into the fibre core in which the changes in the reflected light due to changes in the grating period is measured to detect the effect caused by an external stimulus [13, 14]. Refractometers and chemical sensors based on optical fibre gratings, both FBGs and LPGs, have been extensively employed for refractive index measurements and monitoring associate chemical processes since they offer wavelength-encoded information, which overcomes the referencing issues associated with intensity based approaches.

Among the optical waveguide devices that have been investigated, tapered optical fibre sensors are able to measure environmental parameters (refractive index, chemical concentration, etc.) with high sensitivity owing to the large proportion of the energy of the propagating mode extending into the surrounding environment in the form of an evanescent field [15, 16, 17]. The tapered area of the optical fibre facilitates evanescent wave spectroscopy, in which the absorption spectrum of the surrounding medium is measured. Alternatively, the influence of the surrounding medium on the properties of the optical modes of the tapered waveguide can be explained as a change in the refractive index, i.e. it will operate as a refractometer.

Various deposition techniques, such as dip- and spin-coatings, layer-by-layer deposition (LbL) electrostatic self-assembly, Langmuir-Blodgett deposition, and chemical and physical vapour deposition have been employed for the functional coating of optical fibres. Among these techniques, the LbL technique, which is based on the alternate adsorption of polycations and polyanions onto the surface, has been used as a powerful surface modification method. This alternate adsorption technique is still expanding its potential because of its versatility and convenience for the fabrication of nano-assembled thin films employing various organic and inorganic materials.

In this chapter we will describe recent approaches to the development of fibre-optic chemical sensors utilising different measurement designs based on evanescent wave, tapered and long period gratings functionalized with nanoassembled thin films. Advantages and characteristic features of each measurement design will be discussed and examples of the sensitive and selective detection of various chemical analytes will be demonstrated. In addition, the potential of fibre-optic chemical sensors for future sensor technology will be discussed.

2. Fibre-optic chemical sensor designs

2.1. Evanescent wave fiber-optic sensor

To fabricate the evanescent wave fibre-optic sensor (EWFOS), a short section of the plastic cladding of a multimode optical fibre (HCS silica core/plastic cladding with 200 μm core diameter, Ocean Optics) was replaced with a functional coating of alternate poly(diallyldimethylammonium chloride) (PDDA, Mw: 200000–350000, 20 wt% in H_2O) and tetrakis-(4-sulfophenyl)porphine (TSPP, M_w=934.99) layers, Scheme 1. A schematic illustration of this method is shown in Figure 1a [18]. Before assembly, the previously stripped section of the optical fibre was cleaned with concentrated sulfuric acid (96%), rinsed several times with deionized water, and treated with 1 wt% ethanolic KOH (ethanol/water = 3:2, v/v) for about 10 min with sonication in order to functionalize the surface of the silica core with OH groups. The fibre core was then rinsed with deionized water, and dried by flushing with dry nitrogen gas. The film was prepared by the alternate deposition of PDDA (5 mg mL^{-1} in water) and TSPP (1 mM in water) (where one cycle is considered to be a combined PDDA/TSPP bilayer) by introducing a coating solution (150 μL) into the deposition cell with intermediate processes of water washing and drying by flushing with nitrogen gas being undertaken between the application of layers. In every case, the outermost surface of the alternate film was TSPP. The film is denoted by $(PDDA/TSPP)_x$, where x indicates the number of adsorption cycles.

The measurement principle of the device is based on the analyte-induced optical change in the transmission spectrum of the coated optical fibre.

The penetration depth (d_p) of the evanescent wave is described by [4]:

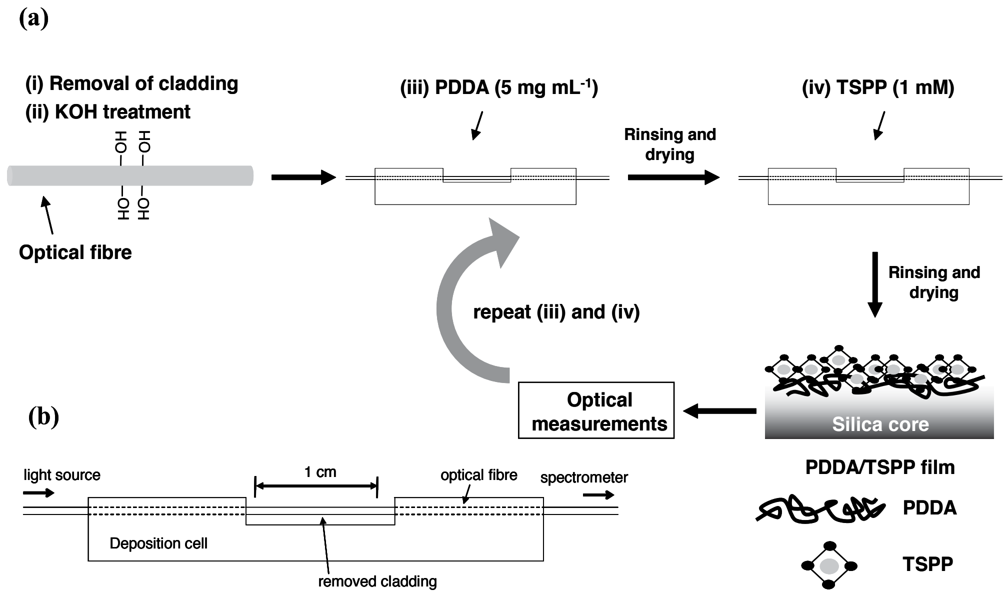

Figure 1. (a) Schematic illustration of the layer-by-layer adsorption of TSPP and PDDA on a multimode optical fibre and (b) deposition cell used for optical fibre coating [18].

$$d_p = \frac{\lambda}{2\pi(n_{eff}^2 - n_c{}^2)^{1/2}} \tag{1}$$

where λ is the wavelength of light in free space, n_c is the refractive index of the cladding and n_{eff} is the effective refractive index of the mode guided by the optical fibre.

Porphyrin compounds can be used as a sensitive element for optical sensors because their optical properties (absorbance and fluorescence features) depends on the environmental conditions in which molecule is present [20]. Porphyrins are tetrapyrrolic pigments that widely occur in nature and play an important role in many biological systems [21]. The optical spectrum of the solid state porphyrin is modified as compared to that of porphyrin in solution, due to the presence of strong π–π interactions [22]. Interactions with other chemical species can produce further optical spectral changes, thus creating the possibility that they can be applied to optical sensor systems. The high extinction coefficient (> 200,000 cm^{-1}/M) makes porphyrin especially attractive for the creation of optical sensors.

2.2. Tapered fiber-optic sensor

A tapered optical fibre may be fabricated by simultaneously heating and stretching a short section of a single mode optical fibre. This creates a region of fibre with reduced and uniform diameter (the waist) that is bounded by conical sections where the diameter of the fibre changes

http://dx.doi.org/10.5772/53399

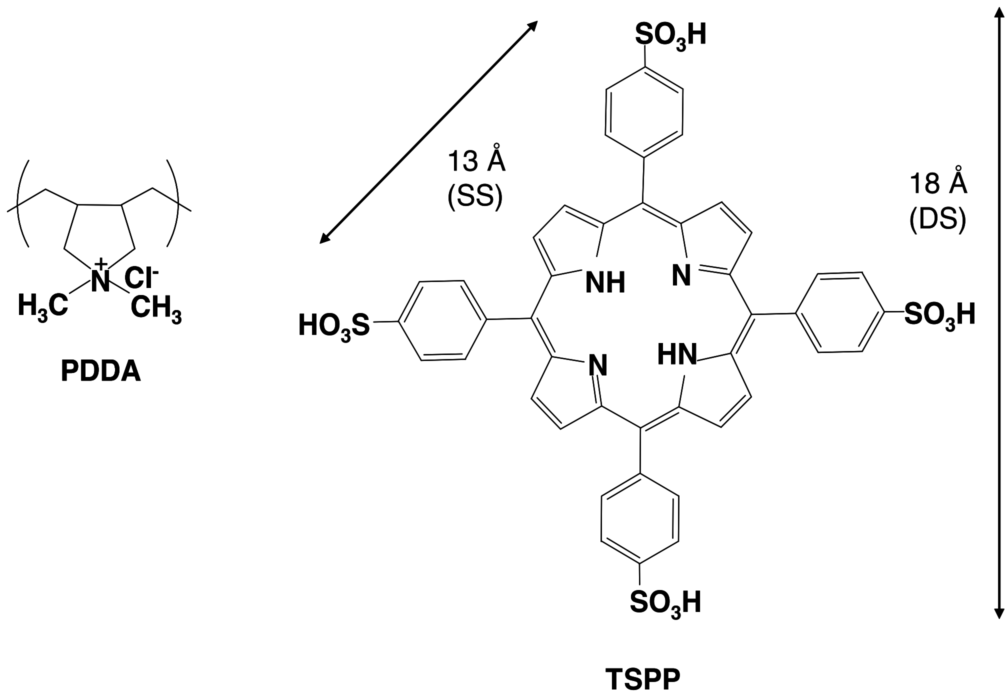

Scheme 1. Structural models of the polycation (PDDA) and porphyrin (TSPP) compounds used for sensor fabrication [19]: SS, side length of square; DS, diagonal length of square.

to merge the tapered section with the unperturbed surrounding single mode fibre. The optical properties of the tapered fibre waveguide are influenced by the profile of the conical tapering sections, by the diameter of the taper waist and by the optical thickness of the surrounding medium. The proportion of the power in the evanescent field, and thus the interaction with the surrounding medium, increases with decreasing diameter of the taper waist [23, 24]. In the tapering section, the guided mode of the single mode fibre is converted into a mode of the waist, Figure 2. In adiabatic tapers this is achieved without coupling to higher order modes. In non-adiabatic tapers the taper profile is such that a proportion of the light is coupled into higher order modes of the tapered section, which interfere to produce the channeled spectra reported for tapers of diameter of order 5 μm [23, 25].

The detailed description of the fibre tapering procedure can be found elsewhere [23]. Briefly, a single mode silica optical fibre was tapered using the heat and pull technique. Firstly, the polymer buffer coating was removed from a 50 mm long section in the middle of a ~1 m length of the single mode optical fibre using a mechanical stripper. The stripped section of the optical fibre was then fixed on a 3-axis flexure stage (NanoMax^{TM}, Thorlabs) and exposed to the flame produced by a gas burner (max temperature 1800ºC) for approximately 60 sec while the ends of the fibre were pulled in opposite directions using translation stages. Nonadiabatic optical fibre tapers of diameters 9, 10 and 12 μm, all having a taper waist of length 20 mm, were fabricated. The dimensions of the tapers were determined using a digital optical microscope, DZ3 Union Optical Co., Ltd., Japan.

The LbL method described above has been used to deposit a multilayer porphyrin film over the tapered region of a single mode optical fibre with the aim of demonstrating a gas sensor, Figure 2a. The effect of the polycation on the optical properties and structure of the multilayer porphyrin film was studied thoroughly. It is suggested that, by using poly(allylamine hydrochloride) (PAH, M_r: 56000) for the porphyrin film preparation instead of PDDA, the form of the aggregation of the TSPP is modified and provides improved optical properties that facilitate the detection of wider class of chemicals. Moreover the analyte-induced refractive index change of the prepared multilayer porphyrin film was monitored using tapered optical fibres.

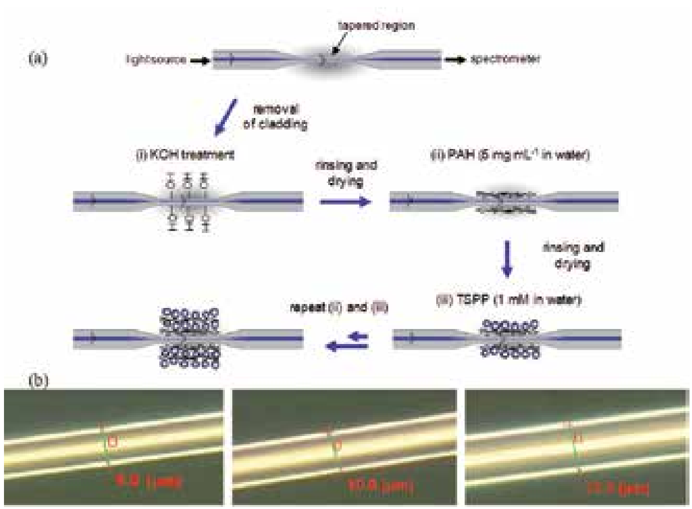

Figure 2. (a) Schematic illustration of the layer-by-layer adsorption of TSPP and PAH on a tapered optical fibre and (b) optical images of the tapered region of the optical fibres with different waist diameter.

2.3. Optical fibre long period gratings

LPGs promote coupling between the propagating core mode and co-propagating cladding modes, i.e. work as transmission gratings. The high attenuation of the cladding modes results in the transmission spectrum of the fibre containing a series of resonance bands centred at discrete wavelengths, each resonance band corresponding to coupling to a different cladding mode, as shown in Figure 3 [26].

The refractive index sensitivity of LPGs arises from the dependence of the phase matching condition upon the effective refractive index of the cladding modes, which is governed by Equation 2 [26]:

$$\lambda_{(x)} = (n_{core} - n_{clad(x)})\Lambda \tag{2}$$

where $\lambda_{(x)}$ represents the wavelength at which the coupling occurs to the linear polarized (LP_{0x}) mode, n_{core} is the effective RI of the mode propagating in the core, $n_{clad(x)}$ is the effective RI of the LP_{0x} cladding mode, and Λ is the period of the grating. The modes to which coupling occurs is dependent upon the period of the grating, and this has a significant influence on the form of the transmission spectrum, as is clear from Figure 3.

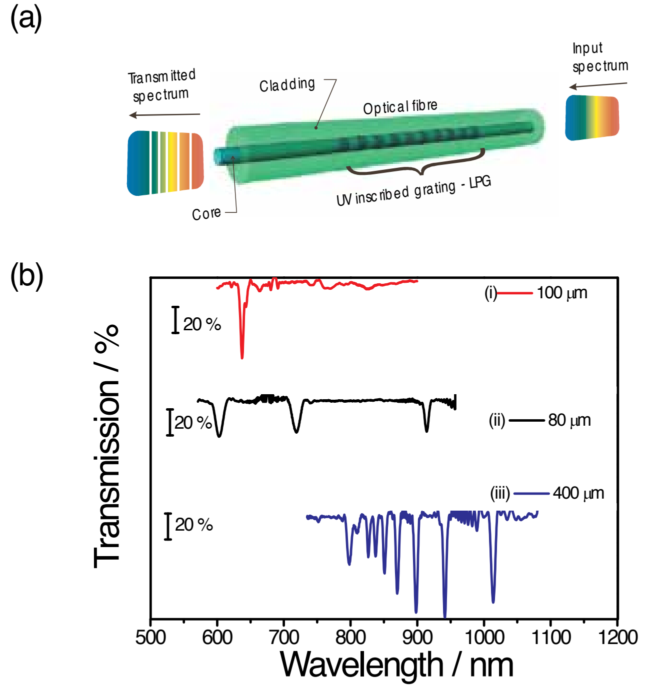

Figure 3. (a) Schematic illustration of the LPG structure and (b) transmission spectra of LPGs with different grating periods fabricated in an optical fibre of cut-off wavelength 670 nm (Fibrecore SM750): (i) 80 μm, (ii) 100 μm, and (iii) 400 μm [27].

The effective indices of the cladding modes are dependent upon the difference between the refractive index of the cladding and that of the medium surrounding the cladding. The highest sensitivity is shown for surrounding refractive indices close to that of the cladding of the optical fibre, provided that the cladding has the higher refractive index [28]. For surrounding refractive indices higher than that of the cladding, the centre wavelengths of the resonance bands show a considerably reduced sensitivity [29].

A detailed description and reference to the optical properties of LPGs can be found elsewhere [27, 30, 31]. In this work, an LPG of length 30 mm with a period of 100 μm was fabricated in a single mode optical fibre (Fibercore SM750) with a cut-off wavelength of 670 nm using point-by-point UV writing process. The photosensitivity of the fibre was enhanced by pressurizing it in hydrogen for a period of 2 weeks at 150 bar at room temperature.

The coated LPG was used for the detection of ammonia in the gas phase and in solution. For the detection of ammonia in solution, the LPG was coated with mesoporous PDDA/SiO_2 nanoparticles (NPs) (SNOWTEX 20L (40–50 nm), Nissan Chemical) film using the LbL process and infused with functional compound, TSPP, as illustrated in Figure 4a. As the LPG transmission spectrum is known to be sensitive to bending, for the film deposition process and ammonia detection experiments the optical fibre containing LPG was fixed within a special holder, as shown in Figure 4b, such that the section of the fibre containing the LPG was taut and straight throughout the experiments [30]. The detailed procedure of the deposition of the SiO_2 NPs onto the LPG and infusion of the TSPP compound has been reported previously [27]. Briefly, the section of the optical fibre containing LPG, with its surface treated such that it was terminated with OH groups, was alternately immersed into a 0.5 wt% solution containing a positively charged polymer, PDDA, and, after washing, into a 1 wt% solution containing the negatively charged SiO_2 NPs solution, each for 20 min. This process was repeated until the required coating thickness was achieved. When the required film thickness had been achieved (i.e. when the development of the second resonance band was observed with the fibre immersed into water), ca. after 10 deposition cycles, the coated fibre was immersed in a solution of TSPP as functional compound for 2 h, which was infused into the porous coating and provided the sensor with its specificity. Due to the electronegative sulfonic groups present in the TSPP compound, an electrostatic interaction occurs between TSPP and positively charged PDDA in the PDDA/SiO_2 film. After immersion into the TSPP solution, the fibre was rinsed in distilled water, in order to remove physically adsorbed compounds, and dried by flushing with N_2 gas. The compounds remaining in the porous silica structure were bound to the surface of the polymer layer that coated each nanosphere. This effectively increased the available surface area for the compounds to bond to. The presence of functional chemical compounds increased the RI of the porous coating and resulted in a significant change in the LPG's transmission spectrum, consistent with previous observations for increasing the coating thickness [32]. All experiments have been conducted at 25°C and 50% of rH.

For the ammonia detection in gas phase the LPG was designed to operate at the phase match turning point. In coated LPGs, for coupling to a particular cladding mode, the phase matching turning point occurs at a specific combination of grating-period and optical thickness of the coating. Near the phase matching turning point conditions, it is possible to couple to the cladding mode at two different wavelengths, with the corresponding resonance band wavelengths showing opposite sensitivity to perturbations to the properties of the coating [33]. LPGs show there highest sensitivity to environmental perturbations when operating in this regime [33]. The LPG was coated with an alternate thin film composed of poly(acrylic acid) (PAA, M_w:4000000) and PDDA, Figure 5. PAA is a promising candidate for the creation of ammonia sensors, of which free carboxylic acid groups lead to the high sensitivity and selectivity toward amine compounds [34]. Recently, we have reported a quartz crystal microbalance (QCM) gas sensor based on the alternate deposition of TiO_2 and PAA for the sensitive detection of amine

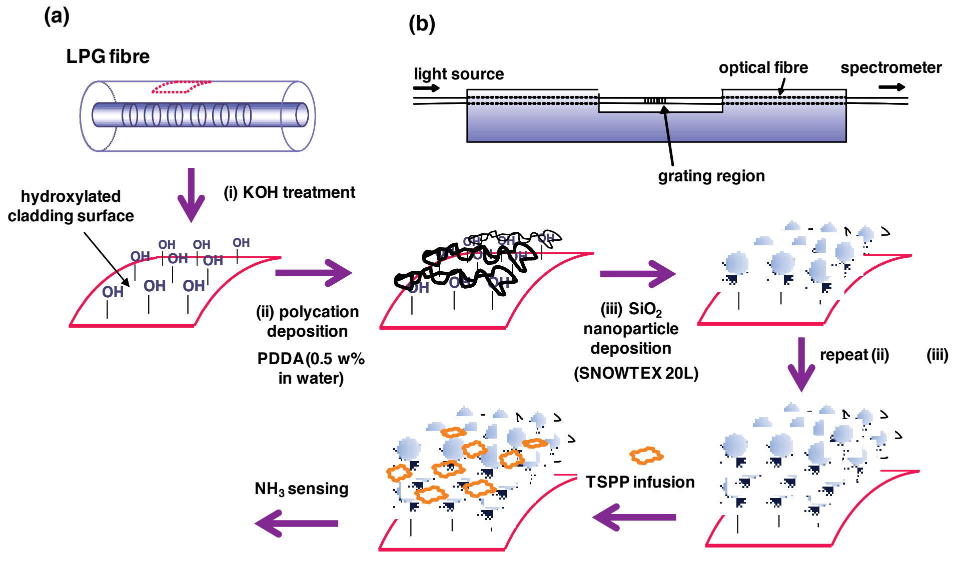

Figure 4. (a) Schematic illustration of the electrostatic self-assembly deposition process and (b) deposition cell with a fixed LPG fibre.

odors. However, QCM sensors still have a weakness that the sensor response can be easily affected by humidity [35]. The current approach would enable the LPG sensor performance based on the acid-base interaction of amine odors to the COOH moiety of PAA under humid conditions.

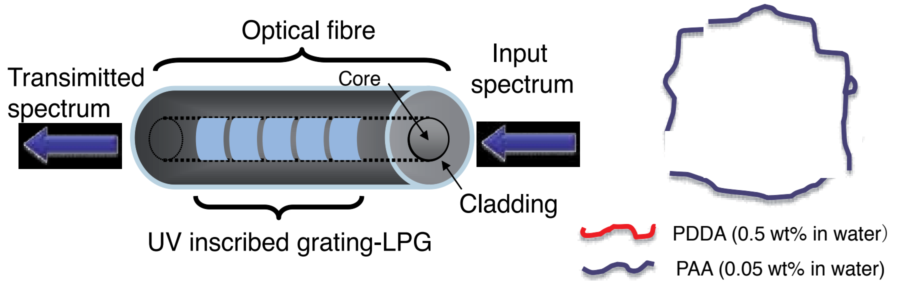

Figure 5. (a) Schemetic illustration of an LPG and its surface modification using PDDA and PAA [34].

3. Sensing approaches

3.1. Sensing based on evanescent wave fiber-optic sensors

Ammonia is one of the major metabolic compounds and the importance of its detection has been recently emphasized because of its correlation with specific diseases [36,37]. At normal physiological conditions ammonia can be expelled from the slightly alkaline blood and emanated through the skin or exhaled with the breath. Dysfunction in the kidneys or liver that converts ammonia to urea can result in an increase of the ammonia concentration in breath or urine. Consequently, the detection of the ammonia gas present in the breath or urine can be used for the early diagnostics of liver or stomach diseases [36].

Ammonia-induced changes in the transmission spectrum of the $(PDDA/TSPP)_5$ film are shown in Figure 6. As ammonia concentration increased from 0 to 20 ppm, a concomitant intensity change is observed at several wavelengths; at 706 nm the intensity increases, whereas at 350 and 470 nm it decreases. Upon exposure of the $(PDDA/TSPP)_5$ film to ammonia, the largest intensity change was observed at 706 nm. The interaction between ammonia and TSPP molecules leads to the deprotonation from the pyrolle ring and hence affects the interaction between TSPP molecules. Similarly, the largest change in absorbance is observed at 706 nm (Q band), which is attributed to the aggregation structure of TSPP [38]. The difference spectra were obtained by subtracting a spectrum measured in ammonia atmosphere from a spectrum measured in air.

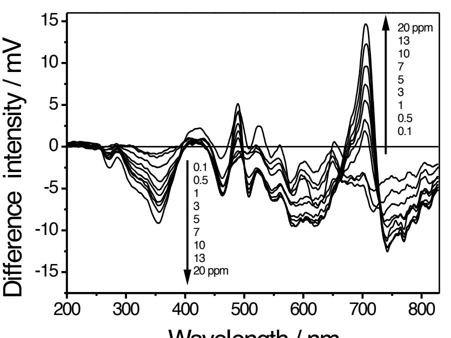

Figure 6. Optical transmission difference spectra of the optical fibre coated with a five-cycle PDDA/TSPP alternate film on exposure to ammonia concentrations ranging from 0–20 ppm.

The dynamic response of the $(PDDA/TSPP)_5$ coated fibre to exposure to ammonia was monitored at 350, 470 and 706 nm (Figure 7a). As can be seen from the result, the sensor response is fully reversible for low ammonia concentrations (up to 1 ppm). However, at higher concentrations the sensor takes a longer time to return to the base line. The base line may be recovered by flushing with air for sufficient time, as shown in Figure 7a. Alternatively, the

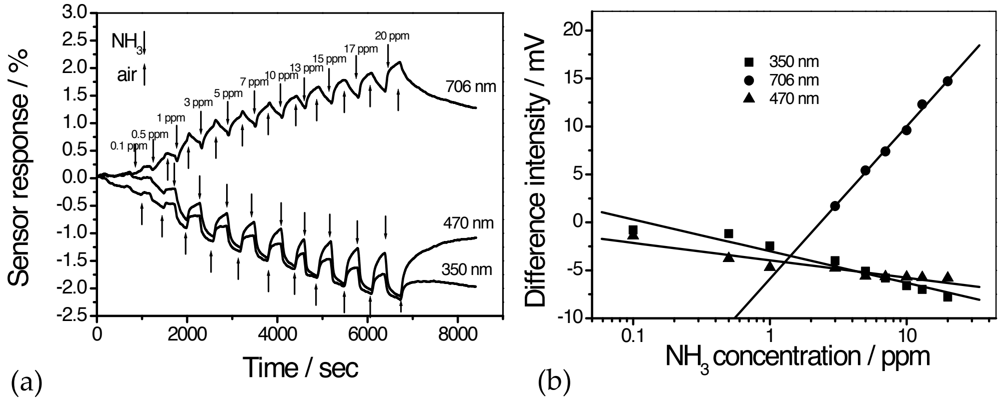

Figure 7. (a) Dynamic response of the optical fibre coated with a five-cycle PDDA/TSPP alternate film for ammonia concentrations ranging from 0–20 ppm at 350, 470, and 706 nm. (b) Calibration curves at 350 nm (squares), 470 nm (rhombuses), and 706 nm (circles). Lines show the linear fitting and are used only as guidance to an eye.

sensor response can be regenerated by rinsing for a few seconds in distilled water [39]. The calibration curve at each wavelength was plotted from the recorded spectra at given ammonia concentrations. The sensor shows linear responses at all wavelengths for a wide concentration range from 0.1 to 20 ppm and the highest sensitivity was observed at 706 nm (Figure 7b).

The response and recovery times (t_{90}) of the sensor to increasing ammonia concentration were within 1.6-2.5 min and 1.8-3.2 min, respectively (see Figure 7a). The sensitivity of the sensor depends on the wavelength and has different directions; for 350 and 470 nm, it is negative, and for 706 nm it is positive. The highest sensitivity was measured at 706 nm, corresponding to the optical change of the Q band of TSPP. The current sensor system has a limit of detection (*LOD*) of 0.9 ppm. The limit of detection was defined according to:

$$LOD = 3s / m \tag{3}$$

where $\sigma \approx 0.31$ is the standard deviation, and m is the slope ($\Delta I/\Delta c$) of the calibration curve, where c is the ammonia concentration and I is the measured intensity (mV) [40].

The results suggest that it will be possible to create a low-cost fibre optic sensor by selecting a LED and a photodiode with parameters that coincide with the wavelength at which the largest ammonia-induced changes were observed (706 nm).

The optical fibre acts as a platform that may be exploited to facilitate the detection of different chemicals by coating the fibre with appropriate functional materials. In order to demonstrate its capability, it was employed for the detection of the gaseous compounds excreted from the human body. Gaseous compounds excreted from the human body are believed to reflect certain metabolic conditions of the organism as well as the blood gaseous content [41]. A lot of information about human skin excretion is present in the literature. In gas chromatography

(GC) based experiments, variety of compounds were found to be emitted by human skin, such as acetone [42], ammonia [43], hydrocarbons [44] and aromatics [45], and the quantity of some of these compounds was correlated to blood content. Ammonia gas has been known to emanate through the skin from serum and its level depends on the humans health conditions [37]. Studies have demonstrated the possibility of identifying human subjects through the examinations of their volatile organic compound (VOC) odour patterns, formulating the idea of personal "smellprint" as an analogue of the fingerprint [46]. Applicability of electronic nose techniques was shown for the classification of bacteria related to human diseases [47,48], urinary tract infections [49] and further progress to metabolic disorders such as diabetes [50] or renal dysfunction [51]. The detection of renal failure in rats [52] and of lung cancer in people [53] was achieved using the breath sniffing method by arrays consisting of appropriately modified chemiresistors. Analysis of gases emitted from skin, however, is mainly being performed with the use of GC, which in spite of its high sensitivity and selectivity is expensive and time-consuming and requires a well- trained operator. Development of miniaturized sensing devices is expected to overcome the drawbacks of conventional approaches.

Here, a preliminary study of an optical fibre based skin gas sensor is discussed.The measurement setup for the skin gas analysis is shown in Figure 8. One end of the optical fibre was connected to a deuterium/halogen tungsten light source (DH-2000-BAL, Micropack) and other end was connected to an optical spectrometer (S1024DW, Ocean Optics) via fibre-optic connectors. The fabricated optical sensor was located inside a small acryl sensing cell (cylinder shape with radius r=3.5 cm, height h=1 cm, volume V=38.5 cm^3) containing a humidity and temperature recording logger (Hygrochron, KN Laboratories: RH range of 0–95%; accuracy ±5% at 25 ^{o}C in the range of 20–80% RH and reading resolution 0.1%).

For skin gas measurements, the top of the acryl cell was completely covered by palm surface. The optical measurement of palm skin emanations inside the chamber was done for 5-30min while the optical output spectrum and optical changes at selected wavelengths were recorded every second using an Ocean Optics software (OOIBase32).

To test the influence of the humidity, the acryl sensing chamber was additionally connected to a humidified air generating system through the additional inlet and outlet of the measuring cell, as shown in Figure 8. Dry compressed air was divided into two flows by the use of flow controllers (FC1 and FC2) and one of the flows passed through a bubbling bottle with deionized water to humidify the air. Recombination of the flows of dry and wet air was used to obtain the different levels of relative humidity.

Sensor response to changes in relative humidity was measured every second by recording the transmission spectrum of the optical fibre coated with a thin film. To explore the reproducibility of the measurements, the response of the fibre optic sensor was recorded twice at three different levels of humidity and flushed with dry air between each measurement.

The sensor response to palm skin gas was assessed by recording the changes of the optical properties of a $(PAH/TSPP)_{10}$ film deposited on the optical fibre. Optical spectral changes induced by the presence of the skin gases emitted from two different people (R and S) are shown in Figure 9a (spectral change) and Figure 9b (dynamic intensity change at selected

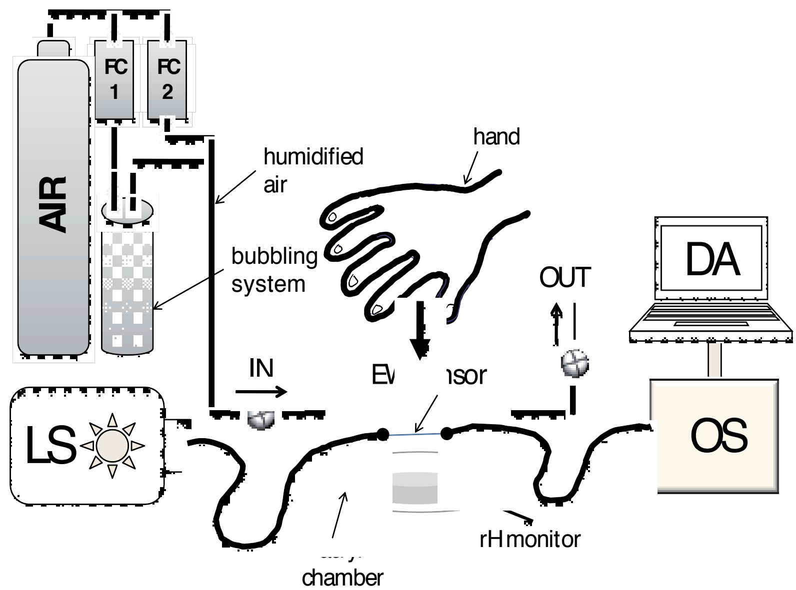

Figure 8. Experimental setup containing light source LS, optical spectrophotometer OS, data acquisition DA and humidified air generating system [54].

wavelengths). Measurements were conducted on the same day at similar conditions: the both participants were healthy, and hands were washed before the experiment with filtrated water. A slightly different response for two different people was observed. It should be noted that relative humidity level measured using a humidity logger, reached equilibrium at a maximum value of 95% within 1 min (data not shown). In general, relative humidity is an important factor that can influence sensor response. The sensor response to the skin gas emanations, however, is much slower as compared to the changes induced by relative humidity.

This difference in the senor response for two different participants suggests that some additional volatile compounds are exhaled by the human skin surface along increasing humidity. Interaction of compounds present in the skin gas with the PAH/TSPP film would contribute to the additional change observed in the output spectra.

From the complex sensor response observed over the wide spectral range, it is not a trivial task to discriminate the influences of humidity and skin gases. For the purpose of qualitative data description, the measured results were analyzed using principal component analysis (PCA, Statistical EXCEL add-in, V. 5.05 by Esumi Co. Ltd.) in order to reduce the multi-dimensionality of the obtained data. The 25 wavelengths at which the biggest intensity changes were observed were manually chosen from the difference spectra. Such selection was sufficient to obtain good separation between qualitatively different samples. The PCA results are shown in Figure 10, with a 96.5% cumulative proportion of PC1 and PC2. General observations are as follows: humidity points are grouped along the positive side of PC1 while most points representing responses to skin gas are located in the negative PC1 region. Additionally, PC2

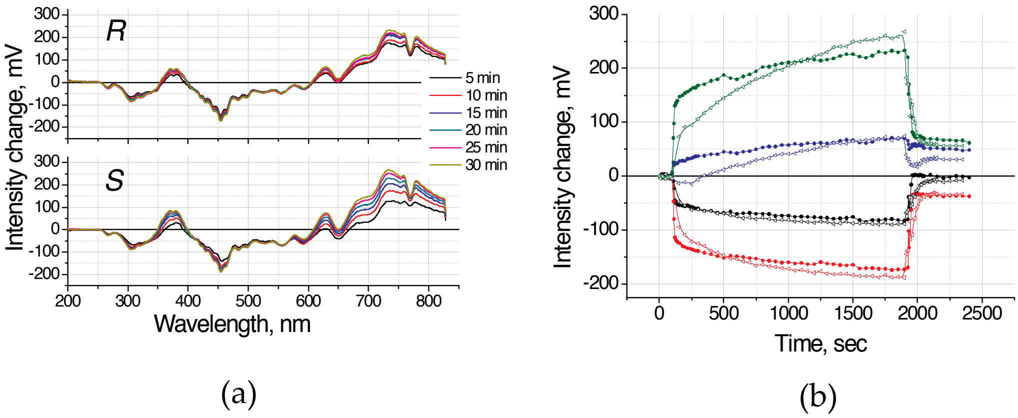

Figure 9. (a) Spectral changes induced by the skin gas emanations and (b) dynamic sensor response measured at selected wavelengths (black line 305 nm, red line 455 nm, blue line 629 nm, green line 733 nm) for different people (R-closed circles, S-open triangles).

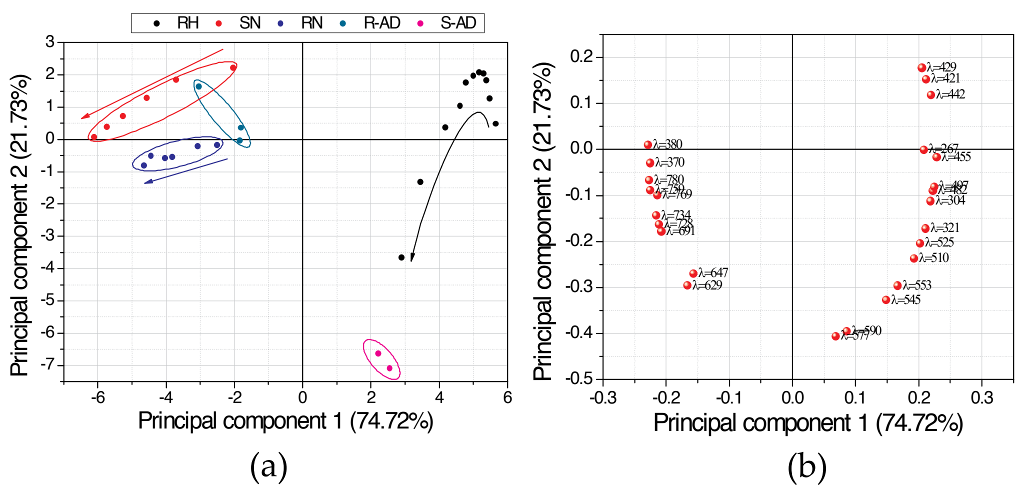

Figure 10. (a) Principal component analysis performed using the data measured at 25 wavelengths. Results measured at relative humidity change (black, with an arrow indicating increase of relative humidity values); Sensor response induced by skin gas emanations from participant R (blue, arrow indicating increase of sampling time of human skin gas emanation; i.e. attachment of the palm to the chamber containing the sensor, green point indicate the response one day after alcohol consumption); and from participant S (red, arrow indicating increase of sampling time of human skin gas emanation, magenta points show the response one day after alcohol consumption). (b) PCA loadings.

can possibly be used for the separation of participants who have different physiological conditions and different skin exhaling properties. The bigger distance between points in the S sample is probably related to the more intensive VOCs emanation. In addition, skin gasses were measured the day after alcohol consumption, and these points are added to the PCA plot.

http://dx.doi.org/10.5772/53399

Those measurements were repeated several times and skin gas sampling was done for 5 min. From the PCA plot, we can see that for the participant R, the points after consuming alcohol lie very close to those of the normal physiological conditions. For participant S, the points after consuming alcohol are located on the opposite side of the both principal component axes, which might be a result of a considerable change in the skin gas content after consuming alcohol. The obtained results further illustrate that the proposed sensor, combined with PCA data analysis, could recognize human samples and humidified air. However, based on the data gathered from only two persons, it is not possible to make a generalization on the behaviour of the sensor and on its ability to distinguish physiological conditions. We can speculate, however, that due to the normal physiological differences (for example in metabolic processes and related products excretion through the skin) between two people, the characteristics of the optical sensor response, such as response time and intensity change at different wavelengths, would be expected to be different. As shown in GC-MS and HPLC studies, variety of compounds can be found from human skin at normal conditions, such as ammonia [43], carbon monoxide [55], acetaldehyde [56], and acetone [42]. These compounds and many other emanations that are constituents of body odor are believed to contribute into the optical spectra of the EW sensor. Measurements using wider group of participants should be conducted, and the physiological condition of the various individuals tested should be considered to clarify the sensor response in more detail. Additionally, the response of the sensor to exposure to particular VOCs should be charcaterised to enable qualitative and quantitative analysis of skin gases.

3.2. Sensing based on tapered fibre optic sensors

A purpose-designed measurement chamber was used in order to characterise the tapered optical fibre sensor performance. The tapered section of the optical fibre, coated with the functional film, was inserted into the chamber. The desired gas concentrations were produced using a two-arm flow system described elsewhere [18]. The dry compressed air that was used as the carrier gas and ammonia gas of 100 ppm concentration were passed separately through two flowmeters. The two flows were combined to produce the desired ammonia concentration in the measurement chamber. The concentration could be controlled by adjusting the flow rates of the ammonia and of the air.

The transmission spectrum was recorded with a 1 Hz update rate as the device was exposed to a given ammonia concentration and subsequently flushed with dry air. The difference spectrum was plotted by subtracting a spectrum measured at a given ammonia concentration from the spectrum recorded in the presence of dry air. The baseline spectrum and sensor response of each experiment were recorded by passing dry air through the measurement chamber until the signal measured at a wavelength of 700 nm reached equilibrium.

The results are shown in Figure 11a–11d. As the ammonia concentration increased from 10 ppm up to 100 ppm, the intensity measured at 700 nm increased for the 10 μm and 12 μm diameter optical fibre tapers (Figure 11b). Interaction of the ammonia molecule with TSPP leads to the deprotonation of the pyrolle ring of TSPP and hence influences the electrostatic interaction between the TSPP moieties in the PAH/TSPP film [18, 39]. Consequently, the biggest change in absorbance is observed at 700 nm (Q band), which may be closely related to the aggregation state of the TSPP molecules [20].

Interestingly, when measurements were conducted using the tapered fibres with 10 and 12 μm waist diameters, the channeled spectra did not exhibit a wavelength shift in response to exposure to ammonia, suggesting that ammonia–induced RI change cannot be measured with tapers of these diameters, possibly because the modes are tightly bound and the influence of the modes' evanescent field interaction with the coatings do not induce significant differential changes in the propagation constants (Figure 11b). When the 9 μm diameter tapered fibre coated with the $(PAH/TSPP)_5$ film was exposed to ammonia, a red–shift of the spectral features at 1000 and 1040 nm was observed that saturates with the increase of the concentration (Figure 11c). We can assume that the wavelength red–shift of the spectral features is caused by the ammonia–induced change in the RI of the PAH/TSPP film. It should be noted that this change is not continuous and saturation occurs between 0 and 50 ppm (Figure 11c). The 9 μm diameter tapered fibre possesses higher sensitivity to RI change as compared to 10 and 12 μm diameter tapered fibres. The absence of the intensity change at 700 nm can be explained by considering the transmission spectrum of the 9 μm diameter tapered fibre obtained after deposition of the 5th bilayer of the PAH/TSPP film (data not shown); the optical power at 700 nm transmitted to the spectrometer is very low, complicating the measurement of the small ammonia–induced intensity change. We can conclude from these results that the wavelength shift near 1000 μm observed in the transmission spectrum of the 9 μm diameter tapered fibre is sensitive to ammonia-induced RI changes of the coating and the change in transmitted power near 700 nm of the 10 and 12 μm tapered fibres can be used to monitor ammonia gas concentration.

Dynamic ammonia–induced changes of the tapered fibres with 10 and 12 μm waist diameters coated with the $(PAH/TSPP)_5$ film were monitored at 700 nm, as shown in Figure 11d. The measurement principle for these waist diameters is based on evanescent wave spectroscopy. The response time and recovery time (t_{90}) of the sensor to increasing ammonia concentration were within 100 sec and 240 sec, respectively. The sensitivity of the device derived from the slope of the calibration curve is 0.440±0.002 mV/ppm and estimated limit of detection (*LOD*) calculated using the 3σ method is 2±0.3 ppm (inset of Fig. 11d). It should be noted that sensitivity of the proposed sensor is ca. 3 times higher as compared to the PDDA/TSPP film assembled onto the quartz substrate (Korposh 2006). This is most plausibly a result of the higher localized energy at the tapered region of the optical fibre and thus increased efficiency of the interaction between the probe light and the functional film. On the other hand, the sensitivity of the fabricated device was ca. 6 times lower than that of a multimode optical fibre coated with the PDDA/TSPP film [18]. This can be attributed to the presence of TSPP in *J*-aggregated form in higher concentration in the PDDA/TSPP film as compared to the PAH/TSPP film used in this study. However, the presence of TSPP in different forms inside the PAH film may allow the coating to exhibit sensitivity to different chemical compounds, thus increasing the application range of the proposed sensor. This hypothesis will be thoroughly explored in the future work. In addition, the tapered fibre may operate as both an evanescent wave spectroscope and as a refractometer. Thus, in contrast to solely evanescent wave spectroscopy, materials without absorbance features in the UV-vis range may be employed as

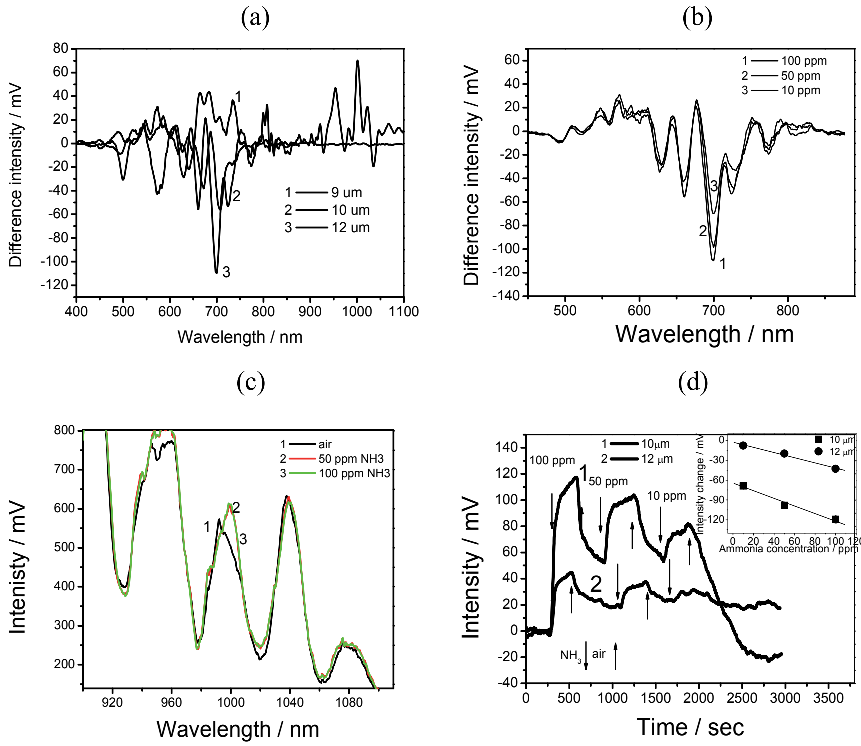

Figure 11. (a) Transmission difference spectra obtained by subtracting a spectrum measured in the 100 ppm ammonia atmosphere from the spectrum measured in air with the tapered fibres of 9, 10, and 12 μm diameter modified with a $(PAH/TSPP)_5$ film, (b) transmission difference spectra of the 10 μm tapered fibre measured at given ammonia concentrations from 10 to 100 ppm, (c) transmission spectra of the 9 μm tapered fibre measured before and after 50 and 100 ppm ammonia exposures, and (d) dynamic responses of the 10 and 12 μm diameter tapered fibres to the varying ammonia concentration (from 100 ppm to 10 ppm) recorded at 706 nm, where arrows indicate the admission time of ammonia and air into the measurement chamber. The inset of Figure 11(d) shows a calibration curve plotted from the difference spectra data taken at 706 nm: squares and circles show the data of the 10 and 12 μm diameter tapered fibres, respectively.

sensitive layers, extending the utility of the chemical fibre optic sensors and the class of the detectable analytes.

The fabricated device was exposed to varying relative humidity to study its effect on the sensor response. When rH was reduced from 70 % to 10% and increased back to 70%, no significant change in the transmission spectra was observed (Figures 12a and 12b) revealing selectivity of the sensor to ammonia over rH. The immunity of the sensor to rH change is very important for real-world practical applications where humidity is one of the major interfering parameters. For example, ammonia detection in breath is highly important non-invasive diagnostic tool in medicine [37], but highly challenging due to the high humidity present in breath. To-date, to the best of our knowledge, there is no sensor with satisfactory sensitivity and selectivity for

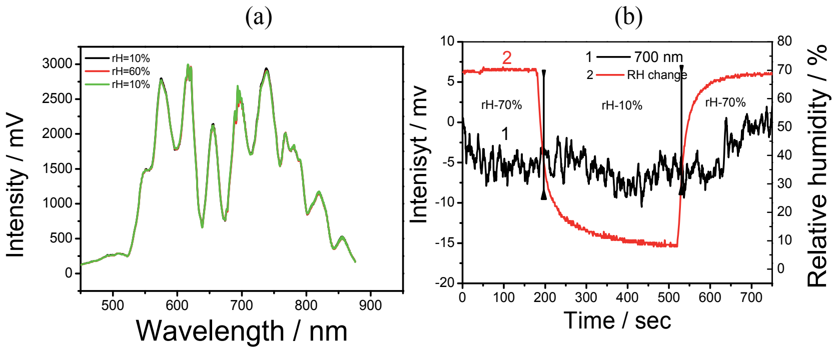

Figure 12. (a) Transmission spectra of the 10 μm diameter tapered fibre modified with a 5-cycle PAH/TSPP film measured before and after change of the relative humidity and (b) dynamic responses of the 10 μm diameter tapered fibre to the varying RH from 70 to 10 % and backwards recorded at 706 nm, where lines indicate the admission time of dry air into the measurement chamber; line 1, sensor response; and line 2, RH change measured using humidity logger.

the detection of ammonia in breath. In our future study of the use of this sensor for ammonia breath measurement, the cross-sensitivity to other gases will be investigated.

3.3. Sensing based on LPG fibre optic sensors

The sensitivity to ammonia in water of an LPG coated with a $(PDDA/SiO_2)_{10}$ film that was infused with TSPP was characterized by sequential immersion of the coated LPG into ammonia solutions with different concentrations (0.1, 1, 5 and 10 ppm). The lower ammonia concentrations were prepared by dilution of the stock solution of 28 wt%. In order to assess the stability of the base line, the coated LPG was immersed several times into 150 μL of pure water. The decrease of attenuation of the second resonance band, LP_{021}, at 800 nm, indicates the partial removal of the adsorbed TSPP molecules. The equilibrium state was achieved after several exposures into water. For the ammonia detection, the LPG fibre was exposed into a 150 μL ammonia solution of 0.1 ppm, followed by drying and immersion into ammonia solutions of 1, 5 and 10 ppm.

The response of the transmission spectrum to varying concentration of ammonia is shown in Figure 13a. The dynamic response of the sensor was assessed by monitoring the transmission at the centre of the LP_{021} resonance band at 800 nm. The response is shown in Figure 13b, where "air" region and "H_2O" and "NH_3" regions correspond to the transmission recorded at 800 nm after drying the LPG and immersing the device into water and ammonium solutions, respectively. After repeating the process of immersion in water and drying 4 times, the recorded spectrum was stable, demonstrating the robustness and stability of the employed molecules in aqueous environments (H_2O regions indicated in Figure 13). On immersion in 1 ppm and 5 ppm ammonia solutions, the transmission measured at 800 nm increases. The transmission when the coated LPG was immersed in a 10 ppm ammonia solution exhibits a further increase, reaching a steady state within 100 s, as shown in Figure 13b. The resonance feature corresponding to coupling to the LP_{020} cladding mode exhibits additional small red shifts of 0.5 and

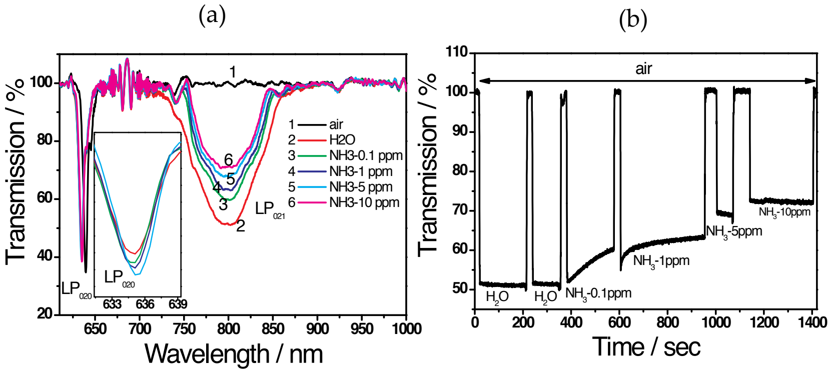

Figure 13. (a) Transmission spectra of the LPG coated with a TSPP infused $(PDDA/SiO_2)_{10}$ film due to immersion into water and into ammonia solutions of different concentrations: "H_2O", LPG exposed into water; "air", LPG in air after drying with N_2 gas; "NH_3 x ppm", LPG exposed into a x ppm ammonia solution, where x = 0.1, 1, 5 and 10. (b) Dynamic response to water and ammonia solutions (0.1, 1, 5 and 10 ppm) recorded at 800 nm; LP_{020} and LP_{021} are labelling the linear polarized 020 and 021 modes, respectively.

1.5 nm when subsequently immersed in solutions of 1 ppm and 10 ppm ammonia concentration, respectively, along with decreases in amplitude, as shown in Figure 13a. The limit of detection (LOD) for the 100 μm period LPG coated with a $(PDDA/SiO_2)_{10}$ film that was infused with TSPP was 0.14 ppm and 2.5 ppm when transmission and wavelength shift were measured respectively. The LOD was derived from the calibration curve and the using equation 3 [40].

Response of the sensor to ammonia gas was measured with ammonia vapor of different concentrations generated from aqueous ammonia solutions in proximity to the modified LPG sensor. Ammonia gas was generated by placing 100 μl of aqueous ammonia solution with different concentrations into the measurement chamber. Concentrations of ammonia in the gas phase were measured using ammonia detection gas tubes (GasTec, Japan) and compared with the values of the corresponding solutions. The sensor response was recorded with a resolution of 1 Hz.

The transmission spectrum was recorded with each analyte solution present in the chamber before and after its removal. To regenerate the sensor response the optical fibre was washed with water and flashed using nitrogen gas.

A linear increase in the separation of the 1st and 2nd bands in the TS was observed at the exposure of the LPG coated with the PDDA/PAA to the increasing ammonia gas concentration, Figures 15a and 15b. The sensitivity of the sensor was estimated to be 0.35 and 0.31 nm/ppm for the 1st and 2nd resonance bands, respectively (Figure 15b). The limit of detection (LOD) for both resonance bands was estimated to be 1.6 and 2.3 ppm ($3\sigma = 0.47$ nm), respectively. The sensor response was fast and almost saturated within 5 min. Along with the wavelength shift, both the extinction of both of the resonance bands also decreased in proportion to the increase of the ammonia gas concentration. Moreover, the sensor response could be easily regenerated by washing the LPG sensor with water (data not shown).

To confirm the selectivity of the sensor, different analyte gases of amine and non-amine compounds were tested (see Figure 15c). The sensor demonstrated higher sensitivity towards amine compounds. It appears that the superior binding of the sensor to amine compounds is assigned to the acid-base reaction between the functional moieties of PAA and the amine compounds. Other parameters of the analytes such as molecular size, solubility to the film, and equilibrium constant (pK_a or pK_b) can be significant factors to determine the selectivity and additional examination is in progress.

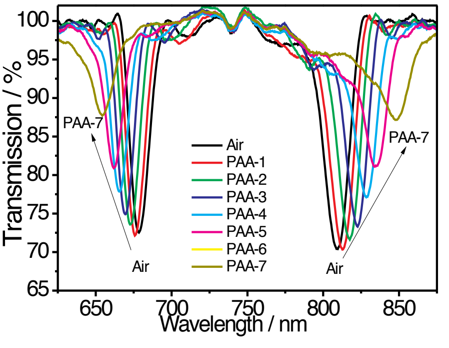

Figure 14. TS changes of the LPG fibre after deposition of PAA.

In order to demonstrate the capabilities and versatility of the coated optical fibre LPG in chemical sensing, a PAH/SiO_2 film was deposited onto the surface for the detection of the organic compounds, namely aromatic carboxylic acids (ACAs, see Scheme 2). The LbL procedure described above was employed for coating the LPG.

After deposition of the PAH/SiO_2 film onto the LPG it was exposed to aqueous solutions of ACAs in the range of 0.001–1000 μM of individual ACAs or their mixtures. All experiments were conducted using the same sensor transducer. After exposure and measurement, the substrate was washed in 0.1 wt% of aqueous ammonia in order to remove adsorbed analytes from the PAH/SiO_2 film.

For the detection of the chemical binding the LPG coated with the $(PAH/SiO_2)_{10}$ film was exposed to different ACAs of concentration 10 μM in water, which lead to a significant change in the TS, Figure 17a. The magnitude of the TS change at 825 nm differed according to the number of carboxylic acid groups in the molecule, the molecular weights and the pKa values of the ACAs. The largest change was observed when the coated LPG was exposed to mellitic acid (MA), as shown in Figures 16a and 16b. As MA has the biggest molecular weight and the highest number of the functional group, suggesting the efficient binding to the amino functional groups of PAH. The response of phthalic acid (PA) is higher than that of BA. These

http://dx.doi.org/10.5772/53399

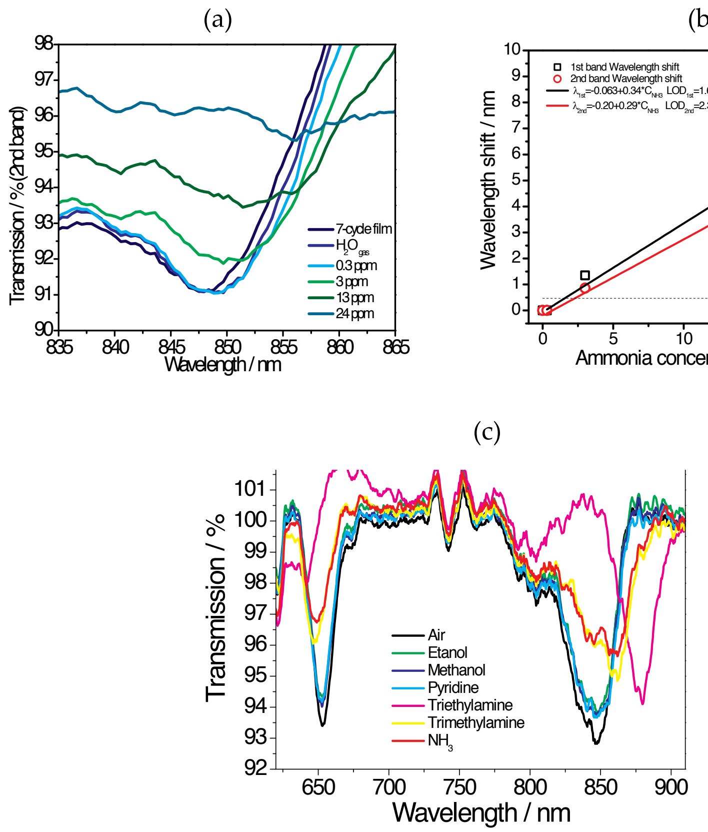

Figure 15. (a) TS changes of the 2nd resonance band of the LPG fibre with a 7-cycle PDDA/PAA film at the exposure to different concentrations of ammonia gas. (b) Ammonia concentration dependence of the 7-cycle PDDA/PAA film coated LPG fibre on wavelength shifts at 654 and 848 nm. (c) TS changes of the LPG fibre modified with a 7-cycle PDDA/PAA film at the exposure to 100 ppm ammonia gas (estimated from the calibration curve of Figure 15b) and to saturated amine and non-amine gases.

results suggest that the sensitivity of the sensor depends additionally on the number of the functional group and increases in the order of MA >> PA > BA (Figures 16a and 16b). It should be noted that, when MA binds to the PAH, the sensor response cannot be regenerated simply by water washing (see “H_2O” after MA exposure in Figure 17b). The sensor response can be perfectly recovered, however, using 0.1 wt% NH_3 aqueous solution for 10 min (see areas marked with “*” in Figures 16b and 16c).

The adsorption of the ACAs in the PAH/SiO_2 film can be described using a Langmuir adsorption curve. The calculated binding constant of BA to the PAH/SiO_2 film is estimated to be 1.36 ± 0.01×10^6 M^{-1}. The lowest measurable concentration was 1 nM when MA was used, with a binding constant of 5.6 ± 0.01×10^8 M^{-1}

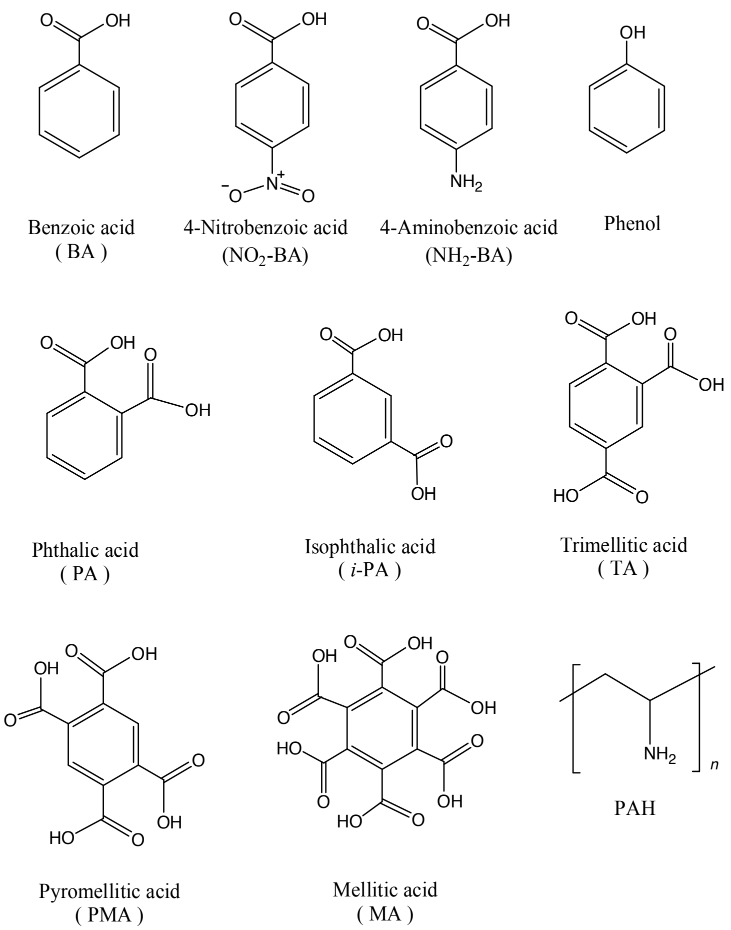

Scheme 2. Structures of ACAs used for binding test and cationic polymer (PAH) used for film assembly.

4. Summary

In summary, in this chapter fibre-optic sensors based on different measurement principles were coated with the nano-assembled thin films for the detection of various chemical compounds. When of the different fibre optic sensor designs were characterised for their response to ammonia gas, the highest sensitivity was observed when EWFOS was coated with the porphyrin based film, showing an LOD of 0.9 ppm. The coated LPG had an LOD of 1.6 ppm and the tapered fibre has an LOD of 2 ppm. The high sensitivity of the EWFOS makes it a promising device for medical applications where there is a requirement of measure low concentrations of specific chemical compounds. The possibility of employing EWFOS for medical diagnosis was explored in the example of skin emanation measurements. In solution, the LOD of LPG sensor was as low as 0.14 ppm for ammonia and the lowest measurable concentration for mellitic acid was 1 nM. From a practical point of view, the EWFOS are limited

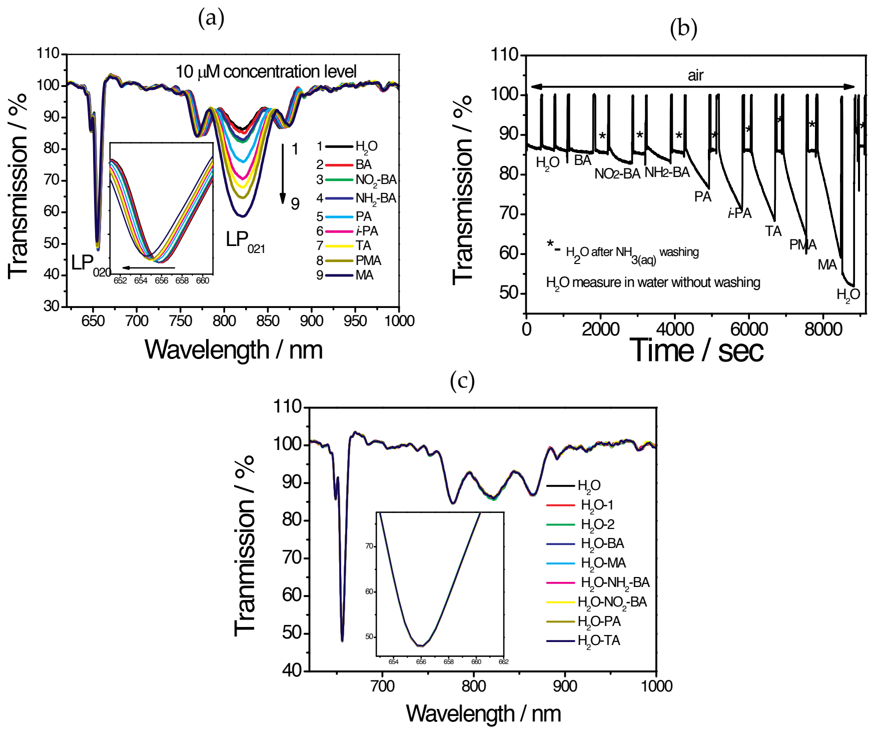

Figure 16. (a) Evolution of the transmission spectra due to the exposure of the optical fibre LPG coated with a $(PAH/SiO_2)_{10}$ film to 10 μM of different ACAs and (b) time-dependence of the transmission measured at 825 nm; "air" arrow indicates signal measured in air, corresponding to spectra 1 in Figure 16a. (c) Transmission spectra measured in water after exposure to ACAs and washing step using NH_3 (aq); inset shows magnified LP_{020} resonance band.

to the materials with the strong absorption features, while tapered and LPGs fibres can be modified with the wider class of materials, including transparent materials. In addition, tapered and LPGs fibres offer wavelength-encoded information, which overcomes the referencing issues associated with intensity based approaches. Moreover, LPGs owing to the multiplexing capabilities enable sensor design for multi-analyte detection using a single optical fibre. Our future work will focus on the creation of multi-analyte detection systems in which the number of individual gratings with the characteristic grating period inscribed in the single optical fibre will be chemically modified for sensitive detection of targeted analytes.

Acknowledgements

This work was supported by the Regional Innovation Cluster Program of the Ministry of Education, Culture, Sports, Science and Technology (MEXT), Japan. The authors from

Cranfield are grateful to the Engineering and Physical Sciences Research Council, EPSRC, UK for funding under grants EP/D506654/1 and GR/T09149/01.

Author details

Sergiy Korposh[1], Stephen James[2], Ralph Tatam[2] and Seung-Woo Lee[1*]

*Address all correspondence to: leesw@kitakyu-u.ac.jp

1 Graduate School of Environmental Engineering, the University of Kitakyushu, Kitakyushu, Japan

2 School of Engineering, Cranfield University, Cranfield, UK

References

[1] Seifert, B, Englert, N, Sagunski, H, & Witten, J. Guidline values for indoor air pollutants. Proc. 8th Int. Con. on Indoor Air Quality and Climate (1999). Indoor Air, Edinburgh, Scotland, 1999) 499.

[2] Natale, C D, Macagnano, A, Martinelli, E, Paolesse, R, Arcangelo, D, Roscioni, G, Finazzi-agrò, C, & Amico, A, D. A. Lung cancer identification by the analysis of breath by means of an array of non-selective gas sensors. Biosens. Bioelectron. (2003). , 18-1209.

[3] Takahara, N, Yang, D-H, Ju, M-J, Hayashi, K, Toko, K, Lee, S-W, & Kunitake, T. Anchoring of cyclodextrin units on TiO2 thin layer for effective detection of nitroaromatics: A novel electrochemical approach for landmine detection. Chem. Lett. (2006). , 35-1340.

[4] Grattan, K. T. V, & Meggitt, B. T. (1999). Chemical and environmental sensing, Dordrecht, Boston : Kluwer

[5] Bucholtz, F, Dagenais, D M, & Koo, K P. High frequency fibre-optic magnetometer with 70 fT per square root hertz resolution. Electronics Letters (1989). , 25(25), 1719-1721.

[6] Dandridge, A. Fibre optic sensors based on the Mach-Zehnder and Michelson interferometers, In: Fiber Optic Sensors: An Introduction for Engineers and Scientists, edited by E. Udd. New York: Wiley (1991).

[7] Yuan, L, & Yang, J. Two-loop based low-coherence multiplexing fibre optic sensors network with Michelson optical path demodulator, Proceedings of 17th International Conference on Optical Fibre Sensors (2005). , 595-598.

[8] Russell, S J, & Dakin, J P. Location of time-varying strain disturbances over a 40 km fibre section, using a dual-Sagnac interferometer with a single source and detector. Proceedings of 13th International Conference on Optical Fibre Sensors (1999). , 580-584.

[9] Rao, Y J, Cooper, M R, Jackson, D A, Pannell, C N, & Reekie, L. High resolution static strain measurement using an in-fibre-Bragg-grating-based Fabry Perot sensor. Proceedings of 14th International Conference on Optical Fibre Sensors (2000). , 284-287.

[10] Cibu, a E, & Donlagic, D. All-fibre Fabry-Perot strain sensor. Proceedings of 2nd European Workshop on OFS (2004). , 180-183.

[11] Lin, C-J, Tseng, Y-T, Lin, S-C, Yang, C-S, & Tseng, F-G. A novel in-vitro and in-situ immunoassay biosensor based on fibre-optic Fabry-Perot interferometry. Proceedings of 2nd European Workshop on Optical Fibre Sensors (2004). , 304-307.

[12] Leung, A, Rijal, K, Shankar, P M, & Mutharasan, R. Effects of geometry on transmission and sensing potential of tapered fibre sensors. Biosensors and Bioelectronics (2006). , 21(12), 2202-2209.

[13] Vohra, S T, Todd, M D, Johnson, G A, Chang, C C, & Danver, B. A. Fibre Bragg grating sensor system for civil structure monitoring: applications and field tests, Proceedings of 13th International Conference on Optical Fibre Sensors (1999). , 32-37.

[14] Schroeder, R J, Yamate, T, & Udd, E. High pressure and temperature sensing for the oil industry using fiber Bragg gratings written onto side hole single mode fiber. Proceedings of 13th International Conference on Optical Fibre Sensors (1999). , 42-45.

[15] Corres, J, Arregui, F, & Matías, I. Sensitivity optimization of tapered optical fiber humidity sensors by means of tuning the thickness of nanostructured sensitive coatings. Sens. and Act. B. (2007). , 122-442.

[16] Leung, A, Shankar, P, & Mutharasan, R. Real-time monitoring of bovine serum albumin at femtogram/mL levels on antibody-immobilized tapered fibers. Sen. and Act.B. (2007). , 123-888.

[17] James, S, & Tatam, R. Fibre optic sensors with nano-structured coatings. J. Opt. A: Pure Appl. Opt. (2006). S430.

[18] Korposh, S, Kodaira, S, Lee, S-W, Batty, W J, & James, S W. Nano-assembled thin film gas sensor. II. An intrinsic high sensitive fibre optic sensor for ammonia detection. Sensor and Materials (2009). , 21(4), 179-189.

[19] Ariga, K, Lvov, Y, & Kunitake, T. Assembling alternate dye-polyion molecular films by electrostatic layer-by-layer adsorption. Journal of American Chemical Society, (1997). , 119(9), 2224-2231.

[20] Takagi, S, Eguchi, M, Tryk, D A, & Inoue, H. Porphyrin photochemistry in inorganic/organic hybrid materials: Clays, layered semiconductors, nanotubes, and mesoporous materials. J. Photochem. Photob. C: Photochem. Rev. (2006).

[21] Kadish, K M, Smith, K M, & Guilard, . . The Porphyrin Handbook, Academic Press, ISBN 0123932009, San-Diego 2007.

[22] Schick, G A, Schreiman, I C, Wagner, R W, Lindsey, J S, & Bocian, D F. Spectroscopic characterization of porphyrin monolayer assemblies. Journal of American Chemical Society, (1989). 1520-5126, 1520-5126.

[23] Jarzebinska, R, Cheung, C S, James, S W, & Tatam, R P. Response of the transmission spectrum of tapered optical fibres to the deposition of a nanostructured coating. Meas. Sci. Technol. (2009). pp).

[24] Jarzebinska, R, Korposh, S, James, S, Batty, W, Tatam, R, & Lee, S. W. Optical gas sensor fabrication based on porphyrin-anchored electrostatic self-assembly onto tapered optical fibres. Analytical Letters. (2012). , 45-1297.

[25] Corres, J M, Matias, I R, Bravo, J, & Arregui, F. G. Tapered optical fiber biosensor for the detection of anti-gliadin antibodies. Sen. and Act.B. (2008). , 135-608.

[26] Bhatia, V, & Vengsarkar, V. A M. Optical fibre long-period grating sensors. Optics Letters(1996). , 21-692.

[27] Korposh, S, James, S W, Lee, S-W, Topliss, S M, Cheung, S C, Batty, W J, & Tatam, R P. Fiber optic long period grating sensors with a nanoasembledmesoporous film of SiO2 nanoparticles. Optics Express (2010). , 18(12), 13227-13238.

[28] Shi, Q, & Kuhlmey, B T. Optimization of photonic bandgap fiber long period grating refractive-index sensors. Optics Communications (2009). , 282-4723.

[29] Patrick, H, Kersey, A, & Bucholtz, F. Analysis of the response of long period fiber gratings to external index of refraction. J. Lightwave Technol. (1998). , 16-1606.

[30] Korposh, S, Selyanchyn, R, Yasukochi, W, Lee, S-W, James, S, & Tatam, R. Optical fibre long period grating with a nanoporous coating formed from silica nanoparticles for ammonia sensing in water. Materials Chemistry and Physics (2012). , 133-784.

[31] Korposh, S, Wang, T, James, S, Tatam, R, & Lee, S-W. Pronounced aromatic carboxylic acid detection using a layer-by-layer mesoporous coating on optical fibre long period grating. Sensors and Actuators B: Chemical(2012). in press.

[32] Ye, C C, James, S W, & Tatam, R P. Simultaneous temperature and bend sensing with long-period fiber gratings. Optics Letters (2000). , 25-1007.

[33] Cheung, S C, Topliss, S M, James, S W, & Tatam, R P. Response of fibre optic long period gratings operating near the phase matching turning point to the deposition of nano-structured coatings. J. Opt. Soc. Am. B (2008). , 25-897.

[34] Wang, T, Korposh, S, Wong, R, James, S, Tatam, R, & Lee, S. W. A novel ammonia gas sensing using a nanoassembled polyelectrolyte thin film on fiber optic long period gratings.Chemistry Letters (2012). in press.

[35] Lee, S-W, Takahara, N, Korposh, S, Yang, D-H, Toko, K, & Kunitake, T. Nanoassembled thin film gas sensors. III. Sensitive detection of amine odors using TiO2/ Poly(acrylic

acid) ultrathin film quartz crystal microbalance sensors. Analytical Chemistry (2010). , 822228-2236.

[36] Timmer, B, & Olthuis, W. Van den Berg A. Ammonia sensors and their applications-a review. Sens. Actuators B, (2005). , 107-666.

[37] Turner, C, Španel, P, & Smith, D. A longitudinal study of ammonia, acetone and propanol in the exhaled breath of 30 subjects using selected ion flow tube mass spectrometry, SIFT-MS. Physiol. Meas. (2006). , 27-321.

[38] Gregory van Patten PShreve A P, Donohoe R J. Structural and photophysical properties of a water-soluble porphyrin associated with polycations in solutions and electrostatically-assembled ultrathin films. Journal of Physical Chemistry:B (2000). , 104(25), 5986-5992.

[39] Korposh, S O, Takahara, N, Ramsden, J J, Lee, S-W, & Kunitake, T. Nano-assembled thin film gas sensors. I. Ammonia detection by a porphyrin-based multilayer film. Journal of Biological Physics and Chemistry (2006). , 6-125.

[40] Swartz, M E, & Krull, I S. Analytical Method Development and Validation, Marcel Dekker, Inc.: NY USA; (1997).

[41] Ohira, S I, & Toda, K. Micro gas analyzers for environmental and medical applications. Anal. Chim.Acta (2008). , 619-143.

[42] Yamane, N, Tsuda, T, Nose, K, Yamamoto, A, Ishiguro, H, & Kondo, T. Relationship between skin acetone and blood beta-hydroxybutyrate concentrations in diabetes. Clin. Chim. Acta, (2006). , 365-325.

[43] Nose, K, Mizuno, T, Yamane, N, Kondo, T, Ohtani, H, Araki, S, & Tsuda, T. Identification of ammonia in gas emanated from human skin and its correlation with that in blood. Anal. Sci. (2005). , 21-1471.

[44] Nose, K, Nunome, Y, Kondo, T, Araki, S, & Tsuda, T. Identification of gas emanated from human skin: methane, ethylene, and ethane, Anal. Sci. (2005). , 21-625.

[45] Akiyama, A, Imai, K, Ishida, S, Ito, K, Kobayashi, T, Nakamura, H, Nose, K, & Tsuda, T. Determination of aromatic compounds in exhalated from human skin by solid-phase micro extraction and GC/MS with thermo desorption system. Bunseki Kagaku (2006). , 55-787.

[46] Penn, D J, Oberzaucher, E, Grammer, K, Fischer, G, Soini, H A, Wiesler, D, Novotny, M V, Dixon, S. J, Xu, Y, & Brereton, R G. Individual and gender fingerprints in human body odour. J. R. Soc. Interface, (2007). , 4-331.

[47] Turner, A, & Magan, F. N. Electronic noses and disease diagnostics. Nat. Rev. Microbiol., (2004). , 2(2), 160-166.

[48] Pavlou, A K, Magan, N, Jones, J M, Brown, J, Klatser, P, & Turner, A. P F. Detection of Mycobacterium tuberculosis (TB) in vitro and in situ using an electronic nose in combination with a neural network system. Biosens. Bioelectron. (2004). , 20-538.

[49] Kodogiannis, V, & Wadge, E. The use of gas-sensor arrays to diagnose urinary tract infections. Int. J. of Neur. Syst. (2005). , 15-363.

[50] Dalton, P, Gelperin, A, & Preti, G. Volatile metabolic monitoring of glycemic status in diabetes using electronic olfaction. Diabetes Technol. The. (2004). , 6(4), 534-544.

[51] Voss, A, Baier, V, Reisch, R, Von Roda, K, Elsner, P, Ahlers, H, & Stein, G. Smelling renal dysfunction via electronic nose. Ann. Biomed. Eng. (2005). , 33(5), 656-660.

[52] Haick, H, Hakim, M, Patrascua, M, Levenberg, C, Shehada, N, Nakhoul, F, & Abassi, Z. Sniffing chronic renal failure in rat models via an array of random network of single-walled carbon nanotubes. ACS Nano (2009). , 3(5), 1258-1266.

[53] Peng, G, Tisch, U, Adams, U, Hakim, M, Shehada, N, Billan, S, Abdah-bortnyak, R, Kuten, A, & Haick, H. Diagnosing lung cancer in exhaled breath using gold nanoparticles. Nat. Nanotechnol. (2009). , 4(10), 669-673.

[54] Selyanchyn, R, Korposh, S, Yasukochi, W, & Lee, S. W. A preliminary test for skin gas assessment using a porphyrin based evanescent wave optical fiber sensor. Sensors & Transducers Journal (2011). , 125(2), 54-67.

[55] Nose, K, Ueda, H, Ohkuwa, T, Kondo, T, Araki, S, Ohtani, H, & Tsuda, T. Identification and assessment of carbon monoxide in gas emanated from human skin. Chromatography (2006). , 27-63.

[56] Sekine, Y, Toyooka, S, & Watts, S F. Determination of acetaldehyde and acetone emanating from human skin using a passive flux sampler- HPLC system. J. Chromat. B (2007). , 859-201.

Chapter 10

Optical Fiber Sensors for Chemical and Biological Measurements

Miguel A. Pérez, Olaya González and José R. Arias

Additional information is available at the end of the chapter

http://dx.doi.org/10.5772/52741

1. Introduction

1.1. Introduction to optical fiber sensors

When the light interacts with matter, some effects are produced that do not affect to electron levels of atoms, and consequently, they do not introduce changes in the light wavelength. Thus, the light is reflected, absorbed, scattered, and transmitted with the original wavelength (λ_1). Absorbed light can produce changes over the electron levels of some molecules, causing a new emission of light (luminescence), with larger wavelength (λ_2) than the original. All these phenomena are shown in Figure 1.

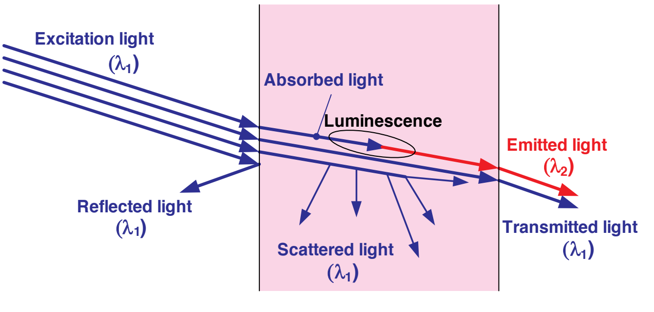

Figure 1. Some phenomena caused by the light-matter interaction.

In addition, other changes can appear, such as light polarization or modification of polarization angle of light. Thus, in a general way, the matter modifies the properties of light (direction, intensity, wavelength and/or polarization).

When the modification of light properties depends on one of the characteristics of the matter, that change can be used to quantify this characteristic, obtaining an optical sensor.

Optical fibers guide the light from excitation source to the sensing area and from the sensing area to the optical detector. During this path, the light hardly suffers any attenuation, and the addition of other sources of optical noise is reduced. So, optical fibers produce a large improvement of Signal-to-Noise Ratio (S/N) in relation to optical sensors without optical fibers.

Besides, optical fibers guide the exciting, the reflected, the scattered, the emitted, and the transmitted light through examining places which would be otherwise difficult to access, making optical fibers quite useful in medicine or biology. It also avoids the need for equipment to be in the vicinity of substance to be measured, which is very interesting for remote operation [30,36,37,48].

Moreover, it is feasible to place several sensors (similar or different) in diverse places along the same optical fiber, obtaining a real sensor network. Several methods for multiplexing excitation signals and demultiplexing signals produced by sensors are available in the domain of time, frequency or light spectrum.

2. Principles of operation and optical fiber measurement systems

The operation of optical fiber sensors requires a light source for exciting the fiber system – including the optical sensor– and a photo detector to read the light emitted by sensing area that includes information about the X, the variable of interest. There are several options for the connection of light source and photo detector as is shown in Figure 2.

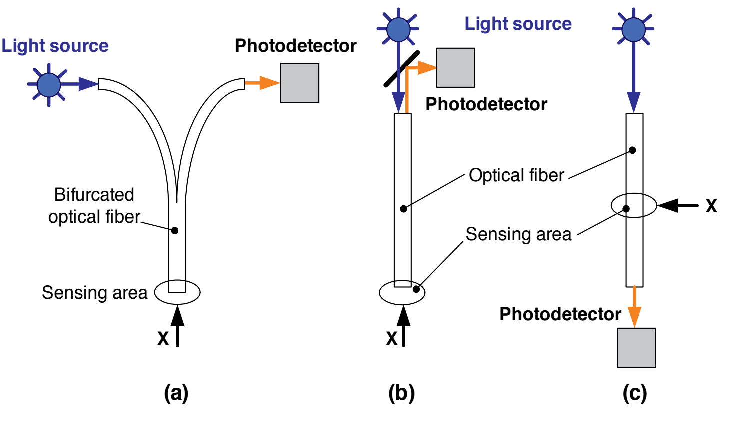

Figure 2. Schemes of possible connections between light source, sensing area and photo detector: (a) bifurcated optical fibers and sensor in the end of fiber; (b) individual fiber with semi-transparent mirror and sensing area in the end of the fiber; (c) individual fiber with sensing area inside the fiber.

Moreover, there are two different types of optical fiber sensor in function of the interaction between the variable, to be measured, and the light: intrinsic and extrinsic sensors.

http://dx.doi.org/10.5772/52741

In intrinsic sensors, the fiber has two functions: first, it is the guiding for exciting and emitting light, and second, the fiber is the transducer. In this case, the variable to be measured modifies some properties of fiber, such as the refraction index or the absorption coefficient (Figure 3). Depending on the magnitude of that variable, the final change of the transmitted radiation will vary, as it happens in evanescence sensors. [13,28].

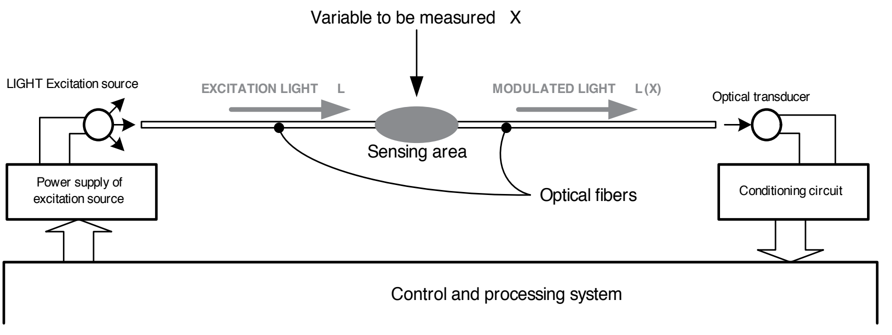

Figure 3. Diagram of the complete intrinsic optical sensor system.

Furthermore, extrinsic sensors use the optical fiber to guide the exciting light from the source to sensing area (outside the optical fiber), and the emitting light, from sensing area to the photo detector (see Figure 4).

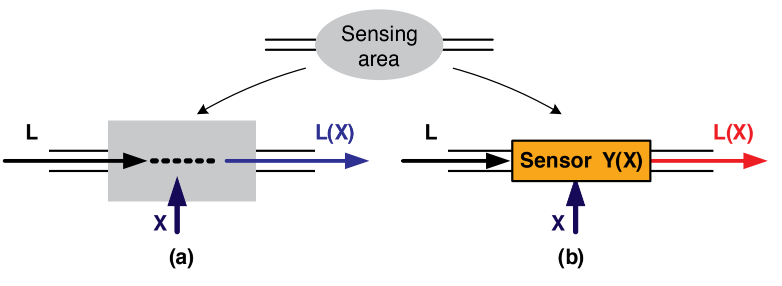

Figure 4. Types of extrinsic optical sensor based on modulation of the light technique: (a) the measured variable produces direct modulation of light; (b) the measured variable, X, produce a change in another variable Y of a sensor, and Y modulates the light.

Sometimes, the observed variable can modulate the light (Figure 4a) but, usually the interaction takes place by means of a specific sensor (Figure 4b) that acts as an interface between the variable X and the optical fiber [41].

For all the above cases, the resulting light contains information about the variable X, that is, the light has been modulated by X. The modulation can modify one or more light characteristic parameters, such as intensity, wavelength, polarization angle, phase or time delay. The type of modulation determines the light source, the photo detector, and the detection procedure [31].

2.1. Measurement based on light intensity

The light intensity is the simplest solution for most of optical fiber sensors and can be used for all cases of Figure 1. However, the use of light intensity introduces some problems in measurement processes because the light intensity is also sensible to other variables. This fact causes both perturbation and noise, and reduces the accuracy of measurement.

The effect of noise could be very important in extrinsic sensors (Figure 4) because the light must leave the optical fiber to reach the sensor, and return into the fiber. During the external path of light, optical noise could be added to the signal, reducing the S/N ratio. Optical filters between the fiber end and the photo detector can increase this ratio by reducing the presence of external sources of light. In addition, the use of a DC source for exciting must be substituted by a fixed frequency source and a narrow band-pass filter after the photodetection to reduce the bandwidth and to increase de S/N ratio. The use of synchronic switched-capacitor filters for both, excitation and received signals, improves the operation of the system because it provides large stability of central frequency [21]. All these solutions are shown in the block diagram of Figure 5.

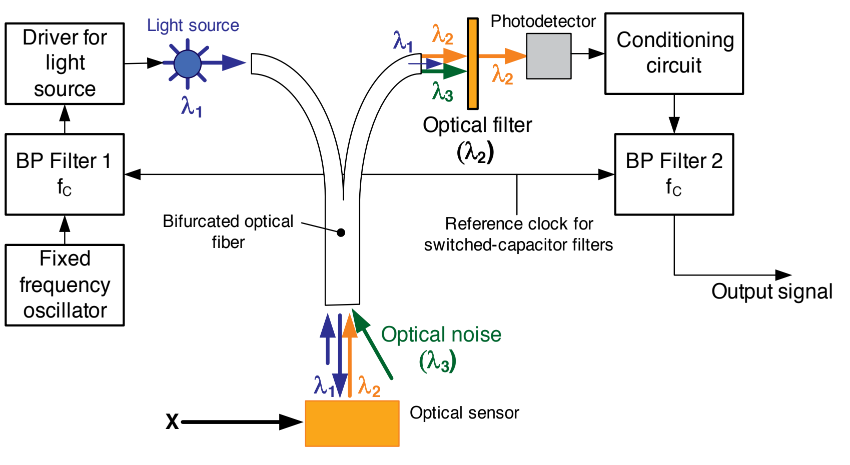

Figure 5. General idea of a light intensity measurement system based upon an optical fiber extrinsic sensor with bifurcated fibers. In case of sensors without modification in wavelength, the emission of sensor has the same wavelength that exciting light ($\lambda_1 = \lambda_2$).

Perturbation of light intensity has a lot of causes: changes in light source, optical fiber couplings (source-to-fiber, fiber-to-sensor, fiber-to-photo detector), and changes in the attenuation of fiber due to curvature, optical fiber length, etc. To prevent the effect of unknown changes in the characteristics of light path in luminescence sensors, it is possible to use a reference signal such as part of the exciting light reflected in optical sensor. The final design is similar to the system in Figure 5, but it uses a tri-furcated optical fiber and two photo detectors, one for the optical sensor emission, and other one for the reflected light from exciting signal (Figure 6).

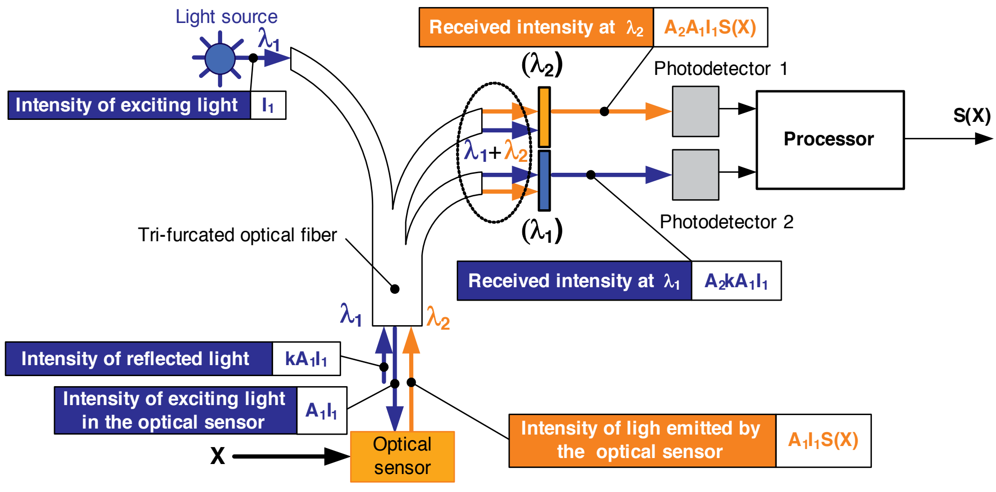

Figure 6. Diagram of the extrinsic optical sensor system with ratiometric measurement to avoid light interferences.

In Figure 6, I_1 is the intensity produced by the excitation source, A_1 is the attenuation coefficient from source to optical sensor, A_2 is the attenuation coefficient from optical sensor to each photo detector, and k is the reflection coefficient in the optical sensor. The processor can evaluate these coefficients by means of the reference signal at wavelength λ_1, and obtain the sensor response at wavelength λ_2, $S(X)$.

2.2. Time domain and frequency domain measurements

The responses of luminescence sensors produce two different measurable effects. The first one is the steady state value of intensity of emitted light that can be processed as is shown in the above point. However, the dynamic response of the optical sensor to a pulse excitation is similar to the plot of Figure 7a, where this response is characterized by the time constant of a mono-exponential decay (in a first approximation). This time constant τ, is dependent on the value of the variable of interest, *X*.

Light intensity and time constant can be used for measurement purposes, but the time constant has a better instrumental behavior [20,23] because the total uncertainty of the measuring instrument is considerably reduced.

However, the analysis is not simple because the emitted light has additional dependences such as the time constant of excitation pulse, the distortions of efficiency of optical sensor and the dynamic response of photo detector.

In the other hand, when the optical response of sensor has a dynamic behavior dependent on the input variable *X* through its time constant, that is, $\tau = f(X)$, this time constant can be evaluated in both, time and frequency domain, because the dependence can be obtained by means of the calculation of his time constant (Figure 7a), or by means of the phase delay in the frequency domain. In the last case, the excitation source is a light with DC + AC components

[1,36], where the alternate signal has a frequency around the one corresponding the time constant of the optical sensor.

The sensor response is a signal with the same excitation frequency, but with a phase delay, φ (Figure 7b) depending on emission time constant τ, by following:

$$\tau(X) = \frac{1}{2\pi f} \tan\left(\varphi\right) \tag{1}$$

Where f is the excitation frequency.

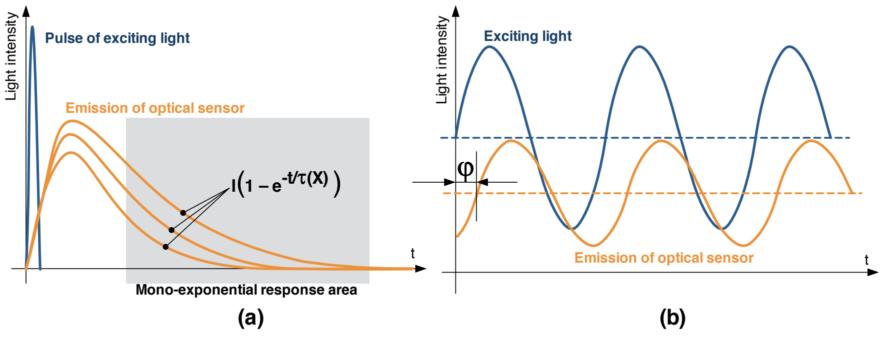

Figure 7. Responses of the luminescence sensor to: (a) a pulse light; (b) a sinusoidal light.

This measurement strategy is very useful for optical sensors with extremely short values of time constant (less than 1 ns), which is very interesting in some fluorescent sensors [17].

2.3. Design considerations of measurement systems based on optical fibers

There is not a universal solution for critical devices in the topologies of optical fiber sensors, because each type of measurement strategy forces the specifications and the requirements for those devices. The measurement system is constituted by the source for exciting light, the optical fibers, and the photo detectors. All these devices must be selected for matching the wavelength spectra of involved phenomena, and according to the measurement strategies. Thus, excitation source must cover the excitation band of the optical sensor; the optical fibers should introduce low attenuation in the involved wavelengths; and the photo detector device has to process all the light emitted by the optical sensor.

Optical filters could be included in the design to guarantee removing the excessive band pass, and to ensure enough noise reduction without decrease the signal power. In the case of optical sensors with wide spectrum sensitivity, too narrow optical filters allow us a heavy reduction of optical noise, but the use of them implies the decrease of the total light power, resulting in a poor S/N ratio.

The choice of source for exciting light depends on measurement type (intensity, and time or frequency domain). For intensity and frequency domain measurement, the source must

http://dx.doi.org/10.5772/52741

produce a DC+AC light signal. The operation frequency of AC component does not have important restrictions in the case of intensity, but must be properly selected for frequency domain operation, according to the expected time delay produced by the sensor response. LEDs and laser diodes (LDs) are excellent solutions for these applications. Pulsating sources are the right selection for time domain measurement; in this case, the total energy of pulse and its duration are the most important parameters that must be taking into account in the design process. Pulse lasers are the best choice for this kind of measurement, because it is possible to obtain extremely short pulses. Other solutions, such as short-arc pulse lamps (Xe, H_2, etc.) could be used in a design [4], but they have some inconvenient: they cannot concentrate the light into the fiber tip and, consequently, need additional –and expensive– optical systems (parabolic mirrors, lenses…) to do it. Moreover, pulse lamps are used to produce wide emission spectrum, forcing the addition of optical filters to reduce the complete spectrum, and to adequate it to the wavelength band.

The photo detector is the device that provides an electrical signal in function on received light signal; its choice is quite similar to the selection of excitation source, because it must have a spectral response including the emission spectrum. Too wide spectral response would include undesirable optical noise, and narrow spectral response reduces the total power of desirable signal; in both cases, the effect becomes negative for S/N ratio.

A common solution for photo detector is the photodiode, a low-volume, low-cost, and versatile device valid for most of applications. However, photodiodes have high noise generation, large dark current, poor sensitivity, and parameter dependence on temperature. Solutions such as avalanche photodiodes (APDs) increase the sensitivity [2], but include additional noise (avalanche noise) and increase the sensitivity dependence on temperature. Sometimes, photodiodes and APDs should be refrigerated to keep a constant temperature by means of Peltier cells and control closed loops for temperature [39]. When the emission level is low (power signal is similar to noise equivalent power (NEP), photodiodes do not have enough sensitivity or introduce intolerable noise level. In these cases, a photomultiplier Tube (PMT) must be used, to guarantee a good behavior of light to electrical signal conversion. In the past, PMTs are complex, expensive; they have a large volume and need high voltage power sources. But, in the present, they are compact solutions, with low voltage supply (5 or 12 V), and reasonable cost. PMTs provides low dark current, produces low noise, and have high sensitivity, being an excellent solution for most of optical fiber sensor based on luminescence phenomenon.

3. Chemical sensors that uses optical fibers

A chemical sensor is a device that can be used for measurement the activity or concentration of chemical specie (analyte) in a sample. It is constituted by two stages [24]. The first stage indentifies and interacts with analyte, and the second one is a transducer, coupled to the first stage (Figure 9).

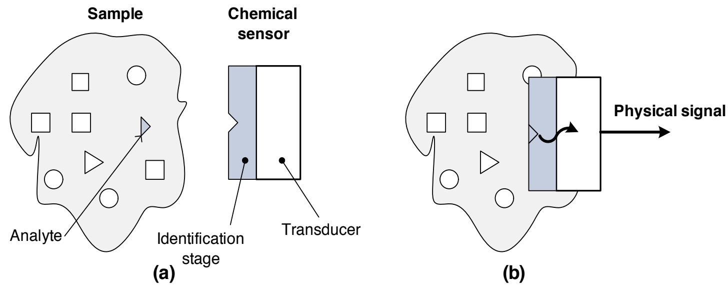

Figure 8. A chemical sensor: (a) sample and sensor; (b) the chemical sensor identifies the analyte, and generates a physical signal.

When the identification stage interacts with the analyte produces changes in its properties (emission and/or absorption of light, electrostatics changes, vibrations, chemical reactions, etc.), that is detected by transducer stage to generate an analytical signal [25,26].

Optical sensors are a type of chemical sensors that provides an optical response depending on analyte concentration in a sample, and they can classify in function of the optical property that has been measured: absorbance, reflectance, fluorescence, phosphorescence, luminescence, Raman dispersion, evanescence, refraction index, etc. When optical fibers are added to these sensors, it is possible to use the fibers for light signal transmission, obtaining an optrode [32].

3.1. Absorbance, transmittance, scattering and reflectance measurements

Light to matter interaction has been above explained (Figure 1), founding various phenomena that modify the properties of exciting (incident) light without changes in its wavelength. For several cases, the behavior of the light in this interaction depends on some characteristics of matter and, consequently, it could be used to identify those characteristics. Thus, the measurement of the light reflected, absorbed, scattered or transmitted is a way for detection or quantification of a property which is able to produce a change in the light.

In transparent media, absorbance and transmittance measurements are closely related because the rest of effects are negligible; consequently, they produce similar results. Absorbance can be used to identify some substances (atoms or molecules) in a medium, because each substance has a specific absorption spectrum. However, a simple quantification in any environment becomes very complex, because there will be more than one chemical specimen in the medium. So, a valid identification and/or quantification require a detailed study of a portion of spectrum. Absorption spectrometry is the technique that can identify and/or quantify the causes of the resulting spectrum, and it involves complex mathematical process and statistical analysis [45].

But, optical sensors based upon absorption are designed for specific analysis, usually in a particular and controlled medium. Hence, these sensors use a small number of wavelengths (even, one specific wavelength), and quantify the change on light intensity when the incident light runs through the sample [7]. By a similar way, reflectance sensors are also designed for specific analysis in opaque or low transparent substances (Figure 10).

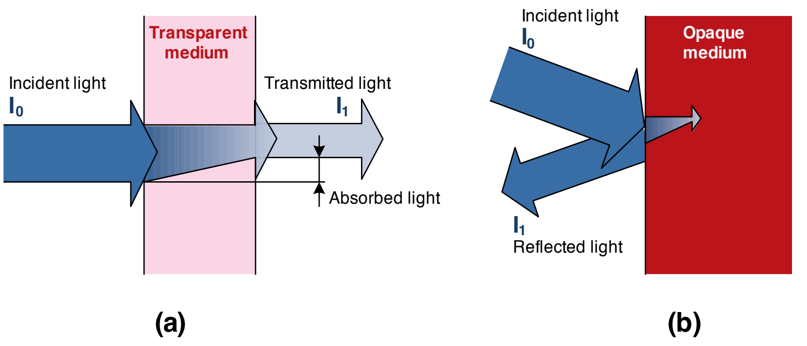

Figure 9. Abortion, transmission and reflection performance of the light: (a) in a transparent medium; (b) to face opaque medium.

In the case of absorbance, the relationship between incident and transmitted light at a specific wavelength can be expressed by means the absorption coefficient, A_λ,

$$A_\lambda = ln\ \frac{I_0}{I_1} \tag{2}$$

When this coefficient A_λ is a function of a chemical or physical parameter of medium, it is possible to use the change in intensity to quantify it, obtaining an absorbance sensor. Usually, that function is not simple and the instrumental design requires an empirical procedure to reach the static transfer curve. A_λ depends on length of optical path through the sample; this fact can be used for adjusting the instrumental sensitivity according to the excitation source and photo detector device.

In the case of reflectance, the hemispherical coefficient of reflectance, ρ_λ, for a wavelength λ, is defined as follows,

$$\rho_\lambda = \frac{I_0}{I_1} \tag{3}$$

This coefficient depends on obvious physical parameters, and sometimes also includes information about the presence of quantity of a specific substance. Thus, the reflectance can be used as an instrumental parameter in the design of a sensor for that substance. As the previous case, a large number of variables can affect the value of reflectance coefficient and an experimental calibration process must be carried out to obtain the static transfer curve.

Scattering light is only used for detection of some physical parameters, such as liquid turbidity [38] or smoke detection, and it is not usual in neither chemical nor biological measurements.

3.2. Fluorescence and phosphorescence measurements

Fluorescence and phosphorescence are two of processes of a photo-luminescence molecule. It absorbs UV or visible radiation to increase the energy level from a fundamental singlet state

S_0 to excited electronic singlet states S_1, as is shown in the Jablonsky diagram of Figure 11. Some low energy changes can occur from this new fundamental state S_1 to near energy levels produced by vibrational relaxation, without radiation emission. When the molecule returns to the original singlet state S_0, can emit a radiation with a longer wavelength than the absorbed radiation; this emission is known as fluorescence. But, the molecule can also return to the original state S_0 through non-radiant transition (vibrational relaxation, internal conversion, external conversion, and intersystem crossing). The most likely path to the fundamental state S_0 will be one that minimizes the mean timelife of the excited state.

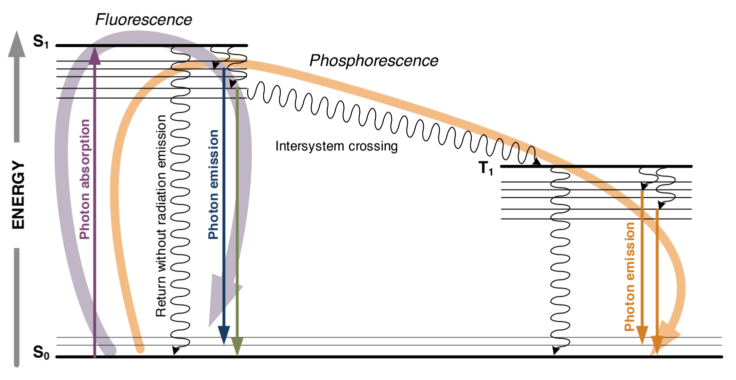

Figure 10. Jablonsky diagram for luminescence processes. Thick lines are fundamental states and fine lines correspond to vibrational states associated to a fundamental state.

Intersystem crossing is an unusual phenomenon that increases the spin multiplicity of electron and drives it to a triplet state (T_1). From this state the molecule returns to its original unexcited state by means an emission of radiation (phosphorescence) or without radiation emission. The phosphorescence phenomenon is longer in time than fluorescence one, and produce longer wavelength. In addition, due to the low probability of the phosphorescence, the total intensity of radiation is very low compared to the fluorescence process.

For both cases, fluorescence and phosphorescence, the kinetic of process can be represented by a first order equation:

$$\frac{d[M^*]}{dt} = -\mathrm{k}\cdot[M^*] \tag{4}$$

Where [M*] is the concentration of molecules in excited states and k is a constant that represents the speed of process and depends on the molecule properties. By integrating,

$$[M^*]=[M^*]_0 e^{-kt} \quad \rightarrow \quad [M^*]=[M^*]_0 e^{-\frac{t}{\tau}} \tag{5}$$

Where $[M^*]_0$ is the initial concentration of excited molecules, and τ = 1/k is known as the medium lifetime of the excited state. As the emission intensity is proportional to the concentration of excited molecules, the previous equation can be rewritten in terms of light intensity, as follows,

$$I = I_0 e^{-\frac{t}{\tau}} \tag{6}$$

In some cases, the deactivation of excited states can be produced by a non-radiant external conversion way due to the interaction of photo-luminescent molecules with external molecules. This implies an energy transfer that reduces the concentration of excited molecules and, consequently, the intensity of light emission decrease. This effect is known as quenching and can be used to determine the concentration of these external molecules (quenchers). This effect can be quantified by means the Stern-Volmer equation,

$$\frac{I_0}{I([Q])} = \frac{\tau_0}{\tau([Q])} = 1 + \tau_0 k_b [Q] \tag{7}$$

Where I_0 and τ_0 are the intensity and medium lifetime of light emission without quencher, I[Q] and τ[Q] are the intensity and medium lifetime in presence of a concentration of quencher [Q], and k_b is the bimolecular constant of quenching. The product $\tau_0 k_b = K_{SV}$ is known as the Stern-Volmer constant. This constant is actually modified by diffusion process and depends on the diffusion coefficients of photo-luminescent and quenchers molecules [3,18]. The Stern-Volmer equation establishes a linear but not-accuracy relationship, due to heterogeneity of chemical sensor. It is possible to correct this relationship, and it must be done. [1,14,15,20,23,46].

3.3. Implementation of chemical sensors with optical fibers

Most of chemical sensors that use optical fibers are extrinsic, because the inclusion of reactive substances inside the fiber (necessary for intrinsic sensor) will increase the response time of recognition stage (Figure 9), due to the slow diffusion process of analyte through the fiber. Hence, most of optical fiber chemical sensors use bifurcated fibers (Figure 2a) or a single fiber with a semi-transparent mirror (Figure 2b). In both cases, the chemical sensor (or the sample to analyze) is placed near or in the end of fiber, depending on fiber type and measurement strategy (Figure 12).

In luminescence sensors, the fiber tip can be shaped to reduce the reflection for exciting wavelength and to prevent the presence of exciting light in the photo detector as a noise. It could include selective membranes to improve the selectivity of sensor (Figure 13); but the membrane increases the sensor settling time due to the diffusion process through it.

The complete sensor includes the source for excitation and the photo detector device. Table 1 shows some consideration about the selection of these systems, taking into account the type of chemical sensor. The most critical specifications for the light source and photo-detector device are for time domain measurements in fluorescence, due to the usual short time response of chemical sensor that forces the selection of extremely short pulse sources and high speed detectors; the low intensity produced by phosphorescence sensors force the use of high sensitivity photo detectors in all cases.

Chemical Sensor	Light source	Photo-detector	Considerations
Absorbance	LED, Laser, LD	Photodiode	AC+DC signal Intensity measurement
Reflectance			
Fluorescence	Pulsating lamps, LED, LD, lasers	Photodiode, APD, PMT	Short time response Time-domain measurement
	LED, Laser, LD		AC+DC signal Frequency-domain measurement
			AC+DC signal Intensity measurement
Phosphorescence	Pulsating, lamps, LD or lasers	APD, PMT	Medium-large time response Time-domain measurement
	LED, Laser, LD	Photodiode, APD, PMT	AC+DC signal Frequency-domain measurement
			AC+DC signal Intensity measurement

Table 1. Light signal, excitation sources and photo detector devices for chemical sensors.

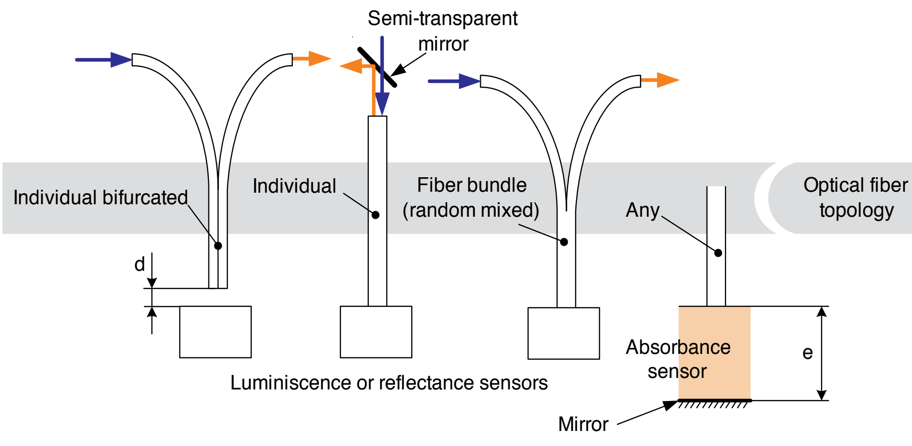

Figure 11. Situation of chemical sensor in the end of fiber considering the optical fiber topology: the parameters *d* and *e* must be calculated to obtain an optimal sensitivity.

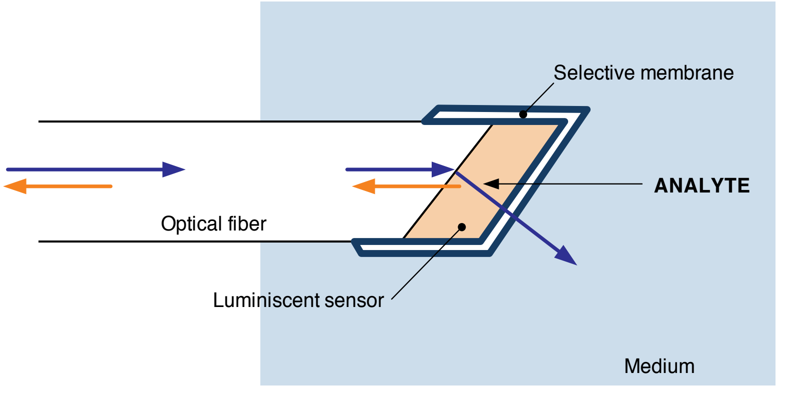

Figure 12. Chemical sensor placed into the fiber tip with a selective membrane.

4. Examples of optical fiber sensors for chemical measurements

4.1. Frequency domain analysis for the fluorescence of ruthenium chemical sensor

The measurements are commonly based in analysis of the time domain or the frequency domain, as it is explained in the above section 2. Time domain measurements have practical difficulties. This method requires a big number of points of the signal response to obtain the time constant, and this is a limitation because of the small size of the sampling period. Due to the characteristics of the physical phenomenon and/or the high cost of the system, it is more efficient using the frequency domain to measure the fluorescence emission, whose lifetime is in a range limited by nanoseconds and a few microseconds [22,47]. In this method, the lifetime is obtained from the phase shift between emission signal from the chemical sensor and the excitation signal used. Currently, some analytical instruments that enable the measurement of a large number of analytes such as pH, carbon dioxide, or oxygen, are known. This section deals with a brief description of the main components of fluorescence sensors, focusing on a sensor for measuring dissolved oxygen concentration.

The system consists of a DC+AC light source which excites the Ruthenium sensor. When this chemical sensor is energized, it produces a fluorescence excitation with a wavelength around 470 nm, and the following fluorescence emission wavelength is near to 600 nm in the case of oxygen measurements.

In fluorescence analysis is not necessary to employ a high intensity light source, but a correct generation of the excitation waveform is very important because this waveform will be used in the final processing. Thus, the best device for been implemented in the emission sub-system (Figure 14) is a LED [11,12,27].

This LED must emit a light with a wavelength close enough to the excitation one (470 nm), and as optic fiber is used to transfer the light, its viewing angle must be small enough to

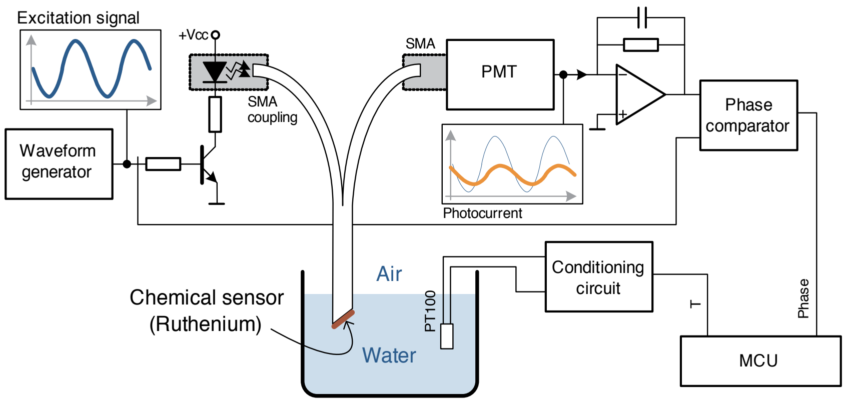

Figure 13. Optical fiber sensor for D.O. based on Ruthenium chemical sensor. It operates with phase detection and temperature correction.

improve the directionality of the emission. So, as LED OVL-5523 also has the intensity needed to excite the Ruthenium sensor, it can be a good solution for the light source of a frequency domain fluorescence system (fluorimeter).

The PIN photodiode is a common photo detector employed in a lot of digital communication systems with optical fiber because it has a good reliability and a quite wide bandwidth. But, considering the disadvantages, it can be mentioned, that it introduces a large noise, it needs an external system to establish its temperature, and its bandwidth is above our specification range. Other interesting photo detector is the APD, it does not have the disadvantages said previously, but in this case, its internal gain is intrinsically unstable. These devices are cheaper and have a smaller volume than PMT, which needs a special enclosure to obtain a correctly amplification of the output current. Nevertheless, their instrumentation characteristics make of this last photo detector, the best option to take part in the fluorescence based system.

In Figure 14, it is possible to appreciate the block diagram of the fluorimeter. The system generates a sinusoidal signal with a DC component for LED excitation. The light is transferred to the Ruthenium sensor by low-cost bifurcated optic fiber (gradual index plastic optical fiber with a diameter of 1 mm). The chemical sensor where the fluorescence phenomenon takes place is in contact with the sample. The fluorescence emission generated goes through the fiber to the PMT. The photo detector output signal (current) and the sinusoidal excitation signal are processed to obtain the frequency response of the fluorimeter.

The data produced by this system can be modelled by a Stern-Volmer equation, but in this case it is better to use a multivariable regression because the influence of the temperature is quite high.

The obtained model has a high correlation considering the phase shift and the temperature as explicative variables of oxygen concentration $[O_2]$. This model is almost linear with 0.9999 of correlation index as it is possible to see in Figure 15, where graphic points produce clearly a

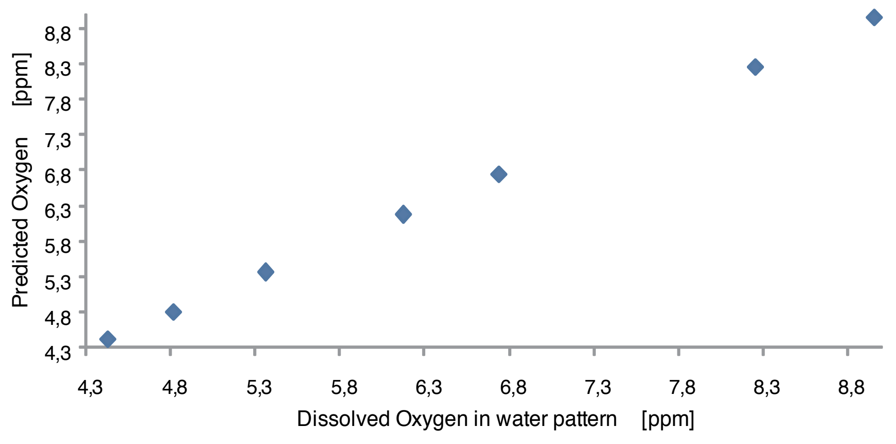

Figure 14. Relationship between the real values of D.O. in water patterns and predicted values from fluorimeter of Figure 14.

straight line. Furthermore, the maximum absolute errors that can be found in this kind of fluorescence systems round 2 ppb, with relative errors values of less than 0.05 %.

4.2. Time-domain analysis of phosphorescence of sol-gel Al-Ferron chemical sensor

Phosphorescence analysis in the domain of time is a well known procedure to carry out several important measurements of several analytes. Concentration of dissolved oxygen in water (D.O.), moisture level, pH value and other chemical parameters can be obtained by means of analysis of phosphorescence emission of a chemical sensor properly excited with light [5,9,18]. In this section, some considerations about main blocks of a time domain phosphorimeter will be discussed, including some improvements.

Light source must excite the chemical sensor that yields a phosphorescence emission with a wavelength quite far from excitation wavelength. In Al-Ferron Sol-gel chemical sensor [18, 48] used for oxygen measurement, excitation wavelength is placed from near UV to violet and the emission takes place around the green light wavelength.

An excitation with high pressure Xe pulse lamps (or similar short-arc lamps) produces a wide spectrum (white light) and high intensity pulses of light, requiring optical filters to reduce optical noise. In addition, these lamps need to include other optical accessories, like parabolic mirrors or lenses to concentrate the light into the optical fibers tip. The final cost of this kind of lamps and associated power and trigger circuits is very high, and these circuits introduce several critical subjects in cabling, housing, protection and/or EMC. Finally, an aging process takes place in arc lamps, reducing the lifetime of lamp, generally due to electrodes are worn out [6].

Laser light sources increase the intensity of pulses, reduce their narrowness, and avoid the use of additional optical systems such as filters and mirrors because the produced light is coherent. But they introduce the same problems in total cost, cabling protection and EMC. Final results of laser-based time domain phosphorimeters are quite similar to results obtained with pulse lamps. The high concentration of power pulse becomes a problem for optical fibers connected to laser sources: the end of fiber has a progressive increase of attenuation by burning.

LD and UV-LEDs are other possible solution for light excitation. They facilitate the connection to optical fiber tip and reduce both, the total cost and the system volume, overcome most of inconvenient of arc lamps and lasers. Moreover, the MTBF of UV-LED is very high in comparison with lasers and lamps, reducing maintenance and replacement costs.

The excitation wavelength of chemical sensor (Al-Ferron immobilized in Sol-Gel) has a maximum peak around 390 nm and its emission spectrum has a peak value around 590 nm. Thus, UV LED like NSHU590 can be a balanced solution for the light source of a time domain phosphorimeter.

The detection of emitted light is critical in phosphorescence based system due to low level of Al-Ferron emission. The best solution –under the instrumental point of view– is the use of a PMT because of its high sensitivity. Moreover, it has low noise, low dark and non dependence on temperature. A comparison between APDs and PMTs results in similar instrumentation characteristics will be that the initial advantages of APD in volume are compensated with the presence of cooling systems [39] for holding constant temperature, and thus, avoiding sensitivity changes. Standard PIN-Photodiodes introduce large noise and need temperature stabilization [6].

Final design of phosphorimeter is shown in Figure 16, where the chemical sensor is included inside a flow cell for calibration purposes, by using a full-controlled gases mixture of argon and oxygen. UV LED output is a waveform that consists of narrow pulses widely separated from each other in order to guarantee tine enough for full extinguishing of chemical sensor emission between pulses. Resulting excitation waveform is shown in that figure.

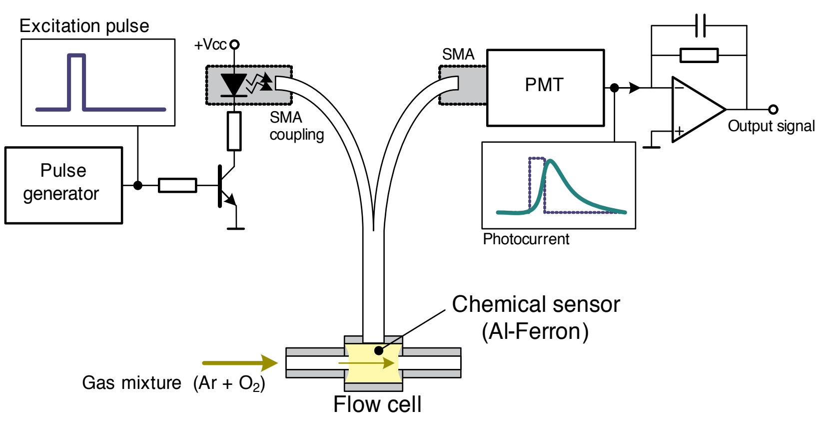

Figure 15. Design of an optical fibers time domain phosphorimeter with Al-Ferron chemical sensor. Bifurcated optical fibers are constituted by a bundle of 1500 borosilicate fibers, in contact with the chemical sensor powder. All optical filters have been removed for this design because the optical noise is not too important.

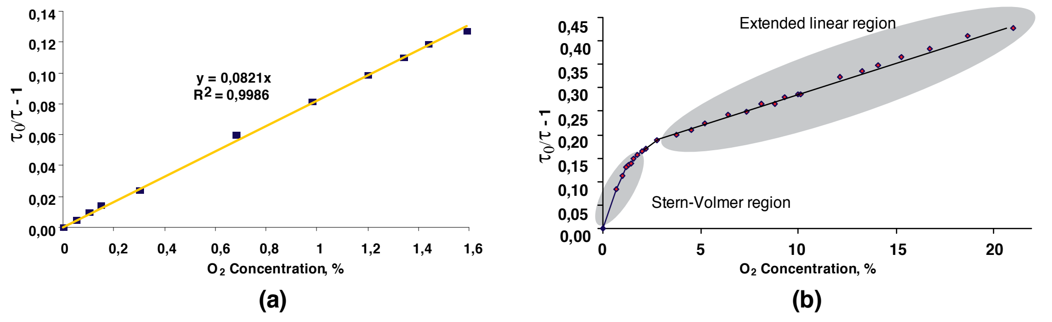

Figure 16. Experimental results of a phosphorimeter using Al-Ferron chemical sensor: (a) for low oxygen concentrations; (b) Extended results of Stern-Volmer relationship with two linear areas.

This system has an excellent behaviour for low level oxygen concentration, obtaining a good correlation coefficient for Stern-Volmer equation (see Figure 16a).

Stern-Volmer equation for low-level oxygen concentration is a well-know fact, but the behaviour of phosphorescence emission at large value of [O_2] is usually described as a 'saturation process' in the chemical sensor. Thus, for [O_2] less than 4%, Stern-Volmer equation can be experimental verified but becomes inexact above this point. However, there is not saturation process but a slope change in plot. In Figure 16b, an extended plot (from 0% to 21% of [O_2]) is displayed, showing two different slopes. The fact of slope change allows us to use phosphorescence lifetime analysis over the limitations of Stern-Volmer equation although the obtained sensitivity is lower. The obtained change in slope is a common question in phosphorescence analysis and it is present in both, medium lifetime analysis and intensity analysis as it has been described for other phosphorescence sensors.

5. Optical fiber sensors for biological applications

Optical fiber sensors can be applied for several biological measurements. However, in most of cases, the final sensor does not have a direct interaction with a biological parameter, but it has a chemical or physical operation principle. The general idea is similar to the exposed in Figure 9, an indirect interaction. In this case, a biological variable produces a chemical or physical change suitable for measurement by light modulation (absorbance, reflectance, luminescence, etc.). So, as a general conclusion, an optical fiber sensor for biological measurement is a type of above discussed solutions.

An example is the well known reaction to detect or determine the quantity of ATP (adenosine triphosphate), a coenzyme used in cell reactions by means luciferine,

$$ATP + Luciferine + O_2 \rightarrow Oxyluciferine + CO_2 + AMP + LIGHT$$

The results of this reaction include adenosine monophosphate (AMP), and it emits light! The light intensity is proportional to the quantity of ATP. This phenomenon is known as bioluminescence but, it could be called chemical-luminescence. There are a lot of applications of this test in the determination of quantity of cells or their activity in a sample.

The main restrictions imposed to the use of any sensor for biological applications are the bio-compatibility and the disturbance for in-vivo measurements; because this kind of sensors is applied in human and veterinary medicine, and in food industry, sectors with extremely restrict conditions and standards. For example, a catheter with a D.O. sensor for determining the oxygen saturation in blood could be a fluorescence sensor based on ruthenium chemical sensor, but it must have a complete bio-compatibility.

In next sections, some examples of sensors for biological applications are presented. In all cases the objective is the monitoring and control of food production.

5.1. Milk quality sensors based upon optical fibers

Daily measurement of nutritional milk parameters could be used for cow selection, cow feed tuning in order to increase economic efficiency, and milk differentiation to obtain predefined values of fat content, total protein or lactose in the farm outlet. Modern dairy farms include several control and automation systems, which are able to provide interesting data for farm management and to improve the economical results of exploitation [44]. NIR spectrometry has been used to estimate milk composition, but previous works are referred to dry milk, homogenised milk, high cost spectrometry equipment [43], or requires sampling and previous treatment of milk samples [16,49], avoiding a cow-side final implementation.

All spectrometry equipment consists of an excitation light source able to produce a continuous spectrum for all wavelengths and a photo-detection system for measuring the received light in the same light spectrum. The reduction of range of interesting light wavelengths simplifies the design of complete system and decreases the final cost because low-cost LEDs and photodiodes can be used for excitation and light detection. Moreover, photodiodes can be used without cooling systems or temperature controllers, keeping an enough S/N ratio.

To investigate the potentiality of VIS-NIR spectrometry, several milk samples has been taken from a farm during milking (along milking and from different cows). Each milk sample is divided into two similar sub-samples and preserved using refrigeration and bronopol (2-Bromo-2-nitro-1,3-propanediol). First sub-sample is sent to a certified laboratory for composition analysis, using standard procedures, obtaining reference values for fat (TG), total protein (TP) and lactose (TL) content; second sub-sample is analyzed by spectrometry. Finally, results of both analyses are compared in order to determine the capability of VIS-NIR spectrometry to estimate the milk composition.

The analysis of each milk sample by spectrometry is carried out using a low-cost VIS-NIR spectrophotometer from Ocean Optics, able to provide 1236 values in the 400.33 to 949.59 nm, resulting in a resolution of 0.444 nm. Three different spectra are obtained by means of custom-designed analyzing cell connected to spectrophotometer and light source using several optical fibers as we can see in Figure 17. When an appropriate excitation lamp is used, this system is able to provide orthogonal spectrum (M90) caused by scattered light, transmittance spectrum

(TR) and reflectance spectrum (RE). All these values are corrected by ratiometric techniques to reduce uncontrolled attenuation and disturbances [7].

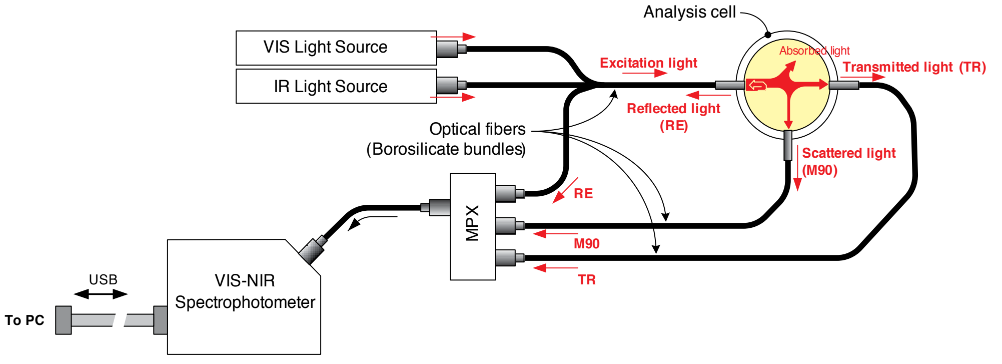

Figure 17. Three spectra analyzer for fresh milk

Spectral data has been smoothed by applying iterative local linear polynomial fit with tricubic weighting [8] to redraw smoothed spectra with low resolution, 20 nm. Thus, the total number of input variables for statistical treatment is reduced and, the problem simplified, without significant data lost. Regression-based methods are used for prediction, using TG, TP and TL as dependent variables and smoothed spectra M90, TR y RE, with 20 nm of resolution as independent variables. For each value of three smoothed spectra, square and cubic terms are generated such as additional input variables to include non-linear behaviour of model. Hence, model includes 504 input variables (56 × 3 ×3), 56 values of each spectrum, and its square and cubic terms).

Total number of input variables is lower than number of observations. So, a multivariate technique for dimensional reduction must be applied, the traditional Principal Component Regression (PCR) or the useful PLS (Partial Least Squares) in univariate response (PLS-1) [29]. Both, PCR and PLS-1 methods are based on calculation of orthogonal components from a linear combination of original variables to reduce the total number of variables. The objective of PLS-1 is to extract the components from correlations between original independent variables and dependent variable. In our case, to choice the final components number, the average squared error of predicted values is calculated for all cases, by means of leave-one-out cross-validation. The use of R statistical environment simplifies these calculations and procedures [40]. Table 2 shows the optimum number of used components for both methods and the percentage of explained variance. The results are quite simple: fat content in milk can be obtained with only one excitation wavelength!

Based on this idea, a low-cost optoelectronic sensor has been developed for working in the NIR region of light spectrum. The developed sensor shown in Figure 18 is a reflectance optical fiber sensor that consists of a stainless steel tube, optical fibers for light conduction from a light emitter to the milk to a light receiver, and circuits for the signal treatment and control unit.

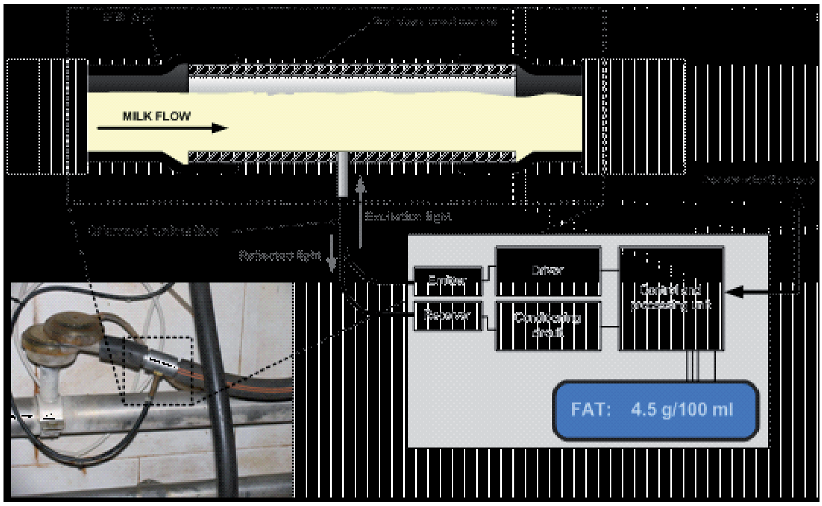

Figure 18. On-line optical fiber sensor for the estimation of fat content in milk. Picture shows an in-farm implementation of this system.

Variable	Number of components		Explained variance (%)
	PCR	PLS-1	
Fat content (TG)	1	1	82
Lactose content (TL)	11	8	62
Total protein content (TP)	2	2	17

Table 2. Comparison of PCR and PLS-1 results in prediction of milk composition. An overall interpretation could establish an excellent behaviour for prediction of fat content (it uses only one component and can explain a high percentage of variance); results are interesting for lactose content, although using many components.

The operation of the system is as follows: the light proceeding from an infrared LED comes into contact with the milk, where part of the light is reflected and then, detected by a photodiode. Due to the fact that the reflected light depends on milk fat, the value of fat can be calculated by a control unit. Figure 19a shows the real behaviour of this sensor for homogenized milk samples, and Figure 19b, for raw milk during milking process. In both cases, the output signal is the voltage produced after conditioning circuit.

5.2. Optical fibers colorimeters in food quality control: Wine and consumption oil

Colour contributes to organoleptic attributes and quality parameters of food. Moreover, it can be used in the production process: to determine the maturation level of fruits and vegetables, in the identification of origin and adulteration of consumption oils, in the fermentation process of grape juice for winemaking or other fermentation process (beer, cider, etc.). In all these cases, colour determination is used to make decisions during the production processes.

http://dx.doi.org/10.5772/52741

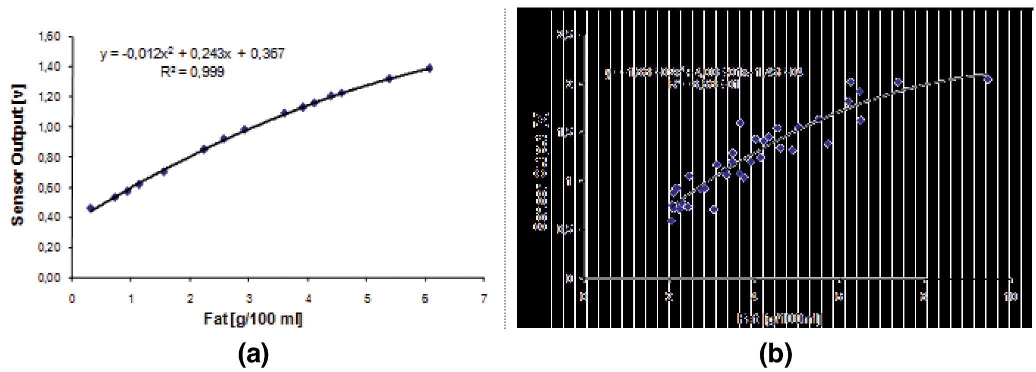

Figure 19. Analysis of 38 samples of fresh un-homogenized raw milk. Actual fat values are provided by a certified laboratory and have and uncertainty less than 2%.

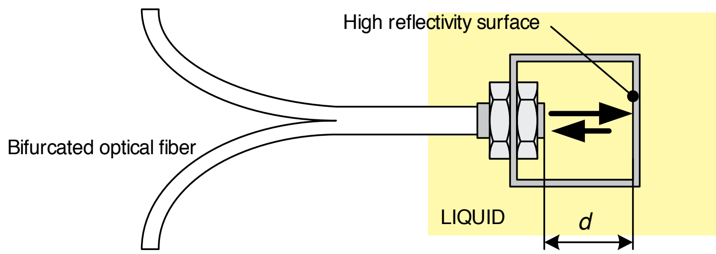

Figure 20. Optical fiber colour probe for liquid foods. The distance d is a design parameter and it depends on liquid transparency. All materials of sensor must accomplish with food industry standards.

In some traditional food industries, the colour is provided by experts, but this introduces subjectivity and uncertainty, and increases the processing time. The final results are a lost of repeatability, reproducibility and quality, and an increase of final cost. Expert estimation of colour can be substituted by a colorimeter that produces on-line results, improves instrumental parameters and reduces cost. A complete colour estimation includes an analysis of reflected (for solid foods) or transmitted/absorbed (for liquid foods) light spectrum in visible wavelengths (400 to 700 nm), but it is usual the reduction of analysis to a short set of wavelengths according to food type and the property that we like to know.

A colour analysis for solid foods such as vegetables, fruits or meat does not require optical fiber sensors and can be carried out by CCD cameras and image analysis; however, sensors for colour estimation of liquid foods can take advantage of optical fibers to reach any measurement place during production process. Figure 20 shows a colour probe with bifurcated optical fibers that uses a transmittance/absorbance measurement.

In wine industry, colour depends on some parameters such as the grape composition, winemaking techniques and several reactions that take place during wine storage. The composition of wine colour changes continuously during winemaking and storage, with associated changes in sensory characteristics. Usual colour analysis for grape juices and wines

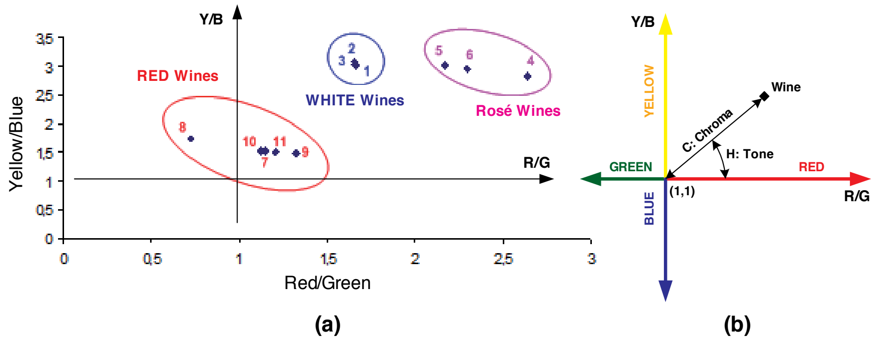

Figure 21. (a) Wine classification in Y/B-R/G coordinates system; (b) Definition of chromaticity parameters of a wine.

is made by measurements at three wavelengths in blue, green and red spectrum areas: 420, 520 and 620 nm [19], but there are several methods to measure the chromatic parameters in all wines types, such as the method based on the CIE [33] or the OIV [34] method to determine the wine colour. These methods use two very similar processes to obtain colorimetric values of wine samples because the wine absorbs the radiation incident, or transmits the one that not absorbed. In both cases, the objective of each method is to obtain three colorimetric values to situate each wine in one point of the specific colour space [34]. Both methods have quite similar characteristics, including their high cost, because they use spectrometers, very expensive and delicate equipment, and other subsystems like special illuminants.

In addition, final colour read-out involves a complex procedure, not allowing on-line operation; this limitation reduces the use of these colorimeters in winemaking process.

On-line requirements and low-cost condition force to explore new methods of colour measurement, that is able to provide on-line chromatic values without punishing the cost, that is: they can be used within the control system of winemaking processes [10]. A new design with RGB colour space simplifies the sensor and reduces the cost of illuminant because a halogen lamp is able to provide enough power excitation in the three selected wavelength. To simplify the fiber topology and connector system it is possible to use a RGB photodiode as photodetector.

The results from this RGB optical sensor can be plotted in the traditional diagram used for wine colour classification (Figure 21a) [42]; thus, the chromaticity values (tone, H and chroma, C) can be derived from measured values (Figure 21b) by,

$$C = \sqrt{(YB - 1)^2 + (RG - 1)^2} \qquad H = \arcsin\left(\frac{YB - 1}{C}\right)$$

where YB and RG are, respectively, the Yellow-to-Blue and the Red-to-Green ratios,.

The use of a colorimetric optical fiber probe has a lot of applications in food industry. Another interesting case is the colour determination of consumption oil, because it can be used to identify the type of oil, even the olive type and the acidity level. Figure 22 shows a diagram block of a RGB colorimeter, applied to oil colour characterization. It includes a full controlled

http://dx.doi.org/10.5772/52741

illuminant (white light emitter) with a feedback of emitted light to avoid long term and temperature derives.

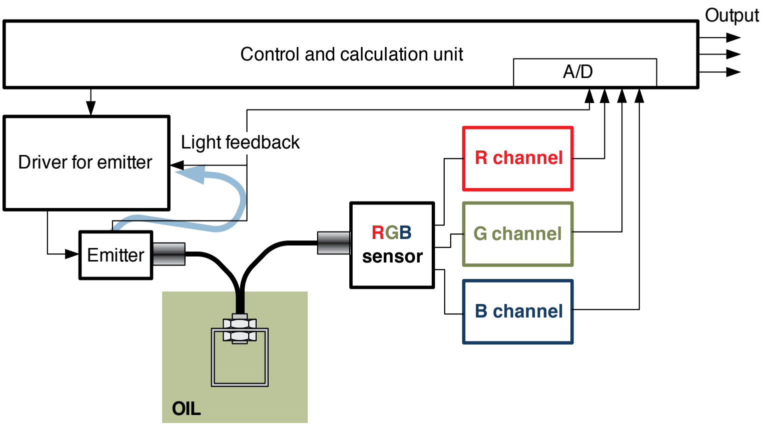

Figure 22. Optical fiber RGB colorimeter applied to oil colour characterization.

As we can see in Figure 23, oil colour can be used to identify the origin of oil, even with only two wavelengths: red (620 nm) and green (540 nm), reducing the blocks of block diagram of Figure 22. A more precise identification needs the value of blue (420 nm) channel and could provide additional knowledge, such as adulteration of oil with dye or the evolution of properties during cycling use for deep frying.

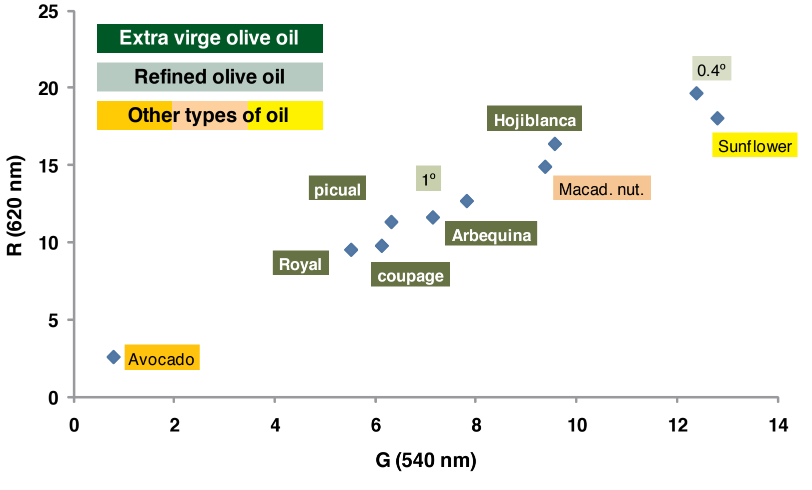

Figure 23. Differentiation of several types of consumption oils by means the values of green (abscissas) and red (ordinates), using arbitrary units.

6. Conclusions

Optical fiber sensors are widely applied for a lot of measurement processes because they have important advantages such as the high noise immunity and the use for remote and multi-position measurement. In particular, the use of optical fibers in combination to chemical sensors increases the potentiality of these sensors and extends their applications.

In above sections, we have presented several operation principles (absorbance, reflectance and luminescence), data processing strategies, and the potential use for measurement purposes by means of some real implementation and the consequent discussion about experimental results. For all these systems, we have taken into account some restrictions and conditions of associated devices such as light excitation sources, photo detector devices and, of course, the design conditions of optical fiber systems and sensors.

Author details

Miguel A. Pérez, Olaya González and José R. Arias

University of Oviedo, Spain

References

[1] Altamirano, M, Senz, A, & Gasponer, H. E. Luminescence quenching of tris (2,2-bi-pyridine) ruthenium(II) by 2,6-dimethylphenol and 4-bromo-2,6-dimethylphenol in sol-Gel processed silicated thin films. J. Colloid Interface Sci, (2004). , 270, 364-370.

[2] Barragán, N. A, Pérez, M. A, Campo, J. C, & Alvarez, J. C. Photo detection of low level phosphorescence produced by low level oxygen concentrations using optical system based on fiber optical and avalanche photodiode. Proc. IEEE-ISIE Puebla (Mexico), (2000). , 596-601.

[3] Basu, B. J, et al. Optical oxygen sensor coating based on the fluorescent quenching of a new pyrene derivative. Sensors and Actuators, (2005). , 104, 15-22.

[4] Campo, J. C, Pérez, M. A, Mezquita, J. M, & Sebastián, J. Circuit-design criteria for improvement of xenon flash-lamp performance (lamp life, light-pulse, narrowness, uniformity of light intensity in a series flashes). Proc. IEEE-APEC, Atlanta (USA), (1997). , 1057-1061.

[5] Campo, J. C, Pérez, M. A, González, M, & Ferrero, F. J. Measurement of air moisture by the phosphorescence lifetime of a sol-gel based sensor. Proc. IEEE-IMTC, Baltimore (USA), (2000).

[6] Campo, J. C, Barragán, N, Pérez, M. A, & Álvarez, J. C. A comparison between different excitation/detection systems for luminescence lifetime based instrumentation. Proc. IEEE-IMTC, Anchorage (USA); May, (2002).

[7] Carleos, C. E, et al. On-line estimation of fresh milk composition by means of Vis-NIR spectrometry and partial least squares method (PLS). Proc. IEEE-IMTC, Victoria (Canada), (2008).

[8] Cleveland, W. S. Robust locally weighted regression and smoothing scatterplots. J Amer Statist Assoc 74: (1979). , 829-836.

[9] Costa, J. M, et al. A critical comparison of different solid supports to develop room-temperature phosphorescence sensing phases in air moisture", Sensors and Actuators B, (1997).

[10] Cozzolino, D, et al. Chemometrics and visible-near infrared spectroscopy monitoring of red wine fermentation in a pilot scale. Biotech. and Bioeng. D01.1002/bit. 21067, (2006).

[11] De Graff, B. A, & Demas, J. N. Luminescence-based oxygen sensors. Reviews in fluorescence. Springer Science, (2005). , 2, 125-151.

[12] Demas, J. N, Degraff, B. A, & Coleman, P. Oxygen sensors based on luminescence quenching. Anal. Chem. (1999). , 793A-7800.

[13] Dessy, R. Waveguides as chemical sensors". Anal. Chem. Nº 19, Oct. (1989). , 61, 1079-1088.

[14] Douglas, P, & Eaton, K. Response characteristics of thin films oxygen sensors, Pt and Pd octaethylporphyrins in polymer films. Sensors and Actuators, (2002). , 82, 200-208.

[15] Draxler, S, et al. Effect on polymers matrices on the time-resolved luminescence of a ruthenium complex quenched by oxygen. J. Phy. Chem., (1995). , 99, 3162-3167.

[16] Eshkenazi, I, et al. A Three-cascade enzyme biosensor to determine lactose concentration in raw milk. J. Dairy Sci. 83, (2000). , 1939-1945.

[17] Fisher, R. P, & Winefordner, J. D. Pulsed source-time resolved phosphorimetry. Analyt. Chem. Nº 6, May, (1972). , 44, 948-956.

[18] Gewehr, P. M, & Delpy, D. T. Optical oxygen sensor based on phosphorescence lifetime quenching and employing a polymer immobilised metalloporphyrin probe. Part 1: theory and instrumentation. Medic. & Biol. Eng. & Comp. Jan (1993). , 2-10.

[19] Gil, R, Gómez, E, Martínez, A, & López, J. M. Evolution of the CIELAB and other spectrophotometric parameters during wine fermentation. Influence of some pre and postfermentive factors. Food Research Internat. (1997). , 30(9), 699-705.

[20] Gillanders, R. N, Tedford, M. C, Krilly, P. J, & Bailey, R. T. A composite Sol-Gel fluoropolymer matrix of dissolved oxygen optical sensing. J. Photochem. Photobiol. (2004). , 163, 193-199.

[21] Grillo, G. J, Pérez, M. A, & Florencias, A. E. Synchronic filter based on switched capacitor filters for high stability phase-detectors systems". Proc. IEEE-IMTC, Sorrento (Italy), April, (2007).

[22] Hercules, D. M. Fluorescence and phosphorescence analysis. J. Wiley and Sons, N. York, (1966).

[23] Hurtubise, R. J, Ackerman, A. H, & Smith, B. W. Mechanistic aspects of the oxygen quenching of the solid-matrix Phosphorescence of perdeuterated phenanthrene on partially hydrophobic paper. App. Spectros. (2001). , 55, 490-495.

[24] Janata, J, & Berzegh, A. Chemical sensors. Analyit. Chem. Nº 12, June, (1988). , 60, 62R-69R.

[25] Janata, J, Josowicz, M, & Devaney, D. M. Chemical sensors. Analyt. Chem. Nº 12, June, (1994). , 66, 207R-228R.

[26] Janata, J, & Josowics, M. Chemical sensors. Analyt. Chem. Nº 12, June, (1998). , 70, 179R-208R.

[27] Kneas, K. A, Xu, W, Demas, J. N, & De Graff, B. A. Dramatic demonstration of oxygen sensing by luminescence quenching. J. Chem. Ed., 696, (1997).

[28] Lechuga, L. M, Calle, A, & Prieto, F. Optical sensor based on evanescent field sensing. Part I: surface Plasmon resonance sensors". Analyt. Chem. suppl 1), Jan, (2000). , 19, 54-60.

[29] Martens, H, & Naes, T. Multivariate calibration". Wiley. Chichester. (1989).

[30] Martin, M. J, Wickramasinghe, Y. A. B. D, Newton, T. P, & Crowe, J. A. Fiber-optics and optical sensors in medicine" Med. Biol. Eng. Comp. (1987). , 25, 597-604.

[31] Mills, A. Response characteristics of optical sensor for oxygen: models based on a distribution on t_0 or Kq", Analyst, (1999). , 124, 1301-1307.

[32] Narayanaswamy, R. Optical chemical sensors: transduction and signal processing. Analyst, April, (1993). , 118, 317-322.

[33] OIVOeno Resolution 1/(2006). Determination of the chromatic characteristics according to CIElab. Certificate as. Paris, July, 28th 2006.

[34] OIVCompendium of international methods of wine and must analysis. International Organisation of Vine and Wine. Edition (2006).

[35] Ogurtsov, V. I, & Papkovsky, D. B. Selection of modulation frequency of excitation for luminescence lifetime-based oxygen sensors. Sensors and Actuators, (1998). , 51, 337-381.

[36] Pawlowsky, M, & Wilson, D. F. Monitoring of the oxygen pressure in the blood of live animals using the oxygen dependent quenching of phosphorescence" Adv. Esp. Med. Biol, (1992).

[37] Pérez, M. A, Campo, J. C, González, M, & López, P. Design of a multi-parameter substance analyzer", Proc. IEEE-IMTC, Baltimore (USA) (2000). , 3, 1584-1589.

[38] Pérez, M. A, & Muñiz, R. Optical fibre turbidimeters. Ch. 8 of Optical Fibre. New developments, Intech, Dec. (2009).

[39] Prieto, M, Braña, E, Campo, J. C, & Pérez, M. A. Thermal performance of a controlled cooling system for low-level optical signals. App. Thermal Eng. March (2004). , 24, 2041-2054.

[40] R Development Core Team. R: A language and environment for statistical computing. R Foundation for Statistical Computing, Vienna, (Austria). 2007.

[41] Seitz, W. R. Chemical sensors based on fiber optics". Analyt. Chem. Nº 1, Jan. (1984). , 56, 16A-34A.

[42] Torre, C, Muñiz, R, García, B, & Pérez, M. A. A new, low-cost RGB colorimeter for wine industry based on optical fibers. Proc. XIX World IMEKO Conf. Lisbon (Portugal), (2009).

[43] Tsenkova, R, et al. Near-infrared spectroscopy for dairy management: measurement of un-homogenized milk composition. J. Dairy Sci. 82: (1999). , 2344-2351.

[44] Tsenkova, R, et al. Near-infrared spectroscopy for biomonitoring: cow milk composition measurement in a spectral region from 1100 to 2400 nm. J. of Animal Sci. 78: (2000). , 515-522.

[45] Tsenkova, R. Visible/near-infrared spectrometry and its device. US Patent 7570357, Aug (2009).

[46] Weiss, G. H, Bendler, J. T, & Schlesinger, M. F. Continuous-side model for Langmuir gas sorption in glassy polymers. Macromol. (1992). , 25, 990-992.

[47] White, C. E, & Argauer, R. J. Fluorescence analysis. CRC Press, Oct. (1970).

[48] Wolfbeis, O. S. Fiber-optic chemical sensors and biosensors, I & II. CRC Press, (1991).

[49] Young-Ha Woo et alDevelopment of a new measuring unit (MilkSpec 1) for rapid determination of fat, lactose and protein in raw milk using NIR transmittance spectroscopy. Appl. Spectros. (2002). , 5(56)

Chapter 11

Investigation of Bioluminescence at an Optical Fiber End for a High-Sensitive ATP Detection System

Masataka Iinuma, Ryuta Tanaka, Eriko Takahama,
Takeshi Ikeda, Yutaka Kadoya and Akio Kuroda

Additional information is available at the end of the chapter

http://dx.doi.org/10.5772/52747

1. Introduction

In biological research, the luminescience from fluorescent proteins or luminescent enzymes is widely applied for monitoring a change of environment at a cell. Biomolecules used as the probe, such as Green Fluorescence Protein (GFP) or luciferase molecules found in fireflies can respond to the existence of specific molecules or ions and subsequently emit a photon. The detection of a specific molecule can then be confirmed by detecting the emitted photons efficiently with a photon detector. A highly efficient detection of the luminescence is normally essential to realization of a high sensitivity to the specific molecules or ions and an improvement of the sensitivity can upgrade the capability of detection in a low concentration of sample solution. Therefore, there are many efforts to improve the efficiency of the collection of emitted photons and of the optical coupling to the photon detector.

A straightforward method is to directly detect the luminescence from the sample solution in a test tube with a single photon detector via simple coupling optics as shown in Fig. 1. This detection system is very simple and easy-operational, so that it has been widely used for various applications so far. To realize high efficiency detection, however, this method needs a single photon detector with the wide photon-sensitive area, which is ideally larger than a photon-emission area in the test tube. Here, we are introducing an alternative method, where the luminescent biomolecules are immobilized at an optical fiber end and the luminescence is detected by a photon detector which is optically coupled to the other optical fiber end. Fig. 2 illustrates the optical fiber-based system. This method has been investigated for application to a fiberoptic biosensor, which is constructed by immobilizing either an enzyme or an antibody. A review of this method is given in reference [1] and [2].

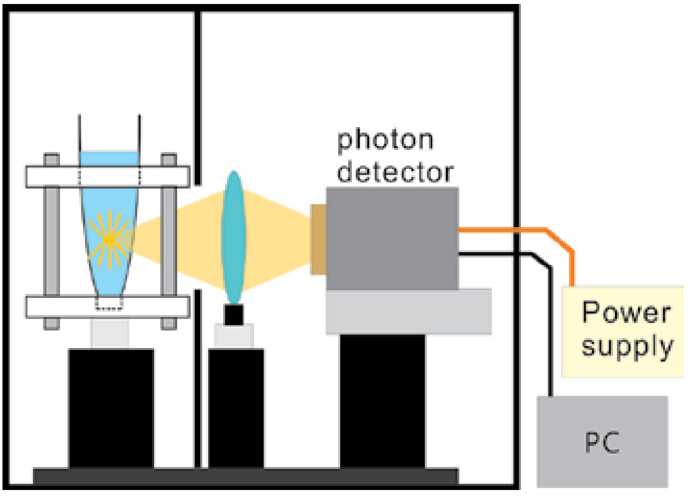

Figure 1. Direct detection system of luminescence

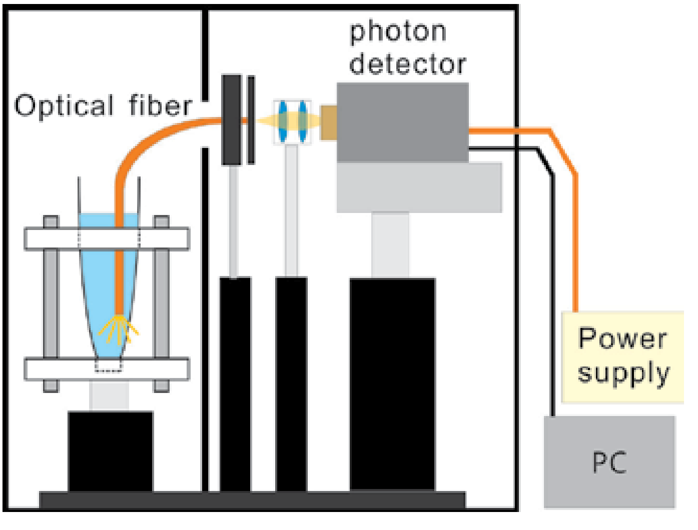

Figure 2. Optical fiber-based system of luminescence

This method has three merits. The first one is to permit a local detection within the sample solution, because the optical fiber end functions as a needle-like probe. Meanwhile, the method as shown in Fig. 1 is suitable for detecting the luminescence from a large area in the sample solution. The second one is that the detection scheme does not require that the photon detection is very close to the sample solution. This feature makes it easier to mount the sensing parts in integrated bioengineering, such as μ -TAS. The third merit is that single photon detectors with a small sensitive area are also available, because the photon-emission area, which is almost identical to the cross section of the core part in the optical fiber, is small. In general, single photon detectors have lower dark counts for smaller sensitive area. Low noise is very important, because it essentially gives the upper limit of the sensitivity of photon detection. Recently, single photon detectors using avalanche photo diodes (APDs) have become widely available with good performance, but their sensitive area is small and typically 0.1 mm. The luminescence detection with the optical-fiber based system allows us to fully use the merits of compactness, high quantum efficiency, and low noise of these APD detectors. On the other hand, single photon detectors using compact and cooled photomultiplier tubes (PMTs) are also available, since they have the characteristics of low noise and much larger sensitive area than the APD's. Moreover, their quantum efficiency is not so much lower than the APD's. The fiber-based system with these PMT detectors can make a fully use of the merits of large sensitive area and low noise of the PMTs, although the quantum efficiency is lower than the APD's.

We have built detection systems of bioluminescence at an optical fiber end and investigated the sensitivity of Adenosine triphosphate (ATP) detections by using an APD-type as described in [3] and [4]. In this chapter, results with a PMT-type detector are presented in comparison with the results by using the APD-type photon detector. We also discuss the reason of limiting the present sensitivity in the system with the PMT-type detector. ATP is a good indicator of biochemical reaction or life activity, since ATP is considered as the universal currency of biological energy for all living things. Therefore, there are many efforts to develop ATP-sensing techniques for compact and efficient ATP detection in reference [5-7]. In particular, high-sensitivity detection of ATP can indicate the existence of microorganisms even in low numbers. Thus, a compact, simple, and easy-operational system with extremely high sensitivity has been desirable.

One well-known and powerful method for highly sensitive ATP detection is to use the chemical reaction involved in thebioluminescence, the luciferin-luciferase reaction in reference [8]. In this reaction, after one ATP molecule and one luciferin molecule are bound to one luciferase molecule, and the luciferin molecule is oxidized using the energy of ATP. As consequence, one photon is emitted during the transition from the excited state to the ground state of the oxidized luciferin molecule bound to the luciferase molecule. The emission of one photon indicates the use of the energy of one ATP molecule. In the method using the luciferin-luciferase reaction, the efficient detection of the bioluminescence is essential for high-sensitivity detection of ATP.

The oxidation of luciferin is catalysed by the enzyme luciferase, so that the immobilization of luciferase molecules on solid probes of various sizes allows highly sensitive and local detection of ATP. Three types of immobilization have been used: firstly attachment to the cell surface in [9], secondary attachment to small particles, such as nanoparticles in [10], glass beads and rods in [11], thirdly attachment to extended objects with a size in the centimeter range, such as strips in [12] and [13], and films in [14]. For the ATP-detection on the intermediate scale below 1 millimeter, a fiberoptic probe employing immobilized luciferase in [2] as well as microchips in [15] and [16] is utilizable. Therefore, the efficient detection system of bioluminescence at an optical fiber end can achieve the local detection of ATP. The realization of highly sensitive detection of ATP potentically provides the local detection of extremely low number of microorganisms. Thus, it is desirable to construct a highly efficient detection system of the bioluminescence at an optical fiber end and to evaluate the detection limit with the system. In order to explore possibilities for improving the detection limit, moreover, it is also necessary to investigate the bioluminescent reaction at an optical fiber end.

The rest of this chapter is organized as follows. In sec. 2, we describe a concept for the construction of the optical fiber-based system and show how to construct the detection systems by using the PMT detector. In sec. 3, we describe the sensitivity test with the constructed system and show the results are consisitent with the APD, but also show that the sensitivity can not reach the expected detection limit. In sec. 4, we present the results of kinetic properties obtained from experimental data on the bioluminescence and clarify a dominant reason of restricting the detection limit.Sec. 5 summarizes prensent results and future problems.

2. Construction of the optical fiber-based system

2.1. General concept

For the construction of an efficient detection of a bioluminescence, it is necessay to consider a collection efficiency of the luminescence at the optical fiber end and a coupling efficiency between the other optical fiber end and a photon detector as described in [4]. Using the optical fiber with a core diameter ϕ_0 and a numerical aperture NA_0, the collection efficiency of the luminescence η at the optical fiber end depends only on NA_0 as shown in Fig.3.

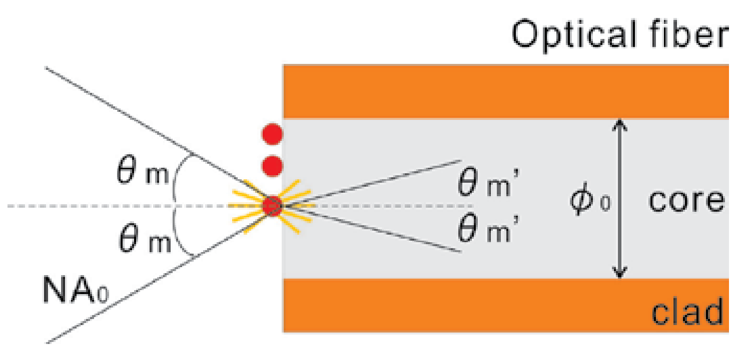

Figure 3. Luminescence at the optical fiber end. θ_m is a maximum opening angle for light propagation in the optical fiber.

From the simple calculation of the solid angle with a maximum open angle θ_m, $\eta(NA_0)$ can be expressed as,

$$\begin{aligned}\eta(NA_0) &= \tfrac{1}{2}(1-\cos\theta_m)\\ &= \tfrac{1}{2}\left[1-\sqrt{1-\left(\frac{NA_0}{n_w}\right)^2}\right],\end{aligned} \tag{1}$$

where n_w is the refraction index of the substance surrounding the optical fiber end. In immersing this optical fiber end into water, its value should be identical to the one of water, which is about 1.33.The caluculated values of the collection efficiency $\eta(NA_0)$ using Eq. (1) at n_w=1.33 are shown in Fig.4 as a function of NA_0. It is easy to see that $\eta(NA_0)$ monotonically increases with NA_0.

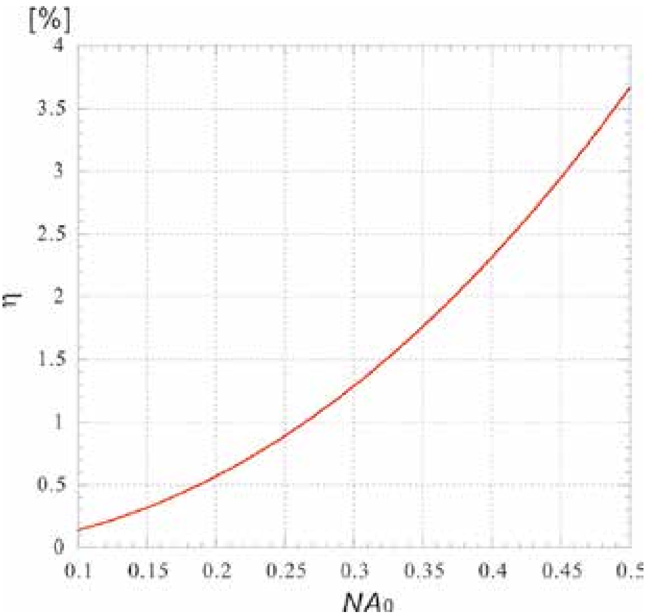

Figure 4. Calculated values of the collection efficiency η as a function of NA_0 at n_w = 1.33.

In the following, let us consider the situation where the other optical fiber end is optically coupled to a photon detector with a detection window of diameter ϕ_4 and with a circular sensitive area having a diameter ϕ_3 and a numerical aperture NA_3. The coupling efficiency ε between the optical fiber end and the photon detector depends on ϕ_0, NA_0 of the optical fiber and ϕ_3, NA_3, ϕ_4 of the photon detector used.The number of emitted photons is proportional to the square of ϕ_0 and $\eta(NA_0)$ monotonically increases with NA_0, so that the number of the transmitted photon to the other optical fiber end is proportional to ϕ_0^2 and $\eta(NA_0)$. On the other hand, the coupling efficiency ε generally decreases as ϕ_0 or $\eta(NA_0)$ increases for the fixed ϕ_3, NA_3, and ϕ_4. Thus, we can define the following formula for a figure of merit (FOM) and optimize ϕ_0, NA_0 and parameters of the coupling optics x_i for the fixed values of ϕ_3, NA_3, and ϕ_4 to maximize the FOM:

$$\mathrm{FOM} = \phi^2 \cdot \eta(NA_0) \cdot \varepsilon(\phi_0, NA_0, x_i, \phi_3, NA_3, \phi_4) \tag{2}$$

It should be noted that the coupling efficiency ε can be ideally 100 % under the condition of $\phi_0 \le \phi_3$ and $NA_0 \le NA_3$.In many cases, the condition $NA_0 \le NA_3$ is satisfied when using the typical photon detector. Under the condition $NA_0 \le NA_3$, thus, we can categorize into two cases: case (1) is $\phi_0 \le \phi_3$ and case (2) is $\phi_0 > \phi_3$. In the case (1), ε is constant and can be ideally 100 %, so that the detection efficiency excluding the quantum efficiency of the photon detector is only limited to $\eta(NA_0)$. Therefore, the optimization of ϕ_0 and NA_0 is not necessary. The conditions of $\phi_0 = \phi_3$ and $NA_0 = NA_3$ both maximize the FOM and the sensitivity becomes highest. In the case (2), however, the optimization of ϕ_0 and NA_0 and a specific design of the coupling optics are necessary, because the coupling efficiency ε decreases as ϕ_0 or NA_0 increases.

2.2. Construction with a cooled PMT detector

2.2.1. Photon detectors

To construct the optical fiber-based system, a choice of a single photon detector is very important. Photon detectors generally have two significant factors contributing to the sensitivity of detection for weak light: the efficiency and the dark counts of the detector. Recently, two types of single photon detectors, which are a cooled APD and a small size of cooled PMT, are available. The cooled APD which can detect for single photons is mostly used because of the high quantum efficiency and the low dark counts. The sensitive area must be very small (ϕ_0 ~0.2mm), but the quantum efficiency is several times larger than that of a typical PMT. Furthermore, it has the useful characteristics of compactness, easy operation, and durability compared to a typical PMT detector. On the other hands, the compact size of cooled PMT is also useful for the optical fiber-based system. The quantum efficiency is typically lower than the APD, but the sensitive area is roughly 10 times larger than the APD's in spite of the same dark counts as the cooled APD. Therefore, it is very easy to construct a coupling optics to the sensitive area of the detector with the high sensitivity.

We selected the PMT counting head (H7421) manufactured by Hamamatsu Photonics K.K. for this system. Its characteristics are summarized in Tab. 1. For comparison, we also present the characteristics of the APD-type photon counting module (SPCM-AQR-14) provided by Perkin Elmer. Ltd. It has already been verified that this APD is applicable to the fiber-based system by our previous investigation as discussed in [3], [4].

	Quantum efficiency (η_{qe})	**Dark noise**	**sensitive area (ϕ_3)**	**Numerical Aperture (NA_3)**	**Detection window (ϕ_4)**
PMT (H7421)	40% at 550nm	100 s^{-1}	5.0 mm	0.123	7.2 mm
APD (SPCM-AQR-14)	55% at 550nm	100 s^{-1}	0.175 mm	0.78	6.16 mm

Table 1. Characteristics of photon detectors in reference [17] and [18]

The value of NA_3 can be calculated from the geometrical structure between the sensitive area and the photon detection window.

2.2.2. Coupling efficiency

As showing in section 2.1, under the condition of $\phi_0 > \phi_3$, it is necessary to optimize ϕ_0, NA_0 and to design the coupling optics for maximal sensitivity. In the use of the PMT detector, it is not absolutely necessary to optimize ϕ_0, NA_0, because the characteristics of ϕ_3=5.0mm sufficiently satisfies the condition of $\phi_0 < \phi_3$ for the typical optical fiber. For easy construction, here, the optical fiber end was directly connected to the attachment of the PMT counting head without the additional coupling optics as shown in Fig. 5.

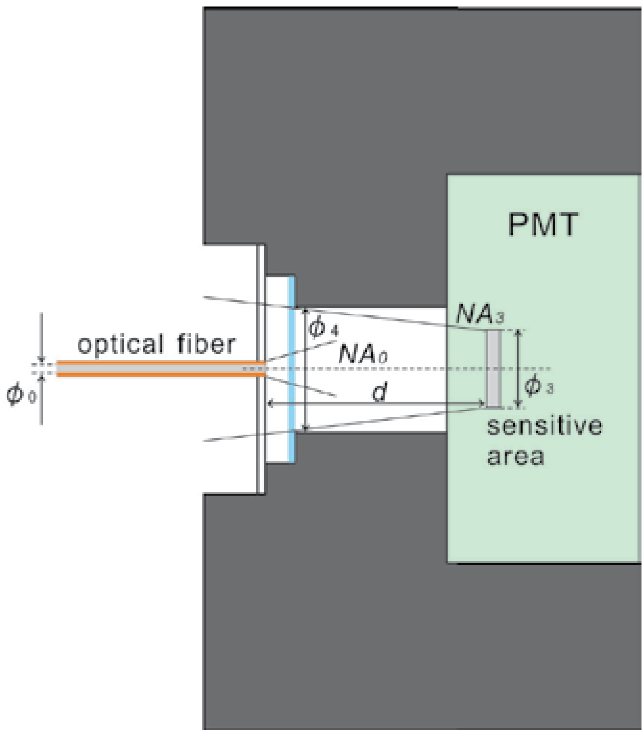

Figure 5. Geometrical structure of the PMT counting head

The coupling efficiency $\varepsilon(\phi_0, NA_0)$ in such geometrical structure can be obtained by the statistical method with matrix formalism in paraxial optics, which can describe the propagation of light. The light at the initial state (r_i, r'_i), where r_i is a distance from an optical axis and r'_i is a slope of the light direction, can be transferred by some matrices. In the case of Fig. 5, the matrix expressing free-space propagation can transfer the initial state (r_i, r'_i) at the optical fiber end to the final state (r_f, r'_f) at the PMT sensitive area. We obtained the value of

$\varepsilon(\phi_0, NA_0)$ by counting the number of the final states inside the sensitive area for many initial states selected with random numbers, which were generated by using the software package based on algorithm of Mersenne Twister in reference [19]. The calculated results are shown as a function of NA_0 in Fig. 6. Since the value of ϕ_3 is approximately 5 times as large as one of ϕ_0, the coupling efficiency $\varepsilon(\phi_0, NA_0)$ is independent of ϕ_0, but monotonically decreasing with NA_0. Therefore, we calculated the FOM for confirming the existence of optimal conditions for ϕ_0, NA_0. Fig. 7 shows the plot of the calculated FOM as a function of NA_0 and obviously indicates that the FOM is almost constant to NA_0. Thus, we determined NA_0=0.37 and ϕ_0=1.0 *mm* because of availability and flexibility of the optical fiber. These values easily give the coupling efficiency $\varepsilon(\phi_0, NA_0)$ of 21.7% and FOM×100 of 0.420.

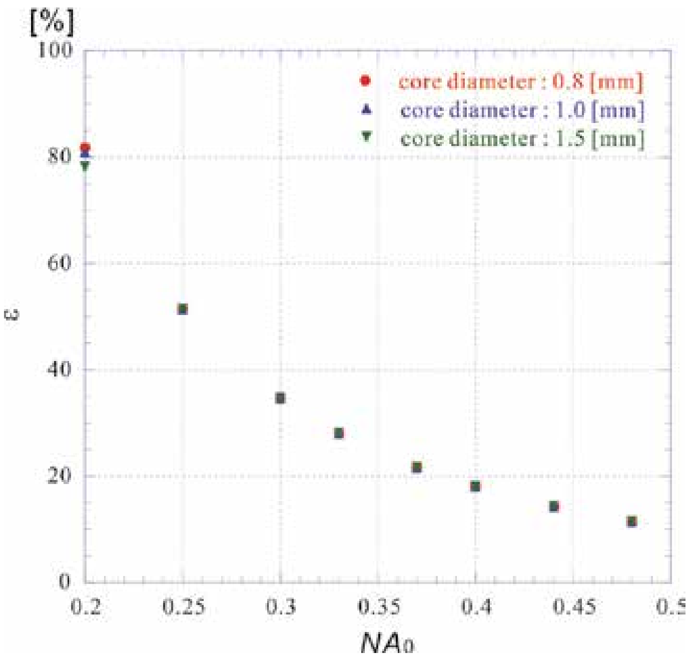

Figure 6. Calculated values of the coupling efficiency ϕ_0 as a function of NA_0. The solid circles represent the values at ϕ_0=0.8 *mm*, the solid triangles are the values at ϕ_0=1.0 *mm*, and the solid inverse triangles are the values at ϕ_0=1.5 *mm*.

On the other hands, in the use of the APD, the optimization of NA_0=0.37, ϕ_0=0.6 *mm* and the design of the optimal coupling optics are absolutely necessary. A simple optically coupling way is shown in Fig. 8. With the above APD, the condition of FOM×100 and $\varepsilon(\phi_0, NA_0)$ maximizes the FOM and the value of $\eta(NA_0)$ is 0.234. The determined design parameters of the coupling optics give the maximum ε of 33.3% and NA_0 of 1.97%. The detailed description about the determination of the design parameters is given in [3] and [4].

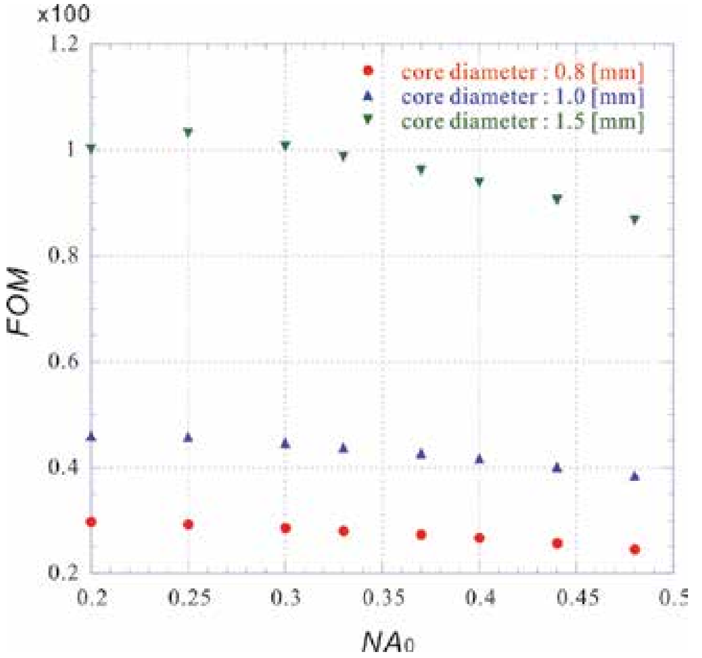

Figure 7. Calculated values of FOM as a function of NA_0. The solid circles represent the values at $\phi_0 = 0.8\ mm$, the solid triangles are the values at $\phi_0 = 1.0\ mm$, and the solid inverse triangles are the values at $\phi_0 = 1.5\ mm$.

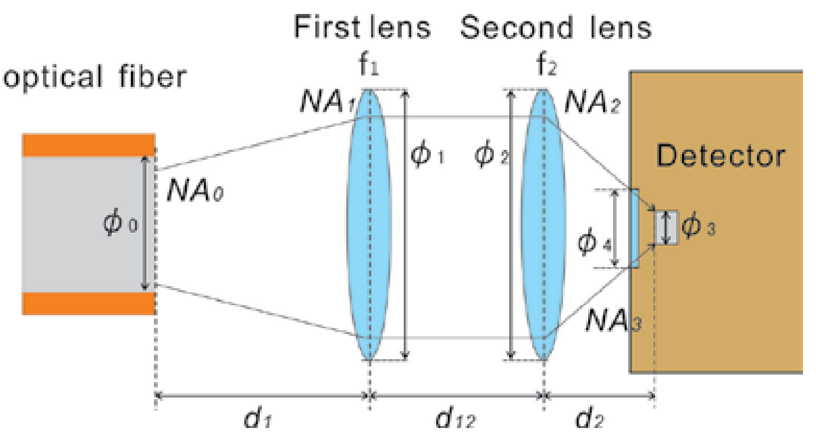

Figure 8. One example of additional coupling optics

The relative sensitivity for the bioluminescence detection can be compared by using a product of FOM and the quantum efficiency η_{qe} of the detector as an indicator. For the PMT, the value of $(\mathrm{FOM} \cdot \eta_{qe}) \times 100$ is 0.168 and 0.129 for the optimal values of the above APD.In such direct connection, the sensitivity with the PMT is almost same as with the APD. For the system with the PMT, furthermore, it should be noted that the coupling efficiency ε at NA_0=0.37 and ϕ_0=1.5 mm can be 100% using the additional coupling optics as shown in Fig. 8. These values give $(\mathrm{FOM} \cdot \eta_{qe}) \times 100 = 1.77$, which is about 10 times larger than the present value.

3. Sensitivity test for ATP detection

3.1. Luciferin-luciferase reaction

Bioluminescence in living organisms, such as fireflies and some marine bacteria, typically occurs due to the optical transition from the excited state to the ground state of oxidized luciferin molecules produced by the luciferin-luciferase reaction under the catalytic activity of luciferase molecules. This reaction can be expressed by the following squential of reaction steps:

$$\mathrm{E} + \mathrm{S} + \mathrm{LH_2} \rightleftarrows \mathrm{C_1} + \mathrm{PP}_i$$

$$\mathrm{C_1} + \mathrm{O_2} \rightarrow \mathrm{C_2} + \mathrm{AMP} + \mathrm{CO_2} + \gamma$$

$$\mathrm{C_2} \rightleftarrows \mathrm{E} + \mathrm{P},$$

where E indicates luciferase, S ATP, LH_2 luciferin, PP_i pyrophoric acid, C_1 is an enzyme-substrate compound $\mathrm{E} \cdot \mathrm{LH_2}$-AMP, AMP adenosine monophosphate, P oxyluciferin (oxidized luciferin), C_2 a luciferase-oxyluciferin compound, and γ a photon in reference [20]. The emission of one photon at the position of luciferase molecule corresponds to the use of the energy of one ATP molecule. Against the second reaction which is a rate-limiting reaction in the above reaction chain, it is known that the following reaction is competitive,

$$\mathrm{C_1} + \mathrm{O_2} \rightarrow \mathrm{C_3} + \mathrm{H_2O_2}$$

$$\mathrm{C_3} \rightleftarrows \mathrm{E} + \mathrm{L\text{-}AMP},$$

where L - AMP represents dehydroluciferyl-adenylate, C_3 is an enyzme-substrate compond $\mathrm{E} \cdot$L-AMP as described in [21]. This reaction does not induce the photon emission. Dehydro-luciferyl-adenylate L - AMP as well as oxyluciferin is known as a competitive inhibitor to the equilibrium reaction in [22].

In the presence of enough luciferin molecules, the immobilization of luciferase molecules at the optical fiber end allows us to sense the present of ATP around the fiber end using single photon counts. For this purpose, we used a compound protein containing a silica-binding protein (SBP) molecule and a luciferase molecule (SBP-luciferase), which were recently synthesized by Taniguchi and co-workers in [23]. This protein makes it possible to immobilize a lucuferase molecule on the optical fiber end through a SBP molecule retaining its activity. The spectrum of the emitted photons shows a central wavelength of 550 nm and a width of about 100 nm in reference [24] and [25]. Both photon detectors of the APD and the PMT have the large quantum efficiency at 550 nm, the photon counting detectors are suitable for ATP sensing.

3.2. Michaelis-Menten formula

In the solution containing nonlocalized homogeneously dispersed luciferase and ATP, the Michaelis-Menten formula is applicable to the enzyme reaction as descibed in [26]. In the presence of sufficient luciferin molecules in the solution, a rate of emitted photons at steady state v_γ can be expressed as the Michaelis-Menten formula,

$$v_\gamma = \frac{V_{max} s}{s + K_M}, \tag{3}$$

where V_{max} is a maximum reaction rate which is equivalent to a product of a concentration of luciferase molecules and a reaction constant h_1 from C_1 to C_2, K_M is the Michaelis constant, and s is the ATP concentration. In the fiber-based system for sensing dispersed ATP molecules, on the other hands, an ATP-flow generated by a gradient of ATP concentration around the luciferase-terminated fiber end carries ATP molecules to the vicinity of immobilized luciferase molecules. One of ATP molecules is bound to one immobilized luciferase molecule near them and subsequently used for the luciferin-luciferase reaction at this fiber end. By solving reaction-diffusion equations, as described in [4], we have confirmed that an ATP diffusion rate is not a rate-limiting process when the number of immobilized luciferase molecules is 10^{11} order and the ATP diffusion constant is $D = 0.5 \times 10^{-3} mm^2 / s$ given in [27]. Therefore, the Michaelis-Menten formula Eq. (3) can be also applied for the fiber-based system without change.

3.3. Mesurement of the sensitivity

3.3.1. Experimental setup

Fig.9 shows the experimental setup for the sensitvity test and the investigation of bioluminescence at the optical fiber end. One optical fiber end was optically connected to the PMT as describing in the previous section. On the other fiber end, the luciferase molecules were immobilized via SBP molecules and the bioluminescent reaction occurs by immersing the luciferase-terminated fiber end into a sample solution. The emitted photons were transmitted to the PMT through the optical fiber and TTL pulses outputted from the PMT were counted by a PC card installed in a personal computer(PC). To reducing the background light, the whole system was put into the dark box.

For the observation of the bioluminescence rising, a test tube containing the sample solution was fixed on the Z-stage, which is a motorized stage and externally controllable. By raising the test tube for immersing the luciferase-terminated fiber end after starting the data acquisition system, the photon counts rising from the background level and subsequently reaching a maximum were observed with time. The numbers of detected photons during 0.0298 s or during 0.1 s were recorded every 0.0321s or every 0.1s by the PC, respectively. These values were obtained from a calibration test of data acquisition system. The details on the experimental setup and the measurements are described in reference [28].

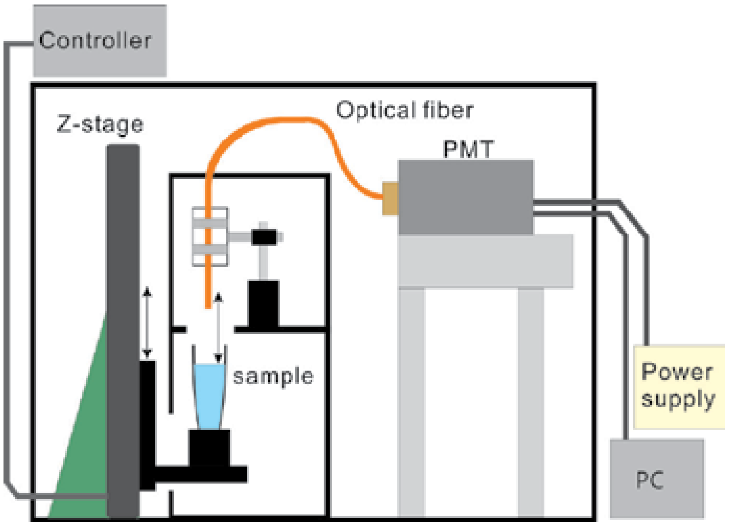

Figure 9. Experimental setup for investigation of bioluminescence at the optical fiber end

3.3.2. Immobilization of luciferase

Before immobilizing luciferase molecules, we cut the optical fiber and cleaned the cut surface with ethanol and Tris buffer (0.25mM Tris-HCl with 0.15 M NaCl). Different from the previous experiments with the APD, we cleaved the optical fiber for making a flat surface on the fiber end, which can reproduce the number of immobilized luciferase. The flat surface also allows us to indivisually evaluate the number of immobilized luciferase molecules by using element analysis, although the sensitivity with the flat surface is about 10 times lower than the one with the appropriately irregular surface cut without the cleaving technique as described in [29]. The cut surface was direcly observed by using the fiber scope and checked its flattness by eyes. After cleaning, the surface was immersed in a solultion of SBP-luciferase and was left at a temperature of 3℃ to 6℃ for a period of about two hours.

For evaluating the number of immobilized luciferase molecules, element analysis to the fiber end was carried out by using Xray Photoemission Spectroscopy (XPS). We measured a spectrum including peaks from nitrogen in the SBP-luciferase and from silicon on the surface of the fiber end which made with the silica and obtained the ratio of the area of the nitrogen-peak to the one of the silicon-peak. Utilizing the absolute number of silicon on the surface of the fiber end, the surface density of immobilized luciferase molecules was determined to be $2.0\times10^{10}mm^{-2}$. By repeating the same measurement and analysis, the error of the surface density was estimated to be 15 %.

3.3.3. Sample solutions

The samples were a 1:4:4:31 mixture of 20 mM D-luciferin solution, Tris buffer solution(250 mM Tris-HCl mixed with 50 mM $MgCl_2$), ATP solution, and distilled water. Several solutions of ATP with different ATP concentrations were made by diluting the ATP standard in ATP Bioluminescence Assay Kit CLS II manufactured by Roche Co. Ltd. A series of sample solutions with different ATP concentrations were prepared in advance. To obtain a background before the ATP measurements, an additional sample without ATP was also produced by mixing distilled water instead of the ATP solution.

3.3.4. Results

The time dependence of photon counts per 0.1-s interval were measured in immersing the luciferase-terminated fiber end into the sample solutions with various ATP concentration and converted to the values of photon counting rate. A typical result for 100 μl at the ATP concentration of 1.65×10^{-6} M is shown in Fig. 10.

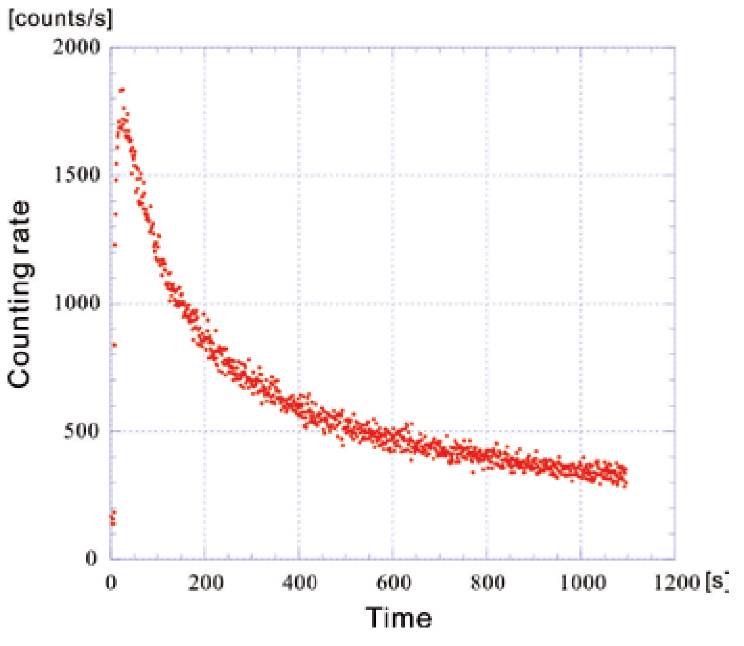

Figure 10. Time dependence of measured counting rate for 100 μl at the ATP concentration of 1.65×10^{-6} M.

The photon counts rise up, reach a maximum at about 100 s, and decrease toward the background level with time scale of 1000 s after the immersion. The background level was about 130 s^{-1}, which was essentially determined by the dark counts. For observing the detection limit of the ATP concentration, we obtained the integrated counts of detected photons over the time range from 0 to 100 s for various ATP concentrations. The result is shown as a function of the ATP concentration in Fig. 11.

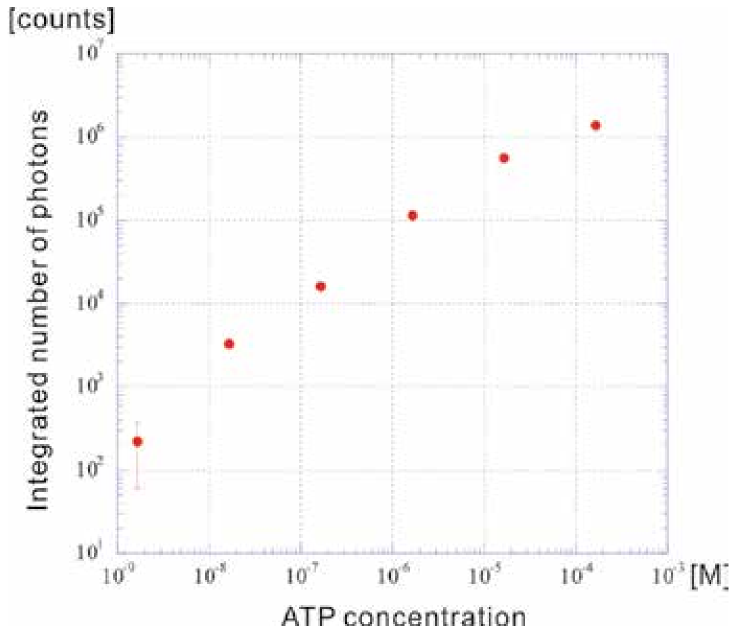

Figure 11. Number of photons integrated over the time range from 0 to 100 s as a function of ATP concentration.

Statistical errors were estimated as one standard deviation assuming Poisson distribution. From Fig. 11, the sensitivity in this system is limited to 1.65×10^{-9} M, whichcorresponds to a number of ATP molecules of about 10^{-14} mol in the 10 μl solution. This value is about 10 times higher than the one in the previous experiment with the APD as described in [3] and [4], although the FOM of this system is almost same as of the APD system. In this experiment, the surface flatness of the luciferase-terminated fiber end makes us identify the effective area as the cross section of the cut surface, as while the effective area of the cut surface in the previous experiment with the APD system was enlarged due to a surface asperity.On the effect of such different cutting ways, we have already confirmed that the sensitivity in the flat surface is about 10 times lower than the one in the appropriately irregular surface cut without the cleaving technique. Therefore, the above results are consistent with our previous results by using the APD.

To check the ATP concentration dependence of the photon counting rate at maximum, the average of counts in sixteen 1-s intervals around the time at which the counting rate become maximal was calculated for each ATP concentration. The results are indicated by the solid circles in Fig. 12. By the analysis of fitting data points in Fig. 12 to Eq. (3), we obtained the Michaelis constant of $K_M = 6.47 \times 10^{-5}$ M and the maximum reaction rate of $V_{max} = 7.38 \times 10^4 s^{-1}$.

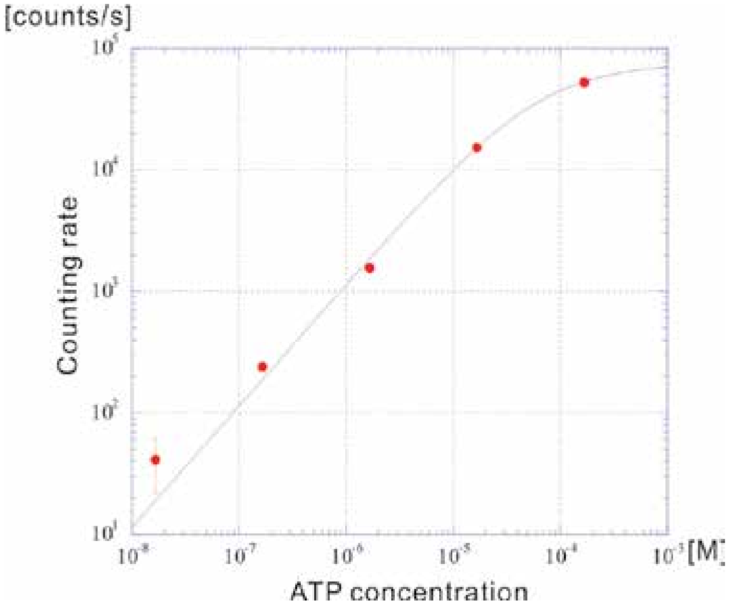

Figure 12. Measured photon counting rate as a function of ATP concentrations. Solid line is a curve obtained by fitting data with the Michaelis-Menten formula.

3.3.5. Discussion

The detection limitis essentially determined by both of the parameter V_{max} and the dark noise of the photon detector. Since the V_{max} can be expressed as $V_{\max} = \varepsilon_{total} \cdot h_1 \cdot e_0$, where h_1 is a reaction rate of one luciferase molecule, e_0 is a total number of immobilized luciferase molecules on the optical fiber end and ε_{total} is a total detection efficiency, we can calculate the value of V_{max} with $\varepsilon_{total} = \eta \cdot \varepsilon \cdot \eta_{qe}$ which is 0.00171 at 550 nm, $\phi_0 = 1$ mm, the surface density of immobilized luciferase given by $2.0 \times 10^{10} mm^{-2}$, and $h_1 = 0.125\ s^{-1}$ in reference [30]. The prediction of V_{max} is $3.36 \times 10^6 s^{-1}$, which is two orders of magnitude larger than the obtained value of $7.38 \times 10^4 s^{-1}$. In our previous experiment with the APD, the predicted value of V_{max} was also one order of magnitude rather than the obtained one. Possible reasons are a reduction of h_1, or an existance of inactive luciferase molecules, or both of them as discussed in reference [4] and [31]. To clarify the reason, it is necessary to individually evaluate the number of active immobilized luciferase molecules e_a and the reaction rate h_1, respectively, from experimental data.

In the PMT system, it is noted that the improvement of two orders of magnitude for V_{max} is promising by using the optimal optics coupled to the optical fiber with $\phi_0 = 1.5\ mm$ and $NA_0 = 0.37$ and the optical fiber end with the appropriately irregular surface cut without the cleaving technique for immobilizing the luciferase.

4. Investigation of bioluminescence at the optical fiber end

4.1. Measurement of the bioluminescence with high time resolution

To obtain the reaction rate h_1, the number of acitve luciferase molecules e_a, and other kinetic parameters from experimental data, the counts of photons with high time resolution and the advaced analysis to such data are necessary. The data acquisition system has a capability of recoding the numbers of detected photons every 0.0321s. By making a full use of this specification, the time dependence of detected photons with high time-resolution at the ATP concentration of 1.65×10^{-4} M was obtained as shown in Fig. 13.

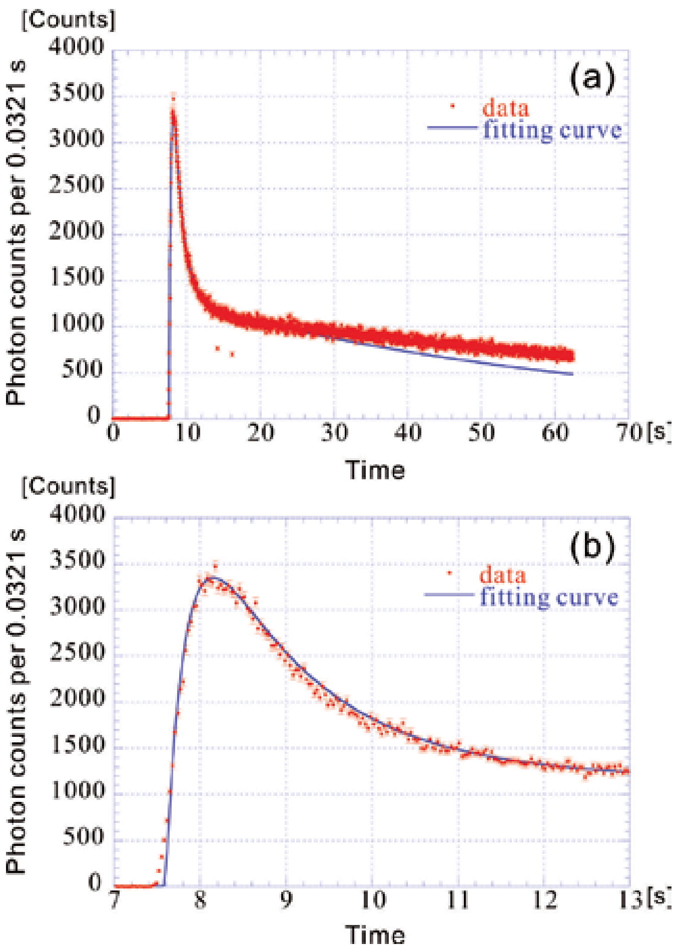

Figure 13. Time dependence of detected photons with the resolution of 0.0312 s at the ATP concentration of 1.65×10^{-4} M. The upper figure (a) shows the result in the solution of 100 μl. Solid line represents an extrapolation of the fitting curve with the parameters obtained by fitting the data from 0 s to 30 s. The lower figure (b) shows a magnified plot around the peak.

http://dx.doi.org/10.5772/52747

Fig. 13 (a) shows the result of the detected photons with the immobilized SBP-luciferase molecules at the optical fiber end into the solution of 100 μl at the ATP concentration of 1.65×10^{-4} M. For comparison, we also measured the time depencence of the photons with homogeniously dispersed SBP-luciferase molecules in the solution of 500 μl. The direct measurement of bioluminescence was carried out with an other type of cooled PMT detector having a huge sensitve area of 1 cm × 1 cm to detect the bioluminescence from a large area of the solution. The details on the direct measurement and the data analysis for dispersed luciferase molecules are given in reference [28].

4.2. Analysis

4.2.1. Reaction model including inhibitors

For obtaining kinetic parameters of bioluminescient reaction, we consider the rate equations including the effects of inhibitors. In the luciferin-luciferase reaction, two kinds of products, oxyluciferin and L - AMP are strong cometitive inhibitors to substrates. Each equilibrium constant for exyluciferin K_i and for L - AMP K_j has been measured and the values of $K_i = 0.5\ \mu$M and $K_j = 3.8$ nM are given in reference [22]. For simplicity of the model, we assume that two inhibitors contribute the competitive inhibition to the equilibrium reactions between luciferase and ATP in the presence of enough luciferin molecules. Fig. 14 shows the reaction steps of luciferin-luciferase reaction including the effects of competitive inhibitors.

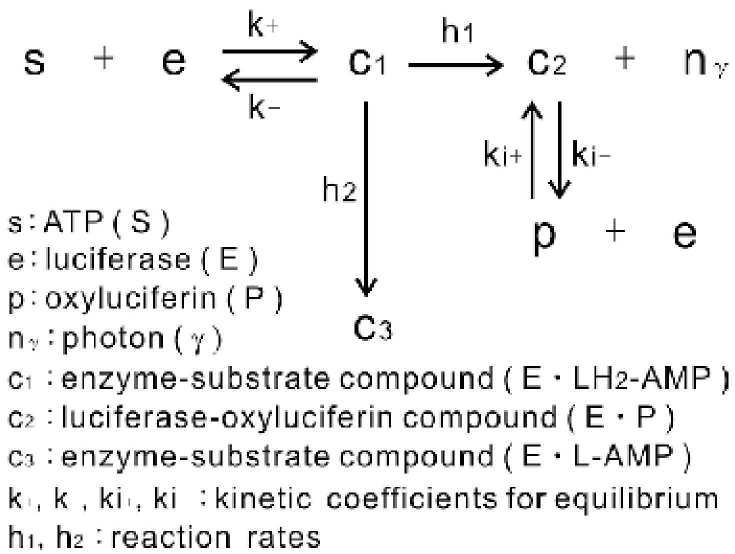

Figure 14. Enzyme reaction including the inhibitors

Here, s, e, p, n_γ, c_1, c_2, c_3 in Fig. 14 represents a concentration of ATP, luciferase, oxyluciferin, photon, $E\cdot LH_2$-AMP, $E\cdot P$, and $E\cdot$L-AMP, respectively, k_+, k_-, k_{i+}, and k_{i-} are kinetic coefficients for equilibrium and h_1 and h_2 are reaction rates. Since the inhibition by L - AMP is much stronger than the ones by oxyluciferin, it can be assumed that the enzymes in the state of the enzyme-susbstrate compound do not release L - AMP molecules and concequently lose the activation in the time scale of our experiment.

In the use of the immobilized luciferase molecules for sensing dispersed ATP molecules, it is natural to consider that the reaction occures in a volume ΔV which is the vicinity of the luciferase-terminated optical fiber end. Therefore, the serise of the rate equations describing the enzyme reaction shown in Fig. 14 in the volume ΔV can be expressed as

$$\frac{de}{dt} = -k_+ es + k_- c_1 + k_{i-} c_2 + k_{i+} ep \tag{4}$$

$$\frac{dc_1}{dt} = k_+ es - (k_- + h_1 + h_2) c_1 \tag{5}$$

$$\frac{dc_2}{dt} = h_1 c_1 - k_{i-} c_2 + k_{i+} ep \tag{6}$$

$$\frac{dc_3}{dt} = h_2 c_1 \tag{7}$$

$$\frac{dn_\gamma}{dt} = h_1 c_1 \tag{8}$$

$$\mathrm{N}_A V_0 \frac{ds}{dt} = -k_+ se + k_- c_1 \tag{9}$$

$$\mathrm{N}_A \Delta V \frac{dp}{dt} = -k_{i+} ep + k_{i-} c_2, \tag{10}$$

where the variable e, n_γ, c_1, c_2, c_3 is a number of each kind of molecules or photon in the volume ΔV. The variable s and p is the concentration of ATP and oxyluciferin, respectively, and their unit is M. The N_A is Avogadro number and the V_0 is a volume of the solution. The unit of k_-, k_{i-}, h_1, h_2 is s^{-1} and of k_+, k_{i+} is $\mathrm{M}^{-1}s^{-1}$. The volume V_0 is explicitly utilized into Eq. (9), since the concentration of ATP in the volume of V_0 is almost same as in the volume of ΔV because of a rapid diffusion rate. The volume ΔV can be approximately considered as a cylinder with a diameter of ϕ_0 =1 mm and a height of 10 nm because the size of SBP-luciferase molecules is about several nanometer, and its value is $\Delta V = 7.85 \times 10^{-12}$ l.

In addition to the above rate equations, the following conditions described as,

$$e_a = e + c_1 + c_2 + c_3 \tag{11}$$

$$n_\gamma = c_2 + \mathrm{N}_A \Delta V p \tag{12}$$

should be satisfied. The condition of Eq. (11) shows that the total number of active luciferase molecules e_a is constant and Eq. (12) means that the total number of photons is equivalent to that of oxyluciferin molecules. The Michaelis constant K_m and the equilibrium constant of oxyluciferin K_i can be expressed as

$$\mathrm{K}_m = (k_- + h_1 + h_2) / k_+ \tag{13}$$

$$\mathrm{K}_i = k_{i-} / k_{i+} \tag{14}$$

Using Eq. (11), Eq. (12), Eq. (13), and Eq. (14) as boundary conditions and inputting the constant values of e_a, h_1, h_2, k_+, k_{i-}, K_m, K_i and the initial values for variables, we can numerically solve the rate equations and obtain the time evolution of n_γ as the numerical solution at each time step. To simplify the numerical calculation, we assumed that oxyluciferin molecules instantaneously move out from the volume of $\Delta\mathrm{V}$ because of the fast diffusion rate of the oxyluciferin molecules. Therefore, the kinetic constant k_{i+} can be practically zero. This treatment means that the influence of the competitive inhibition by the oxyluciferin can be neglected.

In the solution containing non-localized homogenous dispersed SBP-luciferase, the volume of $\Delta\mathrm{V}$ in the equations is replaced with the volume of the solution V_0 and the kinetic constant k_{i+} is treated as non-zero.

4.2.2. Results of analysis

The five parameters $\mathbf{a}(e_a, k_+, k_{i-}, h_1, h_2)$ were treated as fitting parameters and the data was fitted to numerical solution of n_γ for obtaining the values of $\mathbf{a}$. As the first step, by inputting the initial values of $\mathbf{a}$ to the rate equations, the emitted photon $N_{th}^{\,i}(\mathbf{a})$ was calculated every time step of 0.0321 s with $\mathrm{K}_i = 0.5\ \mu\mathrm{M}$ given in [22] and $\mathrm{K}_m = 6.47 \times 10^{-5}$ M, which was deduced from the data analysis shown in Fig. 12. The data-set of $N_{th}^{\,i}(\mathbf{a})$, the n_0 number of measurend counts per 0.0321 s $N_{exp}^{\,i}$, and the background counts $N_{exp}^{\,0}$ enable us to calculate a chi-square χ^2 with the formula given by

$$\chi^2(\mathbf{a}) = \sum_{i=1}^{n_0} \frac{\left\{\left(N_{exp}^{\,i} - N_{exp}^{\,0}\right) - N_{th}^{\,i}(\mathbf{a})\right\}^2}{\left(N_{exp}^{\,i} + N_{exp}^{\,0}\right)} \tag{15}$$

The chi-square $\chi^2(\mathbf{a})$ is a good indicator for fitting data and its minimum gives the optimal combination of probable values in $\mathbf{a}$. Solving the series of the rate equations was executed by using the software package RKSUITE based on the Runge-Kutta method [32] and the minimization of the chi-square was performed with routines of MINUIT package provided by CERN software [33].

The result of fitting the data from 0 s to 30 s is represented as a solid line in Fig. 13 (a), which is extrapolated to 60 s using the obtaind parameters. This result is not reproduced completely in the time range from 0 s to 60 s, because the effect of the competitive inhibition of oxyluciferin is not considered and the fitting fuction includes only the contribution of the deactivation process. The inhibition of the oxyluciferin weakens with time due to its diffusion process, but this diffusion effect is not considered in this analysis. In contrast, the contribution of the deactivation process, which was evaluated by fitting the data around the peak, is concequently overestimated compared to the actual contribution. Therefore, the effect of the relatively strong evaluation for the deactivation process appears in the time range after 30 s.

The parameters obtained by fitting the data are summarized in table 2 together with the results of the dispersed luciferase for comparison. The parameter r represents the activation ratio of the SBP-luciferase, which can be defined as a ratio of the number of active luciferase molecules e_a to the total number of immobilized luciferase molecules e_0, which can be calculatedfrom the surface density of immobilized SBP-luciferase or from the concentration of the dispersed SBP-luciferase. In addtion, the parameter k_- and k_{i+} was derived from Eq. (13) and Eq. (14), respectively. The statistical error was 3 % at the maximum, but the systematical error was estimated to be 20 % taking account of the errors of the numerical calculation and the parameters used.

	dispersed luciferase	**immobilized luciferase**
Volume of solution	**500 µl**	**100 µl**
Region used for fitting	**0 – 60 s**	**0 – 30 s**
$r\ (e_a / e_0)$	0.44	0.010
k_+	$1.7\times10^4 M^{-1}s^{-1}$	$2.1\times10^4 M^{-1}s^{-1}$
h_1	$0.21s^{-1}$	$0.61s^{-1}$
h_2	$0.090s^{-1}$	$0.073s^{-1}$
k_{i-}	$0.090s^{-1}$	$0.25s^{-1}$
k_-	$0.83s^{-1}$	$0.68s^{-1}$
k_{i+}	1.8×10^5	

Table 2. Summary of obtained parameters

4.3. Discussion

In table 2, it is easily seen that the kinetic parameters in the immobilized luciferase are almost same as in the non-localized dispersed luciferase except the reaction rate of h_1. Since the rising time is approximately given by $1/k_+s$, it is useful for checking a consistency of k_+ with the reference. For dispersed luciferase, the rising time of 0.29 s is obtained with $k_+=1.7\times10^4M^{-1}s^{-1}$ and for immobilized luciferase, the rising time of 0.36 s is given by the value of

$k_+ = 2.1 \times 10^4 M^{-1} s^{-1}$. Both of them are close to the value of 0.3 s in reference [34], so that their values are consistent with the reference.

On the reaction rates, the obtained value of $h_1 = 0.61\ s^{-1}$ for immobilized lucifrase is about 5 times larger than the reference value $0.125 s^{-1}$ given in [30], but the order of both values is the same. A more precise comparison is not meaningful, because the surrounding environment of luciferase is not exactly same as in the reference.On the other hands, a branching ratio to the deactivation process, which is given by $h_2 / (h_1 + h_2)$, can be estimated to be 30 % for immobilized luciferase and 10 % for dispersed luciferase, respectively. Since the reference value of 20 % is given in [22], both of them are close to the refrence value. Thus, we can consider the obtained values of the parameters are almost consistent with the values which had been measured so far.

From table 2, the activation ratio r is 44 % for the dispersed SBP-luciferase and 1 % for the immobilized SBP-luciferase, respectively. In contrast, the reaction rate h_1 is the same order as the value we expected. Therefore, the detection limit for ATP detection results in two orders of magnitude larger than the expected one. As a concequence, the results of the sensitivity test described in Section 3 can be explained from the reduction of the activation ratio for the immobilized luciferase molecules.

5. Summary

We introduced a method of high-sensitivity detection of bioluminescence at an optical fiber end for an ATP detection as an efficient alternative to direct detection of bioluminescence for a sample solution. For investigation of the bioluminescence, we constructed an optical fiber-based system, where the luciferase molecules are immobilized on the optical fiber end and the other end is optically coupled to a compact size of cooled PMT-type photon counting head which has a large sensitive area. Although the sensitivity for the bioluminescence is not optimal, it is almost same as the system which had been constructed with an APD-type photon counting detector. We have evaluated the sensitivity for ATP detection and verified the detection limit of 10^{-9} M which is consistent with the previous results with the APD-type detector. This detector limit allows us to detect the absolute ATP number of 10^{-14} mol in a 10 μl solution, but it is two orders of magnitude larger than the expected one. For clarifying the reason, we have performed measurements with high time resolution and analyses of data by using an enzyme reaction model including inhibitors to individulally obtain an activation ratio and a reaction rate of the immobilied luciferase. As the results, the reaction rate of 0.61 s^{-1} and the activation ratio of 1 % have been obtained and these results have explained the reason of two orders of magnitude higher than the expected one. For reducing the detection limit more, it is necessary to improve the activtion ratio of the immobilized luciferase on the optical fiber end as well as the enlargement of the effective area of the cut surface based on a surface asperity and the increase of the FOM with the optimal values of a core diameter ϕ_0, a numerical aperture NA_0 and parameters of the coupling optics.

Acknowledgements

We are grateful to Prof. Hiroyuki Sakaue for supporting the element analysis with XPS and Prof. Kenichi Noda for useful supports to the experiments. This work has been partially supported by the International Project Center for Integration Research on Quantum, Information, and Life Science of Hiroshima University and the Grant-in-Aid for Scientific Research (C) (19560046) of Japanese Society for the Promotion of Science, JSPS.

Author details

Masataka Iinuma, Ryuta Tanaka, Eriko Takahama, Takeshi Ikeda, Yutaka Kadoya and Akio Kuroda

Graduate School of Advanced Sciences of Matters, Hiroshima University, Japan

References

[1] Arnold M. A. Fluorophore- and Chromophore-Based Fiberoptic Biosensors. In: Blum L. J. and Coulet P. R. (ed.)Biosensor principles and applications. New York: Marcel Dekker; (1991), 195-211.

[2] Blum L. J. and Gautier S. M.Bioluminescence- and Chemiluminescence-Based Fiber-optic Sensors. In: Blum L. J. and Coulet P. R. (ed.)Biosensor principles and applications. New York: Marcel Dekker; (1991), 213-247.

[3] Iinuma M., Ushio Y., Kuroda A., Kadoya Y.High Sensitivity Detection of ATP Using Bioluminescence at An Optical Fiber End. Electronics and Communications in Japan (2009), 92(9), 53-59. Available from http://onlinelibrary.wiley.com/doi/10.1002/ecj.10054/abstract (accessed 20 August 2009).

[4] Iinuma M., Ushio Y., Kuroda A., Kadoya Y. High-Sensitivity Detection of Bioluminescence at an Optical Fiber End for an ATP Sensor. In: Yasin M., Harun S. W., Arof H. (ed.) Fiber Optic Sensor. Rijeka; InTech; (2012), 459-474. Available from http://www.intechopen.com/books/fiber-optic-sensor (accessed 22 February 2012).

[5] Stanley P. E.A survey of more than 90 Commercially Available Luminometers and Imaging Devices for Low-light Measurements of Chemiluminescence and Bioluminescence, Including Instruments for Manual, Automatic and Specialized Operation, for HPLC, LC, GLC and Microtitre Plates. Journal of Bioluminescence and Chemiluminescence (1992), 7(2), 77-108. Available from http://onlinelibrary.wiley.com/doi/10.1002/bio.1170070202/abstract (accessed 30 March 2005).

[6] Andreotti P. E., Berthold F. Application of a new high sensitivity luminometer for industrial microbilogy and molecular biology. Luminescence (1999), 14(1), 19-22. Avail-

able from http://onlinelibrary.wiley.com/doi/10.1002/%28SICI%291522-7243%28199901/02%2914:1%3C19::AID-BIO512%3E3.0.CO;2-8/abstract (accessed 26 March 1999).

[7] Gourine A. V., Laudet E., Dale N.,Spyer K. MATP is a mediator of chemosensory transduction in the central nervous system. Nature (2005), 436, 108-111. Available from http://www.nature.com/nature/journal/n7047/full/nature03690.html (accessed 25 April 2005).

[8] Fraga H. Firefly luminescence: A histrical perspective and recent developments. Photochemical and Photobiological Sciences (2008), 7(2):146-158. Available from http://pubs.rsc.org/en/content/articlepdf/2008/pp/b719181b (accessed 23 January 2008).

[9] Nakamura M., Mie M., Funabashi H., Yamamoto K., Ando J, Kobatake E.Cell-surface-localized ATP detection with immobilized firefly luciferase. Analytical Biochemistry (2006), 352(1), 61-67. Available from http://www.sciencedirect.com/science/article/pii/S0003269706001394 (accessed 19 February 2006).

[10] Konno T., Ito T., Takai M., Ishihara K.Enzymatic photochemical sensing using luciferase-immobilized polymer nanoparticles covered with artificial cell membrane. Journal of Biomaterials Sciences, Polymer Edition (2006), 17(12), 1347-1357. Available from http://www.tandfonline.com/doi/abs/10.1163/156856206778937235 (accessed 2 April 2012).

[11] Lee Y., Jablonski I., DeLuca M. Immobilization of Firefly Luciferase on Glass Rods: Properties of the Immobilized Enzyme. Analytical Biochemistry (1977), 80(2), 496-501. Available from http://www.sciencedirect.com/science/article/pii/0003269777906728 (accessed 7 December 2004).

[12] Blum L. J., Coulet P. R., Gautheron D. C.Collagen Strip with Immobilized Luciferase for ATP Bioluminescent Determination. Biotechnology and Bioengineering (1985), 27(3), 232-237. Available from http://onlinelibrary.wiley.com/doi/10.1002/bit.260270304/abstract (accessed 18 February 2004).

[13] Ribeiro A. R., Santos R. M., Rosario L. M., Gil M. H.Immobilization of Luciferase from a Firefly Lantern Extract on Glass Strips as an Alternative Strategy for Luminescent Detection of ATP. Journal of Bioluminescence and Chemiluminescence (1998), 13(6), 371-378. Available from http://onlinelibrary.wiley.com/doi/10.1002/%28SICI%291099-1271%28199811/12%2913:6%3C371::AID-BIO510%3E3.0.CO;2-%23/abstract (accessed 13 January 1999).

[14] Worsfold P. J., Nabi A.Bioluminescent assays with immobilized firefly luciferase based on flow injection analysis. Analytica Chimica Acta (1986), 179, 307-313. Available from http://www.sciencedirect.com/science/article/pii/S000326700084475X (accessed 4 January 2002).

[15] Tanii T., Goto T., Iida T., Koh-Masahara M., Ohdomari I. Fabrication of Adenosine Triphosphate-Molecule Recognition Chip by Means of Bioluminous Enzyme Lucifer-

ase. Japanese Journal of Applied Physics (2001), 40, L1135-L1137. Available from http://jjap.jsap.jp/link?JJAP/40/L1135/ (accessed 24 August 2001).

[16] Tsuboi Y., Furuhata Y., Kitamura N. A sensor for adenosine triphosphate fabricated by laser-induced forward transfer of luciferase onto a poly(dimethylsiloxane) microchip. Applied Surface Science (2007), 253, 8422-8427. Available from http://www.sciencedirect.com/science/article/pii/S0169433207005399 (accessed 13 April 2007).

[17] Hamamatsu Photonics K. K. Manual on H7421 series photon counting head.

[18] Perkin Elmer. Ltd. datasheet of SPCM-AQR-14%2F15%2F16-datasheet.html (accessed 2012).

[19] Matsumoto M., Nishimura T.Mersenne Twister: A 623-dimensionally equidistributed uniform pseudorandom number generator. ACM Transaction modellingand computer simulation (1998), 8, 3-30. Available from http://dl.acm.org/citation.cfm?id=272995&CFID=226399843&CFTOKEN=43874926 (accessed 1 January 1998). l

[20] DeLuca M.Firefly luciferase. In: Meister A. (ed.)Advances in Enzymology. New York; Wiley; (1976), 44, 37-68.

[21] Fraga H., Fernandes D., Novotny J., Fontes R., Esteves da Silva J. C. G. Firefly Luciferase Produces Hydrogen Peroxide as a Coproduct in Dehydroluciferyl Adenylate. ChemBioChem (2006), 7(6), 929-935. Available from http://onlinelibrary.wiley.com/doi/10.1002/cbic.200500443/abstract (accessed 27 April 2006).

[22] Ribeiro C., Esteves da Silva J. C. G. Kinetics of inhibition of firefly luciferase by oxyluciferin and dehydroluciferyl-adenylate. Photochemical and Photobiological Sciences (2008), 7(9), 1085-1090. Available from http://pubs.rsc.org/en/content/articlelanding/2008/pp/b809935a (accessed 1 August 2008).

[23] Taniguchi K., Nomura K., Hata Y., Nishimura Y., Asami Y., Kuroda A. The Si-tag for immobilizing proteins on a silica surface. Biotechnology and Bioengineering (2007), 96(6), 1023-1029. Available from http://onlinelibrary.wiley.com/doi/10.1002/bit.21208/abstract (accessed 29 September 2006).

[24] Denburg J. L., Lee R. T., McElory W. DSubstrate-Binding Properties of Firefly Luciferase 1. Luciferin-binding Site. Archives of Biochemistry and Biophysics (1969), 134(2), 381-394. Available from http://www.sciencedirect.com/science/article/pii/0003986169902975 (accessed 26 October 2004).

[25] Ugarova N. N., Brovko L. Y. Protein structure and bioluminescent spectra for firefly bioluminescence. Luminescence (2002), 17(5), 321-330. Available from http://onlinelibrary.wiley.com/doi/10.1002/bio.688/abstract (accessed 23 September 2002).

[26] Silbery R. J., Alberty R. A., Bawendi M. G. Physical Chemistry 4h edition. Wiley;2004.

[27] Aflao C., DeLuca M.Continuous Monitoring of Adenosine 5'-Triphosphate in the Microenvironment of Immobilized Enzymes by Firefly Luciferase. Biochemistry (1987), 26(13), 3913-3920. Available from http://pubs.acs.org/doi/abs/10.1021/bi00387a026

[28] Tanaka. R., Takahama E., Iinuma M., Ikeda T., Kadoya Y., Kuroda A. Bioluminescent Reaction by Immobilized Luciferase. IEEJ Transactions on Electronics, Information and Systems (2011), 131(1), 23-28. Available from https://www.jstage.jst.go.jp/article/ieejeiss/131/1/131_1_23/_article (accessed 1 January 2011)

[29] Ushio Y. Improvement of the sensitivity for ATP detection by the efficient optical coupling between a biosensor and an APD-type of photon detector. Master thesis. Hiroshima University Higashi-Hiroshima; 2007.

[30] Branchini B. R., Magyar R. A., Murtiashaw M. H., Portier N. CThe Role of Active Site Residue Arginie 218 in Firefly Luciferase Bioluminescence. Biochemistry (2001), 40(8), 2410-2418. Available from http://pubs.acs.org/doi/abs/10.1021/bi002246m (accessed 1 January 2001)

[31] Nishiyama K., Watanabe T., Hoshina T., Ohdomari I.The main factor of the decrease in activity of luciferase on the Si surface. Chemical Physics Letters (2008), 453(4-6), 279-282. Available from http://www.sciencedirect.com/science/article/pii/S0009261408000882 (accessed 21 January 2008).

[32] Netlib Repository Library rksuite. http://www.netlib.org/ode/rksuite/

[33] Minuit home page. http://seal.web.cern.ch/seal/work-packages/mathlibs/minuit/home.html/

[34] DeLuca M., McElory W. D.Kinetics of the Firefly Luciferase Catalyzed Reactions. Biochemistry (1974), 13(5), 921-925. Available from http://pubs.acs.org/doi/abs/10.1021/bi00702a015

Chapter 12

Smart Technical Textiles Based on Fiber Optic Sensors

Katerina Krebber

Additional information is available at the end of the chapter

http://dx.doi.org/10.5772/54244

1. Introduction

Smart technical textiles are by definition textiles that can interact with their environment. They can sense and react to environmental conditions and external stimuli from mechanical, thermal, chemical or other sources. Such textiles are multifunctional or even "intelligent" which is fulfilled by a number of sensors incorporated in the textiles. The embedded sensors are sensitive to various parameters such as temperature, strain, chemical, biological and other substances.

Technical textiles are commonly used within several industrial sectors ranging from medical, healthcare, earthworks, construction, civil engineering, transport, to name a few. Europe has driven substantial developments in technical textile technologies[1]. Smart technical textiles are going to stimulate the European engineering, transportation and construction industry and to improve human performance and health. For example, technical textiles are extensively used in construction in form of geotextiles for the reinforcement of earthworks and masonry structures. The retrofitting of existing masonry walls and soils structures by technical textiles gains more and more importance especially in connection with earthquake protection of historic buildings and protection of roads and railway embankments against landslides. Wearable health systems and protective clothing have been recognized as key technologies to improve the personal protection and health care of Europe's citizens[2]. Smart biomedical garments and clothing act as "a second skin" and detect, for instance, vital signals of the wearer's body or changes in the wearer's environment.

The most effort in the past was made to integrate non-optical sensors into textiles. Optical fibers integrated in textiles were mostly explored for illumination or luminescent purposes. Smart technical textiles containing fiber optic sensors are still an exception. When integration of sensors into textiles is considered, optical fibers have a serious advantage over other kinds of sensors due to their fibrous nature. The optical fiber is similar to textile fibers and can be ideally processed like standard textile yarns. Particularly, the integration of polymer optical fibers (POF), with their outstanding material properties, into technical textiles has not seriously been considered, until now. POF offer additional benefits to users. They are lightweight, robust, cheap and easy to handle. Especially because of their high elasticity and high breakdown strain POF are ideally suited for integration into technical textiles[3].

2. Geotextiles based on distributed fiber optic sensors for structural health monitoring

For stabilization and reinforcement of geotechnical structures like dikes, dams, railways, embankments, landfills and slopes geotextiles are commonly used. The incorporation of optical fibers in geotextiles leads to additional functionalities of the textiles, e.g. monitoring of mechanical deformation, strain, temperature, humidity, pore pressure, detection of chemicals, measurement of the structural integrity and the health of the geotechnical structure (structural health monitoring). Especially solutions for distributed measurement of mechanical deformations over extended areas of some hundred meters up to some kilometers are urgently needed. Textile-integrated distributed fiber optic sensors can provide for any position of extended geotechnical structures information about critical soil displacement or slope slides via distributed strain measurement along the fiber with a high spatial resolution of less than 1 m. So an early detection of failures and damages in geotechnical structures of high risk potential can be ensured.

Geotextiles with incorporated fiber optic sensors based on fiber Bragg gratins (FBG) were demonstrated in the past[4]. Monitoring systems based on such geotextiles can only measure quasi-distributed strain over limited lengths and the relative high price of the FBG-equipped geotextiles might be an additional drawback of the systems. The monitoring of extended geotechnical structures like dikes, dams, railways, embankments or slopes requires sensor technologies with gauge lengths of some hundred meters or even more. Sensor systems based on the stimulated Brillouin scattering in silica fibers have been used for such monitoring purposes. It was reported in the past about a geotextile-based monitoring system using the Brillouin optical-fiber frequency-domain analysis (BOFDA) for measurements of critical soil displacements of dikes[5]. However, the excellent measurement technique based on Brillouin scattering in silica fibers reaches its limits when strong mechanical deformations, i.e. strain of more than 1 % occurs. In such a case sensors based on silica fibers cannot be reliably used. Furthermore, silica fibers are very fragile when installing on construction sites and, therefore, special robust and expensive glass fiber cables have to be used. For that reason, the integration of POF as a sensor into geotextiles has become very attractive because of the high elasticity, high breakdown strain and the capability of POF of measuring strain of more than 40 %. Especially the monitoring of relative small areas with an expected high mechanical deformation such as endangered slopes takes advantage of the outstanding mechanical properties of POF. The monitoring of slopes is a very important task in the geotechnical engineering for prevention of landslide disasters and no reliable sensor methods exist, so far. To overcome the limit of glass-fiber-based geotextiles, a novel distributed fiber optic sensor based on low-priced standard POF and using the OTDR (optical time-domain reflectometry) which is suitable for integration in technical textiles has been developed and demonstrated[6].

Such innovative textile-integrated distributed Brillouin and POF OTDR sensors for the above mentioned monitoring purposes have been developed within several German projects and the European project POLYTECT. The POLYTECT project has particularly focused on the development of polyfunctional technical textiles against natural hazards. The aim of POLYTECT has been to develop and investigate new multifunctional textile structures for the application in construction for the retrofitting of masonry structures and earthworks. The retrofitting of existing masonry walls and soil structures is particularly important for earthquake protection of historic buildings and protection of earthworks against landslides. The new and advanced textile structures containing optical fibers as sensors will be able to increase the ductility and the structural strength of masonry and geotechnical structures and to prevent structural damage[6]. For this, the sensors incorporated into the textile structures will monitor strain, deformation, humidity and will detect presence of chemicals. The development of the sensors carried out within the above mentioned projects has advanced and a number of field tests using distributed Brillouin and POF OTDR sensors have successfully been conducted.

2.1. Monitoring of geotechnical structures using distributed Brillouin sensors embedded in geotextiles

The use of stimulated Brillouin scattering (SBS) for distributed measurement of temperature and strain was already demonstrated 20 years ago[7]. The SBS is the most dominant nonlinear effect in single-mode silica fibers and can be described as a three-wave-interaction of two contra-propagating light waves and an acoustic wave in the fiber. Because of the strain and temperature dependence of the Brillouin frequency shift of the scattered light, sensor systems based on this effect can be used for distributed strain and temperature measurements. The first distributed Brillouin sensing systems named Brillouin optical-fiber time-domain analysis (BOTDA) operated in a time-domain, which means that a short pulse is sent along the fiber and the backscattered light is recorded over time and contains information about the strain or temperature along the fiber[8]. During the last two decades the performance of BOTDA sensor systems has improved steadily. The operating range of these sensors is typically in the order of 20-30 km for 2-3 m spatial resolution. Today, several devises based on this technique are commercially available.

In 1996 an alternative approach named Brillouin optical-fiber frequency-domain analysis (BOFDA) was introduced[9]. The BOFDA operates with sinusoidally amplitude-modulated light and is based on the measurement of a baseband transfer function in frequency domain by a network analyzer (NWA). A signal processor calculates the inverse fast Fourier transform (IFFT) of the baseband transfer function. In a linear system this IFFT is a good approximation of the pulse response of the sensor and resembles the strain and temperature distribution along the fiber (Fig. 1). The frequency-domain method offers some advantages compared to the BOTDA concept. One important aspect is the possibility of a narrow-bandwidth operation in the case of BOFDA. In a BOTDA system broadband measurements are necessary to record very short pulses, but in a BOFDA system the baseband transfer function is determined point-wise for each modulation frequency, so only one frequency component has to be measured by NWA with a narrow resolution bandwidth. The use of a narrow bandwidth operation (detectors) improves the signal-to-noise ratio and the dynamic range compared to those of a BOTDA sensor without increasing the measurement time. Another important advantage of a BOFDA sensor is that no fast sampling and data acquisition techniques are used. This reduces costs. Particularly, the low-cost-potential of BOFDA sensors is very attractive for industrial applications.

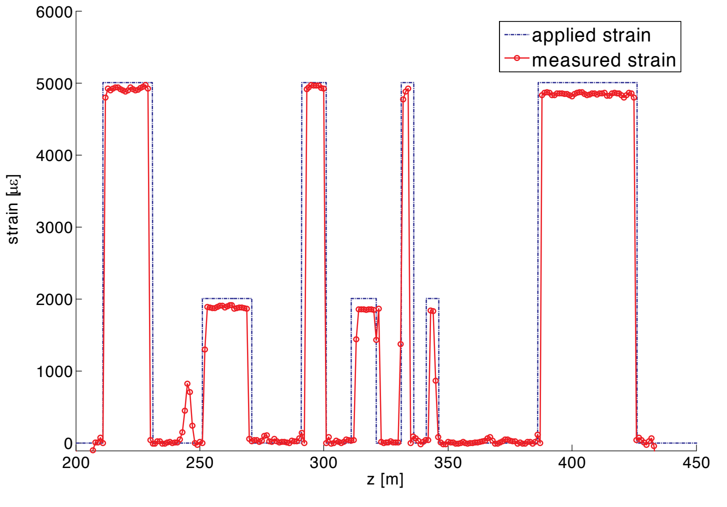

Figure 1. Distributed strain profile measured on a single-mode silica fiber using BOFDA.

As already pointed out, distributed Brillouin sensors are well qualified for the distributed monitoring of mechanical deformation (strain) of extended geotechnical structures like dikes, dams and highways of lengths of some hundred meters up to some kilometers and no alternative sensor techniques for such monitoring purposes exist so far. To push the development of such sensor systems in connection with innovative monitoring solutions based on smart technical textiles, several research projects have been running in Germany and Europe. The German research program RIMAX (Risk Management of Extreme Flood Events) has mainly focused on the development of intelligent monitoring systems for dike protection and was launched as a consequence of extreme floods in Germany in the past decade. A low-cost monitoring system based on the BOFDA technique and geotextiles containing silica fibers as distributed Brillouin sensors have been developed within the program[10].

Geotextiles are commonly used in dikes for reinforcement of the dike body and erosion prevention. By embedding sensing optical fibers in the textiles, distributed measurements of critical mechanical deformations/soil displacements of dikes of several kilometers can be realized. So an early detection of failures in dikes, dams and other large geotechnical structures can be ensured in order to prevent a total collapse of these structures in case of natural disasters. An important task when considering integration of optical fibers in geotextiles is to ensure an accurate transfer of the mechanical quantities to be measured, i.e. of strain, from the soil to the textile and so to the fiber. For this, a stable and damage-free integration of the optical fibers in the geomats is of essential importance. The Saxon Textile Research Institute (STFI) e.V., Chemnitz, Germany has developed a technology to integrate optical fibers into geotextiles so that the sensing fiber is well affixed onto the textile and the integration procedure does not affect the optical and sensing properties of the fibers. Also the use of special coating and cable materials are of crucial importance to protect the fragile single-mode silica fibers against fiber-breakage during the integration into the textiles and the installation on construction sites. For that, a novel glass fiber cable was developed and manufactured by Fiberware, Mittweida, Germany to fulfill the above mentioned requirements on robustness and to assure accurate strain transfer to the sensing fibers[11]. Fig. 2 shows the special cable as well as different types of geotextiles with embedded glass fiber cables.

Figure 2. Special glass fiber cable for strain sensing manufactured by Fiberware, Germany (left) and two different types of geotextiles (middle: nonwoven geotextile, right: geogrid) manufactured by STFI, Germany with embedded glass fiber cables.

The BOFDA monitoring system has been optimized to fit the demands on dike monitoring: detection of mechanical deformation (strain) with a spatial resolution of 5 m over a distance range of up to 10 km. The functionality of the monitoring system and the fiber-sensors-equipped geotextiles has been proven in several installations and field tests in dikes and dams. For example, Fig. 3 shows the installation of geotextiles with embedded Brillouin sensing fibers in a gravity dam in Solina, Poland. A thin soil layer of several 10 cm put onto the geomats after installation has been proven to be a sufficient protection of the textile-integrated glass fiber cables against heavy machinery and construction work.

An application-like test was carried out at a laboratory dike (15 m long) at the University Hannover, Germany[11]. A sensor-based geotextile was installed on top of the dike and was covered with a thin soil layer. To simulate a mechanical deformation/soil displacement, a lifting bag was embedded into the soil and was inflated by air pressure. This induced a break of the inner slope of the dike and a soil displacement (Fig. 4). The soil displacement was clearly detected and localized by the BOFDA system. Fig. 5 shows the distribution of the mechanical deformation (strain) in the dike measured by the BOFDA system at two different air pressure values.

Figure 3. Installation of a non-woven geotextile containing single-mode silica fibers as Brilloin sensors in a gravity dam in Solina, Poland.

Figure 4. Laboratory dike at the University Hannover, Germany and soil displacement in the dike.

As previously mentioned, a geotextile with embedded Brillouin sensing fibers was installed in a gravity dam in Solina, Poland to prove the feasibility of the whole concept in the framework of a real field test Fig. 6. The goal of the field test was to detect possible geophysical activities in the dam by the fiber-sensor-equipped geotextile of a length of 17.5 m manufactured by STFI, Germany and embedded in the soil. Distributed measurements by using a commercially available BOTDA system from Omnisens were conducted. Fig. 7 shows the distributed Brillouin frequency shift measured on the fiber section embedded in the soil. In the fiber sections between 205 m and 240 m (where the geomat was embedded in the soil) a mechanical load is assumed which results in a change of the recorded Brillouin frequency in these fiber sections.

http://dx.doi.org/10.5772/54244

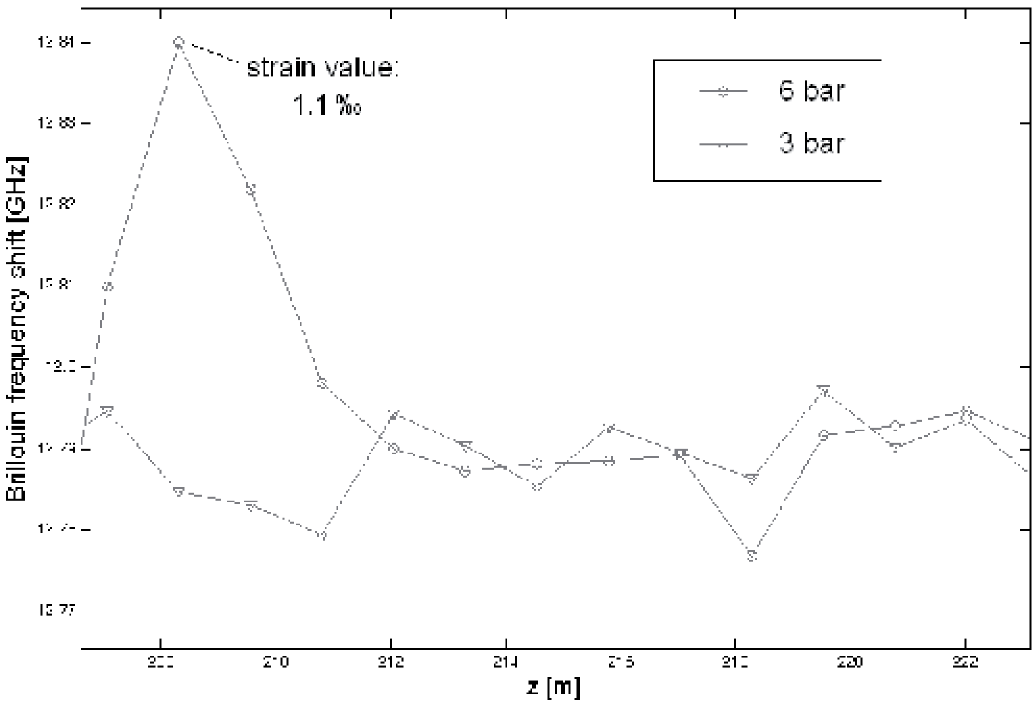

Figure 5. Detection of a soil displacement (strain) in the laboratory dike shown in Fig. 4 using the BOFDA system.

Figure 6. Gravity dam in Solina, Poland (left) and the construction site with the sensor-based non-woven geotextile before embedding in the soil and 3 years later (right).

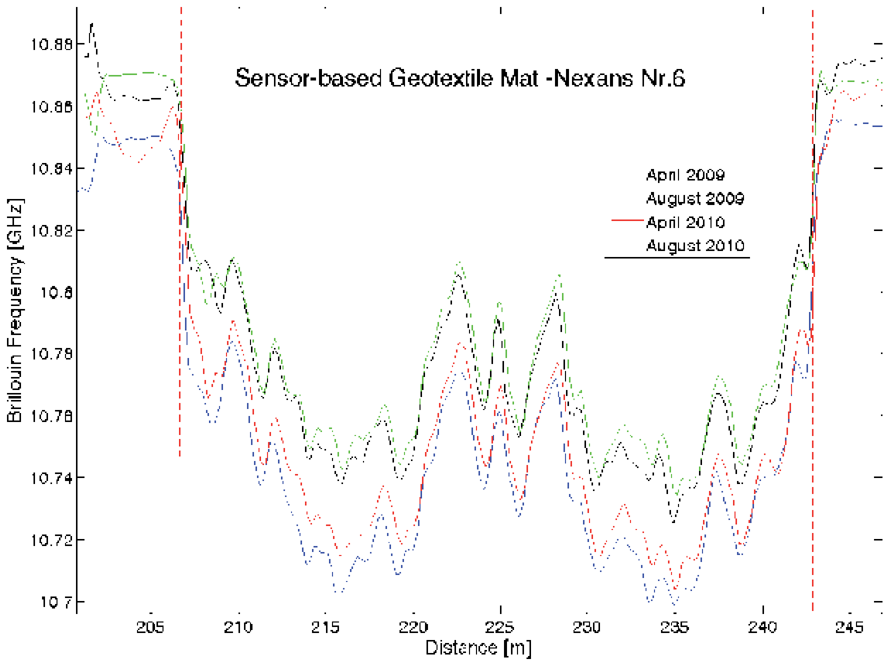

Figure 7. Distributed Brillouin frequency shift measured on the fiber section embedded in the soil (between 205 m and 240 m) 3 years after installation of the geomat.

With the objective of a cost-effective optimization of the BOFDA system a novel measurement concept based on a digital signal processing has been realized[11]. This concept employs a novel digital data acquisition technique, which takes advantage of the reduced bandwidth required in BOFDA sensor systems. The backscattered optical signals can be digitally sampled using state-of-the-art analog-to-digital converters and is processed off-line by means of modern digital signal processing methods, avoiding complex and expensive analog components such as filters, oscillators and circuitry for signal analysis. The digital optical signal processing features several advantages compared to the measurement process using NWA: less hardware is required, an increase of the dynamic range due to the offline signal processing and improvement of the data acquisition time is expected.

2.2. Monitoring of geotechnical structures using distributed POF OTDR sensors embedded in geotextiles

To overcome the limit of silica-fiber-based distributed sensors, a novel distributed strain sensor based on low-priced standard POF and using the OTDR technique for monitoring of mechanical deformations of geotechnical structures has been developed. Already published results showed that it is possible to measure distributed strain in POF using the OTDR tech-

http://dx.doi.org/10.5772/54244

nique[12]. In the framework of the German research project "Sensitive textile structures" (within the German program "ZUTECH" – "Future technologies") and the European project POLYTECT further investigations of this effect with respect to the development of a new, distributed POF sensor embedded in technical textiles have been performed[6], [13].

The functional principle of the POF OTDR technique is very simple. An optical pulse is launched into the fiber and the backscattered light mainly caused by Rayleigh scattering is recorded as a function of time. The time interval from launching the pulse into the fiber until the return of the backscattered light (pulse response) depends linearly on the distance of the scattering location. The level of the backscattered light increases at locations where strain is applied to the POF. Fig. 8 (left) shows the OTDR response of an unstretched POF (solid line) and of a stretched POF (broken line) which is stretched at about 42 m on a 1.4 m long section by 16 %. Fig. 8 (right) shows the relative change of scattering of the stretched POF section at different strain values between 0 % and 16 % (calculated relative to the scattering of the unstretched fiber). The scattered light increases steadily with applied strain. Today, several OTDR devices for POF are commercially available on the market. In the described investigations a photon counting OTDR device from Sunrise Luciol has been used. The device operates at 650 nm, has a dynamic range of 35 dB and allows a measurement of Rayleigh scattering along a length of more than 100 m. The photon counting technique is ideal for achieving high dynamic range on very short sensing lengths. The two-point spatial resolution of the OTDR device is limited to 10 cm. An additional solution to evaluate the strain or length change of a fiber section is to evaluate the shift of reflection peaks along the fiber (see Fig. 8, left). Such peaks originate for example from Fresnel reflections at the fiber end or fiber connectors. This technique provides an absolute length change measurement with a resolution of up to 1.5 mm.

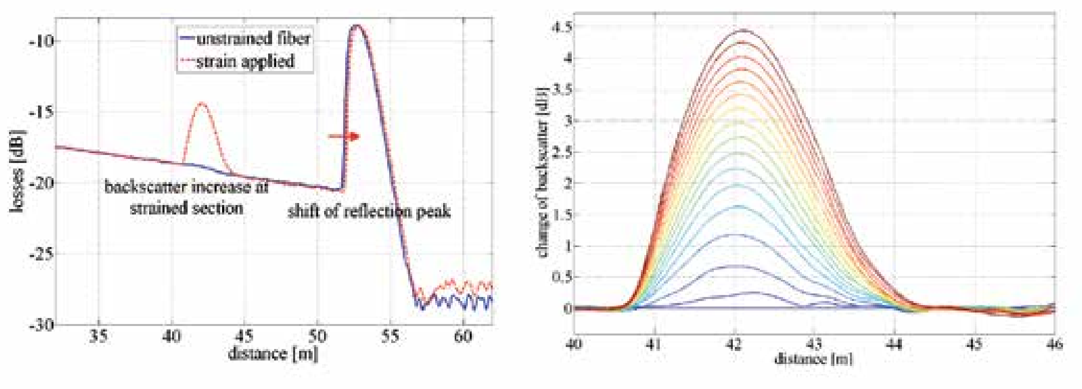

Figure 8. Left: OTDR trace of POF in unstretched condition (solid line) and of POF with a stretched fiber section at about 42 m (broken line). Right: Change of the scattering along a 1.4 m long POF section that is stretched from 0 to 16 % in steps of 1 %.

Fig. 9 shows the increase of the scattered light versus applied strain. A non-linear dependence between the OTDR signal (the backscattering) and the applied strain in the whole strain range was obtained. Strain of up to 45 % was measured using standard PMMA POF.

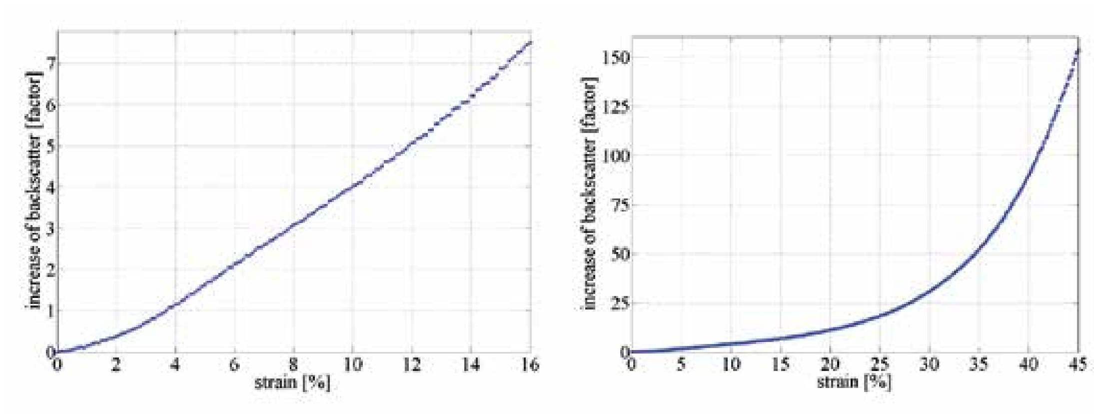

Figure 9. Change of the backscattering as a function of strain measured on standard PMMA POF.

The attenuation of standard PMMA POF limits the distance range of distributed POF OTDR sensors to about 100 m. Low-loss perfluorinated POF show a big potential as distributed strain sensors for long distances[14]. It has been shown that using perfluorinated POF it is possible to monitor fiber lengths of more than 500 m (Fig. 10, left). Recent research has demonstrated, that perfluorinated POF allow the measurement of very high strain values of up to 100 % (Fig. 10, right).

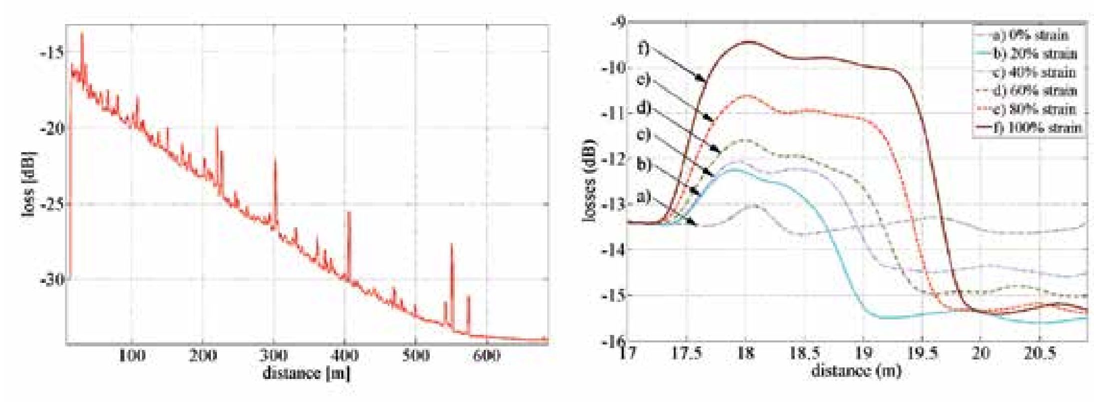

Figure 10. Left: OTDR trace of perfluorinated POF. Right: OTDR signal of perfluorinated POF strained up to 100 %.

Technologies for a damage-free integration of POF into different types of geotextiles have successfully been developed and demonstrated by several textile partners in Europe like STFI, Germany and Alpe Adria Textil, Italy. Fig. 11 shows the integration of POF into non-woven geotextiles at STFI e.V. as well as a geogrid containing POF. Already the first field tests proved that the POF-equipped geotextiles are suited for installation on construction sites. POF-based geomats have successfully been installed in a railway embankment near Chemnitz, Germany (Fig. 12)[6]. All POF sensors have survived the installation on construction site without any damage. Their functionality has been regularly tested (Fig. 12, right).

Figure 11. Integration of POF into nonwoven geotextiles at STFI e.V. (left) and a geogrid containing POF (right).

Figure 12. Installation of POF-equipped geotextiles in a railway embankment near Chemnitz, Germany (left and middle) and OTDR traces measured on the textile-integrated POF (right).

During the last years, the POF-equipped geotextiles have successfully moved from the laboratory to the field. Several field tests have successfully been conducted, e.g. in an open brown coal pit near Belchatow, Poland[15]. The test was initiated, organized and supervised by Gloetzl Baumesstechnik GmbH, Germany in close cooperation with Budokop, Poland and the owner of the coal pit. A sensor-equipped geogrid was installed directly on top of a creeping slope. The 10 m long geogrid was manufactured by Alpe Adria Textil, Italy and comprised one standard PMMA POF. Fig. 13 shows the installation of the sensor textile on top of the slope. It is covered with a 10 cm thick sand layer. The textile is installed with the POF sensor bridging the cleft perpendicular to the opening. The geogrid was installed in a slightly corrugated way simulating realistic installation conditions.

Figure 13. Installation of a geogrid containing PMMA POF at a creeping slope in a brown coal pit near Belchatow, Poland.

Measurements were conducted before and after installation. Fig. 14 (left) shows the OTDR traces of the sensor fiber section (the magnitude of the backscatter increase relative to a reference measurement) in the middle of the textile where the fiber bridges the cleft. The figure clearly shows a backscatter increase due to strain in the fiber at the position where the cleft was opening. The high peak at about 35 m is caused by a very high and confined strain in the sensor fiber and textile. The magnitude of the backscatter increase corresponds to a maximum strain in the fiber of more than 10 %. Such high strain values can only be measured by POF sensors. Silica fiber-based sensor systems would have failed at a strain exceeding about 1 %.

Due to the gradual increase of cleft width, the overlying textile and therefore the sensor fiber change their absolute length. By evaluating the relative shift of the reflection peaks at both ends of the textile-integrated fiber, the values of the total elongation of the fiber sensor indicating the width of the cleft was obtained. Fig. 14 (right) shows a relative linear increase of the POF length with time. The measurements indicate that the creep velocity of the slope was constant during the time of observation with an average rate of about 2 mm per day.

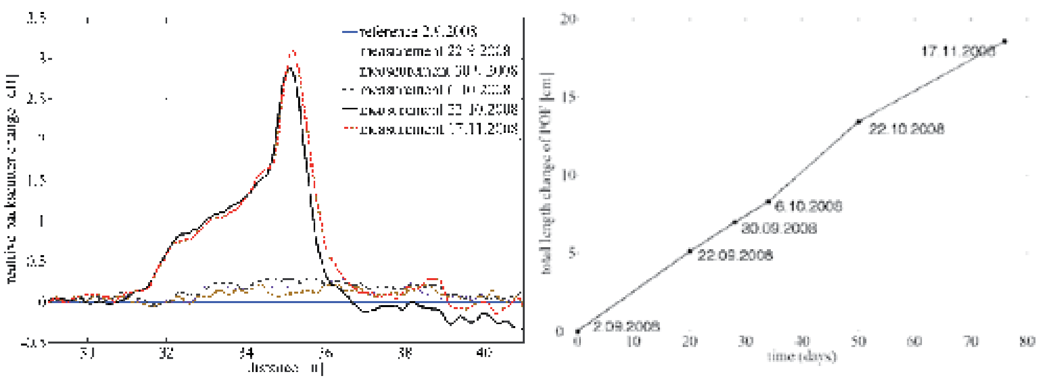

Figure 14. POF OTDR traces at the position of the cleft (left) and total elongation of the POF obtained by a peak-shift evaluation (right).

http://dx.doi.org/10.5772/54244

Recently, novel geogrids containing low-loss perfluorinated POF (PF POF) have been developed and manufactured by Alpe Adria Textil. Already the first field test has proved that the PF POF-equipped geotextiles are suited for installation on construction sites. PF POF-based geomats have successfully been installed at the creeping slope Kap Arkona at the German Baltic coast (Fig. 15, left). All PF POF sensors have survived the installation on construction site without any damage. At present, their functionality has been regularly tested by using the POF OTDR technique (Fig. 15, right).

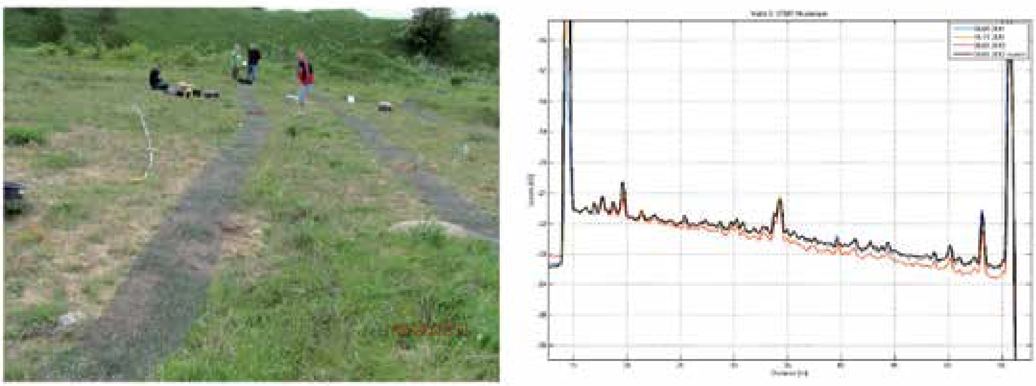

Figure 15. Left: Installation of PF POF-equipped geotextiles at the creeping slope Kap Arkona at the German Baltic coast. Right: OTDR traces measured on the textile-integrated PF POF after installation.

The successful demonstration of the distributed POF OTDR sensors in the field and the huge interest of the geotechnical industry in these sensors resulted in the development of the first commercially available product based on distributed POF sensors – GEDISE: Distributed Sensor Technique in Geotextiles using POF (Fig. 16). GEDISE is commercially available by Glötzl GmbH, Germany.

Figure 16. Leaflet of GEDISE: Distributed Sensor Technique in Geotextiles using POF (www.gloetzl.de).

2.3. Monitoring of masonry structures using distributed POF OTDR sensors embedded in technical textiles

The motivation to monitor masonry structures by sensor-equipped technical textiles is to strengthen the masonry body and enhance the ductility of the structures and at the same time to monitor the structural health and detect any damage of the structures, e.g. due to earthquakes. The development of sensor-based technical textiles containing fiber optic sensors for the retrofitting of masonry structures is an innovative task of the European project POLYTECT. The targeted applications are masonry and heritage structures that are structurally vulnerable, for example in earthquake regions. Typical structural damages that have to be detected are vertical cracks. POF sensors are very promising for that since they not only enable distributed strain measurement, they are also appropriate to detect very short strained fiber sections of a few millimeters that will occur in case of cracks. For example, Fig. 17 shows the monitoring of a crack opening in a masonry structure using a POF OTDR sensor. A technical textile containing POF was applied to the surface of the masonry sample[6]. Using the POF OTDR technique it was possible to detect a crack opening of 1 mm and also the increase of the crack width up to 20 mm in steps of 2 mm (Fig. 17, right).

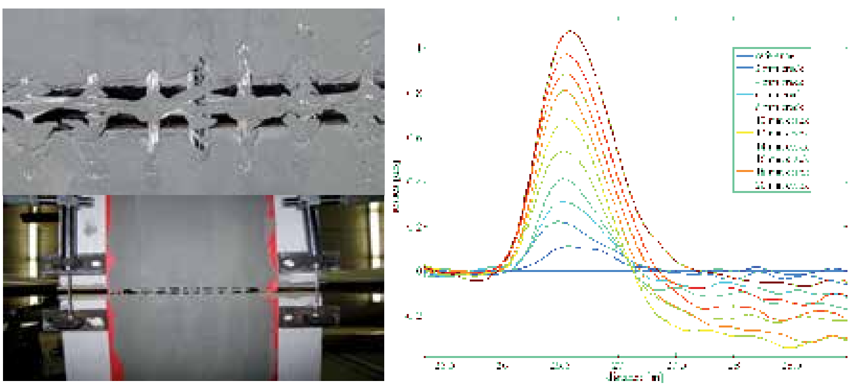

Figure 17. Monitoring of a crack opening in a masonry structure (Institute IfMB at the University of Karlsruhe, Germany) with a POF-equipped masonry textile (STFI e.V., Chemnitz, Germany). The right side of the figure shows POF OTDR backscatter signals at the location of the crack at different crack opening steps.

Using the POF OTDR technique a field test was conducted on an one-storey brick building on a seismic shaking table[16]. The test was organized and supervised by the Institute of Mechanics of Materials and Geostructures (IMMG), Greece. Fig. 18 shows the POF sensors bonded to the wall with a cementitious resin matrix. The testing procedure included several strong shocks, which resulted in structural damage of the building. The task of the distributed POF sensors was to provide information about the existence and location of cracks in the structures. The occurred cracks were detected and localized with the POF OTDR sensor. Fig. 19 shows the OTDR traces measured on one sensor-fiber which was installed diagonally on the wall. Two cracks were detected by the sensor at the locations indicated in Fig. 18. The stronger signal at 27 m is caused by a 2 mm crack at the corner above the door. A smaller, almost invisible crack has been detected at 150 cm distance from the first crack at the lower right corner of the wall.

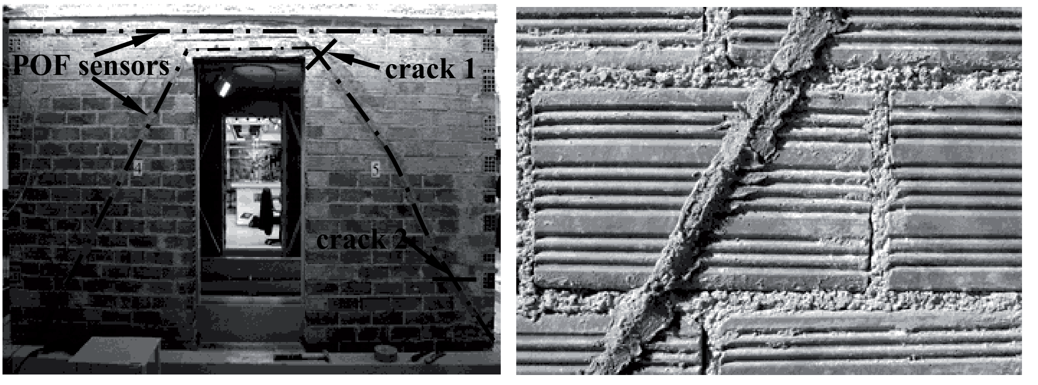

Figure 18. Brick building on a shaking table with POF sensors installed horizontally and diagonally.

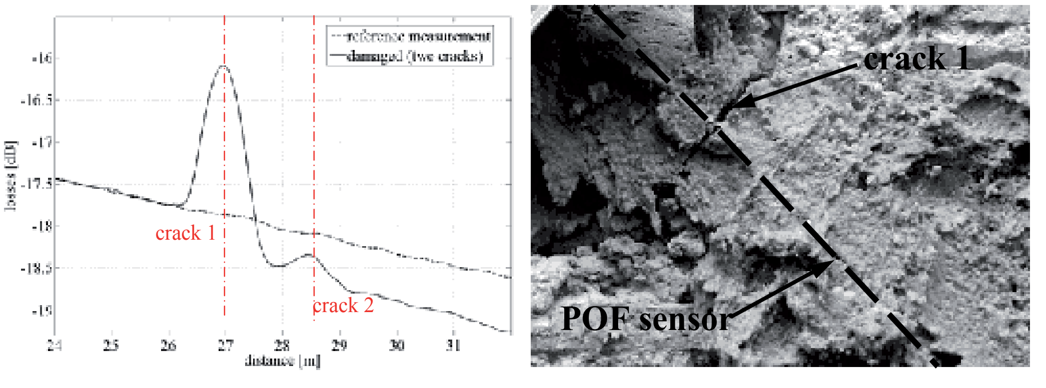

Figure 19. POF OTDR trace showing two cracks at 27.0 m and 28.5 m (left) and the corresponding first crack at 27.0 m of a width of 2 mm (right).

During the last years, several field tests have successfully been conducted on real masonry buildings reinforced by POF-sensors-based technical textiles, one of them on a masonry house at the Eucentre in Pavia, Italy (Fig. 20). The testing procedures of the textile-equipped masonry building included several strong seismic shocks (simulating earthquakes) that resulted in several cracks in the masonry walls. The occurred cracks were clearly detected and localized by the distributed POF OTDR sensor (Fig. 21) which demonstrated the potential of this technique to be used also for damage detection of masonry and heritage structures.

Figure 20. Application of technical textiles containing POF on a masonry building at the Eucentre in Pavia, Italy.

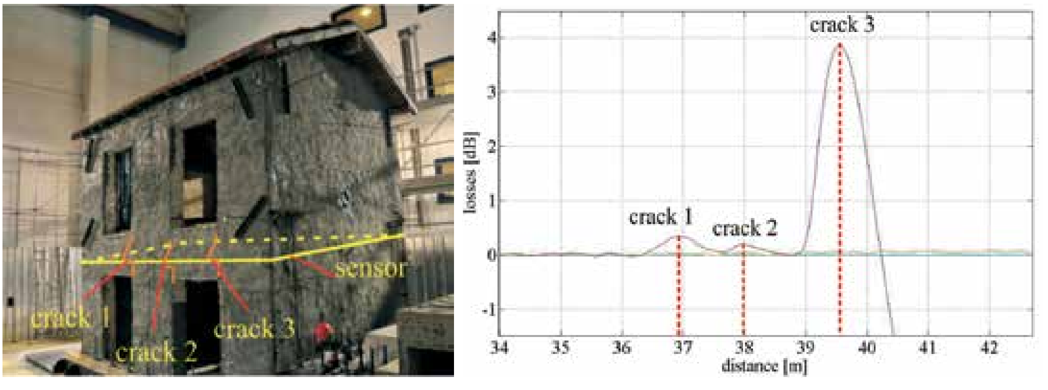

Figure 21. Detection of cracks in a masonry wall by a textile-embedded distributed POF OTDR sensor after several seismic shocks applied to the building.

3. Medical textiles based on fiber optic sensors for healthcare monitoring

Healthcare monitoring of patients and old people who require a continuous medical assistance and treatment is a subject of a number of research activities in Europe. In order to increase the mobility of such patients, the development of wearable monitoring systems able to measure important physiological parameters of the patients is targeted. Europe has considerably pushed the developments of such wearable biomedical clothing containing different types of sensors by a number of research projects.

The European project OFSETH (optical fiber sensors embedded into technical textile for healthcare) supported by the 6th European framework program, has investigated how various vital parameters such as respiratory movement, cardiac rate and pulse oxymetry can be measured by fiber optic sensors based on silica and polymer optical fibers, embedded into medical textiles. As a result, wearable solutions for healthcare monitoring, for patients requiring a continuous medical assistance and treatment, are available. Despite of already existing electrical and also fiber optic sensors, OFSETH has achieved a breakthrough in the healthcare monitoring by combining the advantages of pure fiber optic sensor technologies and wearability of the textiles and so increasing the functionality of the sensor and the comfort of the system.

The OFSETH developments have targeted in the first place on the monitoring of sedated or anaesthetized patients under Medical Resonance Imaging (MRI)[17]. In this case electrical sensors cannot play a role; fiber optic sensors are advantageous because of their electromagnetic compatibility. The use of fiber optic sensors instead of electrical sensors will reduce the electromagnetic disturbance of the MRI field. Additionally, metallic parts and conductive wires of electrical sensors cause burns on the patient's skin in the MRI field. Fiber optic sensors are free from such metallic components and so burning hazard for the patients can be prevented. Besides, fiber optic sensors offer the advantage that the monitoring unit can be placed out of the MRI field and can be connected to the sensor by a fiber cable of some five or ten meters.

Anaesthetized patients are usually transferred from the induction room to the MRI room and back under anesthesia. A continuous monitoring of the patients from the induction to the end of the anesthesia is required but in fact the medical staff usually uses different monitoring devices during the whole procedure, because the most standard monitoring devices are not transportable or not MRI compatible. After the MRI examination, the patient is transferred back, still anesthetized, in the worst case without any monitoring system which puts the patients at risk of anesthetic complications. Therefore, a transportable monitoring system, able to follow the patients from the induction room to the MRI room and back without being removed is needed. The wearability of such a system will increase its functionality and the comfort to the user. Wearable monitoring systems can also be used in the ambulatory healthcare monitoring and the monitoring of Sudden Infant Death Syndrome. Therefore, OFSETH has mainly addressed the textile integration issues and in this context has extended the capability of wearable solutions for healthcare monitoring.

For MRI applications there is especially need to monitor the patients' respiratory parameters: respiratory movement and respiratory rate. Therefore, OFSETH has focused, among other things, on the investigation of textile-integrated fiber optic sensors for respiratory monitoring of patients during MRI examinations. For this purpose, medical textiles that incorporate silica and polymer optical fibers have been investigated where a wearable, adaptable and MRI compatible monitoring system has been targeted.

The feasibility of using fiber optic sensors for respiratory monitoring was demonstrated in the past. It has been reported on fiber sensors woven into bandages or attached onto garments mainly using FBG (fiber Bragg gratings) and LPG (long period gratings) based on silica fibers[18], [19]. However, the poor compatibility of these sensors with industrial textile processes limits their flexibility and use for medical monitoring purposes.

Human breathing movement causes typical elongations of the abdominal circumference of adults of up to 3 %. Using silica fibers, limited strain values of up to 1 % can be measured. Therefore, with a special focus on using POF instead of silica fibers, OFSETH has investigated different fiber sensor techniques for respiratory monitoring[20], [21]. A highly important criterion for selecting POF as medical sensor is its biocompatibility, especially in case of fiber breakage.

3.1. POF OTDR sensor embedded in medical textiles for monitoring of the respiratory movement

For the respiratory monitoring, there is an interest for the doctors to take information from both abdominal (for spontaneous ventilation) and thoracic (for intubated patients) movement[17]. Therefore, a distributed measurement of the respiratory signal, using only one monitor and one sensor fiber would be advantageous. Using an OTDR technique, it is possible to focus on a special part of the fiber and so to differentiate between abdominal and thoracic respiration. A distributed OTDR measurement makes possible to get only the required sensor information and to neglect loss contributions from non-sensing parts. In addition, an OTDR sensor system has the advantage of requiring only one fiber connection, which enables a quicker installation of the system on the patient.

A textile sample based on an elastic fabric containing a POF and manufactured by Centexbel and Elasta, Belgium was tested for the purposes of the respiratory movement monitoring by the OTDR technique. Since it was difficult to integrate a straight optical fiber into an elastic fabric, the textile sample uses a special macrobending sensor design developed by Multitel, Belgium (Fig. 22)[21]. The textile is divided in two sections: a short elastic part of about 10 cm whose length changes during the respiration and a longer non-elastic part. The POF is integrated into the elastic section to measure the elongation of the fabric due to the respiratory movement of the thorax or abdomen. The macrobending sensor design (described more detailed in Chapter 3.2) increases the sensitivity of the POF to the textile elongation and makes possible to detect small changes in the amplitude of the respiratory movement by the OTDR technique. Macrobending effects in POF induce changes of the backscattering in the corresponding area of the fiber that can be easily detected by the OTDR technique.

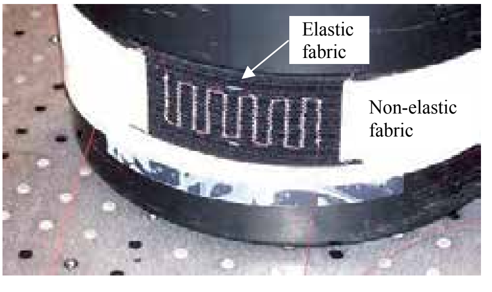

Figure 22. Textile sample containing a POF and based on the macrobending sensor design (textile: Centexbel & Elasta, Belgium; sensor design: Multitel, Belgium).

http://dx.doi.org/10.5772/54244

The feasibility of measuring the respiratory waveform and rate in real time by the POF OTDR technique was demonstrated on a healthy adult during normal breathing[21], [22]. The textile sample was attached around the abdomen of the adult and the elastic part of the textile was placed in the area experiencing the most elongation due to the breathing movement (Fig. 23). The sensor signal was acquired by a fast OTDR device produced by Tempo (OFM20), which operates at 650 nm wavelength, allows a two-point spatial resolution of 5 cm and has a dynamic range of > 20 dB. The device makes possible to measure an OTDR trace in less than 1 s with a sufficient SNR. This acquisition time is fast enough to measure normal human breathing. The changes of the abdominal circumference due to the breathing movement were recorded simultaneously. Fig. 23 shows the result and demonstrates the high potential of the POF OTDR technique for the considered monitoring purposes.

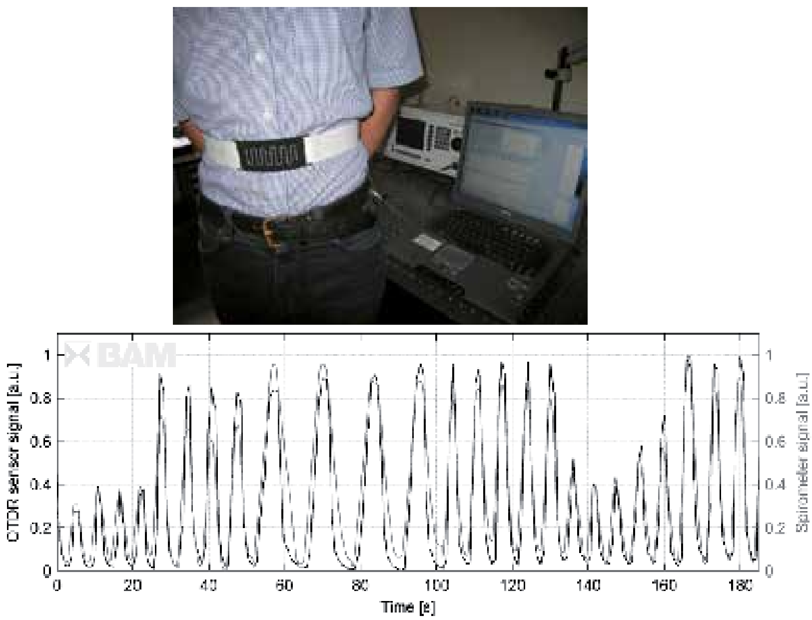

Figure 23. Monitoring of the respiratory abdominal movement of a human adult by POF OTDR sensor embedded in medical textiles (the OTDR sensor signal was compared with the signal measured by a spirometer).

3.2. Sensing harness for monitoring of the respiratory movement

Considering the influence of different patient's morphology as well as textile integration issues to let free all vital organs for medical staff actions during incident or respiratory accidents, different fiber optic sensors have been integrated into a harness allowing an efficient handling and continuous measurement of the respiratory movement[22]. European norms in terms of textile and the medical specification have been taken into account for the design of the sensing harness where the fiber optic sensors are strategically placed for measurement of thoracic and abdominal movements caused by the breathing activity without corruption of one signal by another (Fig. 24). This design is composed of adjustable parts in order to fit the maximum of morphologies and to be worn both by men and women. The harness design keeps some places free, like the pre-cordium in order to facilitate resuscitation in case of cardiac arrest or hemodynamical failure, and give vital information on hemodynamical status during resuscitation. Access to the intra-venous infusion line has also been kept clear, for easy access during anesthesia or for resuscitation purpose. It has been ensured that there is no pressure on venous or arterial blood vessels which could obstruct the regular blood flow.

Figure 24. Sensing harness containing fiber optic sensors for the monitoring of patients under MRI. A thoracic respiration sensor is integrated in the black part (upper right); an abdominal respiration sensor is integrated in the white part (lower middle).

The elongation of the harness belt caused by the respiratory movement is measured using different fiber optic sensing principles based on FBGs and macrobending effects. The abdominal movement causes elongations of about 1-3%, which is much higher than for the thoracic movement which causes only a fractional percentage change. Therefore an FBG sensor which has high accuracy but a low strain limit is used for the thorax while for the abdomen a less accurate macrobending sensor is used which has a much higher strain limit.

The macrobending sensor developed by Multitel (Belgium) is based on bending effect of optical fibers (Fig. 25, left)[22]. Bends cause light coupling from guided modes into radiation modes and thus some power is lost. When the sensor textile is stretched, the curvature radius increases, and the bending loss decreases. Therefore the intensity variations at the output of the optical fiber will reflect the changes of the textile length, due to the respiratory movement. Macrobending sensors have the advantages that their interrogation is very simple: they require measurement of intensity changes, so the main components needed are an LED source and a photodiode. Standard single-mode silica fibers have been integrated into elastic fabrics, manufactured by Elasta (Belgium) during an industrial crochet fabrication process. The bending textile design has the advantage that the integration of the optical fibers into textiles is relatively simple. The bending design also ensures that the optical fiber is not damaged at high strain during integration. Due to the relatively high amplitude of the abdominal movement the signal-to-noise ratio is high enough to monitor the respiratory rate.

For the monitoring of the thoracic respiration movement an FBG sensor developed by Centexbel (Belgium) and Multitel is used. Due to the FBG inscription process the fiber sensor is weakened, which reduces facilities for integration of the fiber into the textiles. For this reason, only optical fibers with sufficient robustness should be used and conventional textile fabrication processes as opted for the macrobending sensor are inadequate for the FBG integration. The optical fiber containing the FBG was thus stitched directly onto an elastic fabric[22]. The robustness of the sensor is guaranteed by an additional silicone coating and polymer attachment points on both sides of the FBG are glued around the fiber for a better adhesion of the sensor onto the fabric and easy stitching without impairing the sensor properties (Fig. 25, right).

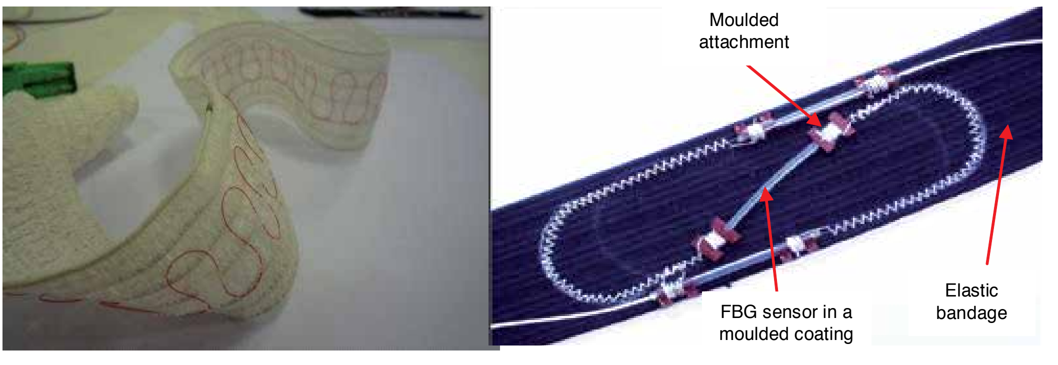

Figure 25. Left: Design of the macrobending sensor. A silica optical fiber was embedded into an elastic fabric during an industrial crochet fabrication process. Right: Design of the FBG sensor. A silica optical fiber containing an FBG was stitched onto an elastic textile.

The harness based on the macrobending and FBG sensor was validated on a simulator in MRI environment[22]. A simulator based on a movable table was used (Fig. 26, left). The displacement of the table was realized by a balloon connected to the medical respirator allowing air-flow circulation by controlling the amplitude and frequency of the movement through the volume or air injected. The signals of the respirator, the fiber sensor response and the gradient signals emitted by the MRI were measured in real-time. Several configurations in terms of volume and/or frequency, in or out of the MRI tube and in presence of or without the MRI gradient were simulated and tested. As a result, it was demonstrated that the displacement of the movable table is detected in terms of amplitude and frequency. The signals of the fiber sensors were not degraded even when the system was submitted to the gradient of the MRI equipment in and out of the magnetic field (inside and outside the MRI tube respectively), as shown in Fig. 26 (right, large picture). At the same time, a clinical validation of the system was carried out at a hospital of Lille, France on several healthy volunteers and patients of the hospital's intensive care unit. Fig 26 (right, small picture) shows the typical signal patterns for both thoracic and abdominal movement detected by the textile-embedded FBG and macrobending sensor on healthy adults.

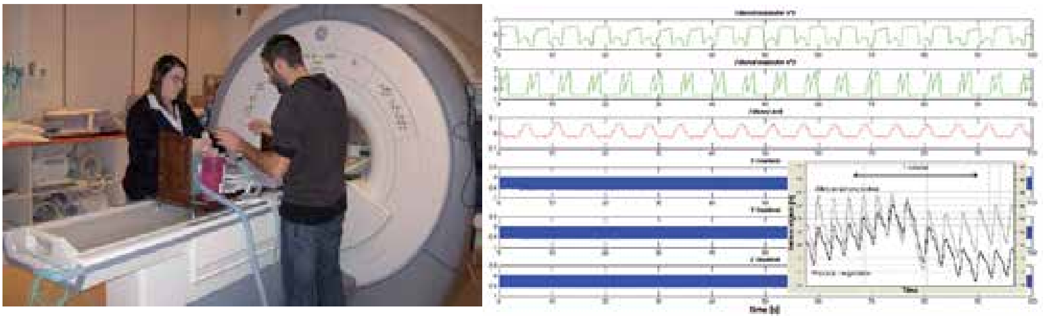

Figure 26. Left: Set-up of the MRI-compatible simulator of CIC-IT de Nancy, France. Right, large picture: Test of the FBG sensor in MRI environment. The first two curves are related to the respiration simulator, the third curve shows the FBG sensor response and the last three curves are related to the magnetic gradients of the MRI equipment. Right, small picture: Abdominal and thoracic respiration signals detected by the textile-embedded macrobending and FBG sensor during a clinical test on healthy volunteers.

3.3. Fiber optic sensors for personal protective equipment

The European project i-Protect (intelligent PPE system for personnel in high-risk and complex environments) develops an advanced personal protective equipment (PPE) system that will ensure active protection and information support for personnel operating in high-risk and complex environments in firefighting, chemical and mining rescue operations[23]. The PPE system will be ergonomically designed and fully adapted to end-users' needs as well as to working conditions. The core of the project is the development of advanced materials and sensors to be used for a multi-functional PPE. This includes a real-time monitoring of risk factors (temperature, gas, oxygen level), users' health status (body temperature, respiratory rate, heart rate) and important protection parameters (end-of-service-life, air pressure in compressed units). The PPE will be wireless connected to a rescue command center.

For the monitoring of the users' health status smart underwear containing fiber optic sensors is being developed. Special attention is paid to the development of a heart rate sensor to be used as a textile-integrated sensor in underwear. A first sensor prototype is based on macrobending effects in POF[23]. The POF macrobending sensor is stitched onto an elastic fabric (the design is similar to this shown in Fig. 25, left) and measures the small elongations of the textile which is caused by the heart movement. To increase the sensitivity of the sensor, the cladding of the POF was treated[23]. A sensor belt containing the POF sensor was tested on a healthy volunteer to measure the circumference changes due to the heart movement. The belt was wrapped around the chest of the volunteer close to the heart. Since the textile design is also sensitive to the respiratory movement, the POF macrobending sensor detects both the respiratory and heart rate at the same time (Fig. 27). A signal processing should be performed to filter the weak heart beats signals. It is expected that by using a modified textile and sensor design it must be possible to improve the sensitivity of the POF macrobending sensor to the heart movement. Alternatively, conventional monitoring techniques like plethysmography could be adapted for the purpose of such applications.

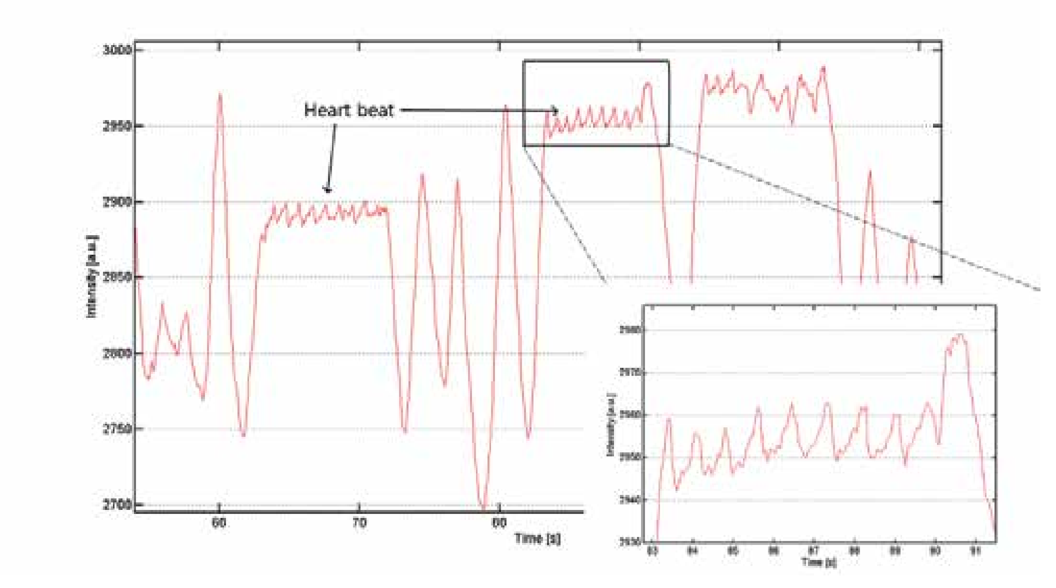

Figure 27. Monitoring of the heart rate of a healthy volunteer by using a textile-embedded POF macrobending sensor.

4. Conclusion

A number of research activities considering the development of novel smart technical textiles based on fiber optic sensors are running in Europe. Such smart technical textiles with embedded optical fibers are a potential new market niche for fiber optic sensors.

Several German projects and the European project POLYTECT have developed novel geotextiles with embedded distributed Brillouin and POF OTDR sensors for monitoring of geotechnical and masonry structures, providing an alarm signal in case of structural damage. Particularly sensors based on POF take advantage of the high robustness, high elasticity and high break-down strain of POF allowing distributed sensing of strong mechanical deformations of soil and masonry walls. Multifunctional, smart technical textiles incorporating fiber optics sensors are a cost-effective solution to increase the structural safety of such structures. The breakthroughs include the use of such textiles for reinforcement and at the same time for monitoring of earthworks and masonry walls, giving online information on the state and the performance of the structures and so preventing a total collapse. Such on-line and long-term monitoring systems will improve the chance of an early detection and the location of “weak points” and damages, and will make it possible to react rapidly and to control damages.

Novel monitoring systems based on medical textiles with embedded fiber optic sensors will be used at medium-term in the healthcare monitoring and for personal protection of rescues in high-risk environments where standard, non-optical monitoring systems show significant limits. Such medical textiles containing fiber optic sensors have been developed in the European projects OFSETH and i-Protect for the monitoring of the respiratory movement of anaesthetized patients under MRI and for the monitoring of the health status of rescues. Especially for MRI applications where transportable and MRI compatible devices are needed, pure fiber optic sensor solutions and the wearability of the textiles are advantageous. The design and comfort of such sensor systems will extend their use from hospitalization to the ambulatory healthcare monitoring and homecare.

Acknowledgements

The research has been carried out in the framework of the German projects "Sensorbasierte Geotextilien zur Deichertuechtigung” (FKZ 02WH0573) and “Sensitive Textilstrukturen” (AiF-Nr. 192 ZBG 1) as well as within the European projects POLYTECT (NMP2-CT-2006-026789), OFSETH (IST-2004-027869) and i-Protect (NMP2-SE-2010-229275). The projects have received research funding from the Federal Ministry of Education and Research (BMBF), the Federal Ministry of Economics and Technology (BMWi) and the European Commission within the European 6th and 7th Framework Programs. The authors are thankful for the financial support and the fruitful cooperation with the project partners.

Author details

Katerina Krebber

Federal Institute for Materials Research and Testing (BAM) Berlin, Germany

References

[1] “The future is Textiles”. Strategic Research Agenda of the European Technology Platform for the future of textiles and clothing, EURATEX (2006).

[2] Lymberis, A. and A. Dittmar, A., “Advanced Wearable Health Systems and Applications”, IEEE Engineering in medicine and biology, pp. 29-33 (2007).

[3] Krebber, K., Lenke, P., Liehr, S., Witt, J. and Schukar, M., “Smart technical textiles with integrated POF sensors”, Proc. SPIE 6933, 69330V-1 – 69330V-15 (2008).

[4] Voet, M. R., Nances, A. and Vlekken, J., “Geodetect: a new step for the use of Fibre Bragg Grating technology in soil engineering”, Proc. of the 17th International Conference on Optical Fibre Sensors, 5855 (1), 214-217 (2005).

[5] Noether, N., Wosniok, A., Krebber, K. and Thiele, E., “A distributed fiber optic sensor system for dike monitoring using Brillouin optical frequency domain analysis”, Proc. SPIE 6933, 69330T-1 – 69330T-9 (2008).

[6] Liehr, S., Lenke, P., Wendt, M., Krebber, K., Seeger, M., Thiele, E., Metschies, H., Gebreselassie, B. and Muenich, J. C., “Polymer Optical Fibre Sensor for Distributed Strain Measurement and Application in Structural Health Monitoring”, IEEE Sensors J., 9 (11), 1330-1338 (2009).

[7] Kurashima, T., Horiguchi, T. and Tateda, M., “Distributed-temperature sensing using stimulated Brillouin scattering in optical silica fibers”, Optics Letters 15 (18), 1038-1040 (1990).

[8] Bao, X., Webb, D.J. and Jackson, D.A., “32-km distributed temperature sensor based on Brillouin loss in an optical fiber”, Optics Letters 18 (18), 1561-1563 (1993).

[9] Garus, D., Krebber, K., Schliep, F. and Gogolla, T., “Distributed sensing technique based on Brillouin optical-fiber frequency-domain analysis”, Optics Letters 21(17), 1402-1404 (1996).

[10] Noether, N., Wosniok, A., Krebber, K. and Thiele, E., ”A Distributed fiber optic sensor system for dike monitoring using Brillouin frequency domain analysis,” Proc. SPIE 7003, 700303 (2008).

[11] Noether, N., Wosniok, A., Krebber, K. and Thiele, E., “A distributed fiber-optic sensor system for monitoring of large geotechnical strutures”, Proc. of the 4th International Conference on Structural Health Monitoring on Intelligent Infrastructure (SHMII-4) (2009).

[12] Husdi, I. R., Nakamura, K. and Ueha, S., ”Sensing characteristics of plastic optical fibres measured by optical time-domain refelectometry”, Meas. Sci. Technol. 15, 1553-1559 (2004).

[13] Lenke, P., Liehr, S. and Krebber, K., „Improvement of the distributed strain sensor based on optical time domain reflectometry measurement in polymer optical fibers”, Proc. of the 17th International Conference on Plastic Optical Fibre, (2008).

[14] Liehr, S., Wendt, M., and Krebber, K., “Distributed strain measurement in perfluorinated polymer optical fibres using optical frequency domain reflectometry,” Measurement Science and Technology 21(9), 094023–1 – 094023–6 (2010).

[15] Liehr, S., Lenke, P., Wendt, M., Krebber, K., Gloetzl, R., Schneider-Gloetzl, J., Gabino, L. and Krywult, L., „Distributed Polymer Optical Fiber Sensors in Geotextiles for Monitoring of Earthwork Strutures”, Proc. of the 4th International Conference on Structural Health Monitoring on Intelligent Infrastructure (SHMII-4) (2009).

[16] Liehr, S., Wendt, M., Krebber, Muenich, J. C., Stempniewski, L. and Metschies, H., „Distributed polymer optical fiber sensors integrated in technical textiles for monitoring of masonry structures", Proc. of the 4th International Conference on Structural Health Monitoring on Intelligent Infrastructure (SHMII-4) (2009).

[17] De jonckheere, J., Jeanne, M., Grillet, A., Weber, S., Chaud, P., Logier, R. and Weber, J. L., "OFSETH: Optical Fibre Embedded into technical Textile for Healthcare, an efficient way to monitor patient under magnetic resonance imaging", Proc. IEEE EMBC conference Engineering in Medicine and Biology Society (2007).

[18] Wehrle, G., Nohama, P., Kalinowski, H.J., Torres, P.I. and Valente, L.C.G., "A fibre optic Bragg grating strain sensor for monitoring ventilatory movements", Meas. Sci. Technol. 12, 805-809 (2001).

[19] Allsop, T., Revees, R., Webb, D. J. and Bennion, I., "Respiratory monitoring using fibre long period grating sensors", Novel Optical Instrumentation for Biomedical Applications II, SPIE-OSA Biomedical Optics, SPIE 5864, Q1-Q6 (2005).

[20] Grillet, A., Kinet, D., Witt, J., Schukar, M., Krebber, K., Pirotte, F. and Depré, A., "Optical Fiber Sensors Embedded into Medical Textiles for Healthcare Monitoring", IEEE Sensors J., 8 (7), 1215-1222 (2008).

[21] Krebber, K., Grillet, A., Witt, J., Schukar, M., Kinet, D., Thiel, T., Pirotte, F. and Depré, A., "Optical fibre sensors embedded into technical textile for healthcare (OFSETH)", Proc. of the 16th International Conference on Plastic Optical Fibre, 227-233 (2007).

[22] Witt, J., Narbonneau, F., Schukar, M., Krebber, K., De Jonckheere, J., Jeanne, M., Kinet, D., Paquet, B., Depré, A., D´Angelo, L.T., Thiel, T. and Logier, R., "Medical textiles with embedded fiber optic sensors for monitoring of respiratory movement", IEEE Sensors J., 12 (1), 246-254 (2012).

[23] Witt, J., Krebber, K., Demuth, J. and Sasek, L., "Fiber optic heart rate sensor for integration into personal protective equipment", Proc. of International Workshop BioPhotonics 2011, Th6.26, 1-3 (2011).

Refractometric Optical Fiber Platforms for Label Free Sensing

Carlos A. J. Gouveia, Jose M. Baptista and
Pedro A.S. Jorge

Additional information is available at the end of the chapter

http://dx.doi.org/10.5772/55376

1. Introduction

The in situ and real time measurement of a variety of chemical and biological parameters is important in diversified environments ranging from industrial processes, medicine to environmental applications. In this context, the demand for novel sensing platforms capable of multiplexing, real time and remote operation in electromagnetic or chemically hazardous environments has increased significantly in recent years.

The combination of fiber optic technology with optical sensing mechanisms has many benefits that make it a promising alternative to standard technologies. Immunity to electromagnetic interferences, small size, and capability for in-situ, real-time, remote, and distributed sensing are some of the most appealing characteristics that motivate a growing scientific community.

Biochemical sensing typically requires that optical signal interacts with the external media, either directly with a given analyte or through an auxiliary membrane, which contains an indicator dye. Some of the most appealing techniques regarding sensitivity and specificity rely on the use of colorimetric or fluorescent indicator dyes. Although some of the intrinsic problems of indicator based sensor like, leaching, photobleaching and temperature dependence have reported solutions, some limitations restrict further developments. A variety of excitation sources, detectors and filters are needed to deal with the large variety of spectral characteristics of dye based sensors. Moreover, these wavelength ranges demand for the use of special optical fibers and optoelectronics, severely limiting its compatibility with the standard telecom optical fiber technology.

In this context, label free optical sensing based on the measurement of refractive index (RI) represents an interesting solution. Such approaches do not interfere with the analyte properties and require, instead, the design of sensitive layers that experience a refractive index change in its presence. This can be achieved by using biomolecules with a natural affinity to the target, or chemical species having analyte specific ligands. The combination of such membranes with refractive index sensors can therefore provide attractive solutions for biochemical sensing.

The aim of this chapter is to expose the basic principles of evanescent field based fiber optic refractometers, suitable to biosensing field and capable to remote and real time operation. Initially, the principles of the technology are described. Thereafter, recent progress in the area is presented where several fiber optic devices will be detailed, ranging from the popular fiber Bragg gratings, the well known long period gratings, a variety of modal interferometers including tapers, mismatched fiber sections and also multimode interference based structures. Emphasis will be given to the description of the sensing structures and its sensing mechanism, advantages and disadvantages and wherever possible, the sensing performance of each sensing device will be compared in terms of sensitivity and detection limit.

2. Fiber optic refractometers: Principle

Optical fiber consists of a core and a cladding with different refractive indices. The refractive index of the core *(n_{core})* is higher than the refractive index of the cladding *(n_{clad})*. Snell's law can describe the propagation of light in optical fibers by the principle of total internal reflection. In optical fibers, the total internal reflection occurs when light is incident from the core to the cladding, at incident angle *(θ_i)*, greater than the critical angle *(θ_c)*, which can be calculated by the following equation;

$$\theta_c = \arcsin\left(\frac{n_{clad}}{n_{core}}\right)$$

Since light is totally reflected inside the core, no electromagnetic field is propagating in to the cladding. Nevertheless, the electromagnetic field actually penetrates a short distance into the lower refractive index medium, propagating parallel to the interface core-cladding and decaying exponentially with the distance from the interface (See figure 1). The physical explanation for this phenomenon is that when applying Maxwell equations to the interface between two dielectrics, the tangential components of both the electric and magnetic fields must be continuous across the interface, this is, the field in the less dense medium cannot abruptly become zero at the interface and a small portion of light penetrates into the reflecting medium. This boundary condition can only be satisfied if the electromagnetic field crosses the interface, creating the so-called evanescent wave [1]. The penetration depth *(d_p)* of the evanescent wave is a key parameter for sensing purposes. It is the distance from the interface at which the amplitude of the electric field is decreased by a factor equal to *1/e* and, following the approximation of geometrical optics, it can be expressed by the following equation:

$$d_p = \frac{\lambda_0}{2\pi}\frac{1}{\sqrt{n_{core}\cdot \sin_2(\theta_i) - n_{clad}}}$$

where λ_0 is the radiation wavelength. The penetration depth of the evanescent field varies from 50 nm to 1000 nm depending on the wavelength, the refractive indices and the angle of incidence.

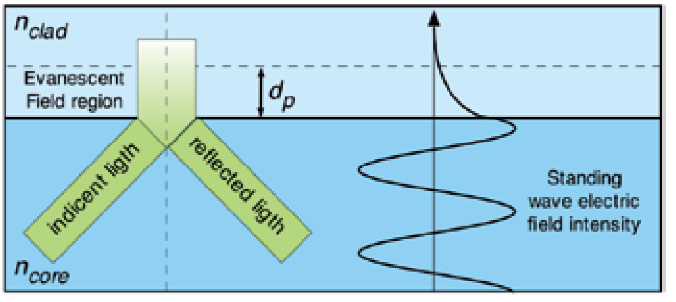

Figure 1. Evanescent field in the core/cladding interface of an optical fiber

The majority of the fiber refractometers are based on evanescent field interactions. However, fibers were originally designed for optical communications. A typical single mode optical fiber has a core diameter between 8 and 10.5 μm, a cladding diameter of 125 μm and light propagates confined in the core. Therefore, the penetration depth is far smaller than the cladding thickness and there is almost no interaction between the optical signal and the external medium. Strategies must be devised in order to provide interaction with the surrounding medium. Typically, the evanescent field can be exposed by removing partially or totally the cladding of the optical fiber. This can be done by chemical etching, tapering or side polishing techniques. In alternative, it is possible to use specific tools capable to transfer energy from the fundamental core mode to cladding modes. Fiber gratings are an example of these devices. In such a cases the optical radiation can interact with the external environment due to the evanescent field formed at the cladding/external medium interface. In this case, the penetration depth is given by:

$$d_p(m) = \frac{\lambda_0}{2\pi \cdot n_{clad}} \frac{1}{\sqrt{\sin^2(\theta_{(m)}) - \sin^2(\theta_{c'})}}$$

where $\theta(m)$ is the incident angle of the geometrical ray associated with the *mth* cladding mode and $\theta_{c'}$ is the critical angle at the interface between the fiber cladding and the external environment. Clearly, $\theta(m)$ is different for each cladding mode and decreases with the increment of the order of the cladding mode. It is important to observe that the *dp* changes as a function of the coupled cladding mode as well as of the external refractive index. The dependence of *dp* on the external refractive index (n_{ext}) is implicitly contained within $\theta_{c'}$, which can be expressed as:

$$\theta_{c'} = \arcsin\left(\frac{n_{ext}}{n_{clad}}\right)$$

Fiber optic biochemical sensors based on evanescent field configurations rely on the use of sensing layers deposited on the sensitive surface that experience a refractive index change in presence of an analyte. This can be achieved by using biomolecules with a natural affinity to the target, or chemical species having analyte specific ligands. When exposed to an analyte, a chemical/biochemical interaction takes place within this layer or on its surface. In this case, only a portion of the optical radiation which comes out of the sensor (evanescent field) is modulated, depending on the thickness of the interaction region.

Biological sensing is based on the specific binding between biorecognition molecules (antibodies, oligonucleotides, aptamers or phages) immobilized on the sensor surface and the targeted biological species, which causes a change in the effective thickness or density of the surface of fiber and consequently a change on the optical signal. Figure 2 conceptually shows an example of label free fiber optic biosensor. A functional coating is used to support and enhance the attachment of the bioreceptor molecules, which bind the analyte [2].

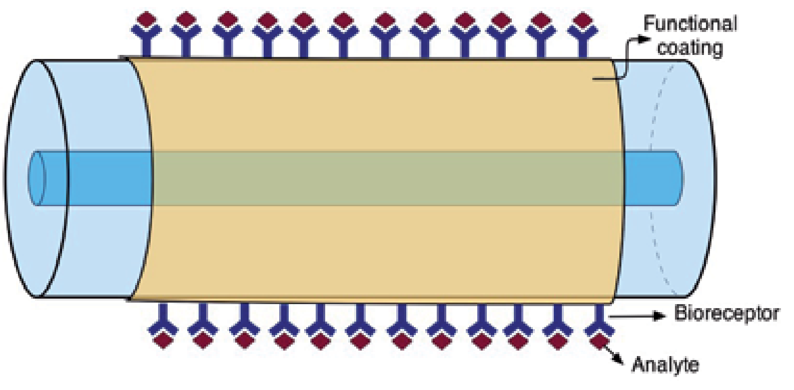

Figure 2. Label free fiber optic biosensor schematic representation

In the following sections the most relevant fiber refractometric platforms based on evanescent field interactions and capable for label free biochemical sensing will be presented, including their measurement principle and some examples of most important works presented till now.

3. Fiber Bragg gratings

Fiber Bragg grating (FBG) sensors have generated great interest in recent years because of their many industrial and environmental applications. FBGs are simple, versatile, and small intrinsic sensing elements that can be written in optical fibers and which consequently have all the advantages normally attributed to fiber sensors. In addition, due to the fact that typically the measurand information is encoded in the resonant wavelength of the structure, which is an absolute parameter, these devices are inherently self-referenced. Moreover there are several intrinsic advantages associated with FBG technology such as reflection operation mode, narrowband spectral response and their compatibility with standard telecom technology, therefore can be easily multiplexed, which is particularly important in the context of remote, multi-point and multi-parameter sensing [3]. Based on diffraction mechanism, they consist on the periodic perturbation of the core of the optical fiber (typically half-wavelength) that is induced by exposing the fiber to an interference pattern of UV light or femtosecond radiation. They are characterized by the periodicity Λ of the refractive index modulation and by the effective refractive index of the waveguide mode $n_{eff.}$ The grating constitutes a wavelength selective mirror or rejection filter defined by the Bragg resonance wavelength (λ_B)

$$\lambda_B = 2 n_{eff} \Lambda$$

The full width at the half maximum (FWHM) of the resonant peak of the Bragg grating is typically a few hundred picometers. It depends on the physical length of the grating, which is usually few millimeters. Figure 3 illustrates the principle of operation of an FBG. When a broadband optical signal reaches the grating, a narrow spectral fraction is reflected and the remaining is transmitted. The peak wavelength of the reflected signal is defined by the Bragg resonance wavelength.

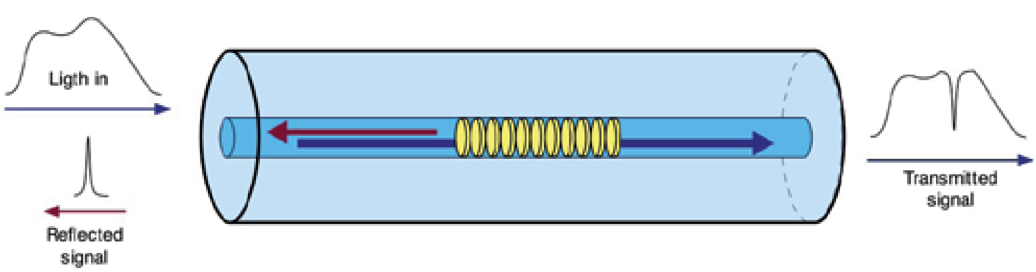

Figure 3. Operation principle of fiber Bragg grating

FBG sensors have been widely used for strain and temperature measurement [4]. Bragg gratings works mainly with radiation confined to the fiber core, this way strategies have to be devised in order for the radiation to interact with the external medium. Typically, FBG based refractometers rely on the evanescent field of the core modes under fiber etching conditions, which enables interaction with the surrounding medium.

The first demonstration of an FBG as a refractometer was done in 1997 by Asseh *et al.* [5], and it was based on the application of chemical etching to the fiber region where the grating was located. The etching process was done by immersing the fiber in a solution of 40% hydrofluoric acid (HF) for approximately 50 min. After etched, the fiber had a diameter of 11μm; thus 1μm of cladding still remained. The sensor was tested in different solutions of sucrose, inferring a variation of refractive index between 1.333-1.345 RIU. The estimated sensibility was 1nm/RIU and the measured resolution was ± 5×10^{-4} RIU. Figure 4 illustrates an FBG based refractometer,

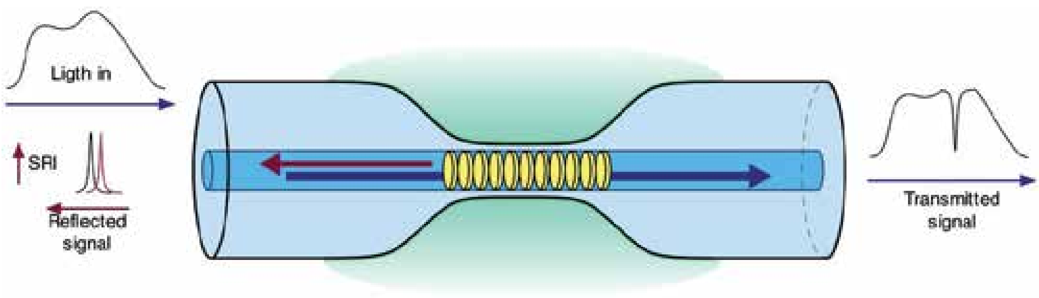

Figure 4. Etched fiber Bragg grating refractometer

when the cladding of the optical fiber was partially etched. Thus, the wavelength of the reflected signal depends on the external refractive index.

Regarding sensitivity enhancement and temperature compensation, in 2001 Schroeder *et al.* [6] presented a two in-line FBGs written on a single-mode depressed-cladding optical fibre of cut-off wavelength 750 nm. One of the gratings was side-polished to become sensitive to the SRI and the second one for thermal compensation. The effect of high refractive index overlays was studied in order to shift the mode field to the surface of the sensor and to enhance the sensitivity for low refractive index analytes. Operation in wavelengths far above the cut-off wavelength was also explored resulting in an improvement of the sensitivity of the sensor. The sensor was tested in different solutions, inferring a variation of refractive index between 1.30-1.46 RIU. The maximum sensitivity for an external refractive index close to 1.45 was found to be 300nm/RIU and the measured resolution was $\pm 2\times10^{-6}$ RIU.

A simpler solution for thermal compensation was published by Iadicicco *et al.* (2005), a single grating half-etched for simultaneous measurement of refractive index and temperature. The operation principle relies on the splitting of the original grating spectral response in two different peaks due to a selective etching over the grating length, where one of them becomes sensitive to the external refractive index and the other one is just sensitive to temperature [7]. Concerning enhancements in sensitivity, in 2005 Chryssis *et al.* [8] has shown that an effective solution is provided by etching the core of a fiber Bragg grating. A maximum sensitivity of 1394 nm/RIU is achieved as the surrounding index approaches the core index when the residual diameter was reduced to 3.4μm.

In the past few years, microfibers have attracted increasing interest due to their intrinsic advantages such as large evanescent field, small effective mode field diameter and low-loss interconnection to single mode fibers. Microfibers can be produced by the use of standard flame brushing technique. Bragg gratings written in microfiber have been also explored for refractive index sensing. In 2010 Fang *et al.* [9] presented FBGs written in microfibers with diameters ranging from 2μm to 10μm by using femtosecond pulse irradiation. The maximum sensitivity obtained was 231.4 nm/RIU for refractive index values near 1.44 for a microfiber with 2μm diameter. However, femtosecond laser Bragg grating inscription relies in the physical deformation of the fibre surface, which can weaken even more the micrometric structure. Concerning with this fact, later in the same year, Zhang *et al.* [10] demonstrated a

http://dx.doi.org/10.5772/55376

microfiber Bragg grating fabrication using a KrF excimer laser in a highly Ge-doped photosensitive microfibers with diameters of 6 and 6.5μm, respectively. Two reflection peaks were observed in the spectrum of FBG. The reflected peak induced by the higher-order mode was used to monitor RI variations, because the higher-order mode has a larger evanescent field outside the microfiber and thus it is more sensitive to the surrounding refractive index, compared with the fundamental mode reflection. The other peak was used for temperature referencing. The maximum sensitivity was ~102 nm/RIU at a refractive index of 1.378, in the 6μm diameter fiber.

Etched FBG, side polished FBG or microfiber Bragg gratings are interesting devices that exploit the influence of the surrounding refractive index (by the evanescent field interaction) on the effective index of the core mode, and consequently on the Bragg wavelength (λ_B). However, in order to enable the interaction with the external medium, the fiber diameter should be reduced, removing the cladding and in some cases partially the core. The sensitivity of the FBG is highly dependent on the diameter of the fiber in the region of the grating. Nevertheless, this process introduces fragility in the fibre sensor especially in cases where maximum sensitivity is required.

A different approach to develop fiber optic refractometers based on FBG technology was proposed in 2001 by Laffont *et al.* [11]. The sensing configuration relies on the use of tilted FBG (TFBG) as refractive index sensors by using the transmission spectrum changes due to the cladding modes resonances sensitivity to the external medium. In TFBGs the modulation pattern is blazed (tilted) by an angle θ with respect to the fiber axis. This asymmetry enables the coupling to circularly and non-circularly symmetric contra-propagating cladding modes and reduces the energy coupling to the contra-propagating core mode. The cladding modes are guided by the cladding boundary, and as a result, their effective index depends on the external index. The sensitivity of the cladding to variations of the SRI increases with mode order, since the penetration depth of the evanescent field increases for higher-order modes. With the increment of the SRI, the center wavelength of the resonances experienced a shift to higher wavelengths. In addition to their spectral shift, the intensity drops progressively, to fit a smooth loss curve. Thus, monitoring the shifts of the cladding modes relative to the Bragg resonance or measuring the normalized envelope of the cladding mode resonance spectrum in transmission can held an accurate measure of the surrounding refractive index. Figure 5 shown a conceptual representation of a tilted FBG.

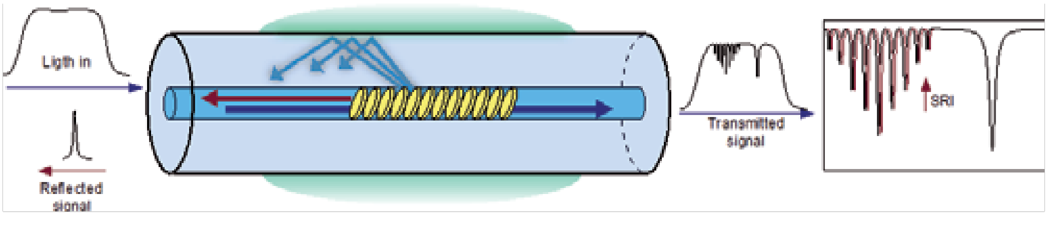

Figure 5. Refractometer based on a tilted fiber Bragg grating

The TFBGs used in the experiment of Laffont *et al.* [11] were written in a standard single mode fiber using a Lloyd mirror interferometer. The measurement of SRI was based on the normalized envelope of the cladding mode resonance spectrum in transmission. It was also shown that this parameter was relatively insensitive to temperature. Another reason for using the envelope of the resonance spectrum is that, choosing the proper tilt angle, this parameter can change monotonically and smoothly for refractive index values between 1.32 and 1.42, with a small change in sensitivity. Using the normalized area parameter and a 16° TFBG a resolution of $\pm 10^{-4}$ RIU was achieved. In 2007 Chan *et al.* [12] proposed a relative measurement of refractive index, based on the separation distance between certain cladding modes that were dependent on the refractive index and temperature and the core mode, which is refractive index independent. A 4° TFBG was used where refractive index sensitivity of 10 nm/RIU was obtained, achieving a resolution of $\pm 10^{-4}$ RIU.

TFBGs are a suitable option for refractometric sensing in terms of performance and robustness of the fiber structure. However, a TFBG couples the core mode to a number of cladding modes in a large wavelength bandwidth, which renders difficult the signal readout and multiplexing. In addition, the fact that the measurement must be made in transmission, requiring access to the sensor from both sides, can represent a difficulty in some applications. Recently a few authors have been exploring the possibility to excite the cladding modes of standard FBG by transferring power from the fundamental core mode to the cladding modes in the upstream of the FBG. Thereby, the FBG will couple back the light to the fundamental core mode. This arrangement enables the possibility to read the cladding mode of the Bragg grating in the reflected spectrum

In 2010 Han *et al.* [13] have shown for first time this method with concatenating a LPG and a FBG. The LPG partially couples light from the core mode to a cladding mode, both of which are reflected by the FBG. The refractive index sensitivity of 2.3 nm/RI was obtained. Recently, based on the same principle, Wu *et al.* [14] presented a singlemode–multimode–singlemode fiber structure (SMS) assisted FBG to measure the SRI. This structure utilizes multimode fiber to excite cladding modes of an FBG written on the singlemode fiber and recouple reflected cladding modes to the input singlemode fiber. The maximum achieved sensitivity was 7.33 nm/RIU in the range from 1.324 to 1.439 RIU. Fiber refractometers based in cladding modes of standard FBGs represent an interesting opportunity for label free sensing, especially by using all-grating devices which enable the possibility of efficiently transfer power to specific high order modes in order to excite specific cladding modes of an FBG. However, work is still to be done concerning the enhancement of sensitivity, which is still far from ideal.

Owing to reflective nature of this devices a few FBG based Fabry-Perot cavities were presented for refractive index measurement. In 2005 Liang *et al.* [15] reported a refractive index sensor based on an etched fiber Fabry-Perot interferometer with a radius of 1.5μm. The sensor showed a sensitivity of 71.2 nm/RIU and a variation of refractive index of $\pm 1.4\times10^{-5}$ can be detected. Table 1 summarizes the most relevant FBG based refractometers presented to date and their performance parameters.

Configuration	Measurement method	Year	RI Range	Sensitivity	Resolution	Ref.
Etched FBG	Spectral Shift	1997	1.333-1.345	1 nm/RIU	5×10^{-4}	[5]
	Spectral Shift	2005	Near 1.44	1394 nm/RIU	$7.2\times10^{-6\,(*)}$	[8]
Polished FBG	Spectral Shift	2001	Near 1.45	300 nm/RIU	$10^{-6(*)}$	[6]
Microfiber FBG	Spectral Shift	2010	Near 1.44	230 nm/RIU	$5\times10^{-6(*)}$	[9]
	Spectral Shift	2010	Near 1.38	102 nm/RIU	$10^{-5(*)}$	[10]
TFBG	Normalized Area	2001	1.32-1.42		10^{-4}	[11]
	Spectral Shift	2007	Near 1.32	11.2 nm/RIU	10^{-4}	[12]
LPG/FBG	Spectral Shift	2010	Near 1.45	2.32 nm/RIU	$10^{-4(*)}$	[13]
MMF/FBG	Spectral Shift	2010	1.40-1.44	7.33 nm/RIU	$10^{-4(*)}$	[14]
FP-FBG	Spectral Shift	2005	Near 1.33	71.4 nm/RIU	1.4×10^{-5}	

(*) Theoretical maximum resolution given by the ratio between the readout device resolution and refractive index sensitivity of the sensor.

Table 1. Comparison of the characteristics of the most relevant FBG based refractometers

3.1. Applications

Several FBG based refractometers have been described rely on the measurement of the refractive index changes for the measurement of sucrose, salt, ethylene glycol, Isopropyl Alcohol among others [5-7]. Using functional layers just few works were presented. The first demonstration of the concept of biosensor based on FBG, was done by Chryssis *et al.* (2005) [16], based on an etched FBG, where single stranded DNA oligonucleotide probes of 20 bases were immobilized on the surface of the fiber grating using relatively common glutarahylde-hyde chemistry. Hybridization of a complimentary target single strand DNA oligonucleotide was monitored in situ and successfully detected. Later, in 2008 Maguis *et al.* [17] presented a biosensor based on a TFBG refractometer that enables to directly detect, in real-time, target molecules. Thus, bovine serum albumin (BSA) (antigen) and anti-BSA (antibody) were used to study the reaction kinetics of the antigen- antibody recognition by changing the antibody concentration in the different configurations for the antigen immobilization.

4. Long period fiber gratings

A Long period grating (LPG) is one of the most popular fiber optic refractive index sensor and it has been widely used for chemical and biological sensing. Like FBG, LPG is also a diffraction structure, where the refractive index of the fiber core is modulated, with a period between 100μm to 1000μm that is induced in the optical fiber using different techniques: UV laser irradiation, CO_2 laser irradiation, electric-arc discharge, mechanical processes and periodic etching [18]. This periodic perturbation satisfies the phase matching condition between the fundamental core mode and a forward propagating cladding mode of an optical fiber. Thereby, in an LPG, the core mode couples into the cladding modes of the fiber, resulting in several attenuation bands centered at discrete wavelengths in the transmitted spectrum, where each attenuation band corresponds to the coupling to a different cladding mode. The spectral width of the resonant dip varies from few nanometers up to tens of nanometers depending on the physical length of the grating.

LPGs are intrinsically sensitive to external refractive index exhibiting changes in the position of the resonance wavelength. The resonant wavelength of light coupling into a particular cladding mode is given by the phase matching condition [19]:

$$\lambda_{res}^{m} = \left(n_{eff,core} - n^{m}_{eff,clad}\right)\Lambda$$

Where Λ is the grating period, $n_{eff,core}$ and $n^{m}_{eff,clad}$ are the effective indexes of the core and *m*th-cladding mode, respectively. Following the phase matching condition, a change in the surrounding refractive index will induce a shift in the resonance wavelength due to the variation of the $n^{m}_{eff,clad}$, which is dependent on the external refractive index. The first long period grating inscribed successfully in an optical fiber was reported in 1996 by Vengsarkar *et al.* [20] for band-rejection filters, and in the same year Bhatia *et al.* [21] presented the first application of long period gratings for refractive index sensing, reporting a wavelength shift of 62nm for a refractive index change between 1.40-1.45 and an average resolution of ± 7.69×10^{-5} RIU in the same range; for an LPG with period of 320μm written by UV radiation exposition in a Corning standard 1310nm fiber. Figure 6 illustrates the principle of operation of long period gratings.

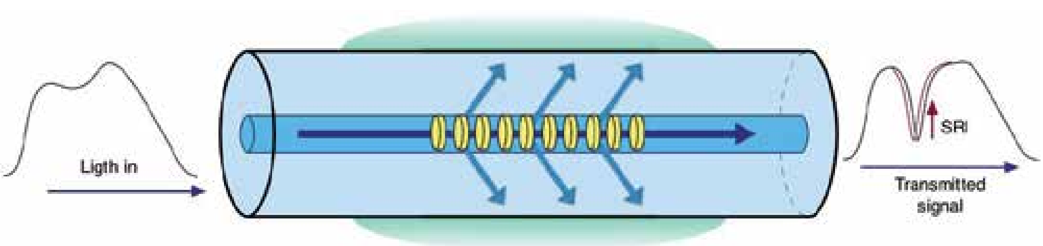

Figure 6. Fiber long period gratings

Shu *et al.* [22] reported in 2002 a Long Period grating written in B–Ge co-doped fiber by UV laser irradiation technique, with a period of 202μm. For the eleventh order mode, a refractive index sensitivity of 1481 nm/RIU was shown in the range between 1-1.36 RIU, which is according with our knowledge the best sensitivity for a bare LPG reported for this range. Electric-arc induced LPGs are attractive due to its simplicity and flexibility, as well as the low cost of the fabrication process and its applicability not only to commonly used photosensitive fibers, but also to photonic crystal fibers, which are made of pure silica. In 2011 Smietana *et al.* [23] published a work on gratings with periods of 345 and 221μm, respectively, for LPGs based on the SMF28 and PS1250/1500 fibers. Which are the shortest periods achieved for this type of fibers using the electric-arc manufacturing technique. Results showed refractive index sensitivities of 302 and 483 nm/RIU in the range between 1.33-1.41 that represent also the highest sensitivity reported for a bare LPG made by electric-arc technique for the specified measuring range.

The sensitivity of an LPG is then typically defined as a shift of the resonance wavelength induced by a measurand. The sensitivity characteristic of a bare LPG to surrounding refractive index changes has an increasing (in modulus) non-linear monotone trend. The result is that the maximum sensitivity is achieved when the external index is close to the cladding index while for lower refractive indices (around 1.33) the LPG is scarcely sensitive. Figure 7 shows the behavior of resonance wavelength and its optical power to refractive index changes. The behavior changes when a thin layer of sub-wavelength thickness (few hundreds of nanometers) and with higher refractive index than the cladding is deposited thereon. The use of high refractive index (HRI) overlays in fiber optic sensors refractometers based on evanescent wave was explored initially by Schroeder *et al.* [6] for a polished FBG. Coated LPGs with thin HRI layers was firstly proposed by Rees *et al.* [24] and since then, several authors have explored its use for LPG RI sensitivity enhancement [24-28] and to develop highly sensitivity chemical devices [29, 30].

The HRI overlay draws the optical field towards the external medium extending its evanescent wave. As a result there is an increased sensitivity of the device to the surrounding RI. Due to the refractive-reflective regime at the cladding-overlay interface, the cladding modes in a HRI coated LPG are bounded within the structure comprising the core, the cladding and the overlay. This means that a relevant part of the optical power carried by the cladding modes is radiated within the overlay. The field enhancement in the overlay depends strongly on the overlay features (thickness and refractive index) and the SRI. For a fixed overlay thickness and refractive index, by increasing the SRI, the transition from cladding to overlay modes occurs: the lowest order cladding mode (cladding mode with highest effective refractive index) becomes guided into the overlay. At the same time, the higher order modes move to recover the previous effective indices distribution. This is reflected through the phase matching condition in the shift of each attenuation band toward the next lower one [31]. Resulting from this modal transition that the attenuation bands can exhibit a sensitivity of thousands of nanometers per refractive index unit.

Pilla *et al.* [32] reported in 2009 a polystyrene coated LPG ($\Lambda = 460\mu m$). For a 5^{th} order resonance, sensitivities of ~ 5000 nm/RIU (near 1.41) and ~ 2500 nm/RIU (near 1.38) were achieved for coating thicknesses of 270nm and 320nm, respectively. The reported data showed how by changing the overlay thickness it is possible to tune the sensitivity characteristic for the considered cladding mode in the desired refractive index.

High order cladding modes that strongly penetrate the external medium, on the other hand, offer higher sensitivity, and obviously these are the most desirable for sensing purposes. An increase in the order of the coupled cladding mode is obtained by decreasing the grating period [33]. Pilla *et al.* [34] reported recently in 2012 a polystyrene coated LPG ($\Lambda = 200\mu m$). The coating thickness was approximately 245nm. For an 11^{th} order resonance, sensitivity over 9000 nm/RIU near 1.347 was achieved, which is so far the best sensitivity obtained for a fiber device

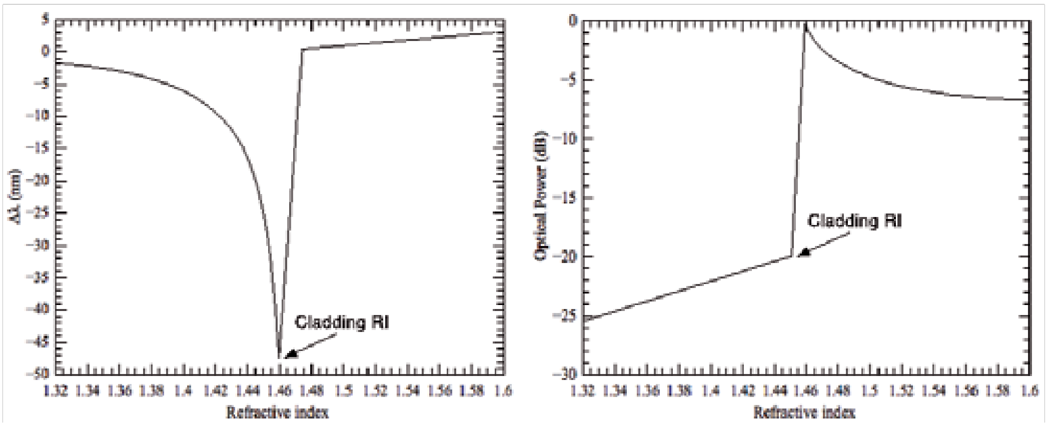

Figure 7. Refractive index response of a LPG

for this range of RI. This result shows HRI coated LPGs as a promising technology for a high-performance label free sensing applications.

LPGs show great sensitivity to the surrounding RI, but also at the same time to temperature. In the other hand, the measurement of the refractive index is strongly dependent on the temperature due to the thermo-optic coefficient. Thus, measurement and compensation of this parameter is an important issue for this kind of platforms. A number of techniques have been proposed in order to get rid of the temperature cross-sensitivity mainly based on the use of a second grating sensitive only to temperature [35, 36].

LPG based interferometers have shown higher resolution to refractive index measurement compared to the use of a single LPG. The advantage of using those structures lies on their interferometric nature and its principle of operation, where the coupled core and cladding modes from one LPG combine again at a second matched LPG to form interference fringes. The core and cladding paths constitute the arms of an all fiber Mach–Zehnder interferometer (see figure 8) [37]. In 2002, Allsop *et al.* [38] presented an LPG based Mach-Zehnder as a refractometer. Using a pair of LPG (Λ = 270μm) apart 100mm from each other, coupling 9th order cladding mode and interrogated by phase generated carrier technique; a resolution of $\pm 1.8\times10^{-6}$ was achieved for a RI range between 1.37-1.40. Later, in 2004 Swart *et al.* [39] presented a refractometer based on Michelson interferometer, by using a single LPG located 45 mm away from the mirrored tip (see figure 9). Compared with the Mach-Zehnder layout, the presented configuration has potential advantages such as reflection operation and compactness, it just need half interaction path length for the same sensitivity.

More recently, in 2010 Mosquera *et al.* [40], presented an optical fiber refractometer based on a Fabry–Perot resonator that incorporates an intracavity long-period grating that couples and recovers energy to the fiber cladding after being phase shifted by the surrounding refractive index. Figure 10 shows the sensing head configuration. The resonator is formed by two high reflectivity (~ 95%) FBGs separated by 47.5 mm. The external refractive index is monitored by the resonant frequencies of the Fabry–Perot interferometer, which can be measured either in transmission or in reflection. Results give a detection limit of $\pm 2.1\times10^{-5}$ RIU at n=1.33.

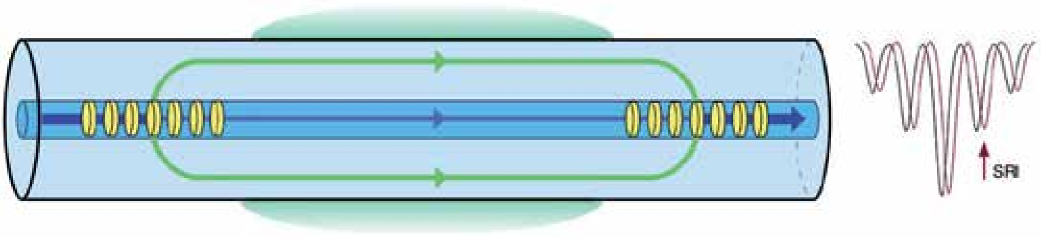

Figure 8. All fiber LPG based Mach-Zehnder interferometer

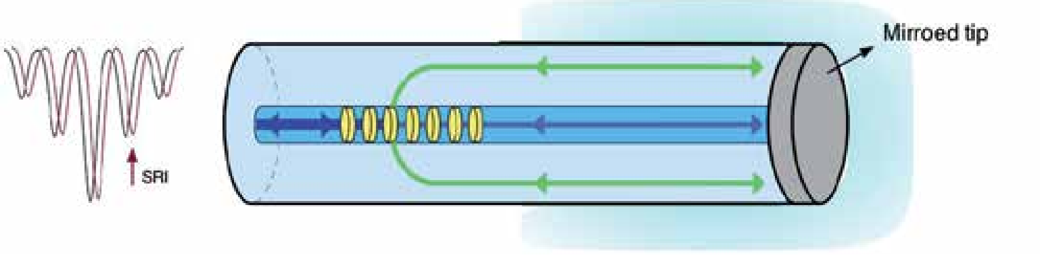

Figure 9. All fiber LPG based Michelson interferometer

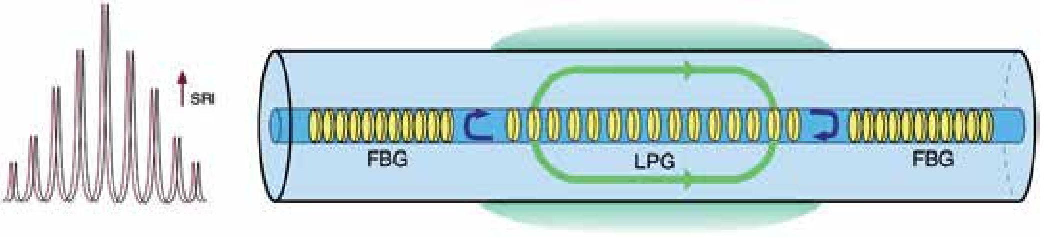

Figure 10. Intracavity LPG Fabry-Perot resonator

4.1. Applications

Long period gratings are the most popular fiber optic sensor for label free sensing, since in 1996 Bhatia *et al.* [21] presented the first LPG based refractometer, many refractive index sensors have been reported along the years, using the refractometric ability to measure parameters such as the concentration of ethylene glycol, sucrose, salt, ethanol among others [33, 41-46]. Although this approach is not the most reliable due to the possible interference of other species present in the solution, which are different from the analyte of interest. Thus, the deposition of sensitive thin layers that can change their own refractive index in presence of a specific analyte have opened a very interesting niche of applications. However, as mentioned above, the thickness and refractive index of the overlay are critical aspects that strongly affect the sensitivity of the device.

LPGs coated by functional layers have been successfully exploited for chemical sensing. Gu *et al.* [30] reported a LPG with a sol-gel derived coating of SnO_2 with optimized thickness. In presence of specific gases, the semiconductor surface energy changes, which leads to the change of conductivity and refractive index. The sensor was tested for Ethanol vapor detection. Corres *et al.* [29] used the electrostatic self-assembled method to create pH sensitive films with an optimal overlay thickness. Two coatings were presented. The first one is based on polyallylamine hydrochloride (PAH), polyacrylic acid (PAA), and the second one was done incorporating the pigment Prussian blue (PB) in the PAH/PAA matrix. Faster response was obtained with the introduction of PB particles in the polymeric matrix. Barnes *et al.* [47] presented a LPG functionalized with a polymethylsiloxane coating; able to perform solid-phase microextraction of organic solvents such as xylene and cyclohexane. The grating was interrogated using cavity ring down spectroscopy. Improvements regarding with sensitivity and miniaturization of the sensing probe were studied recently by the same authors [48]. An LPG coated with a zeolite thin film was used to detect the presence of toluene and isopropanol vapors by Zhang *et al.* [49].

Recently, Korposh *et al.* [50] reported a LPG multilayer film from silica nanoparticles and the subsequent infusion of a porphyrin into the porous coating for ammonia sensing. The infusion of a functional material into the base mesoporous coating, chosen to be sensitive to a specific analyte, represents the novelty of this work. Two possible sensing mechanisms were shown, based upon changes in the refractive index of the coating. Chemically induced refractive index changes of the mesoporous coating at the adsorption of the analyte to the functional material (PAA), and chemically induced desorption of the functional material (tetrakis-(4-sulfophenyl)porphine), from the mesoporous coating.

LPG has been widely used for biochemical sensing; on this case a biomolecule with affinity to a target can be used as functional coating. The earliest demonstration of biomolecule detection using this structure was done by DeLisa *et al.* [51], where the LPG was used for sensitive detection of antibody-antigen reactions. Goat anti-human Immunoglobulin G (antibody) was immobilized on the surface of the LPG, and detection of specific antibody- antigen binding was shown. Later, several works were reported regarding antibody-antigen interaction [32, 52-59] and also DNA hybridization [58, 60-62].

LPGs applied for label free detection of specific bacteria using physically adsorbed bacteriophages were presented for the first time by Smietana *et al.* [63], where T4 phages immobilized onto the surface of an LPG were used as recognition element for *E. Coli* detection. Recently, improvements in sensitivity in a similar work was presented by Tripathi *et al.* [64].

Lately, an enzyme coated LPG was used for glucose detection by Deep et al [65]. The authors demonstrated the successful immobilization of glucose oxidase on to the 3-aminopropyltriethoxysilane (APTES) silanized LPG fibers for the development of a new glucose sensing technique.

5. Modal interferometers

Fiber modal interferometers have recently concentrated the focus of research because of their potential sensing capabilities and in some cases the reduced cost and simplicity of fabrication. In the previous section an LPG based modal interferometer was introduced. The LPGs were used as mechanism to couple light from core to cladding and subsequently from cladding to core. There are different mechanisms through which the high order modes could be selectively excited, by tapering a single mode optical fiber, through a core diameter mismatching structure (larger or thinner) or by a simple misaligned splice. Other kind of devices relies on multimode interference, in such a cases a small section of multimode fiber is properly inserted between single-mode fibers. The aim of this section is to describe the sensing mechanism of this kind of devices and to address the most relevant contributions for chemical and biosensing field.

5.1. Tapered single-mode fiber

Tapering a single mode fiber involves reducing the cladding diameter along with the core and it is made by heating a section of the fiber and pulling on both ends of the fiber in the opposite directions, either under a constant speed, force or tension. The heat source can be a gas burner flame, a focused CO_2 laser beam or an electric arc formed between a pair of electrodes. When the optical fiber is tapered, the core–cladding interface is redefined in such a way that the light propagation inside the core penetrates to the cladding and it is confined by the external medium.

A fiber taper consists of three contiguous parts: one taper waist segment with small and uniform diameter, and two conical transition regions with gradually changed diameter. Depending on the pulling conditions it is possible to fabricate tapers with different shapes and properties. Fiber tapers may be divided into two distinct categories: adiabatic and non-adiabatic. An adiabatic fiber taper is characterized by a very smooth change in the profile (small taper angle) in order to ensure a smooth mode conversion without significant losses in the transmitted signal. In this case, the main portion of the radiation remains in the fundamental mode (LP_{01}) and does not couple to higher order modes as it propagates along the taper.

On the other hand, non-adiabatic fiber tapers (abrupt taper angle) can be done in such a way that coupling occurs primarily between the fundamental mode of the un-pulled fiber and the first two modes of the taper waveguide (LP_{01}, LP_{02}), where due to the large difference of the refractive indexes of air and fiber cladding, the taper normally supports more than one mode. The light propagates at the air/cladding interface of the tapers waist region in which case the single mode fiber is converted into a multimode waveguide. The result of back and forth coupling between the single mode of the fiber and the two (or more) modes of the taper is an oscillatory spectral response. The efficiency of this last coupling is dependent on the relative phase of the participating modes. Therefore, this device behaves as Mach-Zehnder modal interferometer. When there are only two modes, the relative phase is $\Delta\varphi=\Delta\beta L$, where $\Delta\beta$ and L are the difference in propagation constants of the two modes and the interaction length along the taper, respectively. Therefore, the spectral response of the taper will shift correspondingly by changing the above terms. For instance, if the refractive index of the surrounding environment of the taper changes, the difference in propagation constants and the relative phase would be modified leading to a shift of the spectral response. Usually, this devices present waist diameter of few microns, promoting high interaction of the optical signal with the surrounding medium; thereby they are very sensitive to SRI. Figure 11 shows conceptually a non adiabatic (abrupt) fiber taper.

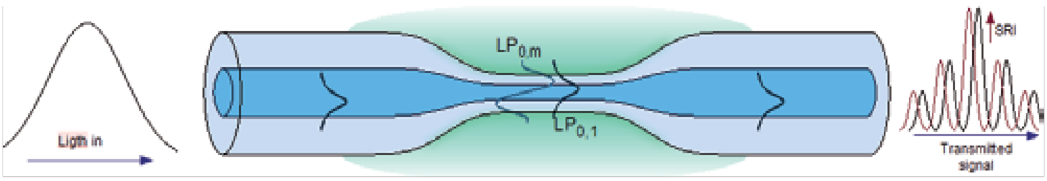

Figure 11. Abrupt taper based refractometer

Fiber refractometer based in non-adiabatic tapers has been proposed recently as platform for label free sensing. Zibaii *et al.* [66] presented a single-mode non-adiabatic tapered optical fiber sensor for sensing the variation in refractive index with concentration of D-glucose in deionized water and measurement of the RI of amino acids (AAs) in carbohydrate solutions. This method showed a rewarding ability in understanding the basis of biomolecular interactions in biological systems. The fiber tapers were fabricated using heat-pulling method with waist diameter and length of 7μm and 9mm respectively. The limit of detection of the sensing probe was 55 ppm for a D-glucose concentration ranging from 0 to 80 mg ml^{-1}. Regarding refractive index measurements a sensitivity of ~ 1150 nm/RIU in the range between 1.3330 - 1.3447. A resolution of ±8.2×10^{-6} RIU was also calculated. Zibaii *et al.* [67] presented also a similar sensing probe for real-time monitoring of the Escherichia coli (E. coli K-12) growth in an aqueous medium. The taper length and waist diameter were 7-9μm and 3nm respectively. The bacteria were immobilized on the tapered surface using Poly-L-Lysine. By providing the proper condition, bacterial population growth on the tapered surface increases the average surface density of the cells and consequently the refractive index of the tapered region would increase. The adsorption of the cells on the tapered fiber leads to changes in the optical characteristics of the taper. This affects the evanescent field leading to changes in optical throughput. Concerning improvements in refractive index sensitivity the same author showed a single-mode non-adiabatic tapered optical fiber sensor inserted into a fiber loop mirror. Adjusting the polarization controllers inserted in the loop allowed to excite different cladding modes in the interferometric taper resulting in different optical paths for the clockwise and the counterclockwise beams. The variation of the polarization settings provided a tuning in the RI sensitivity in a range between 800nm/RIU - 1200 nm/RIU for indices in the range from 1.3380 to 1.3510 [68].

Later, Tian *et al.* [69] published a tapered optical fiber biosensor that enables the label-free detection of biomolecules. The biomolecules bonded on the taper surface were determined by demodulating the transmission spectrum phase shift. The taper waist diameter and length were approximately 10μm and 12mm, respectively. A tapered optical fiber biosensor was fabricated and evaluated with an Immune globulin G antibody-antigen pair.

5.2. Core mismatch

Abrupt Tapered devices show high sensitivity to refractive index measurements. However, after the tapering, due to reduced fiber diameter, the structure becomes very fragile and special handling is needed. Recently, a different approach based on core mismatched sections have been investigated. In this case, mismatched sections are proposed as valid alternatives as mode-coupling mechanisms to transfer optical power between core and cladding modes in optical fiber. The idea is to couple and recouple the fundamental mode and high order cladding modes through two mismatched sections. It can be done by using a misaligned splice or a short section of a special fiber.

A core offset splice based refractometer was presented by Tian *et al.* [70] (2008). Higher order cladding modes were excited by fusion splicing two singlemode fiber (SMF) sections with a certain core offset. Due to asymmetric nature for a core offset splice, coupling mainly occurs between the $LP_{0,m}$ and $LP_{1,m}$ modes. Two layouts were presented, a Mach-Zehnder by concatenating two misaligned splices and a Michelson, realized by a single core offset splice and a layer of ~ 500nm gold coating at the tip of the optical fiber. The Michelson interferometer was tested as refractometer. The response of the device to external variations of refractive index was evaluated by using dimethyl sulfoxide solutions with different concentrations. The sensitivity for a device with 38 mm of interaction length was 33 nm/RIU in the range of refractive index between 1.315-1.362.

The core-offset technique presents difficulties to control the amount of light power splitting. In alternative, Pang *et al.* [71] presented a Mach-Zehnder based standard SMF sandwiched between two double cladding fibers (DCF) sections. Standard SMF were used for both light input and output of the Mach-Zehnder device. The DCF consists of three layers, the core, inner cladding and external cladding. The inner cladding is thin and its refractive index is lower than that of the core and the external cladding. The DCFs serve as the in-fiber couplers that split and combine light propagating in the core and the outer cladding region. Because of the depressed inner cladding structure, the light wave propagating in the core can be partially coupled to the outer cladding through the evanescent wave. Therefore, the DCF can be employed as a core-cladding modes coupler to construct in-fiber interferometers. The DCF length was approximately 5mm (on both sides), and the interferometer interaction length was 93 mm. Sensitivities of 31 nm/RIU and 823 nm/RIU were obtained for the lower refractive index (1.34 range) and the higher refractive index (1.44 range), respectively.

The idea of fiber a core diameter mismatch (CDM) based interferometer for refractive index sensing has been reported by Rong *et al.* [72]. The sensing probe was constituted by a 9mm section of SMF sandwiched between two 2mm segments of thin core fiber (TCF). The two TCF sections act as core-cladding modes coupling and recoupling, and the SMF middle section performs as the interference arm. The first TCF couples part of the core-guided fundamental mode into forward propagating cladding modes of the downstream SMF via CDM. Thus, the cladding modes propagating in the SMF middle section were sensitive to the SRI. Finally, the cladding modes are coupled back to the fiber core of lead-out SMF via the second TCF, mixing with the original core mode and generating the interference signal. The studied refractometer exhibited sensitivity up to 159 nm/RIU over low refractive index values from 1.33 to 1.38. Similar work was presented by the same group [73]. Based on the same principle, but using two sections of multimode fiber (MMF) as a core-cladding modes coupling and recoupling mechanism. The sensing probe was constituted by a 40mm section of SMF sandwiched between two 5mm segments of MMF. The device showed sensitivity up to 188 nm/RIU over low RI values from 1.33 to 1.40. Figure 12 shows schematically the MMF assisted Mach-Zehnder interferometer.

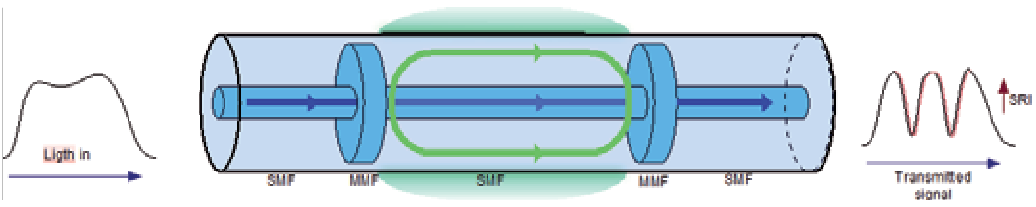

Figure 12. Mach-Zehnder interferometer based on core diameter mismatch

5.3. Multimode interference

Modal interference involving more than two modes has also been studied, resulting into a spectral transfer function that is no co-sinusoidal but instead show sharp peaks at specific wavelengths. It is common to refer this approach as multimode interference (MMI). MMI in optical fiber devices is usually obtained by splicing a MMF section between two single mode fibers, thus forming a SMF-MMF-SMF (SMS) fiber configuration. Based on multimodal interference and the self-imaging or re-imaging effect, the SMS structure acts as an optical band filter that has been widely explored for optical communication and sensing applications.

The SMS fiber concept relies on the fact that when the light field coming from the input SMF enters the MMF, exciting several high order modes, generating a periodic interference pattern along the MMF section. Depending on the wavelength and geometrical length, the light into de MMF can interfere constructively or destructively resulting, at the end, in a device with different spectral characteristics. Therefore the length of the MMF determines the spectral features of the MMI device. Depending where the interference pattern is 'intersected', constructive or destructive interference results, at different wavelengths yielding the transmission of resonant peaks or resonant losses respectively. The transmitted spectral power distribution is, therefore, highly sensitive to the optical path length of the MMF section. It is important to refer that in MMI devices based on standard MMF, the optical signal does not access the external medium. Therefore, they are insensitive to the SRI. MMI based refractometers usually relies on etched cladding MMF, tapered MMF or coreless multimode fibers (CMF). Figure 13 shows conceptually a SMS device based in a CMF, where constructive interference is present resulting in a resonant peak in the transmitted spectrum.

MMI fiber devices are very attractive due to their high potential for refractive index sensing. In 2006, Jung *et al.* [74] presented the first MMI based fiber refractometer. The sensing structure was based in a 125μm diameter coreless silica fiber (CSF) splice between two step index 50/125μm MMF sections. The advantage of use MMF instead SMF is the efficient power coupling and recoupling due to the large core diameter. The refractive index resolution was estimated to be $\pm 4.4\times10^{-4}$ RIU for a refractive index range from 1.30 to 1.44. Later, Wu *et al.* [75] investigated the influence of etched MMF core diameters and on the sensitivity of an SMS fiber based refractometer. They have shown that refractive index sensitivity is highly dependent on the MMF diameter. The SMS fiber structure based refractometer with a core diameter of 80μm has an estimated sensitivity of 180 nm/RIU in the RI range from 1.342 to 1.352 and 1815 nm/RIU in the RI range from 1.431 to 1.437. In another perspective, Biazoli *et al.* [76] studied a tapered SMS structure for high index sensing. The device relies on a coreless MMF, part of which was tapered down by flame brushing technique. For a 55μm MMF taper waist diameter the results showed that in the lower indices range of 1.30–1.33, a sensitivity of 148 nm/RIU was achieved, while in the high sensitivity index region of 1.42–1.43, a value of 2946 nm/RIU was also attained.

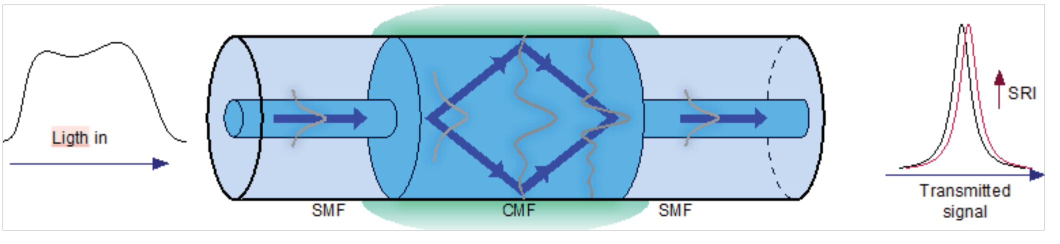

Figure 13. Singlemode-Multimode-Singlemode (SMS) multimodal interferometer

Good sensitivity, ease to fabricate and possibility to build robust devices are some of the advantages of SMS structures for label-free sensing. However, these structures produce a broad optical band spectrum, resulting in a small Q factor and thus poor resolution in the measurement of spectral shift. Concerning improvements in the interrogation schema, Lan *et al.* [77] proposed a SMS fiber structure coated with a zeolite thin film and interrogated by a fiber ring laser for highly sensitive chemical vapor detection. The zeolite-coated SMS structure was used as a bandpass filter and inserted into an Erbium fiber loop to generate a laser line with narrow linewidth and high signal-to-noise ratio. The nanoporous zeolite adsorbs chemical molecules from the surrounding environment to increase its effective refractive index of the coated zeolites, producing a wavelength shift of the SMS filter and a corresponding change in the laser wavelength. The sensor has been demonstrated for detection of ethanol.

A different approach for multimodal interference devices was presented by Xia *et al.* [78]. The authors investigated a fiber modal interferometer constituted by a thin core fiber (TCF) sandwiched between two SMF. The designed TCF modal interferometer was made with a commercial TCF (Nufern 460-HP) whose cut-off wavelength was around three times shorter than normal SMF. In such structure, the high-order cladding modes will be excited when the light reaches the first heterocore interface. The excited high-order cladding modes will interfere with the core mode at the second heterocore interface due to the existing optical path difference between the two modes. The constructive or destructive interference will determine the output intensity maximum or minimum. Both transmissive and reflective TCF modal interferometers were experimentally demonstrated, and showed a good sensitivity to a small change of external refractive index ~ 100 nm/RIU in the range between 1.34 - 1.39. Gu *et al.* [79] presented a pH sensor based on a TCF modal interferometer with electrostatic self-assembled nanocoating. The surface of the sensor is coated with poly(allylamine hydrochloride) and poly(acrylic acid) nanocoating. A fast and linear response was obtained in either acid or alkali solution (in the pH range 2.5 to 10) with resolution of ±0.013 pH unit.

6. Conclusions

In this chapter a review of evanescent field based refractometric platforms for label free sensing was given. Several aspects regarding the implementation of label free biochemical sensors using standard optoelectronics were address. Different structures were described, including fiber gratings, modal interferometers and multimodal devices. Emphasis was given to the description of fiber optic device and their sensing mechanism, advantages and limitations and the sensing performance of each sensing technology was evaluated. Table 2 summarizes the main features of the refractometric configurations.

Technology	Advantages	Limitations
Etched FBG	Well developed technology Multiplexing capability	Fragility Low sensitivity High cost
Tilted FBG	Well developed technology	Low sensitivity High cost
LPG	High sensitivity	Fabrication Temperature cross-sensitivity
LPG based interferometer	High sensitivity	Fabrication Device length
Abrupt taper	High sensitivity	Fragility
CDM based interferometers	Low-cost	Reproducibility
Multimodal interferometer	Low-cost Low temperature cross-sensitivity	Reproducibility Broader resonance

Table 2. Summary of the advantages and limitation of the studied technologies

Optical fiber gratings, including fiber Bragg gratings and long-period fiber gratings, have also been explored for refractive index sensing. They consist in a periodic modulation of the refractive index of the core of the fiber, where the LPG's period is much longer (hundreds of microns) than the FBG's period (typically a half-wavelength). This structural difference results in devices with fundamentally different properties. FBGs work mainly with radiation confined to the fiber core, in this way strategies have to be devised in order for the radiation to interact with the external medium. Typically, FBG based refractometers rely on the evanescent field of the core mode under fiber etching conditions. FBG based configurations are more attractive for the purpose of multipoint sensing due to their very narrow spectral response. Nevertheless, the etching process introduces fragility in the fiber sensor. Tilted FBGs do not require etching therefore maintain the fiber integrity. Although, a TFBG couples the core mode to a number of cladding modes in a large wavelength bandwidth, it renders difficulty for signal readout and multiplexing. The refractive index sensitivity to these devices (FBG and TFBG) in the biological range is quite low which means that these devices are not very promising for field of biosensing.

Long period gratings (LPG), on the other hand, provide evanescent interaction by exciting cladding modes, and are therefore intrinsically sensitive to external refractive index changes. They maintain fiber integrity and probably represent the most popular device for label free sensing. They present high sensitivity to refractive index measurement, which can be increased and tuned by using HRI overlays. The HRI overlay draws the optical field towards the external medium extending its evanescent wave. As a result there is an increased sensitivity of the device to the SRI. The field enhancement in the overlay depends strongly on the overlay thickness and refractive index. This technique allows the coupling of the optical design and sensitivity optimization of the device, together with the functionalization. The careful design by means the proper choice of the grating period, the overlay RI and a very controlled deposition method, together with the integration on the HRI of sensitive materials or biological active agents, provide a powerful platform for advanced optical label free biochemical sensing. However, LPGs are also highly sensitive to temperature, they need an extra mechanism to compensate temperature changes.

LPG interferometers based on Michelson or Mach-Zehnder layouts or even Fabry-Perot intracavity were also demonstrated showing high sensitivity when compared with single bare LPG, and great potential for the biosensing applications. Nevertheless, the device length (few tens of centimeters) can be a constraint for some applications. Fiber tapers, due its highly reduced cladding diameter have an enhanced evanescent interaction and have long been explored for refractive index measurements by monitoring the transmitted optical power. In spite of high sensitivity and very compact size (few millimeters), however, these structures are very fragile and special packaging is needed.

On the other hand, new configurations using special fibers provide new sensing opportunities. Modal interferometers based on core diameter mismatch, by using thin core fibers or multimode fiber used as cladding coupling mechanism have shown good sensitivity, ease of fabrication and potential low cost. Nevertheless, these configurations are difficult to reproduce and to control the mode excitation and the amount of power transferred.

Multimode interference based refractometers are also interesting solutions that rely on the concept of re-imaging effects of MMI patterns present in multimode waveguides. In these devices, the transmitted spectral power distribution is highly sensitive to the optical path length of the multimode fiber and its SRI. Usually based on singlemode-multimode-singlemode structures, they can be easily fabricated and applied in different situations. However, these configurations are also difficult to reproduce and present very broad spectral resonance making for instance multiplexing a very difficult task. The table 2 shows the most relevant evanescent field based fiber refractometers.

Overall, evanescent field fiber refractometers are very attractive due to their immunity to electromagnetic interferences, small size, and capability for in-situ, real-time, remote, and distributed sensing. Most of the applications, however, focus on the measurement of parameters such as the concentration of ethylene glycol, sucrose, salt, ethanol, among others. Nevertheless, this approach is not the most reliable due to the possible interference of other species present in the solution, which are different from the analyte of interest. Thus, the use of sensitive materials containing biomolecules with a natural affinity to the target, or chemical species having analyte specific ligands, has increased, mainly based on LPGs. Several works were reported regarding antibody-antigen interaction and also DNA hybridization. Regarding chemical application several sensing probes were presented to measure pH, Ethanol vapor, ammonia.

Configuration	Measurement method	Sensitivity	Resolution (RIU)	Ref
Microfiber FBG	Spectral Shift	100nm/RIU	-	[10]
TFBG	Spectral Shift	10nm/RIU	10^{-4}	[12]
Bare LPG	Spectral Shift	1481nm/RIU	-	[22]
HRI coated LPG	Spectral Shift	>9000nm/RIU	-	[34]
Mach-Zehnder LPG	Phase	-	$1.8x10^{-6}$	[38]
Fabry-Perot LPG	Spectral Shift	-	$2.1x10^{-5}$	[40]
LPG/FBG	Normalized Optical Power	-	$2x10^{-5}$	[35]
Abrupt Taper	Spectral Shift	1150nm/RIU	$8.2x10^{-6}$	[66]
CDM based Mach-Zehnder	Spectral Shift	188nm/RIU	-	[73]
MMI	Spectral Shift	148nm/RIU	-	[76]

Table 3. Summary of the performance parameters of the most relevant works on fiber based refractometers

Acknowledgements

This work was partially supported by COMPETE program and FCT by funding project n.º FCOMP-01-0124-FEDER-019439 (Refª. FCT PTDC/AGR-ALI/117341/2010). Carlos Gouveia would like to acknowledge the financial support of FCT (SFRH/ BD/ 63758/ 2009)

Author details

Carlos A. J. Gouveia[1,2], Jose M. Baptista[1,2] and Pedro A.S. Jorge[1]

1 INESC-Porto, Rua do Campo Alegre, Porto, Portugal

2 CCCEE, Universidade da Madeira, Campus da Penteada, Funchal, Portugal

References

[1] Hecht, E.: 'Optics 4th edition', Optics 4th edition by Eugene Hecht Reading, MA: Addison-Wesley Publishing Company, 2001, 2001, 1

[2] Fan, X., White, I.M., Shopova, S.I., Zhu, H., Suter, J.D., and Sun, Y.: 'Sensitive optical biosensors for unlabeled targets: A review', Analytica Chimica Acta, 2008, 620, (1-2), pp. 8-26

[3] Kersey, A.D., Davis, M.A., Patrick, H.J., LeBlanc, M., Koo, K.P., Askins, C.G., Putnam, M.A., and Friebele, E.J.: 'Fiber grating sensors', J Lightwave Technol, 1997, 15, (8), pp. 1442-1463

[4] Frazao, O., Ferreira, L.A., Araújo, F.M., and Santos, J.L.: 'Applications of Fiber Optic Grating Technology to Multi-Parameter Measurement', Fiber Integrated Opt, 2005, 24, (3), pp. 227-244

[5] Asseh, A., Sandgren, S., Ahlfeldt, H., Sahlgren, B., Stubbe, R., and Edwall, G.: 'Fiber optical Bragg grating refractometer', Fiber Integrated Opt, 1998, 17, (1), pp. 51-62

[6] Schroeder, K., Ecke, W., Mueller, R., Willsch, R., and Andreev, A.: 'A fibre Bragg grating refractometer', Meas Sci Technol, 2001, 12, (7), pp. 757-764

[7] Iadicicco, A., Campopiano, S., Cutolo, A., Giordano, M., and Cusano, A.: 'Nonuniform thinned fiber Bragg gratings for simultaneous refractive index and temperature measurements', Photonics Technology Letters, IEEE, 2005, 17, (7), pp. 1495-1497

[8] Chryssis, A.N., Lee, S.M., Lee, S.B., Saini, S.S., and Dagenais, M.: 'High sensitivity evanescent field fiber Bragg grating sensor', Photonics Technology Letters, IEEE, 2005, 17, (6), pp. 1253-1255

[9] Fang, X., Liao, C.R., and Wang, D.N.: 'Femtosecond laser fabricated fiber Bragg grating in microfiber for refractive index sensing', Optics Letters, 2010, 35, (7), pp. 1007-1009

[10] Zhang, Y., Lin, B., Tjin, S.C., Zhang, H., Wang, G., Shum, P., and Zhang, X.: 'Refractive index sensing based on higher-order mode reflection of a microfiber Bragg grating', Opt Express, 2010, 18, (25), pp. 26345-26350

[11] Laffont, G., and Ferdinand, P.: 'Tilted short-period fibre-Bragg-grating-induced coupling to cladding modes for accurate refractometry', Meas Sci Technol, 2001, 12, (7), pp. 765-770

[12] Chan, C.-F., Chen, C., Jafari, A., Laronche, A., Thomson, D.J., and Albert, J.: 'Optical fiber refractometer using narrowband cladding-mode resonance shifts', Appl Optics, 2007, 46, (7), pp. 1142-1149

[13] Han, M., Guo, F., and Lu, Y.: 'Optical fiber refractometer based on cladding-mode Bragg grating', Optics Letters, 2010, 35, (3), pp. 399-401

[14] Wu, Q., Semenova, Y., Yan, B., Ma, Y., Wang, P., Yu, C., and Farrell, G.: 'Fiber refractometer based on a fiber Bragg grating and single-mode-multimode-single-mode fiber structure', Optics Letters, 2011, 36, (12), pp. 2197-2199

[15] Liang, W., Huang, Y., Xu, Y., Lee, R.K., and Yariv, A.: 'Highly sensitive fiber Bragg grating refractive index sensors', Appl Phys Lett, 2005, 86, (15), pp. 151122-151122

[16] Chryssis, A.N., Saini, S.S., Lee, S.M., Yi, H.M., Bentley, W.E., and Dagenais, M.: 'Detecting hybridization of DNA by highly sensitive evanescent field etched core fiber bragg grating sensors', IEEE Journal of Selected Topics in Quantum Electronics, 2005, 11, (4), pp. 864-872

[17] Maguis, S., Laffont, G., Ferdinand, P., Carbonnier, B., Kham, K., Mekhalif, T., and Millot, M.-C.: 'Biofunctionalized tilted Fiber Bragg Gratings for label-free immunosensing', Opt Express, 2008, 16, (23), pp. 19049-19062

[18] James, S., and Tatam, R.: 'Optical fibre long-period grating sensors: Characteristics and application', Measurement Science and Technology, 2003, 14, (5), pp. R49-R61

[19] Erdogan, T.: 'Cladding-mode resonances in short- and long-period fiber grating filters', Journal of the Optical Society of America a-Optics Image Science and Vision, 1997, 14, (8), pp. 1760-1773

[20] Vengsarkar, A.M., Lemaire, P.J., Judkins, J.B., Bhatia, V., Erdogan, T., and Sipe, J.E.: 'Long-period fiber gratings as band-rejection filters', Lightwave Technology, Journal of, 1996, 14, (1), pp. 58-65

[21] Bhatia, V., and Vengsarkar, A.M.: 'Optical fiber long-period grating sensors', Optics Letters, 1996, 21, (9), pp. 692-694

[22] Shu, X., Zhang, L., and Bennion, I.: 'Sensitivity characteristics of long-period fiber gratings', Lightwave Technology, Journal of, 2002, 20, (2), pp. 255-266

[23] Smietana, M., Bock, W.J., Mikulic, P., and Chen, J.: 'Increasing sensitivity of arc-induced long-period gratings—pushing the fabrication technique toward its limits', Measurement Science and Technology, 2010, 22, (1), pp. 015201

[24] Rees, N., James, S., and Tatam, R.: 'Optical fiber long-period gratings with Langmuir—Blodgett thin-film overlays', Optics Letters, 2002, 27, (9), pp. 686-688

[25] Cusano, A., Iadicicco, A., Pilla, P., Contessa, L., Campopiano, S., Cutolo, A., Giordano, M., and Guerra, G.: 'Coated long-period fiber gratings as high-sensitivity opto-chemical sensors', Lightwave Technology, Journal of, 2006, 24, (4), pp. 1776-1786

[26] Del Villar, I., Matias, I., and Arregui, F.: 'Optimization of sensitivity in long period fiber gratings with overlay deposition', Opt Express, 2005, 13, (1), pp. 56-69

[27] Ishaq, I., Quintela, A., James, S., Ashwell, G., Lopez-Higuera, J., and Tatam, R.: 'Modification of the refractive index response of long period gratings using thin film overlays', Sensor Actuat B-Chem, 2005, 107, (2), pp. 738-741

[28] Pilla, P., Giordano, M., Korwin-Pawlowski, M.L., Bock, W.J., and Cusano, A.: 'Sensitivity Characteristics Tuning in Tapered Long-Period Gratings by Nanocoatings', Ieee Photonic Tech L, 2007, 19, (19), pp. 1517-1519

[29] Corres, J.M., Matias, I.R., del Villar, I., and Arregui, F.J.: 'Design of pH Sensors in Long-Period Fiber Gratings Using Polymeric Nanocoatings', IEEE Sensors Journal, 2007, 7, (3), pp. 455-463

[30] Gu, Z., and Xu, Y.: 'Design optimization of a long-period fiber grating with sol-gel coating for a gas sensor', Measurement Science and Technology, 2007, 18, (11), pp. 3530-3536

[31] Cusano, A., Iadicicco, A., Pilla, P., Contessa, L., Campopiano, S., Cutolo, A., and Giordano, M.: 'Mode transition in high refractive index coated long period gratings', Opt Express, 2006, 14, (1), pp. 19

[32] Pilla, P., Manzillo, P.F., Malachovska, V., Buosciolo, A., Campopiano, S., Cutolo, A., Ambrosio, L., Giordano, M., and Cusano, A.: 'Long period grating working in transition mode as promising technological platform for label-free biosensing', Opt Express, 2009, 17, (22), pp. 20039-20050

[33] Patrick, H.J., Kersey, A.D., and Bucholtz, F.: 'Analysis of the response of long period fiber gratings to external index of refraction', J Lightwave Technol, 1998, 16, (9), pp. 1606-1612

[34] Pilla, P., Trono, C., Baldini, F., Chiavaioli, F., Giordano, M., and Cusano, A.: 'Giant sensitivity of long period gratings in transition mode near the dispersion turning point: an integrated design approach', Optics Letters, 2012, 37, (19), pp. 4152-4154

[35] Jesus, C., Caldas, P., Frazao, O., Santos, J.L., Jorge, P.A.S., and Baptista, J.M.: 'Simultaneous Measurement of Refractive Index and Temperature Using a Hybrid Fiber Bragg Grating/Long-Period Fiber Grating Configuration', Fiber Integrated Opt, 2009, 28, (6), pp. 440-449

[36] Baldini, F., Brenci, M., Chiavaioli, F., Giannetti, A., and Trono, C.: 'Optical fibre gratings as tools for chemical and biochemical sensing', Anal Bioanal Chem, 2012, 402, (1), pp. 109-116

[37] Duhem, O., Henninot, J.F., and Douay, M.: 'Study of in fiber Mach-Zehnder interferometer based on two spaced 3-dB long period gratings surrounded by a refractive index higher than that of silica', Optics Communications, 2000, 180, (4), pp. 255-262

[38] Allsop, T., Reeves, R., Webb, D.J., Bennion, I., and Neal, R.: 'A high sensitivity refractometer based upon a long period grating Mach-Zehnder interferometer', Rev Sci Instrum, 2002, 73, (4), pp. 1702-1705

[39] Swart, P.L.: 'Long-period grating Michelson refractometric sensor', Meas Sci Technol, 2004, 15, (8), pp. 1576-1580

[40] Mosquera, L., Saez-Rodriguez, D., Cruz, J.L., and Andres, M.V.: 'In-fiber Fabry-Perot refractometer assisted by a long-period grating', Optics Letters, 2010, 35, (4), pp. 613-615

[41] Falciai, R., Mignani, A.G., and Vannini, A.: 'Long period gratings as solution concentration sensors'. Proc. Sensor Actuat B-Chem2001 pp. Pages

[42] Allsop, T., Zhang, L., and Bennion, I.: 'Detection of organic aromatic compounds in paraffin by a long-period fiber grating optical sensor with optimized sensitivity', Optics Communications, 2001, 191, pp. 181-190

[43] Tang, J.-L., Cheng, S.-F., Hsu, W.-T., Chiang, T.-Y., and Chau, L.-K.: 'Fiber-optic biochemical sensing with a colloidal gold-modified long period fiber grating', Sensor Actuat B-Chem, 2006, 119, (1), pp. 105-109

[44] Possetti, G.R.C., Kamikawachi, R.C., Prevedello, C.L., Muller, M., and Fabris, J.L.: 'Salinity measurement in water environment with a long period grating based interferometer', Measurement Science and Technology, 2009, 20, (3), pp. 4003

[45] Manzillo, P.F., Pilla, P., Buosciolo, A., Campopiano, S., Cutolo, A., Borriello, A., Giordano, M., and Cusano, A.: 'Self Assembling and Coordination of Water Nano-Layers On Polymer Coated Long Period Gratings: Toward New Perspectives for Cation Detection', Soft Materials, 2011, 9, (2-3), pp. 238-263

[46] Li, Q., Zhang, X.-l., Yu, Y.-S., Qian, Y., Dong, W.-F., Li, Y., Shi, J., Yan, J., and Wang, H.: 'Enhanced sucrose sensing sensitivity of long period fiber grating by self-assembled polyelectrolyte multilayers', Reactive and Functional Polymers, 2011, 71, (3), pp. 335-339

[47] Barnes, J., Dreher, M., Plett, K., Brown, R.S., Crudden, C.M., and Loock, H.-P.: 'Chemical sensor based on a long-period fibre grating modified by a functionalized polydimethylsiloxane coating', The Analyst, 2008, 133, (11), pp. 1541-1549

[48] Barnes, J.A., Brown, R.S., Cheung, A.H., Dreher, M.A., Mackey, G., and Loock, H.-P.: 'Chemical sensing using a polymer coated long-period fiber grating interrogated by ring-down spectroscopy', Sensor Actuat B-Chem, 2010, 148, (1), pp. 221-226

[49] Zhang, J., Tang, X., Dong, J., Wei, T., and Xiao, H.: 'Zeolite thin film-coated long period fiber grating sensor for measuring trace chemical', Opt Express, 2008, 16, (11), pp. 8317-8323

[50] Korposh, S., Selyanchyn, R., Yasukochi, W., Lee, S.-W., James, S.W., and Tatam, R.P.: 'Optical fibre long period grating with a nanoporous coating formed from silica nanoparticles for ammonia sensing in water', Materials Chemistry and Physics, 2012, 133, pp. 784-792

[51] DeLisa, M.P., Zhang, Z., Shiloach, M., Pilevar, S., Davis, C.C., Sirkis, J.S., and Bentley, W.E.: 'Evanescent Wave Long-Period Fiber Bragg Grating as an Immobilized Antibody Biosensor', Analytical Chemistry, 2000, 72, (13), pp. 2895-2900

[52] Kim, D., Zhang, Y., Cooper, K., and Wang, A.: 'In-fiber reflection mode interferometer based on a long-period grating for external refractive-index measurement', Appl Optics, 2005, 44, (26), pp. 5368-5373

[53] Yang, J., Sandhu, P., Liang, W., Xu, C.Q., and Li, Y.: 'Label-free fiber optic biosensors with enhanced sensitivity', Selected Topics in Quantum Electronics, IEEE Journal of, 2007, 13, (6), pp. 1691-1696

[54] Wang, Z., Heflin, J.R., Van Cott, K., Stolen, R.H., Ramachandran, S., and Ghalmi, S.: 'Biosensors employing ionic self-assembled multilayers adsorbed on long-period fiber gratings', Sensor Actuat B-Chem, 2009, 139, (2), pp. 618-623

[55] Wang, Z., and Xiao, H.: 'Optical intensity-based long-period fiber grating biosensors and biomedical applications [Life Sciences]', Signal Processing Magazine, IEEE, 2009, 26, (2), pp. 121-122, 124-127

[56] Wang, D.Y., Wang, Y., Han, M., Gong, J., and Wang, A.: 'Fully Distributed Fiber-Optic Biological Sensing', Ieee Photonic Tech L, 2010, 22, (21), pp. 1553-1555

[57] Pilla, P., Malachovská, V., Borriello, A., Buosciolo, A., Giordano, M., Ambrosio, L., Cutolo, A., and Cusano, A.: 'Transition mode long period grating biosensor with functional multilayer coatings', Opt Express, 2011, 19, (2), pp. 512

[58] Cooper, K.L., Bandara, A.B., Wang, Y., Wang, A., and Inzana, T.J.: 'Photonic Biosensor Assays to Detect and Distinguish Subspecies of Francisella tularensis', Sensors, 2011, 11, (3), pp. 3004-3019

[59] Pilla, P., Sandomenico, A., Malachovská, V., Borriello, A., Giordano, M., Cutolo, A., Ruvo, M., and Cusano, A.: 'A protein-based biointerfacing route toward label-free immunoassays with long period gratings in transition mode', Biosensors and Bioelectronics, 2012, 31, (1), pp. 486-491

[60] Chen, X., Zhang, L., Zhou, K., Davies, E., Sugden, K., Bennion, I., Hughes, M., and Hine, A.: 'Real-time detection of DNA interactions with long-period fiber-grating-based biosensor', Optics Letters, 2007, 32, (17), pp. 2541

[61] Jang, H.S., Park, K.N., Kim, J.P., Sim, S.J., Kwon, O.J., Han, Y.-G., and Lee, K.S.: 'Sensitive DNA biosensor based on a long-period grating formed on the side-polished fiber surface', Opt Express, 2009, 17, (5), pp. 3855

[62] Hine, A.V., Chen, X., Hughes, M.D., Zhou, K., Davies, E., Sugden, K., Bennion, I., and Zhang, L.: 'Optical fibre-based detection of DNA hybridization', Biochem Soc Trans, 2009, 37, (Pt 2), pp. 445-449

[63] Smietana, M., Bock, W.J., Mikulic, P., Ng, A., Chinnappan, R., and Zourob, M.: 'Detection of bacteria using bacteriophages as recognition elements immobilized on long-period fiber gratings', Opt Express, 2011, 19, (9), pp. 7971

[64] Tripathi, S.M., Bock, W.J., Mikulic, P., Chinnappan, R., Ng, A., Tolba, M., and Zourob, M.: 'Long period grating based biosensor for the detection of Escherichia coli bacteria', Biosensors and Bioelectronics, 2012, 35, (1), pp. 308-312

[65] Deep, A., Tiwari, U., Kumar, P., Mishra, V., Jain, S.C., Singh, N., Kapur, P., and Bharadwaj, L.M.: 'Immobilization of enzyme on long period grating fibers for sensitive glucose detection', Biosensors and Bioelectronics, 2012, 33, (1), pp. 190-195

[66] Zibaii, M.I., Latifi, H., Karami, M., Gholami, M., Hosseini, S.M., and Ghezelayagh, M.H.: 'Non-adiabatic tapered optical fiber sensor for measuring the interaction between alpha-amino acids in aqueous carbohydrate solution', Meas Sci Technol, 2010, 21, (10)

[67] Zibaii, M.I., Kazemi, A., Latifi, H., Azar, M.K., Hosseini, S.M., and Ghezelaiagh, M.H.: 'Measuring bacterial growth by refractive index tapered fiber optic biosensor', J Photoch Photobio B, 2010, 101, (3), pp. 313-320

[68] Zibaii, M.I., Frazao, O., Latifi, H., and Jorge, P.A.S.: 'Controlling the Sensitivity of Refractive Index Measurement Using a Tapered Fiber Loop Mirror', Photonics Technology Letters, IEEE, 2011, 23, (17), pp. 1219-1221

[69] Tian, Y., Wang, W., Wu, N., Zou, X., and Wang, X.: 'Tapered Optical Fiber Sensor for Label-Free Detection of Biomolecules', Sensors, 2011, 11, (4), pp. 3780-3790

[70] Tian, Z., Yam, S.S.H., and Loock, H.-P.: 'Single-Mode Fiber Refractive Index Sensor Based on Core-Offset Attenuators', Ieee Photonic Tech L, 2008, 20, (16), pp. 1387-1389

[71] Pang, F.F., Liu, H.H., Guo, H.R., Liu, Y.Q., Zeng, X.L., Chen, N., Chen, Z.Y., and Wang, T.Y.: 'In-Fiber Mach-Zehnder Interferometer Based on Double Cladding Fibers for Refractive Index Sensor', IEEE Sensors Journal, 2011, 11, (10), pp. 2395-2400

[72] Rong, Q., Qiao, X., Wang, R., Sun, H., Hu, M., and Feng, Z.: 'High-Sensitive Fiber-Optic Refractometer Based on a Core-Diameter-Mismatch Mach-Zehnder Interferometer', IEEE Sensors Journal, 2012, 12, (7), pp. 2501-2505

[73] Ma, Y., Qiao, X., Guo, T., Wang, R., Zhang, J., Weng, Y., Rong, Q., Hu, M., and Feng, Z.: 'Mach–Zehnder Interferometer Based on a Sandwich Fiber Structure for Refractive Index Measurement', IEEE Sensors Journal, 2012, 12, (6), pp. 2081-2085

[74] Jung, Y., Kim, S., Lee, D., and Oh, K.: 'Compact three segmented multimode fibre modal interferometer for high sensitivity refractive-index measurement', Meas Sci Technol, 2006, 17, (5), pp. 1129-1133

[75] Wu, Q., Semenova, Y., Wang, P., and Farrell, G.: 'High sensitivity SMS fiber structure based refractometer - analysis and experiment', Opt Express, 2011, 19, (9), pp. 7937-7944

[76] Biazoli, C.R., Silva, S., Franco, M.A., Frazao, O., and Cordeiro, C.M.: 'Multimode interference tapered fiber refractive index sensors', Appl Opt, 2012, 51, (24), pp. 5941-5945

[77] Lan, X., Huang, J., Han, Q., Wei, T., Gao, Z., Jiang, H., Dong, J., and Xiao, H.: 'Fiber ring laser interrogated zeolite-coated singlemode-multimode-singlemode structure for trace chemical detection', Optics Letters, 2012, 37, (11), pp. 1998-2000

[78] Xia, T.-H., Zhang, A.P., Gu, B., and Zhu, J.-J.: 'Fiber-optic refractive-index sensors based on transmissive and reflective thin-core fiber modal interferometers', Optics Communications, 2010, 283, (10), pp. 2136-2139

[79] Gu, B., Yin, M.J., Zhang, A.P., Qian, J.W., and He, S.: 'Low-cost high-performance fiber-optic pH sensor based on thin-core fiber modal interferometer', Opt Express, 2009, 17, (25), pp. 22296-22302

Chapter 14

Advances in Optical Fiber Laser Micromachining for Sensors Development

João M. P. Coelho, Marta Nespereira, Catarina Silva,
Dionísio Pereira and José Rebordão

Additional information is available at the end of the chapter

http://dx.doi.org/10.5772/52745

1. Introduction

Both lasers and optical fibers technology appeared in the 1960s, being, from the start, close related. Even though the latter gained increased visibility in telecommunications, first experiments using optical fiber sensors are reported from early 1970s. From then on, research in optical fiber sensors has increased taking advantage of their potential when comparing with "traditional" sensors. Although there are many well established techniques to manufacture optical fiber sensors, the use of laser technology as increased as their cost diminishes (at least for older, well matured laser sources technology) and new laser sources appeared. This new tool has the advantage of producing well controlled light beams.

Nowadays, laser processing of optical fibers in the production of fiber-based sensors is an important research theme. In particular, the use of infrared radiation has directed attention as new applications were found and new short pulsed laser technology have been developed. In this chapter we will describe the main technology used and the physical principles involved. The key parameters in laser radiation interaction with the fiber materials will be described as well as the most common types of fiber-based sensors that can be produced. The application of ultraviolet (UV), near-infrared (NIR) and mid-infrared (MIR) radiation in the fabrication of fiber grating(FG) sensors is analysed. The physical principles are described and a comparison between theoretical modelling and experimental results is presented for MIR radiation writing of long-period fiber sensors (LPFG). Micromachining with nanosecond (ns) pulsed near-infrared laser radiation is presented and illustrate an ongoing research in the use of this type of laser to produce new cavity-based optical sensors. Experimental work is presented and its potential application is analysed.

2. Laser interaction with optical fiber materials

Laser interaction with the materials in general and optical fiber material in particular, depends on several parameters. These are related with the laser source (its wavelength and emission regime, mainly) and also on the characteristics of the material itself.

Generally speaking, the common fibers used as sensors are made of glass materials. Although plastic and polymeric materials are also used, usually sensors are produced from fibers made of ultra pure chemicals like silicon tetrachloride ($SiCl_4$), germanium tetrachloride ($GeCl_4$) and also phosphorus oxychloride ($POCl_3$). The improvement of their optical properties is accomplished by doping with germanium, erbium and ytterbium among other rare earths. Nevertheless, in the purpose of this chapter, fused silica (pure or doped) will be considered as the typical bulk material for laser interaction regarding fiber-based optical sensors.

The most common lasers emit either in the UV, visible or infrared (IR). However, UV and IR lasers have been the major players in the field of processing optical fibers given that the resulting interaction mechanisms are more efficient for these wavelengths taking advantage of higher absorption in those regimes.

The two main regimes as laser sources concerns are continuous wave (CW) and pulsed emission. Recent year's laser developments allowed laser sources to present a broad range of available pulsed regimes, from milliseconds (ms) to femtoseconds (fs) pulse widths. This availability has potentiated new ways of using the laser as a tool for optical fiber processing.

Under laser irradiation, and depending on the mentioned source parameters, the main physical mechanisms can be divided in thermal and photonic (non-thermal) effects. These physical processes are used to create different fiber-based sensors, as it will be described in the following sections.

2.1. Thermal effects

Thermal processes arise from absorption of the laser energy in the material, and in general apply for continuous wave (CW) operation, long pulse lengths and high-pulse-repetition-frequency pulse trains. In this case, the absorbed radiation creates an excess of energy due to the excitation of the lattice which is transformed into heat, increasing the material's temperature from its surface to its bulk by heat conduction, so the most basic thermal effect is heating, that depends on irradiation time and thermal diffusivity of the material.

Heating is the effect behind LPFG fabrication using CO_2 laser, where the refraction index change is achieved by heating a fiber submitted to a tensile stress. If the irradiance is high enough, phase transformations are produced. For silica-base materials, melting is produced when the irradiance has a magnitude of ~10^5 W/cm^2 and depending on the irradiation time, the melted material increases its depth into the bulk. Once the boiling point is achieved, if the irradiance reaches values of >> (10^5-10^8) W/cm^2[1] vaporization is initiated. This last step is the basis of the thermal photoablation, which consists in the precise removal of material, by surface vaporization or spallation (due to thermal stresses) [1].

http://dx.doi.org/10.5772/52745

2.2. Photonic effects

Photoionization is a type of laser matter interaction by which a laser pulse modifies the fundamental structure of a material through physical processes like: non- thermal excitation, ionization and dissociation of atoms and molecules, depending on the light and material properties. The simplest process is the single photon ionization (SPI) consisting in the absorption of a single photon with resulting removal of one electron. This process is strongly dependent on the wavelength, laying in the UV for the interaction with glass materials, and requires low irradiance levels (< 10^7 Wcm^{-2}) [1]. This effect is the basis of the laser induced refraction index changes in FG fabrication where this kind of photochemical reaction is produced on UV photosensitive Ge-doped fibers.

The mechanisms of photosensitivity can be explained by the interaction of UV radiation in a special structure in the fiber's bulk named Germanium oxygen deficient center (GODC), which is able to absorb one or two photon. The photosensitivity mechanism is intrinsically associated with the dopants incorporated during the silica-based optical fiber fabrication. Therefore, it is plausible that the origins of this process are related with the germanosilicate glass synthesis, in which a controlled sequence of chemical reactions that involves a mixture of several gases at high temperature occurs accordingly with the reactions [2]:

$$\begin{cases} SiCl_4 + O_2 \xrightarrow{T} SiO_2 + 2Cl_2 \\ GeCl_4 + O_2 \xrightarrow{T} GeO_2 + 2Cl_2 \\ GeO_2 \xrightarrow{T} GeO + O \end{cases} \tag{1}$$

These reactions show that the presence of germanium promotes GeO formation. Truly, the formation of GeO defects is promoted due to the thermodynamics of the gaseous germanium redox reaction at the high synthesis temperature and is dominant, since the Ge-O bond is weaker than the Si-O bond. Despite the possibility of other suboxides being formed, GeOx {x=1 to 4}), the GeO is the most common sub-product inside the germanosilicate glass amorphous structure, GeO_2-SiO_2, as a source of glass defects [3]. The GODC, occurs when a Ge atom is bonded to a Si or Ge atom, in the absence of an oxygen atom, giving rise to a strong absorption at 242 nm band [3]. The model of an oxygen vacancy neighbouring a Ge atom was suggested, based on the analogy of the spectroscopic properties of this Ge-related defect with those monitored on an oxygen vacancy in pure v-SiO_2. This is consistent with the one photon nature pathway, corresponding to the GODC's triplet state andits intensity increases linearly with the concentration of GeO_2 [4].

The photosensitivity mechanism can also be triggered through a two photon absorption mechanism, and its efficiency is affected by several parameters like light's power density, attenuation and light [5]. Despite the fact that pure silica glasses exhibits poor photosensitivity to UV-laser light even if exposed to large accumulated fluence values close to 100 kJ/cm^2, this can be reversed when a fs-laser beam at ≈800nm wavelength is used [6]. In this case, strong permanent changes in the refractive index ($2\text{-}6\times10^{-3}$) are attainable.

The two photon absorption phenomenon is considered one of the multi-photon ionization (MPI) processes which consist in the absorption of two, three or even five photons exciting the electrons to the conduction band. The difference between the two processes can be explained comparing the number of photoproducts versus the irradiation intensity [7]. Typically, this is a high-intensity ($I\sim10^{11}\text{-}10^{13}$ Wcm^{-2}) [7] and very fast process, lying in the fs-range. Two regimes are distinguished, fs-UV and fs-IR, according with the wavelength employed. In the UV regime, the main mechanism is the previously two photon absorption while in the IR mechanism the three and five photon absorption are predominant.

Laser-induced optical breakdown is a process of photoionization which has the result of plasma formation and photoablation. The main photoionization mechanisms are the already mentioned SPI and MPI. For ps- and ns-pulses the optical breakdown is explained by the avalanche model. It's a damage mechanism that starts with one or more electrons in the conduction band, heated by the laser field. The electron collides with the matrix, gaining enough kinetic energy (by inverse *Bremstrahlung*) to free a second electron. The same process repeats until the electron density approaches the critical plasma density $\sim10^9$ $e^-/\mu m^3$, resulting in photoablation. An inconvenient is that in the ns-time scale, most of the plasma energy is transferred to the matrix being able to produce collateral thermal damage and fractures, worsening the quality of ablation [8]. This effect can be avoided in the fs-scale, since there's no time for an avalanche fully develop, and MPI assumes equal importance to electron avalanche. Thus, the heat diffusion is frozen and thermal damages are eliminated. This process is known as "cold ablation" [8].

Theoretically, according to the electron avalanche model, the laser fluence threshold for ablation is strongly dependent to the laser wavelength, implying that this threshold should increase slightly as the wavelength decreases but reported experimental data shows the opposite. This could mean that other photoionization processes could be implied in optical breakdown of silica and having in mind that lattice defects are more absorptive in the UV than in MIR [8].

3. Fundamentals of optical fiber sensors

The understanding of the potential of using laser technology to create fiber-based sensors depends also on the understanding of the requirements those sensors have. The process of interaction must lead to a certain change in the fiber properties that must produce the required sensitivity to an external change. In this section, the fundamentals of the most common fiber-based sensors is presented with focus on those being targeted as able to be produced by laser irradiation. Cavity-based sensors and refractive-index modulated sensors principles will be described.

3.1. Optical fiber grating sensors

FGs are optical devices based in the principle of photo-refractive effect first discovered by Hill *et al.* [9]. Since then, their development had a significant impact on research and development of telecommunications systems and fiber optic sensors. It use as sensing element is advantageous due to the intrinsic characteristics of the fiber sensors, such as multiplexing, remote sensing, high flexibility, low propagating loss, high sensitivity, low fabrication cost, weight and compactness, high accuracy, simultaneous sensing ability, and immunity to electromagnetic interference.

FGs are often classified into two types: Bragg gratings (also called reflection or short-period gratings), in which coupling occurs between modes travelling in opposite directions; and transmission gratings (or LPFGs), in which the coupling is between modes travelling in the same direction. These optical devices are comparatively simple and in its most basic form, it consists on a periodic modulation of the properties of an optical fiber (usually the refraction index of the core). This can be made by permanent modification of the refractive index of the optical fiber core or by the physical deformation of the fibre. In this section, it is presented the fundamental aspects of both types of gratings, and their sensing application.

3.1.1. Fiber Bragg grating

FBGs are spectral filters based on the principle of Bragg reflection. These periodic structures operate in reflection mode and are manufactured with a period of less than 1μm. Their submicron period provide coupling between the modes that propagate in opposite directions. The principle of operation of these optical devices is schematized in Figure 1. A standard FBG consists of a refractive index modulation in the core of an optical fibre that acts to couple the fundamental forward propagating mode to the contra-propagating core mode. When a broad-spectrum light beam inside in the fiber grating, a narrow wavelength range is reflected and all other wavelengths are transmitted. The reflected light signal will be centered at the Bragg wavelength. The spectral response of the FBG is governed by the phase matching condition, $\lambda_B = 2n_{eff}.\Lambda$, where λ_B is the Bragg wavelength, n_{eff} the effective refractive index of the fiber core and Λ the Bragg grating period [10]. Any change in the modal index or grating pitch of the fiber caused by strain or temperature results in a shift of the Bragg wavelength.

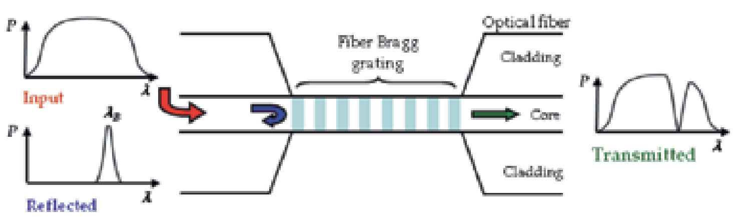

Figure 1. Schematic representation of Fiber Bragg grating principle of operation.

Consider a uniform Bragg grating formed within the core of an optical fiber. The refraction index profile can be expressed as $n(x) = \Delta n.\cos(2\pi/\Lambda)$, where Δn is the amplitude of the induced refractive-index perturbation (typically, 10^{-5}–10^{-2}) and x is the distance along the fiber's longitudinal axis. The coupled-mode theory analytical enables the description of the reflection properties of Bragg gratings. The reflectivity of a grating with length L and constant modulation amplitude and period is given by $R(L,\kappa) = \tanh^2(\kappa.L)$ [11] were the coupling coefficient for a single mode fiber is $\kappa = \pi.\Delta n/\lambda$.

FBGs have been applied in telecommunications[12] and also for a wide variety of sensing applications in several fields [12]. However, FBGs has practical implementation limitations, including the needs of special post-processing for sensing of external refractive index and reduction of the sensor's mechanical strength [13].

3.1.2. Long period fiber gratings

LPFGs are produced by inducing a periodic refractive index modulation (tipically 10^{-4}) in the fiber core with periods typically in the range from 100 μm to 1000 μm [14]. These optical devices operate in transmission mode and their large modulation period promotes the light coupling between co-propagating modes of the optical fibre. In the case of single mode fibers, this takes place between the fundamental and cladding modes, in the same direction. This principle is illustrated in Figure 2. The cladding modes are quickly attenuated resulting in a series of attenuation bands in the transmission spectrum. Each attenuation band corresponds to coupling to a different cladding mode. The phase matching wavelengths are governed by the expression $\lambda_{res}^{m} = (n_{eff,co} - n_{eff,cl}^{m}).\Lambda$ [10,15], where Λ is the grating period, $n_{eff,co}$ and$n_{eff,cl}$ are the effective refractive indexes of the core and mth-cladding modes, respectively. The refractive index sensitivity of LPFGs arises from the dependence of the coupling wavelength upon the effective index of the cladding mode.

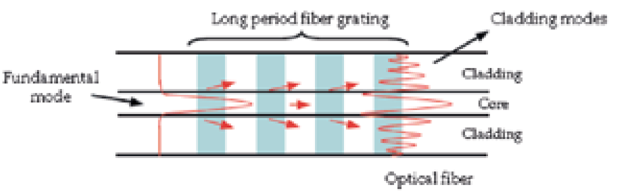

Figure 2. Schematic diagram of long period fiber grating.

Light transmission through the core follows a sinusoidal function of the core refractive index modulation for the wavelengths in the resonance [16] is given by $T = \cos(D.L/2)$, where L is the grating length and D is a coupling coefficient proportional to the core index modulation. The bandwidth of the resonance dips depends on both the coupling coefficient and the difference between the core and cladding indexes:

$$\Delta\lambda_{FWHM} = \frac{\lambda_m^2}{\left(n_{eff,co} - n_{eff,cl}^m\right)}\sqrt{\frac{4D}{\pi L}} \tag{2}$$

External changes in parameters like refractive index, temperature or strain can affect the terms in the ruling equations and consequently shift the attenuation dips and alter their bandwidths [14]).

These optical devices are very sensitive to changes in physical parameters, such as, temperature, strain, bending, torsion, and refractive index of the surrounding medium [17]. This makes possible the use of the LPFGs as a multi-parameter sensor [16]. Their sensibility of to external environment parameters is determined by the magnitude of the perturbation in the refractive index, the period of the grating, and its length.

Compared to other optical devices, LPFGs have a number of unique advantages such as low insertion losses polarization independence, high temperature sensitivity, and relatively simple fabrication. A further advantage of these devices is their higher sensitivity to the environmental refractive index change without the need for access to the evanescent field, as in the case of the FBGs. The extreme sensitivity of the LPFGs to environmental changes could be a disadvantage in telecommunications devices (cross sensitive problems).

3.2. Cavity based optical fiber sensor

Optical fiber Fabry–Perot (FP) interferometric sensors are the main cavity-based type of fiber-sensors and demonstrate a great versatility in different applications [18,19]. The cavity-based sensors are particularly attractive due to its inherent advantages, including small size, relatively low temperature cross-sensitivity and corrosion resistance, high sensitivity, high frequency response and immunity to electromagnetic interference.

In its simplest form, the FP cavity consists in two reflective surfaces arranged in parallel forming a resonant cavity. The reflections at the two end surfaces of the cavity create an interference signal which is a function of the length and refractive index of the cavity. Changes in environment causes a phase shift in the interference pattern and, as a result, a fiber FP sensor is capable of measuring various parameters including temperature, pressure, strain [20]. Considering a general analysis, the transmission function is [13]:

$$T = \frac{\left(1 - R^2\right)}{1 - R^2 - 2R\cos\left(\phi\right)} \tag{3}$$

being R the reflectivity of the surfaces, assuming that both are equal, and that the phase difference between each succeeding reflections is $\varphi = 4\pi.n.L.\cos(\theta)/\lambda$.

The principle of a sensor based in devices like these is based in the fact that changes on the cavity distance (or angle) or in the refractive index of the different media produces a change in the transmitted signal (or reflected, since, the reflected signal is equal to *1-T*, not considering absorption). The resolution of the sensor can be evaluated through a parameter named finesse, *F*, relating the distance between peaks, $\Delta\lambda$, and the full-width half-maximum of the peaks, $\delta\lambda$:$F = \Delta\lambda/\delta\lambda$. Naturally, real fiber sensors are more complex and the applied theory differs from case to case.

Traditionally, FP cavities have been divided in intrinsic (where the sensing element is the fiber itself), extrinsic (two fiber pieces physically separated forming a cavity bounded typically with a capillary glass tube) or hybrid (splicing sections of different types of fibers, for example)[18,21-23]. However, other methods of creating these cavities have been researched like chemical etching and laser processing.

Chemical etching is an efficient and low cost way of producing FP cavities in optical fibers, but the control of the cavity length is less accurate and depends on the precise control of the process, mainly the duration of the etching[24].

Recent methods use laser beams to produce the cavities, either by removing material laterally in the fiber [25] or opening holes on the fiber's end [26] as schematized in Figure 3. Ran *et al.* present an interesting example [26] of a refractive index sensor based on a cavity created by a 157 nm wavelength laser beam on the end of an optical fiber. The micropatterned fiber is then spliced to another fibercreating an air cavity. With this geometry (Figure 3(a)), the refractive index measures can be accomplished without the need of filling the micrometric cavity. In this case, reflection in a third interface must be considered and equation (1) replaced accordingly [20,26], and the analyzed signal is the reflected instead of the transmitted. This type of sensor, with a cavity formed from a hole with a depth of around 20μm and 56 μm diameter (and 1 mm distance to the tip), allowed to measure refractive indexes of liquids with a resolution of ~$4\text{x}10^{-5}$, and is considered as the guideline for the research presented in section 5.

Figure 3. Schematic of two possible configurations for cavity-based optical sensors.

4. FGs sensors fabrication using laser radiation

FGs are important fiber-based sensors. Traditionally they are produced by arc-discharges or UV-exposure. However, in the last years the use of CO_2 lasers, emitting in the MIR, and fs lasers, emitting in the NIR, to write FGs has emerged as an important alternative. In this section, the main laser manufacturing techniques of fiber grating sensors are presented, consid-

http://dx.doi.org/10.5772/52745

ering UV, MIR and NIR radiations. In this scope, an analytical theoretical model for the writing of LPFG by MIR radiation is presented and compared with experimental data.

4.1. FG writing using UV lasers

The use of UV laser radiation was in the base of both FBG and LPFG development. The formation of gratings in an optical fiber was first reported in 1978 by Kawasaki *et al.* [27] using an argon-ion laser at 488 nm UV wavelength. A few years latter, the first LPFG was introduced in 1995 by Vengsarkar who exposed photosensitive optical fibers to 242-248 nm wavelength UV krypton fluoride, KrF, laser light [28].

Although the first FBGs have been manufactured by internal writing [27] (using the interference between the transmitted beam and reflected beams) and holography (two overlapping UV light beams interfere producing a periodic interference pattern) [29], the phase-mask technique has quickly become usual, and even used (in a similar way) from the start for LPFG writing.

Usually, the phase-mask is made from a flat piece of silica glass (transparent to UV radiation) where a one dimensional periodic surface relief is etched (using photolithographic techniques) in one of the surfaces. Thus, the phase-mask becomes an optical element with the capability to diffract the UV beam in transmission. The interference of the transmitted beams corresponds to different diffraction orders in the proximity of the surface, originating a fringe pattern, and leading to Bragg gratings fabrication by modulation of the refractive index in the core of the optical fibre. The profile of the phase grating is chosen such that the zero-order diffracted beam is suppressed to less than 1% of the transmitted power. In addition, the principal beams diffracted by the phase-mask correspond to plus and minus first orders, containing each one, typically, more than 35% of the transmitted power. Then the produced interference pattern photo-imprints a refractive index modulation in the core of the photosensitive optical fibre placed in contact, or in close proximity, immediately behind the phase mask. Typically, the fringe pattern is focused along the fiber's core with the help of a cylindrical lens. The phase-mask technique has the advantage of greatly simplifying the manufacturing process for Bragg gratings, yet yielding high performance gratings. In comparison with the holographic technique, the phase-mask technique offers easier fiber/laser alignment, reduced stability requirements on the writing apparatus and lower coherence requirements on the UV laser beam.

Another writing method uses the point-by-point technique. In this case, single UV laser beam is used to imprint the grating into the fibers equentially along the fiber's length. The incident laser beam is focused on the optical fiber core or cladding (for either FBG or LPFG, respectively) using a lens. The periodic irradiation is accomplished by computer control of the laser beam and the movement of the fiber, so the periods are inscribed. Another way to produce the periodic inscription is by scanning the laser beam focus over the optical fiber, not only to produce the longitudinal modulation but also to produce each transversal refractive index change zone. This process is illustrated in section 4.2.2 regarding MIR irradiation techniques. Figure 4 illustrate both writing techniques.

The mentioned methods apply independently of the UV laser used, and thus from the physical mechanisms involved (see section 2). However, laser technology significantly differs, a characteristic of producing FG using UV laser radiation. Usually, excimer lasers are used to write FGs through the single- or double-photon low energy physical principles described in section 2. Wavelengths of 488 nm, and in the ranges 333 nm to 364 nm or 244 nm to 288 nm are typical either for FBGs or LPFGs. Besides applied wavelength, the required irradiances depend strongly in the optical fiber being considered (mainly its photosensitivity characteristics) but can roughly being considered in the range from a few W/cm^2 to tenths of MW/cm^2 [7].

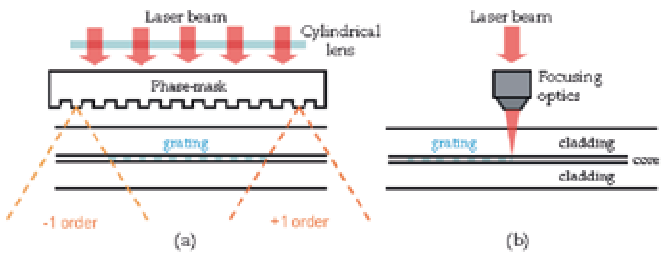

Figure 4. Illustration of (a) phase-mask and (b) point-by-point writing techniques.

Regarding multiphotonic high-excitation energy UV irradiation, this is accomplished using the (relatively) new fs-pulsed laser technology, typically emitting with wavelengths lower than 248 nm. In these cases, irradiances are in the order of GW/cm^2 or higher [7]. This technology based in fs-pulses allows obtaining excellent quality FGs mainly to the laser high spatial uniformity [7]. However, this technology is still very expensive which limits its broader use when comparing with other technologies (either in UV or IR).

4.2. LPFG writing using CO_2 lasers

The use of CO_2 lasers to produce LPFGs was first reported by Davis *et al.* [30] and Akiyama *et al.* [31] in 1998. From then on, the application of this technology has lead to an increasing research on its application for the development of new optical fiber sensors [32].

Using this type of MIR emission laser has several advantages regarding the other two well established methods (UV lasers and arc discharges). The gratings can be inscribed directly in most telecommunication fibers, support high temperatures without vanishing (in opposition to those produced by UV) the process has high repeatability and predictability (in opposition to the arc-discharge method). Also, since CO_2 laser systems are commonly used to process several materials and have a long established industrial application, available systems are robust and low-price.

The application of MIR laser radiation to produce a LPFG has physical principles similar to the ones considered for arc-induced LPFGs [33]. Both rely in thermal effects acting in the fiber bulk materials. However, while the latter can be considered as a volume effect, being applied along the transversal section of the fiber, between the two electrodes, the material's high superficial absorption considered in MIR irradiation promotes heat conduction as a major player in the physical mechanisms involved.

4.2.1. Physical mechanisms

Considering a standard silica-based optical fiber under tension and irradiated by a (Gaussian) 10.6 μm wavelength beam emitted from a CO_2 laser, two main phenomena must be considered: the thermal heating due to the interaction between the photons and the glass molecular structure and the stress due to the differences between a relatively low-viscosity doped silica core and a relatively high-viscosity pure silica cladding [34]. Differences between core and cladding thermal expansion coefficients and viscosity lead to residual thermal stresses and draw-induced residual stresses. These effects are localized and, when periodically induced in the fiber's length, can be responsible for the creation of the gratings. This effect is due to the refractive index change resulting from frozen-in viscoelasticity [35].

The temperature distribution $T(r,z,t)$, with $r^2 = x^2 + y^2$ for laser heating of a homogeneous medium can be obtained by solving the 2D heat flow equation. Considering $K = K(T)$, defining the thermal diffusivity k [$m^2\ s^{-1}$] as $k = K/(\rho\ Cp)$, where ρ is the density, C_p the specific heat, K the thermal conductivity and assuming them constants, the resulting temperature can be approximated for Gaussian elliptical laser beams through [36-40]:

$$T(x,y,z,t)=\frac{(1-R)P}{4\pi k w_x w_y}\int_0^{\sqrt{Kt}}\Psi(x,y,s)\cdot\left[\exp(a_T z)\,erfc\left(\frac{a_T s}{2}+\frac{z}{s}\right)+\right.$$
$$\left.+\exp(-a_T z)\cdot\sqrt{a^2+b^2}\cdot erfc\left(\frac{a_T s}{2}-\frac{z}{s}\right)\right]ds \tag{4}$$

with

$$\Psi(x,y,s)=\frac{a_T s}{\dfrac{s^2}{\left(w_x w_y\right)}+1}\cdot\exp\left[\frac{x^2}{w_x^2+s^2}-\frac{y^2}{w_y^2+s^2}+\frac{\left(a_T s\right)^2}{4}\right] \tag{5}$$

being R the reflectivity at the air/fiber interface for the assumed wavelength, P the laser power, a_T the absorption coefficient (assumed constant) and w_x and w_y the beam's radii at focus (for each axis). With the temperature, T, the resulting residual thermal stresses can be calculated using [37]

$$\sigma_x=\frac{E}{1-\nu}\left[\frac{2\nu}{r_c^2}\int_{r=0}^{r_c}\alpha T r dr-\alpha T\right] \tag{6}$$

beingr_c is the radius (cladding or core), E is the Young's modulus and υ the Poisson's ratio.

If the core is the lower viscosity glass (e.g. Ge-doped silica core with pure silica cladding), the residual axial elastic stresses in the cladding and core, σ_{cl} and σ_{co}, respectively, resulting from a draw tension F, over the equivalent cross-sectional areas A_{cl} and A_{co} can be obtained from [37]:

$$\sigma_{x,cl} = \frac{F}{A_{cl}}\left(\frac{A_{co}E_{co}}{A_{co}E_{co} + A_{cl}E_{cl}}\right) \quad \text{and} \quad \sigma_{x,co} = F\left(\frac{E_{co}}{A_{co}E_{co} + A_{cl}E_{cl}}\right) \tag{7}$$

Taking in consideration the mentioned stresses, the refractive index change in a silica-based optical fiber can be approximated by the relation [35] $\Delta n \approx -6.35\times10^{-6}\sigma$, where σ represents the overall (both thermal and drawn-induced) residual stresses (in MPa) in the fiber's axial direction. Accordingly with Yablon [34], stresses in the other directions can be neglected.

Besides stress-related refractive index change, localized heating can induce microdeformation of the fiber and also changes in its glass structure. The later is likely to occur in the core for which the fictive temperature (below the fictive temperature the glass structure doesn't change) is lower [33,41]. As an example, it can be found that, for a Ge-doped core, the fictive temperature ranges from 1150K and 1500K [41].

These analytical equations don't consider all the physical phenomena (e.g. convection and radiation losses) and were developed assuming several simplifications (mainly, neglecting the temperature dependence of the glass parameters). However, their capability of being used as an engineering tool to develop fiber optic sensors has been demonstrated [40]. A detailed analysis can be made using numerical methods and considering that the absorption coefficient is temperature dependent, e.g. accordingly with MacLachan and Meyer [42].

4.2.2. Irradiation methodologies

Since there is still no phase mask available for CO_2 laser radiation, methodologies rely basically in the point-by-point technique. Nevertheless, several methodologies have been tested since the first experiences in 1998 and are resumed in the schematic of Figure 5. As an example, Davis [30] and Akiyama [31] both have written each single period of a grating by focusingthe laser beam by means of spherical lenses. Spots had dimensions of about 140 μmand translation stages moved the fiber under the laser spot. They used a CW laser, and the single pulse duration was defined through a computer-controlled shutter.

Usually, CW CO_2 laser technology is chosen due to its availability and cost. Low power lasers and mechanical shutters allowing hundreds of ms pulses perform well and accomplish the required performances. Q-switch CO_2 lasers [43] have also been reported by Rao*et al.* [44]. In this case, shorter pulses are available at high frequency rate (in the order of kW). Nevertheless, since fluence is the main parameter involved in the interaction process, setting laser power, pulse duration and spot radius should lead to similar results [40].

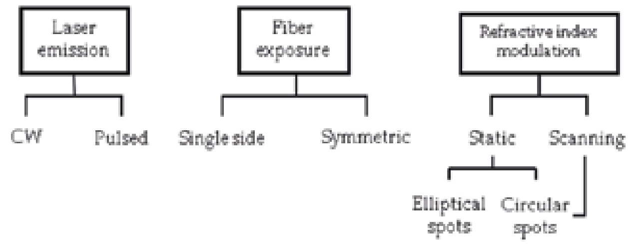

Figure 5. Schematic illustrating the different irradiation methodologies that can be applied for each available operational parameter.

Regarding the way each refractive index modulation is created, there are mainly two options: a static irradiation, for which the laser is applied for a determined amount of time, and a dynamic irradiation where the laser beam is scanned over the region where the refractive index change is to be created. In the first case, basically, one must ensure that the region is fully irradiated (i.e. the focused spot is larger that fiber's diameter) while in the scanning procedure requires the opposite (spot size smaller that the fiber's diameter).

Figure 6 schematizes the two situations considered for the static procedures and the one for scanning. For the latter (Figure 6(a)), the usual procedure is to have the laser beam focused in a small spot and scanned it over the fiber using a galvanometric mirror. If two of such mirrors are used, one of them can be used to move the beam longitudinally and thus write the full LPFG without moving the fiber. However, these scanners and associated optics are expensive, and accomplishing small spots is difficult for the considered wavelength. The diffraction limited spot radius, w_d, resulting from focusing an initial beam of wavelength λ and radius w_0 using a lens of focal distance f is: $w_d = 1.22\lambda . f/w_0$.

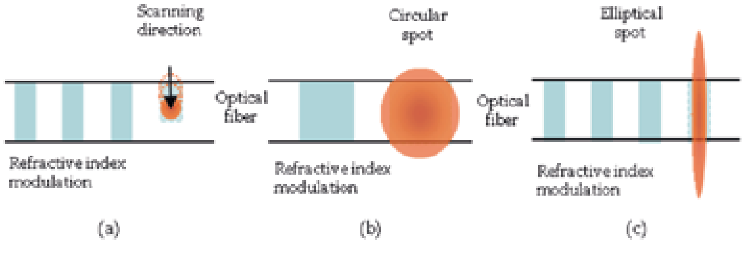

Figure 6. Illustration of (a) dynamic scanning and static (b) circular and (c) elliptical spots procedures in creating LPFG in an optical fiber.

Figure 7 shows the diffraction limited spot radius values for a 10.6 μm wavelength beam focused by different lenses. Two situations are plotted: one considers that the laser has an initial 3.5 mm radius (a usual value) and the other that this value doubles (e.g. using a 2x beam expander). Also plotted is the dimension (cladding radius) of a common optical fiber (for the case, the SMF-28, already considered previously). The plot indicates that only for the lowest focal lengths (< 20 mm, averaging for the two situations) one can obtain spot sizes smaller than the optical fiber radius. The common situation is to use focal lengths in the order of 50 mm, and typically spot sizes are in the order of hundreds of microns. This leads to the fact that usually a static approach is used. Since a circular spot creates (potentially) larger affected zones (Figure 6(b)) and, for smaller beams makes it more difficult to align relatively to the fiber, elliptical beams (Figure 6(c)) are often the preferable choice. This is accomplished by using a cylindrical lens with its axis perpendicular to the fiber's axis.

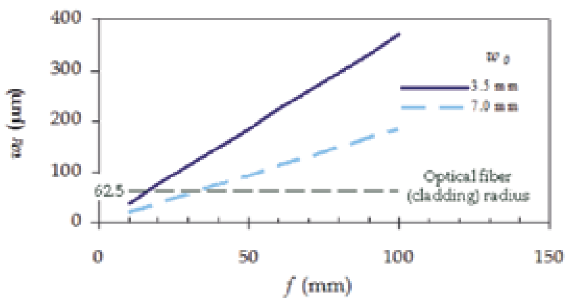

Figure 7. Diffraction limited spots for w_0 = 3.5 mm or w_0 = 7.0 mm CO_2 laser beam radius focused by different focal length lenses.

While no major difference in the LPFG performance has been reported regarding the above mentioned different techniques, the single–side and symmetric exposure to the laser radiation were compared by Oh *et al.* [45], demonstrating that the polarization-dependent loss of the first fabrication method (1.85 dB at 1534 nm) could be significantly reduced to 0.21 dB by applying the second method. Nevertheless, due to its simplicity, the single-side exposure is the most commonly used methodology and the accomplished performance still fulfils the usual requirements.

The same techniques, applied with different parameters (e.g. laser power and applied weight) can produce different devices like based on tapers or grooves along the fiber (i.e., zones were the cladding diameter is reduced) [46]. Other possible advances can be accomplished in the future regarding the writing of non-uniform (or "chirped") LPFG, where the period changes along the grating, and direct writing by MIR interferomety [46].

4.2.3. *An example*

Considering a standard single-mode fiber, SMF-28 [47], consisting of a core of 3.5 mol% Ge-doped SiO_2 and a pure fused silica cladding and irradiating with a common CO_2 laser a simple example can illustrate the application of the formulae and also correlate with experimental data. Table 1 presents the fiber's main parameters considered for the calculations and their references. Values from Yang *et al.* [36] are considered for the 10.6 μm wavelength of a CO_2 laser and equals for both the core and the cladding. This assumption can be made mainly since the Ge concentration in the fiber's core is very low [7,48,49].

Using a static asymmetrical irradiation with a CW CO_2 laser and a cylindrical lens to have a w_x = 0.15 mm and w_y = 1.75 mm elliptical spot on the fiber, the implemented setup is schematized in Figure 8(a) and the considered referential in Figure 8(b). In practice, a Synrad 48-2 laser and a 50 mm focal length lens were used. The laser operation was computer controlled with emissions in the order of hundreds of ms. Experimental set-up also consisted of a broad band light source (Thorlabs S5FC1005S) and an optical spectrum analyzer (OSA) to monitor the LPFG fabrication, while a fast camera (PCO SensiCAM), perpendicular to the irradiation axis, allows to optically visualize the process. The irradiated zones were analyzed using an optical microscope with amplifications up to 1,000×.

Parameter	Core	Cladding
Radius, w (μm) [47]	4.1	62.5
Refractive índex (@ 1550nm, 300K), n [7]	1.449	1.444
Young's modulus, E (GPa) [49]	70.8	72
Poisson's ratio, v [49]	0.165	0.173
Reflectivity (@ 10.6 μm), R [36]		0.15
Density, ρ (kg/cm^3) [36]		2.2×10^{-3}
Specific heat, C_p (J/kg K) [36]		703
Thermal diffusivity, K (m^2/s) [36]		2
Absorption coefficient (@ 300K), a_T (cm^{-1}) [36]		250

Table 1. Optical fiber parameters considered for the calculations.

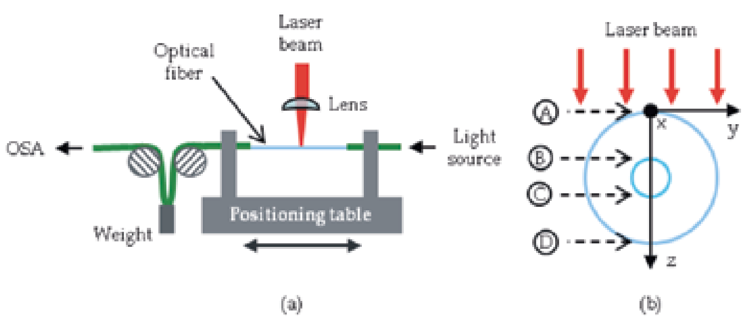

Figure 8. a) Schematic apparatus of a LPFG writing by laser and (b) optical fiber cross-section indicating the considered referential and the interfaces between the different regions: A – irradiated surface, B – core/cladding interface (upper), C – core/cladding interface (lower) and D – bottom surface.

Figure 9(a) shows a microscope photo of an irradiated fiber, part of a 25 mm length grating with a period of 500 μm and Figure 9(b) the resulting relative transmission spectrum.Besides the general conditions previously mentioned, a weight of 16 g was applied and a laser power of 6W was delivered for the duration of 600 ms. In this image it is possible to observe an affected area along the fiber's axis of about 130 μm. Also visible is a (small) micrometric deformation of the fiber.

Using equation (4), one can obtain the temperature distribution at the different regions illustrated in Figure 8(b). Figure 10 shows this distribution along the fiber's axis as well as the equivalent zone regarding the size of the visible affected zone observed in Figure 9(a). From the curves it is clear that the temperature differences along the core are negligible (in depth, the core can be considered at the same temperature) and above the fictive temperature. In the opposite, the cladding shows a significant temperature difference between the fiber's front surface (laser incidence) and its back surface (about 230K).

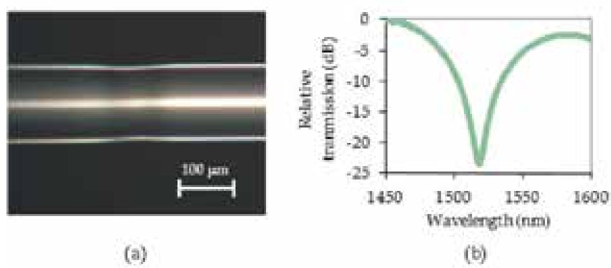

Figure 9. Picture showing (a) an irradiated zone belonging to a 25 mm LPFG with 500 μm period and (b) respective relative transmission. (600 ms exposure time, 6 W laser power).

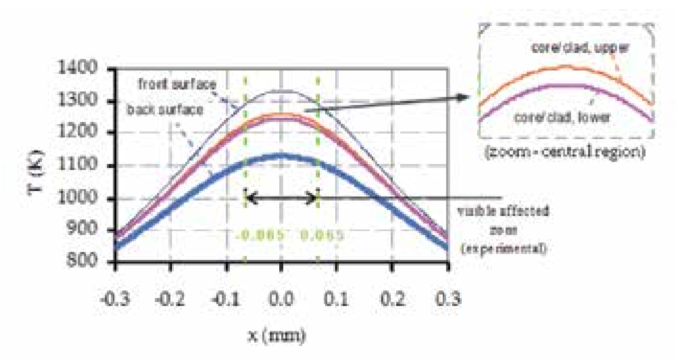

Figure 10. Temperature distribution at the fiber's axial direction at t = 0.6 s. The curves were obtained at the optical fiber's front surface, core/cladding interfaces (upper and lower) and at the back surface of the fiber, and x = y = 0 mm (see Figure 8).

Using the set of equations (7), the residual axial elastic stresses in the cladding and core are approximately 0.05 MPa (cladding) and 12.57 MPa (core). Adding these values to the residual thermal stresses calculated using equation (6) the resulting residual stresses can be obtained. Figure 11(a) plots these values for x = 0 along the z-axis. The asymmetry is clearly visible (mainly in the cladding). However, it has no significant impact in the refractive index profile (obtained by adding the refractive index change Δn to its initial value) resulting from the process as it can be observed in the plot in Figure 11(b).

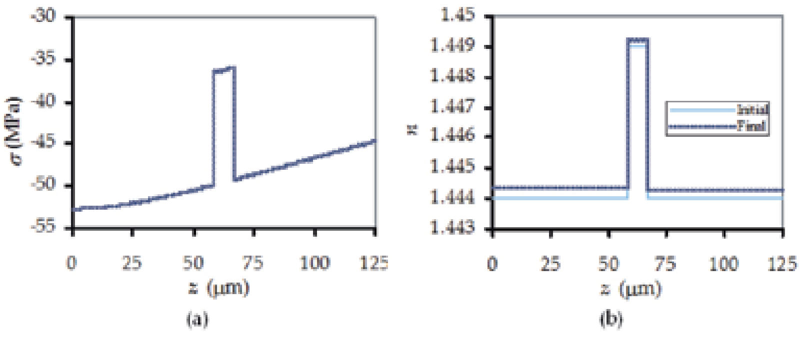

Figure 11. (a) Total residual stress and (b) refractive indexes (before and after laser irradiation) profiles, for the conditions considered.

Also evident is the imposing nature of the thermal component. However, if the drawing force increases, the balance between residual stresses changes. Figure 12 plots the refractive index change Δn calculated for the core and cladding by increasing the weight. For lower weights, the core's refractive index increases while for weights higher than approximately 60 g, it diminishes. At this value, the refractive index modulation is due mainly to the change in the cladding (which has almost no change with the weight value).

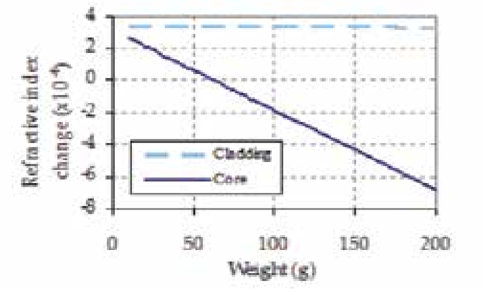

Figure 12. Refractive index change (core and cladding) with increasing weight, for the conditions considered.

4.3. Multi-photonic NIR laser writing of FG sensors

Besides single UV photonic absorption and MIR thermal effects, fs-pulse duration NIR (fs-NIR) lasers appeared in the last years as alternative sources to write LPFG [7,50,51] and FBG [50,52]. In this case, the high peak power irradiation (typically in the order tenth's of thousands of GW/cm^2) produced by the fs-NIR laser induces high refractive index changes in the bulk glass material. This effect is considered as resulting from a non-linear multi-photonic absorption/ionization process in which material compaction and/or defect formation (depending on the intensity of the exposure) can occur [52]. Typically, 800 nm wavelength $Ti^{3+:}Al_2O_3$ lasers are being used with pulses in the order of hundreds of fs. This laser makes use of the five-photon mechanism interaction with the silica-based optical fiber and 7.8 eV band-gap energy for the common 3 mol% Ge-doped fused silica core considered in the examples presented in this chapter [7].

Two types of writing procedures have been researched so far: one using a phase-mask process and the other a point-by-point writing. Both are similar to the techniques described previously for UV and MIR radiation writing. Thermo-stability (up to the glass transition temperature) of both laser written FBG and LPFG, and the ability of record in different types of fibers, as been reported as the main advantage of this technique. However, FBG fabricated using phase masks have strong cladding-mode absorption, only removed with careful relative positioning between the phase mask and the fiber, as well as with the choice of a special high order pitch phase mask [7]. High sensitivity to alignment is also reported [7,52] as one of the major drawbacks in fs-NIR technique regarding LPFGs, not only using masks but also in point-by-point writing. Nevertheless, the latter technique is being researched towards its application in the development of non-uniform (or “chirped”) Bragg gratings [53] and direction-sensitive bending sensors [54].

5. NIR laser micromachining for cavity-based sensors

In recent years fiber micromachining has experienced an increasing development in the context of fiber sensing, the focus being made in creating intrinsic fiber optic structures, such as Fabry-Perot cavities, diffraction elements in the fiber end face, etc. To do so, the most traditional technique is based in the use of chemical etching. However, this technique (as others) is characterized by having low flexibility in its use. In the present, the preferred fabrication technique relies on laser etching, most notably fs or UV laser machining. This is a novel approach (basically following the principles already described in previous sections) being considered as having a huge potential, but the required equipment is complex and highly expensive. To overcome the present limitations the authors have been researching in applying ns-NIR pulses [20]. In this section this new technique is presented and its different applications illustrated. Based in the available experimental data, this optical fiber processing technique is analysed and its potential evaluated.

5.1. Laser micropatterning

Laser micropatterning refers to a material-removal process where micron-level features are fabricated in materials using a highly focused laser beam with high energy density, which is scanned over the material to create a specific feature. Ultra-fast lasers have pulse duration in the ns- through the fs-range which creates material removal by a vaporization process that limits material heating and allows materials to be micromachined with less dependence on laser wavelength absorption.

Micropatterning of hard materials, like glass, with pulsed lasers delivers the highest energy in the shortest possible time, thus reducing the material shock/impact effects. Applying laser energy over a relatively long time results in distortion of the microfeature, and other unwanted results, such as a large heat-affected zone, recast material, microcracking of the surface or inner walls or the laser beam not penetrating completely through the material thickness. These effects can be reduced by using a short (<ms) pulse length.

One of the simplest ways to produce micro-patterns is to apply the concepts of laser drilling and appropriated scanning strategies. Traditional laser drilling techniques are: single pulse drilling, percussion (multiple pulses) drilling and trepanning. In this sequence, the required number of pulses increases, which can increase the machined volume.Basically, material removal in laser hole drilling relates with the vaporization of the material.

When dealing glass materials used in the development of fiber-based sensors, the laser interaction is conditioned by two important parameters: the wavelength and duration of the laser pulses. Since thermal impact can cause cracks in the glass after laser irradiation, UV radiation, having photon energies similar with those of glass, allows material removal by photonic processes without heating the material. Another possibility is to use ultra-short pulses (<ps), so even in the NIR, photonic processes predominate over thermal effects. However, recent studies demonstrated that nanosecond pulses [14,20], in the NIR, can effectively be used to replace UV and fs-lasers in processing silica-based materials.

5.2. Results on nanosecond NIR pulses micropatterning

In 2011, Nespereira *et al.* [20] have presented the first results in creating micrometric holes in optical fibers using nanosecond NIR radiation. Since the tested optical fibers (standard communication silica-based fibers) have reduced absorption in the NIR (absorption coefficient around 1 dB/km) [47], the analysis made in section 4 regarding MIR interaction (with either core or cladding) cannot be made. So, although more research is needed (in particular to fully understand the physical principles involved), experiments allowed determining the conditions to vaporize the required amount of material. Holes with few microns and depths higher than 10 μm were accomplished with multiple superposed shots. The analysis demonstrates the possibility of writing patterns and the potential in the development of fiber-based sensors.

5.2.1. Experimental procedures

Figure 13 illustrates the setup implemented and shows a picture of its implementation. Two main paths can be considered: an irradiation path, combining the laser source and an objective, and an observing path, were light reflected by the targeted fiber is observed by a CCD camera. Together with the fiber, a dichroic mirror is common to both paths allowing reflecting the emitted NIR laser beam, and transmitting visible light reflected by the fiber.

The irradiation procedure was based on a pulsed Nd:YAG laser (BMI model: 5012 DNS 10c) operating at 1064 nm wavelength with a pulse width of 7 ns and 10 Hz repetition rate. The beam has a radius of 3.5 mm and is reflected by a dichroic mirror and focused into a SMF-28 optical fiber. The focusing optics is a 10x objective (ThorLabs LMH) with 0.25 numerical aperture, 20 mm effective focal length, designed to transmit high-power 1064 nm laser radiation and focus it to a diffraction-limited spot [20]. Thus, the spot radius on the fiber top is estimated to be about 3.7μm. However, since the laser beam quality is low, having a M^2 parameter higher than 2 (a Gaussian beam has $M^2 = 1$), the incident beam is expected to be focused into a 7.5 μm spot radius ($M^2 . w_d$).

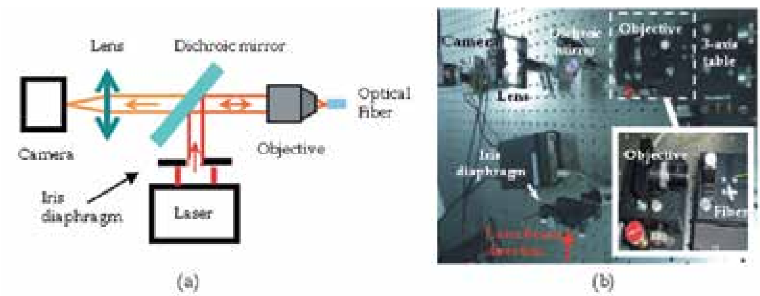

Figure 13. (a) Schematic and (b) photograph of the setup used for nanosecond pulsed NIR laser micropatterning of optical fibers.

Several operational parameters were considered. Besides changing the incident laser energy, the number of superposing pulses changed and it was also tested moving the fiber towards the focus after each pulse. Also tested was the impact of diminishing the spot size just at the laser's output, i.e. changing the depth of focus. This was accomplished with an iris diaphragm which allowed changing the beam from its initial 3.5 mm radius to about 2mm.

5.2.2. Results and analysis

Analysing the resulting data, tests [20] proved that single pulse drilling isn't effective in removing significant amount of material, especially when high depth is required. One laser pulse can produce a perfect round hole at the fiber'ssurface but with a depth less than 1 μm. However, increasing the number of superposing pulses lead effectively increased the hole's depth, while also increasing its diameter (Figure 14). As it can be seen, after about 8 pulses there isn't a significant change in the hole's diameter. However, its depth keeps increasing. More than 20 pulses damaged the fiber (cracks and breakage occurred).

The latter results were obtained with energy of 1.8 mJ and a 2 mm radius vignetted beam. Contrary to what could be expected the beam's size has low impact in the characteristics of the hole: its diameter only varies between 25 μm and 31 μm, while the depth can be considered constant. However, the quality of the holes changes, being better for lower beam sizes as it can be seen in Figure 15 for the same energy and 10 laser pulses/hole. Also unexpected was the fact that increasing the laser energy, for a determined number of superposed pulses, or moving the fiber after each pulse, did not significantly alter the results. This can be a clear indication that some optical breakdown is the physical mechanism responsible by vaporising the material since once delivered enough energy to reach the breakdown threshold any further increase will not contribute for the process.

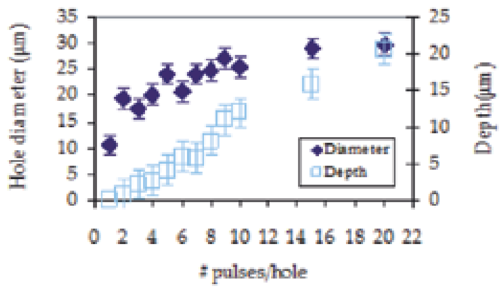

Figure 14. Measured hole's diameter and depth for different number of laser pulses per hole. (2 mm radius vignetted initial laser beam with 1.8 mJ incident energy).

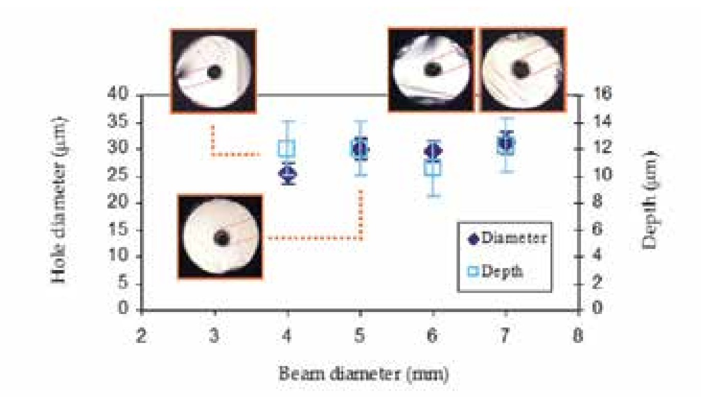

Figure 15. Measured hole's diameter and depth for different emitted laser beam diameter. Tests considered ten 1.8 ml laser pulses/hole.

These tests were made by irradiating the top of the fibers and the technique demonstrated that it is possible to obtain not only cavities for FP fiber sensors but also that different patterns can be inscribed (Figure 16(a)). Using the same parameters, it is also possible to microstructure the lateral side of the fiber. Figure 16, (b) and (c), shows the front and lateral views, taken by a microscope, of two holes opened in the side of a SMF-28 optical fiber.

Future work will focus in using nanosecond NIR pulses micropatterningto produce fiber sensors and also in studying and modelling the physical processes that rule the interaction phenomena. One possible alternative to the production of SPR sensors, while maintaining the same physical principle, is to replace the *a posteriori* metallization of the holes by direct formation of metallic nanoparticles simultaneously with the laser micropatterning of the fiber's top. This would require a metallic ion-doped fiber top. Nevertheless, some successful experiences were already made using NIR laser radiation, in the ns-pulse regime to obtain gold and copper nanoparticles in glass substrates [55,56]. Also, opening apertures along the fiber's length can lead to the development of new optical fiber sensors either by exposing the core or by giving access to inner hollow regions in photonic-crystal fibers.

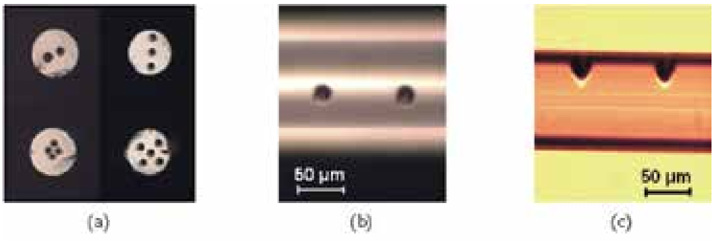

Figure 16. Examples of (a) different patterns written on the optical fiber's topand (b) front and (c) lateral views taken with an optical microscope for an example of two holes opened on the lateral side of a Corning SMF-28 fiber.

6. Conclusions

Laser technology plays an important role in the development of fiber-based optical sensors as its characteristics allow obtaining, in a controlled way, high quality features with good repeatability. Although some techniques are already well established, there still are many improvements and developments being researched. In particular, the use of IR radiation still presents challenges to overcome and promising new sensors are expected to be developed in a near future.

The use of MIR radiation in the writing of LPFG, namely through the use of CO_2 laser systems, has proven to be an efficient tool. However, detail research in the study of the physical mechanisms involved in the process is still being done while its use to create new sensors is a parallel activity in photonic fields. As an engineering tool, a set of analytical expression were presented in this chapter which can give indications to the manufacturing process regarding the required operational parameter to accomplish a determined LPFG.

Recent advances in fs-pulses UV and NIR laser technology were described. In particular, inscribing FBG and LPFG is being researched, although some drawbacks are identified which limits its application. Besides that, an innovative technique that uses ns-NIR laser radiation to micropatterning optical fibers has been presented. These new results are challenging because the irradiated silica-based fibers are mainly transparent to NIR radiation and therefore the usual explanation based in direct heating by molecular or matrix vibrations induced by the laser beam (as in the previous section) should not hold. This leads to the necessity of a further in-depth analysis of the physical mechanisms involved. Nevertheless, the develop-

http://dx.doi.org/10.5772/52745

ment of this technique opens new opportunities in the design of new cavity-based optical fiber sensors which are expected to appear in a near future.

Acknowledgements

This work was partially supported by the Portuguese Fundação para a Ciência e Tecnologia (FCT) through the project PTDC/FIS/119027/2010. The authors gratefully acknowledge José Luis Santos, Orlando Frazão, Pedro Jorge and Paulo Caldas from INESC-Porto for their advices and crucial contributions. A special thanks to Fernando Monteiro and António Oliveira for their technical support to the activities described in this paper.

Author details

João M. P. Coelho[1,2], Marta Nespereira[1], Catarina Silva[1], Dionísio Pereira[3] and José Rebordão[1]

1 Universidade de Lisboa, Faculdade de Ciências, Laboratório de Óptica, Lasers e Sistemas, Pólo do Lumiar, Estrada do Paço do Lumiar, Lisboa, Portugal

2 Universidade de Lisboa, Faculdade de Ciências, Instituto de Biofísica e Engenharia Biomédica, Campo Grande, Lisboa, Portugal

3 Nokia Siemens Networks, Rua Irmãos Siemens 1-1ª, Amadora, Portugal

References

[1] Dahotre NB, Harimkar SP. Laser Fabrication and Machining of Materials. New York: Springer; 2008.

[2] Neustruev VB. Colour centres in germanosilicate glass and optical fibres. Journal of Physics: Condensed Matter 1994; 6(35) 6901–6936.

[3] Kashyap R. Fiber Bragg Gratings. San Diego: Academic Press, 1999.

[4] Williams DL, Davey ST, Kashyap R, Armitage JR, Ainslie, BJ. Photosensitive germanosilicate preforms and fibers. In: Giancarlo C. Righini (ed.) Glasses for Optoelectronics II: proceedings of SPIE: 1513, 12 March 1991, The Hague, Netherlands. Bellingham: SPIE 1991.

[5] Grubsky V, Starodubov DS, Feinberg J. Photochemical Reaction of Hydrogen with Germanosilicate Glass Initiated by 3.4 5.4-eV Ultraviolet Light. Optics Letters 1999; 24(11): 729–731.

[6] Mihailov SJ, Smelser CW, Lu P, Walker RB, Grobnic D, Ding H, Henderson G, Unruh J. Fiber Bragg Gratings Made with a Phase Mask and 800 nm Femtosecond Radiation. Optics Letters 2003; 28(12): 995–997.

[7] Nikogosyan D. Multi-photon High-excitation-energy Approach to Fiber Grating Inscription", Measurement, Science and Technology. 2007; 18 R1-R29.

[8] Smith AV, DoBT. Bulk and Surface Laser Damage of Silica by Picosecond and Nanosecond Pulses at 1064 nm. Applied Optics 2008; 47(26): 4812-4832.

[9] Hill K, Fujii Y, Johnson D, Kawasaki B. Photosensitivity in optical fibre waveguides: application to reflection filter fabrication. Applied Physics. Letters 1978; 32(10): 647–649.

[10] Erdogan T. Fiber grating spectra. Journal of Lightwave Technology 1997;15(8): 1277-1294.

[11] Lee D. Electromagnetic Principles of Integrated Optics. New York: John Willey and Sons; 1986.

[12] Othonos A. Fiber Bragg Gratings-fundamentals and Applications in Telecommunications and Sensing. Boston: Artech House; 1999.

[13] Jiang M, Zhang AP, Wang YC, Tam HY, He S. Fabrication of a Compact Reflective Long-period Grating Sensor with a Cladding-mode-selective Fiber End-face Mirror. Optics Express 2009;17(20): 17976-17982.

[14] Vengsarkar A; Lemaire P; Judkins J, Bhatia V, Sipe J. Long-Period Fiber-Grating-Based Gain Equalizers. Optics Letters 1996;21(5): 335-338.

[15] Erdogan T. Cladding-mode Resonances in Short- and Long-period Fiber Grating Filters. Journal of the Optical Society of America A 1997;14(8): 1760-1773.

[16] Costa RZV, Kamikawachi RC, Muller M, Fabris JL. Thermal characteristics of long-period gratings 266 nm UV-point-by-point induced. Optics Communications 2009;282(5): 816-823.

[17] Patrick H, Chang C, Vohra S. Long Period Fiber Gratings for Structural Bending Sensing. Electronics Letters 1998;34: 1773 – 1775.

[18] Zhang Y, Chen X, Wang Y, Cooper K, Wang A. Microgap Multicavity Fabry-Pérot Biosensor. Journal of Lightwave Technology 2007; 25(7): 1797-1804.

[19] Lee CE, Gibler WN, Atkins RA, Taylor HF. In-Line Fiber Fabry-Pérot-Interferometer with High-Reflectance Internal Mirrors. Journal of Lightwave Technology 1992; 10(10): 1376-1379.

[20] Nespereira M, Silva C, Coelho J, Rebordão J. Nanosecond Laser Micropatterning of Optical Fibers. In: Costa M. (ed.) International Conference on Applications of Optics and Photonics: proceedings of SPIE on CD-ROM: 8001, 3-7 May 2011, Braga, Portugal. Bellingham: SPIE 2011.

[21] Wei T, Han Y, Tsai HL, Xiao H. Miniaturized Fiber Inline Fabry-Perot Interferometer Fabricated with a Femtosecond Laser. Optics Letters 2008: 33(6): 536-538.

[22] Choi HY, Park KS, Park SJ, Paek UC, Lee BH, Choi ES. Miniature Fiber-optic High Temperature Sensor Based on a Hybrid Structured Fabry–Perot Interferometer. Optics Letters 2008; 33(21): 2455-2457.

[23] Rao YJ, Denga M, Duan DW, Zhu T. In-line Fiber Fabry-Perot Refractive-index Tip Sensor Based on Endlessly Photonic Crystal Fiber. Sensors and Actuators A: Physical 2008; 148(1): 33–38.

[24] Tafulo P, Frazão O, Jorge, PAS, Araújo FM. Intrinsic Fabry-Perot Cavity Sensor Based on Chemical Etching of a Multimode Graded Index Fiber Spliced to a Single Mode Fiber. In: Santos JL, Culshaw B, López-Higuera JM, MacPherson, WN. (eds.) EWOFS2010: Fourth European Workshop on Optical Fibre Sensors: Proceedings of SPIE: 7653, 8-10 September 2012, Porto, Portugal. Bellingham: SPIE 2010.

[25] Wei T, Han Y, Tsai H, Xiao H., Miniaturized Fiber Inline Fabry–Perot Interferometer Fabricated with a Femtosecond Laser. Optics Letters 2008; 33(6): 536538.

[26] Ran ZL, Rao YJ, Liu WJ, Liao X, Chiang KS. Laser-micromachined Fabry-Perot Optical Fiber Tip Sensor for High-resolution Temperature Independent Measurement of Refractive Index. Optics. Letters 2008; 16(3): 2252-2263.

[27] Kawasaki BS, Hill KO, Johnson DC, Fujii Y. Narrow-band Bragg reflectors in optical fibers. Optical Letters 1978; 3(2): 66–68.

[28] Vengsarkar AM, Lemaire PJ, Judkins JB, Bhatia B, Erdogan T, Sipe JE. Long-period fiber gratings as band-rejection filters. In Optical Fiber Communication Conference, OFC95, San Diego, CA, Feb. 1995, pp. PD4-2, 1995.

[29] Meltz G, Morey WW, Glenn WH. Formation of Bragg Gratings in Optical Fibers by a Transverse Holographic Method. Optics Letters 1989; 14(15): 823-825.

[30] Davis DD, Gaylord TK, Glytis EN, Kosinski SG, Mettler SC, Vengsarkar AM. Long Period Fibre Grating Fabrication with Focused CO2 Laser Pulses. Electronics Letter 1998;34(3): 302-303.

[31] Akiyama M, Nishide K, Shima K, Wada A, Yamauchi R. A Novel Long-period Fiber Grating Using Periodically Releases Residual Stress of Pure-silica Core Fiber. In: Optical Fiber Communication Conference (OFC), San José, CA, pp. 276-277, Feb. 1998. [Techn. Dig. Conf. Opt. Fiber Commun., 276, 1998].

[32] Wang Y. Review of Long Period Fiber Gratings Written by CO2 Laser. Journal of Applied Physics 2010; 108(8): 081101.

[33] Rego GM. Arc-induced Long-Period Fibre Gratings. Fabrication and their Application in Communications and Sensing. PhD thesis. University of Porto; 2006.

[34] Yablon AD. Optical and Mechanical Effects of Frozen-in Stresses and Strains in Optical Fibers. IEEE Journal of Selected Topics in Quantum Electronics 2004;10(2): 2004.

[35] Yablon AD, Yan MF, Wisk P, DiMarcello FV, Fleming JW, Reed WA, Monberg EM, DiGiovanni DJ, Jasapara J. Refractive Index Perturbations in Optical Fibers Resulting from Frozen-in Viscoelasticity. Applied Physics Letters 2004;84(1):19-21.

[36] Yang S, Matthews M, Elhadj S, Draggoo V, Bisson S. Thermal Transport in CO2 Laser Irradiated Fused Silica: In Situ Measurements and Analysis. Journal if Applied Physics 1998;106(10): 103106.

[37] Grellier A, Zayer N, Pannell C. Heat Transfer Modelling in CO2 Laser Processing of Optical Fibres. Optics Communications 1998;152(4-6): 324-328.

[38] Coelho JMP, Abreu MA, Carvalho-Rodrigues F. Thermal Modeling CO2 Laser Radiation Transmission Welding of Superposed Thermoplastic Films. Optical Engineering 2003;42(11): 3365-3373.

[39] Coelho J, Abreu M, Carvalho-Rodrigues F. Modelling the Spot Shape Influence on High-speed Transmission Lap Welding of Thermoplastics Films. Optics, Lasers in Engineering 2008;46(1): 55-61.

[40] Coelho JMP, Nespereira MC, Abreu M, Rebordão JM. Modeling Refractive Index Change in Writing Long-period Fiber Gratings Using Mid-infrared Laser Radiation. In Proceedings of Summer AOP 2012 / X EONS, CD-ROM, June 27-29th, 2012, Porto, Portugal.

[41] Lancry M, Réginier E, Poumellec B. Fictive Temperature in Silica-based Glasses and its Application to Optical Fiber Manufacturing. Progress in Material Sciences 2012;57(1): 63-94.

[42] Mclachalan A, Meyer F. Temperature Dependence of the Extinction Coefficient of Fused Silica for CO2 Laser Wavelengths", Applied Optics 1987;26(9): 1728-1731.

[43] Xie J, Pan Q. Acousto-Optically Q-Switched CO2 Laser. In: Krzysztof Jakubczak (ed.) Laser Systems for Applications. Rijeka. InTech; 2012. p. 17-38.

[44] Rao YJ, Zhu T, Ran ZL, Wang YP, Jiang J, Hu AZ. Novel Long-period Fiber Gratings Written by High-frequency CO2 Laser Pulses and Applications in Optical Fiber Communication. Optics Communications 2004;229(1-6): 209–221.

[45] Oh ST, Han WT, Paek UC, Chung Y. Azimuthally Symmetric Long-period Fiber Gratings Fabricated with CO2 Laser. Microwave and Optical Technology Letters 2004;41(3): 188-190.

[46] Coelho J, Nespereira M, Silva C, Rebordão J. LOLS Research in Technology for the Development and Application of New Fiber-based Sensors. Sensors 2012;12(3): 2654-2666.

[47] Corning® SMF-28 optical fiber product information. New York: Corning Inc.: 2002.

[48] André P, Rocha A, Domingues F, Facão M. Thermal Effects in Optical Fibres. In: Marco Aurélio dos Santos Bernardes (ed.) Developments in Heat Transfer. Ridjeka: InTech; 2011. p1-20.

[49] Clowes J, Syngellakis S, Zervas M. Pressure Sensitivity of Side-hole Optical Fiber Sensors. IEEE Photonics Technology Letters 2009;10(6): 857-859.

[50] Kondo Y, Nouchi K, Mitsuyu T, Watanabe M, Kazansky P, Hirao K. Fabrication of Long-period Fiber Gratings by Focused Irradiation of Infrared Femtosecond Laser Pulses. Optics Letters 1999;24(19): 646-648.

[51] Hindle F, Fertein E, Przygodzki C, Dürr F, Paccou L, Bocquet R, Niay P, Limberger H. Inscription of Long-period Gratings in Pure Silica and Germano-silicate Fiber Cores by Femtosecond Laser Irradiation. IEEE Photonics Technology Letters 2004;(16)8: 1861-1863.

[52] Mihailov SJ. Fiber Bragg Grating Sensors for Harsh Environments. Sensors 2012;12(2): 1898-1918.

[53] Fu H, Zhou K, Saffari P, Mou C, Zhang L, He S, Bennion I. Microchanneled Chirped Fiber Bragg Grating Formed by Femtosecond Laser-Aided Chemical Etching for Refractive Index and Temperature Measurements. IEEE Photonics Technology Letters 2008;20(19): 1609-1611.

[54] Martinez A, Lai Y, Dubov M, Khrushchev IY, Bennion I. Vector Bending Sensors Based on Fibre Bragg Gratings Inscribed by Infrared Femtosecond Laser. Electronics Letters 2005;41(8): 472-474.

[55] Silva C, Coelho JM, Ruivo A, de-Matos AP. Infrared Nanosecond Laser Effects on the Formation of Copper Nanoparticles. Materials Letters 2010;64(6): 705–707.

[56] Coelho JM, Silva C, Ruivo A, de-Matos A.P. Infrared Nanosecond Laser Radiation in the Creation of Gold and Copper Nanoparticles. In: Book of Abstracts, MATERIAIS 2011: VI International Materials Symposium, 18–20 April 2011 Guimarães: Portugal. Lisbon: SPM; 2011.

Section 4

Fiber Lasers

Chapter 15

Mode Locked Fiber Lasers

Tarek Ennejah and Rabah Attia

Additional information is available at the end of the chapter

http://dx.doi.org/10.5772/46191

1. Introduction

Nowadays, to satisfy the increase of internet demands and requirement, two multiplexing techniques are used: WDM (Wavelength Division Multiplex) and TDM (Time Division Multiplex). WDM still more used than TDM. However, for practical system applications, such as optical CDMA (Code Division Multiplex Access) and OTDM (Optical Time Division Multiplex) systems, high speed optical communications require light sources with a repetition rate control. In this area, pulsed fiber lasers have become very attractive.

Fiber lasers have a number of qualities which make them very attractive for ultra short pulses generation via Q-switching, active or passive mode locking mechanisms. The gain bandwidth of rare-earth-doped fibers is large, typically tens of nanometers, which allows the generation of femtosecond pulses. The high gain efficiency of active fibers makes possible such lasers to operate with fairly low pump powers and tolerate intra cavity optical elements with relatively high optical losses. Fiber laser setups are very compact and can be done with a low cost. Furthermore, mode locked fiber lasers can rely on telecom components.

2. Q-switching mechanism

Storing ions in a higher energy level can be achieved by limiting ions flow to the bottom level. So, it's necessary to prevent stimulated emission prevalence.

By means of light modulators able to generate high optical powers when transiting between the off and on states, we prevent light propagate within the laser cavity. For a radiative transition, the only possible drain to the bottom level is caused by spontaneous emission (see Fig. 1). The E_2 level population very significant, the cavity losses are suddenly reduced and the oscillation becomes possible. The stimulated emission becomes prevalent and the laser starts emitting abruptly. All ions stored up go down emitting stimulated photons (see Fig. 2).

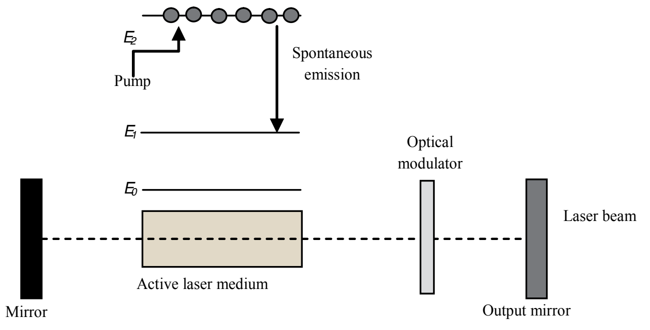

Figure 1. Q-switching first step.

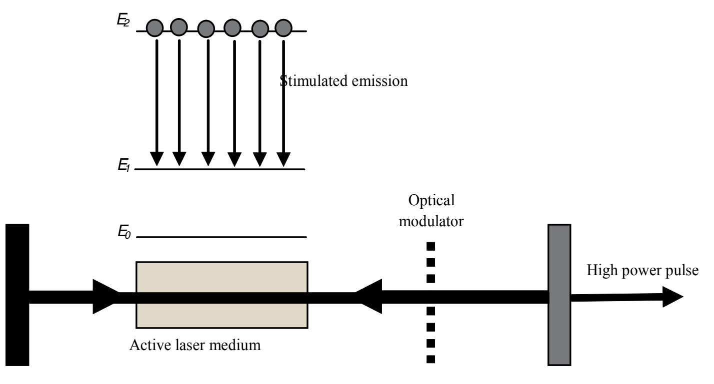

Figure 2. Q-switching second step.

At a given time, there is no way for stimulated emission to happen and the cavity is emptied by resulting losses of the output mirror (see Fig. 3).

The abrupt variation of the number of photons into the cavity results in emitting a high peak power optical pulse. Generally, several journeys between the two mirrors are necessary to completely depopulate the up-level and empty the cavity. So, the pulse width would be higher than the time of a coming and going through the cavity. With lengths lower than one meter, it is possible to generate nanosecond pulses. The repetition rate varies between few hundreds of *Hz* and few hundreds of *KHz*.

The *Q* quality factor of a laser cavity describes its capacity to store the energy light in standing waves. The factor *Q* is the ratio between the stored and the lost energies after each round trip through the cavity. In fact a Q-switch device is an optical modulatorable to control the energy losses of the cavity with generally a repetition rate varying between 1 and $100\ KHz$ [1].

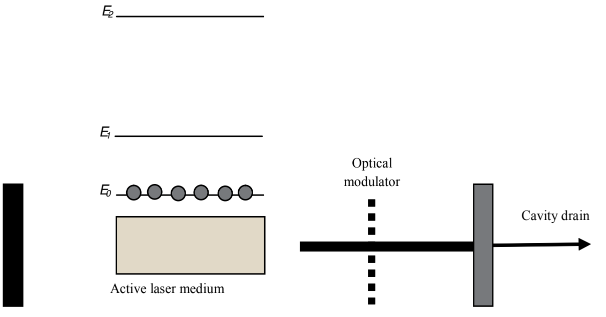

Figure 3. Q-switching third step.

3. Mode locking mechanism

In a laser cavity, frequencies circulating into the resonator and having more gain than losses are called longitudinal modes. They can be considered as an assembly of independent oscillators. These modes gain increases after each round trip through the cavity. These modes are separated by $\Delta F = 1/TF = v/2L$ for a linear cavity case of Fabry Perrot cavity or v/L for a loop cavity case of fiber laser.L is the cavity length and v is the light speed. When these modes oscillate independently of each other, the laser emits continuously. Fig. 4 illustrates a laser cavity output signal resulting on the propagation of three independent longitudinal modes. However, when a fixed phase shift exists between the various modes, the cavity emits a pulses train and becomes phase locked. Fig. 5 shows a mode locked laser cavity output signal resulting on the propagation of three phase dependent longitudinal modes. In fact,the mode locking technique consists in creating a certain phase relationship between the different modes oscillating into the cavity.

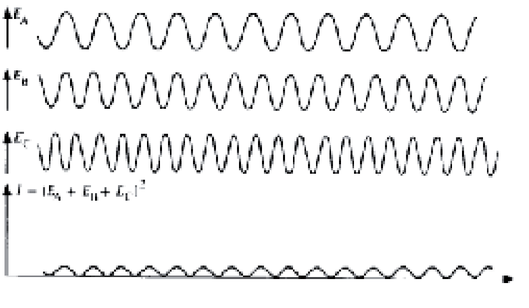

Figure 4. Output signal from laser operating without mode locking mechanism.

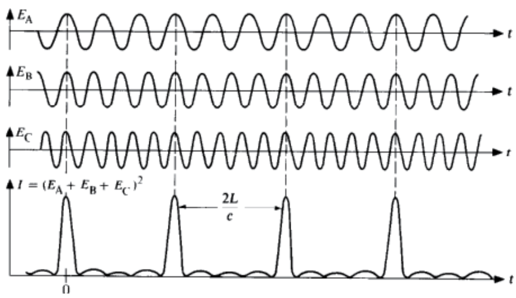

Figure 5. Mode locked laser output signal.

If we consider $M=2S+1$ optical modes with S an integer and A_q the complex envelope of mode q, the complex wave of the q mode and the total signal propagating into the cavity are respectively:

$$
\begin{aligned}
&U_q = A_q \exp\left(j2\pi f_q \left(t - \frac{z}{c} \right) \right) \;;\; f_q = f_0 + q\Delta_f \;;\; U(z,t) = \sum_{q=-S}^{q=S} A_q \exp\left(j2\pi f_q \left(t - \frac{z}{c} \right) \right) \;;\; q = 0; \pm 1; \pm 2; \pm 3; \ldots \\
&\text{If } A(t) = \sum_{q=-S}^{q=S} A_q \exp\left(j\frac{2\pi q t}{T_f} \right) \;;\; U(z,t) = A\left(t - \frac{z}{c} \right) \exp\left(j2\pi f_0 \left(t - \frac{z}{c} \right) \right) \\
&\text{If } A_q = A_0 \;;\; A(t) = A_0 \sum_{q=-S}^{q=S} \exp\left(j\frac{2\pi q t}{T_f} \right) = M A_0 \frac{\sin c\left(Mt / T_f \right)}{\sin c(t / T_f)}
\end{aligned}
\tag{1}
$$

The resulting light intensity is:

$$
I(t,z) = M^2 \left| A_0 \right|^2 \frac{\operatorname{sinc}^2\left(M\left(t - \frac{z}{c} \right) / T_f \right)}{\operatorname{sinc}^2\left(\left(t - \frac{z}{c} \right) / T_f \right)}
\tag{2}
$$

Fig. 6 shows the resulting output pulses sequence of a mode locked laser cavity allowing the oscillation of M longitudinal modes. The mode locking mechanism allows having pulses train with peak power M-times more significant than the average power.

4. Pulsed fiber laser

In case of fiber laser, the *100%* reflective mirror is replaced by the optical fiber loop, the output mirror by an output coupler and the active laser medium by an optical amplifier such as Erbium Doped Fiber Amplifier. Many sophisticated resonator setups have been used particularly for mode-locked fiber lasers, generating picosecond or femtosecond pulses. A fiber laser can contain an electro-optic modulator, an acousto-optic modulator or a saturable absorber to actively or passively mode lock the different longitudinal modes oscillating in the cavity.

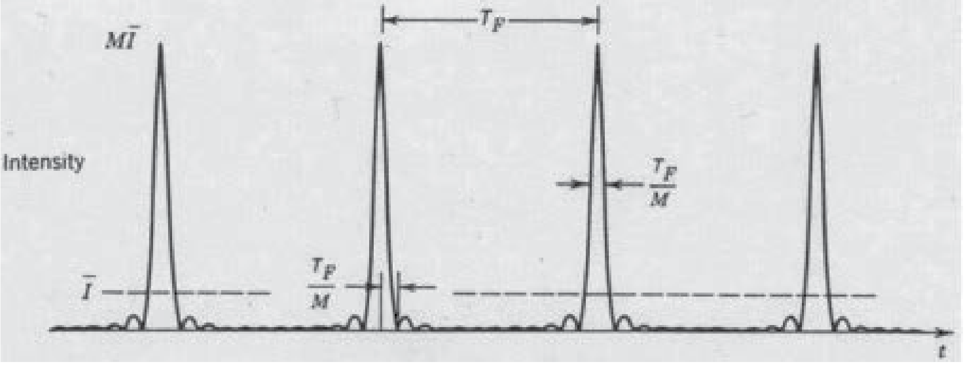

Figure 6. Mode locked laser output *I(t,z)* [2].

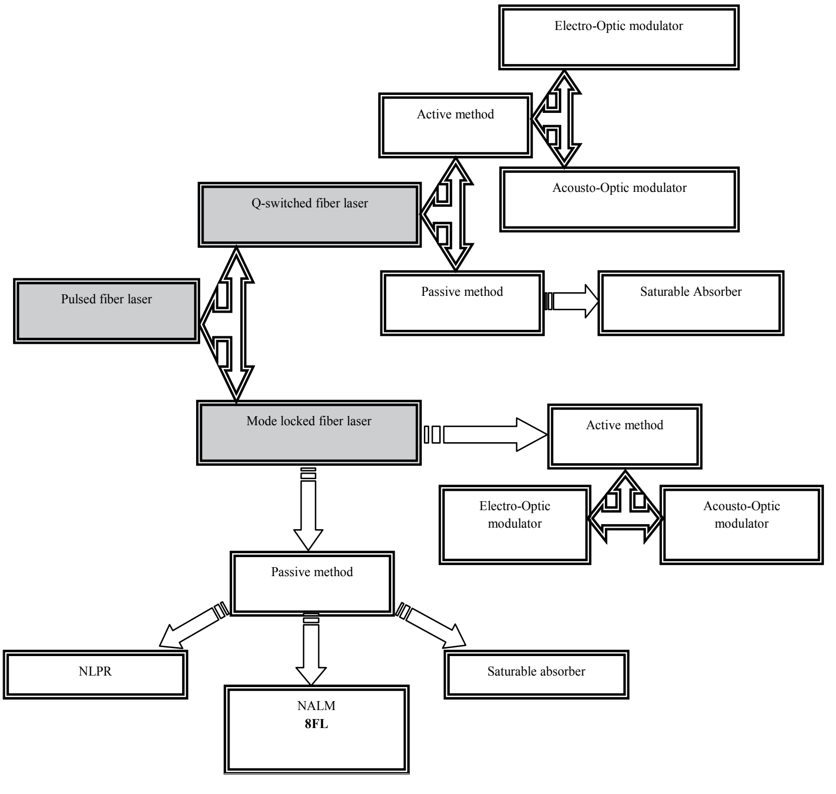

Figure 7. Different types of pulsed fiber lasers.

Passively mode locked fiber lasers have the advantage of being entirely consisted of optical components. They do not require external electrical components and the mode locking mechanism in the cavity is carried out automatically [3-4-5]. However, these lasers can't reach high pulses repetition rates. In fact, the repetition rate of generated pulses depends mainly on the cavity length [6-7]. The laser resonator may contain a saturable absorber such as SESAM (Semiconductor Saturable Absorber Mirror) to passively mode lock the cavity (see Fig. 8).

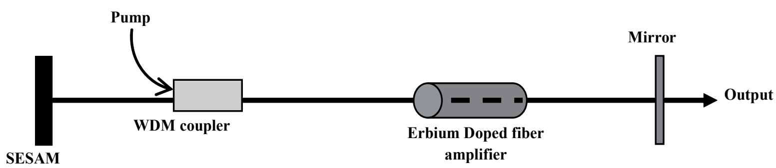

Figure 8. Saturable Absorber passively mode locked fiber laser.

The effect of NLPR(Non Linear Polarization Rotation), as illustrated in Fig. 9, or a nonlinear fiber loop mirror, as illustrated in Fig. 10, can be used as artificial saturable absorbers [8].

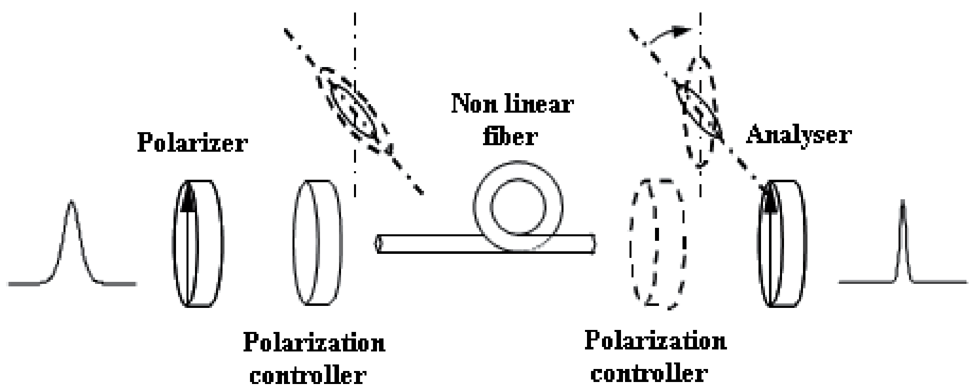

Figure 9. NLPR mechanism.

A nonlinear loop mirror is used in a "figure-of-eight laser". A schematic diagram of the 8FL (Eight Fiber Laser) is shown in Fig. 10. The 8FL overall design is that of a ring cavity with a Sagnac interferometer with a gain medium placed asymmetrically in the loop. By addition of pulses through the central coupler, the NALM (Non linear Amplifying Loop Mirror) transmits highest intensities of pulse and reflects the lowest ones [9-10]. The nonlinear fiber loop amplifies, shapes and stabilizes the circulating ultra short pulse [11]. With the P-APM (Polarization-Additive Pulse Mode-Locking), the polarization state of a pulse propagating through an optical fiber differs from the peak to the wings and the transmission through a polarizer can be adjusted to eliminate the wings [12-13]. The SAs act as intensity dependent elements. The wings of the pulse exhibit more losses than the peak [14].

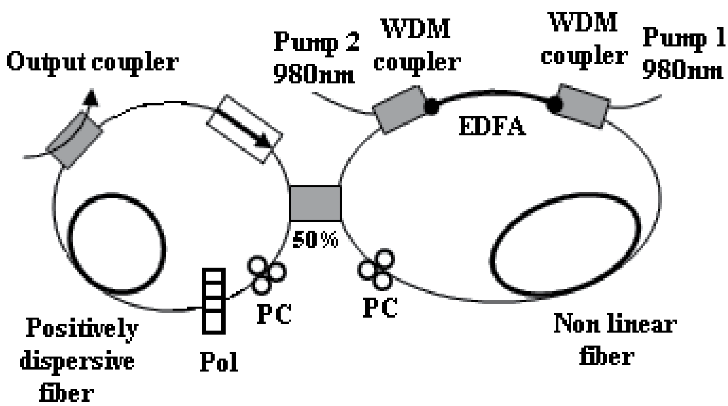

Figure 10. Figure of eight fiber laser.

The PCs (Polarization Controllers) set the input signal in an arbitrary polarization state. The azimuth and elliptical parameters define the polarization state of the output signal. Considering E_{inx} and E_{iny}as the polarization components of the input signal, the output signal is:

$$E_{out}(t)=\begin{pmatrix}\sqrt{(1-k)}\exp\left(j\delta_{xy}(t)\right)\\ \sqrt{k}\exp\left(j\delta_{xy}(t)\right)\end{pmatrix}\sqrt{\left|E_{inx}\right|^2+\left|E_{iny}\right|^2} \tag{3}$$

Where k is the power splitting ratio parameter and $\delta_{yx}(t)$ is the phase difference between the x and y components. The optical isolator is inserted into the loop to allow light circulate only in one direction. The major disadvantage of 8FL is that it requires a special management of the various parameters of the cavity [15]. In the steady state, the various linear and non linear effects are in balance and the pulse output power and width are unchanged or often even nearly constant after each completed round trip. Assuming a single circulating pulse, the pulse repetition rate corresponds to the resonator round-trip time.

In actively mode locked fiber lasers, as shown in Fig. 12, the pulses frequency depends on the electro-optic or the acousto-optic modulator inserted in the cavity [16-17-18]. Generally, these types of laser cavities provide typically pulses larger than those provided by a passively locked laser. This can be explained by the fact that no compression techniques are applied [19]. The most used optical modulator to actively mode lock the different modes oscillating into a fiber laser cavity is the MZM (Mach Zehnder modulator). It's an intensity modulator based on an interferometer principle. It consists of two *3dB* couplers which are connected by two waveguides of equal length (see Fig. 11). By means of electro-optic effects, an externally applied voltage can be used to vary the refractive indices in the waveguide branches. The different paths can lead to constructive and destructive interference at the output, depending on the applied voltage. Then the output intensity can be modulated according to the voltage. A Mach Zehnder Modulator has often only one optical exit, the second one is hidden.

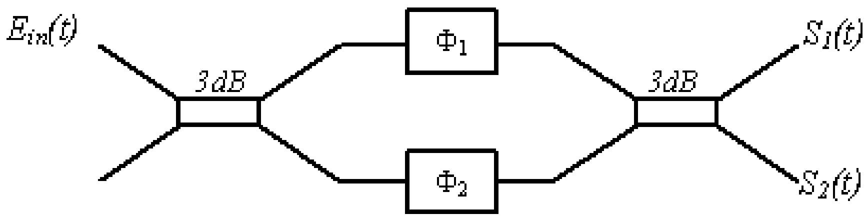

Figure 11. Mach Zehnder Modulator.

$$\begin{aligned}
\begin{pmatrix} S_1(t) \\ S_2(t) \end{pmatrix} &= \frac{1}{\sqrt{2}}\begin{pmatrix} 1 & j \\ j & 1 \end{pmatrix} \cdot \begin{pmatrix} \exp(j\phi_1) & 0 \\ 0 & \exp(j\phi_2) \end{pmatrix} \cdot \frac{1}{\sqrt{2}}\begin{pmatrix} 1 & j \\ j & 1 \end{pmatrix} \cdot \begin{pmatrix} E_{\text{in}}(t) \\ 0 \end{pmatrix} \\
S_1(t) &= j\exp\left(j\left(\frac{\phi_1+\phi_2}{2}\right)\right)\sin\left(\frac{\phi_1-\phi_2}{2}\right)E_{\text{in}}(t) \\
S_2(t) &= j\exp\left(j\left(\frac{\phi_1+\phi_2}{2}\right)\right)\cos\left(\frac{\phi_1-\phi_2}{2}\right)E_{\text{in}}(t)
\end{aligned} \tag{4}$$

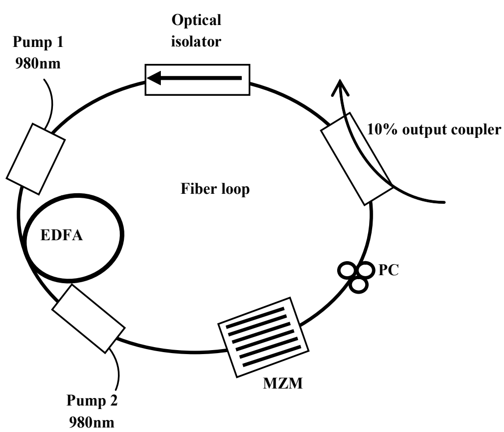

Figure 12. Actively mode locked ring fiber laser.

Aiming to profit at the same of the two configurations advantages: a rather low width and a sufficiently high repetition rate of pulses, new prospects and configurations of fiber lasers, using both the passive and active mode locking techniques, have been proposed. This new generation of pulses generator is called hybrid type mode locked fiber laser [20]. Fig. 13

shows hybrid type mode locked fiber laser using both a machZehnder modulator to actively mode lock the cavity and a non linear amplifying loop mirror to passively mode lock the cavity.

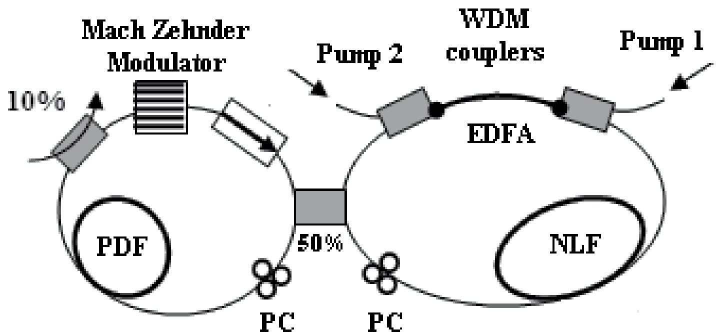

Figure 13. Hybrid type mode locked 8FL.

Being 90% made of fiber; light propagation through a fiber laser can be modeled by the Split Step Fourier Method.

5. Split step fourier method

Light propagation within optical fiber may be expressed by the Generalized Non Linear Schrödinger Equation (GNLSE) as follow:

$$\frac{\partial A}{\partial z} + j\frac{1}{2}\beta_2\frac{\partial^2 A}{\partial T^2} - \frac{\beta_3}{6}\frac{\partial^3 A}{\partial T^3} + j\frac{\beta_4}{24}\frac{\partial^4 A}{\partial T^4} + \frac{\alpha}{2}A = j\gamma|A|^2 A \tag{5}$$

β_2 and β_3 are the second and the third order dispersion terms, α is the attenuation coefficient of the fiber, T is the related time given by $T=t-z/vg$ where z and v_g are the longitudinal coordinate and the group velocity corresponding to the central wavelength λ and γ is the nonlinear parameter of the fiber given by $\gamma=2\pi n_2/\ \lambda A_{eff}$. n_2 is the non linear refractive index and A_{eff} is the effective area of the fiber. When studying the propagation into an EDFA, the GNLSE become:

$$\frac{\partial A}{\partial z} + j\frac{1}{2}\beta_2\frac{\partial^2 A}{\partial T^2} - \frac{\beta_3}{6}\frac{\partial^3 A}{\partial T^3} + j\frac{\beta_4}{24}\frac{\partial^4 A}{\partial T^4} + \frac{\alpha-g}{2}A = j\gamma|A|^2 A \tag{6}$$

The gain of the Erbium Doped Fiber Amplifier (EDFA) can be estimated as $G=exp(gl)$ where l is the length of the doped fiber and g the gain coefficient.

The SSFM consists on transforming the GNLSE as the sum of linear and nonlinear operators:

$$\begin{aligned}
&\frac{\partial A}{\partial z} = (\hat{D} + \hat{N})A \\
&\hat{D} = -\frac{\alpha}{2} + j(-\frac{1}{2}\beta_2 \frac{\partial^2}{\partial T^2} - \frac{\beta_4}{24}\frac{\partial^4}{\partial T^4}) + \frac{\beta_3}{6}\frac{\partial^3}{\partial T^3} \\
&\hat{N} = j\gamma |A|^2
\end{aligned} \tag{7}$$

The SSFM relies on that propagation in each segment of the optical fiber is divided in three steps: two linear and one non linearsteps (see Fig. 14). The nonlinear step is inserted between the two linear steps [21-22].

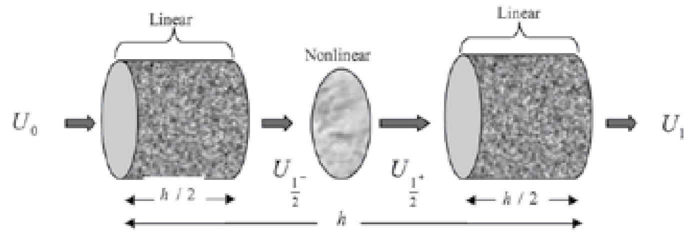

Figure 14. Principle of Split Step Fourier Method SSFM.

So, linear and nonlinear effects are supposed to be applied in the whole segment of the fiber. The linear operator is used in the frequency area and the non linear one is used in time area.

$$\begin{aligned}
&\hat{D} = -\frac{\alpha}{2} + j(\frac{\beta_2}{2}\omega^2 - \frac{\beta_3}{6}\omega^3 - \frac{\beta_4}{24}\omega^4) \\
&U_{\frac{1}{2}^-} = A(z + \frac{h}{2}, T) = FT^{-1}\left(\exp\left(\frac{h}{2}\hat{D}\right)FT\left(A(z,T)\right)\right) \quad ; \quad A(z,T) = U_0 \\
&\qquad = \exp\left(\frac{h}{2}\hat{D}\right)U_0 \\
&U_{\frac{1}{2}^+} = \exp\left(\int_z^{z+h}\hat{N}\left(U_{\frac{1}{2}^-}\right)dz\right) \quad ; \quad U_1 = FT^{-1}\left(\exp\left(\frac{h}{2}\hat{D}\right)FT\left(U_{\frac{1}{2}^+}\right)\right)
\end{aligned} \tag{8}$$

FT is the Fourier transform.

6. Erbium doped fiber amplifier

The EDFA is based on a two-level Er^{3+} system assumption that is usually adapted to model erbium-doped fiber amplifiers. The lifetime transition from level $^4I_{11/2}$ is of the order of microseconds for silicate hosts. Therefore, it is reasonable to neglect the population density N_3 in the rate equations description. A two-level system approximation is used in this case. Under the assumption of the normalized population densities N_1 and N_2 at the ground and metastable energy level, ${}^4I_{15/2}$and ${}^4I_{13/2}$ populations are calculated by numerically solving the rate and propagation equations [23]:

$$\begin{aligned}
&\frac{\partial N_2(z,t)}{\partial t} = -\frac{1}{A_{eff}}\sum_{n=1}^{N}\left\{\Gamma_n\left[\left(\sigma_n^e+\sigma_n^a\right)N_2(z,t)-\sigma_n^a\right]\right\}\left[P_n^+(z,t)+P_n^-(z,t)\right]-\frac{N_2(z,t)}{\tau}\\
&N_2+N_1=1\\
&\frac{\partial P_n^{\pm}(z,t)}{\partial z} = u_n\left\{\rho\times\Gamma_n\left[\left(\sigma_n^e+\sigma_n^a\right)N_2(z,t)-\sigma_n^a-\alpha\right]\right\}P_n^{\pm}(z,t)+2\rho\times\Delta\nu N_2\Gamma_n\sigma_n^e
\end{aligned} \tag{9}$$

Where the optical powers are expressed in units of number of photons per unit time, τ is the metastable spontaneous emission lifetime, N is the number of channels taken into account in the simulation (including signals, pumps, and ASE bins), ρ is the number density of the active erbium ions, α is the attenuation coefficient (which takes into account the background loss of the fiber), $\Delta\nu$ is the frequency step used in the simulation to resolve the ASE spectrum, and A_{eff} is the effective doped area given by πb^2, where b is the Er doping radius (it is considered a uniform distribution of erbium ions in the area given by the Er doping radius region). The n^{th} channel of wavelength λ_n has optical power $P_n(z,t)$ at location z and time t, with emission and absorption cross-section $\sigma^n{}_e$ and $\sigma^n{}_a$ respectively, and confinement factor Γ_n. The superscript symbols + and – are used respectively to indicate channels travelling in forward (from 0 to L_{EDFA}) and backward (from L_{EDFA} to 0) directions. For beams travelling in the forward direction $u_n=1$ and for beams in the opposite direction $u_n=-1$. The overlap integrals Γ_n between the LP_{01} mode intensity distributions doped region areas are given by:

$$\Gamma_n(\nu) = \frac{\int_0^b \left|E(r,\nu)\right|^2 r\,dr}{\int_0^\infty \left|E(r,\nu)\right|^2 r\,dr} \tag{10}$$

7. Interaction between mode locking mechanism and non linear effects in fiber laser

Normally, when designing extremely high output average and peak power fiber laser generating ultra short pulses, the best solution that can be adopted is to enhance the non linear effects in the cavity. This can be achieved either by pumping the piece of doped fiber amplifier with a high input power rate or enhancing the SPM, XPM and FWM effects by reducing the average dispersion of the cavity and the effective area of the different fibers used. In this section, managing the pumping input powers level, the dispersion and the effective area of different microstructured optical fibers inserted into a passively and an hybrid type mode locked 8FLs, we prove that enhancing non linear effects does not lead necessarily to better results. It depends also on the type of mode locking mechanism used. The highest peak powers and the narrowest pulse widths are obtained only for specific parameters.

In spite of their singularities and particularities in managing linear and non linear effects, the exploitation of MOFs in laser cavities has remained a subject of research bit addressed. In fact, MOFs offer many degrees of freedom in the management of dispersion and effective area

A schematic diagram of the first passively mode locked 8FL is shown in Fig.15. It consists of two loops: a ring cavity and a non linear amplifying loop mirror NALM connected to each other through a *50%* central coupler. The linear cavity is made up of *10m* of PDF (Positively Dispersive Fiber: $\beta_2=20ps^2/km$) having $85\mu m^2$ as effective area and aiming to maintain balance between anomalous and normal dispersion within the 8FL, a *10%* output coupler and a polarization insensitive optical isolator to ensure the circulation of light only on the clockwise direction. The NALM includes a MOF (Microstructured Optical Fiber) and a *10m* EDFA (Erbium Doped Fiber Amplifier) having *0.24* as numerical aperture forward and backward pumped by two *980nm* pump laser diodes coupled to the loop through two *980/1550nm* WDM couplers. The Er^{3+} ions density is *700ppm*.

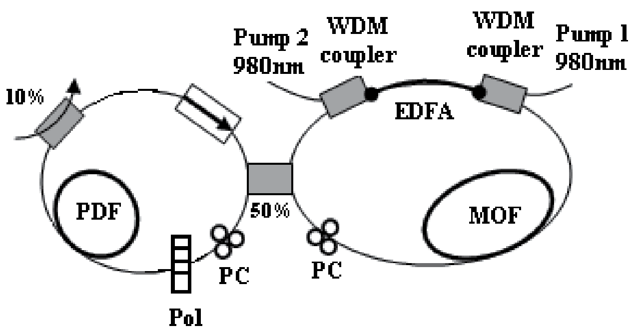

Figure 15. Configuration of passively mode locked 8FL.

The second configuration, shown in Fig.16, is a hybrid type mode locked 8FL. It differs from the first one by the presence of a MZM (Mach Zehnder Modulator) as an electro-optical modulator into the linear ring cavity.

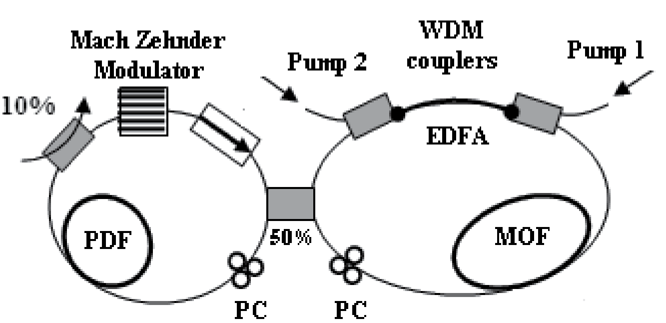

Figure 16. Configuration of hybrid type mode locked 8FL.

http://dx.doi.org/10.5772/46191

By modelling the light propagation through the various components by the SSFM (Split Step Fourier Method), we studied the influence of varying nonlinear parameters of the cavity on the output pulses shape. Light pulse propagation in the 8FL may be expressed by the NLGSE (Non Linear Generalised Schrödinger Equation) and the transfer function of the different components used [12]. The central coupler is a cross-coupler for combining or splitting the optical signal. It is bidirectional, with wavelength independent coupling, insertion loss and return loss. If we consider E_{in}, E_{out}, E_3 and E_4 respectively the input, transmitted, NALM clockwise and counter clockwise circulating light powers, after propagating into an L length loop made of EDFA and MOF, considering only the non linear effects, E_{3L} and E_{4L} are expressed as follow:

$$\begin{aligned} E_{3L} &= \sqrt{k}\sqrt{G}E_{in}\exp(jk2\pi n_2 G\left|E_{in}\right|^2 L / A_{eff}\lambda) \\ E_{4L} &= j\sqrt{(1-k)}\sqrt{G}E_{in}\exp(j(1-k)2\pi n_2\left|E_{in}\right|^2 L / A_{eff}\lambda) \end{aligned} \tag{11}$$

Where k is the power splitting ratio parameter, G is the EDFA gain, λ is the signal wavelength and $A_{eff}$is the MOF effective area. For each round trip through the fiber laser, the transmitted power circulating into the ring linear cavity is:

$$\begin{aligned} E_{out} &= k\sqrt{G}E_{in}\exp(jk2\pi n_2 G\left|E_{in}\right|^2 L / A_{eff}\lambda) - (1-k)\sqrt{G}E_{in}\exp(j(1-k)2\pi n_2\left|E_{in}\right|^2 L / A_{eff}\lambda) \\ \left|E_{out}\right|^2 &= \left|E_{in}\right|^2 G\left(1-2k(1-k)\left(1+\cos\left(\left(kG-(1-k)\right)2\pi n_2\left|E_{in}\right|^2 L / A_{eff}\lambda\right)\right)\right) \end{aligned} \tag{12}$$

A single secant hyperbolic input pulse with *1mW* of peak power and *200ps* FWHM (Full Width at Half Maximum) is launched in the first configuration through the WDM coupler. At the beginning, we studied the output pulses shape for different EDFA pumping power levels and differ4ent MOF effective area's values. The pumping threshold is about *300mW*. In fact, as illustrated in Fig.17 and Fig.18 below, when increasing the pump power of the EDFA, the pulses peak power increases whereas the width decreases. However for very small effective areas like $5\mu m^2$ and $10\mu m^2$, the pulse width reaches a minimum value at a specified pump power level before growing up proportionally to the laser diodes pump powers. In these cases the lowest values of the pulse width are reached respectively for *400mW* and *700mW* of pump powers.

A second approach to study the non linear effects impact in a fiber laser cavity is to use longer portion of the non linear optical fiber used. Fig.19 and Fig.20 show the output pulses peak power and width for different lengths and effective areas of MOF. The pump power delivered by each laser diode is equal to *700mW*.

As shown in Fig.19 and Fig.20, enhancing dramatically the non linear effects, by increasing the MOF length and decreasing its effective area, does not lead necessarily to optimal results. In fact, for each length of one selected fiber there are two optimal effective areas. The first corresponds to the one leading to the highest peak power and the second corresponds to the one leading to the lowest pulse width and conversely. However, there is always an intermediate value of the effective area leading to a high peak and a low pulse width. For *10m* of MOF, the intermediate effective area is $7.5\mu m^2$. The peak power is equal to *16W* and the pulse width to *39.7ps*. However, the highest peak power *18.25W* and the lowest pulse width *39ps* are obtained respectively for $5\mu m^2$ and $10\mu m^2$ effective areas. For *20m* of MOF, the intermediate effective area is $15\mu m^2$. The peak power is equal to *17.25W* and the pulse width to *38.5ps*. However, the highest peak power *20W* and the lowest pulse width *37.5ps* are obtained respectively for $10\mu m^2$and $17.5\mu m^2$effective areas. For *30m* of MOF, the adequate effective area is $15\mu m^2$.

Thus, by reducing the mean dispersion of the cavity with an appropriate choice of the MOF optimal length and effective area, generated ultra short pulses would have the highest peak power and the lowest width.

Unlike the passively mode locked 8FL carried out above, in case of hybrid type 8FL shown in Fig.16, no input pulse is inserted in the cavity to release the cavity oscillation. The first handling aimed to study the average pulses output power fluctuation according to the pump powers of the two lasers diode for different MOF's effective areas. The MOF length and dispersion are respectively *30m* and $-10ps^2/km$. The PDF length and dispersion are respectively *10m* and $20ps^2/km$ with an effective area of $85\mu m^2$. The electrical signal frequency injected into the MZM is *20GHz*. As shown in Fig.23, more the effective area is small and the pumping powers are high more the mean power of output signal is high. So, by increasing non linear effects, we increase the output pulses power.

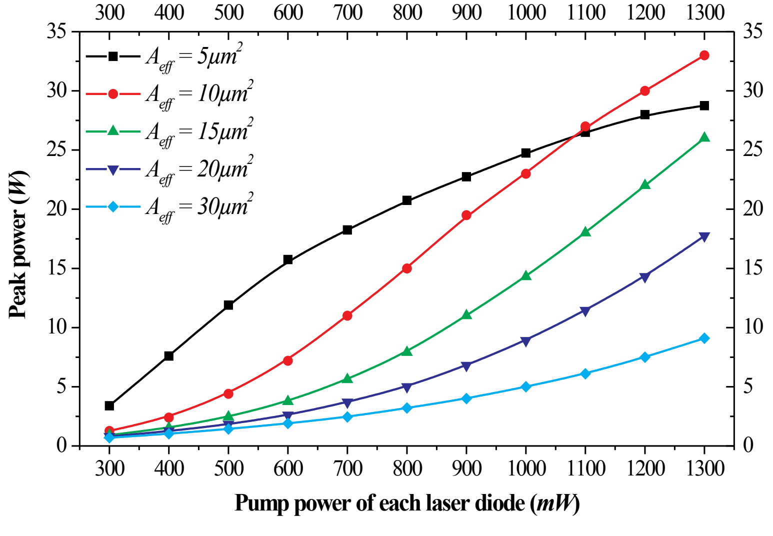

Figure 17. Peak power vs launched pump powers (L_{MOF}=*10m*, β_{2MOF}=$-10ps^2/km$).

http://dx.doi.org/10.5772/46191

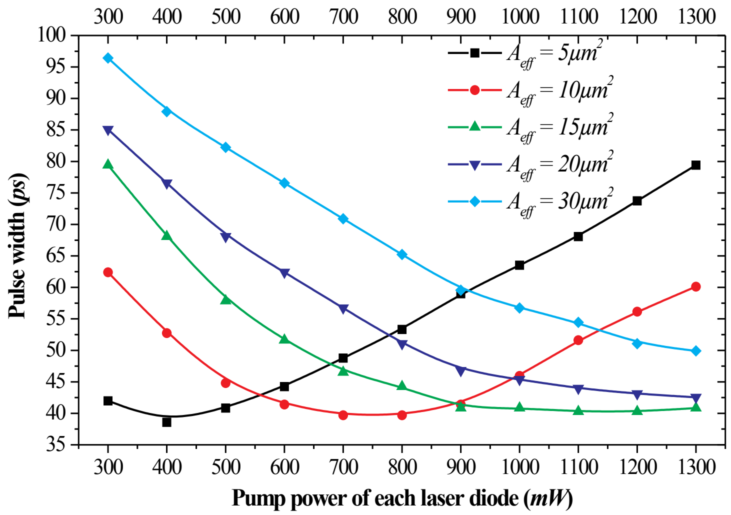

Figure 18. Width vs launched pump powers (L_{MOF}=10m, β_{2MOF}=-10ps²/km).

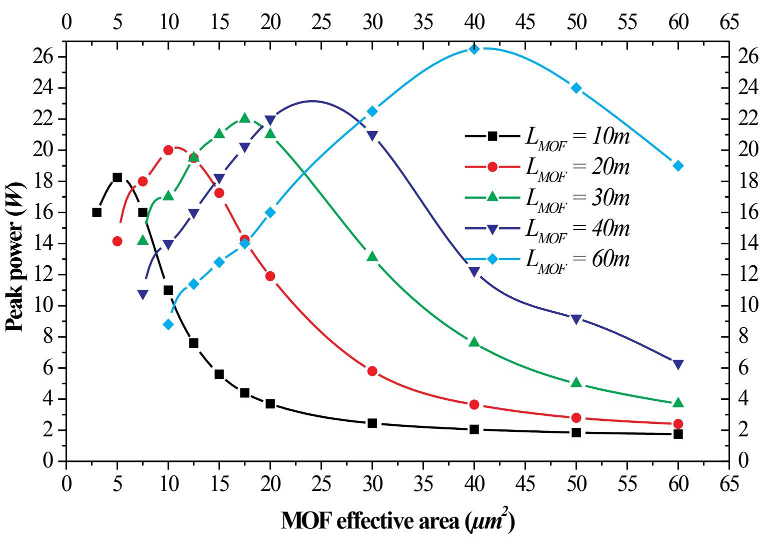

Figure 19. Peak power vs MOF's effective area and length.

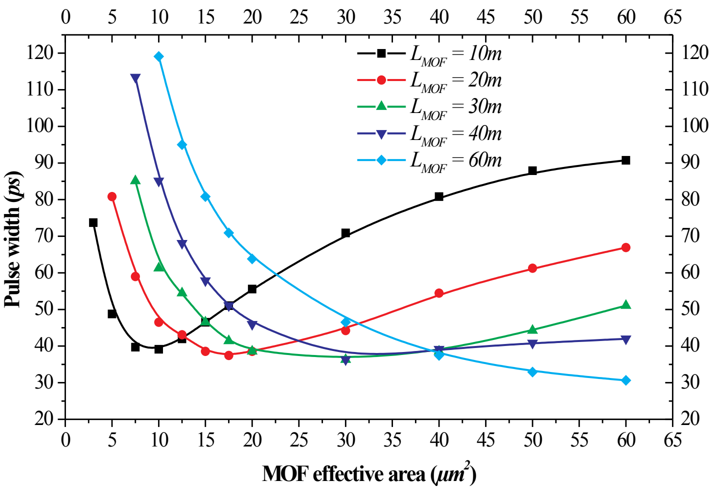

Figure 20. Width vs MOF's effective area and length.

About pulses shape depending on group velocity dispersion, Fig.21 and Fig.22 show that the best results correspond to MOF having negative chromatic dispersions.

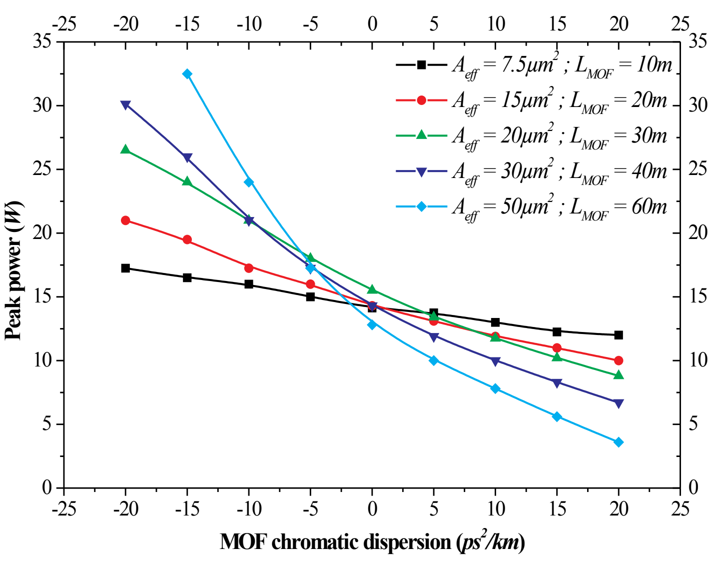

Figure 21. Peak power vs MOF chromatic dispersion.

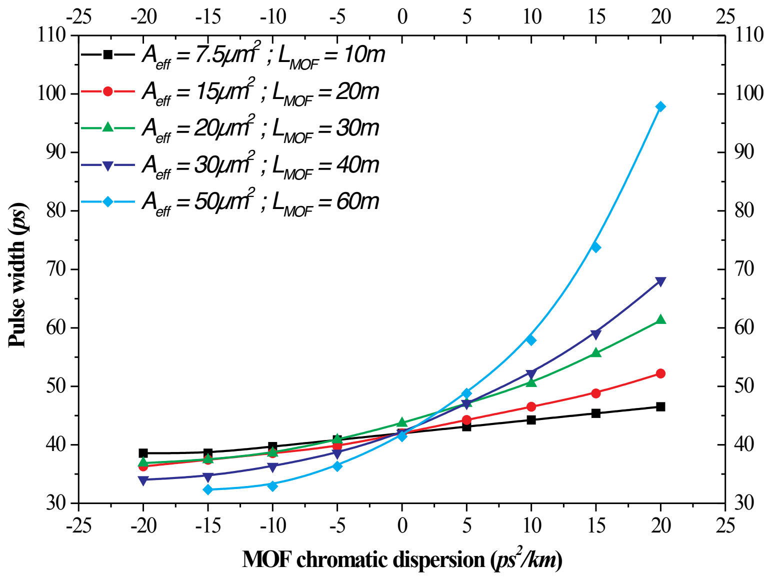

Figure 22. Width vs MOF chromatic dispersion.

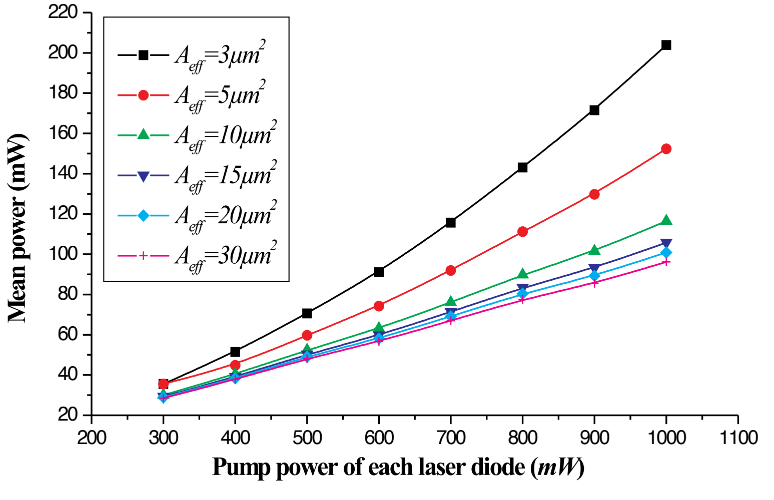

Figure 23. Mean power vs launched pump powers.

The repetition rate and the width of output pulses are fixed by the electro-optical modulator characteristics.

The repetition rate of pulses depends directly on the frequency of the electrical signal injected into the MZM. Fig.24 illustrates the variation of the width of output pulses according to the electrical signal frequency.

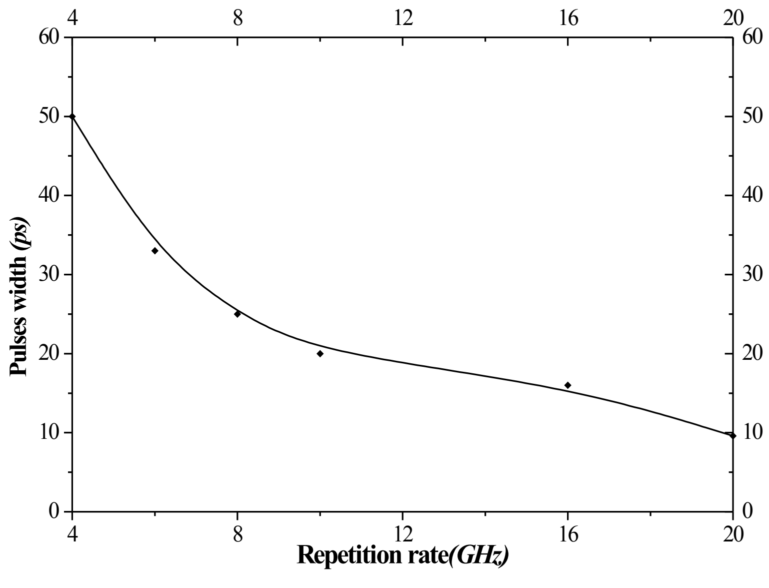

Figure 24. Width vs Repetition rate.

Fig.25 shows hybrid type output pulses with a repetition rate of 20GHz.The second handling aimed to study the average pulses output power fluctuation from a hybrid type 8FL according to non linear effects by varying the length and the effective area of the MOF.

Curves shown in Fig.26 illustrate that more the MOF is long and its effective area is small more the exit power of the laser is significant. However, a significant increase of the MOF length and the effective area leads to a fast power fall. We can also notice that for all different MOF's lengths there is a particular value of the effective area leading always to the same result. In this case, it corresponds to $12\mu m^2$.At the end, we studied the hybrid type 8FL behaviour when decreasing the average chromatic dispersion of the cavity. Contrary to passively mode locked 8FL, the maximum values of exit power, for a hybrid type 8FL, are reached for normal dispersion of the MOF $\beta_{2MOF}>0$ (see Fig.27).

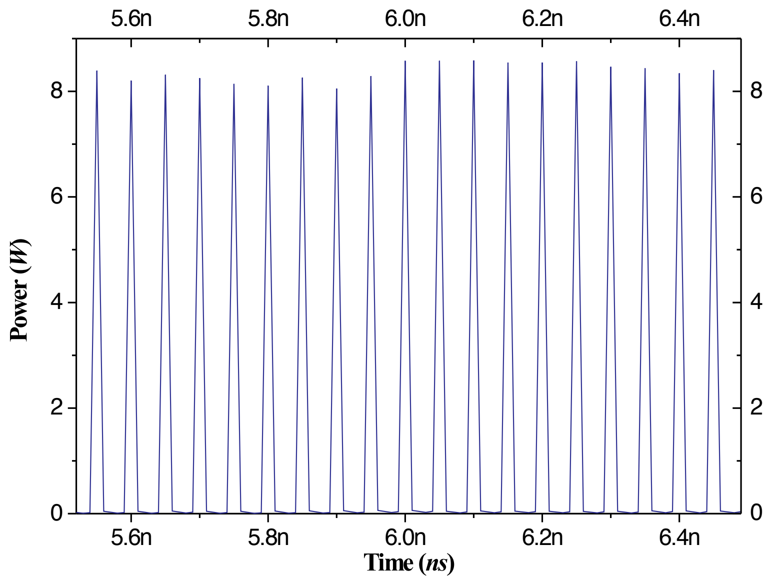

Figure 25. *GHz* hybrid type 8FL output pulses.

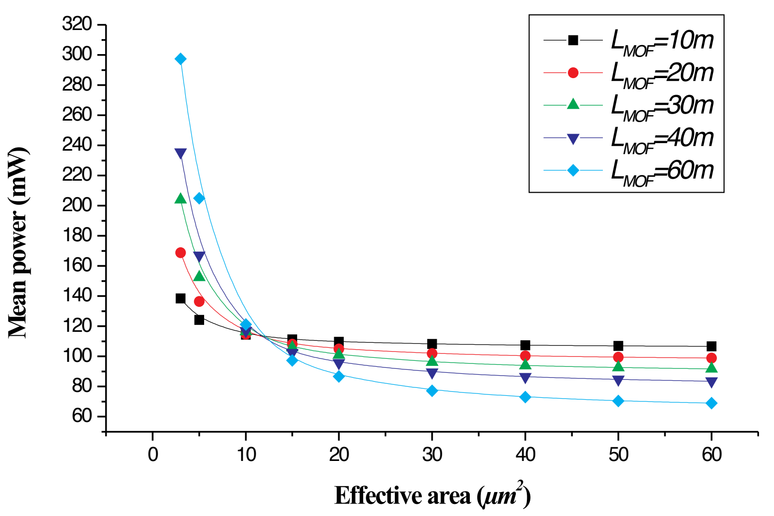

Figure 26. Mean power vs MOF length and effective area (β_{2MOF}=-*10ps²/km*).

Thus, increasing the average exit power of hybrid type 8FL, operating at any pulses repetition rate, can be reached by choosing a rather long MOF having small effective area and normal dispersion.

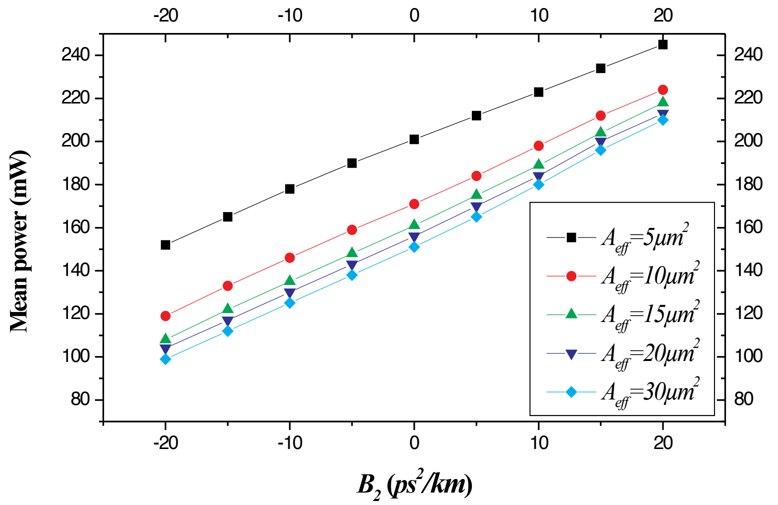

Figure 27. Mean power vs MOF chromatic dispersion.

8. Conclusion

We summarized different techniques used to generate ultra short pulses from a fiber laser. Using the Split Step Fourier Method algorithm to model light propagation within a loop cavity, we described some operating process of different kind of mode locked fiber lasers. We also focused on some optical components operating process used in fiber laser to passively or actively mode lock the different modes oscillating within a laser cavity. In addition, we focused on Erbium Doped Fiber Amplifier operating process. We highlighted the improvement of fiber laser performances does not depend only on the management of the non linear parameters of the cavity. In fact, it depends tightly on the mode locking mechanism used. A passively mode locked 8FL and a hybrid type 8FL do not respond the same way to non linear effects increase. In fact, in case of passively mode locked 8FL, for each length of the high non linear fiber, correspond two associated optimal effective areas: one leading to the highest peak power and one leading to the lowest pulse width. Whereas, increasing the non linear effects by using a rather long high non linear fiber having a reduced effective area leads to the best output results in case of hybrid type 8FL. Moreover, contrarily to hybrid type 8FL, reducing the average dispersion of the cavity leads necessarily to better output passively mode locked 8FL pulses shape. In fact, this work aims to illustrate the existing interaction between non linear effects and mode locking mechanism in fiber laser.

Author details

Tarek Ennejah and Rabah Attia

Unité de Recherche Composants et Systèmes Electroniques UR-CSE, Ecole Polytechnique de Tunisie, EPT, La Marsa, Tunis, Tunisie

References

[1] Liu, J., Shen, D., Tam, S. C., Lam, Y. L., Modelling, "., pulse, shape., of, Q-switched., lasers", I. E. E. E., Journal, of., Quantum, Electronics., vol.3, , & , p. July (2001). , 888 EOF.

[2] K. Merzouk, "Etude d'un système bas coût de transmission optique par multiplexagetemporel", Thèse de doctorat, InstitutPolytechnique de Grenoble, France, Avril 2008.

[3] Salhi, M., Haboucha, A., Leblond, H., Sanchez, F., Theoretical, ., study, of., figure-eight, all., fiber, laser. ., & Phys, . Rev. A, 77, 033828, ((2008).

[4] Zheng, Z., Iqbal, M., Yu, T., Cavity, "., Dynamics, of. a., Figure, of., Eight, Fiber., Laser", International., Journal, of., & Communications, . (2007).

[5] Tarek, Ennejah., Faouzi, Bahloul., Rabah, Attia. "., Generation, of., Non, Uniform., Pulses, by., an, Eight., Microstructured, Optical., & Fiber, Laser". J. Optical. Communications, (2011). , 32, 107.

[6] Theimer, J., Haust, J. W., Figure, "., eight, fibre., laser, stable., operating, regimes"., Journal, of., & modern, Optics. (1997). 919 EOF-928 EOF.

[7] Hofer, M., Ober, M. H., Haberl, F., & , M. E. Fermann "Characterization of ultrashort pulse formation in passively mode-locked fiber lasers. IEEE J. Quantum Electron. 28 (3), (1992). , 720 EOF-728 EOF.

[8] [7], M. E., Fermann, "., Passive, mode., locking, by., using, nonlinear., polarization, evolution., in, a., polarization, maintaining., erbium-doped, fiber"., & Optics, Letters. (1993). 894 EOF.

[9] Richardson, D. J., Laming, R. I., Payne, D. N., Matsas, V., Phillips, M. W., Self, "., starting, passively., mode, locked., erbium, fiber., ring, laser., based, on., the, amplifying., Sagnac, switch"., & Electron, . Lett. 27 (6), 542 ((1991).

[10] Yoshida, E., Kimura, Y., Nakazawa, M., Femtosecond, "., Erbium, Doped., Fiber, Laser., with, Non., linear, Polarization., & Rotation", Jpn. J. Appl. Phys. 33 (10), 5779 ((1994).

[11] Duling, I. N., All-fiber, I. I. I. "., ring, soliton., laser, mode., locked, with. a., nonlinear, mirror"., & Optics, Letters. (1991). 539 EOF.

[12] Theimer, J., Haust, J. W., Figure, "., eight, fibre., laser, stable., operating, regimes"., Journal, of., & modern, Optics. (1997). 919 EOF-928 EOF.

[13] Zheng, Z., Iqbal, M., Yu, T., Cavity, "., Dynamics, of. a., Figure, of., Eight, Fiber., Laser", International., Journal, Of., & Communications, . (2007).

[14] Kuzin, E. A., Andrade-Lucio, J. A., Ibarra, B., Escamilla, R., Rojas-Laguna, , Sanchez-Mondragon, J., Nonlinear, "., optical, loop., mirror, using., the, nonlinear., polarization, rotation., effect", Optics., & Communications, . (1997). 60 EOF-64 EOF.

[15] Faouzi, Bahloul., Tarek, Ennejah., Rabah, Attia. "., Investigation, of., Microstructured, Optical., Fiber, in., Eight, Fiber., & Laser", J. Optical. Communications. (to be published).

[16] Tarek, Ennejah., Faouzi, Bahloul., Rabah, Attia. "., Accordable, Repetition., Rate, Actively., Mode-locked, Fiber., & Laser", J. Optical. Communications, (2010). , 31, 206.

[17] Nakazawa, M., Yoshida, E., Kimura, Y., Generation, "., of, ., fs, optical., pulses, directly., from, an., erbium-doped, fibre., ring, laser., of, 1.., & mm", Electron. Lett, (1993). , 29, 63.

[18] Tamura, K., Ippen, E. P., Haus, H. A., Nelson, I. E., "77fs, pulse., generation, from. a., stretched, pulse., mode, locked., all-fibre, ring., & laser", Opt. Lett, (1993). , 18, 1080.

[19] Spaulding, K. M., Young, D. H., Kim, A. D., Kutz, J. N., Nonlinear, "., dynamics, of., Mode, locking., optical, fiber., & ring, lasers". J. Opt. Soc, Am, B 19, (2002). , 1045.

[20] K.H. Kim, M.Y. Jeon, S.Y. Park, H.K. Lee, and E.H. Lee, "Gain Dependent Optimum Pulse Generation Rates of a Hybrid-Type Actively and Passively Mode-Locked Fiber Lase", ETRI Journal, vol.n°. 1, April (1996). , 1.

[21] G.P. Agrawal, Nonlinear Fiber Optics, 2nded, (1995).

[22] G.P. Agrawal, Applications of Nonlinear Fiber Optics, 2001.

[23] Giles, C. R., Desurvire, E., Modeling, "., erbium-doped, fiber., amplifiers,", Journal., of, Light., wave, Technology., & Vol, . N. 2, (1991). , 271-283.

Chapter 16

Experimental Study of Fiber Laser Cavity Losses to Generate a Dual-Wavelength Laser Using a Sagnac Loop Mirror Based on High Birefringence Fiber

Manuel Durán-Sánchez, R. Iván Álvarez-Tamayo,
Evgeny A. Kuzin, Baldemar Ibarra-Escamilla,
Andrés González-García and Olivier Pottiez

Additional information is available at the end of the chapter

http://dx.doi.org/10.5772/54330

1. Introduction

Dual wavelength fiber lasers (DWFL) research has increased considerably in recent years due to the potential applications of these optical devices in diverse investigation areas. Interest of use of DWFL includes areas such as fiber sensors, wavelength division multiplexing, optical communications systems, optical instrumentation and recently in microwaves generation [1-4], among others.

DWFL are considered profitable optical sources because of their advantages such as low cost, easy and affordable optical structures, low losses insertion and space optimization. Principal issue to generate two simultaneous laser lines resides in the cavity losses adjustment. In DWFL designed with Erbium-doped fiber (EDF) as a gain medium there is a strong competition between the generated laser lines due to the EDF's homogeneous gain medium behavior at room temperature. To reduce the competition between the wavelengths, several techniques have been reported aiming to achieve stable multi-wavelength laser oscillations [5-8].

Moreover, fiber Bragg gratings (FBG) have been extensively used in DWFL cavities design due to their advantages as optical devices including easy manufacture, fiber compatibility, low cost and wavelength selection among others. FBG's wavelength selection property is commonly used as a narrow band reflector inside the laser cavity to generate a laser line at a specific wavelength. Several DWFL experimental setups using FBG's have been reported including use of a FBG written in a high birefringence or in a multimode fiber [6-11].

In a large majority of DWFL using EDF and FBG's, the laser cavity losses correspond to different generated laser lines at a specific wavelength position over the gain medium spectrum. The generated wavelength should be balanced to achieve two simultaneous laser lines. Consequently, both oscillation lines have the same pump threshold. Commonly the wavelengths adjustment is realized through arbitrary methods as use of polarization controllers (PC) and variable optical attenuators (VOA) [7, 12, 13]. With the progress on DWFL research studies have been followed two different pathways in order to enhance stability of the simultaneously generated laser lines by improving the cavity losses adjustment methods.

On the one hand, the research focuses on incorporating of cutting-edge devices in an effort to obtain more stable and efficient dual laser emissions. In such a way that these researching works reports the use of newly developed optical fibers such as photonic crystal fibers, leading to use optical devices that allow the exploit of nonlinear optics [14-16]. Most of the reported works on this area tend to have more complex designs and non-straightforward settings. By the other hand, a second pathway is in function of simplicity and optimization of laser cavity length, taking into account that a reduced cavity length implies a decrease of laser modes within the cavity, allowing, in a first instance analysis, a dual laser emission with lower instability, a simple adjustment of the competition between laser lines with a substantial reduction of implementation space that can improve the results repeatability [17, 18].

In recent years, obtaining of dual-wavelength laser emission does not represent an advance by itself in DWFL progress because the increasing need to analyze the behavior of the competition between the generated laser lines obtained by the cavity losses adjustment methods. Using arbitrary methods like adjustment by polarization controllers and variable optical attenuators do not allow a behavioral analysis of the competition between generated wavelengths because these methods do not have a measurable physical variable to characterize the adjustment and difficultly can provide repeatability in results.

The spectral selectivity of the interferometer is caused by birefringence that has to be introduced to the loop. A lot of effort has been made to suggest and investigate a variety of FOLM designs. Ma et al. [20] demonstrated polarization independence of the Hi-Bi FOLM. Liu et al. [21] reported a study of an optical filter consisting of two concatenated Hi-Bi FOLMs. Lim et al. [22] analyzed the behavior of an FOLM with a fiber loop consisting of two Hi-Bi fibers connected in series. The transmittance spectrum of the FOLM presents a periodic behavior with maxima and minima depending on the Hi-Bi fiber length and birefringence. For dual-wavelength lasers, low contrast offers the advantage of smoother cavity loss adjustment for the generated wavelengths where the principal mechanism of the adjustment of the cavity loss is the shift of the wavelength of the reflection maxima of the FOLM. The wavelength shift is achieved by the change of the temperature of the Hi-Bi fiber. This method allows generating two wavelengths with a well-controlled ratio between their powers [19].

Moreover, the tuning of the laser generated wavelengths promises to be an advantage for DWFL microwave generation application making it possible through the tuning of separation between wavelengths. A simple method of wavelength tuning is related to the Bragg period modification of a FBG. Wavelength tunable DWFL were reported [16-19]. In most configurations the FBG's are used with Bragg wavelength shift by temperature change [23], compression or stretch [18, 24]. Most of the techniques reported before as a matter of fact realize an adjustment of the losses between the two wavelengths to achieve stable dual-wavelength generation. In spite of the numerous papers reporting dual-wavelength generation, to the best of our knowledge no investigations were reported on the relation between the losses for generated wavelengths that enables simultaneous dual-wavelength generation.

M. A. Mirza [25] in 2008 presented the theoretical and experimental analysis of the design of a Sagnac loop filter (SLF) with periodic output spectrum controlled by cascading a small birefringence loop (SBL) with a high birefringence loop (HBL) with a tuning of the amplitude and wavelength of the spectrum of the filter through mechanical rotation. In this work is mentioned that the proposed design may have potential application in the design of Erbium-doped fiber lasers for multiple wavelengths generation in the C band and also can be used as a tuning tool for competition between the generated laser lines.

H. B. Sun [26] published in 2010 a DWFL with wide tuning based on a Hi-Bi FOLM and the use of polarization controllers inside the loop for adjustment of the loss within the ring cavity proposed. The laser wavelength can be tuned flexibly within the range of 1525 nm to 1575 nm by adjusting the polarization controller. The separation between the two generated wavelengths is adjustable by changing the length of the Hi-Bi fiber of the FOLM loop. Also proves the modes stability of the two laser lines at room temperature with a variation of the peak output power of about 0.5 dB over 40 minutes of operation.

K. J. Zhou [27] in 2012 reported the use of an all-PM Sagnac loop periodic filter as a frequency selector in a Erbium-doped fiber ring laser. The laser with a 1 nm interval filter generates four simultaneous and stable wavelengths with equal frequency spacing to overcome the homogeneous broadening of Erbium-doped fiber as a gain medium at room temperature. Polarizer controllers are used inside the ring cavity to adjust the laser lines emissions. The experiment confirm that this kind of filter should be robust to environmental changes.

This chapter proposes the application of a Sagnac fiber optical loop mirror with a high-birefringence fiber on the loop (Hi-Bi FOLM) used as a spectral filter to adjust finely the laser cavity losses, reducing the competition between generated laser wavelengths by temperature variations on the FOLM fiber loop. This control allows characterizing the competition behavior with temperature variations to achieve a better adjustment to obtain dual-wavelength laser emission. The appropriate choice of the angles of both ends of the Hi-Bi fiber allows a reflection minimum between 0 and 0.9 without substantial wavelength shift. The reflection maximum is always equal to 1 [19].

In this chapter the application of an all-fiber Hi-Bi FOLM to balance the losses within a dual-wavelength fiber laser is presented. An analysis of the losses is performed by charactering the FBG's reflections over the transmission spectrum of the FOLM when the laser wavelengths are generated, allowing the study of the fine adjustment of the FOLM transmission spectrum wavelength shift by temperature variation in the Hi-Bi fiber loop of the FOLM necessary to achieve dual-wavelength laser emission.

2. Numerical analysis of Sagnac Hi-Bi FOLM for dual-wavelength laser application

Numerically analysis for variation of the transmission spectrum of a Hi-Bi FOLM with the twist of the fiber in the loop can be an important tool for dual-wavelength fiber lasers design. The Hi-Bi FOLM shown in Figure 1 consists of a fiber coupler with a coupling ratio of $\alpha/1-\alpha$, which is assumed to be independent of wavelength. The output ports (3 and 4) are fusion spliced to a Hi-Bi fiber with arbitrary angles between the axes of the Hi-Bi fiber and the axes of the coupler ports. The segments where the Hi-Bi fiber is spliced to the coupler ports are placed on rotation stages. The Hi-Bi fiber is placed on a thermoelectric cooler to shift the wavelength dependence of the filter transmission. A light beam with electric field E_i enters through port 1; the transmitted beam with electric field E_T exits from port 2.

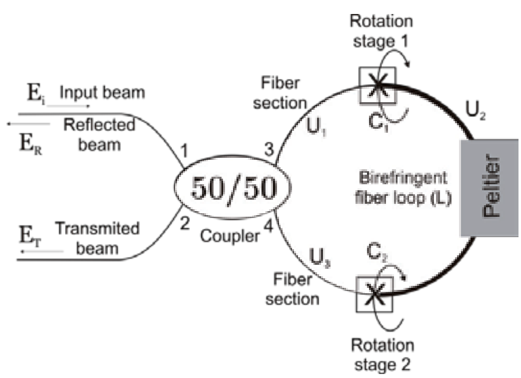

Figure 1. High birefringence fiber optical loop mirror

To calculate the transmission of the FOLM, we used the approach developed by Mortimore [28]. For a single input field E_i, a transmitted field E_T is given by:

$$E_T = \begin{pmatrix} E_{Tx} \\ E_{Ty} \end{pmatrix} = \begin{pmatrix} (2\alpha-1)J_{xx} & (1-\alpha)J_{xy}+\alpha J_{yx} \\ -\alpha J_{xy}-(1-\alpha)J_{yx} & (1-2\alpha)J_{xx} \end{pmatrix} \begin{pmatrix} E_{ix} \\ E_{iy} \end{pmatrix}, \tag{1}$$

where the J matrix is calculated as the product of matrices corresponding to all elements in the loop:

$$J = U_1 \cdot C_1 \cdot U_2 \cdot C_2 \cdot U_3, \tag{2}$$

where matrices U_1 and U_3 represent the coupler ports; the matrices C_1 and C_2 represent the coordinate rotation accounting for the angles between the axes of the Hi-Bi fiber and those of the coupler ports at the splices; finally, the matrix U_2 represents the Hi-Bi fiber. The analysis of the matrices that form the Jones matrix for the Hi-Bi FOLM is presented in detail in reference [19], where matrices U_1, U_2 and U_3 take into account linear birefringence of the fibers and the circular birefringence caused by the fiber twist angle. Matrices C_1 and C_2 transform the Jones vectors from the Cartesian system related with the axes of the port to that related with the axes of the Hi-Bi fiber.

Transmission spectrum of the Hi-Bi FOLM is a periodic function whose period is given by the following expression:

$$\Delta\lambda = \frac{\lambda^2}{B \cdot L}, \tag{3}$$

where B is the fiber loop birefringence, L the fiber loop length and λ the wavelength.

The values of the transmission minima are defined by the coupling ratio and are equal to, the transmission maxima however depends on the rotation of the rotational stages and can be adjusted in the range between $(2\alpha - 1)^2$ and 1 [29]. The adjustment of the values of the transmission maxima can be useful in particularly for dual wavelength laser application. However the rotation of the rotational stages also moves the wavelengths of the maxima and minima.

The numerical simulation for calculated transmission spectrum was performed. The coupler ports with a length of 0.5-m and a beat length of 6 m was used. The length of the Hi-Bi fiber is equal to 28 cm with a beat length of 3.6×10^{-3} m. The angles $\theta_1 = 0.5\pi$ and $\theta_2 = 0.3\pi$ were taken arbitrarily. To obtain the transmission maximum equal to 1 the angles ϕ_1 and ϕ_2 were adjusted with $\phi_2 = -0.8\pi$. Figure 2 shows transmission spectra for angle φ_1 variations in the range between 0 and 1.087π. Transmission maximum depends on the period $\phi_1 = 1.087\pi$. Here we can see than the adjustment of the transmission maximum by angle ϕ_1 variations also causes a wavelength shift of the transmission spectra that depends on the birefringence of the coupler ports.

Figure 3 shows the wavelength as the angle ϕ_1 is varied for different beat lengths of the coupler ports with the same simulation parameters. In a range of the angle ϕ_1 approximately between 0.2π and 0.8π the wavelength shift is less than 1 nm. The wavelength shift is more pronounced for larger birefringence of the coupler ports.

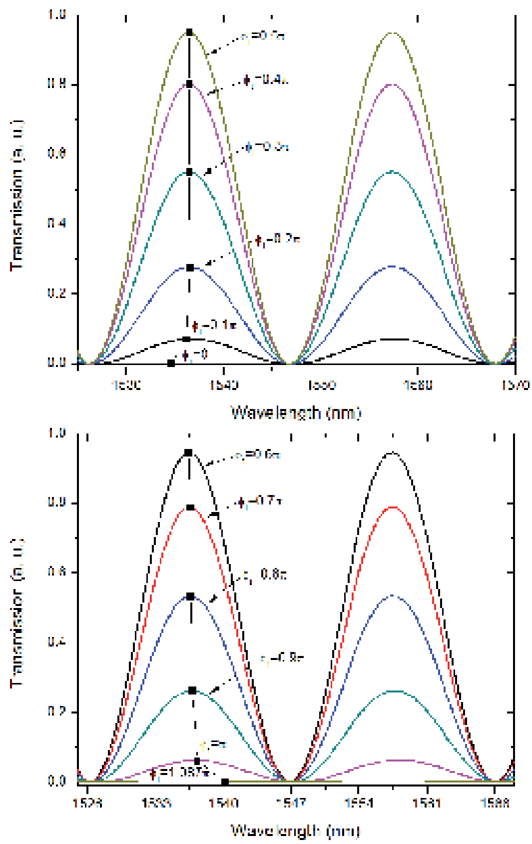

Figure 2. FOLM transmission spectra as a function of angle ϕ_1 with fixed ϕ_2.

The Hi-Bi FOLM transmission spectra amplitude adjustment causes a shift of the maximum/minimum in the reflection spectrum that is undesirable for dual-wavelength laser applications. However, the appropriate choice of the angles of both ends of the Hi-Bi fiber allows a reflection minimum between 0 and 0.9 without substantial wavelength shift. The twist of the fiber offers a simple way to change the ratio between the reflection maximum and minimum that provides a useful and simple method for the FOLM contrast adjustment.

3. Sagnac Hi-Bi FOLM charactization for dual-wavelength laser application

For the experimental investigation we introduce the basic experimental setup used. The all-fiber Fabry-Perot cavity laser is limited at one end by two Bragg gratings and at the opposite end by a Hi-Bi FOLM. Figure 4 shows the configuration where the laser gain medium is EDF with a length of 10-m. The two FBGs at one end of the cavity have 55.4% of maximum reflection at 1547.94 nm and 1546.96 nm to 59.75% respectively. The optical attenuator (OA) is achieved through the introduction of bend loss between the FBG's in a fiber section wounded approximately 6 turns in a circular piece with a 5-cm diameter. The adjustment of the turns was experimentally obtained at a point where both wavelengths (corresponding to FBG1 and FBG2 maxima) compete for the gain of the active medium. With this method we are roughly adjusting the losses within the cavity. The fine cavity loss adjustment is achieved by the FOLM formed by a 3dB optical coupler (Coupler 2) with the output ports interconnected through a high birefringence fiber with 28-cm length.

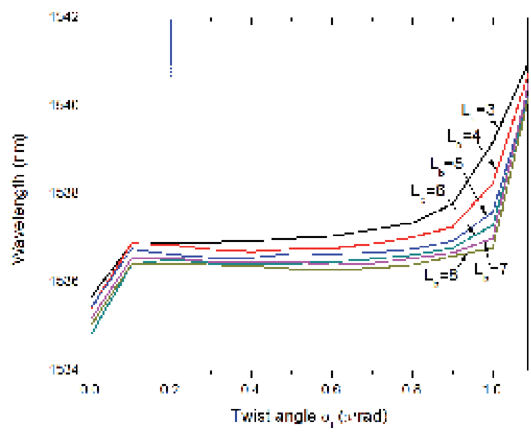

Figure 3. Dependence of the wavelength shift of the transmission maximum on the angle ϕ_1 for different beat lengths L_b.

The EDF is pumped by a 50-mW laser diode at 980-nm through a 980/1550 wavelength division multiplexer (WDM). Coupler 1 is a 90/10 coupling ratio optical coupler used to measure the 10% laser output at Output B, detecting only reflected wavelengths from FBG1 and FBG2. The output signal is launched to a 0.2-nm resolution monochromator, detected by a photodetector and monitored by an oscilloscope. Output A is used to measure the FOLM transmission spectrum at low pump power (below the threshold). Both laser wavelengths and ASE can be detected at this output.

The splices were placed into rotation stages to adjust the transmission of the FOLM. The Hi-Bi fiber temperature is controlled by temperature controller with a precision of 0.1 °C for the purpose of tuning the wavelength of the transmission spectra. The Hi-Bi fiber loop is placed on a thermoelectric cooler (TEC) whose temperature can be adjusted in the range between room temperature (about 25 °C) and 9 °C.

Measure of Hi-Bi FOLM transmission at temperatures in a range between 9 and 20°C was performed. Figure 5 shows the Hi-Bi FOLM transmission for Hi-Bi fiber loop temperatures of 9 and 11°C measured at Output A for low pump power. As it can be seen the transmission curve is shifted towards longer wavelengths when the temperature is decreased however the period remains equal to 20.8-nm. The contrast adjustment by rotation angles twist is near to the maximal contrast.

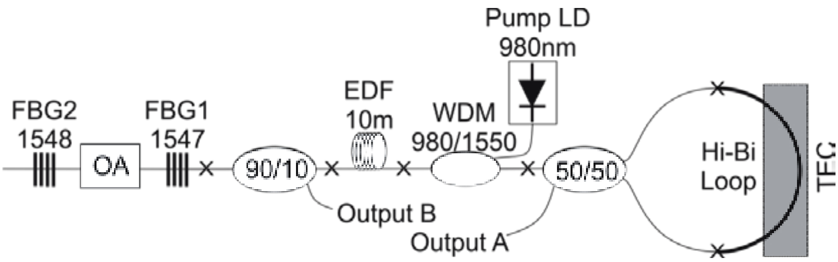

Figure 4. Experimental setup for the dual-wavelength fiber laser.

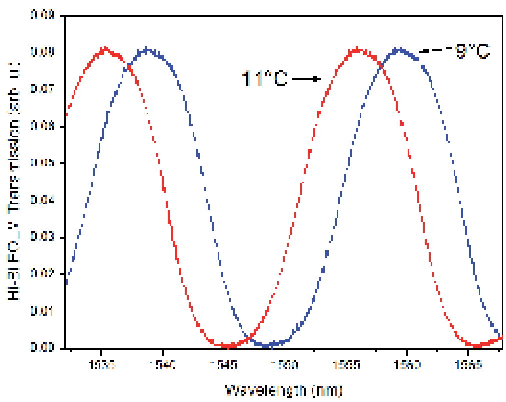

Figure 5. Hi-Bi FOLM transmission spectra wavelength shift by fiber loop temperature variation.

The wavelength dependence shift of the FOLM transmission on Hi-Bi fiber loop temperature is shown on Figure 6. The wavelength shift is well fitted by a linear dependence with a slope of -1.71 nm/°C shown with dashed line, which yields a temperature period equal to 13 °C.

Figure 7 shows output signal spectrum at the output A for the fiber Sagnac loop with a pump power of 25-mW, which is below the threshold for generating laser amplification. The measurement was performed with a temperature of 22.7 °C. Rotation angles adjustment is close to a minimum FOLM spectra output with ϕ_1=40^o (angle which we take as zero for rotation ϕ_1, we rotate 180° in ϕ_1 from this position of the rotator C_1) and ϕ_2=120^o reference to the axis of laboratory table. With fixed ϕ_2, rotation is performed in ϕ_1 with a 15° step.

http://dx.doi.org/10.5772/54330

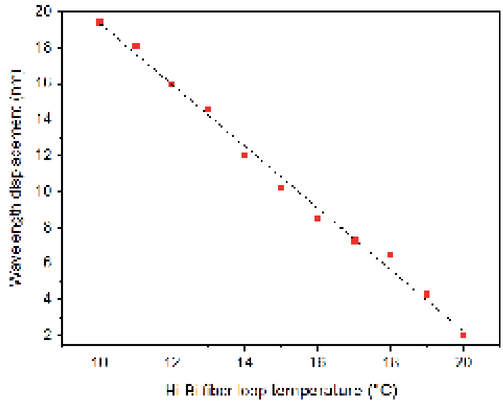

Figure 6. Wavelength displacement for Hi-Bi fiber loop temperature variations.

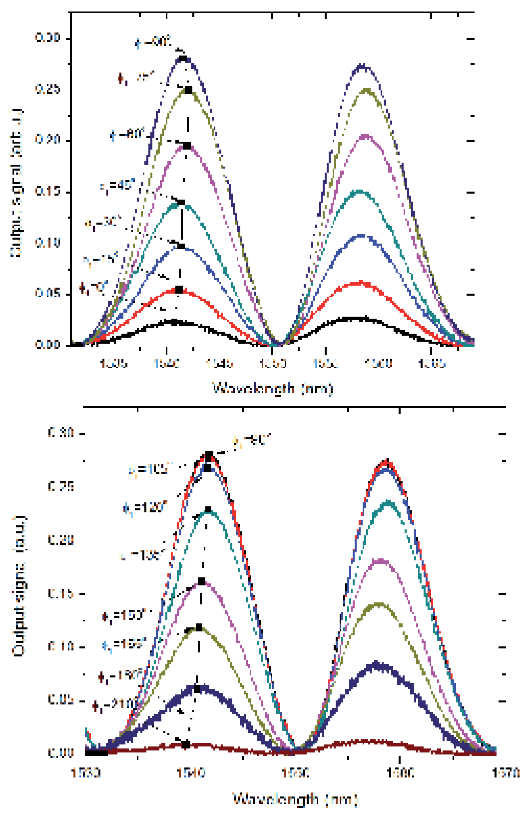

Figure 7. Spectrum at the FOLM output for different angles ϕ_1 with fixed ϕ_2.

The FOLM transmission presents periodic wavelength dependence with a period of 20.8 nm. It can be seen that the position of the maximum is shifted when the angle ϕ_1 is changed. The maximum is connected by a solid line in Figure 7. However, the period remains the same.

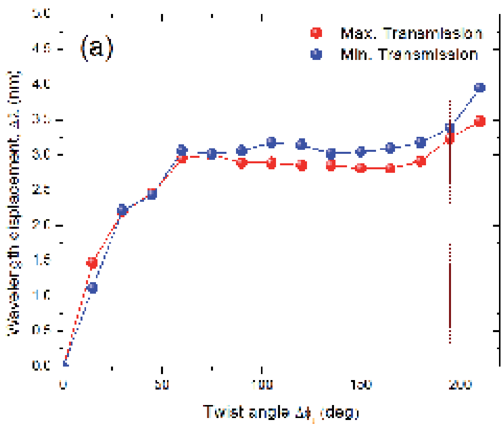

Figure 8. Dependence of wavelength shift of the transmission maximum and minimum on the angle ϕ_1 with ϕ_2=55°.

Figure 8 shows the wavelength shift of the maximum and the minimum of transmission due to the variation of the ϕ_1 angle for an angle ϕ_2 adjustment to 55°. The angle ϕ_1 was referred as 0 in the same manner as for Figure 7. The experimental dependences show a behavior similar to that obtained in simulations in Figure 3. It can be seen that there exists a range of the angle from about 60° to 180° where the dependence of the wavelength shift is almost flat with variations of less than 0.5-nm (corresponding to only a few percent of the transmission period).

The FOLM is used to adjust the loss of the cavity for wavelengths λ_1 and λ_2 corresponding to the FBG1 and FBG2 to obtain dual-wavelength operation. The application of the FOLM for dual-wavelength lasers was reported for the first time in Ref. [30].

4. Dual-wavelength fiber laser cavity loss fine adjustment by Sagnac Hi-Bi FOLM

Figure 8 presents the laser spectrum for different temperatures of the Hi-Bi fiber with the experimental setup shown in Figure 4. Laser output is measured in Output B for a pump power of 50-mW. The temperature of the Hi-Bi fiber was chosen to have a maximum of reflection of the FOLM close to the wavelengths of maximal reflection of the FBG's. Rotation stages fiber twist is set near to the 70% of FOLM transmission spectrum amplitude contrast.

A change of the temperature moves the maxima of FOLM transmission and so changes the ratio between the reflections for λ_1 and λ_2.

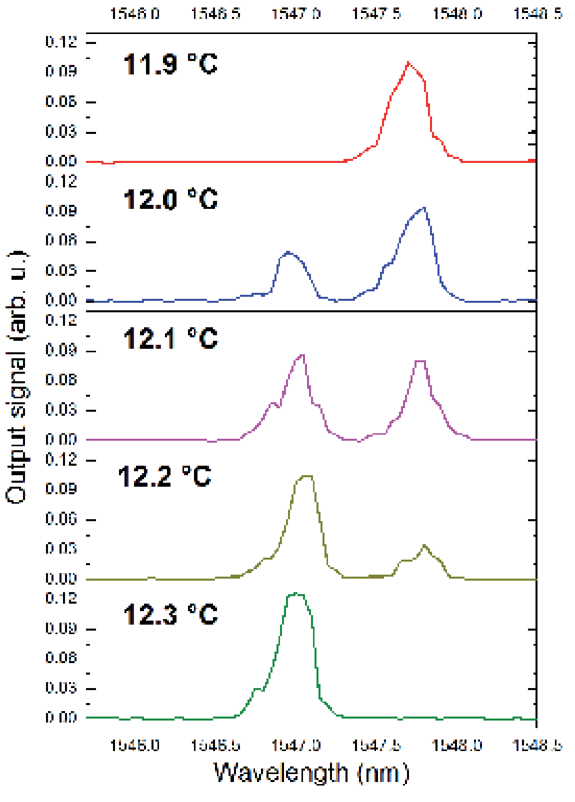

Figure 9. Measured output laser spectra for different Hi-Bi FOLM fiber loop temperatures.

As can be seen at the temperature of 12.0 °C two peaks are still observed however the amplitude of the peak with shorter wavelength is less than that of the peak with longer wavelength. At the temperature of 12.1 °C two peaks with equal amplitudes were observed. The increase of temperature to 12.2 °C results in a lower amplitude of the peak with longer wavelength. Finally for the temperature shift larger than 0.2 °C only one wavelength is generated by the laser, the shorter wavelength at 12.3 °C and for the longer wavelength at 11.9 °C.

Here we show the usefulness of the adjustment of the values of the reflection maxima by tuning the angles of the rotation stages. Figure 10a shows the laser transmission spectra obtained with the FOLM at high contrast between maxima and minima of reflection, while Figure 10b shows the results obtained with low contrast with the change of contrast achieved through a rotation of the rotational stages. In the results with lower contrast (Figure 10b) the dependence of the reflection on the temperature is slower, then, the range of temperatures over which dual-wavelength generation is observed is larger than in Figure 10a, providing higher tolerance with respect to the temperature stability. In figure 10a the FOLM spectrum was adjusted to have the highest contrast between the reflection maximum and minimum with ϕ_1=120°. In figure 10b results, the FOLM spectrum was adjusted to have a low contrast with ϕ_1=30°.

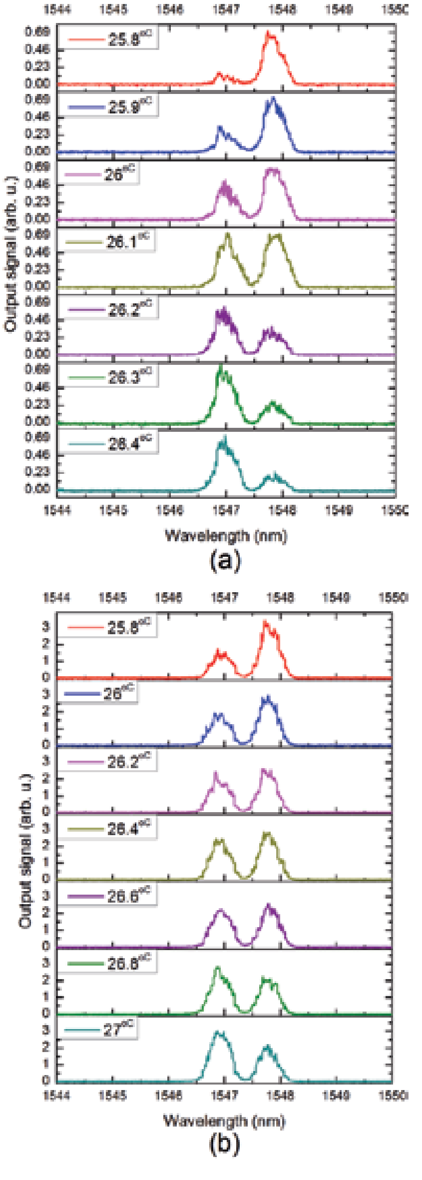

Figure 10. Laser output spectra at different temperatures with different contrasts.

Figure 11 shows the measured power of the two laser lines for the same FOLM adjustment as for Figures 10a and 10b for the maximal transmission amplitude point. Insets in the figures show reflection of the FOLM used for each measurement. We can see that the temperature tolerance of the dual-wavelength operation for the case shown in Figure 11b is much higher than the temperature tolerance for the case shown in Fig. 11a.

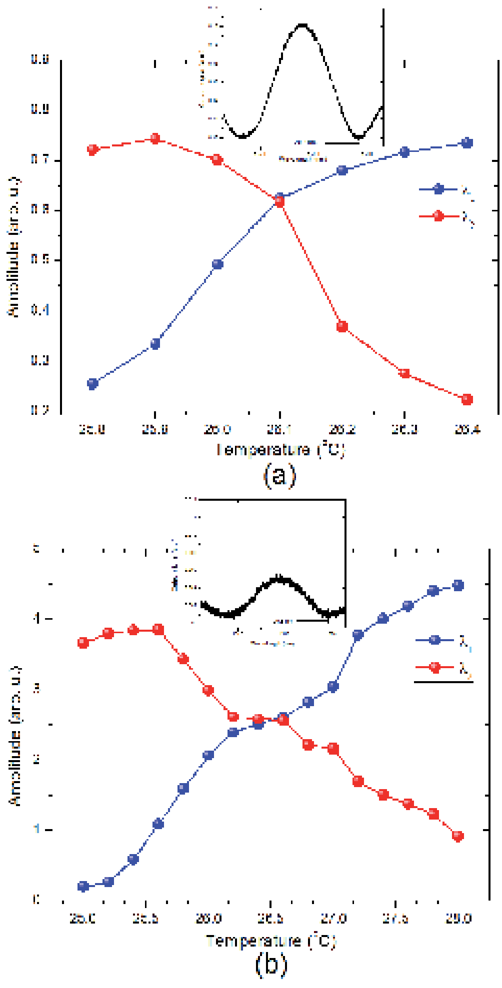

Figure 11. Power at wavelengths λ_1 and λ_2. (a) Highest contrast between reflection maxima and minima, (b) low contrast between reflection maxima and minima.

For dual-wavelength lasers, low contrast offers the advantage of smoother cavity loss adjustment for the generated wavelengths where the principal mechanism of the adjustment of the cavity loss is the shift of the wavelength of the reflection maxima of the FOLM. The wavelength shift is achieved by the change of the temperature of the Hi-Bi fiber. This method allows generating two wavelengths with a well-controlled ratio between their powers.

5. Tunable dual-wavelength fiber laser with Sagnac Hi-Bi FOLM and a polarization-maintaining FBG

Here, experimentally operation of a linear cavity dual-wavelength fiber laser using a polarization maintaining fiber Bragg grating (PM-FBG) is presented. PM-FBG is used as an end mirror that defines two closely spaced laser emission lines and it is also used to tune the laser wavelengths. The total tuning range is around 8 nm. The laser operates in a stable dual-wavelength mode for an appropriate adjustment of the cavity losses for the generated wavelengths. The high birefringence (Hi-Bi) fiber optical loop mirror (FOLM) is used as a tunable spectral filter to adjust the losses as can be seen before in topics 3 and 4 [31].

The experimental setup used is similar to in figure 4 and it can be seen in figure 12. The linear laser cavity is formed by the Hi-Bi FOLM analyzed before and a PM-FBG mounted in a mechanical device allowing compression/stretch and a polarization controller (PC). The PM-FBG spectrum presents two peaks with separation of 0.3-nm centered at 1549 nm. Both peaks have 99.5% maximum reflection. The 90/10 coupler is used as the laser output (Output A). The output radiation was launched to a monochromator with 0.1-nm of resolution, detected by a photodetector and monitored by an oscilloscope. Output B is used to monitor FOLM transmission spectra.

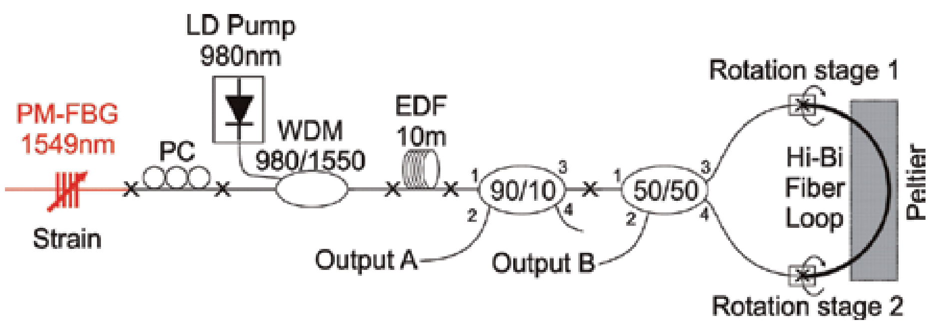

Figure 12. Tunable dual-wavelength fiber laser with PM-FBG experimental setup.

The laser cavity is set to have the transmission minimum at approximately 1549 nm where the PM-FBG reflection is centered by temperature variations of the Hi-Bi FOLM fiber loop.

Figure 13 shows the reflection spectrum of the PM-FBG and ASE at Output B for a pump power near the laser threshold (around 25-mW) and a temperature of 24.5 °C. No strain is applied to the PM-FBG then, PM-FBG reflection peak is centered at 1549 nm.

Figure 13a shows the FOLM transmission spectrum for a high contrast between minima and maxima of reflection. Figure 13b shows the FOLM transmission spectrum for a low contrast adjustment. The low contrast adjustment allows a smoother change of the FOLM reflection with temperature such that this is the adjustment of contrast used in measurements of the generation of laser lines.

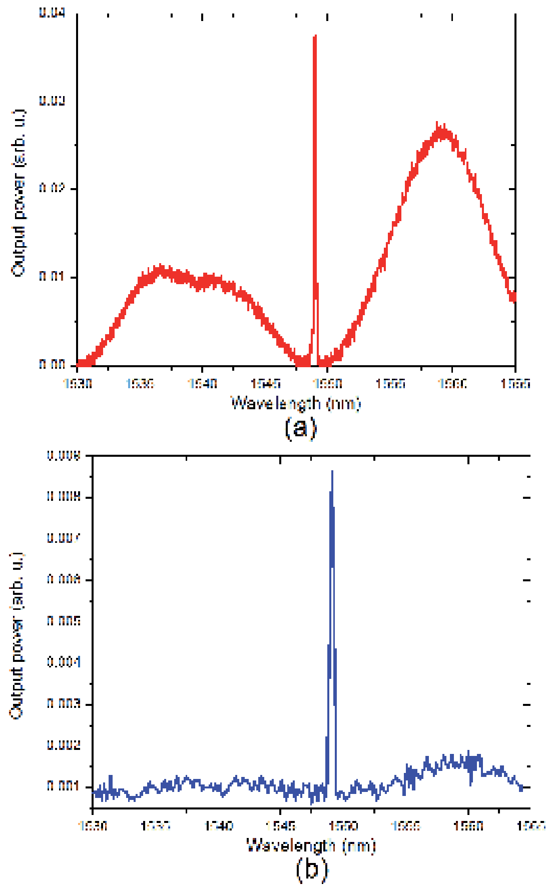

Figure 13. Measured Hi-Bi FOLM transmission spectra at Output B. (a) High contrast adjustment. (b) Low contrast adjustment.

For dual-wavelength generated laser lines measurement, both laser lines at 1548.86 and 1549.18 nm are monitored at Output A. Adjust of PC allows to obtain stable dual wavelength generation. However the compression/stretch of the PM-FBG causes the loss of the dual wavelength generation and further adjustment of the PC is required. The adjustment of the PC however is not a straightforward procedure. An adjustment of the temperature of the Hi-Bi fiber in the FOLM was performed then. Figure 14 shows the shift of the two wavelengths for different values of compression/stretch applied to the PM-FBG. Micrometer screw positions are shown in the graphics; negative values are assigned to the compression, positive to the stretch.

The resolution of the monochromator was not sufficient to measure the bandwidth of lines. To be sure that we have two well separated laser lines we monitored the output also with a scanning Fabry–Perot.

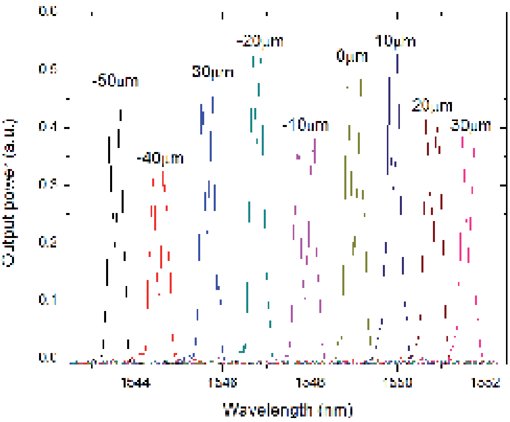

Figure 14. Fiber laser spectra at the compressed/stretched PM-FBG.

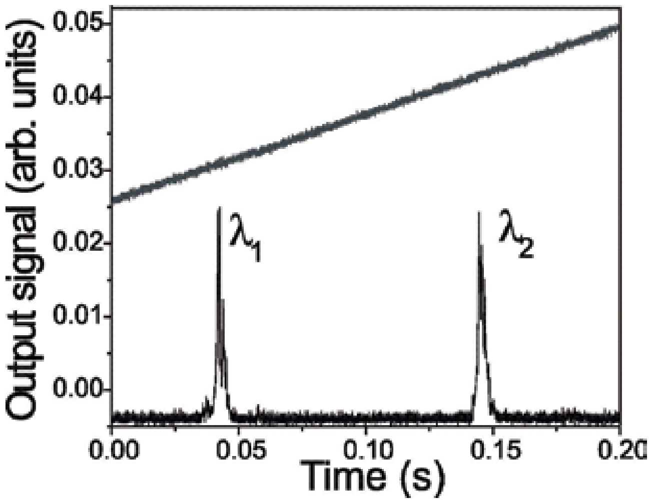

Figure 15. Output signal from the Fabry-Perot scanning with no strain applied to the PM-FBG.

Figure 15 shows the oscilloscope trace of the signal at the FP output with no strain applied to the PM-FBG. As can be seen there are two well separated lines with separation of 0.34 nm. The free space of FP shown in the inset is equal to 0.6 nm. The total power inside the cavity is about 1-mW and was measured at the output A through a photodetector and an optical power meter.

Axial compression or stretch was applied by using a micrometric screw mechanical system. The maximum compression applied was 50 μm causing a maximum wavelength displacement of 5.5 nm. The corresponding wavelengths shift rate is about 1.1 nm/10 μm. The maxi-

http://dx.doi.org/10.5772/54330

mum stretch was 30 μm, causing a wavelength shift of about 2.58 nm, which corresponds to a rate of 0.86 nm/10 μm. The total laser wavelength shift is 8.09 nm with average rate of 1 nm/10 μm approximately. For each compression/stretch of the PM-FBG we adjusted the temperature of the Hi-Bi fiber to obtain dual-wavelength generation.

Figure 16 shows the temperature required for dual-wavelength generation. As one see the dependence is well fitted linearly with a slope of –1.39 nm/°C so the adjustment procedure is very simple and straightforward.

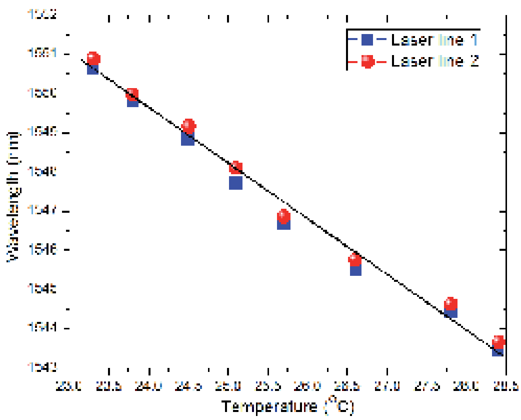

Figure 16. Required Hi-Bi FOLM temperature for dual-wavelength laser operation at stretched/compressed PM-FBG.

This method allows to estimate a reflection change for shorter and longer wavelengths of the PM-FBG under compression/stretch. Figure 17 shows the FOLM minimum transmission wavelength and the central wavelength of the dual line laser. If the wavelength of the FOLM minimum transmission coincides with the central wavelength of the laser, the reflection of the FOLM is equal for both wavelengths. We observe this for compression/stretch around 0.

To have dual wavelength generation under compression or stretch the minimum of the FOLM transmission (corresponding to maximum reflection) has to be displaced to shorter wavelength with respect to the central lasing wavelength, which means that the FOLM reflection for the shorter wavelength line is slightly higher than the reflection for the longer wavelength.

From this we can conclude that the reflection of the PM-FBG for shorter wavelength line became slightly smaller at compression/stretch than for the longer wavelength line.

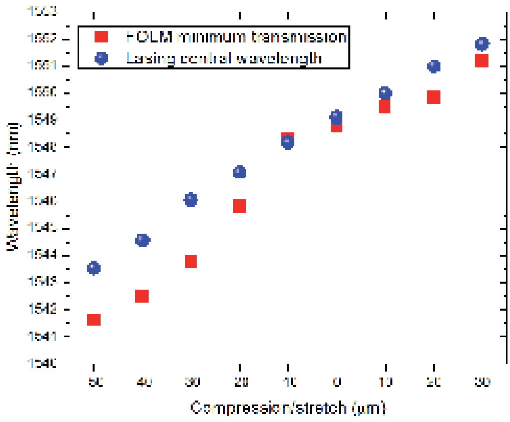

Figure 17. Wavelengths of the FOLM minimum transmission and lasing central wavelengths at the stretched/ compressed PM-FBG.

6. Conclusions

In the first part we present numerical and experimental analysis of a high birefringence fiber optical loop mirror (Hi-Bi FOLM) to use in lasers with dual wavelength. The adjustment in the amplitude spectrum because of the reflectivity was considered as a tool for the dual wavelength laser stability. This is accomplished by adjusting the angles in one of the ports of the FOLM where we in which we may have a minimum and maximum of reflectivity the laser cavity. Also that we can select the best performing region in terms of period, amplitude spectrum of the FOLM and by temperature we can shift the wavelength in the FOLM and equalize the two wavelengths required to generate a laser with dual wavelength emission.

In the second part we propose to apply the FOLM to generate a laser with dual wavelength emission. We propose and demonstrate experimentally a laser with dual wavelength and stable, we can make the laser having laser emission at single or dual wavelength by adjusting the temperature in the loop FOLM and we demonstrate how to improve the stability of the laser by adjusting the amplitude using the optical fiber twisters in the FOLM.

In the third part we explain the implementation of the FOLM to generate tunable dual wavelength using a polarizer maintaining fiber Bragg grating (PM-FBG). We propose and demonstrate experimentally a tunable wavelength laser. The tuning range was 8.06-nm; this tuning was achieved by stretching and compressing the PM-FBG. For each tuning was only necessary to adjust the temperature in the FOLM. As a result of this application of the FOLM to generate a dual wavelength laser, we present two simple configurations that can be used for future applications.

http://dx.doi.org/10.5772/54330

Acknowledgements

This work is supported by CONACYT grant 151434.

Author details

Manuel Durán-Sánchez[1], R. Iván Álvarez-Tamayo[2], Evgeny A. Kuzin[3], Baldemar Ibarra-Escamilla[3], Andrés González-García[3] and Olivier Pottiez[4]

1 Mecatrónica, Universidad Tecnológica de Puebla (UTP), Puebla, México

2 Facultad de ciencias físico-matemáticas Benemérita Universidad, Autónoma de Puebla (BUAP), Puebla, México

3 Departamento de Óptica, Instituto Nacional de Astrofísica, Óptica y Electrónica (INAOE), Puebla, México

4 Departamento de Fibras Ópticas, Centro de Investigaciones, en Óptica (CIO), León, Guanajuato, México

References

[1] Talaverano L., Abad S., Jarabo S., and Lopez-Amo M. Multiwavelength fiber laser souces with Bragg-grating sensor multiplexing capability. J. Lightwave Technology 2001; 19(4) 553-558.

[2] Liu D., Ngo N. Q., Tjin S. C., and Dong X. A dual-wavelength fiber laser sensor system for measurement of temperature and strain. IEEE Photonics Technology Letters 2007; 19(5) 1148-1150.

[3] Mao Q., and Lit J. W. Y. Switchable multiwavelength Erbium-doped fiber laser with cascaded fiber grating cavities. IEEE Photonics Technology Letters 2002; 14(5) 612-614.

[4] Zhang H., Liu B., Luo J., Sun J., Ma X., Jia C., Wang S. Photonic generation of microwave signal using a dual-wavelength single-longitudinal-mode distributed Bragg reflector fiber laser. Optics Communications 2009; 282(20) 4114-4118.

[5] Liu Z., Liu Y., Du J., Yuan S., Dong X. Switchable triple-wavelength Erbium-doped fiber laser using a single fiber Bragg grating in polarization-maintaining fiber. Optics Communications 2007; 279 168-172.

[6] Latif A. A., Ahmad H., Awang N. A., Zulkifli M. Z., Pua C. H., Ghani Z. A., Harun S. W. Tunable high power fiber laser using AWG as the tuning element. Laser Physics 2011; 21(4) 712-717.

[7] Han. Y., Lee J. H. Switchable dual wavelength Erbium-doped fiber laser at room temperature. Microwave and Optical Technology Letters 2007; 49(6) 1433-1435.

[8] Ahmad H., Zulkifli M. Z., Norizan S. F., Latif A. A., Harun S. W. Controllable wavelength channels for multiwavelength Brillouin Bismuth/Erbium based fiber laser. Progress in Electromagnetics Research Letters 2009; 9 9-18.

[9] Ahmad H., Sulkifli M. Z., Thambiratnam K., Latif A. A., Harun S. W. Switchable semiconductor optical fiber laser incorporating AWG and broadband FBG with high SMSR. Laser Physics Letters 2009; 6(7) 539-543.

[10] Feng S., Xu, O., Lu S., Mao X., Ning T., Jian S. Switchable dual-wavelength Erbium-doped fiber-ring laser based on one polarization maintaining fiber Bragg grating in a Sagnac loop interferometer. Optics and Laser Technology 2009; 41 264-267.

[11] Ahmad H., Zulkifli M. Z., Thambiratnam K., Latif A. A., Harun S. W. High power and compact switchable Bismuth based multiwavelength fiber laser. Laser Physics Letters 2009; 6(5) 380-383.

[12] Liu D., Ngo N. Q., Chan H. N., Teu C. K., Tjin S. C. A switchable triple –wavelength Erbium-doped fiber laser with a linear laser cavity. Microwave and Optical Technology Letters 2006; 48(4) 632-635.

[13] Feng S., Xu O., Lu S., Ning T., Jian S. Switchable multi-wavelength Erbium-doped fiber laser based on cascaded polarization maintaining fiber Bragg gratings in a Sagnac loop interferometer. Optics Communication 2008; 281 6006-6010.

[14] El-Tasher A. E., Alcon-Camas M., Babin S. A., Harper P., Ania-Castañon J. D., Turitsyn S. K. Dual-wavelength, ultralong Raman laser with Rayleigth-scattering feedback. Optics Letters 2010; 35(7) 1100-1102.

[15] Parvizi R., Harun S. W., Ali N. M., Shahabuddin S., Ahmad H. Photonic crystal fiber-based multiwavelength Brillouin fiber laser with dual-pass amplification configuration. Chinese Optics Letters 2011. 9 021403.

[16] Im J. E., Kim B. K., Chung Y. Tunable single and dual-wavelength Erbium-doped fiber laser based on Sagnac filter with a high-birefringence photonic crystal fiber.

[17] Liu D., Ngo N. Q., Liu H., Liu D. Microwave generation using an all polarization-maintaining linear cavity dual-wavelength fiber laser with tunable wavelength spacing. Optics Communications 2009; 282 1611-1614

[18] Moore P. J., Chaboyer Z. J., Das G. Tunable dual-wavelength fiber laser. Optical Fiber Technology 2009; 15 377-379.

[19] Alvarez-Tamayo R. I., Duran-Sanchez M., Pottiez O., Kuzin E. A., Ibarra-Escamilla B., Flores-Rosas A. Theoretical and experimental analysis of tunable Sagnac high-bi-

refringence loop filter for dual-wavelength laser application. Applied Optics 2011; 50(3) 253-260.

[20] Ma X., Kai G., and Wu Z. Study of polarization independence for high birefringence fiber Sagnac interferometers. Microwave Optical Technology Letters 2005; 46 183–185.

[21] Liu L., Zhao Q., Zhou G., Zhang H., S Chen., Zhao L., Yao Y., Guo P., Dong X. Study on an optical filter constituted by concatenated Hi-Bi fiber loop mirrors. Microwave Optical Technology Letters 2004; 43 23–26.

[22] Lim K. S., Pua C. H.,N. Awang A., Harun S.W., Ahmad H. Fiber loop mirror filter with two-stage high birefringence fibers. Progress in Electromagnetics Resarch C 2009; 9 101–108.

[23] Li S., Ngo N. Q., Tjin S. C., Binh L. N. Tunable and switchable optical bandpass filters using a single linearly chirped fiber Bragg grating. Optics Communication. 239 (2004) 339-344.

[24] Moon D. S., Sun G., Lin A., Liu X., Chung Y. Tunable dual-wavelength fiber laser based on a single fiber Bragg grating in a Sagnac loop interferometer. Optics Communications 2008; 281 2513-2516.

[25] Mirza M. A., Stewart G. Theory and design of a simple tunable Sagnac loop filter for multiwavelength fiber lasers. Applied Optics 2008; 47 5242–5252.

[26] Sun H. B., Liu X. M., Gong Y. K., Li X. H., Wang R. Broadly tunable Dual-Wavelength Erbium-Doped Ring Fiber Laser Based on a High-birefringence Fiber Loop Mirror. Laser Physics 2010; 20(2) 522-527.

[27] Zhou K. J., Ruan Y. F. Fiber ring laser employing an all-polarization-maintaining loop periodic filter. Laser Physics 2012; 20(6) 1449-1452.

[28] Mortimore D. B. Fiber loop reflectors. J. Lightwave Technology 1988; 6(7) 1217–1224.

[29] Kuzin E.A., Cerecedo-Nuñez H., Korneev N. Alignment of a birefringent fiber Sagnac interferometer by fiber twist. Optics Communications 1999; 160 37-41 (1999)

[30] Durán-Sánchez M., Flores-Rosas A., Alvarez-Tamayo R. I., Kuzin E. A., Pottiez O., Bello-Jimenez M., Ibarra- Escamilla B. Fine adjustment of cavity loss by Sagnac loop for a dual wavelength generation. Laser Physics 2010; 20(5) 1270–1273.

[31] Alvarez-Tamayo R. I., Durán-Sánchez M., Pottiez O., Kuzin E. A., Ibarra-Escamilla B. Tunable Dual-Wavelength Fiber Laser Based on a Polarization-Maintaining Fiber Bragg Grating and a Hi-Bi Fiber Optical Loop Mirror. Laser Physics 2011; 21(11) 1932-1935.

Chapter 17

Multi-Wavelength Fiber Lasers

Rosa Ana Perez-Herrera and Manuel Lopez-Amo

Additional information is available at the end of the chapter

http://dx.doi.org/10.5772/53398

1. Introduction

A fiber amplifier can be converted into a laser by placing it inside a cavity designed to provide optical feedback. Such lasers are called fiber lasers. In this kind of lasers there are optical fibers that act as gain media such as erbium or ytterbium doped fibers among other, although some lasers with a semiconductor gain medium and a fiber resonator have also been called fiber lasers.

Nowadays, multiwavelength lasers are of great interest for telecommunications and sensors multiplexing. These lasers also have a great potential in the fiber-optic test and measurement of WDM components. The requirements for such optical sources are: a high number of channels over large wavelength span, moderate output powers (of the order of 100μW per channel) with good optical signal to noise ratio (OSNR) and spectral flatness, single longitudinal mode operation of each laser line, tunability and accurate positioning on the ITU frequency grid. Reaching all these requirements simultaneously is a difficult task, and many different approaches using semiconductor or erbium-doped fiber technology have been proposed and experimented in order to obtain multiwavelength laser oscillation.

Fiber lasers also offer great possibilities as multiwavelength sources. Their ease of fabrication has yielded many ingenious designs. The main challenge in producing a multiline output with and erbium doped fiber laser (EDFL) is the fact that the erbium ion saturates mostly homogeneously at room temperature, preventing stable multiwavelength operation.

Single longitudinal mode operation of fiber lasers is desirable for many potential applications where coherence is necessary. These include coherent communications, interferometric fiber sensors and coherent light techniques in bulk or micro-optics, such as holography or spatial filtering. [1]. However, these lasers normally operate in multiple longitudinal modes because of a large gain bandwidth (>30 nm) and a relatively small longitudinal-mode spacing (< 100 MHz). The spectral bandwidth of laser output can exceed 10 nm under CW operation [2]. Many applications of continuous wave (CW) lasers require operation in a narrow-linewidth single mode whose wavelength can be tuned over the gain bandwidth. Numerous methods have been used to realize narrow-linewidth fiber lasers, however fiber Bragg gratings (FBGs) are preferred for this purpose since they can be fabricated with a reflectivity spectrum of less than 0.1 nm.

It is also worth noting that the large gain bandwidth of fiber lasers is useful for tuning them over a wavelength range exceeding 50 nm [2]. Several other methods have been used to achieve single longitudinal mode operation of fiber lasers and these include unidirectional ring resonators [3], intracavity wave-mixing in a saturable absorber [4], fiber Fox-Smith resonators [5] and injection locking using the line narrowed output form a separate source [6]. Nevertheless, no technique is free from operating difficulties due to the problems of isolating the fiber laser resonator from environmental influences, such as vibrations and temperature drift among other factors. Most of these problems can be addressed by using some clever schemes, as will be presented in this work.

2. Fiber lasers design

Fiber lasers can be designed with a variety of choices for the laser cavity [2]. One of the most common type of laser cavity is known as the Fabry-Perot cavity, which is made by placing the gain medium between two high-reflecting mirrors. In the case of fiber lasers, mirror often butt-coupled to the fiber ends to avoid diffraction losses.

Several alternatives exist to avoid passing the pump light through dielectric mirrors. For example, one can take advantage of fiber couplers. It is possible to design a fiber couple such that most of the pump power comes out of the port that is a part of the laser cavity. Such couplers are called wavelength-division-multiplexing (WDM) couplers. Another solution is to use fiber gratings as mirrors. As it is known, a FBG can acts as a high-reflectivity mirror for the laser wavelength while being transparent to pump radiation. The use of two such gratings results in an all-fiber Fabry-Perot cavity. An added advantage of Bragg gratings is that the laser can be forced to operate in a single longitudinal mode. A third approach makes use of fiber–loop mirrors that can be designed to reflect the laser light but transmit pump radiation.

Ring cavities are often used to force unidirectional operation of a laser. In the case of fiber lasers, an additional advantage is that a ring cavity can be made without using mirrors, resulting in an all-fiber cavity. In the simplest design, two ports of a WDM coupler are connected tighter to form a ring cavity containing the doped fiber, as shown in Figure 1.

An isolator is inserted within the loop for unidirectional operation. However, some alternative fiber laser configurations have been shown, where these kinds of devices can be suppressed from the cavity rings by using optical circulators [7]. Theoretically, a polarization controller is also needed for conventional doped fiber that does not preserve polarization. However, some works [7] have demonstrated that this device has little influence on the multiwavelength regime.

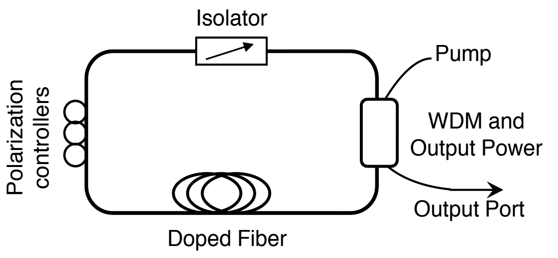

Figure 1. Schematic of a unidirectional ring cavity used for fiber lasers.

Ring fiber lasers are also known to be susceptible to power fluctuations. These instabilities can significantly degrade the characteristics of a sensor array based on a tunable ring laser interrogation scheme [8]. Although the laser output power stability usually depends on many parameters like the EDF lengths, the coupling ratio on the output and the total cavity length [9], [10]-[15], it can be improved through an appropriate choice of laser parameters.

For sensor applications, a tunable narrow-band laser source is very attractive since it significantly simplifies the detection scheme. However, the interaction of laser relaxation oscillations with external perturbations induces self-pulsation and output power variations. In addition, the long coherence length of the radiation emitted by a single-mode laser may result in Fabry-Perot type unwanted interference within the sensing arm. In a few-mode regime, mode-hopping results in power fluctuations. To avoid these fluctuations the laser must operate in a many-mode regime, in which the power carried by each mode is sufficiently small. Specifically, the spacing between longitudinal modes is defined by the length of the cavity which is usually a few tens of meters. The number of modes (N) and modes spacing ($\Delta\lambda$) in a fiber ring laser are given by:

$$\Delta\lambda = \frac{\lambda^2}{nL} \tag{1}$$

$$N = \frac{nL}{\lambda} \tag{2}$$

where n: is the refractive index of the Er fiber, L: the ring length, and λ: the centered mode wavelength.

Some experimental studies have been carried out with the purpose of enabling an erbium doped fiber ring laser (EDFRL) design to be optimized, by using highly Er-doped fiber instead of conventional one [16], in order to meet the required performance by analyzing several configurations. In that way, the optimal EDF length [17] required to generate both the highest possible gain for a given signal and output power oscillations as low as possible under certain constraints can be found.

Thus, several EDFL hybrid cavity configurations, combining both EDFR and short cavity fiber laser, have been designed and experimentally analyzed [18], [19]. Figure 2 shows the experimental setup of a short-cavity fiber laser. These studies were focused on the optimization of laser parameters, which include EDF lengths, pump power and diverse configurations, without changing the basic scheme, which was kept as simple as possible.

Figure 2. Experimental setup of a short-cavity fiber laser

Regarding to the spectral characterization of these kind of EDFLs, Figure 3 shows the exit amplified spontaneous emission (ASE) measured in the amplifier configuration, i.e., when the free end of the EDF was connected to an optical spectrum analyzer (OSA). It may be useful to note that the steady-state ASE spectra can be accurately simulated with the standard static model [20] based on the doped fiber parameters provided by the fiber manufacturer.

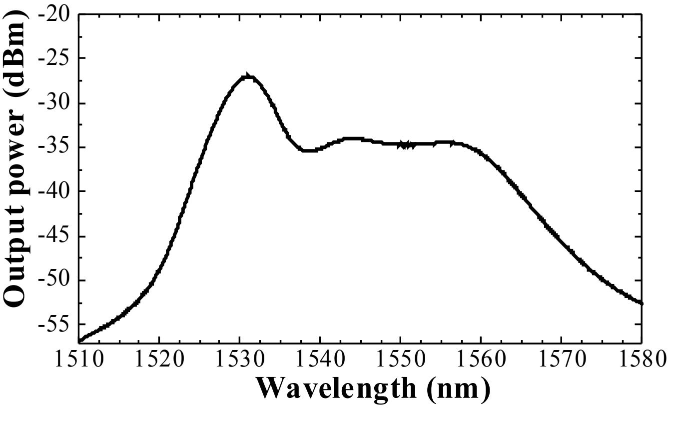

Figure 3. ASE obtained from a 1 m length of Er-80 when it is pumped by a 980nm light source.

http://dx.doi.org/10.5772/53398

Spectrally resolved measurements of the laser (i.e., closed cavity) output with different EDF lengths as the gain medium (and 500mW of input power) show a multiple-wavelength operation. The position of the comb depends on the fiber length. For a 25cm-long fiber, the generation occurs at shorter wavelengths values, while already for a 1m-long fiber the generation shifts to longer wavelengths (Figure 4). This shift is due to an increase of the effective fiber length when the cavity is closed and it corresponds to the L-band operation of an EDFA with an increased fiber length.

Frequency hopping to other longitudinal cavity modes is possible since neighboring modes may have a higher (unsaturated) gain. Usually, when no cavity filters are used, linear cavity lasers are less stable in power and frequency than ring cavity lasers. Ring cavity EDFLs use the gain provided by the EDF more efficiently and have a cavity free spectral range (FSR) that is twice as large for the same cavity length compared to linear cavity lasers [16].

On the other hand, the linear, or Fabry–Perot cavity, is the most common laser cavities, and the first EDFL cavity that was explored. Its main advantages are its simplicity and the possibility to make very short cavities. It is thus well suited for robust single longitudinal mode operation. They are also suitable for master oscillator power amplifier (MO-PA) [21] applications since it is usually easy to recover unabsorbed pump power at the output coupler.

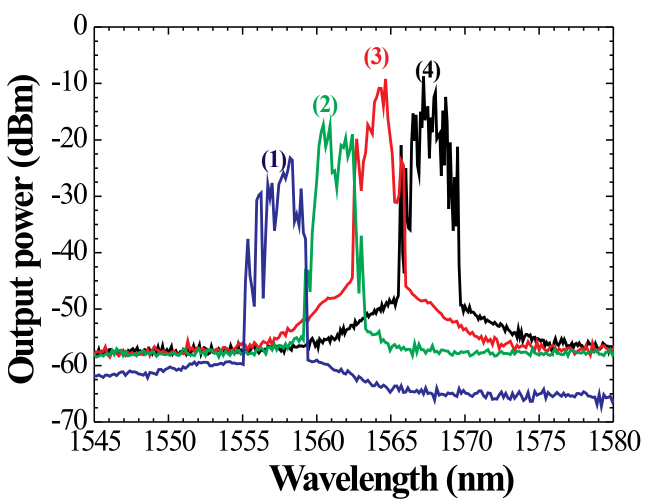

Figure 4. Output power spectra for closed cavity configuration with different EDF lengths. (1) 25, (2) 50, (3) 75 and (4) 100 cm length of the erbium-doped fiber. 500mW pump power.

An example of a linear cavity is presented in Figure 5. In a forward pumped linear cavity EDFL, the pump light is injected through a wavelength-dependent reflector (WDR) which is, ideally, perfectly transparent at the pump wavelength and perfectly reflective at the signal wavelength. The output coupler completes the linear cavity. It is preferable that the output coupler be highly reflective at the pump wavelength to recycle unused pump power thus providing optimized pumping and no residual pump at the output.

The output coupler must also have a reflectivity at the signal wavelength that optimizes the output power [22]. The output coupler reflectivity in the signal band can either be broadband, leading to a lasing wavelength determined by the erbium-doped fiber gain curve, or wavelength-selective, leading to a lasing wavelength selected, and possibly tuned, by the output coupler. Linear cavities are also ideal for compact single-longitudinal mode lasers and for high power applications.

Many other cavity designs are possible. For example, one can use two coupled Fabry-Perot cavities. In the simplest scheme, one mirror is separated from the fiber end by a controlled amount. The 4% reflectivity of the fiber-air interface acts as a low-reflectivity mirror that couples the fiber cavity with the empty air-filled cavity. Because of that, all the free terminations on the systems have to be immersed in refractive-index-matching gel to avoid undesired reflections. Such compound resonator has been used to reduce the line width of an Er-doped fiber laser [23]. Three fiber gratings in series also produce two coupled Fabry-Perot cavities. Still another design makes use of a Fox-Smith resonator [5].

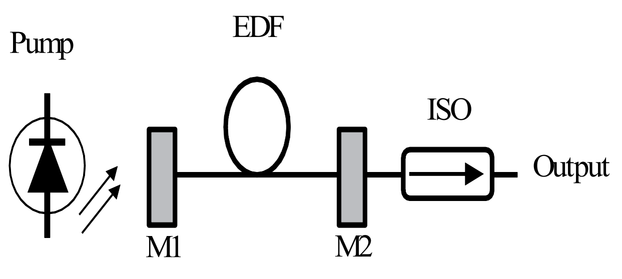

Figure 5. General schematic diagram of a linear cavity EDFL. M1: pump WDR mirror, M2: output coupler, EDF: erbium-doped fiber, ISO: optical isolator.

As it was previously pointed out, multiwavelength lasers are of great interest for telecommunications and sensors multiplexing. These lasers also have a great potential in the fiber-optic test and measurement of WDM components. The requirements for such optical sources are: a high number of channels over large wavelength span, moderate output powers (of the order of 100μW per channel) with good OSNR and spectral flatness, single longitudinal mode operation of each laser line, tunability and accurate positioning on the ITU frequency grid [25].

2.1. Laser output fluctuations

Many lasers, exhibit fluctuations in their output intensity that appear as either a sequence of sharp, narrow pulses (spikes) or a small oscillation "ripple" superimposed upon the steady-state laser output signal. The lasers that experience these fluctuations are lasers in which the recovery time of the excited-state population inversion is significantly longer that the laser cavity decay time.

It has been recognized that such instabilities can significantly degrade the performance characteristics of a sensor array based on a tunable ring laser interrogation scheme. Most of the factors influencing stability of the output power of fiber laser have been analyzed theoretically in detail [23]. A systematically effort to study these causes has been carried out. Based on previous experience these studies have been focused on optimization of some the following parameters: pump power [19], doped fiber length and ions concentration [26], output coupling ratio [7], total cavity length [26], spectral hole-burning effect [27] or the cavity losses [28]. However, polarization control seems not very important for the multimode regime [7].

2.2. Room temperature operation of fiber lasers

Multiple gain medium: In a manner similar to semiconductor laser arrays, it is possible to create multifrequency EDFLs that use a single gain medium per wavelength. In 1994, Takahashi et al. [29] demonstrated a multifrequency ring EDFL oscillating simultaneously over four wavelengths spaced 1.6 nm apart by using an 8 x 8 AWG and four EDFAs. Later, Miyazaki and his co-worker [30] showed a ring EDFL that lases on 15 lines separated by 1.6nm. Again, the laser consisted of 15 EDFAs placed between two 16 x 16 AWGs. The light from a 1480 nm pump laser was evenly distributed to N fiber segments by a 1 x N broadband coupler. Each segment was composed of a piece of EDF followed by an optical isolator, a tunable optical filter and variable attenuator. By adjusting each attenuator it was possible to establish multifrequency oscillation in this ring cavity. Independent wavelength tuning of each laser line was the main feature of this structure.

Various schemes have been demonstrated to show both SLM and tunability simultaneously, for example, using such schemes as a multi-ring cavity with a band pass filter [31], a tunable fiber Bragg grating (FBG) Fabry-Perot etalon [32] and a saturable absorber with a tunable FBG [33]. It has been shown in prior works that a section of unpumped EDF in a Sagnac loop can be used as a saturable absorber in which two counter-propagating waves form a standing wave and induce spatial-hole-burning (SHB). The refraction index of the unpumped EDF changes spatially due to SHB and this results in an ultra-narrow bandwidth self-induced FBG [34], [35].

By means of optimized length of unpumped EDF, the beat frequencies corresponding to the multimode lasing disappeared when a saturable absorber is introduced [36] so, lasers that can be wavelength-swept over the entire C-band (1520nm-1570nm) window with linewidth less than 0.7 kHz [37], laser that can also achieve switching modes among several wavelengths by simple adjustment of two polarization controllers in the cavities [38], C- plus L-band fiber ring laser with wide wavelength tunability and single-longitudinal-mode oscillation [39], generation of terahertz (THz) electromagnetic waves by photomixing two wavelengths in a high speed photodetector [40] can be obtained among others.

In 2008, Tianshu Wang [41] reported a novel high power tunable single-frequency erbium-doped fiber laser. The single-frequency operation was realized by using the FBG as a narrow band filter and a section of unpumped EDF as a saturable absorber in the cavity. The obtained slope efficiency was more than 20%, the stability was less than 0.005 dB and the modes adjacent to the lasing mode were completely suppressed.

Single gain medium: The very first attempts [42], [43] at room temperature operation of single gain stage multifrequency EDFLs showed, notwithstanding their inefficiency, the great potential of these sources. Later, Hübner et al. [44] proved that a multifrequency EDFL could be obtained through writing a series of DFB (distributed feedback laser) fiber Bragg gratings in a single erbium-doped fiber. Their laser produced five lines over a 4.2 nm range. The use of specialty doped fiber has also led to very elegant designs. A twincore EDF was used by Graydon et al. [45] as an inhomogeneous gain medium in a multifrequency ring EDFL. In that fiber, wavelength-dependent periodic coupling between the two cores partially decouples the available gain for each wavelength, since they interact with a different subset of erbium ions. Poustie et al. [46] used a multimode fiber to create a frequency periodic filter based on spatial mode beating and showed multi-wavelength operation over four lines spaced by 2.1 nm. In 1992, Abraham et al. [47] conceived a multifrequency hybrid laser composed of a 980 nm pump laser diode with antireflection coating coupled to an EDF with a fiber mirror. That laser produced an output spectrum with six lines spaced by 0.44 nm. In 1997, Zhao et al. [48] demonstrated that the control of optical feedback in a modified S-type cavity allowed stable multifrequency operation. In addition to this, a very interesting scheme to realize room temperature operation of a multifrequency EDFL was demonstrated by Sasamori et al. [49]. They used an acousto-optic modulator to prevent the laser from reaching steady-state operation. Initially, the authors believed that the repeated frequency shifting of the circulating ASE by the acousto-optic modulator prevented laser oscillation and yielded an incoherent source. Recently, it was shown that this source is in fact a laser and its potential as a frequency reference was demonstrated [9], [50], [51].

X.S. Liu et al. [52] experimentally demonstrated a simple-structure but efficient multiwavelength EDFL based on dual effects of nonlinear polarization rotation (NPR) and four-wave-mixing (FWM). With this structure, a maximum of 38-lines output in C-band and 28-wavelength flattened output within 3 dB bandwidth in L-band, both with the same spacing of about 0.4 nm, was obtained. Through the comparative experiments, it was demonstrated that introducing hybrid nonlinear effects by using a length of DSF is more efficient to generate multiwavelength lasing than using SMF.

2.3. Liquid nitrogen cooled multifrequency fiber lasers

The most obvious way to force multifrequency operation in a single gain medium EDFL is to cool the EDF by immersion in a bath of liquid nitrogen (77 K). At these temperatures the erbium ions become inhomogeneous, and multifrequency operation is much easier. It must be noted that this complex and unreliable approach is not recommended for field applications. Nonetheless, many potent experimental results have been published using this method and it is worthwhile to review them. In 1996, Chow et al. [53] published results concerning a multifrequency ring EDFL using two different types of frequency periodic filters. They obtained eleven laser peaks spaced by 0.65nm using a Fabry–Perot filter based on chirped fiber Bragg gratings

http://dx.doi.org/10.5772/53398

[54], and five laser peaks spaced by 1.8 nm with a sampled fiber Bragg grating. An example of these kind of structures can be seen in Figure 6.

That same year, Yamashita et al. [55] proposed a single-polarization linear cavity multi-frequency EDFL. This laser does not use polarization-maintaining fiber and operates in a travelling-wave mode, thus preventing spatial hole burning, since cavity feedback is provided by Faraday mirrors. A Fabry–Perot etalon is used as the frequency periodic filter. A polarizer and a Faraday rotator are placed on each side of the etalon to prevent parasitic reflections. With this setup, the authors obtained simultaneous oscillation over 17 wavelength spaced by 0.8 nm. Simultaneous lasing of up to 24 wavelengths has been demonstrated by Park et al. [56] using controlled polarization evolution in a ring cavity and liquid nitrogen cooling to enhance spectral hole burning, polarization hole burning, and polarization selectivity. A polarizer and a polarization controller were placed before a piece of polarization maintaining fiber to form a Lyot filter with a free spectral range of 1.1 nm. Finally, Yamashita et al. [57] realized a multiwavelength Er:Yb Fabry–Perot micro-laser with 29 0.4 nm-spaced lines.

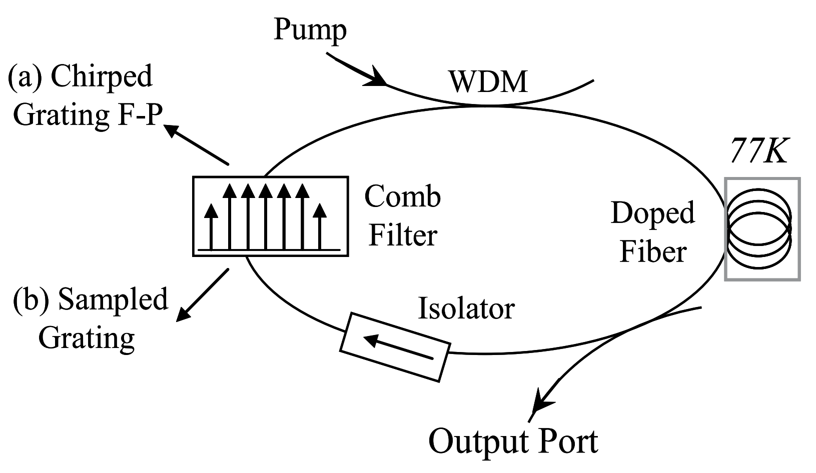

Figure 6. Schematic diagram of a nitrogen-cooled multifrequency EDFL.

2.4. Multiwavelength fiber laser-based multiplexing systems

One of the major difficulties to detect the sensing signals when broadband light sources are more than 50 km long is the Rayleigh scattering-induced optical noise as well as loss of background signal in the transmission fiber [58]. To increase the performance of sensing systems, a fiber laser-based sensing probe with a narrow bandwidth and a high extinction ratio should be considered.

As it was said, FBGs are suitable for use as spectrally narrowband reflectors for creating cavities for fiber lasers. Multisensor fiber Bragg grating lasers utilizes several FBGs normally at different wavelengths, an amplification section and a mirror (or structure acting as a mirror) to create an in-fiber cavity [59]. The utilization of an amplifying medium between the gratings and the mirror pumped inside or outside the cavity provides gain and thus lasing. The cavity may show single mode or multimode performance depending on the gratings and the cavity length. This multimode performance can be seen in Figure 7, where the output optical spectrum measured by a BOSA (Brillouin optical spectrum analyzer) for a multiwavelength erbium doped fiber ring laser tested by heating one FBG on a climatic chamber in the range of 30˚C to 100˚C is shown. In addition to this, a linear relation between each lasing wavelength with the temperature can be observed. For single mode operation using typical FBG bandwidth, the cavity required to be on the order of a few cm, thus most part of remote sensing system are multimode. Numerous configurations to multiplex a number of FBGs have been carried out. These new sensing configurations offer a much improved SNR than the non-lasing ones. Initially Er-doped fiber amplifiers were utilized, being nowadays utilized Raman amplification, EDFAs and SOAs depending on the application and distance to be achieved [7].

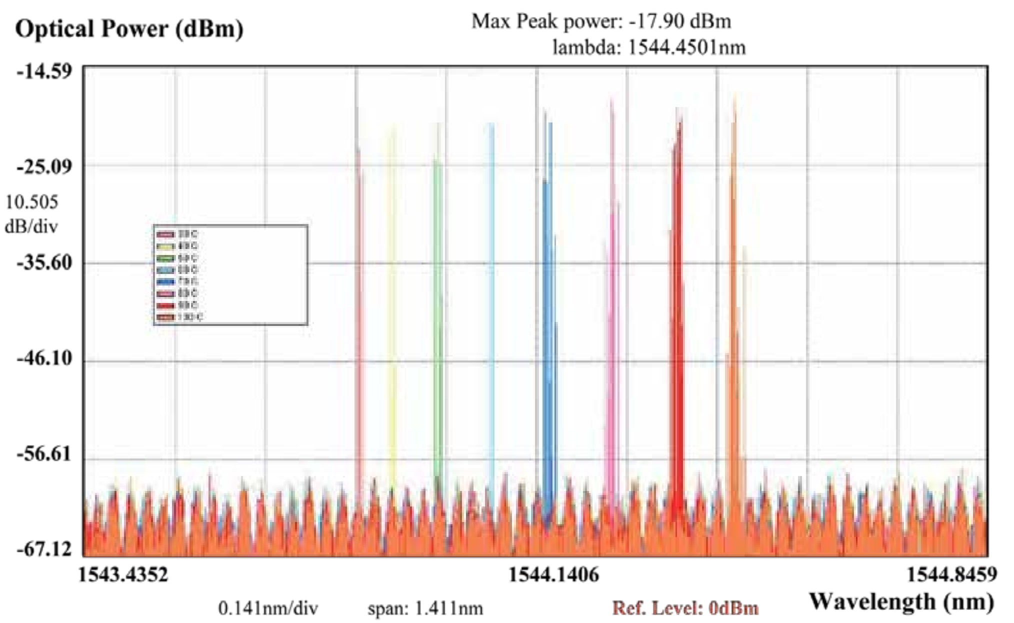

Figure 7. Output optical spectrum measured by the BOSA for the MEDFRL (with 1.5m of highly doped Er-fiber (Er-80) from Liekki) tested by heating one FBG on a climatic chamber in the range of 30˚C to 100˚C.

Several approaches based on fiber lasers have been reported in order to realize long-distance and remote sensing. Peng et al. [60] proposed an advanced configuration based on the use of a linear cavity Raman laser configuration formed by FBGs and a fiber loop mirror to achieve a high optical signal-to-noise ratio (50 dB), but in such a system the number of FBG sensors was limited by the relatively low Raman gain, which is difficult to improve even by using a high Raman pump power and multiwavelength lasing characteristics.

Another approach, also proposed by Peng et al., [61] was a multiwavelength fiber ring laser configuration with an erbium doped waveguide amplifier and a semiconductor optical amplifier (SOA), but only six or so FBG sensors can be used in such a system with its narrow effective bandwidth of 20 nm, which depends on the overlap of the spectrum between the EDFA and the SOA. Moreover, its sensing distance is limited by the SOA, which cannot be pumped remotely.

Recently, numerous multiwavelength switchable erbium-doped fiber lasers have been developed [62]. These topologies offer a stable operation without the necessity of passive multi-ring cavities [63] or polarization maintaining fiber [64], are suitable for the selection of all the possible output combinations of several different lasing wavelengths and they have been used for remote sensing up to 50 km [65]. In addition to this, in [66], an approach using a tunable fiber ring laser with hybrid Raman–Erbium-doped fiber amplification was demonstrated, obtaining an optical SNR of 60 dB for 50 km. However, ultra-long distance FBG multiplexing systems have been demonstrated [67] without using optical amplification, obtaining acceptable signal to noise ratios (20 dB) after 120 km. Besides, a 200 km long fiber ring laser for multiplexing FBG arrays was recently developed [68] and it was also able to detect four multiplexed FBGs placed 250 km away, offering a signal to noise ratio of 6–8 dB [69].

As can be seen in [70] backward Raman amplification approach is an effective way to realize ultra-long distance FBG sensing systems. Because of that, a 300km transmission distance has been recently achieved with an optical SNR of 4 dB [71], which is the longest FBG sensing distance, to the best of our knowledge.

3. Laser cavity resonance modes

In a typical laser, the number of cavity resonances that can fit within the gain bandwidth is often plotted as a function of laser output power versus wavelength. This subsection deals with how varying the appropriate frequencies can alter curves describing the number of cavity modes and gain bandwidth of a laser.

One can suppress all but one lasing mode by increasing the spacing between adjacent modes such that other modes lie outside the width of the laser gain curve. This is usually achieved by designing very short cavity lasers. In fiber lasers, this can be achieved by designing a very short (few centimeters long) standing-wave cavity combined with one or two narrow band Bragg gratings that select a single longitudinal mode.

A common misconception about lasers results from the idea that all of the emitted light is reflected back and forth within the cavity until a critical intensity is reached, whereupon some "escapes" through the output mirror as a beam [72]. In reality, the output mirror always transmits a constant fraction of the light as the beam, reflecting the rest back into the cavity. This function is important in allowing the laser to reach an equilibrium state, with the power levels both inside and outside the laser becoming constant.

Due to the fact that the light oscillates back and forth in a laser cavity, the phenomenon of resonance becomes a factor in the amplification of laser intensity. Depending upon the wavelength of stimulated emission and cavity length, the waves reflected from the end mirrors will either interfere constructively and be strongly amplified, or interfere destructively and cancel laser activity. Because the waves within the cavity are all coherent and in phase, they will remain in phase when reflected from a cavity mirror. The waves will also be in phase upon reaching the opposite mirror, provided the cavity length equals an integral number of wavelengths. Thus, after making one complete oscillation in the cavity, light waves have traveled a path length equal to twice the cavity length. If that distance is an integral multiple of the wavelength, the waves will all add in amplitude by constructive interference. When the cavity is not an exact multiple of the lasing wavelength, destructive interference will occur, destroying laser action. The following equation defines the resonance condition that must be met for strong amplification to occur in the laser cavity:

$$N \cdot \lambda = 2 \cdot (Cavity\ length) \tag{3}$$

where N is an integer, and λ is the wavelength. The condition for resonance is not as critical as it might appear because actual laser transitions in the cavity are distributed over a range of wavelengths, termed the gain bandwidth [72]. Wavelengths of light are extremely small compared to the length of a typical laser cavity, and in general, a complete roundtrip path through the cavity will be equivalent to several hundred thousand wavelengths of the light being amplified.

Resonance is possible at each integral wavelength increment and because the corresponding wavelengths are very close, they fall within the gain bandwidth of the laser. Figure 8 illustrates a typical example in which several resonance values of N, referred to as longitudinal modes of the laser, fit within the gain bandwidth.

Laser beams have certain common characteristics, but also vary to a wide degree with respect to size, divergence, and light distribution across the beam diameter. These characteristics depend strongly upon the design of the laser cavity (resonator), and the optical system controlling the beam, both within the cavity and upon output. Although a laser may appear to produce a uniform bright spot of light when projected onto a surface, if the light intensity is measured at different points within a cross section of the beam, it will be found to vary in intensity. Resonator design also affects beam divergence, a measure of beam spreading as distance from the laser increases. The beam divergence angle is an important factor in calculating the beam diameter at a given distance.

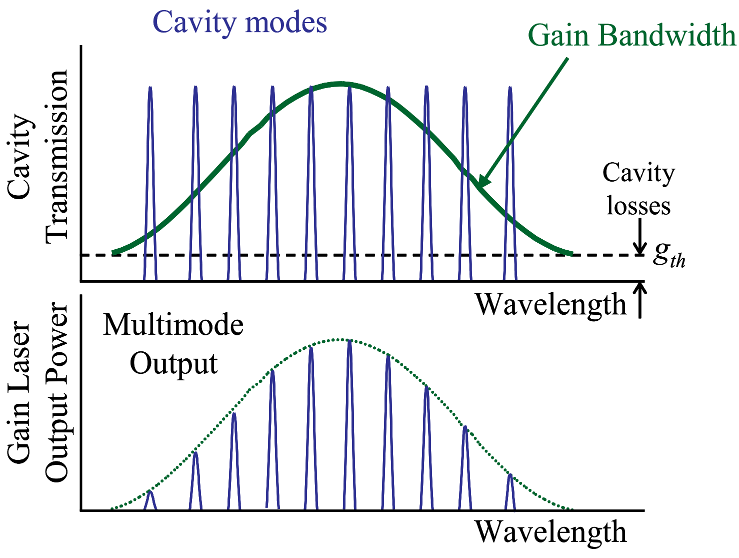

Figure 8. Cavity resonance modes and gain bandwidth.

In order to obtain monochromatic or single-mode laser radiation, it is usually necessary to insert a frequency dependent loss element (a filter) to insure that gain exceeds loss for only a single longitudinal mode.

4. Fiber lasers

4.1. Rare earth doped optical fiber lasers

Rare earth doped optical fibers are now a well-established class of gain media with many diverse applications that extend far from the original conceived application; namely, in-line amplifiers [73], [74]. Erbium-doped silica fiber lasers have been use, for example, for distributed sensing applications [75], remote sensing of magnetic fields [76], and as sources of optical solitons for all-optical fiber-based communications networks [77]. Many of these applications have evolved because of the advantages accrued from placing the rare earth ion in the optical fiber host lattice. The interaction between the rare earth ion and the intrinsic electric field associated with the host results in a broadening of the absorption and emission lineshapes associated with the rare earth ion. It is fortuitous that the absorption bands associated with many of the rare earth ions occur at wavelengths that are common to well-established laser diodes. The broadening of the absorption bands removes some of the wavelength-tailoring problems encountered with rare earth doped crystalline materials [78]. In fact, the ability to convert the output radiation from low-cost laser diodes, which generally occurs in a low-quality output mode with a poor frequency definition, into a high-brightness coherent source, is beneficial to applications, such as remote sensing and fiber-based communication systems, because it results in compact systems with low power requirements. The broadband emission of trivalent rare earth ions allows the development of sources emitting either broad continuous-wave (CW) spectra or ultrashort pulses, as well as widely tunable narrow-linewidth operation [73].

A fiber laser using a trivalent rare earth as the active element has the potential for very narrow linewidth operation compared with other sources that oscillate in the same spectral regions, such as semiconductor lasers [73]. The output radiation from a single-frequency laser is not monochromatic, but has a finite bandwidth. The theoretical limit for the bandwidth is known as the Schalow-Townes limit and depends on both the linewidth of an individual longitudinal mode of the cavity and the amount of amplified spontaneous emission coupled to the oscillating longitudinal mode [22]. The cavity linewidth scales inversely with the cavity length of the laser, and the waveguiding nature of a fiber allows cavity lengths of many meters to be established. In comparison, the cavity length of semiconductor lasers is typically a fraction of a centimeter. Also, the optimum linewidth that can be expected from a fiber laser is significantly smaller than that of a semiconductor laser, making the fiber a suitable tool for narrow-linewidth applications [22].

Because of potential applications of multiwavelength fiber lasers, such as the fields of optical communication, optical fiber sensing, optical component testing and microwave photonics among other, erbium-doped fiber lasers emitting in multiple wavelengths simultaneously have attacked much interest recently [79],[80]. The multiwavelength fiber lasers used have various advantages such as the wavelength multiplexing operation, simple and compact structure, low cost, and small insertion loss, etc. It is worth mentioning than another important application of these multiwavelength fiber lasers is their use as light sources themselves in WDM systems.

Erbium-doped fiber is rarely employed to implement a stable multiwavelength lasing at room temperature owing to the homogeneous line-broadening property of the EDF. Over the last decade, various approaches have been proposed to address the above issue, for example, as it was previously pointed out in section 2.3, the EDF cooling the frequency shifting [9], the spatial and polarization hole-burning-effect-based [81], the nonlinear effects, and the nonlinear polarization rotation-based methods [82]. Most of these aspects have the following drawback: they use to offer few lasing wavelengths or they use to show a rather broad linewidth.

Moreover, EDFLs can operate in several wavelength regions, ranging from visible to far infrared. The 1.55 μm region has attracted the most attention because it coincides with the low-loss region of silica fibers used for optical communications.

The performance of EDFLs improves considerably when they are pumped at the 0.98 or 1.48 μm wavelength because of the absence of excited-state absorption. Indeed, semiconductor lasers operating at these wavelengths have been developed solely for the purpose of pumping Er-doped fibers. Their use has resulted in commercial 1.55-μm fiber lasers.

EDFLs pumped at 1.48 μm also exhibit good performance. In fact, the choice between 0.98 and 1.48 μm is not always clear since each pumping wavelength has its own merits. Both have been used for developing practical EDFLs with excellent performance characteristics [83], [84].

http://dx.doi.org/10.5772/53398

An important property of continuously operating EDFLs from a practical standpoint is their ability to provide output that is tunable over a wide range and many techniques can be used to reduce the spectral bandwidth of tunable EDFLs [2]. Ring cavities can also be used to make tunable or switchable EDFLs [62], [65], [85].

Besides, fiber gratings can also be used to improve the performance of EDFLs. Since 1990, when a Bragg grating was used to realize a line width of about 1 GHz [86], fiber gratings have been used in EDFAs for a variety of reasons [87]. The simplest configuration splices a Bragg grating at each end of an erbium-doped fiber, forming a Fabry–Perot cavity. Such devices are called distributed Bragg reflector (DBR) lasers. These fiber lasers can be tuned continuously while exhibiting a narrow line width. They can also be made to oscillate in a single longitudinal mode by decreasing the fiber length. Multiple fiber gratings can be also used to make coupled-cavity fiber lasers. Figure 9 shows an example of the output power spectral density of a single-stage EDFA (with two FBGs centered at 1540 and 1545nm and pump power of 90mW at 980nm. This EDFA (Photonetics, model BT 1300) provides 13 dBm output saturation power and a maximum 35 dB small signal gain.

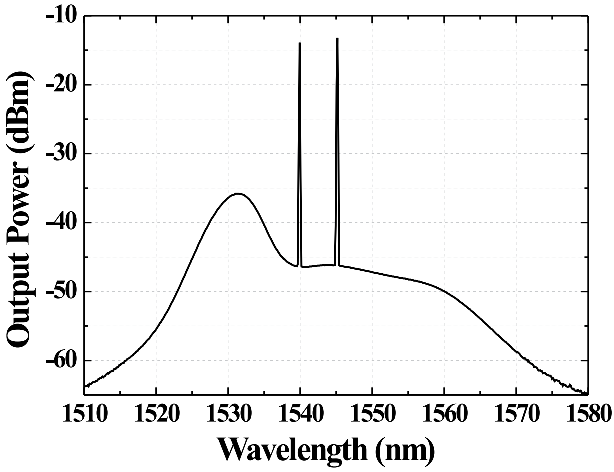

Figure 9. Output power spectral density (res=0.1nm) of a single-stage EDFA with λ_1=1540nm, λ_2=1545nm, P_p=90mW, L= 32 m, and λ_p=980nm.

Multiwavelength optical sources, capable of simultaneously emitting light at several well defined wavelengths, are useful for WDM lightwave systems. Fiber lasers can be used for this purpose, and numerous schemes have been developed [88]. The cavity length is made quite small (~ 1 mm or so) since spacing between the lasing wavelengths is governed by the longitudinal-mode spacing. A 1mm cavity length corresponds to a 100 GHz wavelength spacing. Such fiber lasers operate as standard multimode lasers. Cooling of the doped fiber helps to reduce the homogeneous broadening of the gain spectrum to below 0.5 nm. The gain spectrum is then predominantly inhomogeneously broadened, resulting in multimode operation through spectral hole burning. Long cavities with several meters of doped fibers can also be used. Wavelength selection is then made using an intracavity comb filter such as a Fabry–Perot interferometer.

Many other rare-earth ions can be used to make fiber lasers. Holmium, samarium, thulium, and ytterbium have been used in nearly simultaneous experiments to make fiber lasers emitting at wavelengths ranging from visible to infrared. Attention later shifted to Pr3+ ions in an attempt to realize fiber lasers and amplifiers operating at 1.3 μm. Pr-doped fiber lasers can also operate at 1.05 μm. Thulium-doped fiber lasers have attracted considerable attention because of their potential applications. Operation at several other important wavelengths can be realized by using fluoride fibers as a host in place of silica fibers.

Holmium-doped fiber lasers have attracted attention because they operate near 2 μm, a wavelength useful for medical and other eye-safe applications. Thulium codoping permits these lasers to be pumped with GaAs lasers operating near 0.8 μm. Ytterbium-doped fiber lasers, operating near 1.01 μm and tunable over 60 nm, were first made in 1988 [89]. In 1992, the use of fluoride fibers as the host medium provided output powers of up to 100 mW. In a later experiment, more than 200-mW power with a quantum efficiency of 80% was obtained from a silica-based Yb-doped fiber laser pumped at 869 nm [90].

4.1.1. Single longitudinal mode operation

A number of schemes have also been demonstrated to show single-longitudinal mode (SLM), using such schemes as a multi-ring cavity with a band pass filter [31], a tunable fiber Bragg grating (FBG) Fabry-Perot etalon [32] and a saturable absorber with a tunable FBG [33]. In addition to this, it has been experimentally demonstrated [36] that the beat frequencies corresponding to the multimode lasing disappeared when saturable absorber (an optimized length of unpumped EDF) is introduced.

Even when single-mode regime is achieved, these lasers suffer from multi-gigahertz mode hopping. However these rings are at least several meters long so thermally induced hops to adjacent cavity modes still occur. An alternative approach is to use gratings, or distributed Bragg reflectors (DBR), in a linear cavity. These can be fabricated directly into an optical fiber through refractive index changes induced by short wavelength radiation to provide both optical feedback and wavelength selectivity [91]. Such a linear laser must possess better wavelength selectivity than a ring to overcome spatial hole burning. However, because the cavity losses can be so low, the resonator can potentially be made much shorter and with greater finesse. Singlemode operation has been reported in erbium-doped fiber DBR lasers with cavity lengths of 50cm [91] and 10cm [87]. To assure that the singlemode operation is robust, the cavity should be sufficiently short such that the mode spacing is comparable to the grating bandwidth.

On the other hand, and as reported in [92], a SLM fiber ring laser can be made to annihilate the mode competition with an auxiliary lasing. Owing to the interaction of the seed light produced from one channel to the other one and vice versa, multiple-longitudinal-mode oscillation can be suppressed, and thus the mode competition and mode hopping is not produced. Therefore, the laser oscillation is rather stable. In a single-wavelength operation of these lasers, has been experimentally demonstrated that multiple longitudinal modes are supported by the cavity. However, for similar pumping levels, a single-mode operation of the laser when we emit simultaneously several wavelengths using a special ring cavity configuration has been achieved [85]. The stable SLM operation is guaranteed if the output power of both channels is similar. This implies that it is possible to avoid the utilization of additional optical filtering techniques (that reduce the optical efficiency) to achieve the SLM operation.

4.1.2. Applications of single frequency fiber lasers

The narrow linewidhs and excellent frequency noise characteristics of single-frequency fiber lasers make them ideal form many applications. One key area for which the fiber geometry is attractive is remote sensing. The advent of fiber lasers based on Bragg reflectors has triggered a revolution in sensing applications, making possible, for example, the ustrasensitive detection of strain and magnetic fields. The narrowband reflection of the Bragg reflector meant that only a small precentage of the incident signal was reflected by the device, resulting in difficulties in extracting the optical signal from the background noise. The ability to incorporate Bragg gratings into fiber lasers has allowed the development of high-power (> 1mW) sensitive optical sensors and alleviated these signal to noise problems [73].

Several approaches have been investigated to developed fiber laser based strain sensors [93]. Also, cavities for narrow-linewidth fiber lasers can be made with matched pairs of fiber Bragg reflectors. These lasers have been employed to produce both single point and multipoint sensors [94]. Instead of using the Bragg reflector to sense the environmental change, the actual laser acts as the sensor. As it is well known, a change in the optical path length induces a change in the frequency, so by monitoring the wavelength change the environmental perturbation can be monitored. The multipoint sensor consists of a series of fiber lasers made from Bragg reflectors peaking at different wavelengths. In addition to this, magnetic fields can be detected using an active fiber laser sensor [76]. A single frequency fiber laser was attached to a magnetostrictive element. This element exhibits a quadratic dependence to the applied field, and it can be used to detect either AC or DC magnetic fields [73].

The foregoing sensors rely on changes in laser wavelength to provide information on the perturbation applied to the active sensor. The polarization properties of fiber lasers can be also be exploited to produce a sensor. Dual-frequency operation can be obtained in narrow-linewidth fiber lasers by exiting the orthogonal polarization axes of the weakly birefringent laser cavity. Because the refractive indices associated with polarization axes are different, the oscillating frequencies of the two modes are also different. Detection of these two frequencies result in a beat note at the detector. By applying to the cavity a perturbation that alters its birefringence, the beat frequency changes, and by monitoring this frequency change the applied perturbation can be quantified.

The need for a suitable standard close to 1.5 μm is driven by the use of narrow-linewidth lasers for wavelength multiplexed communication systems. In general, the light sources used for these systems have been distributed feedback semiconductor lasers. However, it has been demonstrated that narrow-linewidth fiber lasers are a potentially suitable replacement [73].

5. Raman lasers

Raman fiber lasers (RFLs) are attractive light sources for generating laser light at wavelengths which are difficult to obtain with other lasers. One of the most significant characteristics of these lasers is versatility in terms of wavelength, since Raman gain is achievable throughout the complete window of transparency of silica (300-2200nm). Providing that a suitable high power pump is provided, the Raman amplification process can be cascaded several times [95] allowing lasing in a broad wavelength range. Such wavelength versatility cannot be achieved using traditional lasers based on rare-earth-doping that have limited emission bands not broader than a few tens of nanometers. The nonuniform nature of the Raman gain spectrum is of concern for wavelength-division-multiplexed (WDM) lightwave systems because different channels will be amplified by different amounts. This problem is solved in practice by using multiple pumps at slightly different wavelengths. Each pump provides nonuniform gain but the gain spectra associated with different pumps overlap partially. With a suitable choice of wavelengths and powers for each pump laser, it is possible to realize nearly flat gain profile over a considerably wide wavelength range.

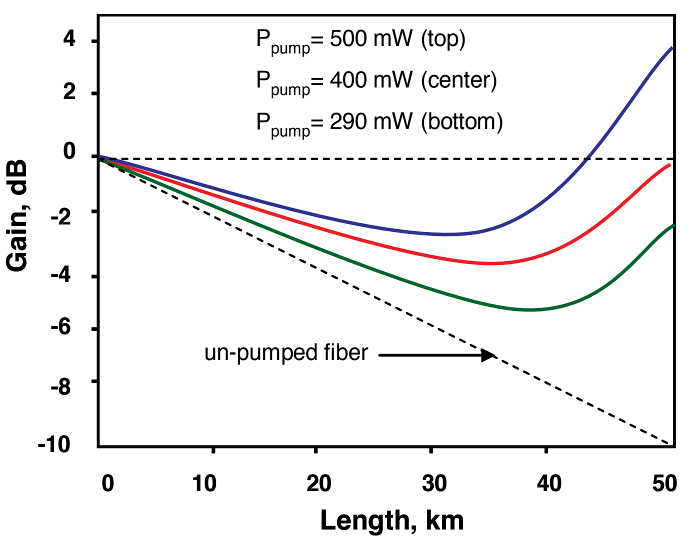

Figure 10. Measured gain evolution observed within a 50 km standard fiber transmission span for different pump powers.

In addition to this, and besides the advantages due to distributed amplification, another merit of the Raman amplifier is that any gain band can be tailored by proper choice of pump wavelength. One of the main purposes of discrete Raman amplifiers is to realize an amplifier operating in different windows than EDFA. There have been many efforts to develop discrete Raman amplifiers operating in 1.3 [96], 1.52 [97], and 1.65 μm [98] bands. Because the interaction length of the Raman amplifier is typically orders of magnitude longer than that of EDFA, nonlinearity, saturation, and double Rayleigh backscattering may become serious issues.

However, by optimizing the length of the gain fiber (see Figure 10) and using a two-stage structure, one may be able to design discrete Raman amplifiers that are good for signal transmissions. Raman fiber lasers have been used in several of the pioneering experiments in distributed Raman amplification. For example, the first demonstrations of (a) capacity upgrades using Raman amplification by Hansen et al. [99], (b) multiwavelength pumping for large bandwidth by Rottwitt and Kidorf [100], and (c) higher order pumping by Rottwitt et al. [101] all used single wavelength Raman fiber lasers. Many other systems' results have also established an RFL as a viable Raman pump source.

In long-distance FBG systems, the most important problem is Rayleigh scattering in the transmission fiber connecting the FBGs and interrogator. The noise floor of the FBG reflection spectrum is caused by Rayleigh-scattered light. The FBG reflection spectrum detected by the interrogator decreases and the power of the Rayleigh-scattered light increases as the length of the transmission fiber increases. When the length is about 70 km, the signal to noise ratio (OSNR) of the FBG reflection spectrum becomes very low, limiting the practical length of the transmission fiber for FBG sensor systems of about this length (70 Km). A number of long-distance remote sensing systems using multiwavelength Raman lasers have been also proposed [102].

There were several methods used to improving the sensing distance of FBG-based sensor systems [103]. Based on a tunable laser and optical amplification, a sensing distance of 100km was achieved with a SNR of about 57 dB [104]. Takanori Saitoh et al. developed a FBG sensor system based on EDFA, whose performance was highly dependent on the quality of the light source and sensing distance of 230 km was obtained with a SNR of 4dB [70]. On the other hand, Fernandez-Vallejo et al. developed an ultra-long range fiber Bragg grating sensor interrogation system able to detect four multiplexed FBGs placed 250 km away, offering a signal to noise ratio of 6–8 dB [104]. Due to in many applications, such as railway, oil or gas pipelines, FBG sensor systems with even longer sensing distance are needed. Recently, a novel tunable fiber ring laser configuration with combination of hybrid Raman amplification and EDFA has been presented [105] to improve the sensing characteristics of the FBG-based ultra-long sensor system. A maximum sensing distance of 300 km with an SNR of about 4 dB has been obtained.

6. Random lasers

Random lasers are miniature sources of stimulated emission in which the feedback is provided by scattering in a gain medium [107]. Random lasers have currently evolved into a large research field. The recent review of random lasers can be found in [108]. Since scattering provides the feedback in random lasers, they do not require any external cavity or mirrors. However, external mirrors enhance the performance of random laser if they are positioned close enough to the gain medium and help to increase the feedback of stimulated emission or the efficiency of utilization of pumping. The random laser with one mirror, which had high transmission at the pumping wavelength and high reflection at the stimulated emission wavelength, was demonstrated in [109]. It has been shown that the mirror helps to reduce the threshold by~25% and increase the slope efficiency by~30%. The relatively moderate improvement was explained by the fact that the mirror and the laser powder in [109] were separated by a1 mm thick wall of the cuvette.

An intrinsic fundamental loss mechanism of an optical fiber is Rayleigh scattering (RS) [110]. When using Raman amplification besides losses due to RS there will also be losses due to double Rayleigh scattering (DRS). The long lengths of fiber used for Raman amplification make the Rayleigh scattering associated noise an issue. As the gain in Raman amplifiers increases so will RS and DRS, which eventually limit the achievable gain [111]. An interesting approach in order to diminish these losses is using this Rayleigh associated noise as an active part of the laser. It can be used as a distributed random mirror transforming what were losses in gain in the output signal [112], [113]. Lasers taking advantage of cooperative Rayleigh scattering as a self-feedback mechanism of Brillouin-Rayleigh scattering have been reported [114]-[116]. Schemes have been implemented by using four-wave mixing method through the use of reduced high nonlinear Bismuth-erbium doped fiber for Brillouin-Raman multiwavelength lasing with comb generation [117], or high-reflectivity mirror in the linear cavity for distributed feedback [118], [119]. Different multiwavelength Raman fiber lasers based in these same structural setups have been recently developed: a multiwavelength Raman fiber laser based in highly birefringent photonic crystal fiber loop mirrors combined with random mirrors [110] or based in Sagnac structures [120], [121].

7. Other fiber lasers

Besides the fiber lasers previously pointed out, there are other fiber lasers that it is worth taking into consideration. This subsection is devoted to show some of the most common types.

Different techniques have been used to Q-switch a fiber laser. Q-switching can be achieved actively through the action of an electrically controlled loss modulator. It can also be carried out passively [73]. For example, a saturable absorber placed in the cavity acts as a loss modulator, with an intensity-dependent transmission controlled by the laser field itself. Active Q-switching has been used preferentially with fiber lasers. Ideally, in its low-transmission state the loss modulator should introduce a loss high as possible, to maintain the laser below threshold while gain is built-up to high values. On the other hand, it should be as transparent as possible in its high-transmission state, to minimize the loss it adds to the laser field. Finally, the switching time of the loss modulator should be short enough to accommodate the rapidly expanding laser field. A slow-opening modulator is a source of loss and can also result in multiple pulsing [22], [122].

Mode-locked fiber lasers are capable of producing pulses with widths from close to 30 fs to 1ns at repetition rates, ranging from less than 1 MHz to 100 GHz. This versatility, as well as the compact size of optical fibers, is quite unique in laser technology, and thus open up fiber lasers to a large range of applications. Indeed, mode-locked fiber lasers have been established as a premier source of short optical pulses, ranking equally with semiconductor and solid-state lasers. As mode-locked fiber laser technology matured and these lasers became commercially available, they have been used in many different fields, such as laser radar, all-optical scanning delay lines, nonlinear frequency conversion, injection-seeding, two-photon microscopes, THz generation, and optical telecommunications, just to mention the most widely publicized areas [73].

Separately, stimulated Brillouin scattering (SBS) is a nonlinear process that can occur in optical fibers at input power levels much lower than those needed for stimulated Raman scattering (SRS). It manifests through the generation of a backward-propagating Stokes wave that carries most of the input power, once the Brillouin threshold is reached. For this reason, SBS limits the channel power in optical communication systems. At the same time, it can be useful for making fiber-based Brillouin amplifiers and lasers.

Brillouin fiber lasers consisting of a Fabry–Perot cavity exhibit features that are qualitatively different from those making use of a ring cavity. The difference arises from the simultaneous presence of the forward and backward propagating components associated with the pump and Stokes waves. Higher-order Stokes waves are generated through cascaded SBS, a process in which each successive Stokes component pumps the next-order Stokes component after its power becomes large enough to reach the Brillouin threshold. At the same time, anti-Stokes components are generated through four-wave mixing between copropagating pump and Stokes waves. The number of Stokes and anti-Stokes lines depends on the pump power. Most Brillouin fiber lasers use a ring cavity to avoid generation of multiple Stokes lines through cascaded SBS. The performance of a Brillouin ring laser depends on the fiber length used to make the cavity.

Considerable attention was paid during the 1990s to developing hybrid Brillouin erbium fiber lasers capable of operating either at several wavelengths simultaneously or in a single mode, whose wavelength is tunable over a wide range [106]. Besides the foregoing fiber lasers, some novel FBG interrogation techniques for remote sensing using a hybrid Brillouin-Raman fiber laser (100 km) [123] or combining Raman, Brillouin and erbium gain in a fiber laser (155 km) [124] have experimentally demonstrated.

8. Conclusions

This work dealt with various aspects of the multiwavelength fiber lasers. These kinds of lasers can be designed with a variety of choices for the laser cavity, because of that a brief explanation about the suitable configuration design has been shown.

There are a number of fiber lasers with different configurations and amplification methods; however this work has been centered on the erbium doped and Raman fiber lasers. The importance of the multiwavelength fiber lasers has been pointed out. Some of their problems, such as the laser output fluctuations, have been explained just as several reported stabilization techniques.

Finally, it is worth highlighting that multiwavelength fiber lasers are the hot topic in industrial-laser circles. They promise to revolutionize the laser industry through a disruptive combination of high reliability, high efficiency, low cost, and excellent beam quality. Fiber lasers are merely the most prominent example of these technologies' proliferation in industrial lasers.

Acknowledgements

The authors are grateful to the Spanish Government project TEC2010-20224-C02-01.

Author details

Rosa Ana Perez-Herrera* and Manuel Lopez-Amo

*Address all correspondence to: rosa.perez@unavarra.es

Department of Electric and Electronic Engineering, Universidad Pública de Navarra, Campus Arrosadia S/N,Pamplona, Spain

References

[1] López Higuera JM. Advanced Photonic Topics. Universidad de Cantabria; 1997

[2] Liu K. et al. Broadband diode-pumped fibre laser. Electronics Letters 1988; 24(14) 838-840.

[3] Fernandez-Vallejo M, Diaz S, Perez-Herrera RA, et al. Comparison of the stability of ring resonator structures for multiwavelength fiber lasers using Raman or Er-doped fiber amplification. IEEE Journal of Quantum Electronics 2009; 45(12) 1551-1557

[4] Horowitz M, et al. Narrow-linewidth, singlemode erbium-doped fibre laser with intracavity wave mixing in saturable absorber. Electronics Letters 1994; 30(8) 648-649

[5] Barnsley P, et al. Fiber Fox-Smith resonators: application to single-longitudinal-mode operation of fiber lasers. Journal of the Optical Society of America 1988; 5(8) 1339-1346

[6] Jones JDC, et al. An injection-locked erbium fibre laser. Optics Communications 1990; 76(1) 42-46

[7] Perez-Herrera RA, et al. Stability comparison of two ring resonator structures for multiwavelength fiber lasers using highly doped Er-fibers. IEEE Journal of Lightwave Technology 2009; 27(14) 2563-2569

[8] Chan CC, Jin W, Ho HL, Demokan MS. Performance analysis of a time-division-multiplexed fiber Bragg grating sensor array by use of a tunable laser source. IEEE J. Selected Topics Quantum Electronics 2000; 6(5) 741–749

[9] Bellemare A, Karasek M, Rochette M, LaRochelle S, Tetu M. Room temperature multifrequency erbium-doped fiber lasers anchored on the ITU frequency grid. Journal of Lightwave Technology 2000; 18(6) 825–831

[10] Gusarov A, Liegeois F. Experimental study of a tunable fiber ring laser stability. Optics Communications 2004; 234(1-6) 391-397

[11] Chen X, Yao J, Zeng F, Deng Z. Single-longitudinal-mode fiber ring laser employing an equivalent phase-shifted fiber Bragg grating. IEEE Photonics Technology Letters 2005; 17(7) 1390-1392

[12] Bellemare A, Karásek M, Riviere C, Babin F, He G, Roy V Schinn GW. A Broadly Tunable Erbium-Doped Fiber Ring Laser: Experimentation and Modeling. IEEE Journal on Selected Topics in Quantum Electronics 2001; 7(1) 22-29

[13] Liu CK, Jou JJ, Liaw SK, Lee HC. Computer-aided analysis of transients in fiber lasers and gain-clamped fiber amplifiers in ring and line configurations through a circuit simulator. Optics Communications 2002; 209(4-6) 427–436

[14] Yeh CH, Chi S. A broadband fiber ring laser technique with stable and tunable signal-frequency operation. Optics Express 2005; 13(14) 5240-5244

[15] Yeh CH, Shih FY, Chow CW, Chi S. Dual-Wavelength S-Band Erbium-Doped Fiber Double-Ring Laser. Laser Physics 2008; 18(12) 1553-1556

[16] Talaverano L, Abad S, Jarabo S, López-Amo M. Multiwavelength Fiber Laser Sources with Bragg-Grating Sensor Multiplexing Capability. Journal of Lightwave Technology 2001; 19(4) 553-558

[17] Bellemare A. Continuous-wave silica-based erbium-doped fibre lasers. Progress in Quantum Electronics 2003; 27(4) 211-266

[18] Perez-Herrera RA, Chen S, Zhao W, Sun T, Grattan KTV, Lopez-Amo M. Stability performance of short cavity Er-doped fiber lasers. Optics Communications 2010; 283(6) 1067-1070.

[19] Perez-Herrera RA, Chen S, Zhao W, Sun T, Grattan KTV, Lopez-Amo M. Experimental optimization in terms of power stability and output power of highly Er-doped fiber lasers with single and hybrid cavities. Fiber & Integrated Optics 2010; 29(2) 106-120

[20] Giles CR, Desurvire E. Modeling erbium-doped fiber amplifiers. Journal of Lightwave Technology 1991; 9(2) 271-283

[21] Ball GA, Holton CE, Hull-Allen G, Morey WW. 60mW 1.5μm single-frequency low-noise fiber laser MOPA. IEEE Photonics Technology Letters 1994; 6(2) 192–194

[22] Siegman AE., editor. Lasers. University Science Books: Mill Valley; 1986

[23] O'Sullivan MS, Chrostowski J, Desurvire E, Simpson JR. High-power narrow-line-width Er3+-doped fiber laser. Optics Letters 1989; 14(9) 438-440

[24] Pang H-W, Cui H-M, Lian H., Zhao R-M, Hu B-N, Wang Y-F. Design of erbium-doped fiber laser based on linear multi-cavity. In: Yang L, Chen Y, Kley E-B, Li R (eds.) 3rd International Symposium on Advanced Optical Manufacturing and Testing Technologies: Advanced Optical Manufacturing Technologies, AOMATT 2007, 8-12 July 2007, Chengdu, China

[25] International Telecommunication Union (ITU-T). Optical interfaces for multichannel systems with optical amplifiers. Recommendation G.692, 40pp, 1998

[26] Liegeois F, Gusarov AI. Mid-term stability of a fiber ring laser with a wavelength-tunable Fabry-Perot filter. In proceedings of SPIE - The International Society for Optical Engineering 2004; 5480(36) 36-45

[27] Liu Y, Dong X, Shum P, Yuan S, Kai G, Dong X. Stable room-temperature multi-wavelength lasing realization in ordinary erbium-doped fiber loop lasers. Optics Express 2006; 14(20) 9293-9298

[28] Deepa V, Vijaya R. Linewidth characteristics of a filterless tunable erbium doped fiber ring laser. Journal of Applied Physics 2007; 102(8), art. no. 083107-4

[29] Takahashi H, Toba H, Inoue Y. Multiwavelength ring laser composed of EDFAs and an arrayed waveguide wavelength multiplexer. Electronics Letters 1994; 30(1) 44–45

[30] Miyazaki T, et al. A multiwavelength fiber ring-laser employing a pair of silica-based arrayed-waveguide-gratings. IEEE Photonics Technology Letters 1997; 9(7) 910–912

[31] Yeh CH, Huang TT, Chien HC, Ko CH, Chi S. Tunable S-band erbium-doped triple-ring laser with single-longitudinal-mode operation. Optics Express 2007; 15(2) 382-386

[32] Cheng XP, Shum P, Tse CH, Zhou JL, Tang M, Tan WC, Wu RF, Zhang J. Single-longitudinal-mode erbium-doped fiber laser based on high finesse fiber Bragg grating Fabry-Perot Etalon. IEEE Photonics Technology Letters 2008; 20(12) 976-978

[33] Song YW, Havstad SA, Starodubov D, Xie Y, Willner AE Feinberg J. 40-nm-wide tunable fiber ring laser with single-mode operation using a highly stretchable FBG. IEEE Photonics Technology Letters 2001; 13(11) 1167-1169

[34] Fischer B, Zyskind JL, Sulhoff JW, DiGiovanni DJ. Nonlinear wave mixing and induced gratings in erbium-doped fiber amplifiers. Optics Letters 1993; 18(24) 2108-2110

[35] Frisken SJ. Transient Bragg reflection gratings in erbium-doped fiber amplifiers. Optics Letters 1992; 17(24) 1776-1778

[36] Sharma U, Kim CS, Kang JU. Highly Stable Tunable Dual-Wavelength Q-Switched Fiber Laser for DIAL Applications. IEEE Photonics Techn. Letters 2004; 16(5) 1277-1279

[37] Zhang K, Kang JU. C-band wavelength-swept single-longitudinal mode erbium-doped fiber ring laser. Optics Express 2008; 16(18) 14173-14179

[38] Liu Y, Feng X, Yuan S, Kai G, Dong X. Simultaneous four-wavelength lasing oscillations in an erbium-doped fiber laser with two high birefringence fiber Bragg gratings. Optics Express 2004; 12(10) 2056-2061

[39] Yeh C-H, Chi S. A broadband fiber ring laser technique with stable and tunable signal-frequency operation. Optics Express 2005; 13(14) 5240-5244

[40] Sun J, Yuan X, Zhang X, Huang D. Single-longitudinal-mode dual-wavelength fiber ring laser by incorporating variable saturable absorbers and feedback fiber loops. Optics Communications 2007; 273(1) 231–237

[41] Wang T. Study on high power single-frequency erbium doped fiber laser for long distance communications. Microwave and Optical Techn. Letters 2008; 50(6) 1660-1662

[42] Schmuck H, Pfeiffer T. Fibre-pigtailed Fabry-Perot filter used as tuning element and for comb generation in an erbium doped fibre ring laser. In proceedings of the Technical Digest of 17th European Conference on Optical Communication, ECOC'91, 9-12 Sept 1991, Paris, France.

[43] Park N, Dawson JW, Vahala KJ. Multiple wavelength operation of an erbium-doped fiber laser. IEEE Photonics Technology Letters 1992; 4(6) 540–542

[44] Hübner J, Varming P, Kristensen M. Five wavelength DFB fibre laser source for WDM systems. Electronics Letters 1997; 33(2) 139–140

[45] Graydon O, Loh WH, Laming RI, Dong L. Triple-frequency operation of an Er-doped twincore fiber loop laser. IEEE Photonics Technology Letters 1996; 8(1) 63–65

[46] Poustie AJ, Finlayson N, Harper P. Multiwavelength fiber laser using a spatial mode beating filter. Optics Letters 1994; 19(10) 716–718

[47] Abraham D, Nagar R, Ruberto MN, Eisenstein G, Zyskind JL, DiGiovanni D, Koren U Raybon G. Intracavity-diode-pumped erbium doped fibre laser. Electronics Letters 1992; 28(19) 1830–1832

[48] Zhao Y, et al. Multiple wavelength operation of a unidirectional Er-doped fiber ring laser with optical feedback. In proceedings of the Technical Digest of Lasers and Electro-Optics, CLEO'97, 18-23 May 1997, Baltimore, Maryland

[49] Sasamori H, Isshiki K, Watanabe H, Kasahara K. Multi-wavelength erbium-doped ring light source with fiber grating filter. Technical Digest of Optical Amplifiers and Their Applications, OAA'97, 1997, paper WC3, pp. 235–238

[50] Bellemare A, Rochette M et al. Multifrequency erbium-doped fiber ring lasers anchored on the ITU frequency grid. In proceedings of the Technical Digest of Conference on Optical Fiber Communication, OFC'99, 21-26 Feb 1999, San Diego, California.

[51] Karásek M, Bellemare A. Numerical analysis of multifrequency erbium-doped fiber ring laser employing a periodic filter and a frequency shifter. IEE Proceedings-Optoelectronics 2000; 147(2) 115–119

[52] Liu XS, Zhan L, Hu X, Li HG, Shen QS, Xia YX. Multiwavelength erbium-doped fiber laser based on nonlinear polarization rotation assisted by four-wave-mixing. Optics Communications 2009; 282(14) 2913–2916

[53] Chow J, Town G, Eggleton B, Ibsen M, Sugden K, Bennion I. Multiwavelength generation in an erbium-doped fiber laser using in-fiber comb filters. IEEE Photonics Technology Letters 1996; 8(1) 60–62

[54] Town GE, Sudgen K, Williams JAR, Bennion I, Poole SB. Wide-band Fabry-Perot-like filters in optical fibers. IEEE Photonics Technology Letters 1995; 7(1) 78–80

[55] Yamashita S, Hotate K. Multiwavelength erbium-doped fiber laser using intracavity etalon and cooled by liquid nitrogen. Electronics Letters 1996; 32(14) 1298–1299

[56] Park N, Wysocki PF. 24-line multiwavelength operation of erbium-doped fiber-ring laser. IEEE Photonics Technology Letters 1996; 8(11) 1459–1461

[57] Yamashita S, Hsu K, Loh WH. Miniature Erbium:Ytterbium fiber Fabry-Perot multiwavelength lasers. IEEE Journal of Selected Topics in Quantum Electronics 1997; 3(4) 1058–1064

[58] Lopez-Amo M, López-Higuera JM. Multiplexing Techniques for FBG Sensors. In: Cusano A, Cutolo A, and Albert J. (eds.) Fiber Bragg Grating Sensors: Research Advancements, Industrial Applications and Market Exploitation. Oak Park, Illinois: Ed. Bentham Science Publishers Ltd; 2010.

[59] Koo KP, Kersey AD. Bragg grating based laser sensor systems with interferometric interrogation and wavelength division multiplexing. Journal of Lightwave Technology 1995; 13(7) 1243-1249.

[60] Peng PC, Tseng HY, Chi S. Long-Distance FBG Sensor System Using a Linear-Cavity Fiber Raman Laser Scheme. IEEE Photonics Technology Letters 2004; 16(2) 575-577

[61] Peng PC, Feng KM, Peng WR, Chiou HY, Chang CC, Chi S. Long-distance fiber grating sensor system using a fiber ring laser with EDWA and SOA. Optics Communications 2005; 252(1-3) 127-131

[62] Perez-Herrera RA, Fernandez-Vallejo M, Diaz S, Quintela MA, Lopez-Amo M, López-Higuera JM. Stability comparison of two quadruple-wavelength switchable erbium-doped fiber lasers. Optical Fiber Technology 2010; 16(4) 205-211

[63] Liaw S-K, Lee C-C, Ho K-P, Chi S. Power equalized wavelength-selective fiber lasers using fiber Bragg gratings. Optics Communications1998; 155 (4-6) 255–259.

[64] Feng S, Xu O, Lu S, Ning T, Jian S. Switchable multi-wavelength erbium doped fiber ring laser based on cascaded polarization maintaining fiber Bragg gratings in a Sagnac loop interferometer. Optics Communications 2008; 281(24) 6006– 6010.

[65] Perez-Herrera RA, et al. Switchable multi-wavelength erbium-doped fiber laser for remote sensing. In proceedings of the SPIE 20th International Conference on Optical Fiber Sensors, OFS-20, 5-9 Oct 2009, Edinburgh, United Kingdom, 75031Y-1. 75031Y-4.

[66] Rao YJ, Ran ZL, Chen RR. Long-distance fiber Bragg grating sensor system with a high optical signal-to-noise ratio based on a tunable fiber ring laser configuration. Optics Letters 2006; 31(18) 2684-2686

[67] Saitoh T, Nakamura K, Takahashi Y, Iida H, Iki Y, Miyagi K. Ultra-Long-Distance Fiber Bragg Grating Sensor System. IEEE Photonics Technology Letters 2007; 19(20) 1616-1618

[68] Fernandez-Vallejo M, Bravo M, Lopez-Amo M 200-km long fiber ring laser for multiplexing fiber Bragg gratings arrays. In proceedings of the SPIE 22th International Conference on Optical Fibre sensors, OFS-22, 15-19 October 2012, Pekin, China, 84218J.

[69] Fernandez-Vallejo M, Rota-Rodrigo S, Lopez-Amo M. Remote (250 km) fiber Bragg grating multiplexing system. Sensors 2011; 11(9) 8711-8720

[70] Saitoh T, Nakamura K, Takahashi Y, Iida H, Iki Y, Miyagi K. Ultra-long-distance (230 km) FBG sensor system. In proceedings of the SPIE 19th International Conference on Optical Fiber Sensors, OFS-19, 14-18 April 2008, Perth, Western Australia, 70046C-70046C-4

[71] Rao YJ, Feng S, Jiang Q, Ran Z. Ultra-long distance (300km) fiber Bragg grating sensor system using hybrid EDF and Raman amplification. In proceedings of the SPIE 20th International Conference on Optical Fiber Sensors, OFS-20, 5-9 Oct 2009, Edinburgh, United Kingdom, 75031Q-75031Q-4

[72] http://www.olympusmicro.com/primer/java/lasers/gainbandwidth/index.html

[73] Digonnet MJF, editor. Rare-Earth-Doped Fiber Lasers and Amplifiers. Second Edition. Boca Ratón, EEUU: CRC Press, Taylor & Francis Group; 2001

[74] Snitzer, E. Optical Maser Action of Nd+3 in a Barium Crown Glass. Physical Review Letters 1961; 7(12) 444-446

[75] Kersey AD, Morey WW. Multi-element Bragg-grating based fibre-laser strain sensor. Electronics Letters 1993; 29(11) 964-966

[76] Koo K, Kersey A, Bucholtz F. Fiber Bragg grating laser magnetometer. In proceeding of the Conference on Lasers and Electro-Optics, postdeadline paper PD41, 1995, Baltimore, Maryland

[77] Taylor JR. Soliton fiber lasers. In proceedings of the Conference on Lasers and Electro-Optics, paper CWM3, 1995, Baltimore, Maryland

[78] Koechner W, editor. Solid State Laser Engineering. Berlin: Springer, 2006.

[79] Liu XS, Zhan L, Hu X, Li HG, Shen QS Xia YX. Multiwavelength erbium-doped fiber laser based on nonlinear polarization rotation assisted by four-wave-mixing. Optics Communications 2009; 282(14) 2913-2916

[80] Zhang K, Kang JU. C-band wavelength-swept single-longitudinal mode erbium-doped fiber ring laser. Optics Express 2008; 16(18) 14173-14179

[81] Ibsen M, Ronnekleiv E, Cowle GJ, Zervas MN, Laming RI. Multiple wavelength all-fibre DFB lasers. Electronics Letters 2000; 36(2) 143-144

[82] Yamashita S, et al. Multiwavelength Er-Doped Fiber Ring Laser Incorporating Highly Nonlinear Fiber. Japanese Journal of Applied Physics 2005; 44(33-36) L1080-L1081

[83] Humphrey PD, Bowers JE. Fiber-birefringence tuning technique for an erbium-doped fiber ring laser. IEEE Photonics Technology Letters 1993; 5(1) 32-34

[84] Chieng YT, Minasian RA. Tunable erbium-doped fiber laser with a reflection Mach-Zehnder interferometer. IEEE Photonics Technology Letters 1994; 6(2) 153-156

[85] Quintela MA, Perez-Herrera RA, Canales I, Fernandez-Vallejo M, Lopez-Amo M, Lopez Higuera JM. Stabilization of dual-wavelength erbium doped ring fiber lasers by single-mode operation. IEEE Photonics Technology Letters 2010; 22(6) 368-370

[86] Kashyap RP et al. All-fibre narrowband reflection gratings at 1500 nm. Electronics Letters 1990; 26(11) 730-732

[87] Ball GA, Morey WW. Continuously tunable single-mode erbium fiber laser. Optics Letters 1992; 17(6) 420-422

[88] Perez-Herrera RA, et al. L-Band Multiwavelength Single-Longitudinal Mode Fiber Laser for Sensing Applications. IEEE Journal of Lightwave Technology 2012; 30(8) 1173-1177, art. no. 6062627

[89] Hanna DC, et al. Continuous-wave oscillation of a monomode ytterbium-doped fibre laser. Electron. Letters 1988; 24(17) 1111-1113

[90] Allain JY, Bayon JF, Monerie M, Bernage P, Niay P. Ytterbium-doped silica fiber laser with intracore Bragg gratings operating at 1.02 μm. Electronics Lett. 1993; 29(3) 309-310

[91] Ball GA, Morey WW, Glenn WH. Standing-Wave Monomode Erbium Fiber Laser. IEEE Photonics Technology Letters 1991; 3(7) 613-615

[92] Sun J, Huang L. Single-longitudinal-mode fiber ring laser using internal lasing injection and self-injection feedback. Optical Engineering 2007; 46(7) 074201-1-6

[93] Kim HK, Kim SK, Kim BY. Polarimetric fibre laser sensors using Er-doped fibre. Optical and Quantum Electronics 1995; 27(5) 481-485

[94] Ball GA, Morey WW, Cheo PK. Singlepoint and multipoint fiber-laser sensors. IEEE Photonics Technology Letters 1993; 5(2) 267–270

[95] Lin C, Cohen LG, Stolen RH, Tasker GW, French WG. Near-infrared sources in the 1–1.3 μm region by efficient stimulated Raman emission in glass fibers. Optics Communications 1977; 20(3) 426–428

[96] Gapontsev DV, Chernikov SV, Taylor JR. Fibre Raman amplifiers for broadband operation at 1.3 μm. Optics Communications 1999; 166(1) 85-88

[97] Kani J, Jinno M, Oguchi K. Fibre Raman amplifier for 1520nm band WDM transmission. Electronics Letters 1998; 34(18) 1745-1747

[98] Masuda H, Kawai S, Suzuki K-I, Aida K. 1.65 μm band fibre Raman amplifier pumped by wavelength-tunable amplified spontaneous emission light source. Electronics Letters 1998; 34(24) 2339-2340

[99] Hansen PB, Eskildsen L, Grubb SG, et al. Capacity upgrades of transmission systems by Raman amplification. IEEE Photonics Technology Letters 1997; 9(2) 262–264

[100] Rottwitt K, Kidorf HD. A 92 nm bandwidth Raman amplifier. In proceedings of Optical Fiber Communication Conference, OFC, 22 Feb 1988, Postdeadline Paper PD6, San Jose, California.

[101] Rottwitt K, Stentz A, Nielson T, Hansen P, Feder K, Walker K. Transparent 80 km bidirectionally pumped distributed Raman amplifier with second order pumping. In proceedings of the European Conference on Optical Communication, ECOC′99, 26-30 Sept 1999, II-144–145, Nice, France.

[102] Fernandez-Vallejo et al. Resilient long-distance sensor system using a multiwavelength Raman laser. Measurement Science and Technology 2010; 21(9), art. no. 094017.

[103] Rao Y-J, Ran Z-L, Chen R-R. Long-distance fiber Bragg grating sensor system with a high optical signal-to-noise ratio based on a tunable fiber ring laser configuration. Optics Letters 2006; 31(18) 2684-2686

[104] Fernandez-Vallejo M et al. Remote (250 km) Fiber Bragg Grating Multiplexing System. Sensors 2011; 11(9) 8711-8720

[105] Rao Y-J, Feng S, Jiang Q, Ran Z-L. Ultra-long distance (300km) fiber Bragg grating sensor system using hybrid EDF and Raman amplification. In proceedings of the SPIE 20th International Conference on Optical Fiber Sensors, OFS-20, 5-9 Oct 2009, Edinburgh, United Kingdom, 75031Q-75031Q-4

[106] Al-Mansoori MH et al. Widely tunable linear cavity multi-wavelength Brillouin-Erbium fiber lasers. Optics Express 2005; 13(9) 3471-3476

[107] Noginov MA, Zhu G, Small C, Novak J. Neodymium random laser with external mirrors. Applied Physics B: Lasers and Optics 2006; 84(1-2) 269-273

[108] Noginov MA, editor. Solid-State Random Lasers. USA: Springer, 2005

[109] Noginov MA, Noginova N, Egarievwe SU, Wang JC, Caulfield HJ. Nonlinear Optical Phenomena and Coherent Optics in information Technologies. In: Chesnokov SS, Kandidov VP, Koroteev NI (Eds.) ICONO'98, 29 June-3 July 1998, Moscow, Russia

[110] Pinto AMR, Frazão O, Santos JL, Lopez-Amo M. Multiwavelength Raman Fiber Lasers Using Hi-Bi Photonic Crystal Fiber Loop Mirrors Combined With Random Cavities. Journal Of Lightwave Technology 2011; 29(10) 1482-1488

[111] Headley C, Agrawal GP, editor. Raman Amplification in Fiber Optical Communication Systems. London, U.K.: Elsevier Academic Press, 2005

[112] Pinto AMR, Frazao O, Santos JL, Lopez-Amo M. Multiwavelength fiber laser based on a photonic crystal fiber loop mirror with cooperative Rayleigh scattering. Appl. Phys. B. 2010; 99(3) 391–395

[113] Zamzuri AK, et al. Contribution of Rayleigh scattering on Brillouin comb line generation in Raman fiber laser. Appl. Opt. 2010; 49(18) 3506–3510

[114] Park KD, et al. Dynamics of cascaded Brillouin-Rayleigh scattering in a distributed fiber Raman amplifier. Optics Letters 2002; 27(3) 155–157

[115] Giraldi MTM, et al. Rayleigh assisted Brillouin effects in distributed Raman amplifiers under saturated conditions at 40Gb/S. Microw. Opt. Technol. Lett. 2010; 52(6) 1331–1335

[116] Min B, Kim P, Park N. Flat amplitude equal spacing 798-channel Rayleigh-assisted Brillouin/Raman multiwavelength comb generation in dispersion compensating fiber. IEEE Photon. Technol. Lett. 2001; 13(12) 1352–1354

[117] Shahi S, Harun SW, Norizan SF, Moghaddam MRA, Ahmad H. Brillouin-Raman multi-wavelength laser comb generation based on Bi-EDF by using dual-wavelength in dispersion compensating fiber. J. Nonlinear Opt. Phys. 2010; 19(1) 123–130

[118] Zamzuri AK, et al. Flat amplitude multiwavelength Brillouin-Raman comb fiber laser in Rayleigh-scattering-enhanced linear cavity. Opt. Exp. 2007; 15(6) 3000–3005

[119] Zamzuri AK, Ali MIM, et al. Brillouin-Raman comb fiber laser with cooperative Rayleigh scattering in a linear cavity. Opt. Lett. 2006; 31(7) 918–920

[120] Pinto AMR, Lopez-Amo M. Double random mirror Hi–Bi photonic crystal fiber Sagnac based multiwavelength fiber laser. Applied Physics B: Lasers and Optics 2011; 103(4) 771-775

[121] Pinto AMR, Bravo M, Fernandez-Vallejo M, Lopez-Amo M, Kobelke J, Schuster K. Suspended-core fiber Sagnac combined dual-random mirror Raman fiber laser. Optics Express 2011; 19(12) 11906-11915

[122] Midwinter, JE. The theory of Q-switching applied to slow switching and pulse shaping for solid state lasers. British Journal of Applied Physics 1965; 16(8) 1125-1133

[123] Fernández-Vallejo M, et al. Fiber Bragg Grating interrogation technique for remote sensing (100km) using a hybrid Brillouin-Raman fiber laser. In proceedings of the SPIE 21st International Conference on Optical Fiber Sensors, OFS-21, 15-19 May 2011, Ottawa, Canada, 77537I

[124] Leandro D. et al. Remote (155 km) Fiber Bragg Grating Interrogation Technique Combining Raman, Brillouin, and Erbium Gain in a Fiber Laser. IEEE photonics technology letters 2011; 23(10)

Section 5

Optical Fiber Measurement and Device

Characterization of Optical Fibers by Multiple-Beam Interferometry

Fouad El-Diasty

Additional information is available at the end of the chapter

http://dx.doi.org/10.5772/54720

1. Introduction

Optical fibers as circular dielectric optical waveguides made of silica glass with the lowest loss and the most carefully controlled index. Doping with impurity oxides such as Germenia GeO_2, Titania TiO_2, Caesia Cs_2O, Alumina Al_2O_3, Zirconia ZrO_2 and Phosphorus pentaoxide P_2O_5 rises the refractive index of pure silica in the core region. [1] Doping with Boria B_2O_3 or Fluorine F inferiors the refractive index of the cladding. [2] Rare-earth ions such as $ErCl_3$ and Nd_2O_3 have been used in order to make fiber amplifiers and fiber lasers. [3] Polymer optical fibers are also achieved with increased attention for short-haul transmission of light, although these fibers are limited to multi-mode dimensions. [4]- [9]

In addition to the application in fast high capacity telecommunication, optical fibers are used as sensors to measure many different quantities. [10]- [11] Fiber gratings can function as mirrors [12], in which a forward-propagating mode guided by the fiber core couples to a backward-propagating mode of the same type [13]. They also can be used as mode converters, in which one type of guided core mode couples to different type of cladding mode. [14] Great interest is being paid to fiber-optic devices like modulators, coupler and switches. [15]- [16]

1.1. Type of optical fibers

The structure (geometric shape and index profile) basically establishes the information carrying capacity of the fiber and also influences the response of the fiber to environmental perturbations. Fiber modes mean field solutions of Maxwell's equations to the transverse boundary-value problem of waves that propagate without changing shape along the fiber optical axis. In case of a single-mode fiber, the fiber sustains only one mode of propagation, whereas the total number of modes M in case of multi-mode step-index fiber is given by [17]

$$M = \frac{V^2}{2} \tag{1}$$

while in case of parabolic multi-mode GRIN fiber, the number of modes is given by:

$$M = \frac{V^2}{4} \tag{2}$$

where V is the normalized frequency which can be defined as:

$$V = \frac{2\pi\ a}{\lambda}\ (\text{N.A}) \tag{3}$$

Here a is the core radius, λ is the wavelength of propagated light and N.A is the numerical aperture which is defined as:

$$\text{N.A} = \sqrt{n_{co}^2 - n_{cl}^2} \tag{4}$$

where n_{co} and n_{cl} are the core and cladding indices, respectively. Higher number of propagated modes means higher mode dispersion and hence lower data rate and less efficient transmission. This gives the reason why the single-mode fibers are preferable in very high speed telecommunication.

The refractive index profile of graded-index (GRIN) fiber is classified by two-system parameters which are giving by

$$n(r) = n_{co}\left[1 - 2\Delta n\left(\frac{r}{a}\right)^{\alpha}\right]^{1/2} \quad \text{for} \ \ r < a \tag{5}$$

$$n(r) = n_{co}\left(1 - 2\Delta n\right)^{1/2} \quad \text{for} \ \ r > a \tag{6}$$

and

$$\Delta n = \frac{n_{co}^2 - n_{cl}^2}{2n_{co}^2} \tag{7}$$

http://dx.doi.org/10.5772/54720

or

$$\Delta n = \frac{n_{co} - n_{cl}}{n_{co}} \quad \text{for} \quad n_{co} \cong n_{cl} \text{ or } \Delta n << 1 \tag{8}$$

where r is the radial distance, and α is a parameter that describes the shape of the core index profile. Δn is a measure of the index difference between the peak refractive index at the core center $n(0)$ and the cladding refractive index. For the single-mode fiber, Δn is usually in the range of $0.2\% < \Delta n < 1.5\%$; but for multi-mode fiber, the typical range is $1\% < \Delta n < 3\%$.

1.2. Dispersion and pulse propagation in optical fibers

Since the fiber is carrying a time-varying signals that comprise of multiple frequency components, so the chromatic dispersion must be considered. A medium exhibits chromatic dispersion if the propagation constant (the logarithmic rate of change with respect to the distance in a given direction of the complex amplitude of the field component) for a wave or mode varies nonlinearly with frequency. Signal distortion caused by group-velocity dispersion occurs as the different frequency components of the signal travel with different group velocities. Thus the signal components emerg from the medium with different relative time delay. Chromatic dispersion in a single-mode of optical is caused by two dependent sources:

- Material Dispersion; the refractive indices of the materials that make up the fiber waveguide depend on the optical frequency or wavelength (i.e., $n_{co} = n_{co}(\lambda)$ and $n_{cl} = n_{cl}(\lambda)$).
- Waveguide Dispersion; the effective-index of each waveguide-mode depends on the frequency or wavelength due to frequency dependence of the mode dispersion relation (i.e., $n_{eff} = n_{eff}(\lambda)$).

Material dispersion is compensated by waveguide dispersion described by the index profile. [18]- [19]

2. Characterization of optical fibers

Characterization of optical fibers means determination of both the fiber numerical aperture and the normalized frequency. This of course requires precise and sensitive measurements of very important parameters such as the index profile of both of core and cladding, index difference Δn, and the profile shaping parameter α as in case of GRIN fiber. Many of the fiber properties such as the cutoff wavelength, connection losses, and launching efficiency are determined by the refractive index profile. Also different fiber parameters can be measured from the index profile such as the induced-birefringence in optical fibers (due to external mechanical perturbations like elongation or bending of fibers [20]- [24]) or due to irradiation of the waveguide. [25]- [32] Another fiber parameters such as acceptance angle, dispersion per unit length and modal dispersion are functions of the fiber index and they need a precise measurement of the fiber index profiles. [17] As a result different methods and techniques for characterizing optical fibers and for determining their refractive indices have been developed.

2.1. Methods for investigation the structure and index of optical fibers

Various methods are reported and applied to characterize optical fibers. They are mainly:

1. Optical microscopy [33]- [34],
2. Scanning electron microscopy [35],
3. Transmission electron microscopy;
4. X-ray spectrometry [36],
5. Infrared spectroscopy [37],
6. Speckle interferometry [38], [39],
7. Reflection method [40],
8. Quarter wave plate method [24],
9. Two-beam interference microscopy [41],
10. Multiple-beam interference,
11. Tomographic back projection [42].
12. Laser Sheet of light and lens-fiber interferometer. [43]- [47]
13. Diffraction techniques. [48]- [50]

Among them, the most reliable and precise technique is the interferometric method. [41] From the obtained interferogram the method determines the path shift of the ray transmitted through the fiber sample (the fiber is considered as a phase object). The method resolves relatively the fiber structure in detail with a higher resolution giving more quantitative and qualitative results.

3. Interferometry

Superposition of two or more coherent waves (beams) originating from the same source, but traveling different paths, results dark and bright interference fringes. A bright fringe will be observed if the path difference between the interfering beams equals an integer number of wavelength. The beams, being in phase, reinforce each other and a constructive interference occurs. Destructive interference occurs and a dark fringe result if the interfering beams are 180° out of phase or half an integer number of wavelength. Thus, the interferograme is considered as a distribution of intensity and phase. Interferometers are classified by the number of interfering beams. There are; a) two-beam interferometers (TBI) or b) multiple-beam interferometers (MBI). Semi transparent mirror or beam splitter is used to separate the beams and to produce the interfering beams.

Amplitude objects vary in their light absorption with respect to surrounding medium. They do also refraction and deviation to the light beam passing through them. In contrast, phase objects produce no variation in light intensity but differ merely from the surrounding medium by their optical thickness. Optical thickness is the multiplication of refractive index of the object n by the object's metric thickness t. Application of interferometry in the field of optical fiber research considers primarily the optical fiber waveguides as a phase object. So, the variations in the fiber refractive index or its thickness, or both do shifts in the fringe position which can be measured to get information about the fiber structure.

3.1. Two-beam interferometers

The main interferometers that were developed utilizing the two-beam interference technique are; Michelson interferometer, Twyman-Green interferometer, Mach-Zehnder interferometer, Nomarski interferometer, Pluta polarizing interference microscope, Interphako interference microscope, and Baker, Dyson, Leitz, and Zeiss-Linnik interference microscopes. [51]- [54] As in Michelson interferometer, the two interfering beams have equal amplitudes but they differ in phase (δ). The resultant intensity distribution (I) follows a cosine square law given by:

$$I = I_{\circ} \cos^2\left(\frac{\delta}{2}\right) \tag{9}$$

The fiber under study is placed in quartz cell filled with an immersion liquid of uniform and known refractive index. The fiber is introduced into the path of one of the interfering beams. If the fiber axis is chosen as the z-axis while the x-axis is perpendicular the axis fiber, the equation that describes the fringe shift due to the existence of an optical fiber inside the interferometer is given by:

$$z = \frac{2\Delta z}{\lambda}\left[\left(n_{cl} - n_L\right)\left(r_{cl}^2 - x^2\right)^{1/2} + \left(n_{co} - n_L\right)\left(r_{co}^2 - x^2\right)^{1/2}\right] \tag{10}$$

where Δz is the interfringe spacing (free spectral range between two adjacent fringes) and n_L is the refractive index of immersion liquid.

If n^{II} and $n^{\perp}$ are the mean refractive indices of the fiber for plane polarized light vibrating in two planes parallel and perpendicular to the fiber z-axis respectively, then both of n^{II} and $n^{\perp}$ and the index difference Δn, for fiber with irregular and/or non-irregular transverse sections, are given by:

$$n^{\mathrm{II}} = n_L + \frac{F^{\mathrm{II}}\lambda}{\Delta z A} \tag{11}$$

$$n^{\perp} = n_L + \frac{F^{\perp}\lambda}{\Delta z A} \tag{12}$$

and

$$\Delta n = \left(\frac{F^{\mathrm{II}} - F^{\perp}}{\Delta z} \right) \frac{\lambda}{A} \tag{13}$$

where A and F are the mean cross sectional area of the fiber and the area under the fringe shifts.

According to the interferometric slab method [55]- [64], a thin slab of thickness 0.1 - 0.5 mm is cut out perbendicular to the fiber optic axis remaining the thickness t of the slab constant over the entire slab area to within a fraction of the wavelength of light. To measure the index profile of the fiber, the slab is placed in one arm of an interference microscope, and a reference slab with a refractive index equals the cladding index is placed in the second arm of the microscope. If the two mirrors are slightly inclined, a system of equally spaced fringes with two-beam intensity distribution is formed, see Fig. 1. The core refractive index can be described by:

$$n(x,y) = n_{cl} + \frac{\lambda\lambda\, z(x,y)}{t\, \Delta z} \tag{14}$$

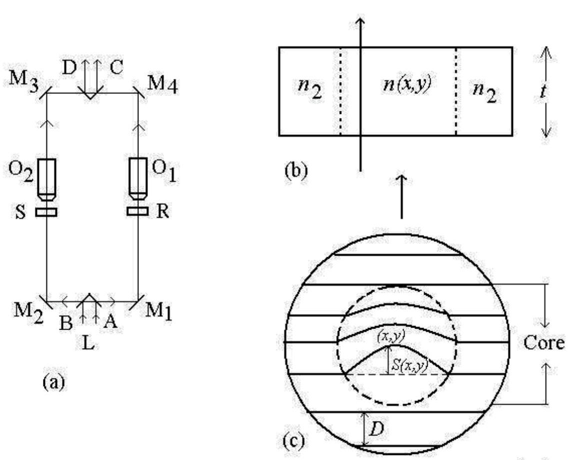

Figure 1. (a) A two-beam single-pass interference microscope. L is the incident light, M_1, M_2, M_3, and M_4 are mirrors. S is the slab, R is the reference slab, O_1 and O_2 are microscope objectives. A, B, C, and D are semi-transparent mirrors. (b) A slab of thickness t for a graded-index core with a cladding of refractive index n_2. (c) Interferogram in which the fringe shift $Z(x, y)$ in the core region is a function of point position x, y is shown.

Transverse two-beam interference technique [65]- [80] applied to study optical fibers requires the light to be incident perpendicular to the fiber axis. The fiber is immersed in a matching liquid whose refractive index is nearly equal to that of the fiber cladding. The technique avoids the time consuming for sample preparation which is needed in the slab method. The propagation problem associated with the reflection technique can be avoided.

Barakat et al. [81] used a Zeiss-Linnik as a two-beam interferometer to obtain interferograms of fusion-spliced fibers. A common feature is the presence of buckling of the fiber material on both sides of the splicing point. This resulted from the fusion splicing process. Their heights ranged from 1 to 10 μm, some 300 μm apart for graded-index fibers of 50 μm core and 125 μm cladding diameters. The power loss resulting from fusion splicing for the specimens examined interferometricaly is measured. It is found that the greater the buckling, the greater the power loss. A height of 2λ or less (λ = 535 nm) gave no detectable loss.

White-light spectral interferometric technique employing a low-resolution spectrometer is used to measure intermodal dispersion for LP_{01}^{x} and LP_{11}^{x}modes of elliptical-core optical fibers in a spectral range approximately from 540 to 870 nm. [82] The technique utilizes a tandem configuration of a Michelson interferometer and an optical fiber to measure the equalization wavelengths as a function of the optical path difference (OPD) between beams of the interferometer, or equivalently, the wavelength dependence of the intermodal group OPD in the optical fiber.

3.2. Multiple-beam interference

Multiple-beam interferometer is a device utilizes the fringes produced after multiple reflection in air film between two plates (mirrors) that thinly silvered onto their inner surfaces. The fringes (Fizeau fringes) in this case are much narrower than that in case of two-beam interference. This narrowing in the multiple-beam interference fringes gives more resolution for the spectroscopic measurements and also provides the ability to study the fine details of studied fibers and their inner structure. Fabry-Perot interferometer is an example of the multiple-beam Fizeau fringes. The two mirrors are parallel to each other to form an inner air film of constant thickness (i.e., etalon). The types of multiple-beam interference fringes that usually applied to optical fibers are:

1. multiple-beam Fizeau fringes in transmission characterized by sharp bright fringes on a dark background,
2. multiple-beam Fizeau fringes at reflection characterized by sharp dark fringes on a bright background,
3. multiple-beam fringes of equal chromatic order both in transmission and at reflection.

The theoretical expression for the intensity of the fringes was given by Airy in 1831. [83] The intensity distribution of the fringe system has the following general expression [41]

$$I = A + B + \frac{C}{1 - 2r_2 r_3 \cos\Delta + r_2 r_3} \tag{15}$$

For the transmitted system;

$$\begin{aligned} A &= B = 0 \\ C &= t_1^2 t_2^2 \end{aligned} \tag{16}$$

where A, B and C are constants depend on the used system. r_2^2 and r_3^2 are the fractions of light intensity reflected at the inner layers (glass/metal/medium and medium/metal/glass). Also t_1^2 and t_2^2 are the fractions of light intensity transmitted through the metallic layers for the upper and lower mirrors, respectively. Whereas Δ is the phase difference between any successive beams.

3.2.1. Silvered wedge interferometer

Tolansky [84] carried out analysis for the conditions needed to produce multiple-beam localized Fizeau fringes using a wedge interferometer. The successively multiple-reflected beams are not in phase in exact arithmetic series. The phase lag of the multiple-reflected beams from the arithmetic series with normal incidence is equal to [42]

$$\delta = \frac{4}{3} m^3 \varepsilon^2 \ d \tag{17}$$

where ε is the angle of the wedge, m is the order of the beam, and d is the interferometric gap thickness. To secure the Airy sum condition, the interferometric gap thickness d and the wedge angle ε must be small. The permitted limit to the phase lag (retardation) is equal to $\lambda/2$ which gives the upper limit values of d and ε. Barakat and Mokhtar [85] found out the permitted limit which gives the maximum intensity to be $\lambda / 8$ which inturn brings down the upper limit of d.

3.3. Theory of transverse multiple-beam Fizeau fringes

Since the pioneer work of Barakat [86] utilizing multiple-beam Fizeau fringes to study fibers of circular cross section and composed of single and double layers, and the Fizeau interferometry has wide applications in the fiber researches. The following section is concerned with the mathematical equation of a family of Fizeau fringes across a graded-index optical fiber. The fiber is assumed to be of a perfectly circular cross section. The fiber axis is introduced in a silvered liquid wedge and the fiber is adjusted perpendicular to the apex. Both the wedge angle and the interferometric gap should be kept small to reduce the phase lag between successive beams to produce the sharpest fringes. A parallel beam of monochromatic light presented by AB and CD is incident normal to the lower mirror of the wedge. The Fiber axis is chosen as the z-axis, and the edge of the wedge is parallel to the x-axis, see Fig. 2. For the optical path length (OPL) of the ray AB [87]

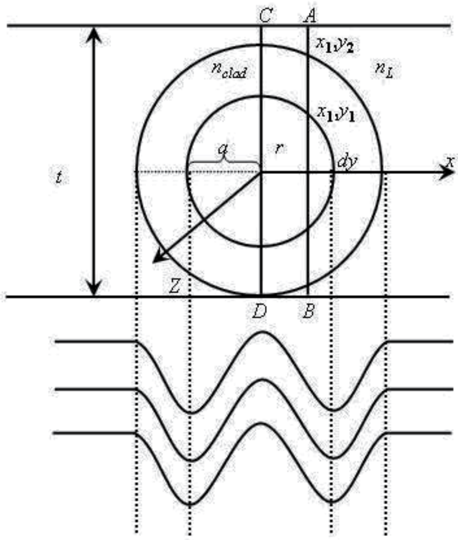

Figure 2. Cross section in a silvered liquid wedge interferometer with graded-index optical fiber of variable index core $n(r)$. A schematic representation of the resulting fringes is shown.

$$\mathrm{OPL} = (t - 2y_2)n_L + 2(y_2 - y_1)n_{cl} + \int_0^{y_1=\sqrt{a^2-x_1^2}} n(r)\,dy, \tag{18}$$

where t is the interferometric gap thickness and $n(r)$ is the core index which is defined by Eq. (5). For index difference $\Delta n \ll 1$, therefore

$$\mathrm{OPL} = (t - 2y_2)n_L + 2(y_2 - y_1)n_{cl} + 2n(0)\sqrt{a^2 - x_1^2} - 2\frac{\Delta n}{a^\alpha}\int (x_1^2 + y^2)^{\alpha/2}dy \tag{19}$$

On a fringe of order of interference N,

$$N\lambda \ = \ 2(\mathrm{OPL}) = 2n_L t + 4y_2(n_{cl} - n_L) + 4\Delta n y_1 - \frac{4\Delta n}{a^\alpha}\int_0^{\sqrt{a^2-x_1^2}} (x_1^2 + y^2)^{\alpha/2}dy \tag{20}$$

For $t = z \tan \varepsilon$

$$(N\lambda \ -2n_L z \tan\varepsilon \ ) = 4y_2(n_{cl}-n_L) + 4\Delta n y_1 - \frac{4\Delta n}{a^\alpha}\int_0^{\sqrt{a^2-x_1^2}}(x_1^2+y^2)^{\alpha/2}dy \tag{21}$$

Transforming to the point (0, $N\lambda/2n_L$ tanε) it gives

$$z\cdot 2n_L \ \tan\varepsilon = 4y_2\left(n_{cl}-n_L\right) + 4\Delta n y_1 - \frac{4\Delta n}{a^\alpha}\int_0^{\sqrt{a^2-x_1^2}}\left(x_1^2+y^2\right)^{\alpha/2}dy \tag{22}$$

The fringe spacing between any two consecutive fringes in the liquid region and is equal to $\lambda/2n_L$ tanε. If z is the fringe shift of the Nth order in the fiber region from its position in the liquid region, this leads to

$$\begin{aligned}\left(\frac{z}{\Delta z}\right)\cdot\lambda/2 &= 2\left[y_2\left(n_{cl}-n_L\right)+\Delta n y_1 - \frac{\Delta n}{a^\alpha}\int_0^{\sqrt{a^2-x_1^2}}\left(x_1^2+y^2\right)^{\alpha/2}dy\right] \\ &= 2\left[\left(n_{cl}-n_L\right)\sqrt{r_f^2-x_1^2}+\Delta n\sqrt{a^2-x_1^2} \ -\frac{\Delta n}{a^\alpha}\int_0^{\sqrt{a^2-x_1^2}}\left(x_1^2+y^2\right)^{\alpha/2}dy\right]\end{aligned} \tag{23}$$

This gives the required equation giving ($z/\Delta z$) for any value of x_1 where $0 \le x_1 \le a$ in terms of Δn and α. Substituting for $x_1 = 0$ gives the following expression

$$\left(\frac{z}{\Delta z}\right)\cdot\frac{\lambda}{2} = \left(n_{cl}-n_L\right)t_f + t_{co}\cdot\Delta n\frac{\alpha}{\left(\alpha+1\right)} \tag{24}$$

where $t_{co} = 2a$ and $t_f = 2y_2$.

In contrast with the case of step-index fibers when $\alpha = \infty$, the following equation can be given:

$$\left(\frac{z}{\Delta z}\right)\cdot\frac{\lambda}{2} = \left(n_{cl}-n_L\right)t_f + t_{co}\left(n_{co}-n_{cl}\right) \tag{25}$$

Fig. 3 illustrates an interferogram of Fizeau fringe in case of straight fiber immersed in a matching liquid and non-matching one. While in the second case the liquid index is less than that of fiber cladding. It could be seen that, the refractive index profile of the cladding of a straight fiber is symmetric at each point across the fiber cross section. Instead of measuring the fringe shift, the refractive index of a regular multi-layer fiber can be measured by another method developed by Hamza et al. [86] where it depends on measuring the enclosed area under the interference fringe shift F_m of mth fiber layer and the mathematical expression is given by:

$$\frac{\lambda\ F_m}{4\Delta z} = \sum_{j=1}^{m} (n_j - n_{j-1})\ A_{j,m} \tag{26}$$

where j is the number of layers and $A_{j,m}$ is the cross-sectional area of the fiber layers that is defined as

$$A_{j,m} = \int_{r_{m-1}}^{r_m} \sqrt{r_m^2 - x^2}\, dx \tag{27}$$

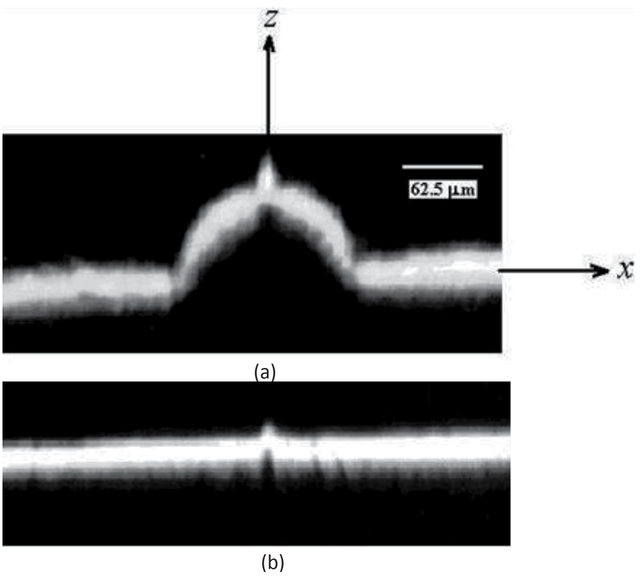

Figure 3. Interferograms of Fizeau fringe shape in case of straight fiber immersed in; (a) non-matching liquid and (b) matching liquid.

The advantage of this method is the ability to determine the refractive indices of fibers which have irregular cross-sections, where the optical properties of multiple-skin fibers of elliptical and rectangular cross sections are obtained. [88]- [91]

The minimum variance technique is used to calculate both α and Δn from the fringe shift. [92] The effect of the immersion liquid on the shape of the fringes crossing the core and the cladding has been dealt with to examine the fiber cladding and its index homogeneity, presenting a method to control the process of cladding production. [93] Barakat et al. [94] studied also the existence of successive layers forming a graded-index fiber core. Both thickness and approximate refractive index graded from one layer to another have been estimated. The fiber is found to be formed from a succession of step-index layers, $n(r)$, which remains constant over the interval thickness Δr, follows the known function relating $n(r)$ with r in terms of $n(r = 0)$ and

α, see Fig. 4. Making an analysis to the shape of a Fizeau fringe crossing GRIN fiber to its elements, it is found that the fringe is consist of two half ellipses and a saddle. [95] For a step-index fiber, the elements contributing to its fringe shape are merely two half ellipses. Using a matching liquid they could cancel the outer half ellipse in both cases. The central dip contributes an extra half ellipse and a saddle over the dip but in reverse direction away from the wedge apex. Canceling the cladding by using a matching liquid and measured the area enclosed under the core shift, an exact solution of the integration which is required to get the values of α and Δn is found. [96] An image processing system is used to analyze the multiple-beam fringes crossing optical fiber immersed in matching and non-matching liquids. [97]

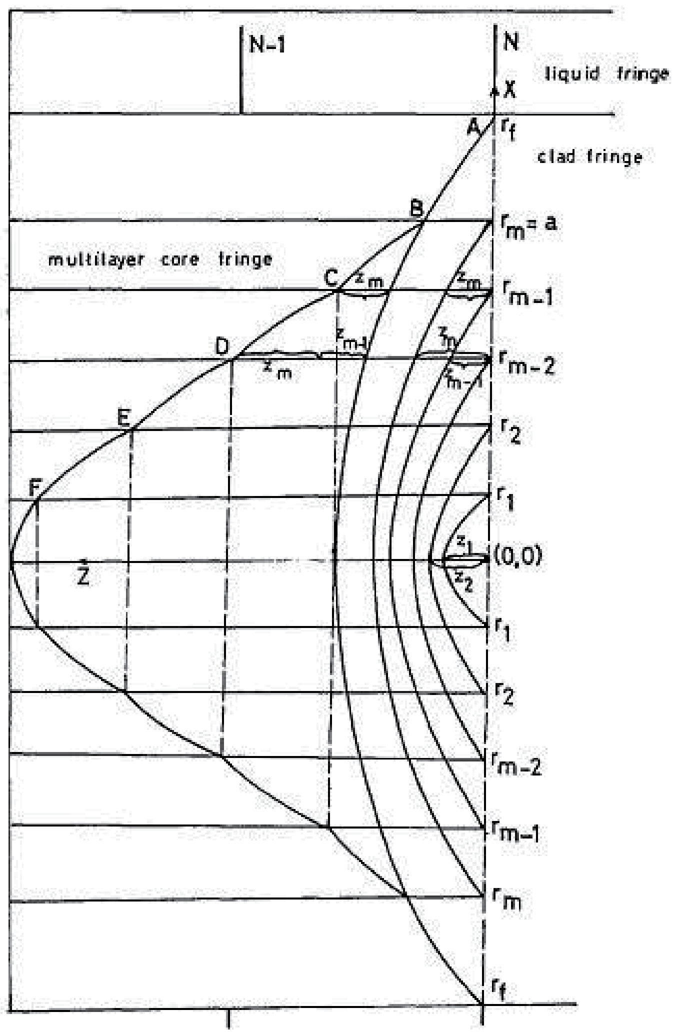

Figure 4. Shape of multi-layer core fringes, resulting from summing the contribution of each core layer in addition to the cladding of the fiber whrn immersed in a silvered liquid wedge.

http://dx.doi.org/10.5772/54720

Multiple-beam Fizeau fringes acrossing a GRIN fiber immersed in a silvered liquid wedge together with computerized optical tomographic back projection technique are used to obtain a three-dimensional refractive index profile of optical fiber core. [98] An opto-thermal device attached to automate Fizeau interferometer is used to investigate the influence of temperature on opto-thermal properties of multi-mode graded-index (GRIN) optical fiber and on fiber strucutre in a range from 27 to 54 °C. [99]- [101] Multiple-beam interferometry (MBI) of the Fizeau type is used to investigate multi-mode step-index optical fibers. Two different types of multi-mode step-index optical fibers are studied. [102]- [105] The first has a plastic cladding and silica core (the problems of studying this type of fiber and how to overcome these problems are outlined). The second fiber is a multi-mode multi-step-index (quadruple-layer) optical fiber.

Since the fringe shift across the fiber region is a function in the geometry of the different regions of the fiber and the refractive index profile of the fiber, therefore theoretical models for the fringe shift across double-clad fibers (DCFs) with rectangular, elliptical, circular, and D-shaped inner cladding are developed. [106] An algorithm to reconstruct the linear and nonlinear terms of the refractive index profile of the DCF is outlined where numerical examples are provided and discussed.

Derived mathematical expressions are used to determine the fiber dip parameters such as index difference and the dip shape parameter from interferograms of multiple-beam Fizeau fringes crossing GRIN fibers, as shown in Fig. 5. The optical fiber is of radius r_f and having a cladding of constant refractive index n_{cl}, a graded-index core of variable refractive index $n_c(r)$ and radius r_c and a graded-index dip of variable refractive index $n_d(r)$ and radius r_d. The fiber is immersed in a liquid of refractive index n_L close to n_{cl}. The equation represents the shape of multiple-beam Fizeau fringes in the dip region, i.e., for a radial distance x_1, where$0 \le x_1 \le r_d$, is given by: [107]

$$\begin{aligned}\left(\frac{z}{\Delta z}\right)_{x_1} \cdot \frac{\lambda}{2} = 2\{&(n_{cl} - n_L)\sqrt{r_f^2 - x_1^2} + \Delta n_c \sqrt{r_c^2 - x_1^2} \\ &- \frac{\Delta n_c}{(r_c - r_d)^{\alpha_c}} \int_{\sqrt{r_d^2 - x_1^2}}^{\sqrt{r_c^2 - x_1^2}} \left[\sqrt{x_1^2 + y^2} - r_d\right]^{\alpha_c} dy - \Delta n_d \sqrt{r_d^2 - x_1^2} \\ &+ \frac{\Delta n_d}{r_d^{\alpha_d}} \int_0^{\sqrt{r_d^2 - x_1^2}} \left(x_1^2 + y^2\right)^{\alpha_{d/2}} dy\}\end{aligned} \tag{28}$$

where $\Delta n_c = n_c(r_d) - n_{cl}$ and α_c is a shaping parameter controlling the shape of the core index profile. Also, $\Delta n_d = n_c(r_d) - n_d(0)$and α_d is a parameter controlling the shape of the dip index profile. $\Delta z = \lambda / z n_L$ is the fringe spacing in the liquid region and z is the fringe shift in the fiber region. In the case of GRIN optical fiber having a dip of constant refractive index n_d, the mathematical expression of the shape of Fizeau fringes across this type of optical fiber will take the form: [107]

$$\left(\frac{z}{\Delta z}\right)_{x_1}\cdot\frac{\lambda}{2}=2\{(n_{cl}-n_L)\sqrt{r_f^2-x_1^2}+\Delta n_c\sqrt{r_c^2-x_1^2}-[n_c(r_d)-n_d]\sqrt{r_d^2-x_1^2}$$
$$-\frac{\Delta n_c}{(r_c-r_d)^{\alpha_c}}\int_{\sqrt{r_d^2-x_1^2}}^{\sqrt{r_c^2-x_1^2}}\left[\sqrt{x_1^2+y^2}-r_d\right]^{\alpha_c}dy\} \tag{29}$$

So, in case of GRIN optical fibers having no cetral index dip Eq.(28) is converted to be Eq.(23).

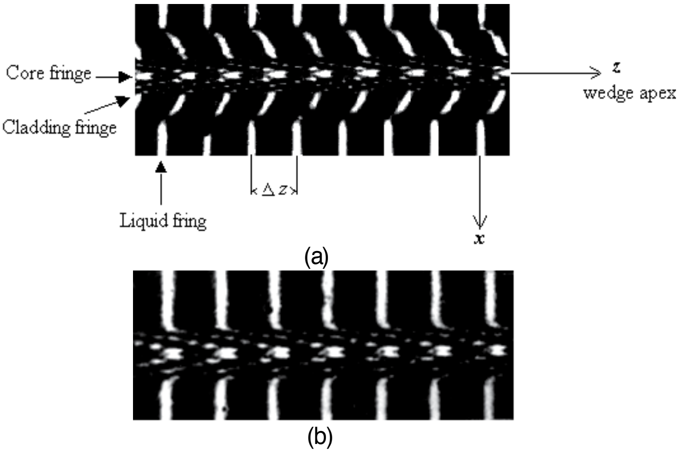

Figure 5. Multiple-beam Fizeau fringes interferogram in transmission crossing immersed GRIN fiber in a) liquid has a small refractive index than the fiber cladding and b) matched liquid.

3.4. Fiber-index determination considering refraction due to fiber layers

Fiber that being used in telecommunication has a small numerical aperture. Therefore, the change in optical path due to refraction must be taken in account to get an precise measurement of the fiber index profiles. Kahl and Mylin [108] used the ray tracing method to study analytically the effect of refractive deviation on interferograms of cylindrical and planer objects. The results indicated that the effects are additive and classified into three categories: disturbed deviation due to object only, misfocusing deviation and deviation in dense thick plates. The effect of refraction on a ray crossing the fiber perpendicular to its optic axis is studied [87]- [88] where the defocusing effect and the immersion-object index mismatch is taken into account. [109]- [111] The fringe shift and ray deflection function has been correlated to determine precisely the index profiles of preforms and optical fibers.

http://dx.doi.org/10.5772/54720

3.5. Multiple-beam interferometry for studing bent fibers

The induced-birefringence due to bending in the cladding of single-mode optical fiber has been investigated applying interferometric method. [112]- [128] Using wedge interferometer, the refractive indices for plane polarized light vibrating parallel (‖) and perpendicular (⊥) to the optic axis of a bent fiber represent the parameters that characterize the induced-birefringence (β) where the induced-birefringence is is given by:

$$\beta = n^{\parallel} - n^{\perp} \tag{30}$$

Considering the photo-elastic theory, the induced-birefringence as a measure of index isotropy is a second-rank tensor. It represents the changes of coefficients in the optical indicatrix or ellipsoid in the presence of applied stresses. The principal birefringence axes in case of elastic deformation coincide with the principal stress-strain axes. Fresnel's refractive index, cauchy's stress and the indicatrix or the strain ellipsoide are coaxial. [112] Due to the existence of a compression stress on one side of the fiber and a tensile stress on the other side, the fringe shift of the Fizeau fringe system of a bent single-mode optical fiber appears as anti-parallel hook-like shape fringe shifts one in each cladding side as shown schematically in Fig. 6. [113] The fringe shift $z(x)$ is considered positive in the direction of increasing n (towards the apex), while the shift is considered negative in the direction of decreasing n (away from the apex).

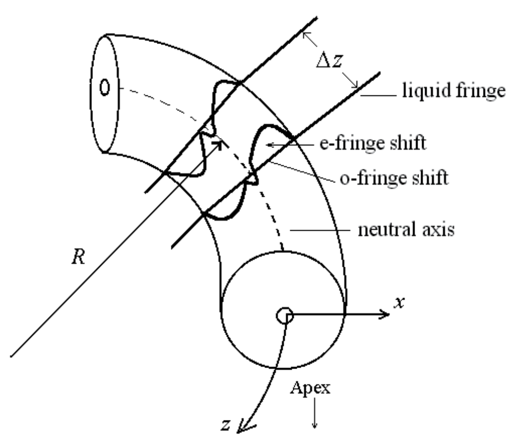

Figure 6. Schematic representation of multiple-beam Fizeau fringes in transmission applied to determine the refractive index profiles of a bent step-index optical fiber.

With a matching immersion liquid, the interferogram of the induced-birefringence of the cladding is composed of two components. One of the two fringe components ($n^{\perp}$) that represents ordinary index component shows no fringe deviation with respect to the liquid fringe position. It means that variation of the bending radius has no detectable influence on this component. Therefore $n^{\perp}$ is equal to n_L, while the shifted component (n^{II}) of β which represents the extra-ordinary index component is dependent on the radius of curvature, R.

Considering the parallel component of the refractive index of the cladding, at the compressed side of the fiber the cladding index increases and it is given by:

$$n_{cl}^{\mathrm{II}} = n_L + \frac{z_{com}(x)\lambda}{4\Delta z}\left(r^2 - x^2\right)^{-1/2} \tag{31}$$

Whereas in the tensile side of the fiber the cladding index decreases and it is described by:

$$n_{cl}^{\mathrm{II}} = n_L - \frac{z_{ten}\left(x\right)\lambda}{4\Delta z}\left(r^2 - x^2\right)^{-1/2} \tag{32}$$

The extra-ordinary component of the refractive index of bent fiber n^{II} as a function of radius of curvature is given by: [114]

$$n^{\mathrm{II}} = n_o + (n_{\mathrm{o}}^3/2)[\rho_{12}(1-\nu) - \nu\rho_{11}](x/R) \tag{33}$$

where n_{o} is the index of straight and strain-free fiber, v is Poisson's ratio. $\rho_{11}$and ρ_{12} are the strain-optic coefficients. For a fused silica fiber ρ_{11}= 0.12, ρ_{12}= 0.27 and ν = 0.17 ± 0.02. [112], [115], [116]

The radial change of the refractive index and the related induced-birefringence in the cladding of a bent single-mode optical fiber has been measured to an accuracy of 1×10^{-4}. [113] The principal stresses in the cladding of single-mode optical fiber due to bending are demonstrated. [117] The study represented a nonlinear relation between the difference of maximum radial values of the cladding's refractive indices versus the radii of curvature in the cladding of the bent optical fibers.

The relation discribes the asymmetric distribution of the compression and tensile stresses over the fiber cross section rather than the shift in the centroid (neutral axis). An inverted Z-like shape has been detected in the fiber cladding between the maximum birefringence across the fiber and the radii of curvature, as shown in Fig. 7. [119] The angle between the direction of the fringe shift representing the birefringence and the radial direction provides a direct measure of the induced-birefringence. The method requires no precise polarizing optics, or complicated mechanical equipment, or variation of angle of incidence, or precise light intensity comparisons. Applying the forward scattering technique confirmed that the asymmetry distribution of the modulus value due to asymmetric index profile could be attributed to a shift in the fiber centroid (neutral axis) rather than a deviation in the circular fiber cross section due to a deformed elliptical cross section which could result under the effect of bending. Multiple-beam Fizeau interferometry is used to evaluate the acceptance angle, numerical aperture, and V number profiles of the bent multimode graded-index (GRIN) fiber, as shown in Fig. 8. [122]

http://dx.doi.org/10.5772/54720

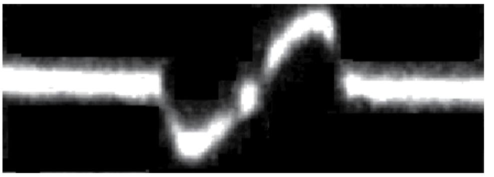

Figure 7. Interferogram of extraordinary Z-like shap fringe shift of bent sigle-mode optical fiber.

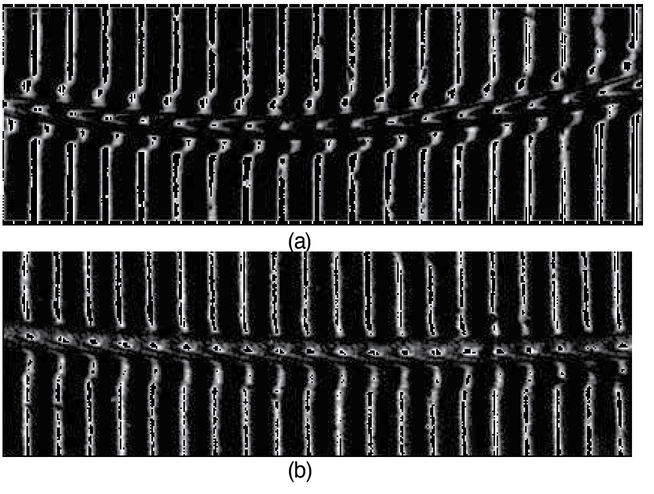

Figure 8. Multiple-beam Fizeau fringes interferogram in transmission crossing an immersed GRIN bent fiber in a) extrordinary fringe shift component and b) ordinary one.

3.6. Nonlinearity in bent optical fibers

In addition multiple-beam interferometry provides determination of nonlinearity (due to Kerr effect) in fibers such as third-order susceptibility $\chi^{(3)}$ and second-order refractive index n_2 are usually associated with all-optical effects such as modulation, soliton, switching, etc. Therefore the profiles of the induced variations of second-order refractive index and complex nonlinear third-order susceptibility components, i.e., the dispersive and absorptive are investigated in both the core and cladding of straight double-clad and macro-bent single-mode optical fibers are studied applying Fizeau interferometry. [129]- [131] The study is done on a standard single-mode fiber at two IR fundamental operating wavelengths, 1300 and 1550 nm and at radii of curvature from 5 mm to 11mm. The studies revealed an asymmetry in optical nonlinearity subsisted between the tensile and compressed sides of bent fibers due to the asymmetry in Young's modulus of the fiber material.

Multiple-beam white light interference fringes or fringes of equal chromatic orders (FECOs) are powerful and sensitive method in many field of applications. [132] The fringes are used to determine optical properties of a monomode fiber and a GRIN optical waveguide. [133]- [136]

By this method, a single interferogram of FECOs is enough to give all the needed information revealing the optical fiber parameters across the visible spectrum with sufficient accuracy.

4. Experimental setup for multiple-beam Fizeau fringes

Figs. 9 and 10 represent the wedge interferometer and setup used to produce multiple-beam Fizeau fringes in transmission. S is a low pressure Hg lamp with a green filter, L_1 is a condensing lens with a wide aperture and a short focal length, and P is an adjustable pinhole. L_2 is a collimating lens with a long focal length, W is the liquid wedge interferometer, and M is a microscope with a CCD camera attached with a PC computer. This processing enable the locateation of the peak of the fringe with an accuracy of approximately 1 pixel, i.e., 1.39 μm. The wedge interferometer consists of two circular optical flats usually 60 - 100 mm in diameter, 10 mm thick and flat to ± 0.01 μm. The inner surface of each flat is coated with a highly reflecting partially transmitting silver layer (reflectivity ≈ 70%). The two optical flats are fixed in a special jig. A drop of immersion liquid with a refractive index near by the cladding index is introduced on the sliver layer of the lower optical flat. The fiber under investigation is immersed in the liquid and the second flat is brought to form a silvered liquid wedge.

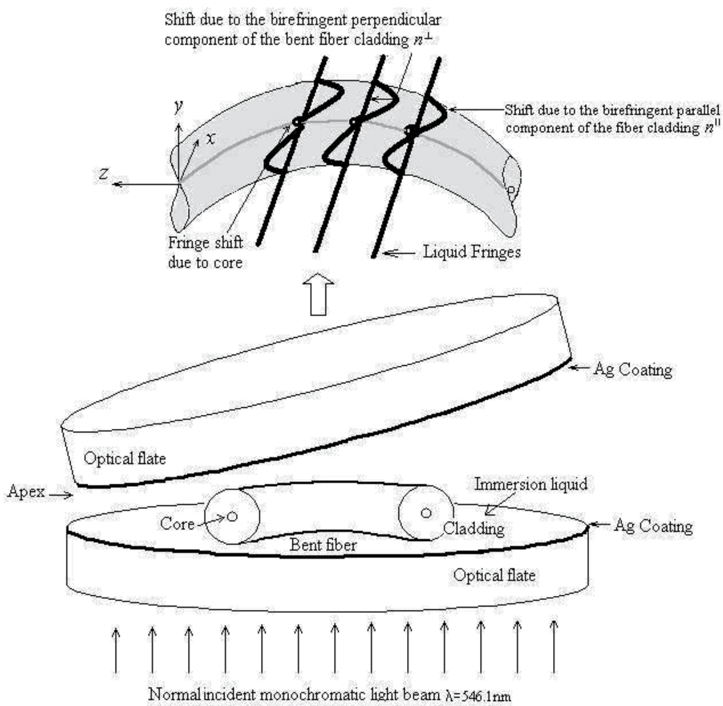

Figure 9. A schematic diagram represents the wedge interferometer and the Fizeau fringes at transmission crossing perpendicularly a bent single-mode fiber.

http://dx.doi.org/10.5772/54720

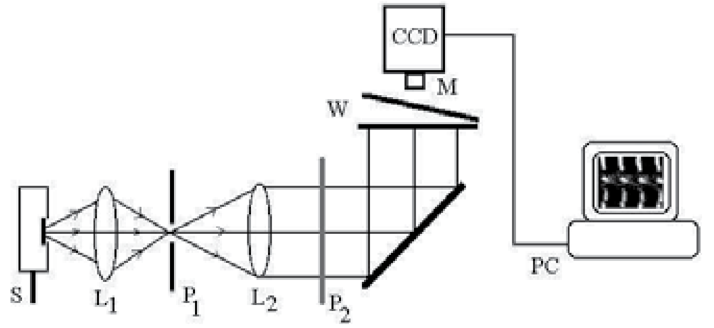

Figure 10. The optical setup for measuring the refractive index profiles of optical fibers using wedge interferometer.

A suitable immersion liquid could be prepared by mixing two different volumes of stable, clear and non-volatile liquids. α-boromonaphtalene (n = 1.6585 at 293 K) and liquid paraffine (n = 1.4500 at 293 K) might be chosen. In case of mixture of two liquids 1 and 2, the refractive index of the mixture of the immersion liquid is

$$n_L = \frac{(n_1 \mathrm{v}_1 + n_2 \mathrm{v}_2)}{\mathrm{v}_1 + \mathrm{v}_2} \tag{34}$$

where n_1 and n_2 are the refractive indices of the components, respectively. v_1 and v_2 are the volumes of the components, respectively. The interferometer is set on the microscope stage. A parallel beam of monochromatic light of known wavelength illuminates the wedge interferometer. The interferometer is adjusted so that the Fizeau fringes crossed the fiber nearly perpendicular to its optic axis, while in the liquid region they are straight lines parallel to the edge of the wedge (apex).

To obtain the sharpest fringes across the fiber, capable of revealing the fiber structure and to measure its index profile, the phase lag has to be suppressed. Both the gap thickness and the wedge angle are adjusted to reduce the phase lag and thus produce sharpest fringes across the fiber. [85]The wedge angle has to be in the range of 5×10^{-3} to 1×10^{-4} rad to be able to suppress the phase lag. The refractive index profile of the bend fiber is divide into two components; normal and parallel one. For the ordinary component (the normal one), the refractive index profile is kept unchanged similar to the case of straight fiber. But for the extra ordinary component, parallel component, the refractive index profile change across the fiber radius. In the compressed region the refractive index increases as it goes away from the fiber optic axis, i.e., neutral axis. While in tensile region, the refractive index decreases reaching its minimum values at the fiber outer surface. Fig. 11 shows interferograms of multiple-beam Fizeau fringes of the birefringence shift components in the cladding of a bent single-mode fiber immersed in a matching liquid with radius of curvature R = 9 mm. (a) the two components, (b) the perpendicular component and (c) the parallel component.

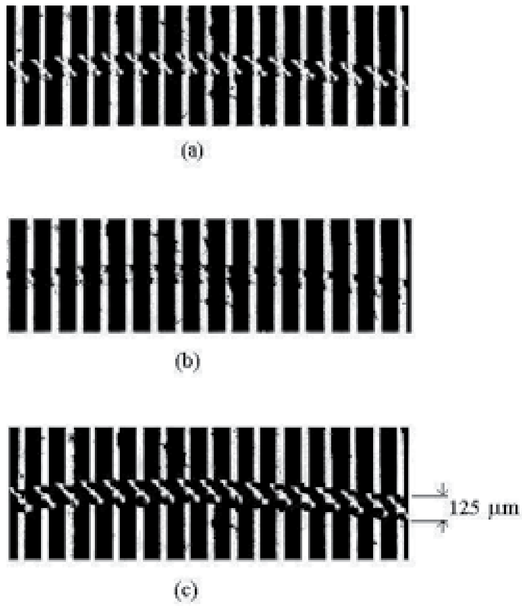

Figure 11. Interferograms of multiple-beam Fizeau fringes showing the birefringence shift components in the cladding of a bent single-mode fiber immersed in a matching liquid, $R = 9$ mm. (a) the two components, (b) the perpendicular component and (c) the parallel component.

5. Automatic analysis of micro-interferograms

Three different methods were usually used to analyze the fringe patterns (interferograms); traveling microscope, slide projection and image processing system. El-Zaiat and El-Hennawi [137] discussed the relative error in measuring refractive index by these methods. At constant wedge angle the relative error was ranging from 0.002 to 0.0006. Application of digital electronic provides picture acquisition, digitization and storage of the images. It also provides picture analysis, recording, printing, and reporting. Wonsiewiez et al. [63] developed a machine-aid technique of data reduction for interference micrographs. The technique was applied with the slab method and it consists of digitizing the interferogram with a scanning microdensitometer attached with computer to determine the position of the center line of each fringe. Presby et al. [64] used an automated setup of a video camera, a digitizer and computer to process the output of the interference microscope using the interferometric slab method. Many investigators used the transverse interferometric method with an immersion liquid matching to the cladding refractive index to study optical fibers electronically. [72], [73], [127], [132]- [141] A Leitz dual-beam, single-pass, transmission interference microscope is used with a video camera and video analysis system. Their measurement procedure involves video detection and digitization of interference fringes controlled by computer. The data obtained are then converted into refractive index and fiber radius information.

http://dx.doi.org/10.5772/54720

6. Conclusion

Using a silvered liquid wedge interferometer, multiple-beam Fizeau fringes at transmission crossing the fiber perpendicular to its axis suffer a shift. The shape, magnitude, and direction of the fringe shift provide quantitative and qualitative information about optical fiber structure and their index parameters. The state of polarization of the used light has an effect in the fringe shift specially in case of irregular fibers which suffer from external perturbation effects. Since the information is encoded in the phase of a fringe pattern, many practical disadvantages such as nonuniform intensity of illumination, inhomogeneous reflectivity distribution, nonlinearity of recording device, low or nonuniform contrast, and unavoidable noise affect the accuracy of determination of spatial localization of the fringe. Thus, the problem of ultra-high precise phase extraction (skeleton) is quite challenging. But the research in the field of digital fringe pattern analysis [142]- [152] is the only way to overcome this problem extending in the same time the limits of applicability of interferometry in the field of fiber researches and related devices.

Author details

Fouad El-Diasty

Department of Physics, Faculty of Science, Ain Shams University, Abbasia, Cairo, Egypt

References

[1] Midwinter, J. E. Optical fibers for transmission", (John Wiley (1979).

[2] Payne, D. N, & Gampgling, W. A. Electron. Lett. 10, 289 ((1974).

[3] Hall, D. R, & Jackson, P. E. The Physics and Technology of Laser Resonators", 1st ed. (Institute of physics publishing, Bristol and Philadelphia (1992).

[4] Ishigure, T, Nihei, E, & Koike, Y. Appl. Opt. 33, 4261 ((1994).

[5] Koike, Y, Ishigure, T, Nihei, E, & Lightwave, J. Technol. 13, 1475, ((1995).

[6] Koike, Y. nd European Conference on Optical Communication", ECOC'96, Oslo, , 1.

[7] Koike, Y, Ishigure, T, Satoh, M, & Nihei, E. th Optical Fiber Measurement Conference", OFMC'97 Teddington, UK, , 99.

[8] Koeppen, C, Shi, R. F, Chen, W. D, Garito, A. F, & Opt, J. Soc. Am. B 15, 727 ((1998).

[9] Koike, Y, Ishigure, T, Satoh, M, & Nihei, E. (1998). IEEE/LEOS Summer Topical Meeting" Monterey, CA, , 13.

[10] Decusatis, C. Opt. Eng. 37, 3082 ((1998).

[11] Dde, E. Fiber Optic Sensors: An Introduction for Scientists and Engineers", 1st ed. (Wiley, New York (1991).

[12] Erdogan, T, & Lightwave, J. Technol. 15, 1277 ((1997).

[13] Melz, G, Morey, W, & Glenn, W. H. Opt. Lett.14, 823 ((1997).

[14] Hill, K. O, Malo, B, Vineberg, K. A, Bilodeau, F, Johnson, D. C, & Skinner, I. Electron. Lett. 26, 1270 ((1990).

[15] De Paula, R. P, & Moore, E. L. In Proc. SPIE Int. Soc. Opt. Eng. 478 ((1984).

[16] Sharif, M. A. IEEE trans. Instrum. Measur. 38, 595, ((1989).

[17] Zanger, H, & Zanger, C. Fiber Optics Communication and other Applications", (Maxwell Macmillan International Publishing Group, New York, (1991).

[18] Jurgensen, K. Appl. Opt. 18, 1259 ((1979).

[19] Chang, C. T. Appl. Opt. 18, 2516 ((1979).

[20] Nagano, K, Kawakami, S, & Nishida, S. Appl. Opt. 17, 2080 ((1978).

[21] Taylor, F. F, Lightwave, J, & Technol, L. T. (1984).

[22] Sakai, J, Kimura, T, & Ieee, J. Quantum Electron. QE-17, 1041 ((1981).

[23] Smith, A. M. Appl. Opt. 19, 2606 ((1980).

[24] Ulrich, R, Rashleigh, S. C, & Eichoff, W. Opt. Lett. 5, 273 ((1980).

[25] Friebele, E. J. Opt. Eng. 18, 552 ((1979).

[26] Sigel, G. H, & Proc, J. R. IEEE 68, 1236 ((1980).

[27] Rao, R, & Mitra, S. S. Appl. Phys. Lett. 36, 948 ((1980).

[28] Friebele, E. J, Askins, C. G, & Gingerich, M. E. Appl. Opt. 23, 4202 ((1984).

[29] Chigusa, Y, Watanabe, M, Kyoto, M, Ooe, M, & Matsubara, T. IEEE Trans. Nuclear Science 35, 894 ((1988).

[30] Iida, T, Ire, S, & Sumita, K. IEEE Trans. Nuclear Science 35, 898 ((1988).

[31] Leskovar, B. IEEE Trans. Nuclear Science 36, 543 ((1989).

[32] Kyoto, M, Chigusa, Y, Ohe, M, Okamoto, S, & Lightwave, J. Technol. 10, 289 ((1992).

[33] Stoves, J. L. Fibre Microscopy", (London: National Trade Press, (1957).

[34] Francon, M. Progress in Microscopy", (Oxford: Pengamon Press, (1961).

[35] Wells, O. C. Scanning Electron Microscopy", (McGraw-Hill, New York, (1974).

[36] Kita, H, Kitano, I, Uchida, T, Furukawa, M, & Am, J. Ceramic Soc., (1971). , 54

[37] Meredith, R, & Hearle, J. W. S. Physical Methods of Investigating Textiles", (Interscience Publishers, New York, (1959).

[38] Verrier, I, & Goure, J. P. Opt. Lett. 15, 15 ((1990).

[39] Anderson, D. Z. Opt. Lett. 21, 685 ((1996).

[40] Ikeda, M, Tateda, M, & Yoshikiyo, H. Appl. Opt. 14, 814 ((1975).

[41] Barakat, N, & Hamza, A. A. Interferometry of Fibrous Materials", (Adam Hilger, Bristol and New York, (1990).

[42] Fariz, G. W, & Byer, R. L. Opt. Lett. 11, 413 ((1986).

[43] El Ghandoor, H, & Nasser, I. Afaf Abdel-Hady, A. Al-Shukri, Opti. Lasers Eng. 41, 277 ((2004).

[44] Hamza, A. A, Mabrouk, M. A, Ramadan, W. A, & Wahba, H. H. Opt. Lasers Eng. 42, 121 ((2004).

[45] Ghandoor, H, Nasserb, I, Abd-el, M. A, & Rahman, R. Hassan, Opt. Laser Technol. 32, 281 ((2000).

[46] Ghandoor, H, Abd, E, & Ghafar, R. Hassan, Opt. Laser Technol. 31, 481 ((1999).

[47] Ghandoor, H, Hennawi, H, Diasty, F, Soliman, M. A, & Mater, J. Sci. Eng. B 1, 148 ((2011).

[48] Diasty, F, & Lightwave, J. Technol. 22, 1539 ((2004).

[49] Diasty, F, Heaney, A, & Erdogan, T. Appl. Opt. 40, 890 ((2001).

[50] Thyagarajan, K. Mini Das, M. N. Satyanarayan, Opt. Commun. 218, 67 ((2003).

[51] Tolansky, S. An Introduction to Interferometry", (Longman Press, London (1973).

[52] Barakat, N, & Sorour, D. Proc. The mathematical and Physical Society of U.A.R. 28, 93 ((1966).

[53] Pluta, M. Optica Acta 18, 661 ((1971).

[54] Pluta, M, & Microsc, J. (1972).

[55] Rawson, E. G, Murray, R. G, & Ieee, J. Quantum electron. QE-9, 1114 ((1973).

[56] Martin, W. E. Appl. Opt. 13, 2112 ((1974).

[57] Cherin, A. H, Cohen, L. Q, Holden, W. S, Burrus, C. A, & Kaiser, P. Appl. Opt. 13, 2359 ((1974).

[58] Presby, H. M, & Brown, W. L. Appl. Phys. Lett. 24, 511 ((1974).

[59] Burrus, C. A, & Standley, R. D. Appl. Opt. 13, 2365 ((1974).

[60] Burrus, C. A, Chinnock, E. L, Gloge, D, Holden, W. S, Li, T, Standley, R. D, & Keck, D. B. Proc. IEEE 61, 1498 ((1973).

[61] Stone, J, & Burrus, C. A. Appl. Opt. 14, 151 ((1975).

[62] Presby, H. M, & Kaminow, I. P. Rev. Sci. Instrum. 47, 348 ((1976).

[63] Wonsiewiez, B. C, French, W. G, Lazay, P. D, & Simpson, J. R. Appl. Opt. 15, 1048 ((1976).

[64] Presby, H. M, Marcuse, D, & Astle, H. Appl. Opt. 14, 2209 ((1978).

[65] Shiraishi, S, Tanaka, G, Suzuki, S, & Kurosaki, S. Natl. Conv. Rec., IECE Japan paper 891, 239 ((1975). , 2

[66] Stone, J, & Earl, H. E. Appl. Sci. Inst. 4, 348 ((1976).

[67] Marhic, M. E, Ho, P. S, & Epstein, M. Appl. Phys. Lett. 26, 574 ((1975).

[68] Saunders, M. J, & Gardner, W. B. Appl. Opt. 16, 2369 ((1977).

[69] Iga, K, & Kokubun, Y. Tech. Digest Int. Conf., IOOC Tokyo, 403 ((1977).

[70] Kokubun, Y, & Iga, K. Trans. IEEC Japan E60, 702 ((1977).

[71] Iga, K, Kokubun, Y, & Yamamoto, N. Record of Natl. Symp. Light Radio Waves, IECE Japan paper s3-1 ((1976).

[72] Boggs, L, Presby, H. M, & Marcuse, D. Bell Syst. Tech. J. 58, 867 ((1979).

[73] Presby, H. M, Marcuse, D, Boggs, L, & Astle, H. Bell Syst. Tech. J. 58, 883 ((1979).

[74] Presby, H. M, & Opt, J. Soc. Am. 64, 280 ((1974).

[75] Presby, H. M, & Marcuse, D. Appl. Opt. 13, 2882 ((1974).

[76] Hannes, H. Koloid Z-Z Polymere 250, 765 ((1972).

[77] Witkins, L. S. Appl. Opt. 18, 2214 ((1979).

[78] Rogus, D. SPIE 1121, 317 ((1989).

[79] Bozyk, M. SPIE 1121, 284 ((1989).

[80] Pluta, M. Optica Applicata 16. 375 ((1985).

[81] Barakat, N, Hennawi, H. A, Medhat, M, Sobie, M. A, & Diasty, F. Appl. Opt. 25, 3466 ((1986).

[82] Hlubina, P. Opt. Commun. 218, 283 ((2003).

[83] Tolansky, S. Multiple-Beam Interference Microscopy of Metals", (Academic Press, London, (1970).

[84] Tolansky, S. Multiple-Beam Interferometry of Surfaces and Films (Oxford: Clarendon (1948).

[85] Barakat, N, Mokhtar, S, & Opt, J. Soc. Am. 53, 1153 ((1963).

[86] Barakat, N. Textile Res. 41, 167 ((1971).

[87] Barakat, N, Hamza, A. A, & Goneid, A. S. Appl. Opt. 24, 4383 ((1985).

[88] Hamza, A. A, Kabeel, M. A, Phys, J, & Appl, D. Phys. 19, 1175, ((1986).

[89] Hamza, A. A, Kabeel, M. A, Phys, J, & Appl, D. Phys. 20, 963, ((1987).

[90] Hamza, A. A, Sokkar, T. Z, Shahin, M. M, & Appl, J. Phys. 70, 4480 ((1991).

[91] Hamza, A. A, Mabrouk, M. A, & Modern, J. Opt. 38, 97 ((1991).

[92] Hennawi, H. A, Medhat, M, Diasty, F, & Egypt, J. Phys. 18, 179 ((1987).

[93] Hennawi, H. A, Diasty, F, Meshrif, O, & Appl, J. Phys. 62, 4931 ((1987).

[94] Barakat, N, Hennawi, H. A, & Diasty, F. Appl. Opt. 27, 5090 ((1988).

[95] Barakat, N, Hennawi, H. A, & Sobeah, H. E. Pure Appl. Opt. 2, 419, ((1993).

[96] Mabrouk, M. A, & Bawab, H. F. Pure Appl. Opt. 6, 247 ((1997).

[97] Barakat, N, Hennawi, H. A, Zaiat, S. Y, & Hassan, R. Pure Appl. Opt. 5, 27 ((1996).

[98] Barakat, N, Hennawi, H. A, Abd, E, Ghafar, H, Ghandoor, R, & Hassan, F. El-Diasty, Opt. Commun. 191, 39 ((2001).

[99] Hamza, A. A, Belal, A. E, Sokkar, T. Z. N, & Agour, H. M. E. L-D. e. s. s. o. u. k. y, M. A. Optics and Lasers Eng. 45, 145 ((2007).

[100] Hamza, A. A, Sokkar, T. Z. N, & Opt, K. A. E. L-F. a. r. a. h. a. t. y, H. M. E. L-D. e. s. s. o. u. k. y. Lasers Eng. 41, 261 ((2004).

[101] Hamza, A. A, Mabrouk, M. A, Ramadan, W. A, & Shams-eldin, M. A. Opt. Commun. 200, 131 ((2001).

[102] Hamza, A. A, & Nasr, A. M. Pure Appl. Opt. 7, 449 ((1998).

[103] Hamza, A. A, Sokkar, T. Z. N, Ghander, A. M, Mabrouk, M. A, & Ramadan, W. A. Pure Appl. Opt. 4, 161 ((1995).

[104] Hamza, A. A, Ghander, A. M, Sokkar, T. Z. N, Mabrouk, M. A, & Ramadan, W, A. Pure Appl. Opt. 3, 943 ((1994).

[105] Hamza, A. A, Ghander, A. M, & Mabrouk, M. A. Pure Appl. Opt. 1, 71 ((1992).

[106] Abd, R. H. El-Maksoud, M. F. Omar Appl. Opt. 50, 5957 ((2011).

[107] Hennawi, H. A, Diasty, F, Ghandoor, H, & Soliman, M. A. Opt. Quant. Electron. 43, 35 ((2012).

[108] Kahl, G. D, Mylin, D. C, & Opt, J. Soc. Am. 55, 364 ((1965).

[109] Sochacki, J, & Appl, J. Opt. 25, 3473 ((1986).

[110] Sochacki, J, Rogus, D, & Sochacka, M. Fibre Intg. Opt. 6, 279 ((1987).

[111] Hennawi, H. A, & Egypt, J. Phys. 19, 91 ((1988).

[112] Durelli, A. J, & Riley, W. F. Introduction to Photomechanics (Prentice-Hall, Englewood Cliffs, NJ, (1965).

[113] Diasty, F, & Opt, J. A: Pure Appl. Opt. 1, 197 ((1999).

[114] Diasty, F. Appl. Opt. 39, 3197 ((2000).

[115] Bertholds, A, Dandliker, R, & Lightwave, J. Technol. 6, 17-20 ((1988).

[116] Pinnow, D. A. Electrooptic materials," in Handbook of Lasers, R. J. Presley, ed. (CRC, Cleveland, Ohio, (1971).

[117] Diasty, F, & Appl, J. Phys. 87, 3254 ((2000).

[118] Diasty, F, & Opt, J. Soc. Am. A 18, 1171 ((2001).

[119] Diasty, F, & Egypt, J. Phys. 33, 359 ((2001).

[120] Diasty, F, & Opt, J. A: Pure Appl. Opt. 4, 575 ((2002).

[121] Diasty, F. Opt. Commun. 212, 267 ((2002).

[122] Diasty, F. Appl. Opt. 42, 5263 ((2003).

[123] Diasty, F. Meas. Sci. Technol. 14, 1734 ((2003).

[124] Diasty, F. Opt. Commun. 225, 61 ((2003).

[125] Diasty, F, & Opt, J. Soc. Am. A 21, 1496 ((2004).

[126] Diasty, F. F. Abdel Wahab, Opt. Eng. 45, 035003/1-7 ((2006).

[127] Diasty, F, Hennawy, H, & Soliman, M. A. Opt. Commun. 267, 394 ((2006).

[128] Diasty, F, & Amichi, A. Opt. Commun. 281, 4329 ((2008).

[129] Diasty, F, & Hennawi, H. A. Appl. Opt. 48, 3818 ((2009).

[130] Diasty, F. Opt. Eng. 51, 015007 ((2012).

[131] Abd, R. H. El-Maksoud, M. F. Omar, Appl. Opt. 50, 5957 ((2011).

[132] Malacara, D. Optical Shop Testing," Wiley: New work ((1992).

[133] Medhat, M, Zaiat, S. Y, Omer, M, & Mod, J. Opt. 43, 2205 ((1996).

[134] Medhat, M, Zaiat, S. Y, Omer, M, Barakat, N, & Mod, J. Opt. 44, 461 ((1996).

[135] Medhat, M, Zaiat, S. Y, Radi, A, Omer, M, & Opt, J. A: Pure Appl. Opt. 4, 174 ((2002).

[136] Medhat, M, Zaiat, S. Y, Saleh, M. A, Radi, A, Omer, M, & Opt, J. A: Pure Appl. Opt. 4, 485 ((2002).

[137] Zaiat, S. Y, & Hennawi, H. A. Meas. Sci. Technol. 7, 1119 ((1996).

[138] Marcuse, D, & Presby, H. Proc. IEEE 68, 676 ((1980).

[139] Ferrari, J. A, & Garcia, P. Appl. Opt. 39, 5667 ((1996).

[140] Presby, H. M. Appl. Opt. 20, 446 ((1981).

[141] Betts, R. A, Lui, F, & Whitbread, T. W. Appl. Opt. 30, 4384 ((1991).

[142] Chitti, Y. Graph. Model Image Proc. 59, 139 ((1997).

[143] Gureyev, T. E, Nugent, K. A, & Opt, J. Soc. Am. A 13, 1670 ((1996).

[144] Beniere, A, Goudail, F, Dolfi, D, Alouini, M, & Opt, J. Soc. Am. A 26, 1678 ((2009).

[145] Ma, J, Wang, Z, & Vo, M. Opt. Commun. 285, 3917 ((2012).

[146] Cai, Z, Liu, Q, & Yang, X. L. Opt. Laser Technol. 35, 295 ((2003).

[147] Vikram, Z. . H, & Caulfield, H. J. Appl. Opt. 46, 5137 ((2007).

[148] Gurov, I. P, & Opt, J. Technol. 67, 313 ((2000).

[149] Singh, H, & Sirkis, J. S. Appl. Opt. 33, 5016 ((1994).

[150] Gurov, I, Ermolaeva, E, Zakharov, A, & Opt, J. Soc. Am. A 21, 242 ((2004).

[151] Hamza, A. A, Sokker, T. Z. N, Farahaty, K. A, & Raslan, M. I. Poly. Test. 29, 1031 ((2010).

[152] Gurov, I, & Volynsky, M. Opt. Laser Technol. 50, 514 ((2012).

Chapter 19

Fiber Measurement Technique Based on OTDR

Masaharu Ohashi

Additional information is available at the end of the chapter

http://dx.doi.org/10.5772/54243

1. Introduction

An optical time domain reflect-meter (OTDR) has been developed for detecting the fault location and estimating the average loss of the installed fiber cables. The resolution of the distance has been improved up to a few centimeters. Recently, OTDR has been used for measurements of the transmission characteristics in fiber and optical fiber properties based on the backscattered signal power [1, 2].

As a result of the rapid progress made in the field of optical fiber amplifiers (OFA's), it has become possible to construct long distance transmission systems without conventional 3R repeaters [3, 4]. However, the use of OFA's gives rise to the problems of optical nonlinearities such as four-wave mixing (FWM), stimulated Brillouin scattering (SBS), and self-phase modulation (SPM). In OFA-based optical transmissions, both the chromatic dispersion distribution along a fiber and the average chromatic dispersion influence signal performance. Therefore, it has become important to know the longitudinal chromatic dispersion distribution for sophisticated transmission systems such as wavelength multiplexed and optical soliton transmission systems. However, conventional measurement techniques [5, 6] can only determine the average chromatic dispersion of either a short or a long fiber. Recently, there have been some reports on measurement techniques for estimating chromatic dispersion distribution along a fiber [7-9]. As these measurement techniques are based on optical nonlinear effects, the measurement distance is limited. On the other hand, we have reported the principle of a technique based on bidirectional measurement with OTDR [1].

In this chapter, we describe the measurement techniques for the longitudinal fiber parameters or transmission characteristics along the fiber. The backscattered power contains information on the fiber parameters at the scattered position such as mode field diameter, refractive index, and relative-index difference. Such information can be obtained by extracting the capture fraction from the backscattered power.

There are two types of techniques based on OTDR for measuring the longitudinal fiber properties by analyzing the backscattered power. One is the way of extracting the required information on the parameter from the capture fraction in the backscattered power just as it is. This technique is called "indirect method" in this section. The other is the way of adding the information into the backscattered power by utilizing the phenomenon between the signal and pump lights and required information can be easily obtained from the additional information in the backscattered power. This method is called "direct method". By using two types of techniques, the required information can be extracted from the backscattered power in the fiber.

In section 2, the principle of measurement technique for longitudinal fiber parameters such as the mode field diameter and relative-index difference and the reduction of polarization fluctuation influence in a fiber are described[2,10]. In section 3, the measurement technique for longitudinal transmission characteristics such as chromatic dispersion and the Raman gain efficiency are described. In this section, the direct and the indirect methods are described. In section 4, we summarize the measurement technique based on OTDR.

2. Measurement technique for longitudinal fiber parameters

This section describes the measurement techniques for longitudinal fiber parameters such as mode field diameter and relative-index difference.

2.1. Mode field diameter distribution

2.1.1. Measurement principle

The backscattered power *P(z)* received from a given position z in a single-mode fiber can be expressed as [2, 11]

$$P(z) = P_0 \alpha_s(z) B(z) \exp\left[-2\int_0^z \gamma(x)dx\right] \tag{1}$$

where P_0 is the input power, α_s(z) the local scattering coefficient, *B(z)* the backscattering capture fraction, and $\gamma(z)$ the local attenuation coefficient.

A reliable way to separate the effects of decay and waveguide imperfections from backscattered signals has already been described [1, 2, 10]. For OTDR signals $S_1(\lambda, z)$ and $S_2(\lambda, L\text{-}z)$ (in dB) launched from opposite ends (subscripts 1 and 2) of a fiber of length L, the imperfection contribution $I(\lambda,z)$ can be expressed as [2]

$$
\begin{aligned}
I(\lambda,z) &= \frac{S_1(\lambda,z)+S_2(\lambda,L-z)}{2} \\
&= a_0 + 10\log[\alpha_s(z)B(\lambda,z)] - 2(10\log e)\int_0^z \gamma(x)dx
\end{aligned}
\tag{2}
$$

where a_0 is a constant independent of distance z and is expressed as

$$
a_0 = 5\log(P_0P_1) - 10(\log e)P_0\alpha_s(z)\int_0^L \gamma(x)dx \tag{3}
$$

Therefore, the imperfection contribution $I(\lambda,z)$ depends on the local scattering coefficient α_s (z) and the backscattered capture fraction $B(\lambda,z)$, which is given by[12]

$$
B(\lambda,z) = \frac{3}{2}\left(\frac{\lambda}{2\pi n(z)w(\lambda,z)}\right)^2 \tag{4}
$$

where $n(z)$ and $2w(\lambda,z)$ denote the refractive index of the core and the mode field diameter (MFD) at a wavelength of λ, respectively.

With conventional single-mode fibers, the variation in the local scattering coefficient $\alpha_s(z)$ is negligible compared to that in the mode field diameter $2w(\lambda,z)$[13]. Therefore, the imperfection contribution $I_n(\lambda,z)$ normalized by the value at a reference point $z=z_0$ is

$$
I_n(\lambda,z) \equiv I(\lambda,z) - I(\lambda,z_0) = 20\log\left[\frac{2w(\lambda,z_0)}{2w(\lambda,z)}\right] \tag{5}
$$

When the mode field diameter $2w(\lambda,z_0)$ at $z=z_0$ is given, the mode field diameter distribution $2w(\lambda,z)$ can be obtained as

$$
2w(\lambda,z) = 2w(\lambda,z_0)10^{-\frac{I_n(\lambda,z)}{20}} \tag{6}
$$

However, in a fiber link composed of different kinds of fiber, the local scattering coefficient $\alpha_s(z)$ and refractive index of the core $n(z)$ of each fiber should be taken into account because these values are different.

Here, we consider the measurement procedure for a fiber link composed of different types of fibers, by taking into account the difference between the scattering coefficients of the composed fibers.

When the scattering coefficient and the refractive index change along the fiber are taken into account, the imperfection contribution $I(\lambda,z)$ can be expressed as

$$I(\lambda,z) = 10\log\left[\frac{\alpha_s(\lambda,z)}{n^2(z)}\right] + 20\log\left[\frac{1}{2w(\lambda,z)}\right] + a_1 \tag{7}$$

$$a_1 = 10\log\left[\frac{3\lambda^2}{8\pi^2}\right] + a_0 \tag{8}$$

where a_1 is a constant independent of distance z. The imperfection contribution $I_n(\lambda,z)$ normalized by that at $z=z_0$ can be written from (7) as

$$I_n(\lambda,z) \equiv I(\lambda,z) - I(\lambda,z_0) = 10\log\left[\frac{\alpha_s(z)n^2(z_0)}{\alpha_s(z_0)n^2(z)}\right] + 20\log\left[\frac{2w(\lambda,z_0)}{2w(\lambda,z)}\right] \tag{9}$$

Here, we define the first term on the right hand side in (9) as a correction factor *K*. The local scattering coefficient $\alpha_s(z)$ is propotional to the Rayleigh scattering coefficient R. The Rayleigh scattering coefficient R for GeO_2-doped core fiber is expressed as [14]

$$R = R_0(1 + 0.62\Delta) \tag{10}$$

where R_0 and Δ denote the Rayleigh scattering coefficient of SiO_2 glass and the relative-index difference in %, respectively [14]. The refractive index n of the core can be expressed using the relative-index difference Δ as

$$n = n_0 \big/ \sqrt{1 - 2\Delta / 100} \tag{11}$$

where n_0 is the refractive index of the cladding. Using this relation, the correction factor *K* is written as

$$K = 10\log\left[\left\{\frac{1 + 0.62\Delta(z)}{1 + 0.62\Delta(z_0)}\right\}\left\{\frac{50 - \Delta(z)}{50 - \Delta(z_0)}\right\}\right] \tag{12}$$

Therefore, the mode field diameter $2w(\lambda, z)$ distribution can be obtained as

http://dx.doi.org/10.5772/54243

$$2w(\lambda,z) = 2w(\lambda,z_0)10^{-\left\{\frac{I_n(\lambda,z)-K}{20}\right\}} \tag{13}$$

On the contrary, another procedure has been proposed [15]. To circumvent this difficulty, a procedure similar to that introduced in [16], but with an easier implimentation is used. Like [16], two fitting coefficients *A(λ)* and *C(λ)* are introduced so that

$$\begin{aligned} I_n(\lambda,z) &\equiv I(\lambda,z) - I(\lambda,z_0) \\ &= 20A(\lambda)\log\left[\frac{2w(\lambda,z_0)}{2w(\lambda,z)}\right] + C(\lambda) \end{aligned} \tag{14}$$

Suppose to set a second reference point $z=z_1$. Two subscriptions can be made in (14), $z=z_0$ for the first reference point and $z=z_1$ for the second reference one. The resulting values for the coefficients *A(λ)* and *C(λ)* are

$$A(\lambda) = \frac{I(\lambda,z_1) - I(\lambda,z_0)}{20\log\dfrac{2w(\lambda,z_0)}{2w(\lambda,z_1)}}, \quad C(\lambda) = 0 \tag{15}$$

From (14) and (15), the MFD becomes

$$2w(\lambda,z) = 2w(\lambda,z_0)\left[\frac{2w(\lambda,z_1)}{2w(\lambda,z_0)}\right]^{\frac{I(\lambda,z)-I(\lambda,z_1)}{I(\lambda,z_0)-I(\lambda,z_1)}} \tag{16}$$

Thus, we need to know the MFD at the two reference points z_0 and z_1. From a experimental view point, two reference fibers have to be connected in front of the fiber link. This method is very effective when these fibers have different material characteristics.

2.1.2. Reduction of polarization fluctuation influence in a fiber

The polarization state of an optical pulse is continuously changing as the pulse propagates in a fiber, and this polarization fluctuation causes measurement error. This fluctuation must therefore be reduced during the backscattered power accumulation. It is believed that the polarization fluctuation can be reduced by switching the polarization state from 0 to 90 linear polarization during the measurement [2]. Figure 1 shows a block diagram of our experimental setup for measuring the backscattered power.

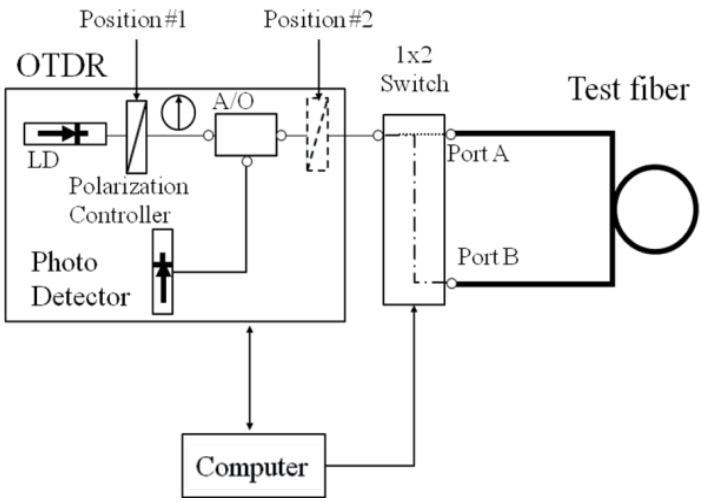

Figure 1. Block diagram of experimental setup

In our investigation, we refer to the positions of the polarization controller shown in Fig. 1 as positions #1 and #2. For simplicity, we defined the Jones matrix of the models shown in Fig. 1 as

$$\mathbf{M} = \mathbf{R}(\theta)\mathbf{F}\mathbf{R}(-\theta) \tag{17}$$

where $\mathbf{R}$ is the rotation matrix and θ denotes the angle from the principal axis. The rotation matrix $\mathbf{R}$ is expressed as

$$\mathbf{R}(\theta) = \begin{bmatrix} \cos\theta & -\sin\theta \\ \sin\theta & \cos\theta \end{bmatrix} \tag{18}$$

$\mathbf{F}$ is the Jones matrix of the fiber which is expressed as

$$\boldsymbol{F} = \begin{bmatrix} 1 & 0 \\ 0 & \exp(j\phi) \end{bmatrix} \tag{19}$$

where ϕ is the birefringence of the fiber. Jones matrices for the detector through the A/O switch $\mathbf{M}_{AO}$, the polarization controller $\mathbf{P}_c$ and input electric field vector $\mathbf{E}$ can be expressed as the following equations:

$$\mathbf{M}_{AO} = \begin{bmatrix} m_1 & 0 \\ 0 & m_2 \end{bmatrix} = m_1 \begin{bmatrix} 1 & 0 \\ 0 & k \end{bmatrix} \tag{20}$$

$$\mathbf{P}_{C_x} = \begin{bmatrix} 1 & 0 \\ 0 & 0 \end{bmatrix},\ \mathbf{P}_{C_y} = \begin{bmatrix} 0 & 0 \\ 0 & 1 \end{bmatrix} \tag{21}$$

$$\mathbf{E}_x = \begin{bmatrix} 1 \\ 0 \end{bmatrix},\ \mathbf{E}_y = \begin{bmatrix} 0 \\ 1 \end{bmatrix} \tag{22}$$

When x-polarized light is launched into the fiber, the detected power P_x, shown in Fig. 1 as position #1, is expressed as

$$P_x = \left|\mathbf{M}_{AO}\mathbf{M}\mathbf{E}_x\right|^2 = m_1^2\left\{1 + 4(k^2 - 1)\sin^2\theta\cos^2\theta\sin^2(\phi/2)\right\} \tag{23}$$

The detected power P_y for -polarized light input is expressed as

$$P_y = \left|\mathbf{M}_{AO}\mathbf{M}\mathbf{E}_y\right|^2 = m_1^2\left\{k^2 - 4(k^2 - 1)\sin^2\theta\cos^2\theta\sin^2(\phi/2)\right\} \tag{24}$$

Using (23) and (24), the total detected power P is expressed as the sum of the polarization components

$$P = P_y + P_y = m_1^2(1 + k^2) \tag{25}$$

Equation (25) shows that the obtained power P is independent of θ and ϕ. The total detected power $P^\#$, shown in Fig. 1 as position #2, is expressed as

$$\begin{aligned} P^\# = P_x^\# + P_y^\# &= \left|\mathbf{M}_{AO}\mathbf{P}_{Cx}\mathbf{M}\mathbf{E}_x\right|^2 + \left|\mathbf{M}_{AO}\mathbf{P}_{Cy}\mathbf{M}\mathbf{E}_y\right|^2 \\ &= m_1^2(1 + k^2)\left\{1 - 4k^2\sin^2\theta\cos^2\theta\sin^2(\phi/2)\right\} \end{aligned} \tag{26}$$

From (26), it is found that the obtained power depends on θ and ϕ. Therefore, the polarization controller must be located between the LD and the A/O switch, shown in Fig. 1 as position #1.

By using the polarization controller, the backscattered power can be suppressed due to the polarization fluctuation.

2.1.3. Experimental results

To confirm the present technique, the mode field diameter distribution along the fiber link composed of the three fibers was measured. OTDR was used to measure the backscattered power of the fiber link. Table I summarizes the fiber parameters in the fiber link.

Parameters	Fiber A	Fiber B	Fiber C
MFD (μm) at 1310nm at 1550nm	9.02 10.17	6.47 7.86	6.49 7.86
Cutoff wavelength λ_c (nm)	1260	1150	1010
Relative-index difference Δ (%)	0.37	0.78	0.77
Chromatic dispersion D (ps/km/nm) at 1550 nm	16.72	-0.29	-0.27
Fiber length (km)	25.0	9.99	20.19

Table 1. Parameters of test fibers

Figure 2 shows the bi-directional OTDR traces of the fiber link at λ=1550 nm. OTDR (Agilent E6003) with wavelengths of 1550 and 1310 nm was used to measure the backscattered signal powers for the fiber link. In our measurements, the pulse width of the OTDR was 1 μs and the averaging time was 10 minutes.

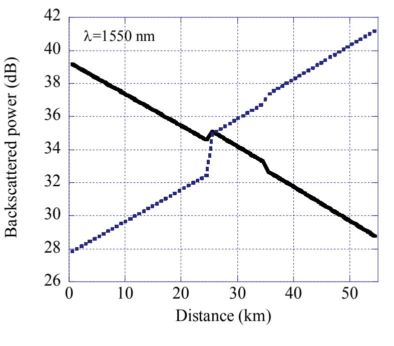

Figure 2. Bi-directional OTDR traces at λ=1550 nm

It is found that three fibers were spliced in the fiber link. The imperfection loss obtained from (2) was shown by using the Fig.1. Figure 3 shows the inperfection loss of the fiber link.

It is found that the losses of Fibers A, B, and C fluctuate along the fiber length. This fluctuation has an effect on the mode field diameter of each fiber. The MFD distribution at λ=1550 nm using Fig. 3 is shown in Fig. 4.

The MFD was estimated by using double reference method. When we measure the MFD distribution of the fiber link, Fibers A and B was used as reference fibers. The MFD was estimated by using (16) and MFDs at the double reference points. The deviations of the MFD for Fiber A, B and C were 0.039 μm, 0.023 μm, and 0.046 μm, respectively. It is clarified that the longitudinal MFD deviation is negligible small for the fibers fabricated by the present fabrication technique.

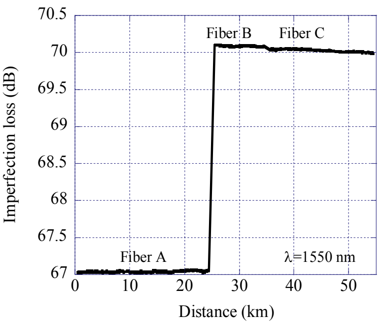

Figure 3. Imperfection loss of the fiber link

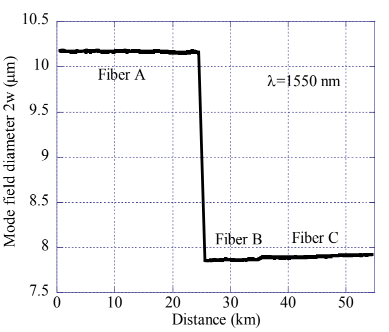

Figure 4. MFD distribution of the fiber link at λ=1550nm

2.2. Relative-index difference distribution

2.2.1. Measurement principle

The first term on the right hand side in (9) depends on the variations in the scattering coefficient and refractive index of the core. The local scattering coefficient is proportional to the Rayleigh scattering coefficient. The Rayleigh scattering coefficient R for GeO_2 doped core fiber is expressed as [14]

$$R = R_0(1 + k\Delta) \tag{27}$$

where R_0 and Δ denote the Rayleigh scattering coefficient for SiO_2 and the relative index difference Δ in %, respectively. The k value was estimated experimentally to be 0.62 in [14].

As the variation in the refractive-index $n(z)$ of the core along the fiber link is negligible, the following equation holds very well even if the fiber link is composed of different kinds of fiber[10].

$$n^2(z_0)/n^2(z) \cong 1 \tag{28}$$

Thus, (9) can be rewritten as by using (27) and (28).

$$\begin{aligned} I_n(\lambda,z) &\equiv I(\lambda,z) - I(\lambda,z_0) \\ &\cong 10\log\left[\frac{\alpha_s(z)}{\alpha_s(z_0)}\right] + 20\log\left[\frac{2w(\lambda,z_0)}{2w(\lambda,z)}\right] \\ &= 10\log\left[\frac{1+k\Delta(z)}{1+k\Delta(z_0)}\right] + 20\log\left[\frac{2w(\lambda,z_0)}{2w(\lambda,z)}\right] \end{aligned} \tag{29}$$

Here, if the MFD distribution and the relative index difference $\Delta(z_0)$ are known, the relative index difference $\Delta(z)$ can be derived from (29) as follows[10].

$$\Delta(z) = \frac{1}{k}\left[(1+k\Delta(z_0)10^{\frac{I_n(\lambda,z)-20\log\left[\frac{2w(\lambda,z_0)}{2w(\lambda,z)}\right]}{10}} - 1\right] \tag{30}$$

The MFD distribution along the transmission line can be easily estimated by using the double reference method [15]. With this technique, the imperfection loss of each test fiber along the transmission line can be estimated by comparing it with the imperfection losses at two reference points.

Next, the principal estimation error of the proposed method is discussed. The Δ estimation error was calculated by using (9) and (30) and can be written as

$$\Delta_E(z) - \Delta_R(z) = \frac{1}{k}\left[\left\{\left(\frac{n^2(z_0)}{n^2(z)}\right) - 1\right\}\left(1 - k\Delta_R(z)\right)\right] \tag{31}$$

where Δ_R and Δ_E denote the correct and estimated Δ values, respectively. From (31) we find that the Δ estimation error is directly proportional to$[n^2(z_0)/n^2(z) - 1]$.

Figure 5 shows the relationship between the correct relative index difference Δ_R and the relative Δ estimation error (%) against the refractive index at the 0.35 % and 0.8 % reference points. Here, a k value of 0.62 was used. It is seen that the relative Δ estimation error increases as the relative index difference between the test fiber and the reference fiber increases. Therefore, a reference fiber should be selected that has almost the same refractive index as that of the test fiber in order to estimate the relative index difference accurately.

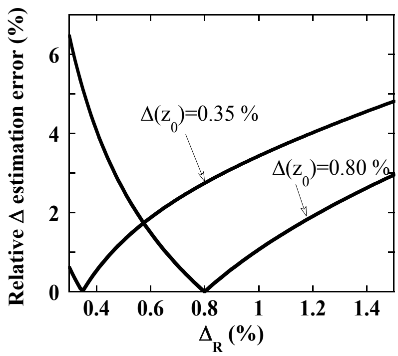

Figure 5. Relationship between the correct index difference Δ_R and relative Δ estimation error against refractive index as reference points of 0.35 % and 0.8%

2.3. Experimental results

To confirm the effectiveness of the present method, I measured the relative index difference distribution *Δ(z)* along a fiber link composed of one single-mode fiber (Fiber A) and two dispersion-shifted fibers (Fibers B and C). The parameters of these test fibers are listed in Table 1.

OTDR (Agilent E6003) with wavelengths 1550 and 1310 nm was used to measure the backscattered signal powers for the fiber link. In our measurements, the pulse width of the OTDR was 1 μs and the averaging time was 10 minutes. The spatial resolution of the relative index difference Δ estimation depends on the OTDR pulse width. In the experiments, the spatial resolution was about 200 m.

Figure 6 shows the relative index difference distribution $\Delta(z)$ in the fiber link by using the MFD distribution as shown in Fig. 4. k=0.62 was used in (17). The Δ distribution of Fibers B and C are also shown in Fig. 6. It is found that the $\Delta(z)$ of Fiber C decreases slightly along the fiber length. The Δ variation of Fiber C was estimated to be 0.01 % from Fig. 6. In addition, the experimental results for the relative index difference obtained with the present method are in good agreement with the values measured with refractive near field (RNF) method.

This study proposed a novel relative-index difference distribution measurement method for a fiber link based on the use of an OTDR. It was clarified experimentally that the method can be applied to fiber links composed of different kinds of fiber. The relative-index difference is one of important parameters to estimate the chromatic dispersion. However, there have been no reports on the technique for estimating the relative-index difference distribution. As far as we know, for the first time, we proposed the novel technique for estimating the relative-index difference distribution of the fiber link based on the OTDR.

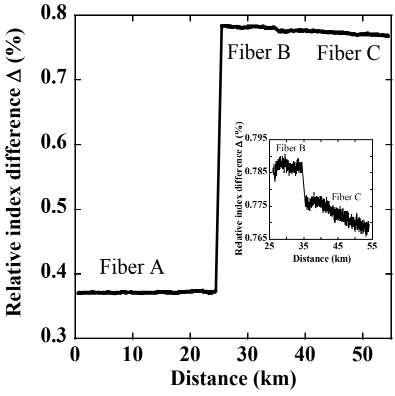

Figure 6. Relative-index difference distribution *Δ(z)* in the fiber link

3. Measurement technique for longitudinal transmission characteristics

This section describes the measurement techniques for longitudinal transmission characteristics such as chromatic dispersion and Raman gain efficiency and the experimental results.

3.1. Chromatic dispersion distribution

3.1.1. Measurement principle

The chromatic dispersion is expressed as the sum of the material dispersion D_m and the waveguide dispersion D_w.

$$D = D_m + D_w \tag{32}$$

Here, D_m and D_w [17] are expressed as

$$D_m = -\frac{\lambda}{c}\frac{d^2 n}{d\lambda^2} \tag{33}$$

$$D_w = \frac{\lambda}{2\pi^2 cn} \frac{d}{d\lambda} \left(\frac{\lambda}{w^2} \right) \tag{34}$$

where c is the light velocity. The material dispersion can be estimated from the dopant concentration in an optical fiber by using Sellmeier's coefficients [18]. The dopant concentration can be obtained from the relative-index difference Δ of the core. By contrast, the waveguide dispersion D_w can be estimated by determining the wavelength dependence of the mode field diameter.

The empirical relationship between the mode-field diameter $2w$ and the normalized frequency v has been reported by Marcuse as [19]

$$\frac{w}{a} = b_0 + b_1 v^{-1.5} + b_2 v^{-6} = c_0 + c_1 \left(\frac{\lambda_c}{\lambda} \right)^{-1.5} + c_2 \left(\frac{\lambda_c}{\lambda} \right)^{-6} \tag{35}$$

where $2a$ is the core diameter and λ_c the cutoff wavelength.

Here, we approximated the wavelength dependence of the mode-field diameter(MFD) $2w$ as

$$w(\lambda, z) = g_0(z) + g_1(z)\lambda^{1.5} + g_2(z)\lambda^{6} \tag{36}$$

Substituting (36) into (34), the waveguide dispersion can be expressed as

$$D_w = \frac{\lambda}{2\pi^2 cnw^2(\lambda, z)} \left\{ 1 - \frac{2\lambda}{w(\lambda, z)} \left(\frac{3}{2} g_1(z)\lambda^{0.5} + 6 g_2(z)\lambda^{5} \right) \right\} \tag{37}$$

Therefore, the waveguide dispersion $D_w(z)$ at the position z can be evaluated from the coeffcients $g_0(z)$, $g_1(z)$ *and* $g_2(z)$. To obtain the coefficients $g_0(z)$, $g_1(z)$ and $g_2(z)$, the MFD has to be measured at more than three wavelengths.

In general, as the coefficient of g_2 is negligible small compared with that of g_1, the wavelength dependence of the MFD can be expressed as

$$w(\lambda, z) = g_0(z) + g_1(z)\lambda^{1.5} \tag{38}$$

In this case, the coefficients g_0 and g_1 can be estimated by using the MFDs at the two wavelengths. The two wavelengths of 1.31 and 1.55 μm are usually used for these measurements, which are the operating wavelengths in the current transmission systems.

Substituting (38) into (34), the waveguide dispersion can be expressed as

$$D_w = \frac{\lambda}{2\pi^2 cnw^2(\lambda,z)}\left\{1 - \frac{2\lambda}{w(\lambda,z)}\left(\frac{3}{2}g_1(z)\lambda^{0.5}\right)\right\} \tag{39}$$

Here, we assume that the MFDs at the two wavelength λ_1 and λ_2 are respective $2w(\lambda_1)$ and $2w(\lambda_2)$. In this case, the coefficients g_0 and g_1 which represent the wavelength dependence of the MFD can be obtained as

$$g_0 = \frac{w(\lambda_2)\lambda_1^{1.5} - w(\lambda_1)\lambda_2^{1.5}}{\lambda_1^{1.5} - \lambda_2^{1.5}} \tag{40}$$

$$g_1 = \frac{w(\lambda_1) - w(\lambda_2)}{\lambda_1^{1.5} - \lambda_2^{1.5}} \tag{41}$$

The chromatic dispersion can be measured by using the wavelength dependence of the MFD and the relative-index difference of the core. Both parameters MFD and the relative-index difference can be easily estimated by using the OTDR. The MFD $2w(z)$ and the relative-index difference $\Delta(z)$ can be measured by the technique as mentioned in section 2.

3.1.2. Experimental results

The chromatic dispersion measurements were made on the fiber link composed of three different fibers. The parameters of these test fibers are listed in Table 1. The chromatic dispersion is sum of waveguide and material dispersion. The material dispersion can be estimated from the dopant concentration corrssponding to the relative-index difference. On the contrast, the waveguide dispersion can be obtained by using the wavelength dependence of MFD. The fiber link was measured by bi-directional OTDR with both wavelengths of 1310 and 1550 nm. Figs. 4 and 7 show the MFD distributions at λ=1550 nm and 1310 nm. estimated by using the bi-directional OTDR traces, respectively. To estimate the MFDs, Fibers A and B were used as the reference fibers[15].

The waveguide dispersion can be estimated by using the MFD distributions at both 1310 and 1550 nm and (30). Figure 8 shows the waveguide dispersion of the fiber link at λ=1550 nm.

It is found that the waveguide dispersion of Fiber A (conventional single-mode fiber) was smaller than that of Fiber B and C (dispersion-shifted fibers). This is because the zero-dispersion wavelength can be shifted to the longer wavelength. On the other hand, the material dispersion can be calculated by using Sellmeire equation when the relative-index diffence is known. The relative-index differnce was estimated by using the technique presented in 2.2. Figure 9 shows the material dispersion of the fiber link at λ=1550 nm.

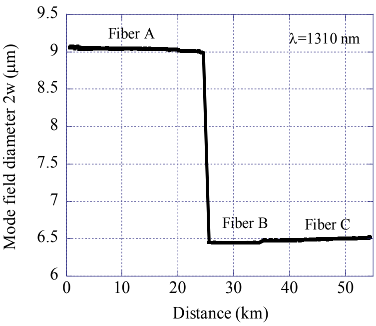

Figure 7. MFD distribution of the fiber link at λ=1310 nm

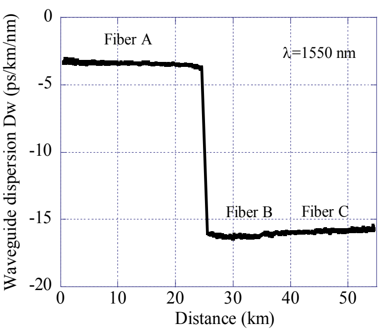

Figure 8. Waveguide dispersion of the fiber link at λ=1550 nm

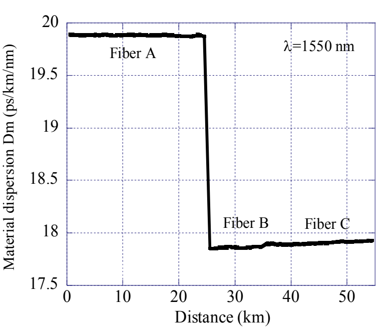

Figure 9. Material dispersion of the fiber link at λ=1550 nm

The chromatic dispersion at λ=1550 nm can be estimated by using Figs 9 and 10. Figure 10 shows the chromatic dispersion of the fiber link at λ=1550 nm.

We described a nondestructive technique for measuring the chromatic dispersion distribution along a single-mode fiber based on bidirectional OTDR measurements. This technique was compared with the destructive interferometric technique and found to be in good agreement. We also proposed a measurement procedure for a transmission line composed of different types of single-mode fibers. We confirmed experimentally that our technique can be applied to a transmission line. Our technique for estimating chromatic dispersion distribution will be a powerful tool for designing WDM and FDM transmission systems.

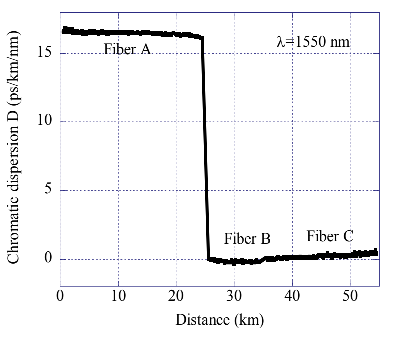

Figure 10. Chromatic dispersion distribution of the fiber link at λ=1550 nm

3.2. Raman gain efficiency distribution

The development of various kinds of Internet services has led to a rapidly increase in transmission capacity. With a view to realizing ultra-wide band transmission systems, wavelength division multiplexing (WDM) systems have been introduced together with Raman amplification technology [20]. Raman amplification technology is an attractive technology whereby the amplification wavelength region can be adjusted by changing the wavelength of the pump light wavelength. Technologies have been reported for measuring the Raman gain efficiency distribution using pump and signal lasers [21]. In this section, two types of techniques for measuring the Raman gain efficiency is described based on the OTDR. The first one is the direct method using pump lasers. The other is the in direct method without pump lasers.

3.2.1. Measurement principle

a. Direct method

Figure 11 shows the schematic diagram for measuring the Raman gain efficiency distribution in the optical fibers by using an OTDR.

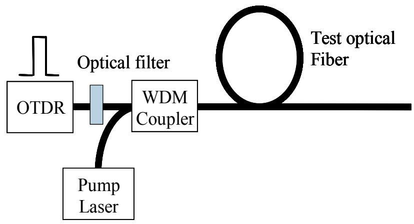

Figure 11. Schematic diagram of the proposed Raman gain efficiency measurement method

The pulsed signal and the continuous wave pump lights are launched into the test fiber through the WDM coupler. These lights co-propagate through the test optical fiber. An optical filter is inserted between the OTDR and the WDM coupler to eliminate the Rayleigh backscattering of the pump light.

Here, we derive the signal power at the distance of z. The signal power P_s can be obtained by solving the coupled power equation with regard to the signal P_s and the pump powers P_p. If the pump is un-depleted, the pump power can be expressed by the following equations [22].

$$\frac{dP_s}{dz} = \frac{g_R}{A_{eff}} P_p P_s - \alpha_s P_s \tag{42}$$

$$\frac{dP_p}{dz} = -\alpha_p P_p, \tag{43}$$

where g_R is the Raman gain coefficient. α_s and α_p are the attenuation coefficients of signal and pump wavelengths, respectively. A_{eff} denotes the effective area, which corresponds to the overlapping area between pump and signal lights and is defined as

$$A_{eff} = 2\pi \frac{\int \phi_s^2(r) r dr \int \phi_p^2(r) r dr}{\int \phi_s^2(r) \phi_p^2(r) r dr} \tag{44}$$

where ϕ_s and ϕ_p are the field distributions of the fundamental mode of the fiber at radius r at the respecitive signal and pump wavelengths.

In particular, when the field distribution is Gaussian, the effective area A_{eff} is obtained as

$$A_{eff} \cong \pi \left(w_s^2 + w_p^2 \right) / 2 \tag{45}$$

where w_s and w_p denote the mode field radii of the signal and pump wavelengths, respectively.

From (43), the pump power P_p at the position of z can be obtained as

$$P_p(z) = P_p(0)\exp(-\alpha_p z). \tag{46}$$

Substituting (46) into (42), the signal power $P_s(z)$ at the position of z can be obtained as

$$P_s(z) = P_s(0)\exp\left[\int_0^z \left(\frac{g_R P_p(0)}{A_{eff}}\exp(-\alpha_p z) - \alpha_s\right)dz\right]. \tag{47}$$

The signal power $P_s(z)$ at the position of z is reflected and it travels toward the input direction. The backscattered light can be expressed as the product of the signal power $P_s(z)$ and $B(z)$ α, where α is the scattering coefficient and $B(z)$ is the backscatterd capture fraction. Then, the backscattered signal light $P_s(z)B(z)\alpha$ is amplified by the counter propagating pump light. Therefore, the backscattered power $P(z,P_p)$ from the position of z can be expressed as

$$\begin{aligned} P(z,P_p) &= P_s(0)\alpha B(z)\exp\left[2\int_0^z \left(\frac{g_R P_p(0)}{A_{eff}}\exp(-\alpha_p z) - \alpha_s\right)dz\right] \\ &= P_s(0)\alpha B(z)\exp\left[2P_p(0)G(z)\right]\times\exp\left[-2\alpha_s z\right] \end{aligned} \tag{48}$$

where $G(z)$ is defined as

$$G(z) = \int_0^z \frac{g_R(z)}{A_{eff}(z)}\exp(-\alpha_p z)dz. \tag{49}$$

On the contrary, when the pump light is off, the backscattered power $P(z,0)$ can be obtained by substituting $P_p(0)$ =0 into (48) as

$$P(z,P_p) = P_s(0)\alpha B(z)\exp\left[-2\alpha_s z\right]. \tag{50}$$

The backscattered power of OTDR, $S\ (z,P_p)$ [=10log {$P\ (z,P_p)$}] can be expressed as

$$S(z,P_p) = 10\log\left[P_s(z,P_p)\right] = 10\log\left[P_s(0)\right] + 10\log\left[\alpha B(z)\right] \\ + 2P_p(0)G(z)\cdot 10\log(e) - 2\alpha_s z 10\log(e) \tag{51}$$

The backscattered power at $z=z+\Delta z$ can be also expressed as

$$\begin{aligned} S(z+\Delta z,P_p) = 10\log\left[P_s(z+\Delta z,P_p)\right] \\ &= 10\log\left[P_s(0)\right] + 10\log\left[\alpha B(z+\Delta z)\right] \\ &+ 2P_p(0)G(z+\Delta z)\cdot 10\log(e) \\ &- 2\alpha_s\left(z+\Delta z\right)10\log(e) \end{aligned} \tag{52}$$

The following equation can be derived from (50) and (51).

$$\frac{dS(z,P_p)}{dz} = \frac{d\left\{10\log\left[\alpha B(z)\right]\right\}}{dz} + 2P_p(0)\cdot 10\log(e)\frac{dG(z)}{dz} - 2\alpha_s 10\log(e) \tag{53}$$

On the contrary, when $P_p=0$, the following equation can be also derived in the same manner.

$$\frac{dS(z,0)}{dz} = \frac{d\left\{10\log\left[\alpha B(z)\right]\right\}}{dz} - 2\alpha_s 10\log(e) \tag{54}$$

From the definition of G, $dG(z)/dz$ can be expressed as

$$\frac{dG(z)}{dz} = \frac{g_R(z)}{A_{eff}(z)}\exp(-\alpha_p z). \tag{55}$$

Therefore, the Raman gain efficiency $g_R(z)/A_{eff}(z)$ at the position of z can be derived from (52) to (54) as

$$\frac{g_R(z)}{A_{eff}(z)} = \frac{dS_d(z)}{dz}\cdot\frac{1}{2P_p(0)\cdot 10\log(e)\exp(-\alpha_p z)} \tag{56}$$

Here, $S_d(z)$ corresponding to the backscattered power difference between with and without pumping is defined as

$$S_d(z) = S(z, P_p) - S(z, 0). \tag{57}$$

Therefore, the Raman gain efficiency distribution can be estimated from the length dependence of the pump power and the derivative of $S_d(z)$ with regard to the fiber length z. It is also found from (56) that the Raman gain efficiency distribution $g_R(z)/A_{eff}(z)$ can be estimated by using the conventional OTDR.

b. Indirect method

The Raman gain coefficient g_R of GeO_2-doped core fiber can be expressed by the following equation [23, 24].

$$g_R = g_0(1 + 80\Delta) / \lambda_p \tag{58}$$

where Δ is the relative-index difference in % and g_0 denotes the Raman gain coefficient of pure silica glass. λ_p is the pump wavelength.

The Raman gain efficiency can be expressed as g_R/A_{eff}. Thus, the Raman gain efficiency can be obtained by using (44) and (58) as

$$\frac{g_R}{A_{eff}} = \frac{g_0(1 + 80\Delta)}{\lambda_p A_{eff}} \tag{59}$$

From (59), we can approximate the Raman gain coefficient by using the relative-index difference Δ and mode field diameter (MFD) $2w$. In the fiber link, the MFD $2w$ and relative-index difference Δ distributions can be estimated by using the bi-directional OTDR technique as described in section 2.

If we know the Raman gain efficiency ($g_R(z_0)/A_{eff}(z_0)$) of the reference fiber at the position z=z_0, the Raman gain efficiency ($g_R(z)/A_{eff}(z)$) of the test fiber at the position z can be estimated from (59) as

$$\frac{g_R(z)}{A_{eff}(z)} = \frac{g_R(z_0)}{A_{eff}(z_0)} \frac{(1 + 80\Delta(z))}{\left(w_s^2(z) + w_p^2(z)\right)} \frac{\left(w_s^2(z_0) + w_p^2(z_0)\right)}{(1 + 80\Delta(z_0))} \tag{60}$$

Here, if we assume that the wavelength dependence of MFD is negligible, (60) can be approximated as

http://dx.doi.org/10.5772/54243

$$\frac{g_R(z)}{A_{eff}(z)} = \frac{g_R(z_0)}{A_{eff}(z_0)}\left[\frac{w_s^2(z_0)}{w_s^2(z)}\frac{1+80\Delta(z)}{1+80\Delta(z_0)}\right] \tag{61}$$

The Raman gain efficiency can be estimated by measuring both the MFD and the relative-index difference distributions of the test fiber. Thus, the Raman gain efficiency can be obtained indirectly by using OTDR without pump lasers. This technique is a relative measurement method, so the measurement accuracy depends on the Raman gain efficiency of the reference fiber.

3.2.2. Experimental results

a. Direct method

The Raman gain efficiencies for a conventional single-mode fiber with a length of 25 km and a fibre link installed in the field with a length of 11km composed of 22 conventional single-mode fibers with a piece length of 500 m were measured to confirm the effectiveness of our technique.

Figure 12 shows the backscattered powers with and without pumping for the conventional single-mode fiber. OTDR (Anritsu) with a wavelength of 1550 nm was used to measure the backscattered power. The OTDR pulse width was 1μs and the averaging time was 5 min. The pump laser with a wavelength of 1475 nm was used. It is found that the signal power is amplified by the pump power.

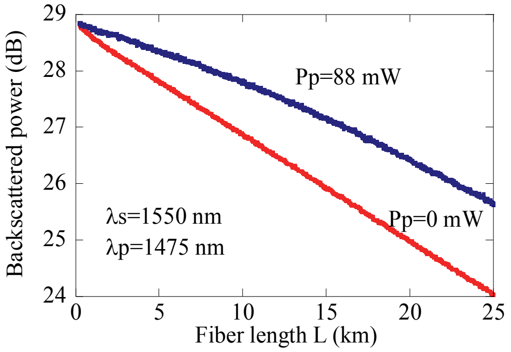

Figure 12. Backscattered powers with and without pumping

Figure 13 shows the backscattered power difference S_d defined in (14) plotted as a function of fiber length.

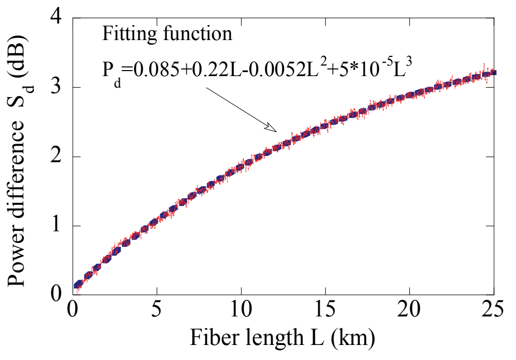

Figure 13. Backscattered power difference S_d

$S_d(z)$ was best fitted to the polynomial function as to calculate its derivative.

$$S_d(z) = 0.085 + 0.22 \cdot z - 0.0052 \cdot z^2 + 5.0 \times 10^{-5} \cdot z^3 \tag{62}$$

The attenuation coefficient of the test fiber at λ=1475 nm was 0.217 dB/km. The pump power $P_p(0)$ was 88 mW. The Raman gain efficiency distribution along the fiber length can be estimated by using (56) and (62). Figure 14 shows the Raman gain efficiency distribution estimated by our technique.

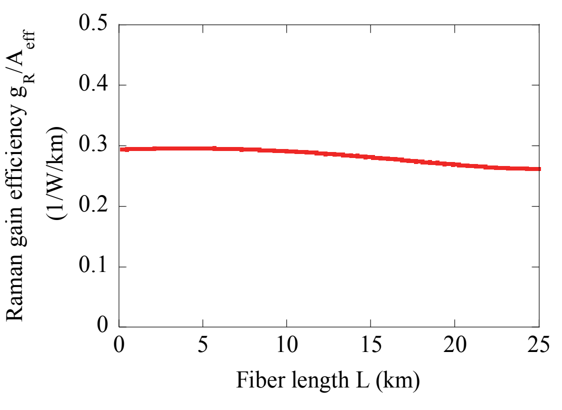

Figure 14. Raman gain efficiency distribution

It is seen that Raman gain efficiency along the fiber length is almost the same as 0.3 $W^{-1}km^{-1}$.

Next, the Raman gain efficiency for the fiber link composed of 22 conventional single-mode fibers was measured. Figure 15 shows the backscattered powers with and without pumping and the backscattered power difference S_d plotted as a function of fiber length.

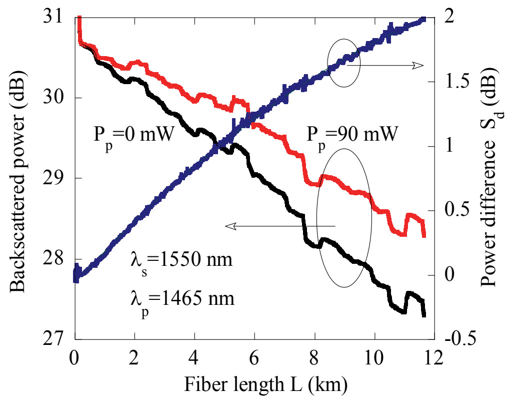

Figure 15. Backscattered powers with and without pumping and the backscattered power difference S_d plotted as a function of fiber length

The attenuation coefficient α_p was measured by the OTDR with a wavelength of 1450 nm. The length dependence of the pump power $P_p(z)(=P_p(0)\exp(-\alpha_p z))$ was estimated from the OTDR trace at the pump wavelength λ_p. By using the length dependence of the pump power, and the derivative of S_d with regard to the fiber length z, the Raman gain efficiency distribution of the fiber link was estimated. The Raman gain efficiency of the fiber link is shown in Fig. 16.

It is found that the Raman gain efficiency distribution in the fiber link varies from 0.22 to 0.32 $W^{-1}km^{-1}$. The Raman gain efficiency distribution of the fiber link installed in the field shows the appropriate value. As a result, it is confirmed that our technique can be applied to the fiber link.

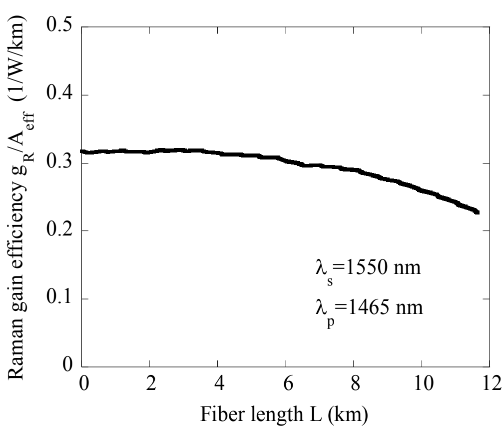

Figure 16. Raman gain efficiency of the fiber link

b. Indirect method

The Raman gain efficiency of the concatenated fiber link as shown in Fig. 17 was measured to confirm the effectiveness of our technique.

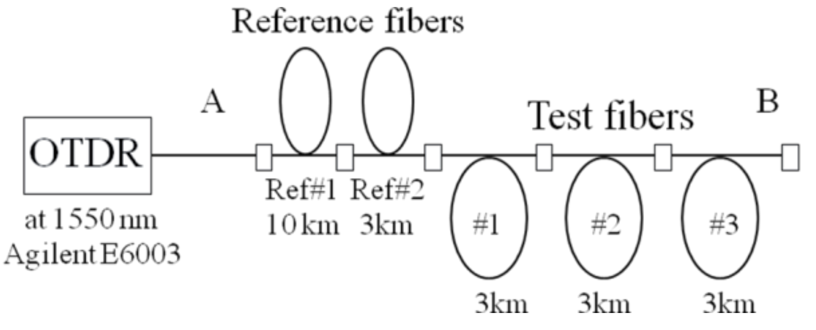

Figure 17. Concatenated fiber link

The fibers Ref#1 and Ref#2 were used as reference fibers for estimating the MFD and the relative-index difference Δ distributions in the concatenated fiber link. The parameters of these two reference fibers are listed in Table 2. Ref#2, #1, #2 and #3 are the conventional single-mode fibers. OTDR (Agilent E6003) was used to measure the backscattered signal powers for the concatenated fiber link.

Parameters	Ref#1	Ref#2
MFD (μm) at 1550nm	7.86	10.2
Cutoff wavelength λ_c (nm)	1150	1130
Relative-index difference Δ (%)	0.78	-
Fiber length L (km)	10.0	3.0
Loss (dB/km)	0.20	0.19

Table 2. Parameters of reference fibers

Figure 18 shows the MFD distribution at λ=1550 nm in the concatenated fiber link estimated by [4]. In this measurement, the OTDR pulse width was 1 μs and the averaging time was 3 min. The parameters of test fibers #1 to #3 are listed in Table 3.

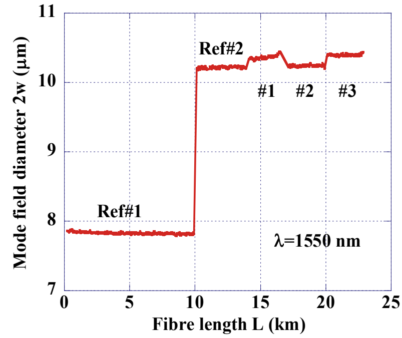

Figure 18. MFD distribution in the concatenated fiber link

Parameters	#1	#2	#3
MFD(μm) at 1550 nm	10.4	10.2	10.4
Cutoff wavelength λ_c (nm)	-	1250	-
Fiber length L (km)	3.0	3.0	3.0
Loss (dB/km) at 1550 nm	0.18	0.19	0.19
Raman gain efficiency* (1/W/km)	0.66	0.75	0.64

* The value measured by the direct technique.

Table 3. Parameters of test fibers

Figure 19 shows the relative-index difference *Δ(z)* distribution in the concatenated fiber link which was obtained by using the MFD distribution as shown in Fig. 19. It is seen that the relative-index differences *Δ* of Ref#2, #1, #2, and #3 are almost the same and the *Δ* of the Ref#1 is the largest among the test fibers.

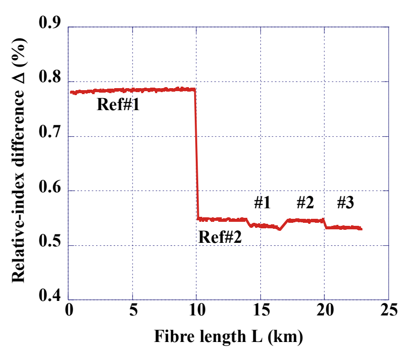

Figure 19. Relative-index difference *Δ(z)* distribution in the concatenated fiber link

The Raman gain efficiency normalized by that of Ref#2 was estimated from Figs. 18 and 19 by using (61), which is shown in Fig. 20. The Raman gain efficiency of Ref#2 was estimated to be 0.75 by the direct measurement technique. It is seen that the Raman gain efficiency of Ref#1 is the largest among the test fibers because the relative-index difference Δ is large and the MFD is small. We found that the Raman gain efficiencies of Ref#2 and #2 (group A) are larger than those of #1 and #3 (group B). Each group was fabricated by the same manufacturer. The ratio of the Raman gain efficiency of group B fiber to that of group A fiber was about 1.1.

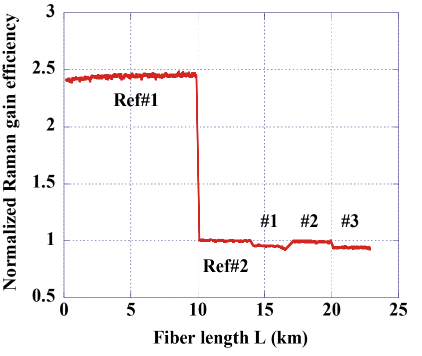

Figure 20. Normalized Raman gain efficiency in the concatenated fiber link

Next, we measured the Raman gain efficiency of the test fibers directly by using a pump laser. The experimental results are summarized in Table 3. We found that each group fiber has almost the same the Raman gain efficiency. We also found that the ratio of the Raman gain efficiency of group B to that of group A is about 1.2, which is in good agreement with the results obtained with the present technique.

We described a new technique for measuring Raman gain efficiency distribution using a conventional OTDR. The Raman gain efficiency in the 25km long single-mode fiber and the fiber link installed in the field with a length of 11 km composed of 22 conventional single-mode fibers were successfully estimated experimentally.

4. Conclusion

We described the measurement techniques for the longitudinal fiber parameters or transmission characteristics along the fiber based on the OTDR.

We described two types of techniques based on OTDR for measuring the longitudinal fiber properties by analyzing the backscattered power. One was the way of extracting the required information on the parameter from the capture fraction in the backscattered power just as it is. This technique is called "indirect method". As the backscattered capture fraction contains the information on the fiber parameters, the fiber parameters distibution can be ob-

http://dx.doi.org/10.5772/54243

tained by analizing the backscattered capture fraction. The other was the way of adding the information into the backscattered power by utilizing the phenomenon between the signal and pump lights and required information can be easily from the additional power in the backscattered power. This method is called “direct method”. By using two types of techniques, the required information can be extracted from the backscattered power in the fiber.

OTDR based measurement techniques will be powerful to estimate the various kinds of properties in the fibers or the optical transmission lines.

Acknowledgements

The author would like to express sincere thank to Prof. Tateda M. and Dr. Nakajima K. for their fruitful discussions. He would like to also thank Dr. Yamashita I., Dr. Tsutsumi Y. and Mr. Hatada H. for their helps during measurements.

Author details

Masaharu Ohashi

Address all correspondence to: ohashi@eis.osakafu-u.ac.jp

Osaka Prefecture University, Gakuen-cho, Naka, Sakai, Osaka, Japan

References

[1] Ohashi M. and Tateda M., ”Novel technique for measuring longitudinal chromatic dispersion distribution in single-mode fibres,” *Electron Lett.*, vol. 29, pp. 426-427, 1993.

[2] Nakajima K., Ohashi M. and Tateda M., “Chromatic dispersion distribution measurement along a single-mode optical fiber,” *J. Lightwave Technol*., vol. 15, pp. 1095-1101, 1997.

[3] Hagimoto K., Iwatsuki K., Takada A., Nakazawa M., Saruwatari M., Aida K., and Nakagawa K., “250 km nonrepeated transmission experiment at 1.8 Gb/s using LD pumped Er_{3+}-doped fiber amplifiers in IM/direct detection system,” *Electron. Lett.*, vol. 25, no. 10, pp. 662–664, 1989.

[4] Nakazawa M., Kimura Y., Suzuki K., Kubota H., Komukai T., Yamada E., Sugawa T., Yoshida E., Yamamoto T., Imai T., Sahara A., Nakazawa H., Yamauchi O., and Umezawa M., “Field demonstration of soliton transmission at 10 Gbit/s over 2000 km in

Tokyo metropolitan optical loop network," *Electron. Lett.*, vol. 31, no. 12, pp. 992–994, 1995.

[5] Tateda M., Shibata N., and Seikai S., "Interferometric method for chromatic dispersion measurement in a single-mode optical fiber," *J. Quantum Electron.*, vol. QE-17, pp. 404–407, Mar. 1981.

[6] Daikoku K. and Sugimura A., "Direct measurement of wavelength dispersion in optical fibers - Difference method," *Electron. Lett.*, vol.14, no. 5, pp. 149–151, 1978.

[7] Jopson R. M., Eiselt M., Stolen R. H., Derosier R. M., Vengsarkar A. M., and Koren U., "Non-destructive dispersion-zero measurements along an optical fiber," *Electron. Lett.*, vol. 31, no. 24, pp. 2115–2117, 1995.

[8] Nishi S. and Saruwatari M., "Technique for measuring the distributed zero dispersion wavelength of optical fibers using pulse amplification caused by modulation instability," *Electron. Lett.*, vol. 31, no. 3, pp. 225–226, 1995.

[9] Onaka H., Otsuka K., Miyata H., and Chikama T., "Measuring the longitudinal distribution of four-wave mixing efficiency in dispersionshifted fibers," *Photon. Technol. Lett.*, vol. 6, pp. 1454–1456, Dec. 1994.

[10] Ohashi M.,"Novel OTDR technique for measuring relative-index difference of fiber links", *IEEE Photon. Technol. Lett.*, vol. 18, pp. 2584-2586, 2006.

[11] Vita P. Di. and Rossi U., "Backscattering measurements in optical fibers: Separation of power decay from imperfection contribution," *Electron. Lett.*, vol. 15, pp. 467–469, 1979.

[12] Brinkmeyer E., "Analysis of the backscattering method for single-mode optical fibers," *J. Opt. Soc. Amer.*, vol. 70, pp. 1010–1012, 1980.

[13] O'Sullivan M. S. and Ferner J., "Interpretation of SM fiber OTDR signatures," in *Proc. SPIE'86 Optic. Testing Metrology*, vol. 661, pp. 171–176, 1986.

[14] Tsujikawa K., Ohashi M., Shiraki K., and Tateda M., "Scattering property of F and GeO_2 codoped silica glasses," *Electron. Lett.*, vol.30, pp. 351–352, 1994.

[15] Rossaro A., Schiano M., Tambosso T. and D'Alessandro D., "Spatially resolved chromatic dispersion measurement by a bidirectional OTDR technique," I*EEE J. Select. Topics Quantum Electron*., vol. 7, pp. 475-483, 2001.

[16] ITU-T Recommendation COM15-55-E, Dec. 1997.

[17] Pask C., "Physical interpretation of Peterman's strange spot size for single-mode fibers," *Electron. Lett.*, vol. 20, pp. 144–145, 1984.

[18] Shibata N., Kawachi M., and Edahira T., "Optical loss characteristics of high-GeO_2 content silica fibers," *IECE(J) Trans.*, vol. E63, pp. 837-841, 1980.

[19] Marcuse D., "Loss analysis of single mode fiber splice," *Bell Syst. Tech. J.*, vol. 56, pp. 703–718, 1977.

[20] Takachio N., Suzuki H., Masuda H., and Koga M., "32x10 Gb/s distributed Raman amplification transmission with 50-GHz channel spacing in the zero-dispersion region over 640 km of 1.55-μm dispersion- shifted fiber," presented at *the Optical Fiber Communication Conf. and Int. Conf. Integrated Optics Optical Fiber Communication (OFC/IOOC'99)*, Postdeadline Paper PD9.1, 1999.

[21] Nissov M., Davidson C. R., Rottwitt K., Menges R., Corbett P. C., Innis D., and Bergano N. S., "100 Gb/s (10x10 Gb/s) WDM transmission over 7200 km using distributed Raman amplification," in *Proc. Eur. Conf. Opt. Commun. (ECOC)*, Edinburgh, Scotland, pp. 9–12, 1997.

[22] Agrawal G. P., *Nonlinear Fiber Optics*, 3rd ed. New York: Academic Press, 1995.

[23] Shibata N., Horiguchi M., and Edahiro T., "Raman spectra of binary high-silica glasses and fibers containing GeO_2, P_2O_5 and B_2O_3, " *J. Non-Cryst. Solids*, vol. 45, pp. 115-126, 1981.

[24] Nakashima T., Seikai S., and Nakazawa M., "Dependence of Raman gain on relative index difference for GeO_2-doped single-mode fibers," *Opt. Lett.*, vol. 10, pp. 420-422, 1985.

Chapter 20

Optical Fibre on a Silicon Chip

A. Michael, C.Y. Kwok, Md. Al Hafiz and Y.W. Xu

Additional information is available at the end of the chapter

http://dx.doi.org/10.5772/54246

1. Introduction

Silicon is a typical substrate on which most devices on chip are made. It is a common platform for integrated circuits due to its well understood and established technological processes such as ionic implantation, diffusion, oxidation and others. Silicon has excellent mechanical properties, which make it suitable for realizing sensors and actuators on chip, which are often classified as Micro-Electro-Mechanical Systems. Integrated optics and planar light wave circuits have also extensively employed silicon as a substrate. Currently, silicon-photonics have become a promising technology to increase processing speed and reduce power consumption in multi-core micro-processor architecture.

Whenever optical interface to a silicon chip is required, optical signals must be coupled to optical components on the chip via optical fibres. These optical components include planar optical waveguides, micro-mirrors, photo-detectors, optical-switches, and micro-lenses among others. Precise alignment is necessary to increase the optical coupling. Such precise alignment is enabled by the formation of structures and mechanical components on the chip that positions the core of the fibre at the desired location with sub-micron precision. Silicon micro-machining is the technology that is instrumental for realizing such alignment structures and mechanical components on the chip for optical coupling purposes.

In this section, the various silicon micro-machining technologies available and the fundamental principles behind the technologies will be described. Special emphasis will be given to those which are particularly useful for optical MEMS applications.

1.1. Silicon micro-machining

Silicon micro-machining refers to the physical and chemical mechanisms of removing silicon material in a precisely controlled fashion, with the precision going down to a nano-scale. It can be achieved through various technologies. These technologies can be broadly categorized as wet and dry etch.

The wet etch can be further classified into isotropic and anisotropic silicon etch. Isotropic etch displays the same etch rate in all directions while anisotropic etch has directional etch rate dependency, which arises from differences in the etching rates of various crystallographic orientations in silicon by certain chemical solutions. For example, 25% TMAH water solution etches (100) crystal planes at 300 times faster than (111) crystal planes.

Dry etch in silicon is often accomplished by generating RF driven plasma. Positively charged ions and reactive species are created in the plasma. They are responsible for physical and chemical etching effects in dry etch. Although there are also other forms of dry etch that involve ion creation other than plasma, our focus will be on plasma based dry etch. As in the wet etch, dry etch can also be divided into isotropic and anisotropic. Positively charged ion bombardment and polymer deposition from reactive and neutral species are responsible for providing directionality and physical etchings in dry etch. Reaction between reactive species and silicon, on the other hand, yields chemical etching behavior to dry etch. The diagram in Figure 1 summarizes the classifications of silicon micro-machining technologies and commonly used etchants.

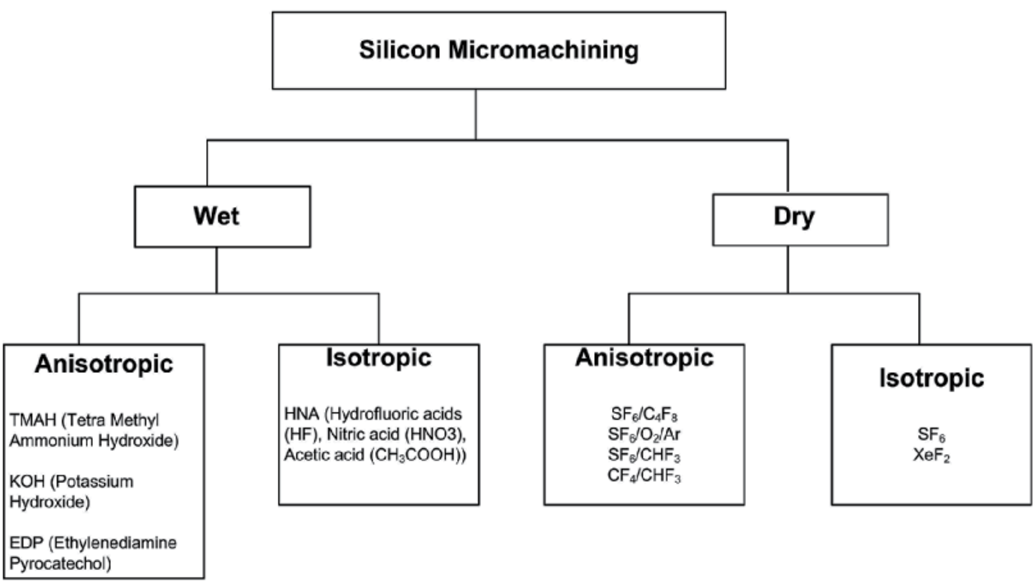

Figure 1. Classification of silicon micromachining

http://dx.doi.org/10.5772/54246

1.2. Silicon wet etch

1.2.1. Isotropic silicon wet etch

Acidic solutions containing oxidizing agents are used in an isotropic silicon wet etch. HNA, the solution of HF (hydrofluoric acid)/HNO_3(Nitric acid)/CH_3COOH (Acetic acid), is typical isotropic silicon and poly-silicon wet etchant. The dissolution of silicon proceeds with injection of holes into valance band of covalently bonded silicon structures. The source of the hole is the oxidizing agent, HNO_3, in the solution. The result is oxidation of silicon, which reacts readily with hydroxide ions in the solution to produce SiO_2 layer. The resulting SiO_2 layer will dissolve in HF by forming water soluble H_2SiF_6. Etching process of silicon in HNA can be summarized by the following simplistic reactions:

$$HNO_3 + HNO_2 \rightarrow 4NO^- + 2h^+ + H_2O \text{ (holes generation)}$$

$$Si + 4h^+ \rightarrow Si^{4+} \text{(holes injection)}$$

$$Si^{4+} + 4OH^- \rightarrow 2\, SiO_2 + 2H_2 \text{ (silicon oxide formation)}$$

$$SiO_2 + 6HF \rightarrow H_2SiF_6 + O_2 + 2H_2 \text{ (dissolution of silicon-dioxide)}$$

The overall reaction can be simplified to

$$Si + HNO_3 + 6HF \rightarrow H_2SiF_6 + HNO_2 + H_2O + H_2$$

The role of CH_3COOH (Acetic acid) in HNA is to dilute the solution. It is preferred to H_2O as it can better control the dissociation of HNO_3, and hence preserve its oxidizing power [1]. Due to the hole injection mechanism, etch rate of silicon in HNA depends on the type and concentration of dopants in silicon. Heavily doped silicon substrates etch faster. The etch rate reduces by 150 times when the concentration of dopants in silicon goes below 10^{17}atoms/cm^3 [2]. Table 1 summarizes the etching characteristics of HNA including suitable masking materials.

Parameter	Characteristics
Typical composition	250ml HF (49.2 wt%) + 500ml HNO_3(69.5 wt%) + 800ml CH_3COOH [3]
Etch rate	4um/min – 20um/min (at room temperature and increases with agitation) [4]
Surface roughness	Rough- with more proportion of HNO_3 Smooth – with more proportion of HF [1]
Temperature dependent	10-20Kcal/mol activation energy for concentrated HNO_3, and 4Kcal/mole for concentrated HF [5]
Masking material	Silicon-nitride is the best mask material with only 10°A-100°A/min etches rates in HNA. Other masking materials include Au/Cr at room temperature, and thick thermal oxide.

Table 1. Etching characteristics of HNA

Although isotropic wet etch of silicon has a wide range of application in making micro-needles for drug delivery and micro-probes for scanning microscopy, it is not suitable for formation of optical fiber insertion grooves as it may be difficult to control precisely the etched sizes of the grooves.

1.2.2. Anisotropic silicon wet etch

Anisotropic silicon wet etch is based on alkaline solution, which exhibits different etch rates depending on the crystal orientation of the exposed surface. Although there is still disagreement on why such crystallographic dependent phenomenon occurs, there are various models suggested to explain the behavior. These models include: (i) the number of silicon atoms on various crystallographic planes varies, with (111) plane having the largest density. However, such differences between the crystallographic planes do not explain the significant etch rate variations; (ii) The bond between the silicon atoms on the surface and the underlying atoms has different energy levels depending on the orientation of the surface [6]; (iii) the variations in nuclear roughness of various crystallographic planes, with (111) plane having the highest nuclear roughness of all planes [7]. Nuclear roughness is characterized as a nuclear barrier that reduces the etch rate by several dimensions.

Etching of silicon in such crystallographic dependent solutions proceeds with injection of electrons into the conduction band of silicon that results in oxidation of Si atoms on the surface by the following reaction

$$Si + 4OH \rightarrow Si(OH)_4 + 4e-$$

In the presence of H_2O, the silicate complex will be transformed into hexahydrosilicate complex due to the reduction of hydrogen in the water.

$$Si(OH)_4 + 4e- + 4H_2O \rightarrow Si(OH)_6^{2-} + 2OH^- + 2H_2$$

The overall reaction becomes

$$Si + 4H_2O + 2\,OH^- \rightarrow Si\,(OH)_6^{2-} + 2H_2$$

From the overall reaction, one can see that anisotropic wet etch solution requires OH^- groups, water solution, and results in the formation of H_2 that rises as bubbles. It is also important to note that the etching process is based on the transfer of electrons into the conduction band of the silicon, and as such the etching rate can be controlled by applying bias voltage. In fact, electrochemical etch stop is based on applying bias voltage that effectively stops the transfer of electrons into the silicon conduction bands.

Typically used alkaline solutions and their selectivity between the major crystallographic planes are summarized in Table 2. It will be worthwhile to note that selectivity between major crystallographic planes can vary by changing the composition of the solution and adding additives. Isopropanol and surfactants are commonly used additives in alkaline solutions. Although surfactants are added in order to reduce roughness of the etched surface and formation of hillocks, they are also found to affect etching characteristics of TMAH solutions. Generally, it slows down the etch rate of (110) oriented silicon surface.

Description	KOH	TMAH (1)	TMAH (2)	TMAH (3)	EDP
Etching solution	Potassium Hydroxide (24%) water solution, 85°	Tetra Methyl Ammonium Hydroxide (25%) water, 90°C	Tetra Methyl Ammonium Hydroxide (25%) water with 0.1% surfactants, 60°C	Tetra Methyl Ammonium Hydroxide (25%) 60°C	Ethylendiamin, NH_2-$(CH_2)_2$-NH_2,Pyrocatechol $C_6H_4(OH)_2$
R(100)	100μm/hr	55μm/hr	7.2 μm/hr	7.8 μm/hr	75
R(110)	-	65μm/hr	2.7 μm/hr	18 μm/hr	-
R(111)	0.25μm/hr	1.4 μm/hr	0.6 μm/hr	0.6 μm/hr	35
Masking layer	Si_3N_4 (70nm/hr) Thermal SiO_2 (0.43μm/min) PECVD-SiO_2 (0.7μm/min)	SiO_2(10^{-4} R(100)), Si_3N_4	SiO_2, Si_3N_4	SiO_2, Si_3N_4	SiO_2 (12nm-30nm/hr), Si_3N_4(6nm/hr), Au, Cr, Ag, Cu
R(100) (P^{++} - Si):R(100)	1:20	1:40	-	-	

Table 2. Typical anisotropic wet etching solutions

Three factors play important roles in determining the shape of the volume that will be formed in anisotropic wet etching solution. They are (i) the shape of the mask that determines the exposed pattern of silicon; (ii) the orientation of the mask edges; (iii) crystallographic etching characteristics (etch rate diagram) of the alkaline solutions. The crystallographic etching characteristic (etch rate diagram) is often given in a polar diagram form, where the angle from the reference orientation plane indicates the particular crystallographic direction and the magnitude corresponds to the etch rate. Considering the above three factors, creation of three-dimensional structure that results in is a complex process and various soft wares have been developed to assist engineers to perform simulation and prepare the right mask layout. Nonetheless, one can apply Wulff-Jaccodine method [8] along with the following etching behaviors at the convex corner, concave corner, and straight mask edge to make simple constructions of the resulting feature.

- At the straight mask edge: the etching progresses parallel to the mask edge and its shifting represents the etching-off of a side wall.
- At the Concave corners: sidewalls with the lowest etch rate are formed
- At the Convex corners: sidewalls with the maximum etch rate are formed

There are five important etching behaviors that worth discussing due to their significant application in creating grooves for optical fibre insertions, vertical micro-mirrors and side-walls, and 45° micro-mirrors.

1. Formation of V-grooves

The first requirement in the formation of V-grooves is to use (100) oriented silicon substrate. (100) oriented silicon substrate has its primary flat cut in <110> direction. The second requirement is to align square or rectangular window openings on the mask, as illustrated in Figure 2(a), along <110> direction which is parallel to the primary flat. The third requirement is to use anisotropic etchant with etching rate diagram showing minima at {111} planes. Etching with the above three requirements fullfilled will result in the formation of V-grooves (see Figure. 2(b)) or pyramidal pit bounded by (111) planes that are at 54.7° from (100) surface plane.

Let us now design the window opening size, w_o, of the mask that is required to form a V-groove to precisely position the core of an optical fibre at a distance, R, from the surface. Figure.2(c) illustrates optical fibre positioned in the V-groove and all the relevant dimensions including the depth of the V-groove from the surface, d_e, the radius of optical fibre including the cladding (the standard size is 125μm in diameter), and the position of the core from the surface, R. It should be noted that R will be negative if the core is positioned below the surface. The depth of the V-groove from the surface, d_e, is related to the radius of the optical fibre and the position of the core, Ras

$$d_e = 108.2 - R \tag{1}$$

It can also be related to the window opening size, w_o, and lateral under-etching of (111) plane, t_u , which is of course minimal, as

$$d_e = \tan(54.7)\left(\frac{w_o}{2} + t_u\right) \tag{2}$$

Eq. (1) and (2) can be combined and the window opening size can be expressed

$$w_o = 2\left(\frac{108.2 - R}{\tan(54.7)} - t_u\right) \tag{3}$$

The lateral under-etching of (111) plane, t_u, can be determined from the etching rate of (111) plane, $R_{(111)}$, and the etch time,t.

$$t_u = \frac{R_{(111)}\, t}{\sin(54.7)} \tag{4}$$

From Eq.(3),and (4), the window opening size can be simplified to

$$w_o = 153.2 - 1.416R - 2.45R_{(111)}t \tag{5}$$

where the etch time should be carried out for at least etching duration of, t , given the etch rate of the (100) plane is $R_{(100)}$

$$t \geq \frac{108.2 - R}{R_{(100)}} \tag{6}$$

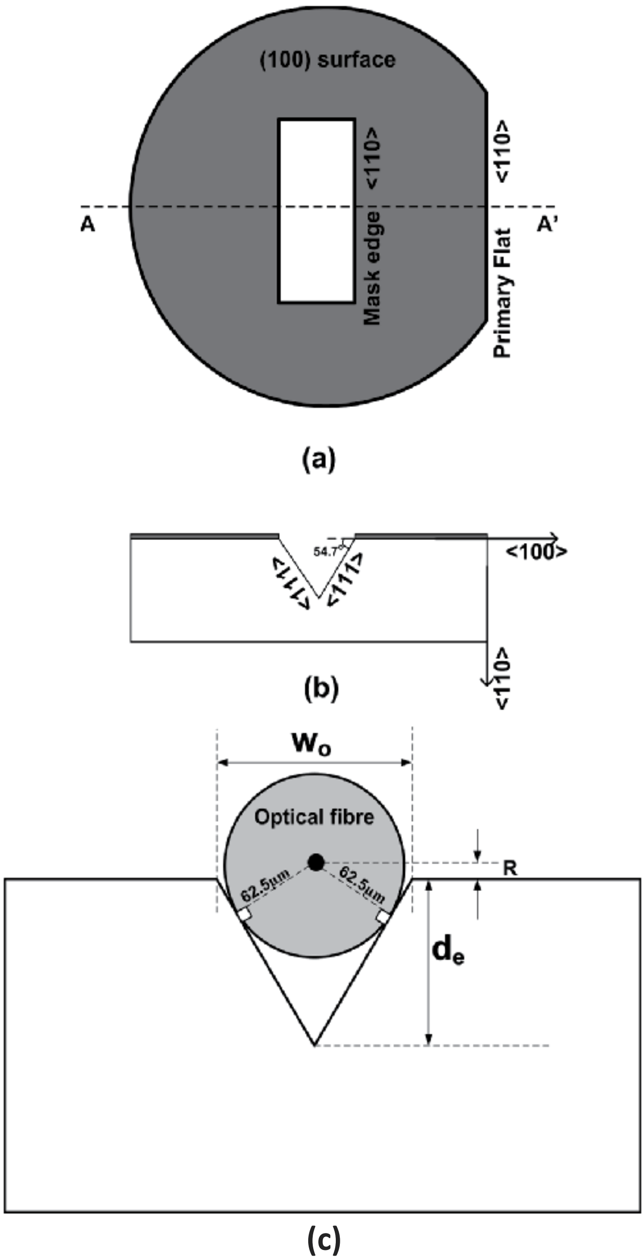

Figure 2. (a) Mask alignment in (100) type silicon; (b) the resulting V-groove after wet anisotropic etch; (c) optical fiber inserted in the V-groove

2. Formation of U-grooves

In this case, (110) type wafer will be used. (110) silicon substrate can be cut with primary flat in <111> direction. This direction can be used as a rough guide to align the window opening. However, for precise alignment of the mask in <111> direction, other techniques of locating the exact <111> direction should be employed. One of these techniques is to incorporate a wagon-wheel mask which extends from -3º to 3º with a pitch of 0.1º. The direction which displays the smallest lateral under-etch indicates the exact location of <111> direction. The (111) planes intersect on (110) surface to each other to form a parallelogram with 109.3º obtuse and 72.7º acute angles. The planes are either perpendicular or form 35.6º with the (110) surface. With etching solution that shows high (110) and (100) etch rates with respect to very slowly etching (111) planes, it is possible to make U-grooves with (111) vertical sidewalls. The same principle has also been applied to make vertical (111) micro-mirrors.

The primary flat of (110) wafer in <111> direction, the parallelogram window opening mask aligned to <111> direction, and the U-groove formed after etching are illustrated in Figure 3(a) and (b). Designing the window size opening for positioning the core of an optical fiber at a desired position in this case is easier than the case before. The depth of U-groove from the surface, d_e, is related to the radius of the optical fibre and the position of the core, R as

$$d_e = 62.5 - R \tag{7}$$

The window opening size can be expressed

$$w_o = 2(62.5 - t_u) \tag{8}$$

The lateral under-etching of (111) plane, t_u, can be determined from the etching rate of (111) plane, $R_{(111)}$, and etch time, t.

$$t_u = R_{(111)}\, t \tag{9}$$

From Eq.(8),and (9), the window opening size can be simplified to

$$w_o = 125 - 2R_{(111)}t \tag{10}$$

While Eq.(10) determines the required window opening size, the location of core is controlled with etch time, t

$$t \ge \frac{62.5 - R}{R_{(110)}} \tag{11}$$

3. Formation of rhombus channels

The etching characteristic, mask alignment direction, and wafer types needed for this purpose are similar to that of the formation of V-grooves, which is discussed earlier. In this case, the V-grooves are etched sideways in horizontal direction (as shown in Figure. 4(a)) as opposed to

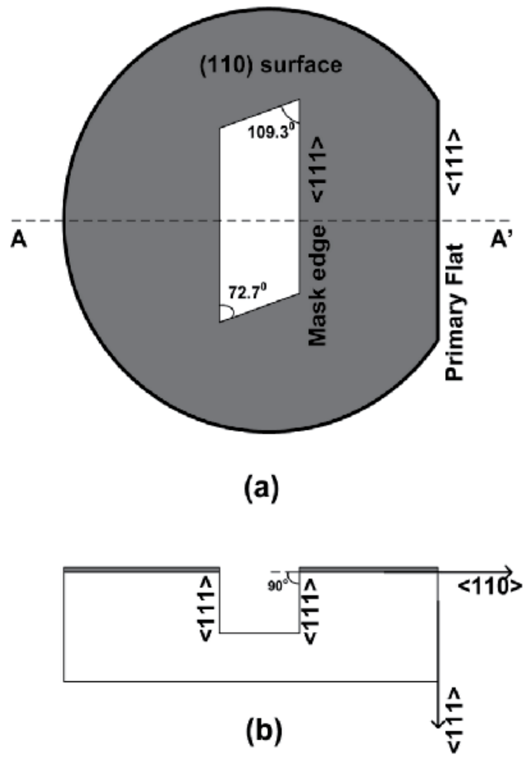

Figure 3. (a) Mask alignment for (110) type wafer with primary flat in (111) direction; (b) the resulting vertical trench after wet anisotropic etch

the previous case, where the V-grooves are etched down in the vertical direction. A narrow vertical opening is first made to expose (100) oriented vertical sidewalls by deep reactive ion etching of silicon as illustrated in Figure 4(b). The exposed vertical (100) silicon surfaces will be etched into a rhombus channels in anisotropic wet etch with sides being in (111). Hoffmann et al [9] has used 20% KOH solution at 60° to form the rhombus channels. Such channels are preferred to other grooves such as V or U-shaped ones because they provide self-clamping mechanism to the fiber inserted into the position. In V or U shaped grooves, other clamping or gluing mechanism will be required to keep the fiber in the required position.

Considering a narrow vertical opening with width,ω , and depth,d , before wet anisotropic etch, the final size of the rhombus channel after the wet etch is desired to precisely position the optical fiber as shown in Figure 4(c). The minimum depth, d, is related to the width, ω, and the optical fibre radius, r as [9]

$$d = \frac{2r}{\cos(\alpha)} - \omega\tan(\alpha) = 2r\sqrt{3} - \sqrt{2}\omega \tag{12}$$

For (100) silicon, α=54.7°.

With the optical fiber of the diameter of 125μm, and it is completely buried under the wafer, the minimum depth has to be 125μm and hence the width of the opening at the top should be 64.5μm. This is smaller compared to the width openings 241μm for V-grooves and 125μm for U-grooves.

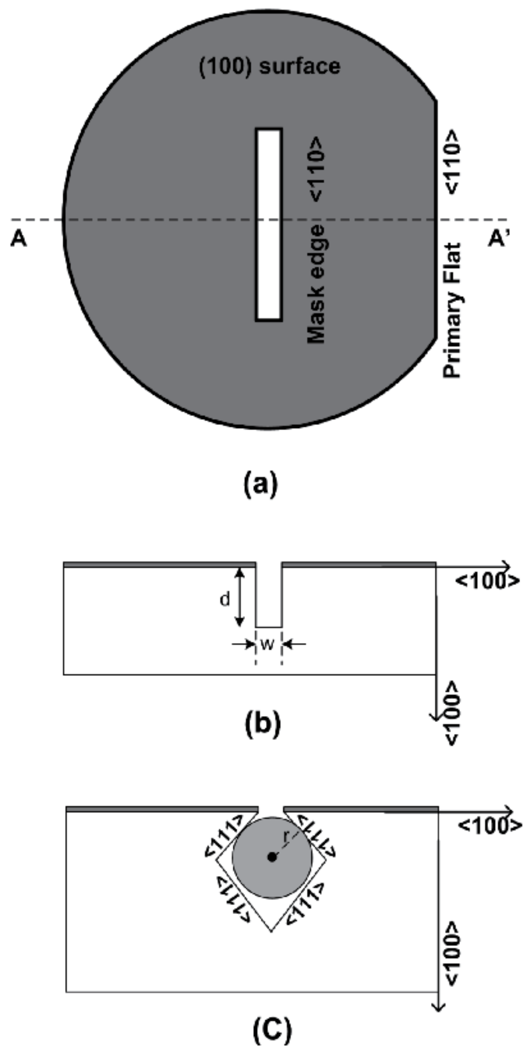

Figure 4. (a) Mask alignment in (100) type wafer for forming rhombus channels; (b) DRIE of narrow vertical trench in silicon defined by the mask; (c) the rhombus channel made after wet anisotropic etch with optical fiber inserted

4. Formation of vertical (100) micro-mirrors or sidewalls

Vertical mirrors that can precisely be aligned with optical fibers inserted into V-grooves are desired for MEMS based optical switches as it enables self-aligned switching architecture.

Although such optical switching architectures are possible with dry etching techniques, anisotropic wet etch is preferred due to the better mirror surface quality that is resulted.

For this case, (100) silicon wafer should be employed. The edge of the mask is aligned along <100> direction which is 45^o rotated from the orientation of the primary flat. With etching characteristics, where (110) planes are etching faster than (100) planes, vertical sidewall of (100) planes emerge as the etching progresses, and these planes etch sideways at the same rate as the horizontal (100) planes. With time controlled strategy, it is possible to form (100) vertical micro-mirror of the desired thickness. Such kind of etching behavior has been observed with KOH solutions [12]. However, TMAH and HNZ have not shown such etching characteristics.

5. Formation of 45^o micro-mirrors

The requirement to form such mirror is to use (100) silicon wafer, and align the edge of the mask at 45^o off the primary flat. This is similar to the case where vertical (100) micro-mirror is formed. The difference lies on the etching characteristics of the anisotropic wet etchant. In this case, the etching characteristics should display slower etching rate for (110) plane as compared to all other exposed planes between (100) and (110) planes. Other consideration that needs to be taken into account is the smoothness quality of the resulting surface. It is not easy to find the right etchant composition to satisfy both the requirements: (i) etching characteristics and (ii) surface smoothness. Solutions with the desired etching characteristics (etch diagrams) have displayed a rough 45^o surface. On the other hand, those with smooth surface quality tend to provide inferior etching characteristics. The resulting etched surface becomes more curved than slanted 45^o surface. As a compromise solution and in order to achieve both the requirements, techniques involving multi-step etching have been proposed and demonstrated to provide significant improvement. The first technique [10] involves the use of etching solution with the desired etching characteristics (etch diagrams) as the first step and the use of etching solution with smooth surface quality as the second step. In this technique, the first etching step provides the desired 45^o slope and the second etching step smoothens the rough surface resulted from the first etching step. The end result is slanted 45^o slope with smooth surface. The other technique [11] involves the use of etching solution that provides smooth surface and applying successive removals of suspended oxide mask. This method has improved the 45^o degree portions of the curved mirror by straighten up the top portion.

Table 3 reviews some of the anisotropic wet etchant solutions that have been used by various authors in forming V- grooves, U-grooves, rhombus channels, Vertical and 45^0 micro-mirrors.

1.2.3. Silicon dry etch

1.2.3.1. Isotropic silicon dry etch

An isotropic dry etch of silicon involves etching of silicon using chemical reactive species that are in vapor form. Various forms of mechanism are employed to form chemical reactive vapor species. They include sublimation of solid sources at low pressure [17], laser assisted etching [18], and plasma [19]. Although all these methods have been proved to be useful, plasma based dry etching process has been a common and standard practice.

Optical fibre insertion, alignment structures, and micro-mirrors	V-groove	U-groove	Rhombus-Channels	Vertical mirror	45° micro-mirror
Wet etch	33% KOH[12] KOH[13] 20%KOH[15]	25% TMAH [14]	20% KOH [9]	25% TMAH[14] 33%KOH[12] 20%KOH[15]	5% TMAH 1% Surfactant [11] 25%TMAH 0.1% surfactant[10] 36%KOH \IPA(isoproponal)[16]

Table 3. Anisotropic wet etching solution for forming optical MEMS

Hecht et al [20] and Hoffman et al [21] have used Xenon difluoride (XeF_2) to etch silicon isotropically and release CMOS circuitry, and form sensors and actuators. They produced vapour form of XeF_2 by sublimating solid Xenon difluoride at 1 torr and room temperature in a simple bell-jar setup. The etchant has shown excellent selectivity with respect to CMOS process layers. The etching process proceeds with spontaneous reaction of XeF_2 with solid Si to generate volatile gaseous by products of SiF_4 and Xe. Etching rates of 1-3μm/min are typical with XeF_2. The disadvantage of XeF_2 etch is that it causes rough surface. As a remedy to reduce roughness of the etched silicon, XeF_2 has been mixed with other halogen fluoride such as BrF_3 and ClF_3 [22].

The other common dry etching of silicon in isotropic manner is based on generation of fluorine reactive species from RF plasma. Fluorine, unlike chlorine and bromine, reacts with silicon to produce volatile SiF_4 spontaneously. In the absence of polymer deposition, fluorine reactive species from RF plasma produce pure isotropic etch. SF_6 is the typical source gas used for this purpose.

Although isotropic dry etches are important to release sensors, actuators, and CMOS circuitry, their applications in forming alignment grooves for inserting optical fibers in silicon are very limited.

1.2.3.2. Anisotropic silicon dry etch

Plasma driven dry etch process can be made directional by controlling ionic energy bombardment and allowing fluorocarbon polymer deposition. Ionic energy bombardment is controlled by the DC bias voltage between the plasma and electrode. Polymer deposition may be allowed by introducing carbon containing gases into the recipe. Directionality of ionic bombardment along with polymer deposition provides anisotropic plasma based silicon etching characteristics. For etching deep and high aspect ratio silicon structures, special reactive ion etching systems are commonly employed. These systems are often referred as Deep Reactive Ion Etchers. Such systems are capable of generating large density of reactive species (plasma), and controlling ionic energy bombardment independent of ionic density. They can also allow the substrate to be maintained at cryogenic temperature as low as 77K. At this cryogenic temperature, films can also be deposited from condensations of reactive gases. Sidewall deposition prevents sidewall etching while vertical ionic bombardment removes films deposited on horizontal surface, and allows directional etch [23,24].

Other deep silicon etch is based on alternate etching and deposition steps [25]. The etching step may use SF_6, SF_6/O_2, SF_6/Ar and can be purely isotropic. After a short time of pure etching, pure deposition step will follow. The deposition step will often use fluorocarbon gases such as C_2F_8 or CHF_3. $(CF_2)_n$ polymers are deposited on the substrate during this step. When these etching and deposition steps are repeated, they yield vertically etched structures.

Deep reactive ion etching of silicon is a very versatile micromachining technique which does not rely on crystalline orientation or type of silicon substrate. It has been used to form U-grooves for fiber insertion and alignment. Spring structures can easily be integrated with the U-grooves to provide fiber holding mechanism. Ji et al [26] and Marxer et al [27] have used this powerful technique in their 2X2 optical switch architecture. The actuator, micro-mirror, and fiber insertion and alignment grooves are all made in a single mask.

2. Thick silica film deposition

In addition to micro-machining techniques for silicon substrate, formation of optical components on silicon chip will require deposition and micro-machining of optical quality films. One of such films is silicon-dioxide (silica). Silica planar waveguides have been for a decade a key platform for fabrication of photonics circuits and optical Micro-Electro-Mechanical Systems (MEMS) devices. They can be easily coupled to optical fibre due to their low index contrast. Fabrication of silica waveguide requires deposition of silica film and consequently micro-machining the film to the desired waveguide core size. The thickness of silica for such purpose is usually in the range of 6μm-8μm depending on the wavelength of the light for which the waveguide is designed. Such thick silica films have to be deposited using chemical vapor deposition techniques. When their integration with integrated circuits is considered, chemical vapor deposition need to be carried out to maintain low thermal budget. In such case, plasma enhanced chemical vapor deposition is an appropriate technique. Moreover, it provides an efficient method of controlling film stoichiometry, refractive index, and surface roughness.

Plasma enhanced chemical vapor deposition of silica film based on the reaction of SiH_4 and O_2 gaseous has been reported to produce low loss silica waveguides [28,29] although other mixtures of gaseous can be used to deposit silica films. Controlling refractive index of silica film is essential to enable the formation of core and cladding of the waveguide. Silica film has been doped with Ge by introducing GeH_4 into the gaseous mixture, and the refractive index of the silica film has been controlled by varying the doping level of Ge in the silica film [30]. Silica films can also be doped with fluorine to change their refractive index [28,29,31,32]. In this case, CF_4 will be introduced as the source of fluorine to the gaseous mixture of SiH_4 and O_2. Another important parameter of the film that is critical for deposition of thick silica film is stress in the film. The stress should be minimized not only to maintain structural integrity of the deposited film but also to avoid stress related birefringence leading to polarization dependence losses. Controlling the stress of Ge-doped silica film has been found difficult [30]. From such perspective, F-doped silica films are preferred ways of minimizing stress and researches have been directed toward achieving this. Bazylenko et al. [28] has reported the experimental results of characterization pure and F-doped silica films using Hollow Cathode PECVD system for fabrication of silica waveguides. Their results have shown that fluorine incorporation into silica film reduces both stress and refractive index. However, this trend of stress and refractive index reduction does not continue as more CF_4 is introduced into the mixture, but reverses trend and causes more abrupt increase of stress and refractive index. The reason is attributed to the scavenging of O_2 by CF_4 to cause silicon rich film. Increasing the flow rate of O_2 has been suggested as a way of mitigating the scarcity of O_2 in the plasma. However, stress in the film increases as more oxygen is added into the plasma at the same flow rate of CF_4. Moreover, it does not stop the occurrence of reversal trend at higher CF_4 flow rate. The characteristics of F-doped silica films deposited at various RF powers and $O_2/CF_4/SiH_4$ flow rates in HC-PECVD have been studied [31]. Figure.5 shows the refractive index and stress of silica films as the RF power varies from 100W-300W. The results in the figure are obtained for the flow rates of CF_4= 30sccm, O_2=50sccm, and SiH_4=20sccm. The stress in the silica film reduces as the RF power increases up to 220W. From 220W onwards, the stress starts to increase rapidly. XPS analysis of the films has revealed that the stress reversal behavior at 220W attributes to the onset of oxygen depletion in the plasma and hence silicon richness of the film. As the flow rate of CF_4 is reduced maintaining the same flow rates of SiH_4 and O_2, the RF power, at which the onset of oxygen depletion occurs, increases markedly. On the other hand, for higher CF_4 flow rates, the RF power, at which the onset of oxygen depletion occurs, reduces only slightly. For instance, the increase in CF_4 flow rates from 30sccm to 46sccm has reduced the required RF power for oxygen deficiency slightly by only 4W. The RF power, required for onset of oxygen deficiency in the plasma, for various CF_4 flow rates has been obtained and plotted in Figure 6. The results clearly indicates that for a given SiH_4 and O_2 flow rates, there is a threshold RF power below which oxygen depletion in plasma will not occur even at practically higher CF_4 flow rates. This means that continuous reduction in silica film stress as well as refractive index can be achieved with incorporation of more fluorine into the film. It is even possible to deposit oxide film with slightly tensile stress at higher CF_4 flow rates. This is particularly useful to reduce the overall stress in thick film deposition [33] and to form MEMS structures that are not prone to buckling [34].

It has been indicated before that it is possible to shift the occurrence of oxygen depletion in the plasma to a higher CF_4 flow rate by increasing oxygen flow rate in the gaseous mixture. This is an obvious solution as more oxygen will be available in the plasma, and causes oxygen rich film. However, the film becomes more stressed. In order to reduce the stress in the film while increasing permissible CF_4 flow rate range in which oxygen depletion does not occur, SiH_4 flow rate is reduced. This has lowered the silicon content of the silica film and less stressed film results [31]. Figure 7 (a) and (b) show stress and refractive index of silica film deposited at various CF_4 flow rates at 300W RF power and O_2=100sccm for SiH_4=20sccm and SiH_4 = 15sccm, respectively.

http://dx.doi.org/10.5772/54246

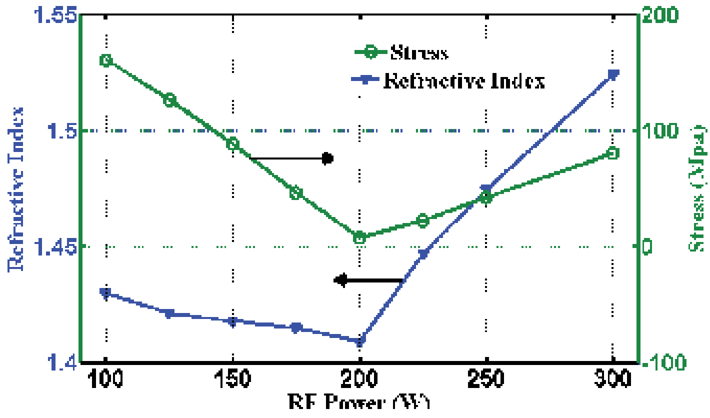

Figure 5. Refractive index (green) and stress (blue) as a function of RF powers

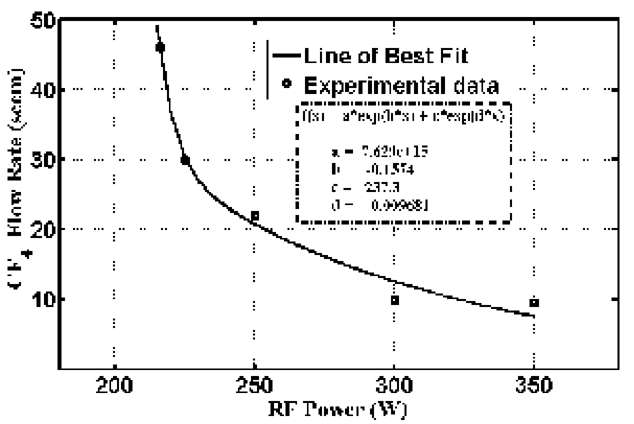

Figure 6. RF powers and CF_4 flow rates at which oxygen depletion starts to occur

Depositing a desired film thickness is based on characterizing deposition rate at the given deposition condition. Measuring deposition rates of silica films at various CF_4 flow rates have shown that deposition rates are almost constant independent of CF_4 flow rates [31,32]. This behavior is quite attractive for depositing F-doped graded index layers for making planar waveguides and planar grin lenses. Figure 9 shows the constant deposition rate of silica film at RF power = 300W, O_2 = 100sccm and SiH_4 = 15sccm for various CF_4 flow rates.

The above deposition techniques have been used to form silica films as thick as 90μm as shown in Figure 8. Such successful thick film deposition is attributed to the reduction of stress in the film to almost zero. This is useful characteristics for realizing optical components on silicon chip including planar silica waveguides, planar silica lens and 3D micro-lens.

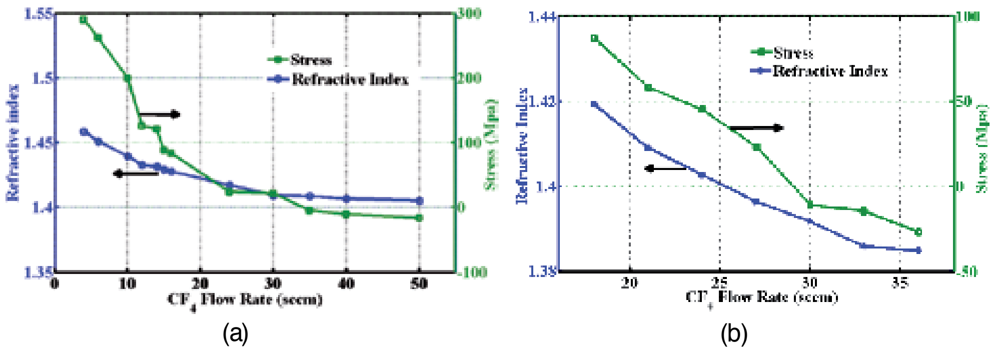

Figure 7. Refractive index and stress for various flow rates at (a) SiH_4= 20sccm (b) SiH_4=15sccm

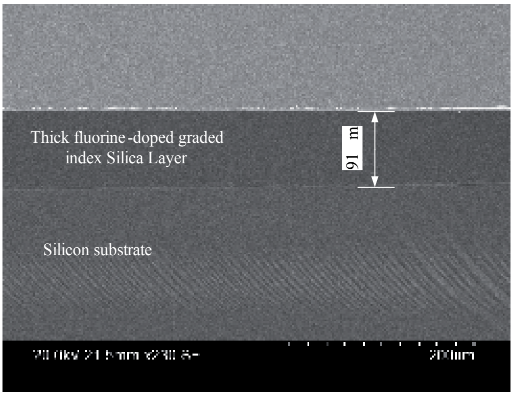

Figure 8. SEM cross-sectional view of thick fluorine-doped graded index silica layer deposited by HC-PECVD deposited on a plane silicon substrate;

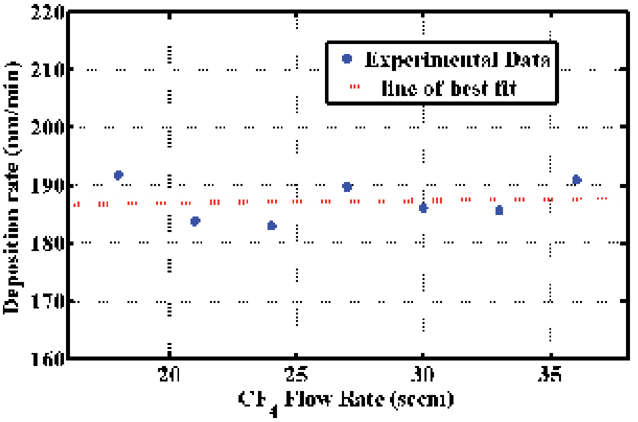

Figure 9. Deposition rate as a function of CF4 flow rates

By depositing silica films with parabollically graded refractive index profile, planar silica lens can be fabricated [32, 35]. The desired graded index profile as a function of thickness is represented by step wise approximation. An index step of 0.001 has been found to minimize optical loss due to the approximation to only 0.5dB [30]. The step index of 0.001 or less is, therefore, often chosen for step-wise approximation of the desired refractive index profile. Based on the chosen step index, the corresponding step height at a desired thickness can be computed from the refractive index profile. The refractive index value at the desired height corresponds to a unique CF_4 flow rate (depending on other deposition conditions such as Figure 7(a) or (b)), and the step height corresponds to deposition duration (based on deposition rates) for the constant and corresponding CF_4 flow rate. Thus, the desired refractive index profile can be translated into a deposition schedule which indicates what CF_4 flow rate to use, for how long and when. The CF_4 flow rate at the scheduled time determines the refractive index. How long the CF_4 is maintained at the scheduled time determines the step height at the desired thickness, which is related to the scheduled time.

It is important to confirm that the deposition schedule has resulted in the desired parabolic graded index profile. This is done by confirming experimentally the periodic refocusing characteristic of the graded index profile. To measure the periodic refocusing length, first spin Polymer poly (N-vinylpyrrolidone) (PVP) doped with Xanthene dye, Phloxine B, on top of the deposited graded index layer. A green light from a single mode fiber coupled to a frequency doubled Nd:YAG laser (532 nm) source can then be shined onto the graded index silica side of cleaved sample. The resulting periodic yellow emissions due to the excitation of the dye from the extension of the evanescent field into the polymer layer can be measured to determine periodic refocusing length.

4. Silica micro-machining

In addition to the ability to deposit thick and refractive index modulated silica layers, capability of micro-machining thick silica film is also necessary to form micro-optical components on silicon substrate. Vertical and relatively smooth sidewalls are desired in most situations. Reactive ion etching is capable of providing such etching characteristics. Unlike silicon, reactive ion etching of silica is a more aggressive process as there are no gaseous species that react with silicon-dioxide spontaneously. Some level of reactive ion bombardment and fluorocarbon polymer film deposition are needed. The fluorocarbon film reacts with silica in the presence of ion bombardment to form a volatile SiF_4. To increase the etch rate of silica and improve mask selectivity, the ionic current density, ionic energy, and F/C reactive ion species are required not only to be boosted [36] but also independently controlled. Inductively coupled plasma (ICP) reactive ion etching system can fulfill these requirements. The substrate potential with respect to the plasma can be independently controlled by the platen RF power. High density plasma, controlled by the RF coil power, can be generated at low pressure to result in the desired ionic current density. Advanced Oxide Etch STS ICP has been used to etch thick silica and glass layers using various masks [37]. Photoresist masks are acceptable when the etch depth of less than 6μm are required. For deeper etches in a range of 6μm-50μm, polysilicon masks are more appropriate. When the etch depth of greater than 50μm is desired, metal masks should be used. We have done thick silica film etching using amorphous silicon as a mask in Advanced Oxide Etch STS-ICP (AOE STS-ICP) system. The etching experiments are discussed below.

Amorphous silicon film is deposited onto a thick silica layer using HC-PECVD system as an etch mask for deep silica etch. Mixture of SiH_4 and Ar gases at 4mtorr chamber pressure and 300W RF power are employed as process parameters for depositing amorphous silicon film. Photoresist is spun on amorphous silicon film and photo lithographically patterned. Figure 10(a) shows the cross-sectional view of the patterned photoresist on the top of the amorphous silicon film. Using the photoresist as the mask, the amorphous silicon film is dry-etched. SF_6 and C_4F_8 chemistry at 20mtorr chamber pressure and 600W (RF coil power)/30W (RF platen power) are used to etch the amorphous silicon at 1μm/min and expose the silica in AOE STS-ICP. Figure 10(b) is the cross-sectional SEM images of the patterned amorphous layers on the top of thick silica.

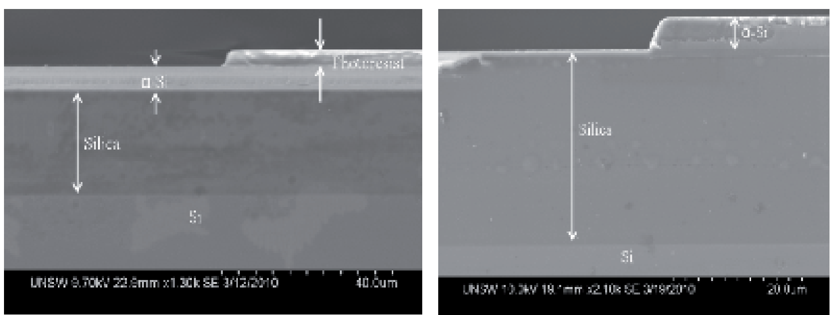

(a) (b)

Figure 10. Cross-sectional image of patterned (a) photoresist on the top of amorphous silicon (b) amorphous silicon on the top of thick silica

Various recipes have been investigated to etch thick silica. The recipes are based on varying the coil and platen powers while keeping other parameters constant. C_4F_8 (at 30sccm) and He (at 300sccm) are used as the process gases at 6mtorr chamber pressure. The coil powers of 1000W, 1400W, and 1800 W and platen powers of 200W, 400W and 500W have been investigated to optimize the etching process for achieving vertical side wall, high selectivity between silica and amorphous silicon, and high etching rate. Figure 11 (a) and (b) plot the etch rate, selectivity between the silica and amorphous silicon layer, and sidewall angle as a function of coil powers with 400W platen power, and as a function of platen power with 1000W coil power, respectively. The results indicate that the etch rate, selectivity, and sidewall angle are improved by increasing platen power at a given coil power or vice versa. Large coil and platen power, however, have caused the receding of the mask. The mask receding increases proportionally with coil and platen power and is attributed most likely to the fast erosion of the mask at the corner edges due to the concentration of electric field at those spots. In order to avoid such mask receding and achieve the desired etching profile (vertical sidewall and fast etch rate),

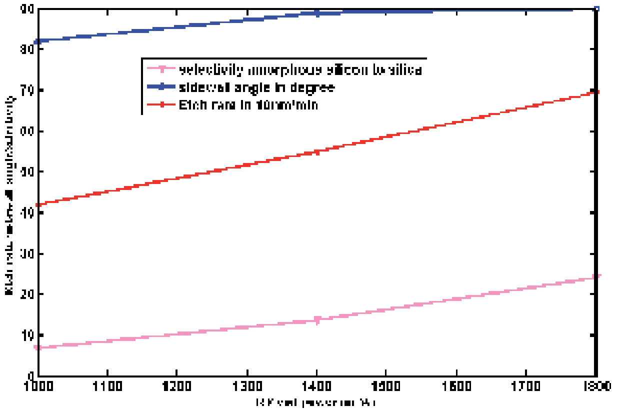

(a)

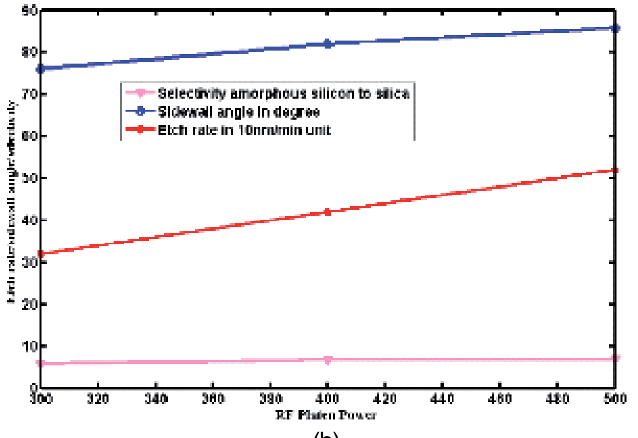

(b)

Figure 11. Etch rate, selectivity, and sidewall angle for (a) various RF coil power with 400W platen power (b) various RF platen power with 1000W RF coil power.

coil RF power of 1400W and platen RF power of 400W have been chosen as best compromising process parameters. Figure 12 shows the SEM image of the cross-sectional view of the etched silica layer at the chosen process parameter. Vertical and relatively smooth sidewall has been achieved.

5. Planar silica lens pairs

Before we look at some applications of silicon and silica micro-machining in optical switching and optical interconnects, it is important to first present planar silica lens pair. This is because of the significant applications that this planar ens pair has for optical switching and interconnect. Hence, the design principles and fabrication of the planar lens pair will be described in this section.

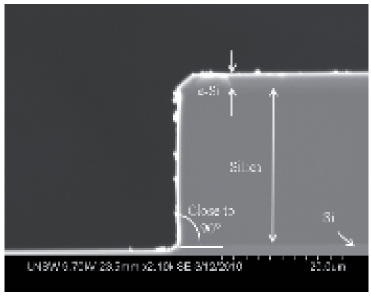

Figure 12. Cross-sectional SEM image of deep etched silica film using the optimized etching recipe

Optical beam will be required to propagate in free space from one planar silica waveguide to another in Planar Light wave Circuits (PLC). Free Space optical switch and interconnect systems are based on such requirements. The design of such systems should ensure the propagation loss be minimized. The free space propagation loss between two planar waveguides depends on the optical beam size, propagation distance, and misalignment (both lateral and angular) between the waveguides. These losses have been well understood and the behaviors can be summarized as follows

- The propagation loss increases with propagation distance.
- The propagation loss increases with lateral and angular misalignments.
- The propagation loss increases as the beam spot size reduces. Such losses are significant even for small propagation distances, in a range of 10μm-100μm, for the spot sizes of typical silica waveguides, in a range of 2μm-6μm.

Significant free-space propagation loss at smaller spot size attributes to the large divergence angle of the optical beam. Such large divergence angle associated with smaller optical beam size can be reduced by collimating the optical beam at the source and re-focusing the beam back to the original beam size at the receiving end. Although traditional 3D lens can do the collimation and re-focusing, it will be difficult to integrate them with planar waveguides. Therefore, planar lens pairs are needed for planar waveguides.

Planar lens pairs with parabolically graded index profile in a vertical direction and convex curvature in horizontal direction have been proposed [30]. The design of such lens has been discussed in detail [30, 35, 38]. Here, the design flow chart will be presented to illustrate the design methodology. Relevant articles and associated equations are referred in the flow chart to direct interested readers for more detailed information.

The schematic of the planar lens pair with design parameters is shown in Figure 13(a), in which, dT is the free-space propagation distance, ω_0 is the input spot-size of the Gaussian beam. The graded index profile of silica, defined by $n(x)=\left\{n_0{}^2[1-2\Delta(x/\rho)^2]\right\}^{1/2}$, is used for the design of micro-lens pair, where $\Delta=(n_0^2-n_{cl}^2)/2n_0^2$ is the relative index change, and x is the transverse (vertical) coordinate. n_0, n_{cl} and ρ are the maximum refractive index, minimum refractive index and half-width of the graded index profile, respectively. Other system parameters required for the planar lens pair design, but not shown in Figure 13(a), are the maximum refractive index in the graded index profile, n_0, the relative index change, Δ, the vertical spot-size ωcx, at mid-point of the free-space propagation distance and the wavelength λ. The evolution of the Gaussian input spot-size as it propagates through the micro-lens pair and the free-space in between is illustrated schematically in Figure 13 (b) and (c). Figure 14 shows the flow chart of a planar lens pair design procedure for an ideal free-space propagation distance, dT, with zero loss. Design parameters are taken as inputs to the design flow. Other parameters that will be calculated during the planar lens pair design include (i) horizontal spot-size at the micro-lens/air interface, ωiy, (ii) horizontal spot-size at mid-point of the free-space propagation distance, ωcy, (iii) maximum vertical spot-size in the micro-lens section, ωmx, (iv) radius of curvature defining the convex shape, R, (v) planar lens length, L, (vi) focusing parameter, $\alpha = \sqrt{2\Delta}/\rho$, (vii) minimum refractive index of the graded index profile, n_{cl}, and (viii) half-width of the parabolic graded index profile, ρ.

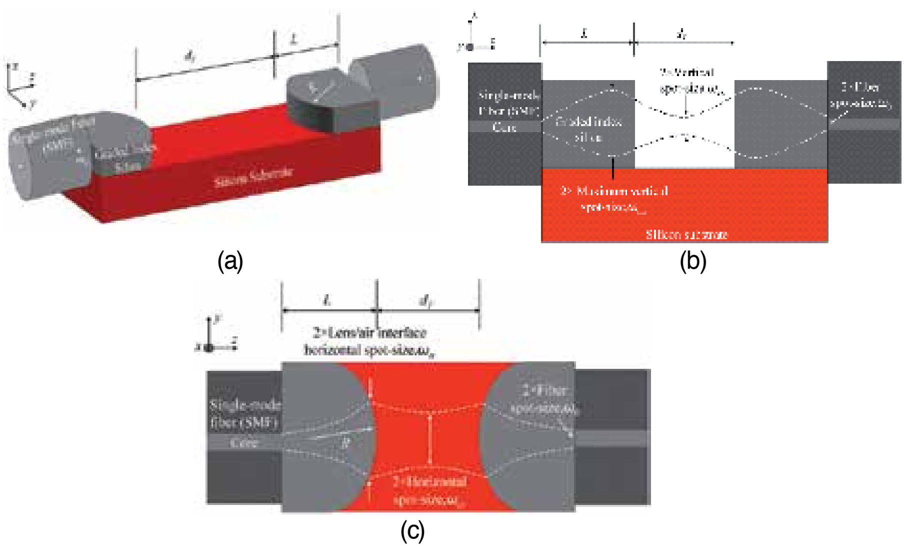

Figure 13. (a) Schematic of a planar silica planar lens pair with input and output fibre, (b) side view, and (c) top view, showing the Gaussian beam evolution in the micro-lens pair and in the free-space.

At the beginning of the design flow, the design parameters, λ, n_0, ω_0, ωcx, $dT/2$ and Δ are used to find the ABCD parameters [38] in the vertical direction. The outputs of this stage are planar lens length L and the half-width of the parabolic refractive index profile ρ. Using the value of ρ, the length of one fourth of the ray period, $\pi\rho/4\sqrt{2\Delta}$, is calculated where the vertical beam diameter reaches its maximum value. The maximum vertical beam spot-size ωmx is then computed. At this stage of design flow, a decision has to be made as to whether the vertical beam spot-size is sufficiently small or not because this parameter determines the thickness of the graded index film to be deposited for the planar lens fabrication. If the decision is 'No', the design process will go back to the input stage to change the vertical spot-size at mid-point of the free-space propagation distance ωcx. Otherwise, the design flow will continue to the next step to find the lens/air interface horizontal spot-size ωiy, from which the horizontal spot-size at mid-point of the free-space propagation distance ωcy, is obtained. Using L, n_0, λ, ωcy, ω_0 and $dT/2$ together with ωiy and ωcy, the ABCD parameters in the horizontal direction are calculated. Finally, the radius of curvature of the planar lens front-face R, is determined from the ABCD parameters in the horizontal direction [38].

Based on the design flow chart and design parameters indicated in Table 4(a), planar lens pairs for dT=200 μm is designed. The calculated parameters for the planar lens pair are provided in Table 4(b).

d_T=200 μm	
Design parameters	Value
λ	0.633 μm
Δ	0.01
n_0	1.40
ω_0	2.1 μm
ω_{cx}	5 μm
(a)	

d_T=200 μm	
Calculated parameter	Value
ω_{iy}	12.67 μm
ω_{cy}	12.57 μm
ω_{mx}	6.69 μm
R	52.45 μm
L	182.36 μm
$\alpha = \sqrt{2\Delta} / \rho$ ncl ρ	10.24×10^{-3} μm -1 1.386 13.8 μm
(b)	

Table 4. (a) Design parameters and (b) Calculated parameters for the micro-lens pairs designed for d_T=200 μm.

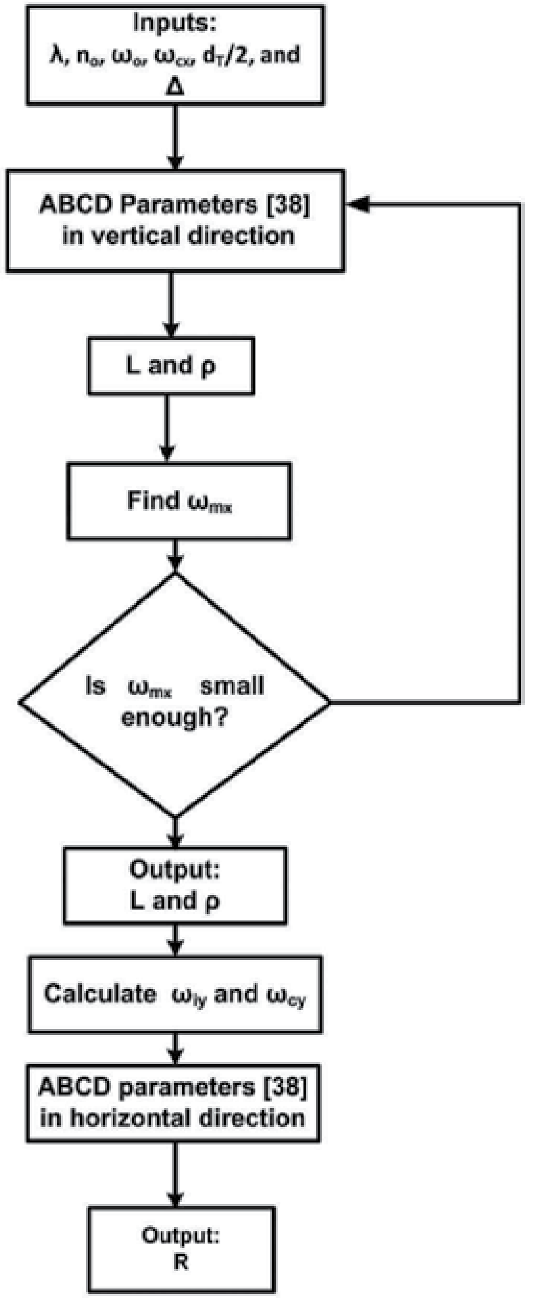

Figure 14. Design flow chart.

It can be shown from the design methodology of the planar silica lens that as the design parameter, d_T, free-space propagation distance increases the required thickness of the lens increases provided that other design parameters are kept the same. For example, for d_T=500 μm, the required thickness of the silica planar lens almost doubles. The thickness of the planar lens pairs for d_T=200 μm is 2* ω_{mx}+ buffer layer (6μm) + capping layer (4μm)) whereas for d_T=500 μm, the thickness has to increase to 32μm. The implication is that deposition of low stress thick silica film and its micro-machining will be necessary to create low loss long free-space optical link on chip. It also signifies the importance of deposition and micro-machining techniques discussed earlier.

The planar lens pairs designed for d_T=200 μm have been fabricated and tested to substantiate the design [35]. The SEM image of the planar lens pairs with V-grooves for optical fiber insertion and alignment is shown in Figure 15. The fabrication process steps consists of thick graded silica film deposition, silica micro-machining, and wet anisotropic etching of silicon using TMAH. The process starts with (100) silicon wafer. The graded index silica film with buffer and capping layers is then deposited on the silicon wafer according to the deposition schedule obtained from the step-wise approximation of the parabolic graded index profile designed for d_T=200 μm. An amorphous silicon layer is deposited on the top of the thick silica layer and patterned. Using the patterned amorphous silicon as a mask, the thick silica layer is etched to define the convex curvature of the lens, the free space distance between the lens pairs, and openings on silicon for forming the V-grooves. Finally, the sample is etched in 25% TMAH with 0.1% of surfactants to form the V- grooves and the free space between the lens pairs. Figure 16 illustrates the fabrication process steps.

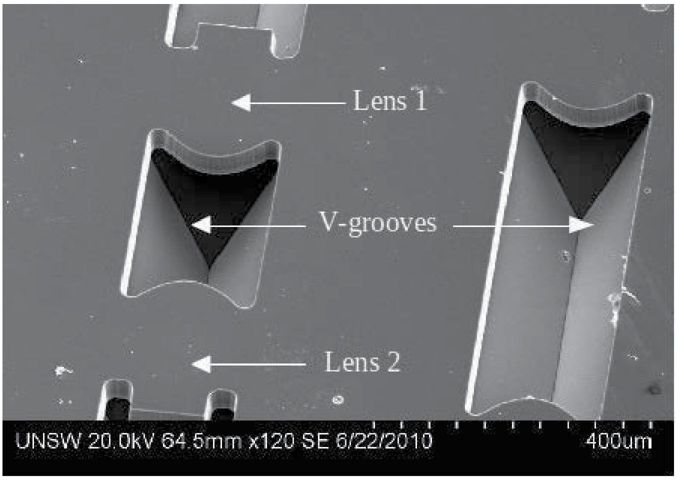

Figure 15. The SEM image of fabricated micro-lens pairs with V-grooves

After fabrication, the input and output optical fibers are inserted into the V-grooves and butt coupled to the planar lens pair. A 633nm optical signal from a pigtailed laser source is coupled to the input fiber while the output optical power at the output optical fibre is measured. The power at the output of the input fiber is measured to be used as a reference power to calculate the optical loss in the system.

http://dx.doi.org/10.5772/54246

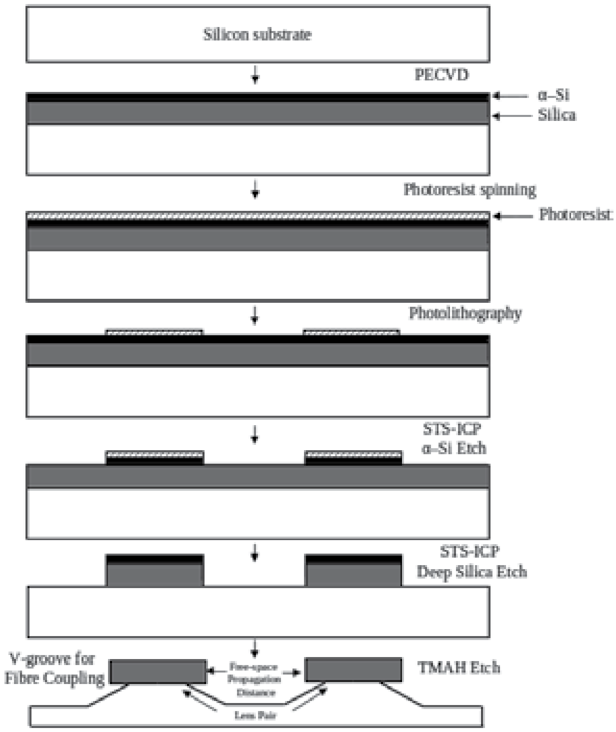

Figure 16. Fabrication process flow.

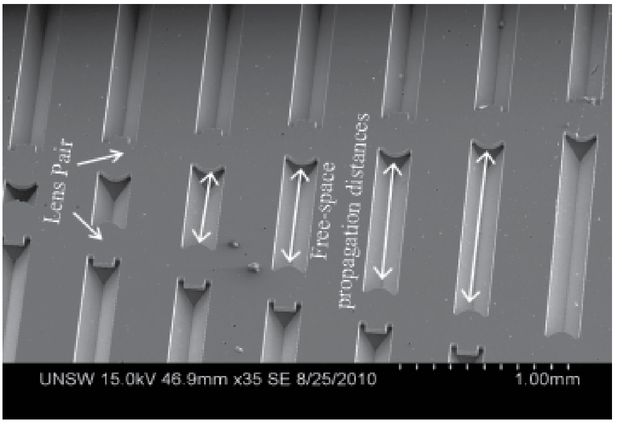

Figure 17. SEM image of identical micro-lens pairs with various free-space propagation distances

To evaluate the performance of the planar lens pair, various free-space propagation distances were fabricated, apart from the ideal free-space propagation distance of 200 μm as shown in Figure 17. The measured and theoretically calculated losses for the planar lens pairs are plotted in Figure 18 for free-space propagation distances of 50, 100, 200, 300, 400 and 500 μm.

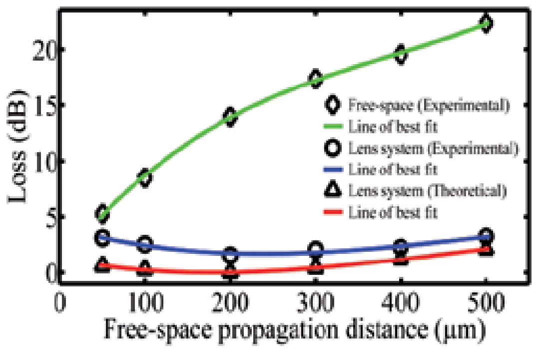

Figure 18. Free-space propagation losses with and without the micro-lens pair set ups designed for d_T = 200 μm.

The measurement indicates that there is a good agreement between the theoretical calculations and experimental results. It can also be seen that the planar lens pair is best suited for 200μm free-space propagation distance, for which it is designed, and the increase in loss from the minimum is only about 1dB for ± 50% departure from the optimal free-space distance of 200 μm.

Loss reduction in using the planar lens pair in free-space propagation distances in comparison to the case without the lens pair is also plotted in Figure 18. The coupling loss for 200 μm free-space propagation distance is measured to be 13.95dB whereas by using the planar lens pair the loss is reduced to 1.56 dB, which is 12.4 dB reductions in loss. For longer free-space propagation distances, the loss improvement is even more significant. For example, 19 dB of measured reduction in loss is obtained for 500 μm of free-space distance using the micro-lens pair designed for 200 μm. This is particularly significant as it compares to a theoretical 21 dB loss improvement expected for a micro-lens pair designed for an ideal zero loss free-space propagation distance of 500 μm.

The application of this planar lens pairs for optical switching and interconnects in a free-space can be significant as it can be used to collimate light for waveguides integrated on the chip, and optical fibers coupled to the integrated circuits. The applications of planar lens in MEMS based optical switch architectures and 3D optical interconnect systems will be described.

6. Applications

6.1. MEMS based optical switching

MEMS based optical switches have been described extensively in the literature. The following are some characteristic advantages that make MEMS especially suitable for optical switching applications compared to other optical switching mechanisms such as those based on change in the refractive index due electro-optic, thermo-optic, acoustic-optic, or free carrier effects [39-42] and bubble switches [43-45].

http://dx.doi.org/10.5772/54246

- Low insertion loss and cross talk
- Independent of optical wavelength, polarization and data modulation.
- small size
- Reliability
- Mass-production at low cost
- Enable large matrix switching to be monolithically integrated in a single chip

The continuing increase in the high speed transfer of large data size using the internet and large increase in the WDM channel count have led to the increased demand for compact and multi-channel optical switches. MEMS technology has been proposed as a means of meeting these requirements. As a result, many new developments have been reported in MEMS optical switches. In fact, it is evolved into a new field of MEMS called MOEMS (Micro- Opto-Electro-Mechanical Structures).

MEMS optical switches are generally classified as 3-D MEMS optical switches and 2-D MEMS optical switches. In 3-D MEMS optical switches [46, 47], micro-mirrors are rotated into two axes to steer optical beam in any desired direction. Because the mirrors can assume any possible positions, they are also referred as 'Analog optical switches'. On the other hand, in 2-D MEMS optical switches, the micro-mirrors assume only two-positions and move into or out of the optical beam direction. As a result of assuming only two positions, they are called 'Digital optical switches'.

6.1.1. 2D MEMS optical switch

The 2D MEMS optical OXC architecture uses a dedicated mirror to cross connect an input port to a particular output port. The mirror is manipulated by an actuator to assume one of two positions. When it is in one position, it establishes a connection by directing light from an input port to an output port. In another position, it moves out of the optical path and ends the connection. 2-D MEMS switches have been commonly implemented using two approaches: free-space and guided-wave. Free-space approaches are characterized by the presence of fairly long, typically larger than 200μm, free space travel and optical fibers as waveguides. On the other hand, guided-wave approaches are characterized by a short free space propagation distance and the presence of planar wave guides instead of optical fibers. However, the coupling of the planar waveguides with optical fibers is required to interface optical signals from off-chip sources. This is especially the case for telecommunication application where optical fibers are signal carriers.

6.1.1.1. MEMS Actuators for 2-D MEMS Free space optical switches

Various MEMS actuators are used in 2-D MEMS free space optical switches. These actuators include Scratch Drive Actuators (SDA) [48, 49], Cantilever, Comb-drive, Torsion Beam, Hinged Plates and Bridges.

Lin *et al* [50, 51] have used arrays of SDAs to make flip-up mirrors for optical switching applications as shown in Figure 19 (a) and (b). Lee *et al*[52] and Chen *et al*[53] used SDAs to create self assembly mechanism for their optical switching system. SDAs were also employed to drive a cam-micromotor for optical fiber switching by Kanamori *et al* [54] as shown in Figure 19 (c) and (d). Although SDAs are in-plane actuator, not intrinsically bi-stable and move only in one direction, it is possible to create bi-stable, two-way actuated, out-of-plane optical switches by using interleaved micro-hinges, pushrods and two sets of SDAs such as the one developed by Lin *et al*[50]. The only disadvantage of SDAs is that they require large voltage for operation, typically larger than 100V.

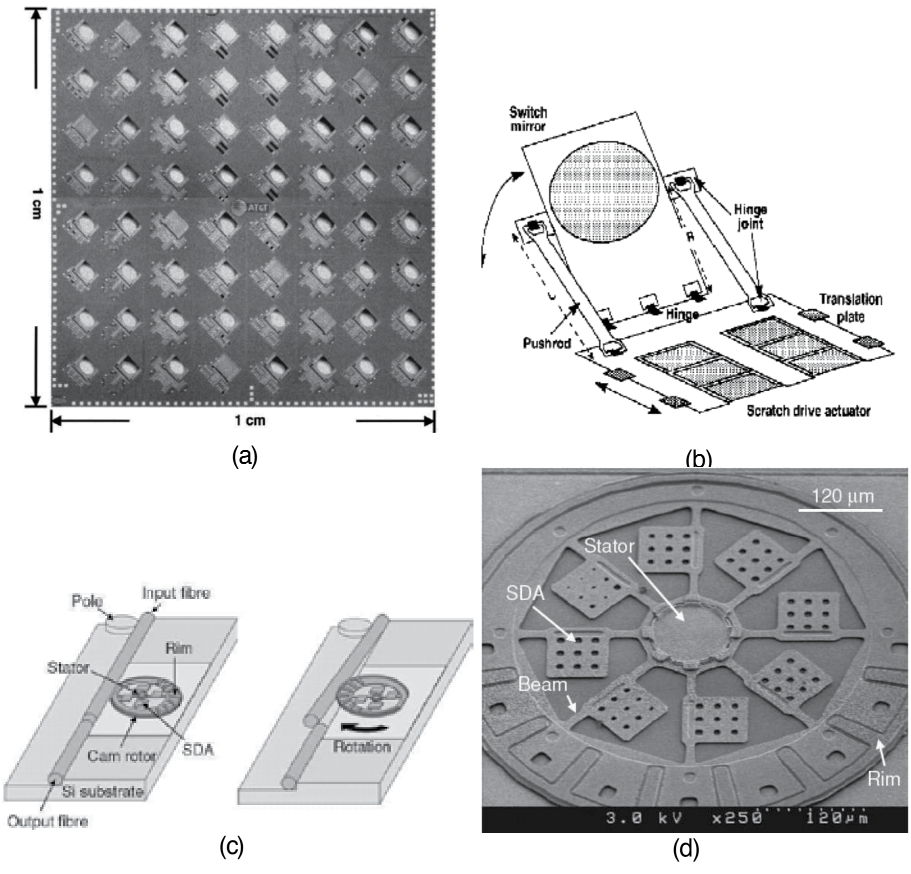

Figure 19. (a) An array of 8X8 Optical Cross Connect switches from Lee *et al* [50]. (b) Schematic illustration of SDA actuated flip-up mirror [50].(c) SDA driven cam-micromotor for optical switch with 'ON' and 'OFF' position Kanamori *et al*[54] (d) SDA driven cam-micromotor [54]

Helin *et al*.[55] presented a self-aligned bulk-micro-machined optical switch using a cantilever actuator. The vertical mirror is integrated to the tip of the silicon cantilever beam and V-grooves for optical fiber insertion and alignment are made in a single wet anisotropic silicon etch as shown in Figure 20.

http://dx.doi.org/10.5772/54246

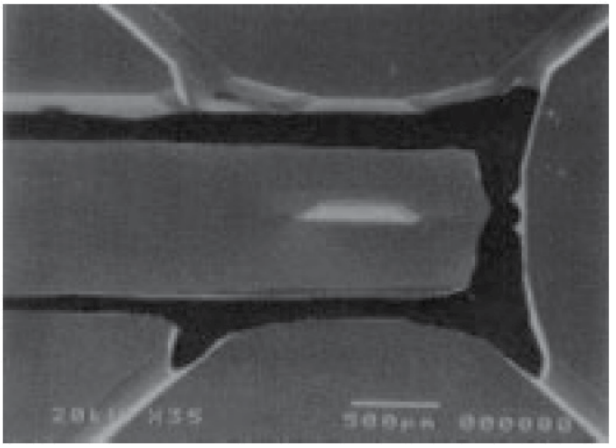

Figure 20. Bulk micro-machined self aligned 2X2 optical switch [55].

Electro-magnetically actuated vertical cantilever actuator is also used by Ji *et al* [56] to realize MEMS optical switch using DRIE technology as shown in Figure 21(a) and (b). The vertical cantilever beam is supported by torsion beams. The vertical micro-mirror, U-grooves with clip structures for optical fiber insertion and alignment, and actuation structures are all made in a single dry anisotropic etch.

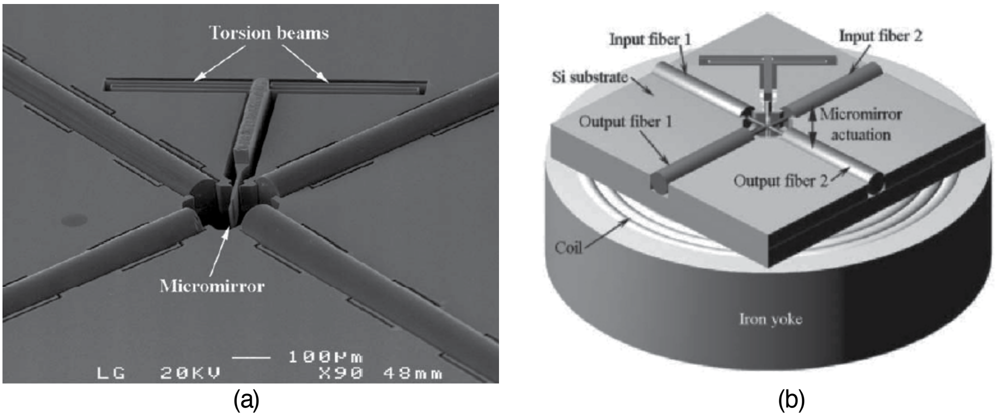

Figure 21. (a) 2X2 optical switch array from Ji *et al* [56] (b) illustration of magnetic field source and optical switch system[56]

The cantilever actuators such as the ones used by Helin *et al* [55] and Ji *et al*[56] are bi-stable as a result of employing permanent magnet in electro-magnetic actuation. Two-way out-of-plane actuation and low-voltage drivability are also other important features of these actuators.

Comb-drive actuator is commonly used for in-plane actuation. Marxer *et al* [57] used comb-drive actuator to make an optical switch as shown in Figure 22. DRIE is used to form U-grooves for optical fibers insertion and alignment, the vertical mirror and the comb drive actuators in one mask step.

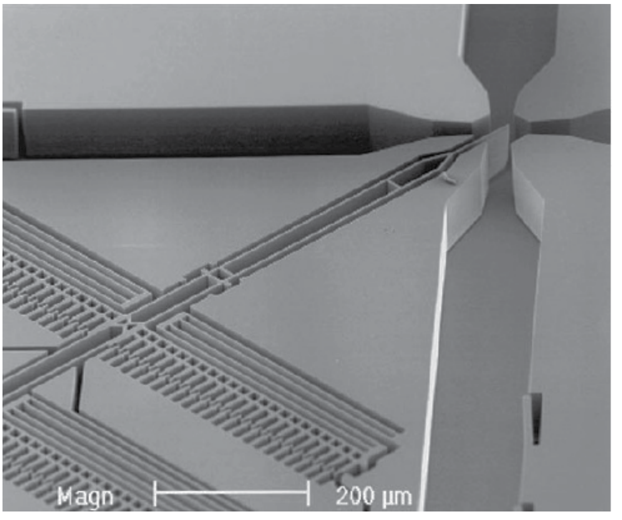

Figure 22. SEM of actuator-mirror system from Marxer *et al* [57]

6.1.1.2. MEMS actuators for Guided-Wave 2-D MEMS optical switching

Although MEMS actuators like comb-drives, cantilevers, and suspended plates have been used in planar waveguide switching, they are developed in a different fashion and actuation mechanism so that they can be appropriate to PLC applications. This is because the approach employed for free-space optical switching was not suitable for planar waveguide switching due to some fundamental differences.

- Large mirror sizes, commonly in the range of 200μm, are required for optical fiber switches compared to small mirror sizes, in the range of 40μm-50μm, for PLC depending on the beam waist. Related to this difference, SDA actuators used for optical fiber switching in [50-53] and Torsion beam and hinges in [58-59] are not appropriate for planar waveguide switching.
- Optical fibers are placed in and aligned using V-grooves (or U-grooves) in free space optical switches. These grooves can be precisely designed and fabricated to position the core of the fiber at any level relative to the surface of the wafer. The core can be positioned on or below the plane surface of the wafer. This flexibility of positioning optical fibers is not possible with planar waveguides. Planar waveguides are usually fabricated in a different substrate and assembled above the surface of the wafer. As a result of this inflexibility, cantilever actuators with electromagnetic actuation similar to those of Helin *et al* [55] and Ji *et al* [56] may not suitable for planar waveguide switching applications.

http://dx.doi.org/10.5772/54246

- Figure 23(a) and (b) shows the comb-drive configuration used by Dellmann *et al* [60] for guided wave optical switching. The actuator, the mirror and the trenches were fabricated in one substrate using DRIE on SOI. The arrays of planar waveguides were fabricated on another substrate. The two wafers were then assembled together by aligning the waveguides into the trenches.

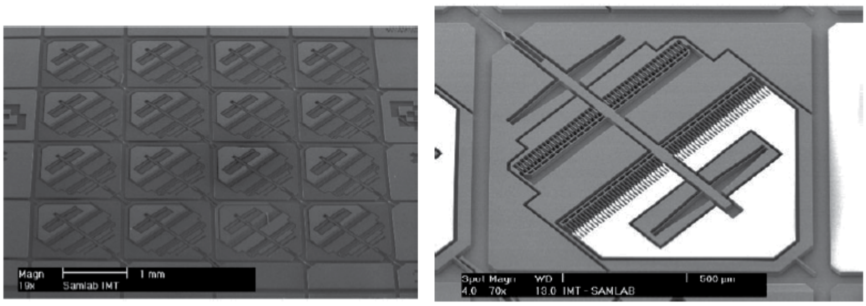

(a) (b)

Figure 23. (a) planar waveguide optical switch matrix[60] (b) Single optical switch[60]

In another configuration for guided wave switching, an actuator consisting of a plate suspended by four symmetric beams (springs) is used by Iyer *et al* [61]. The actuator and a single switch arrangement are illustrated in Figure 24(a) and (b).

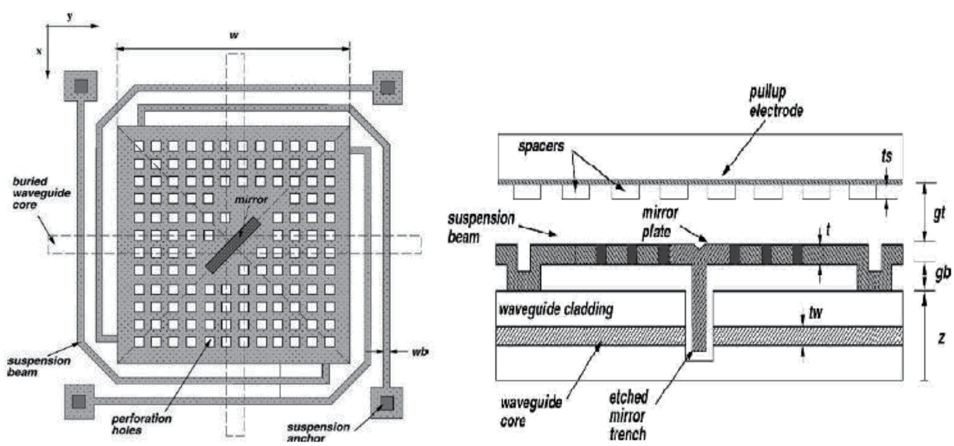

(a) (b)

Figure 24. (a) illustration of actuator used and (b) a single planar waveguide optical switch from Iyer *et al*[61].

Guerre *et al*. [62] used a simple cantilever and bridge actuator in the configuration shown in Figure 25(a) and (b) for PLC switching application.

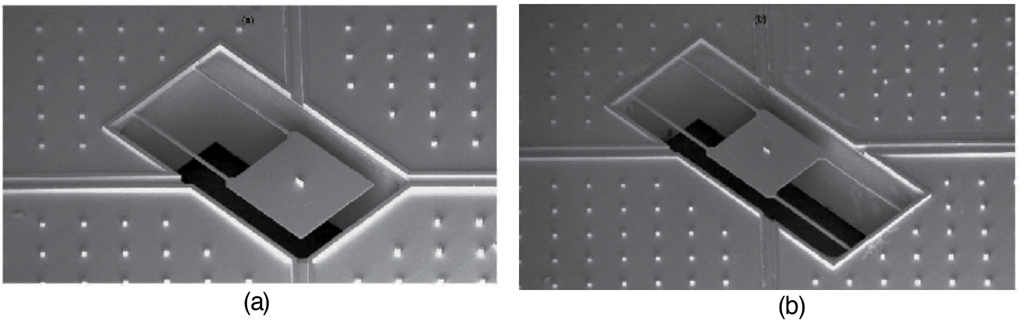

Figure 25. (a) Cantilever actuator with a micro-mirror[62] and (b) Bridge actuator with a micro-mirror Guerre *et al*[62]

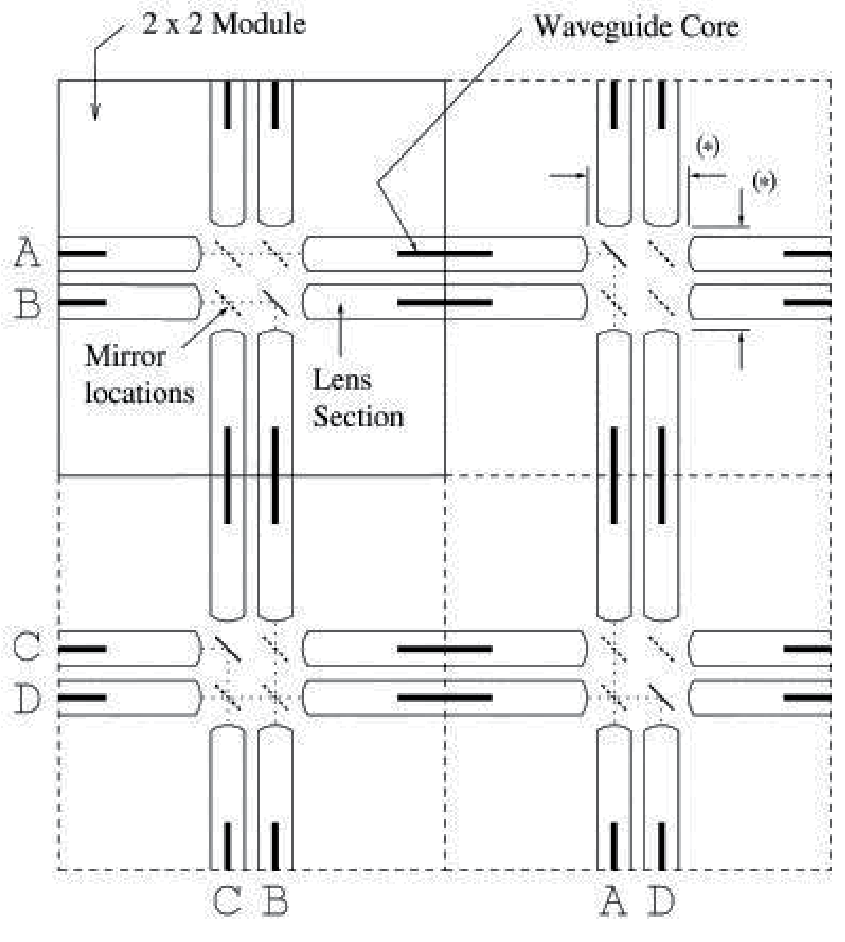

Figure 26. Optical switching architecture combining both Free space and guided wave features[63].

http://dx.doi.org/10.5772/54246

6.1.1.3. Combined free space and guided-wave MEMS optical switching

The major drawback of guided wave MEMS optical switching architectures is the requirement to employ two separate substrates to form the optical switch. This is mainly due to the incompatibility between the PLC and MEMS actuator fabrication processes employed in the guided wave optical switching schemes. Thus, developing MEMS actuation mechanism that is compatible with PLC fabrication processes is necessary to solve the drawback. Moreover, such actuation mechanism may enable to realize new optical switching architecture proposed by Mackenzie *et al* [63]. The architecture is based on planar lens pairs and their integration with MEMS actuation mechanism. It combines both free-space and guided wave approaches and is illustrated in Figure 26. It incorporates the advantages of simplicity in free-space architectures and large port count in guided wave approaches.

The same authors [64] later also suggested a 1X4 modular optical switching layout, which can be cascaded to make larger matrix optical switches. This switching layout, based on the planar lens pair, can theoretically minimize propagation loss regardless the matrix size. As a result, it is expected to provide a significant possibility of realizing multi-channel 2-D MEMS optical switching.

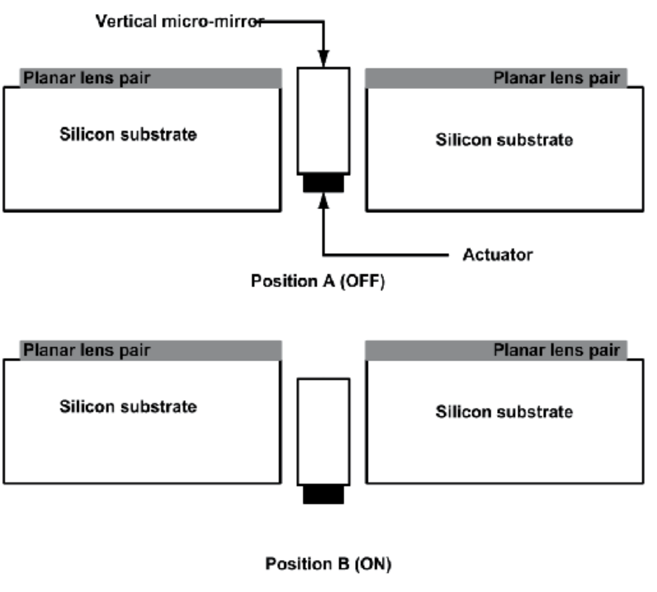

Figure 27. Desired positions of micro-mirror for planar lens pair optical switching

For such combined Free Space and guided-wave MEMS optical switching architecture to be realized, micro-mirror actuation mechanism that fulfills the following characteristics is required: (i) compatibility with planar lens fabrication process; (ii) large out-of-plane deflections; (ii) bi-stabilty. Figure 27 illustrates the switching positions of the micro-mirror actuation mechanism with respect to planar lens pairs. When the micro-mirror is moved to position A, it defines an OFF state. To switch ON the optical link between planar waveguides, the micro-mirror will be moved down to position B. Since bi-stability is desired for optical switch, the out-of-plane deflections that define the ON and OFF positions of the micro-mirror should be stable posi-

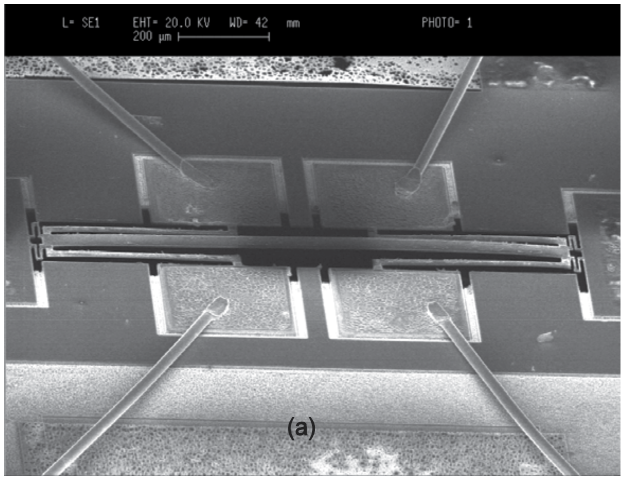

Figure 28. Bi-stable thermally actuated micro-bridge actuator

tions. Previously realized micro-mirror actuation mechanism for free space or guided wave MEMS optical switches do not fulfill the above requirements, and hence are not suitable for planar silica lens. Bi-stable thermally actuated micro-bridge [65] has been developed to enable micro-mirror actuation mechanism that is compatible with planar lens pairs fabrication process steps and provides the required out-of-plane movement. Figure 28 shows the SEM image of thermally actuated micro-bridge actuator. The actuator has 1200μm length, 80μm width, and 5.5μm effective thickness. It has provided 30μm range of out-of-plane movement. The fabrication process [65] is based on releasing a silicon membrane on which the micro-bridge is defined using wet anisotropic TMAH silicon etch with electro-chemical etch stop. When the micro-mirror is integrated with the micro-bridge, the length of the micro-bridge is increased to compensate for the size of the mirror that integrates to the mid-portion of micro-bridge. In addition, the effective length, the length of the micro-bridge minus the length the mirror, should be chosen to provide the required out of plane movements for optical switching. In the case of planar silica lens with d_T=200um, the micro-mirror must travel at least 24μm (the thickness of the planar lens) out-of-plane from the surface of substrate in order to fully intercept the optical path for either ON or OFF switching operation. Not only the mirror is required to be moved at least by 24um out-of-plane but also it should stay in that position without requiring power for bi-stability operation. In other words, the micro-bridge should provide at least 24μm initial out-of-plane deflection. Based on buckling behavior [66] and bi-stability criteria [67] of the micro-bridge, the effective length of 1500μm has been calculated. The fabricated micro-mirror actuator designed for such purpose is shown in Figure 29. The vertical mirror is monolithically integrated with micro-bridge. The mirror has an initial out-of-plane deflection of 27μm as seen from SEM image taken at 80^o tilt in Figure 30, and confirmed by MSA Polytech surface analyzer. For this monolithic integration of micro-mirror, (110) oriented silicon wafer with the primary flat in (111) is used. This enables to form vertical micro-mirror with sidewall having (111) orientation. Other (111) planes at 35.6^o from the sides also emerge. The final shape of the micro-mirror is more like trapezoidal than a perfect rectangle with the top length of 100μm and bottom length of around 850μm for 270μm thick silicon substrate. The total length of the micro-mirror actuator is, therefore, about 2350μm as can be measured from Figure 29. The optical characterization of the micro-mirror actuator [14] has demonstrated less than 0.9dB optical insertion loss during ON state and more than 60dB isolation loss during OFF state at 1.3μm wavelength. Combining this micro-mirror actuator with planar lens pairs in 1X4 modular optical switch architectures can provide optical switch with the maximum optical loss of only 2.46dB. The optical switch can be extended to 2X4 matrix with the maximum loss of 4.02dB. The maximum loss for any NX4 matrix based on 1X4 modular unit is 2.46 + (N-1)*1.56. For an allowable optical loss of 16dB, for example, the optical switch matrix can be extended to 9X4.

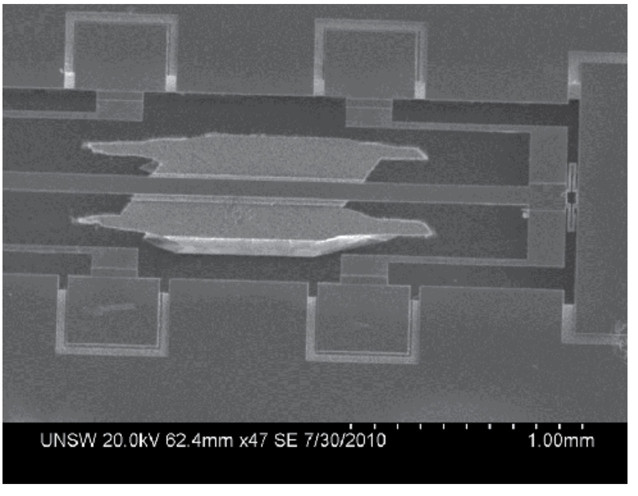

Figure 29. The micro-mirror actuator with monolithically integrated vertical micro-mirror.

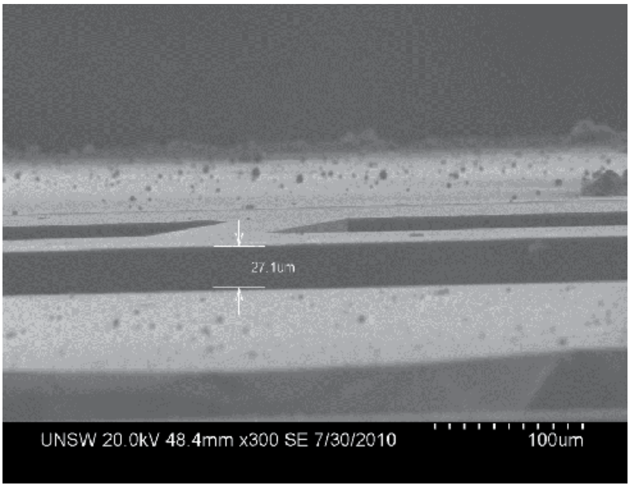

Figure 30. Initial out-of-plane deflection of micro-mirror as viewed at 80° tilt

6.2. MEMS based 3D optical interconnect

Optical link has provided a solution to bandwidth limitation exhibited by wire link. It has been found to be effective when the length of the link is substantial depending on the data speed. Optical link is now ubiquitous form of interconnect for switching nodes in telecommunication network, and for rack to rack communication. As the communication speed goes beyond 10GHz, optical links for board-to-board communication on the PCB and core-to-core communication on multi-core process on a single chip become viable solutions not only to resolve the bandwidth limitation of wire interconnects but also to reduce cost and save power consumption. As the number of cores in multi-core architecture increases, it is envisaged that communication speed in order of THz will be reached. Although TSV (Through Silicon Via) technology is used to reduce the wire interconnect distance between integrated circuits in 3D stack to increase bandwidth, it is inevitable that optical link in 3D stack will be cost driven solution. A number of solutions have been proposed to create such optical link. One of these solutions involves optical propagation in free-space. Focusing elements are required for low-loss free space optical link. Focusing techniques based on Micro-ball lens [68], fluidic membrane lens [69], a planar PDMS lens [70] and a polymer lens [71] are not compatible with planar waveguides and requires separate assembly processes. Planar silica lens pair discussed earlier in this chapter is well suited for such purpose. The integration of this planar lens in the 3D optical interconnect system has been demonstrated [72].

The 3D optical interconnect system employs a pair of 45° micro-mirrors in order to establish an optical path between stacked silicon dies, as illustrated schematically in Figure 31. The fabrication processes have been developed to form both facing-down and facing-up 45° micro-mirrors. The formation of ultra-smooth facing-up 45° micro-mirrors using surfactant added low concentration TMAH has been established [11]. The process starts with p-type (100) silicon wafer with primary flat in (110) direction. The silicon wafer is then thermally oxidized to grow silicon dioxide. The grown oxide is patterned to expose silicon surface using a rectangular mask rotated by 45° from the primary flat so that its edge can orient in (100) direction. Performing wet silicon etch in surfactant added (1%) low TMAH concentration (5%) with successive removal of over-hanging oxide mask produces ultra-smooth 45° micro-mirror whose surface is in (110) plane. Figure 32(a) shows the SEM cross-sectional view for the fabricated 45° facing-up micro-mirror.

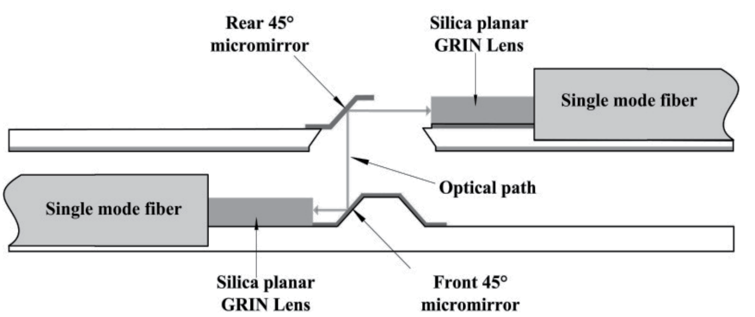

Figure 31. Optical interconnect system with planar silica lens pairs

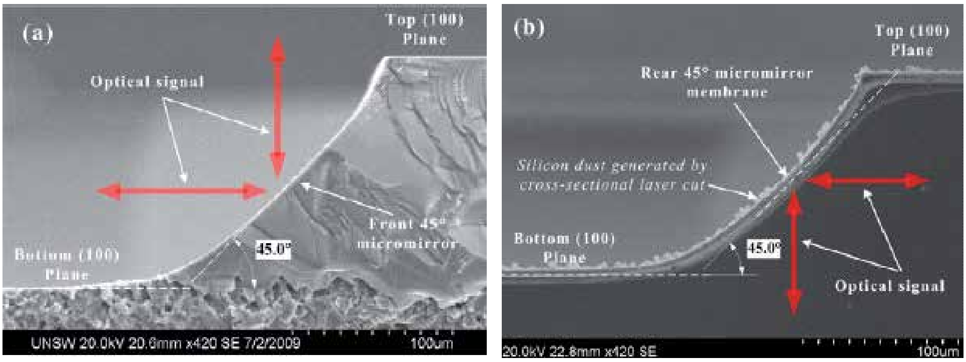

Figure 32. (a) Facing-up 45° micro-mirror; (b) Facing-down 45° micro-mirror

Based on the formation of facing-up 45° micro-mirrors, phosphorus diffusion on p-type substrate on the side where the facing-up 45° micro-mirror is formed, and electro-chemical etch stop technique at p-n junction, facing-down 45° has been released[73]. The cross-sectional view of the released facing-down 45° micro-mirror is shown in Figure 32(b).

The fabrication techniques to form facing-up and down 45° micro-mirrors have been modified to integrate planar silica lens pairs and U-grooves for single-mode optical fiber insertions [74, 75]. Figure 33 and 34 show the modified fabrication process steps for integrating planar lens pairs with facing-up and facing-down 45° micro-mirror, respectively.

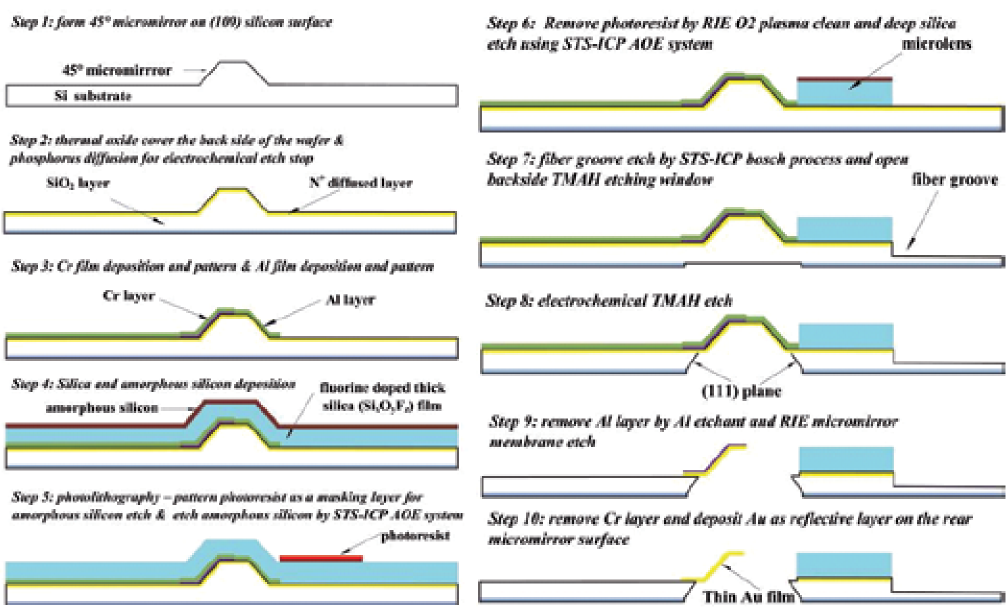

Figure 33. Fabrication process flow for silica lens integrated facing-down 45° micromirror.

It should be noted that in both fabrication process steps, the thick silica film deposition and micro-machining techniques are based on the discussion we had earlier in section 4. In this case, however, the planar lens pair designed for a free-space propagation distance of 500μm is employed. The SEM images of the fabricated top die consisting of the facing-down micro-mirror and one of the planar lens pair and bottom die having facing-up micro-mirror and the other planar lens pair are given in Figure 35 and 36, respectively.

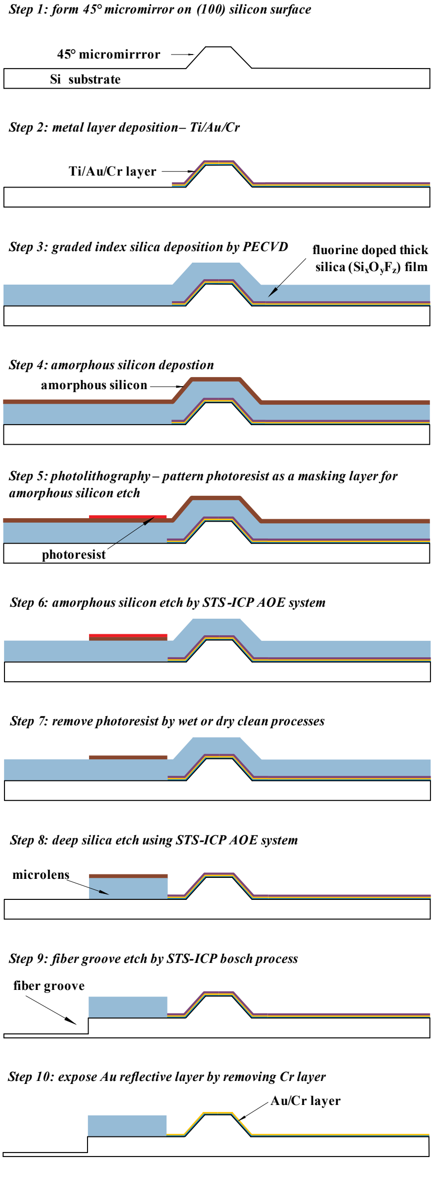

Figure 34. Fabrication process flow for silica lens integrated facing-up 45° micromirror.

http://dx.doi.org/10.5772/54246

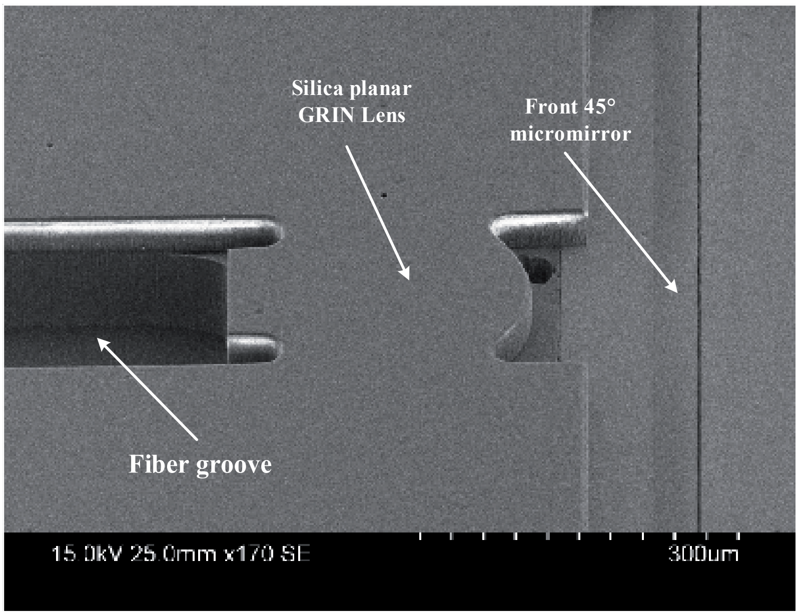

Figure 35. Front facing micromirror with planar silica graded index lens.

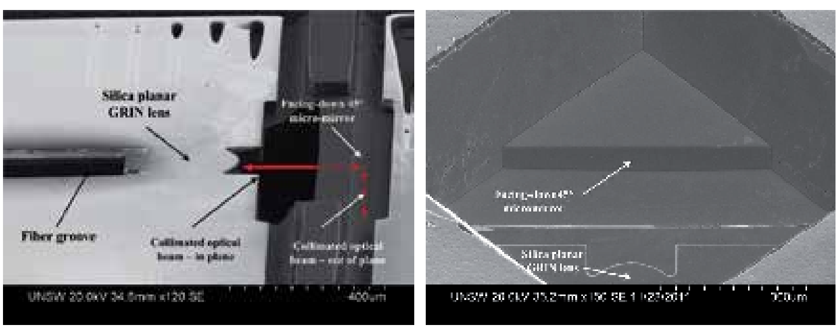

(a) (b)

Figure 36. (a) SEM image of silica planar GRIN lens integrated with facing-down 45º micro-mirror.Flerioof silica planar; (b) backside view of facing-down 45º micro-mirror

After fabricating the top and bottom dies separately, they are assembled and aligned one on the top of the other using micro-positioning system. Input and output single mode optical fibers are inserted into the U-grooves formed on the dies and butt-coupled to the respective planar lenses. The input optical fiber is coupled to the pig-tailed laser diode source at 633nm wavelength. The output fiber is coupled to optical power to measure the received power. The total optical power loss in the system is measured to be 8.5dB. This is an improvement of more than 25dB and demonstrates the effectiveness of the planar silica GRIN lens in reducing optical loss in 3D optical interconnect systems.

Author details

A. Michael, C.Y. Kwok, Md. Al Hafiz and Y.W. Xu

School of Electrical Engineering and Telecommunication, UNSW, Australia

References

[1] H.Robbins and B.Schwartz, "Chemical Etching of Silicon-II: The system HF,HNO_3, $HC_2C_3O_2$," J. Electrochem. Soc.,vol. 107, pp. 108-11, 1960.

[2] H.Muraoka, T.Ohahi, and T.Sumitomo, "Controlled Preferential Etching Technology," in semiconductor silicon 1973, Chicago, pp. 327-38

[3] Marc J. Madou, Fundamentals of Microfabrication, second edition

[4] G.T.Kovacs, N.I.Maluf, and K.E. Peterson, "Bulk Micromachining of Silicon," in proceedings of the IEEE, Vol. 86, IEEE, 1998, pp. 1536-51.

[5] B.Schwartz, and H.Robbins, "Chemical etching of Silicon-IV: Etching Technology," J.Electrochem. Soc.,Vol. 123, pp. 1903-9,1976.

[6] H. Seidel, L.Csepregi,A.Heuberger, H. Baumgartel, "Anisotropic etching of crystalline silicon in alikaline solutions. Part I. Orientation dependence and behaviour of passivation layers. Journal of the Electrochamical Society 137, pp. 3612-3626.

[7] M. Elwenpoek, H.V. Jansen, Silicon Micromachining, Cambridge university press.

[8] R.J.Jaccodine, "Use of modified free energy theorems to predict equilibrium growing and etching shapes," Journal of Applied Physics, 33(1962), pp.2643-2647.

[9] Martin Hoffman, Sabine Dickhut, and Edgar voges, "Fiber Ribbon Alignment Structures Based on Rhombus Shaped Channels in Silicon," IEEE Photonics Technology Letters, Vol. 12, No.7, (2000), pp. 828-830.

[10] D.Cheng, M.A.Gosalvez,T.Hori, K.Sato, M.Shikida, "Improvement in smoothness of anisotropically etched silicon surfaces: effects of surfactant and TMAH concentrations," Sensors and Actuators A: Physical, Vol. 125, (2006), pp. 415-421.

[11] Y.W.Xu, A.Michael, C.Y.Kwok, "Formation of ultra-smooth 45^o micromirror on (100) silicon with low concentration TMAH and surfactant: Technique for enlarging the truly 45^o portion," Sensors and Actuators A: Physical, Vol.166 (2011),pp. 164-171.

[12] Philippe Helin, Makoto Mita, Tarik Bourouina, Gilbert Reyne, and Hiroyuki Fujita, "Self-Aligned Micromachining Process for Large-Scale, Free-Space Optical Cross-Connects," Journal of Light wave Technology, Vol. 18, No. 12, 2000, pp. 1785-1791.

[13] Shi-sheng Lee, Long-sun Huang, Chang-Jin Kim, and Ming C. Wu, "Free-Space Fiber-Optic Switches Based on MEMS Vertical Torsion Mirrors," Journal of Lightwave Technology, Vol. 17, No. 1, January 1999, pp. 7-12.

[14] A.Michael, C.Y.Kwok, "Monolithically integrated out-of-plane micro-mirror," Sensors and Actuators A: physical, Vol.179, pp. 263-276, 2012.

[15] Martin Hoffman and Edgar Voges, "Bulk Silicon Micromachining for MEMS in optical communication systems," Journal of Micromechanics and Micro engineering, Vol. 12 (2002) pp. 349-360.

[16] C.Strandman, L.Rosengren,H.G.A. Elderstg, Y.Backlund, "Fabrication of 45^{o} mirrors together with well-defined V-grooves using wet anisotropic etching of silicon," Journal Microelectro mechanical systems, 4(4) (1995), 75-79.

[17] H.F.Winters and J.W.Coburn, " The etching of silicon with XeF_2 vapor," Applied Physics Letter, Vol.34, No.1,pp 70-73,1979.

[18] R.S.Osgood, Jr., H. H. Gilgen, and P. Brewer, "summary abstract: Low temperature deposition and removal of material using laser-induced chemistry," J. Vac. Sci Technology,, Vol. 2, no. 2, pp. 504-505, Apr.-June 1984.

[19] J.W.Coburn and H.F.Winters, "Plasma etching- A discussion of mechanisms," J.Vac. Sci. Tehcnology, Vol. 16, no. 2, pp. 391-403,Mar./Apr 1979.

[20] M.H.Hecht, R.P.Vasquez, and F.J.Grunthaner, " A novel x-ray photoelectron spectroscopy study of the Al/SiO_2 interface," J.Appl. Phys., Vol.57, no. 12, pp. 5256-5261, 1985.

[21] E.Hoffman, B.Warneke, E.Kruglick, and K.S.J.Pister, "3D structure with piezoresistive sensors in standard CMOS," in Proc. IEEE Micro Electro Mechanical Systems Conf., Amsterdam, The Netherlands, Jan. 29-Feb. 2, 1995, pp. 288-293.

[22] U.Kohler, A.E.Guber, W.Bier, M.Heckele, and Th.Schaller, "Fabrication of microlenses by combining silicon technology, mechanical micromachining and plastic molding," in Proc. SPIE Miniaturized Systems with Micro-Optics and Micromechanics, San Jose, CA, Jan. 30-31, 1996, Vol. 2687, pp. 18-22.

[23] K.Murakami, Y.Wakabayashi, K.Minami, and E.Esashi, "Cryogenic dry etching for high aspect ratio microstructures," in Proc. IEEE Microelectromech. Syst. Conf., Fort Lauderdale, FL, Feb. 1993, pp. 65-70.

[24] M.Esashi, M.Takinami, Y.Wakabayashi, and K.Miniami, "High-rate directional deep dry etching for bulk silicon micromachining," J.Micromech Microeng, Vol. 5, No. 1, pp. 5-10, Mar. 1995.

[25] F.Larmer and P.Schilp, "Method of anisotropically etching silicon," German Patent DE 4 241045, 1994.

[26] Chang-Hyeon Ji, Youngjoo Yee Yunghoon Choi, Seong-Hyok Kim, and Jong-Uk Bu, "Electromagnetic 2X2 MEMS Optical Switch," IEEE Journal of selected topics in quantum electronics, Vol. 10, No. 3, 2004, pp 545-550.

[27] Cornel Marxer and Nicolaas F. de Rooij, "Micro-Opto-Mechanical 2X2 switch for Single Mode Fibers Based on Plasma-Etched Silicon Mirror and Electrostatic," Journal of Lightwave Technology, Vol. 17, No.1, 1999, pp. 2-6.

[28] M.V.Bazylenko, M.Gross, A.Simonian and P.L.Chu, "Pure and Flourine-doped silica films deposited in a hollow cathode reactor for integrated optic applications, J.Vacuum Sci.Technology. A, 14(1996), 336-345.

[29] M.V.Bazylenko, M.Gross, P.L.Chu, and D. Moss, "Photosensitivity of Ge-doped silica deposited by hollow cathode PECVD," Electron Letter, 32(196), 1198-1199.

[30] M.R. Mackenzie, "collimating lens pair for planar silica waveguides" PhD Thesis, 2005, University of New South Wales, NSW, Australia.

[31] A.Michael, Md.Hafiz, T.Puzzer, C.Y.Kwok, "Fabrication and optical characterization of planar silica lens pair," Electron Letter,2011, 46(21), pp. 1459-1460.

[32] D.R.Betltrami, J.D.Love, A.Durandet, A.Samoc, M.Samoc, B.Luther-Davies and R.W.Boswell, "Planar graded-index (GRIN) PECVD lens," Electron letter, 32(1996), pp. 548-550.

[33] X. Zhang, K.-S. Chen, R.Ghodssi, A.A.Avon, and S.M Spearing, "Residual stress and fracture in thick tetraethylorthosilicate (TEOS) and silane-based PECVD oxide films," Sensors and Actuators A, 91(2001), pp.379-386.

[34] Patrick J. French et al, "The development of a Low-Stress Polysilicon Process Compatible with Standard Device Processing, " Journal of Microelectromechanical Systems, Vol. 5, No. 3, September 1996.

[35] Md.Al Hafiz, A.Michael, C.Y.Kwok and T. Puzzer, "Fabrication and optical characterization of planar silica lens pair," Electronics Letters, Vol. 46, No. 21, 2010 pp.

[36] N.R.Rueger, M.F.Doemling, M.Schaepkens, J.J.Beulens, T.E.F.M.Standaert, and G.S.Oehrieina, "Selective etching of SiO_2 over polycrystalline silicon using CHF_3 in an inductively coupled plasma reactor," J.Vac.Sci. Technology A, Vol 17, No.5, 1999, pp. 2492-2502.

[37] D.Bien et al, "Characterization of masking materials for deep glass micromachining," J. Micromech. Microeng. 13 (2003) 34–40.

[38] Md. Abdullah Al Hafiz, Mark R. Mackenzie, Chee Yee Kwok, "Design Methodology of focusing elements for multilevel planar optical systems in optical interconnects," Optical Engineering, 48(12), 2006,125401-(1-9).

[39] P.D.Dobbelaere, K.Falta, L.Fan, S.Gloeckner, and S.Patra, "Digital MEMS for optical switching," IEEE Commun.Mag., pp. 88-95, Mar.2002.

[40] A.Dugan, L.Lightworks, and J.-C.Chiao, "The optical switching spectrum: A primer on wavelength switching technologies," Telecommunication Mag., May 2001.

[41] J.Sapriel, D.Charissoux, V.Voloshinov, and V.Molchanov, "Tunable acoustooptic filters and equalizers for WDM applications," Journal of Lightwave Technology, vol. 20, pp.892-899, May 2002.

[42] B.Mukherjee, Optical Communication Networks. New York: Mc-Graw-Hill, 1997.

[43] J.L.Jackel, J.J.Johnson, and W.J.Tomlinson, "Bistable optical switching using electrochemically generated bubbles," Opt.Lett.,vol. 15, no.24, pp. 1470-1472, Dec. 1990.

[44] M.Makihara, M.Sato, F.Shimokawa, and Y.Nishida, "Micromechanical optical switches based on thermocapillary integrated in waveguide substrate," J.Lightwave technology, Vol.17, No.1, pp.14-18, Jan. 1999.

[45] J.E.Fouquet, S.Ventkatesh, M.Troll, D.Chen, S.Schiaffino, and P.W.Barth, "Compact, scalable fiber optic cross-connect switch using total internal reflection due to thermally-generated bubbles," in Proc. IEEE/LEOS Annu. Meeting, Orlando, FL, 1998, pp.169-170.

[46] P.B.Chu, S.Lee, and S.Park, "Mems: The path to large optical cross connects," IEEE Communication Magazine, pp.80-87, March 2002.

[47] J.Kim et al, "1100x1100 port mems-based optical crossconnect with 4-db maximum loss," IEEE Photonics Technology Letters, Vol.15, no.11, pp.1537-1539, 2003.

[48] T.Akiyama and K.Shono, "Controlled Stepwise Motion in Polysilicon Microstructures," IEEE JMEMS, Vol.2, No.3, pp. 106-110 Sep.1993.

[49] T.Akiyama and H.Fujita, "A Quantitative Analysis of Scratch Drive Actuator Using Buckling Motion," in IEEE workshop of MEMS, Amestrdam, The Netherlands, Jan. 29-Feb.2, 1995.

[50] L.Y.Lin, E.L.Goldstein, R.W.Tkach, "Free-Space Micromachined Optical Switches for Optical Networking", IEEE Journal of Selected Topic in Quantum Electronics, Vol.5, pp. 4-9, 1999.

[51] L.Y.Lin, E.L.Goldstein, R.W.Tkach, " On the Expandability of Free-Space Micromachined Optical Cross Connects", Journal of Lightwave Technology, Vol 18, No.4, 482-489, 2000.

[52] S.S.Lee,L.S.Haung,C.J.Kim and M.C.Wu, "Free-Space Fiber-Optic Switches Based on MEMS Vertical Torsion Mirrors", Journal of Lightwave Technology, Vol.17, pp 7-14, 1999.

[53] R.T.Chen, H.Nguyen, M.C.Wu, "A High-Speed Low-Voltage Stress-Induced Micromachined 2X2 Optical switch", IEEE Photonics Technology Letters, Vol.11, pp. 1396-1399, 1999.

[54] Y.Kanamori, Y.Aoki, M.Sasaki, H.Hosoya, A.Wada, and K.Hane, "Fiber-Optical Switch using Cam-Micromotor Driven by Scratch Drive Actuators," Journal of Micromechanics and Microengineering, vol.15, pp. 118-123, 2005.

[55] P.Helin,M.Mita,T.Bourouina,G.Reyne, and H.Fujita, "Self Aligned Micromachining Process for Large-Scale, Free-Space Optical Cross-Connects", Journal of Lightwave technology, vol.18, pp.1785-1791, 2000.

[56] C.H.Ji, Y.Yee, J.Choi, S.H.Kim, and J.U.Bu, "Electromagnetic 2X2 MEMS Optical Switch", IEEE Journal of Selected Topics in Quantum Electronics, Vol.10, pp.545-550, 2004.

[57] C.Marxer, C.Thio, M.A.Gretillat, N.F.de rooij, R.Bättig, O.Anthamatten, B.Valk and P.Vogel, "Vertical Mirrors Fabricated by Deep Reactive Ion Etching for Fiber-Optic Switching Applications", Journal of MicroElectroMechanical Systems, Vol.6, pp. 277-285.

[58] H.Toshiyoshi and H.Fujita, "Electrostatic Micro Torsion Mirrors for an Optical Switch Matrix", Journal of MicroElectroMechanical Systems, Vol.5, pp. 231-237, 1996.

[59] D.A.Horsley, W.O.Davis, K.J.Hogan, M.R.Hart, E.C.Ying, M.Chaparala, B.Behin,M.J.Daneman and M-H Kiang, "Optical and Mechanical Performance of a Novel Magnetically Actuated MEMS-Based Optical Switch", Journal of Microelectromechanical systems, Vol 14, pp.274-284.

[60] L.Dellmann, W.Noell, C.Marxer, K.Keible, M.Hoffmann, and N.F.De Rooij, "4x4 Matrix switch based on MEMS switches and integrated waveguides", in Proc. Transducers, Munich, Germany, Jun. 10-14, pp.1332-1335,2001.

[61] N.Iyer, C.H.Mastrangelo, S.Akkaraju,C.Brophy,T.G.McDonald, R.Dureiko, and E.T.carlen, "A two-dimensional optical cross-connect with integrated waveguides and surface micromachined cross-bar switches", Sensors and Actuators A: physical, Vol.109, pp.231-241, 2004.

[62] R.Guerre, C.Hibert,Y.Burri,Ph.Flückiger,P.Renaud, "Fabrication of vertical digital silicon optical micromirrors on suspended electrode for guided-wave optical switching applications", Sensors and Actuators A: physical, Vol. 123-124, pp. 570-583, 2005.

[63] M.R.Mackenzie and C.Y.Kwok, "Theoretical analysis of integrated collimating waveguide lens," IEEE Journal of Lightwave Technology, vol.21, no.4,pp.1046-1052, 2003.

[64] M.Mackenzie, "Collimating lens pair for planar silica waveguides", Ph.D thesis, School of Electrical Engineering and Telcommunication, The university of New South wales, May 2005.

[65] A.Michael, C.Y.Kwok, K.Yu, and M.Mackenzie, "A Novel Bi-stable Two-Way Actuated Out-of-Plane Electro-Thermal Micro-Bridge," IEEE Journal of MEMS, Vol.17, No. 1,pp. 58-69, 2008.

[66] A.Michael, C.Y.Kwok, "Buckling shape of elastically constrained multi-layered micro-bridges," Sensors and Actuators A: Physical, Vol.135, No.2, pp.870-880, 2007.

[67] A.Michael, C.Y.Kwok, "Design Criteria for Bi-stable Behavior of Buckled Multi-layered MEMS Bridges," J. Micromechanics and Micro engineering, Vol.16, pp. 2034-2043, 2006.

[68] Lee, C.-C., Hsiao, S.-Y., and Fang, W.: 'Implementation of a micro ball lens on a silicon optical bench using insoluble two-phase liquid immersion technology', *J. Micromech. Microeng.*, 2010, 20, 085015 (7pp)

[69] Draheim, J., Schneider, F., Kamberger, R., Mueller, C., and Wallrabe, U.: 'Fabrication of a fluidic membrane lens system', *J. Micromech. Microeng.*, 2009, 19, 095013 (7pp),

[70] Chang, S.-II, and Yoon J.-B.: 'A 3-D planar microlens for an effective monolithic optical interconnection system', *IEEE Photonics Tech. Letters*, 2006, 18, (7), pp. 814-816

[71] Shen, S. C., Pan, C. T., Liu, K. H., Chao, C. H., and Huang, J. C.: 'Fabrication of an eyeball-like spherical micro-lens array using extrusion for optical fiber coupling', *J. Micromech. Microeng.*, 2009, 19, 125017 (9pp).

[72] Y W Xu, A.Michael, C.Y.Kwok, T.Puzzer, G.D.Peng, "Integration of 1D Planar Silica Grin Lenses in 3D Optical Interconnect System," Vol 48, No. 1, pp. 585-586, 2012

[73] Y.W.Xu, A.Michael, Kwok C Y, Peng G.D, "A Novel stacked die optical Interconnect Prototype system: Fabrication technique for front and rear 45^o micro-mirror pair", The 5th Asia-Pacific conference on Transducers and Micro-Nano Technology, Perth, 6-9 July 2010.

[74] Y.W.Xu, A.Michael, C.Y.Kwok, G.D.Peng, "Integration of 1D planar silica GRIN lens with upward facing 45^o micro-mirror", APCOT, July 2012.

[75] Y.W.Xu, A.Michael, C.Y.Kwok, T.Puzzer, G.D.Peng, "1D Planar Silica Lens Integrated 3D Optical Interconnect System – fabrication techniques of Lens Integrated Facing-down 45^o micro-mirror", Eurosensors XXVI, Krakow, Sept 9-12, 2012.

Edited by Sulaiman Wadi Harun and Hamzah Arof

This book is a compilation of works presenting recent advances and progress in optical fiber technology related to the next generation optical communication, system and network, sensor, laser, measurement, characterization and devices. It contains five sections including optical fiber communication systems and networks, plastic optical fibers technologies, fiber optic sensors, fiber lasers and fiber measurement techniques and fiber optic devices on silicon chip. Each chapter in this book is a contribution from a group of academicians and scientists from a prominent university or research center, involved in cutting edge research in the field of photonics. This compendium is an invaluable reference for researchers and practitioners working in academic institutions as well as industries.

Photo by ktsimage / iStock

IntechOpen

ISBN 978-953-51-6348-0